



Proceedings of the 11th Thermal and Fluids Analysis Workshop

The NASA STI Program Office . . . in Profile

Since its founding, NASA has been dedicated to the advancement of aeronautics and space science. The NASA Scientific and Technical Information (STI) Program Office plays a key part in helping NASA maintain this important role.

The NASA STI Program Office is operated by Langley Research Center, the Lead Center for NASA's scientific and technical information. The NASA STI Program Office provides access to the NASA STI Database, the largest collection of aeronautical and space science STI in the world. The Program Office is also NASA's institutional mechanism for disseminating the results of its research and development activities. These results are published by NASA in the NASA STI Report Series, which includes the following report types:

- **TECHNICAL PUBLICATION.** Reports of completed research or a major significant phase of research that present the results of NASA programs and include extensive data or theoretical analysis. Includes compilations of significant scientific and technical data and information deemed to be of continuing reference value. NASA's counterpart of peer-reviewed formal professional papers but has less stringent limitations on manuscript length and extent of graphic presentations.
- **TECHNICAL MEMORANDUM.** Scientific and technical findings that are preliminary or of specialized interest, e.g., quick release reports, working papers, and bibliographies that contain minimal annotation. Does not contain extensive analysis.
- **CONTRACTOR REPORT.** Scientific and technical findings by NASA-sponsored contractors and grantees.

- **CONFERENCE PUBLICATION.** Collected papers from scientific and technical conferences, symposia, seminars, or other meetings sponsored or cosponsored by NASA.
- **SPECIAL PUBLICATION.** Scientific, technical, or historical information from NASA programs, projects, and missions, often concerned with subjects having substantial public interest.
- **TECHNICAL TRANSLATION.** English-language translations of foreign scientific and technical material pertinent to NASA's mission.

Specialized services that complement the STI Program Office's diverse offerings include creating custom thesauri, building customized data bases, organizing and publishing research results . . . even providing videos.

For more information about the NASA STI Program Office, see the following:

- Access the NASA STI Program Home Page at <http://www.sti.nasa.gov>
- E-mail your question via the Internet to help@sti.nasa.gov
- Fax your question to the NASA Access Help Desk at 301-621-0134
- Telephone the NASA Access Help Desk at 301-621-0390
- Write to:
NASA Access Help Desk
NASA Center for Aerospace Information
7121 Standard Drive
Hanover, MD 21076



Proceedings of the 11th Thermal and Fluids Analysis Workshop

Proceedings of a conference held at The Forum Conference Center and
cosponsored by the NASA Glenn Research Center and the Ohio Aerospace Institute
Cleveland, Ohio
August 21–25, 2000

National Aeronautics and
Space Administration

Glenn Research Center

Trade names or manufacturers' names are used in this report for identification only. This usage does not constitute an official endorsement, either expressed or implied, by the National Aeronautics and Space Administration.

Available from

NASA Center for Aerospace Information
7121 Standard Drive
Hanover, MD 21076

National Technical Information Service
5285 Port Royal Road
Springfield, VA 22100

Available electronically at <http://gltrs.grc.nasa.gov/GLTRS>

Table of Contents

On the Adaptation of the ADI-Brian Method to Solve the Advection-Diffusion Transport Equation Dean S. Schrage, Zin Technologies, Inc.	1
Initial Thermal Modeling of the Constrained Vapor Bubble Heat Exchanger Using TSS/SINDA S. Basu, P.C. Wayner, Jr., and J.L. Plawsky, Rensselaer Polytechnic Institute	17
An Analysis and Procedure for Determining Space Environmental Sink Temperatures With Selected Computational Results Albert J. Juhasz, NASA Glenn Research Center	27
Thermal Design and Analysis of the Stratospheric Aerosol and Gas Experiment III (SAGE III) for the ISS Mission Dana C. Gould, NASA Langley Research Center	37
Thermal Analysis of an MEMS Broadband Light Source Eric Golliher, NASA Glenn Research Center	51
Modeling the Specular Exchange Between Concentric Cylinders in a Radiative Shielded Furnace R. Gregory Schunk, NASA Marshall Space Flight Center; and Francis C. Wessling, University of Alabama in Huntsville	57
Photophoresis of Micronized Particles in the Free-Molecular Regime Shahram Tehranian, George Mason University; Frank Giovane and Jurgen Blum, Naval Research Laboratory; and Yu-Lin Xu and Bo A.S. Gustafson, University of Florida.....	81
Remote Thermal Analysis Through the Internet Eric T. Malroy, NASA Glenn Research Center.....	95
Correlation of Annular Diffuser Performance With Geometry, Swirl, and Blockage David Japikse, Concepts ETI, Inc.....	107
The Effect of Orientation on Flow Boiling in Single-Side Heated Channels Quaid Peatiwala, Haidry Memorial Market; and Ronald D. Boyd, Sr., Prairie View A&M University.....	119
Mathematical Physics of the Propagation of a Laminar Aerodynamic Boundary Layer, Using the Kenetic Theory of Gases Albert L. de Graffenried, Aero-Electronic Leasing Corporation	129
The Use of Mathcad in Thermal/Fluids Calculations B.K. Hodge and Robert P. Taylor, Mississippi State University	143
A Modified NPARC Code: The Burnett Equations Solver K.L. Guo and G.S. Liaw, Alabama A&M University	161
Multidisciplinary Analysis of a Microsystem Device for Thermal Control Matthew E. Moran, NASA Glenn Research Center	173
Thermal Analysis Methods for an Earth Entry Vehicle Ruth M. Amundsen, John A. Dec, and Michael C. Lindell, NASA Langley Research Center	187
Inclusion of Thermal Protection Systems in Spacecraft Thermal-Stress Analysis Using Concurrent Engineering Techniques Steven L. Rickman, NASA Lyndon B. Johnson Space Center	205

The U.S. STEP–TAS Pilot Georg Siebes, Jet Propulsion Laboratory, California Institute of Technology; Hans Peter de Koning, European Space Research & Technology Centre/European Space Agency; and Eric Lebegue, SIMULOG	215
Reliability Engineering and Robust Design: New Methods for Thermal/Fluid Engineering Brent A. Cullimore, C&R Technologies, Inc.; and Glenn T. Tsuyuki, Jet Propulsion Laboratory	225
Design Study of a Low-Cost LOX Turbopump David Japikse, Nicholas Baines, and Michael J. Platt, Concepts ETI, Inc... ..	241
Unsteady Phenomena During Operation of the SSME Fuel Flowmeter Bogdan Marcu, Boeing, Rocketdyne Propulsion and Power	253
Interfacing SINDA/FLUINT With ROCETS Barbara A. Sakowski, NASA Glenn Research Center	263
Numerical Modeling of Drying Residual RP–1 in Rocket Engines Alok Majumdar, Robert Polsgrove, and Bruce Tiller, NASA Marshall Space Flight Center	271

On the Adaptation of the ADI-Brian Method to Solve the Advection-Diffusion Transport Equation

Dean S. Schrage
Zin Technologies Inc.
3000 Aerospace Parkway
Glenn Research Center Group
Brook Park, Ohio 44142
dean.schrage@grc.nasa.gov

ABSTRACT

The focus of the present study is a semi-direct solution to the linearized Burger's advection-diffusion (AD) equation using alternating direction implicit (ADI) methods. In particular, the paper features the adaptation of the *Brian* ADI method, originally designed for stable three dimensional (3D) solutions of the parabolic heat equation, to include the advection component of the Burgers equation. The present study presents a method to split up the advection component in a manner which is consistent with the splitting of the diffusive terms in the Brian method. Upon implementing upwind differencing, this new method offers very robust stability margins and is capable of issuing stable solutions at Courant numbers exceeding 10. The upwind scheme applies only the left or right diagonals of the ADI coefficient matrix to register the advection term depending on the direction of the velocity vector. For this reason, upwind differencing is an ideal starting point for the ADI solution method because ADI methods depend on a direct inversion of a tri-diagonal coefficient matrix. However, for large Peclet numbers, the advection term dominates the diffusion term in the Burgers equation and the solution is hampered by the classical numerical diffusion induced by upwind differencing. This motivates the search for enhanced differencing schemes which can be implemented with the ADI method. A central differencing scheme produces second-order spatial accuracy and can be differenced within the tri-diagonal band and eliminates numerical diffusion, but generates dispersion errors. To mitigate both diffusion and dispersion errors, *third-order upwind differencing* is implemented. Third-order upwinding requires four points ($i - 2$, $i - 1$, i , $i + 1$). In the tri-diagonally bound ADI method, the fourth point ($i - 2$) is registered as a source term using the belated ADI state. Effectively, the third-order upwinding is implemented as either central differencing with a *smoother* or upwind differencing with a *sharpeners*. Both give the same numerical results. All three advection differencing methods are compared to a showcase of steady and transient exact solutions to the Burgers equation which demonstrates the combined utility of the new advection method with an ADI solution engine.

INTRODUCTION

The focus of this paper is the general advection-diffusion transport equation which is described by a series of terms (read from left to right): capacitive, advection, diffusion and a source term:

$$\frac{\partial \phi}{\partial t} + \mathbf{v} \cdot \nabla \phi = \Gamma \nabla^2 \phi + s \quad (1)$$

The balance between advective and diffusion terms is governed by the Peclet number:

$$Pe = \frac{U_{Char} L_{Char}}{\Gamma} \quad (2)$$

In this equation, ϕ is a general state variable. As discussed below, it can take on several values such as a velocity component or temperature or mass fraction. This is demonstrated pictorially in the following figure.

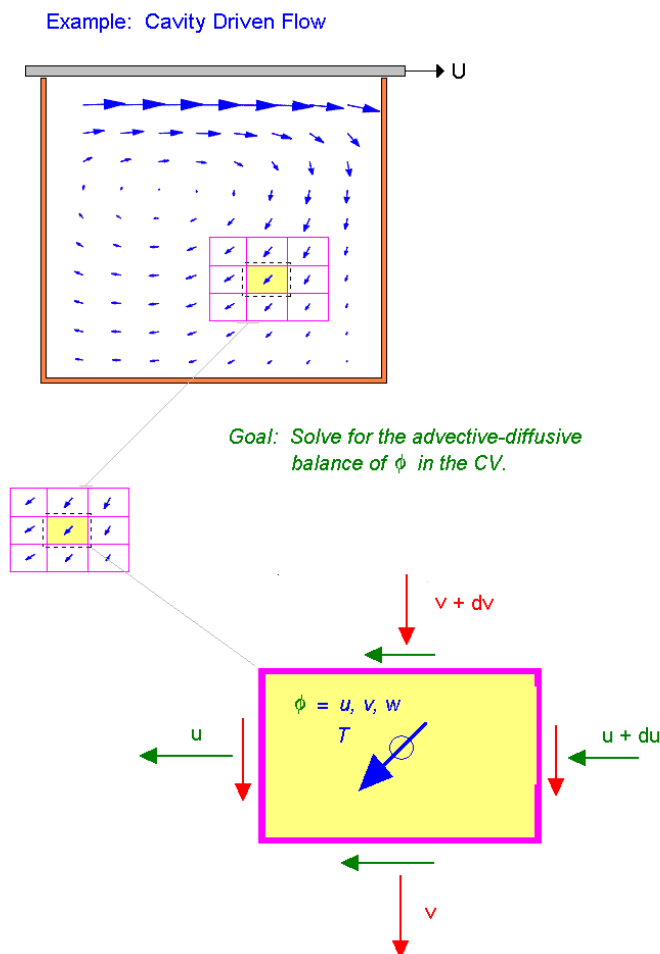


Figure 1. General control volume showing cell centered velocity components and temperature.

A simple vectorized form is generated by simply stacking these scalar states into a vector:

$$\vec{\phi} = [T, u, v, w]^T \quad (3)$$

One of the difficulties in solving the vectorized equation is the non-linear advection term. The velocity appears two times in the advection term for CFD solutions. As we discuss below, ADI methods can only be applied to a linear system of discrete equations. To support the implementation of an ADI solution, we apply a simple linearization to this equation by applying a velocity vector which is belated by one time step (n-1):

$$\frac{\partial \vec{\phi}}{\partial t} + \mathbf{v}^{(n-1)} \cdot \nabla \vec{\phi} = \Gamma \nabla^2 \vec{\phi} \quad (4)$$

$$\text{where } \vec{\phi} = [T, u, v, w]^T$$

This form will produce a series of linear equations for spatial discretization and also appears to offer reasonable CFD solutions to classical test cases such as the backwards facing step. Typical of discrete solutions to the Navier Stokes equation, the discretized advection term $\mathbf{v}^{(n-1)} \cdot \nabla \vec{\phi}$ introduces a constraint on the time step. This constraint is related to the Courant number:

$$CFL = \frac{\Delta t}{\frac{\Delta x_i}{|\mathbf{v}|}} \quad (5)$$

and is a function of the combination of time-space discretization. For example time-explicit and space-central differencing will produce unstable simulations while time-explicit space-upwind will produce stable simulations provided that $CFL < 1$. This paper will not attend to development of the various differencing techniques but will instead focus on an application of two select methods and their implementation in ADI methods.

Discretization of The Conservation Equation

The discretized form of the vectorized conservation equation can be written using the Tilde symbol to represent the numerical equivalent of the Laplacian and gradient operators $\tilde{\nabla}, \tilde{\nabla}^2$

$$\frac{\phi_i^{(n)} - \phi_i^{(n-1)}}{\Delta t} + \mathbf{v}^{(n-1)} \cdot \mathbf{e}_p \tilde{\nabla}(\phi_i^{(n)}, \mathbf{e}_p) = \Gamma_i \left(\tilde{\nabla}^2(\phi_i^{(n)}, \mathbf{e}_x) + \tilde{\nabla}^2(\phi_i^{(n)}, \mathbf{e}_y) + \tilde{\nabla}^2(\phi_i^{(n)}, \mathbf{e}_z) \right) + s_i \quad (6)$$

$$\text{where } \mathbf{e}_p = \mathbf{e}_x, \mathbf{e}_y, \mathbf{e}_z$$

The numerical Laplacian operator is described by the standard 3 point space difference:

$$\tilde{\nabla}_n^2 \phi_i = \frac{\phi_{i+1} - 2\phi_i + \phi_{i-1}}{\Delta n_i^2} \quad (7)$$

The numerical gradient operator $\tilde{\nabla}$ will be cast for the upwind differencing and third order upwind differencing. These definitions will be presented below.

RATIONALE for ADI IMPLEMENTATION

One method to solve the above discrete equation is to application of successive over relaxation (SOR) to solve for a residual form of the state ϕ . This involves rewriting the above equation in residual form:

$$R(\phi_i^{(n)}) = \frac{\phi_i^{(n)} - \phi_i^{(n-1)}}{\Delta t} + \mathbf{v}^{(n-1)} \cdot \mathbf{e}_p \tilde{\nabla}(\phi_i^{(n)}, \mathbf{e}_p) - \Gamma_i \left(\tilde{\nabla}^2(\phi_i^{(n)}, \mathbf{e}_x) + \tilde{\nabla}^2(\phi_i^{(n)}, \mathbf{e}_y) + \tilde{\nabla}^2(\phi_i^{(n)}, \mathbf{e}_z) \right) \quad (8)$$

where the residual vector \mathbf{R} is driven to acceptably small values using successive updates and iterations.

Two limitations are presented with SOR. First, for systems with wide varying values of the diffusivity coefficient Γ , the solution times can be very lengthy. Second, the SOR method tends to exacerbate the problems with stability introduced by the advection term. The following example illustrates. The test case is a simple 1D bar with high Peclet number. The solution using SOR can be driven unstable at the first time step with very moderate values of Courant number.

It is these restrictions that motivates us to search for better solution algorithms. Alternating direction implicit algorithms (ADI) would appear to offer the desired benefits. Specifically, the non-iterative aspect should aid in enhancing stability margins and computational efficiency. However, ADI methods were designed for just the diffusional term in the transport equation. The implementation of ADI methods for the transport equation with the additional advection term is not well documented. This is the focus of the present study.

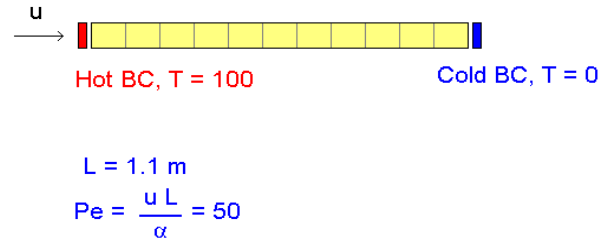


Figure 2. 1D slab example demonstrating SOR solution

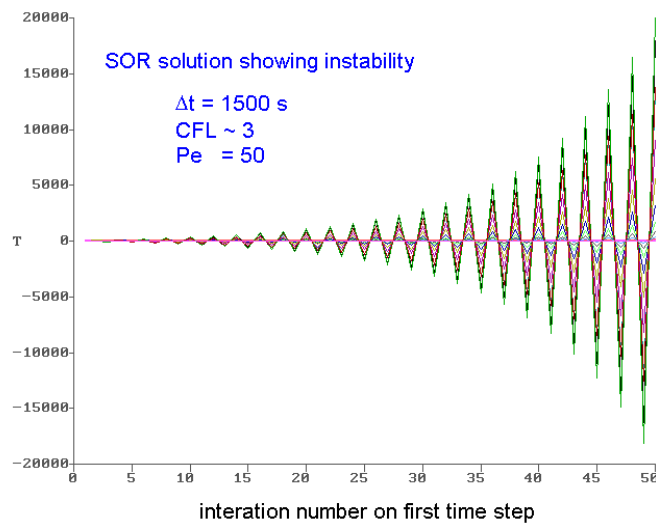


Figure 3. Time trace of ϕ at each control volume during the iteration process.

OBJECTIVES and APPROACH

The objective of this study is to develop a computationally efficient and robust general advection-diffusion transport solver offering improved performance over standard relaxation techniques. The performance of this new method will be measured by:

- *decrease wall clock time in a simulation*
- *enhanced stability margins by increasing CFL number*
- *minimized numerical diffusion introduced by the differencing method of the advection term*

The approach is to modify a standard *diffusionally-designed* Alternating Direction Implicit (ADI) method for the general advection-diffusion equation by implementing a stable splitting of the advection term. The advection-diffusion ADI solution will then be benchmarked using exact solutions to the linear Burger equation. Finally, the validated ADI method will be compared to SOR in application studies, demonstrating the achievement of speed and stability sub-objectives.

ADI SOLUTION METHOD - DIFFUSIONAL DESIGN

In this section, the implementation of ADI to solve the heat diffusion equation is discussed. These ADI implementations are referred to as *diffusional designs* (to delineate the advective-diffusional design). We begin with the discretized diffusional transport equation:

$$\frac{\phi_i^{(n)} - \phi_i^{(n-1)}}{\Delta t} = \Gamma \tilde{\nabla}^2 \phi_i^{(n)} + s_i \quad (9)$$

This equation can be written as a system of linear equations of the form:

$$\mathbf{A} \boldsymbol{\phi} = \mathbf{f} \quad (10)$$

where matrix \mathbf{A} is banded and sparse. The central feature of ADI is the approximation of this single equation, which cannot be inverted numerically, with a series of 3 sweep equations which have tri-diagonal matrices which can be inverted directly using the computationally efficient Thomas algorithm. These sweep equations can be written in a general form as a function of a succession of ADI-states (\mathbf{U} , \mathbf{V} , $\boldsymbol{\phi}^{(n)}$):

$$\begin{aligned} \mathbf{A}_X \mathbf{U} &= \hat{\mathbf{f}}_X(\boldsymbol{\phi}^{(n-1)}) \\ \mathbf{A}_Y \mathbf{V} &= \hat{\mathbf{f}}_Y(\boldsymbol{\phi}^{(n-1)}, \mathbf{U}) \\ \mathbf{A}_Z \boldsymbol{\phi}^{(n)} &= \hat{\mathbf{f}}_Z(\boldsymbol{\phi}^{(n-1)}, \mathbf{U}, \mathbf{V}) \end{aligned} \quad (11)$$

This general form of an ADI implementation is made specific when the tridiagonal matrices $\mathbf{A}_X, \mathbf{A}_Y, \mathbf{A}_Z$ and the source vectors $\mathbf{f}_X, \mathbf{f}_Y, \mathbf{f}_Z$ are defined. This is a subject of considerable detail. Two competing methods are the basic splitting method and the ADI-Brian method. The ADI-Brian method is ideal because it can be applied at larger time steps than splitting, retarding banding effects and is stable for 3D diffusion networks. The banding effect is demonstrated in the following figure showing a comparative evaluation between ADI-splitting and ADI-Brian methods. Thus, the present paper will select the **ADI-Brian** method in the implementation of these matrices and vectors. All subsequent derivations will be specific to this method.

Analysis of a copper backed circuit board with coupling through discrete pins to the cold boundary condition

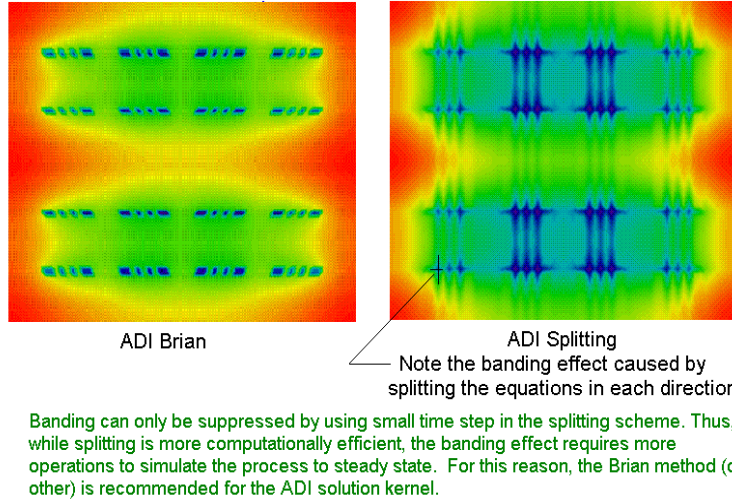


Figure 4. Comparison of Brian and splitting ADI solution methods at equivalent time step for heat conduction problem demonstrating banding effect.

ADI BRIAN IMPLEMENTATION - DIFFUSIONAL DESIGN

The solution method using ADI involves solving a general tridiagonal sweep equation of the form:

$$b_{i_n} \psi_{i-1} + a_{i_n} \psi_i + c_{i_n} \psi_{i+1} = f_i \quad \text{for } n = X, Y, Z \quad (12)$$

The solution variable ψ is one of the ADI-states described above. It can be described as the following vector:

$$\bar{\psi} = [\phi^{(n-1)}, U, V, \phi^{(n)}]^T \quad (13)$$

The solution variable changes with each sweep equation. For example, when solving for the scalar state $\phi = T$, we require intermediate values of the temperature field; when solving the Y-sweep equation, equivalently sweep number 2, we apply the following value of the ADI-state:

$$\begin{aligned} \bar{\psi}[2] &= [\phi^{(n-1)}, U, V, \phi^{(n)}]_{row\ 2}^T \\ &= V \end{aligned} \quad (14)$$

In other words, the second sweep corresponding to the Y direction, will solve for a temperature vector which is held in the storage location V . This notation allows for simple coding of the method, and is further highlighted in the pseudo code presented below

The following table defines the tridiagonal coefficients b , a , c and source vector f for the Brian method. As shown, the coefficients b , a , c need only be calculated once in a diffusional thermal simulation while the source vector is updated at each time step. The next section introduces the convection augment to these coefficients.

Table 1. ADI coefficients for Brian Method - diffusional design

sweep	b_i	a_i	c_i	f_i
x	$-\frac{\Gamma_i}{\Delta X^2}$	$\frac{1}{\Delta t/2} + \frac{2\Gamma_i}{\Delta X^2}$	$-\frac{\Gamma_i}{\Delta X^2}$	$s_i + \frac{1}{\Delta t/2} \phi_i^{(n-1)} + \Gamma_i \left(\tilde{\nabla}_y^2 \phi_i^{(n-1)} + \tilde{\nabla}_z^2 \phi_i^{(n-1)} \right)$
y	$-\frac{\Gamma_i}{\Delta Y^2}$	$\frac{1}{\Delta t/2} + \frac{2\Gamma_i}{\Delta Y^2}$	$-\frac{\Gamma_i}{\Delta Y^2}$	$s_i + \frac{1}{\Delta t/2} \phi_i^{(n-1)} \Gamma_i + \left(\tilde{\nabla}_x^2 U_i + \tilde{\nabla}_z^2 \phi_i^{(n-1)} \right)$
z	$-\frac{\Gamma_i}{\Delta Z^2}$	$\frac{1}{\Delta t/2} + \frac{2\Gamma_i}{\Delta Z^2}$	$-\frac{\Gamma_i}{\Delta Z^2}$	$s_i + \frac{1}{\Delta t/2} V_i + \Gamma_i \left(\tilde{\nabla}_x^2 U_i + \tilde{\nabla}_y^2 V_i \right)$

ADI BRIAN IMPLEMENTATION - ADVECTION AUGMENT

The advection term can be included by simply augmenting the diffusional coefficients with a differential term which accounts for the presence of a flow velocity at each control volume. The general augmented equation can be written:

$$(A + \delta A) [\phi] = f + \delta f \quad (15)$$

Each of the $\delta(\cdot)$ coefficient vectors is described in the following table. These are activated according to an advection logical. This logical indicates if a particular control volume has flow associated with it or, depending on differencing method, if the adjoining control volume used to compute the gradient, has a flow associated with it. As described in these equations, the augmenting matrix and source vector are zero if there is no flow and the method reverts back to the diffusional designed ADI method.

Table 2. ADI coefficients for Brian Method - advection augment

sweep	δb_i	δa_i	δc_i	δf_i
x	$-L_{Advect_{i-1_x}} u_i^{(n-1)} \frac{1}{\Delta X}$	$-\delta b_{i_n} - \delta c_{i_n}$	$+L_{Advect_{i+1_x}} u_i^{(n-1)} \frac{1}{\Delta X}$	$-\left(v_i^{(n-1)} \tilde{\nabla}_y \phi_i^{(n-1)} + w_i^{(n-1)} \tilde{\nabla}_z \phi_i^{(n-1)} + u_i^{(n-1)} M_x \right)$
y	$-L_{Advect_{i-1_y}} v_i^{(n-1)} \frac{1}{\Delta Y}$	$-\delta b_{i_n} - \delta c_{i_n}$	$+L_{Advect_{i+1_y}} v_i^{(n-1)} \frac{1}{\Delta Y}$	$-\left(u_i^{(n-1)} \tilde{\nabla}_x U_i + w_i^{(n-1)} \tilde{\nabla}_z \phi_i^{(n-1)} + v_i^{(n-1)} M_y \right)$
z	$-L_{Advect_{i-1_z}} w_i^{(n-1)} \frac{1}{\Delta Z}$	$-\delta b_{i_n} - \delta c_{i_n}$	$+L_{Advect_{i+1_z}} w_i^{(n-1)} \frac{1}{\Delta Z}$	$-\left(u_i^{(n-1)} \tilde{\nabla}_x U_i + v_i^{(n-1)} \tilde{\nabla}_y V_i + w_i^{(n-1)} M_z \right)$

The advection logical for upwind differencing can be defined by the following convention: ¹

$$\begin{aligned}
 L_{Advect_{i-1_n}} &= NOT(v_{i-1_n}^{(n-1)} \cdot e_n = 0) \times (v_i^{(n-1)} \cdot e_n > 0) \\
 L_{Advect_{i+1_n}} &= NOT(v_{i+1_n}^{(n-1)} \cdot e_n = 0) \times (v_i^{(n-1)} \cdot e_n < 0)
 \end{aligned} \quad (16)$$

¹ The convention to reference an adjoining control volume is simplified with the symbol $i \pm 1_n$. For example, the control volume which is North in the Y direction above CV-i is defined by CV $i + 1_y$. Similarly the CV which is West of CV-i is defined by $i - 1_x$. This notation eliminates confusing i, j, k indices.

Next we will define the numerical gradient operator. As indicated above, the ADI method applies upwind differencing as the basic method. The functions M_x, M_y, M_z which appear in the source vector on Table 2 are called *modulator functions*. These are used to create the effect of 3rd order upwind differencing to lesson the numerical diffusion caused by upwind differencing. This is explained in the next section.

Numerical Gradient - Upwind Differencing

The advection term is implement with an upwind differencing scheme where the numerical gradient operator is defined:

$$\tilde{\nabla}_{n_{Upwind}} \phi_i = \text{sign}(\mathbf{v} \cdot \mathbf{e}_n) \left(\frac{\phi_i - \phi_j}{\Delta} \right) \quad (17)$$

In this equation the subscript n is the differencing direction ($X, Y, \text{ or } Z$). The index j is the number of the upwind node and is determined by:

$$j = i - \text{sign}(\mathbf{v} \cdot \mathbf{e}_n) 1_n \quad (18)$$

There are two reasons that upwind differencing is selected as the basic method. First, it requires only one control volume outside of the control volume of interest to evaluate the gradient. With the ADI method limited to tri-diagonal inversion, this single point always lies somewhere on the tri-diagonal (either left or right). Second, the upwind method is very robust and computational robustness is one of the goals of this study. However, the central disadvantage of upwind differencing is the introduction of numerical diffusion into a simulation. Numerical diffusion can be reduced by implementing central space differencing, and an ADI implementation is still possible because both diagonals would be applied, accessing both the $i-1$ and $i+1$ points on a sweep direction. But central differencing introduces dispersion errors. Thus, we explore the use of 3rd order upwind differencing.

Numerical Gradient - 3rd Order Upwind Differencing

To create 3rd order upwinding requires four points (control volumes) to approximate the gradient. The differencing equation for a positive flow velocity in the n direction can be written:

$$\tilde{\nabla}_n \phi_i = \left(\frac{\frac{1}{6} \phi_{i-2_n} - \phi_{i-1_n} + \frac{1}{2} \phi_i + \frac{1}{3} \phi_{i+1_n}}{\Delta} \right) \quad (19)$$

This stencil requires a fourth point at $i \pm 2_n$ but the tri-diagonal in any sweep direction encompasses $i \pm 1_n$. Clearly this point is outside the tri-diagonal and it cannot be directly included in the application of the tri-diagonal inversion routine. This is the motivation behind the modulator function which was hinted at in Table 2. That is, we can bias or modulate the 1st order upwind gradient to look like 3rd order upwinding by multiplying the simple upwind differencing by a modulator function, but still cast the equation with tri-diagonals. The following equation is an approximation to 3rd order upwinding which can be implemented in an ADI tri-diagonal inversion:

$$\tilde{\nabla}_n \phi_i = \tilde{\nabla}_{n_{Upwind}} \phi_i + M(\psi) \quad (20)$$

The modulator function M can be determined by removing the upwind gradient from the above equation and observing the remaining terms:

$$\tilde{M}_n(\psi_i) = - \left(\frac{-\psi_{i-2n} + 2\psi_{i-1n} - \psi_i}{6\Delta} \right) \quad (21)$$

As shown, the modulator function is represented as a function of the ADI sweep state ψ and the reason for this is related to how the ADI states evolve. After each ADI sweep direction, the past and local states are known. These states are used in the modulator function to augment the source vector δf . The most simple implementation would be to evaluate M using the initial ADI state, that is, compute using $\phi^{(n-1)}$ based on the initial temperature (or velocity) vector at the start of each time step. However, as the sweeps are computed, updated information on temperature (or velocity) can be applied in the following convention which has been shown to give very reasonable results in practical simulation:

$$\begin{aligned} M_n &= \hat{M}(\psi[n]) \text{ where } n=1,2,3 \\ M_x &= \hat{M}(\phi^{(n-1)}) \\ M_y &= \hat{M}(U) \\ M_z &= \hat{M}(V) \end{aligned} \quad (22)$$

This definition of the modulator, as will be shown below, effectively *sharpens* the 1st order upwind gradient by suppressing diffusion errors. One could also extracting a different modulator function for central differencing, having the effect of a *smoother* which suppresses dispersion errors endemic to central differencing. In each case, the simulation results are exactly the same. For simplicity the basis used is always upwind differencing.

ADI Pseudo Code

```

step 1  read initial conditions on velocity and temperature
step 2  set the initial conditions on first ADI state  $\phi^{(n-1)}$ 
step 3  for p = 1 to 3    (sweep directions corresponding to X, Y, Z)
    •    point to ADI sub level  $\psi[p] = [\phi^{(n-1)}, U, V]^T$ 
    •    compute diffusion matrix coefficients  $b, a, c$  for each sweep direction (done only once)
    •    compute augment in the matrix coefficients  $\delta b, \delta a, \delta c$  for each sweep direction
    •    perform the LDU decomposition of matrix  $A + \delta A$ 
    •    compute the forcing vector coefficients  $f$  and  $\delta f$  specific to sweep direction
    •    apply Thomas algorithm to arrive at ADI solution  $\psi[p+1] = [U, V, \phi^{(n)}]^T$ 
    •    if (p = 2 or 3) renumber ADI sub levels  $\psi[p+1] = [V, \phi^{(n)}]^T$  consistent with X sweep
        node numbering
    next p
step 4  update ADI state  $\phi^{(n-1)} \leftarrow \phi^{(n)}$  and reenter time loop at step 3

```

VALIDATION - BENCHMARK COMPARISONS

In this section, the new ADI method is validated by comparing the numerical predictions and comparisons to exact analytical solution of the linear Burger equation. The linear Burger equation is defined by the general transport equation with the velocity term replaced by a constant velocity U :

$$\frac{\partial \phi}{\partial t} + U \nabla \phi = \Gamma \nabla^2 \phi + s \quad (23)$$

There are several exact steady and transient solutions to this equation. These can be solved for a simplified 1D slab geometry with fixed and variable inlet and fixed outlet boundary conditions. This basic geometry is shown in Figure 5. The thermal-fluid conditions are set to produce a Peclet number of $Pe = 10$. The number of space nodes is set to 11. The following figures show the time-space plot for the steady state and transient solutions, and a direct numerical to analytical comparison at select points in time. The steady state comparison is prepared at $t = 15000$ seconds and the transient comparison is compared at $t = 2400$ seconds. As evident, the ADI solution gives a very good prediction of the exact temperature when using the modulator function to create 3rd order upwinding and as expected the 1st order upwinding produces numerical diffusion. This is particularly pronounced in these figures showing a lower gradient at the outflow boundary which is the result of the artificially enhanced conductivity of the fluid.

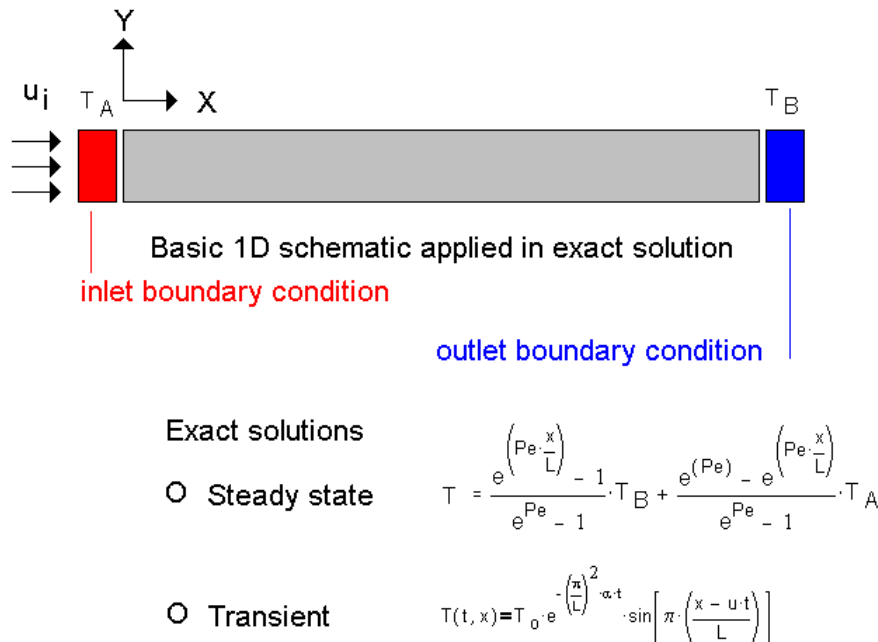


Figure 5. 1D slab geometry used to evaluate steady and transient solutions.

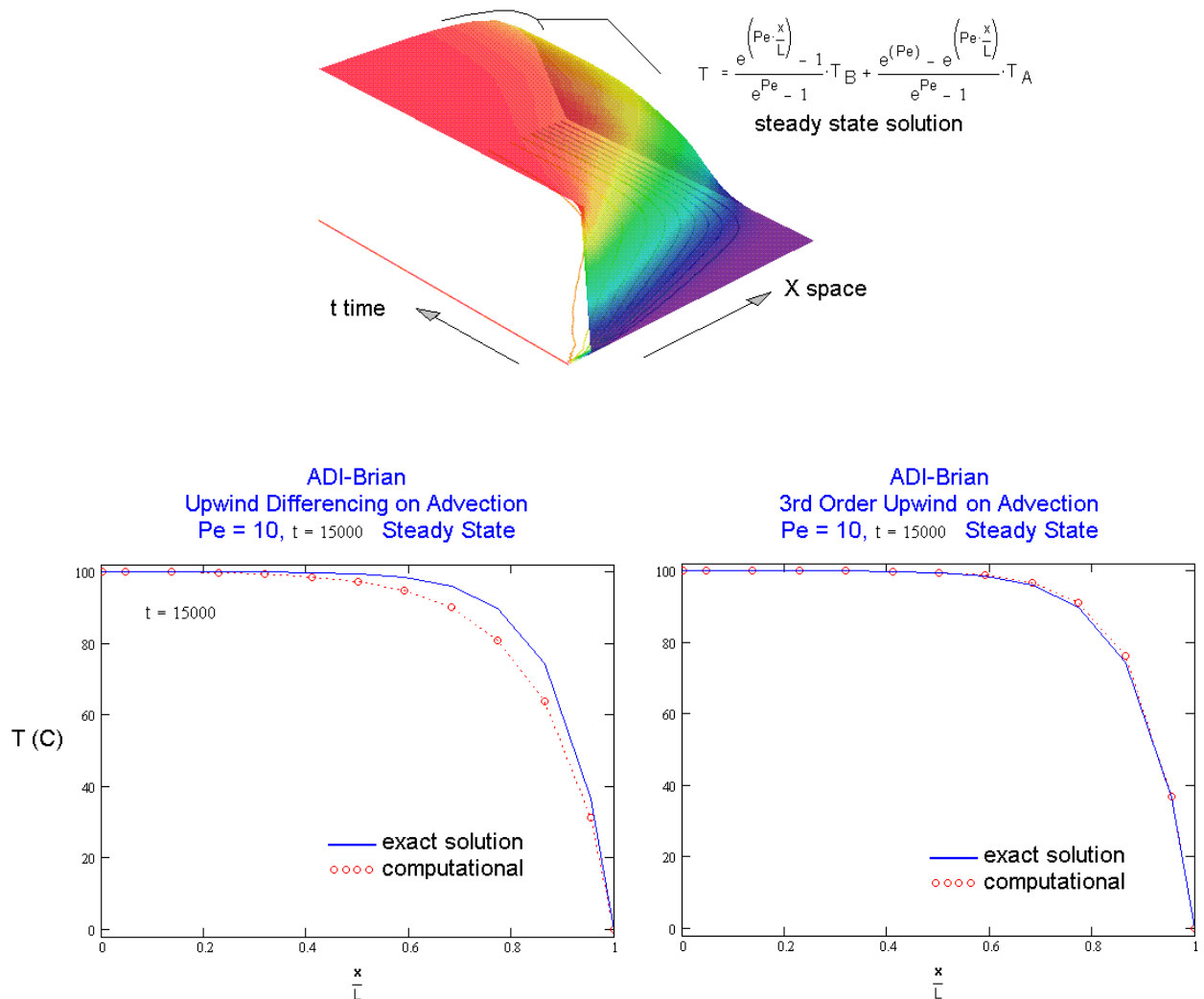


Figure 6. Comparison of numerical and exact solutions to the 1D slab with 2 fixed boundary conditions at each end. Demonstrates numerical diffusion caused by upwinding and sharpening produced by 3rd order upwinding.

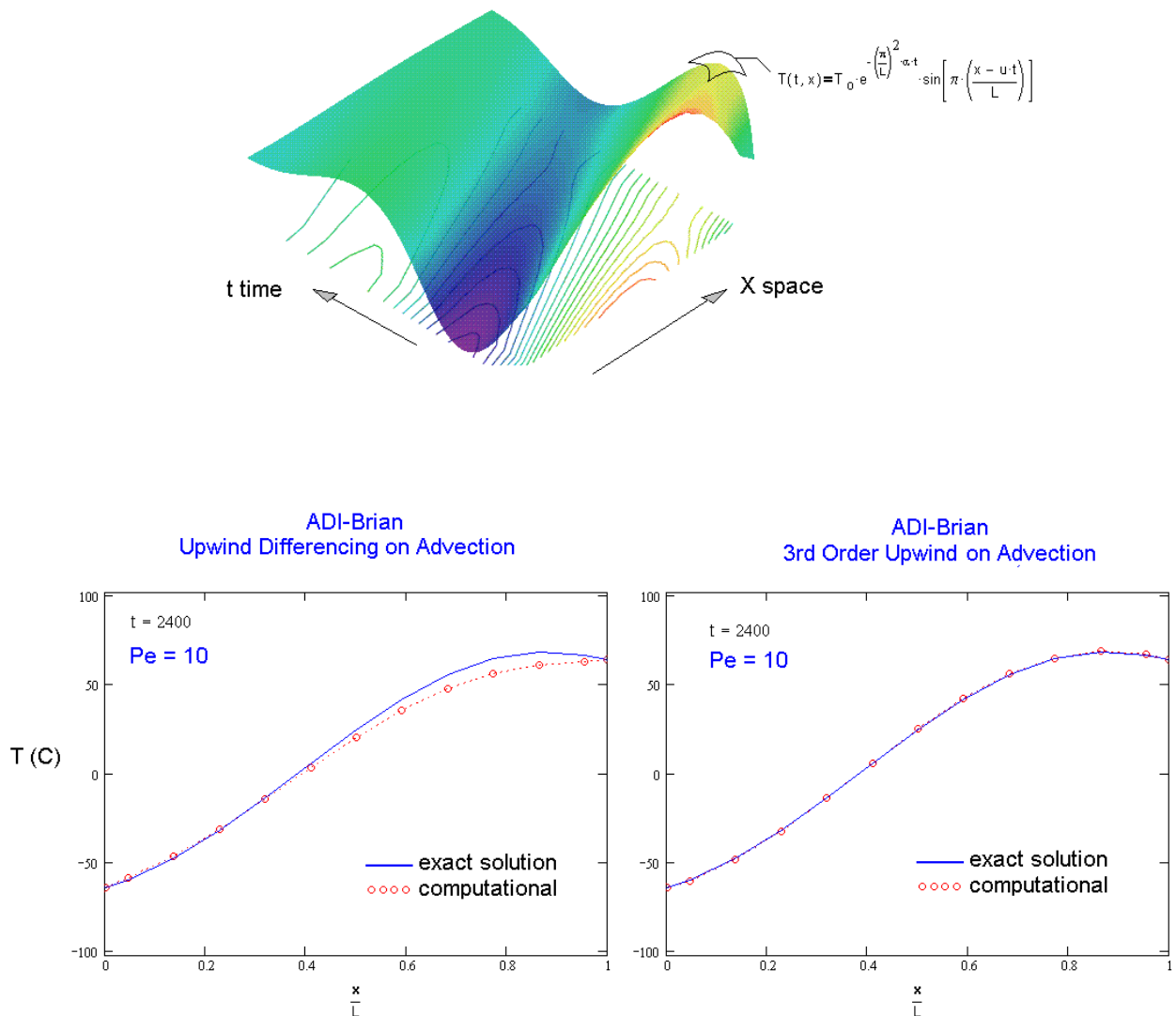


Figure 7. Comparison of numerical and exact solutions to the 1D slab with time varying inlet boundary condition and sinusoidal initial condition of $T_0 \sin\left(\pi \frac{(x - U t)}{L}\right)$ boundary conditions at each end.

APPLICATION STUDY

The application study is used to evaluate the computational performance of the new ADI solver. The problem selected is the classical backwards facing step. The geometry of the step and velocity field is shown in the following figure. The Reynolds number is $Re = 34$ and the separation length compares closely with published results. The velocity field computed in the CFD simulation was then directly applied in a thermal simulation. An adiabatic purge test case is analyzed. The inlet temperature is adjusted from 0 to 100 °C in a step change. The temperature contour plots at several instances in time are layered to show the transient evolution of the temperature field.

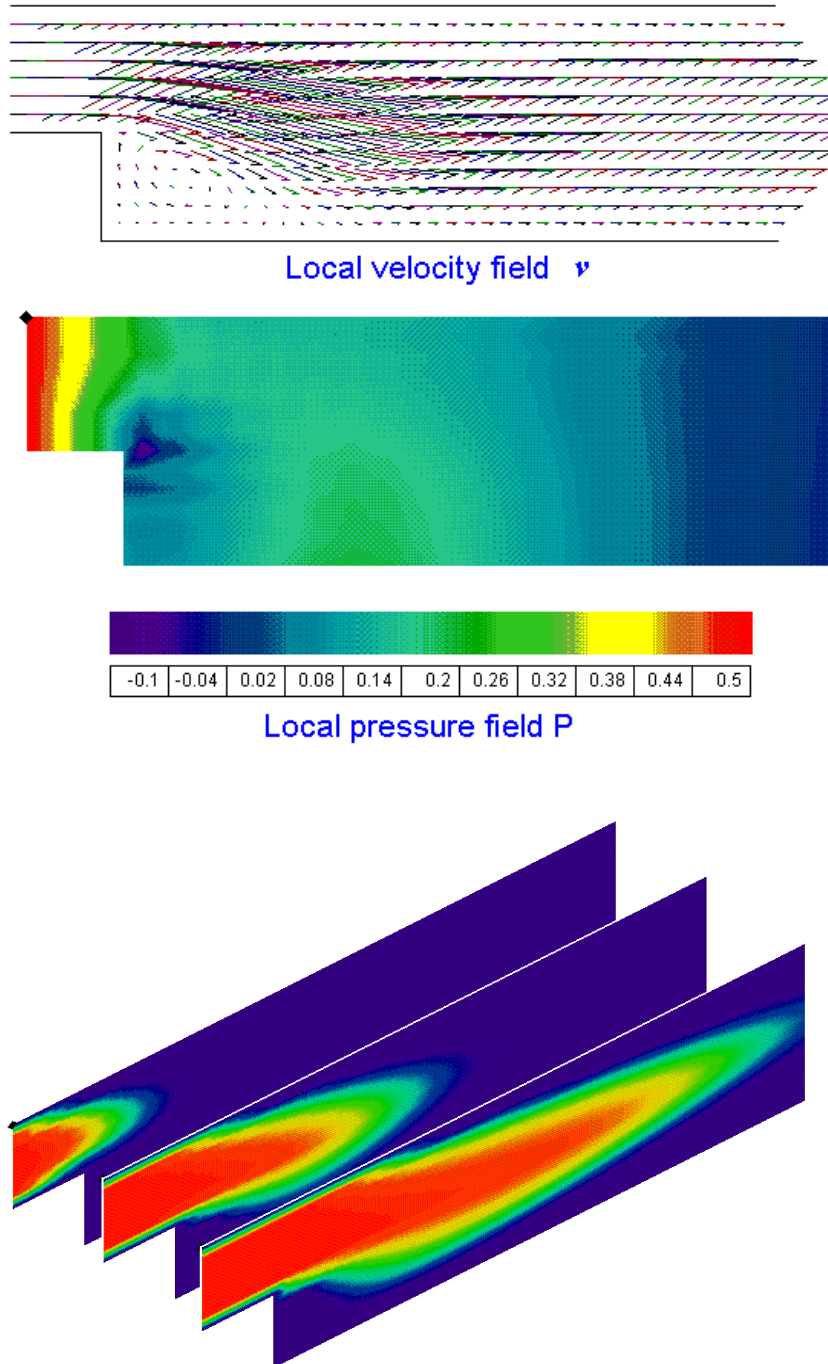


Figure 8. Temperature field for the an inlet purge case.

Performance Assessment

The following plot shows the evolving wall clock time as a function of the location simulation time comparing the relaxation solution to the new ADI solution. As evident, the ADI solution outpaces the SOR solution by a factor of x3. This is a conservative speed increase because the ADI solution is effectively a 3D solver while the SOR solution was a 2D solver. In other words, the 3rd Z sweep which is executed in the ADI solution is fundamentally unnecessary. Equivalently, an SOR solution would be even slower if the geometry was actually 3D because the ADI solution would not be beleaguered by the added third dimension. This is even more pronounced for problems with wide varying values of the diffusivity. Moreover, the actual simulations were performed at equal Courant numbers where as the ADI solution can be executed at much higher numbers or in fewer time steps. Thus, nominal speedup factors with the new ADI method are expected to range around x10; peak speedup factors as high as x40 have been observed in some 3D thermal simulations.

The robustness of the ADI solution is evidenced by the magnitude of the Courant number. The contour plots presented above were obtained with a time step giving a CFL ~ 10 . Even at these excessive Courant numbers, the thermal simulation with the ADI method maintains stability, while a comparative simulation with the SOR solution becomes unstable. The qualitative reasons are suggested to originate from the direct inversion process and the reduction of the single time step into two half-steps. The direct inversion appears to minimized reflection and amplification of waves which rebounding off of boundaries. In contrast, these tend to build with SOR. Second, in any sweep direction, the actual Courant number in the ADI solution is $\frac{1}{2}$ the value given by the overall time step selected for the simulation because each sweep equation takes a value of $\frac{1}{2}$ for the capacitive term (see Table 1).

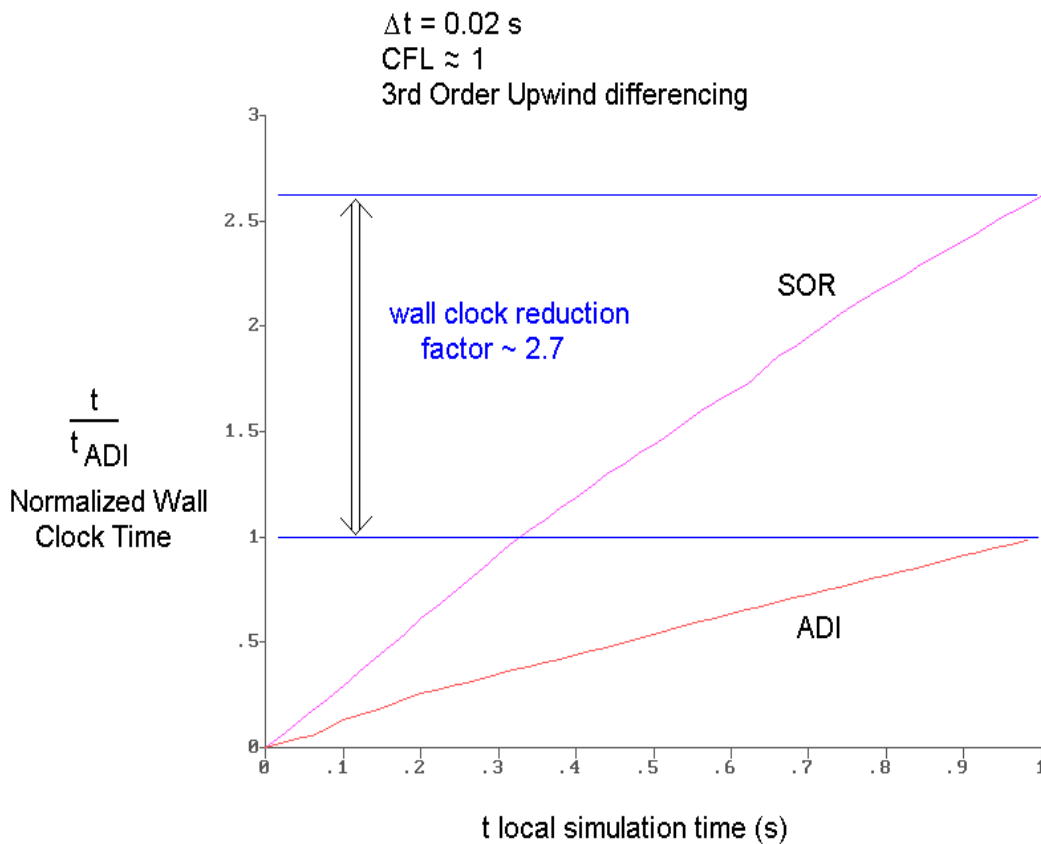


Figure 9. Evolving wall clock time for ADI and SOR thermal purge simulations of backwards facing step.

CONCLUSIONS

This paper presents a study of the adaptation of the conventional ADI solution method for diffusion transport to include advective transport. The study has shown it is feasible to modify a diffusional-designed ADI method for the advection terms to derive a general purpose transport equation solver. The ADI-Brian method can be implemented by splitting the advection term in analogous fashion to the splitting of the diffusional operators. The augmenting of the advection term can be adjusted by implementing a modulator function which can sharpen a standard upwind differencing method to 3rd order upwind and still be implemented with a standard tridiagonal solver. The new ADI solution method offers robust efficient performance with Courant numbers in excess of 10 and wall clock time conservatively x3 faster conventional SOR solution. The new ADI method can be structured for efficient code implementation and can be easily extended to operate on a general solution vector of unknowns such as temperature and velocity.

INITIAL THERMAL MODELING OF THE CONSTRAINED VAPOR BUBBLE HEAT EXCHANGER USING TSS/SINDA

S. Basu,* P.C. Wayner, Jr., and J.L. Plawsky
The Isermann Department of Chemical Engineering
Rensselaer Polytechnic Institute
Troy, NY 12180-3590

*2001 Aerospace Parkway
Brook Park, Ohio 44142

ABSTRACT

Heat transfer systems operating under interfacial free-energy gradients to control the fluid flow are simple and light due to the absence of mechanical pumps. These have been proposed as reliable cooling systems in microgravity environments (Wayner, 1999). The Constrained Vapor Bubble (CVB) heat exchanger is being designed as a microgravity (μg) fluid physics experiment for the Fluids Integrated Rack (FIR) aboard the International Space Station (ISS). The aim of this study is to characterize the heat flow mechanisms of such a device operating as a wickless heat pipe, using the TSS/SINDA software. The geometry and nodal meshwork was created using TSS, the graphics interface to SINDA. A SINDA (thermal) model was created to study steady state and transient solutions to heat transfer under the influence of conduction, convection and radiation. Experiments were performed with the CVB in vacuum and air, for various power inputs. An initial thermal model using TSS-SINDA is presented for the dry, evacuated CVB cell. The temperature profile data collected from the experiments were compared to the results of the model to provide significant insights to the losses due to radiation and convection. In view of expected flight-data trends (where convection is essentially negligible), the importance of radiation is discussed. The presence of a good heater-insulation is essential for high heat input to the cell.

INTRODUCTION

The Constrained Vapor Bubble or the CVB, is a miniature heat transfer device whose principle of operation is similar to the mechanism of conventional and micro heat pipes. Many applications including cooling of electronic equipment require efficient heat dissipation for their safe and reliable operation. Attaching fins to high temperature zones is a common solution. The work of Bowman et al (1998) has shown that not only are heat pipe fins lighter than standard fins, they can be significantly more efficient depending on their mode of operation. The purpose of this study is to use the CVB heat exchanger to study heat transfer characteristics of the heat pipe fin with special emphasis on radiation. Most of the work done on such heat pipes has neglected the effects of radiation. Our long-term aim is to understand all the inside and outside heat transfer mechanisms. An understanding of dry-out conditions and the heat transfer capacity of the working fluid in the corner arteries would help assess the capabilities of the CVB heat pipe.

EXPERIMENTAL

A simplified general concept of the CVB is presented in Figure 1. This small-scale device works on the principle of closed-loop change of phase heat transfer with capillarity to re-circulate the working liquid. The set-up consisted of a fused quartz tube (square in cross-section with inside dimensions measuring 3mm X 3mm and outside dimensions of 5.5mm X 5.5mm), a resistance copper heater with insulation attached on one end and a cooler assembly at the opposite end of the vapor bubble. The bubble length can be varied by under-filling the evacuated cuvette with different amounts of liquid. The transparent nature of the fused quartz aids in interferometry and imaging the bubble shape and size. Interferometric studies provide information about liquid curvature and the apparent contact angle (Wang, 2000). The resistance heater was attached to the quartz cuvette using a thermally conductive/electrically insulating epoxy (Epo-Tek T6081). Super FiretempTM L insulation was used to enclose the heater. A portion of the insulation near the cuvette-end was chamfered to reduce shadow effects during microscopy. Type T thermocouples were placed 2mm (3mm in two cases) apart along the entire length of the cuvette. The cooler-system was mounted on the quartz cell approximately 40 mm away

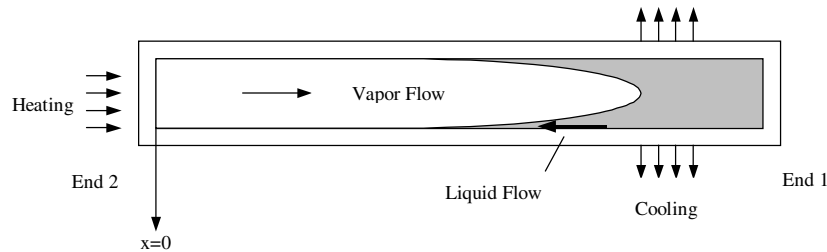


Figure 1. General Concept of the Constrained Vapor Bubble.

from the heater end. It consists of a sleeved-on square copper block with four thermoelectric coolers (one on each side of the four walls) and aluminum fins. One of the aluminum fins was attached to the base of the setup to provide a conduction path for heat removal from the thermoelectric coolers. This assembly provided the cooling mechanism required to condense the vapors when operated in the wet mode. When a working liquid exists inside the cuvette, energy flows from End 2 (heater end) to End 1 (cooler end) by a combination of conduction in the walls, evaporation - vapor flow and finally condensation. Liquid flows back to the heater end by capillarity in the corners. There is a small amount of heat loss to the surrounding.

In the dry mode, the cuvette is evacuated to hold a vacuum of 10-Torr and is referred to as the 'dry cell'. In order to calibrate the CVB, it is necessary to run it first in the dry mode. We present an effort toward estimating the effective thermal emissivity, the radiation and convection heat transfer coefficients in the dry heat pipe fin.

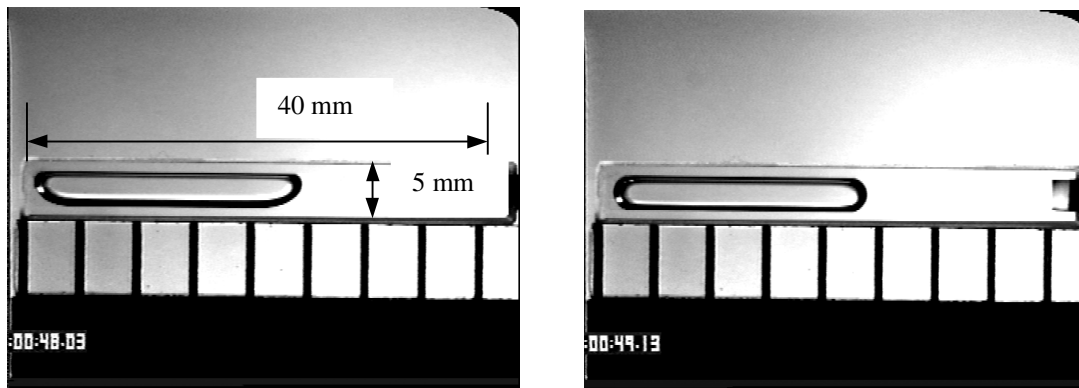


Figure 2. Shape of pentane vapor bubble under gravity (left) and microgravity.

Choice of orientation of the setup was the first important design decision. On earth, gravity forces are known to influence liquid flow in systems the size of ours, leading to an asymmetric bubble shape. This was proven by a 2.2-second drop tower test at the Glenn Research Center in Cleveland, OH as shown in Figure 2. While operating the setup in a horizontal mode, the asymmetric bubble-shape gave rise to a number of problems. The presence of excess liquid on the bottom surface of the cuvette hampered uniform heat transfer and fluid flow. Moreover, curvature differences resulted between the top, bottom and side faces. To ensure symmetry in operation of the CVB, the setup was mounted vertically with the heater on top. In this type of setup condensation becomes very important since the liquid has to rise in the capillary channels (corner arteries) of the cell against gravity forces. The efficiency does fall off as compared to other orientations (Bowman, 1999) but the heat transfer characteristics can be studied more uniformly.

Two sets of experiments were run. The first set consisted of runs with the dry cell inside the vacuum chamber, while the other consisted of repeating the same runs in air. The CVB test module was placed inside a vacuum chamber as shown in Figure 3. T-type thermocouple wires attached to the quartz surface were connected to a data acquisition system (pDaqView) through a series of connectors (blue). A total of twenty-two thermocouples were used, with one of them measuring ambient temperature in the immediate vicinity of the cuvette (for air runs). A thermocouple was attached to the inside wall of the vacuum chamber. The chamber was closed and pumped down to a pressure of 6×10^{-6} Torr. The data



Figure 3. CVB test configuration inside the vacuum chamber (left) and a close-up view of the cell.

acquisition system was configured to automatically record the axial temperatures from the thermocouples at 20-second intervals from start to end of each run. Five different levels of power were fed to the heater from a voltage source. The whole setup was held at a given power level until the cuvette temperatures reached steady state. The cuvette was allowed to run at steady state for at least fifteen minutes in each case before switching off the heater. Care was taken to ensure the proper recording sequence of the data for the various runs. The heater power was varied from 0.13W to 1.5W in three intervals. Inside the vacuum chamber the heater-power could not be increased beyond 1.5W as the temperature of the heater exceeded 210°C, a limiting factor for the epoxy. There was a significant difference for runs in air wherein the heater power could be raised to as high as 2.5W due to the presence of convection cooling in addition to radiation and conduction.

A few additional tests were performed inside the vacuum chamber to improve our understanding of the thermal emissivity of the quartz in the region closest to the heater and insulation. These used the same vertical configuration at three power levels with an aluminum foil barrier on the cuvette nearest to the heater end to shield it from the white insulation. As before, temperature data from each run was recorded at 20-second intervals using the acquisition system.

The second set of experiments was conducted in air. The same configuration was mounted vertically on to an optics table. The room was selected such that presence of overhead ducts/vents and fans were eliminated. This was done to ensure no forced convective currents near the experimental setup. The CVB was allowed to operate under seven different power-levels. As mentioned before, the limiting temperature of the epoxy (~250°C) permitted us to go to a heater power of 2.55W only. Data was collected in the same manner as before.

THEORY AND MODELING

Figure 4 depicts the CVB heat pipe control volume. Assuming steady state operation and variation of temperature in the axial (x) direction only, an energy balance over the differential element of the wall gives

$$kA_c \frac{\partial^2 T}{\partial x^2} - h_{oc} P_o (T_x - T_\infty) - h_{or} P_o (T_x - T_\infty) - h_{ic} P_i (T_x - T_v) - h_{ir} P_i (T_x - T_\infty) = 0 \quad (1)$$

where k is the thermal conductivity of fused quartz, A_c is the cross-sectional area of the solid heat pipe wall (total area minus area of vapor space), T_x is the temperature of the wall at a distance x , h_{oc} is the outside convective heat transfer coefficient, h_{ic} is the inside convective heat transfer coefficient, h_{ir} and h_{or} are the inside and outside radiation heat transfer coefficient respectively, P_o is the outside perimeter of the cuvette, P_i is the inside perimeter of heat pipe or vapor space depending on mode of operation, T_∞ is the temperature of the surrounding ambient or vacuum chamber wall and T_v is the temperature of the vapor in the cuvette.

For operations conducted on the *dry cell inside the vacuum chamber*, there is no convective heat transfer. As such Equation 1 reduces to:

$$kA_c \frac{\partial^2 T}{\partial x^2} - h_{or} P_o (T_x - T_\infty) - h_{ir} P_i (T_x - T_\infty) = 0 \quad (2)$$

We assume $T_\infty = T_{chamber-wall} = T_{sur}$ for calculating radiation exchanges. The reading from the thermocouple placed on the chamber wall was taken to be $T_{chamber-wall}$. Equation 2 can thus be rewritten as

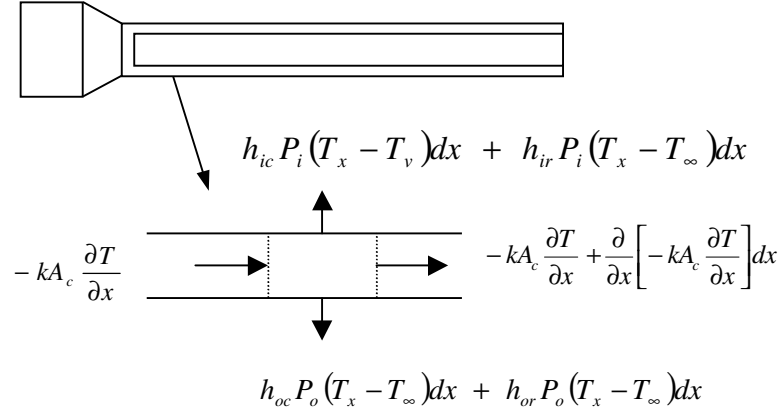


Figure 4. Control volume of CVB heat pipe cuvette

$$kA_c \frac{\partial^2 T}{\partial x^2} = (h_{or} P_o + h_{ir} P_i)(T_x - T_{chamber-wall}) \quad (3)$$

Heat exchange in the form of radiation may be written as

$$Q_{rad} = h_r A(T_s - T_{sur}) \quad (4)$$

where h_r denotes the radiation heat transfer coefficient, A is the surface area, T_s is the surface temperature and T_{sur} is the surrounding temperature with which radiation exchange occurs. In general the radiation heat transfer is given by

$$Q_{rad} = F_{cell-sur} \epsilon \sigma A (T_s^4 - T_{sur}^4) \quad (5)$$

where $F_{cell-sur}$ is the view factor for cell surface to surrounding (assumed to be unity), ϵ is the emissivity and σ is the Stefan-Boltzmann constant.

Comparing Equations 4 and 5 we get the expression for the radiation heat transfer coefficient to be

$$h_r = F_{cell-sur} \epsilon \sigma (T_s + T_{sur}) (T_s^2 + T_{sur}^2) \quad (6)$$

Owing to the high transmissivity of fused quartz in our temperature range, we assume that

$$h_r = h_{or} = h_{ir} \quad (7)$$

We define:

$$\begin{aligned} \theta &= (T_x - T_\infty) \\ \theta_{base} &= (T_{base} - T_\infty) \end{aligned} \quad (8)$$

$$m^2 = (h_{or} P_o + h_{ir} P_i) / kA_c$$

L is the total length of the CVB cell and $x=0$ is defined at the inside face of the end-block (Figure 1). Using the boundary condition $\theta_L = \theta(L)$ for the cell, and assuming that the radiation heat transfer coefficient is constant, the temperature distribution profile is

$$\frac{\theta}{\theta_{base}} = \frac{(\theta_L / \theta_{base}) \sinh mx + \sinh m(L-x)}{\sinh mL} \quad (9)$$

For tests conducted on the dry, evacuated cuvette **in air**, Equation 1 is modified to include convection on the outside. There are still no convective currents inside the cell as there is no air or liquid present there. (Convective heat transfer coefficient is also assumed to be a constant). The modified Equation 1 thus becomes:

$$kA_c \frac{\partial^2 T}{\partial x^2} - h_{oc} P_o (T_x - T_\infty) - h_{or} P_o (T_x - T_\infty) - h_{ir} P_i (T_x - T_\infty) = 0 \quad (10)$$

and the parameter m^2 is redefined as

$$m^2 = (h_{oc}P_o + h_{or}P_o + h_{ir}P_i)/kA_c \quad (11)$$

T_∞ is now the ambient temperature of the surrounding vicinity of the experimental setup.

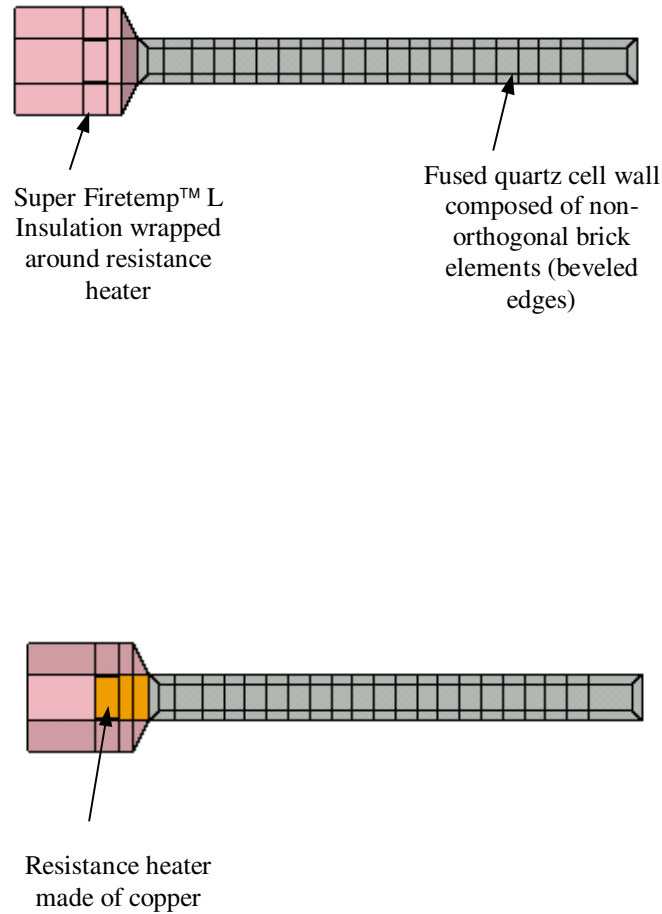


Figure 5. CVB Heat Exchanger Geometry on TSS

The geometric model of the CVB heat exchanger as set up on TSS is shown in Figure 5. The cooler assembly was not required for the dry runs and was thus left out. Each wall was composed of twenty-one non-orthogonal brick elements to simulate the real cell edges, walls and corners. The sizes of the elements were selected so as to generate data near the actual positions of the thermocouples on the cell. The end block was attached to the copper heater. We assumed that the temperature drop across the very thin layer of epoxy was negligible. Diffusion nodes were used at the centroid-position of the elements and arithmetic nodes were generated to connect elements and represent surface nodes. Table 1 lists some of the thermo-physical properties of the materials used.

Boundary nodes, obtained from the thermocouples included the ambient temperature, the boundary temperatures at length L , wall temperature of the vacuum chamber for radiative exchange and the heater temperature. Figure 6 shows

the node/conductor meshwork. Radiation from interior nodes was modeled using view factors, while exterior nodes were ‘connected’ to the chamber wall by radiation conductors, assuming the view factors to be unity. For runs in air, the exterior nodes were also attached to the ambient through convective conductors. The cuvette was divided into six regions for

Table 1. Thermo-physical properties of CVB materials

Material Name	Thermal Conductivity, k W/m-K	Specific Heat, C_p J/kg-K	Density, ρ kg/m ³
Copper	401	385	8933
Fused Quartz	1.38	745	2220
Insulation	0.06	810	288

fine-tuning the temperature profile. Narrower sections were allocated closer to the heater. Final heater temperatures for the various power loads were fed to the model and steady state runs obtained. The output was collected in the form of discrete data points. However for ease of viewing, the model data has been presented as dotted curves in the graphs to follow.

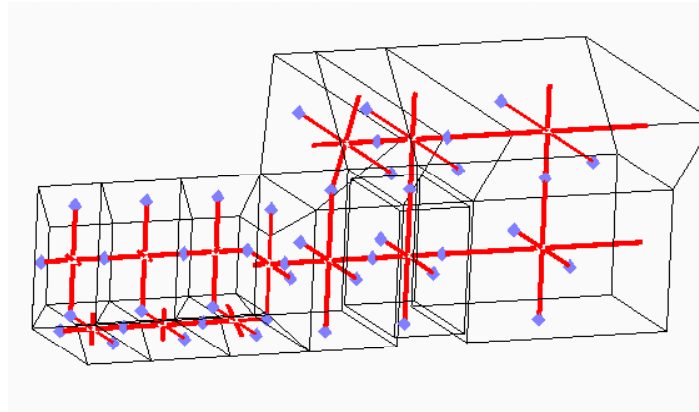


Figure 6. General concept of the node/conductor meshwork of TSS-SINDA model.

RESULTS AND DISCUSSION

Figure 7 shows the experimental and theoretical temperature profiles obtained inside the vacuum chamber. The heater position is approximately at $x = -2.0 \text{ mm}$. Equation 9 was iterated to best fit the theoretical profile to the experimental data from the vacuum chamber tests. This gave a value for m and using Equation 8 & 6 with values of temperature from the thermocouple measurements, an effective thermal emissivity (ϵ) for the whole cell was obtained. Using the emissivity we get an *average* radiation heat transfer coefficient (see Table 2). It was found that the effective emissivity decreased with an increase in the heater power (and hence overall temperatures), for 3-5 μm range of operation. Not surprisingly, the spectral emissivity of fused quartz increases with increasing wavelength in the same range (Thermo-physical Properties of Matter, 1972). This leads to the conclusion that although spectral distribution is approximately independent of temperature there is proportionately more emission at higher wavelengths with increasing temperature. Other factors contributing to the observed phenomena may be a high hydroxyl ion content in the material leading to ionic absorption, the thickness of the glass itself and its appreciable transmissivity in the 3-5 μm range.

The values of emissivity were compared to those obtained from the Sinda model. Figure 8 shows the (discrete) Sinda model distributions with respect to the experimental data sets. The good match of the numerically computed values to the experimental data proved the validity and reliability of the model. The view factors used for the inside wall-elements varied from 0.2 – 0.8 depending on position with respect to other walls. The predicted emissivity matched the experimental emissivity over most of the cell while the region closest to the heater showed a lower emissivity in general. This was attributed to the presence of the heater insulation, which was affecting the net emissivity in that region. Once the cell was shielded from the insulation by a piece of aluminum foil, the emissivity increased.

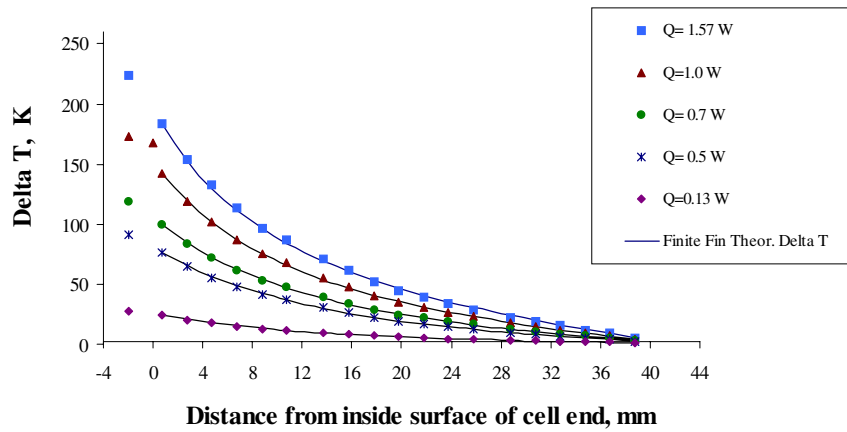


Figure 7. Experimental and Theoretical Thermal Profiles of vertical CVB in vacuum.

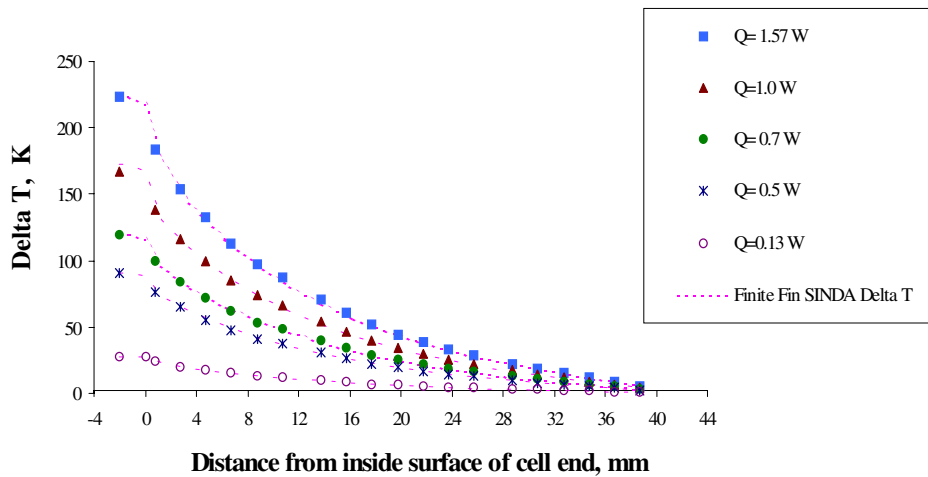


Figure 8. Experimental and Sinda Thermal Profiles of vertical CVB in vacuum.

Table 2. Thermal Emissivity and Radiation h.t.c.'s for various power inputs

Heater Power, Watts	Effective Thermal Emissivity	Average Radiation h.t.c., W/m ² -K
0.13	0.67	4.22
0.50	0.65	4.59
0.70	0.63	4.74
1.06	0.61	5.01
1.55	0.57	5.23

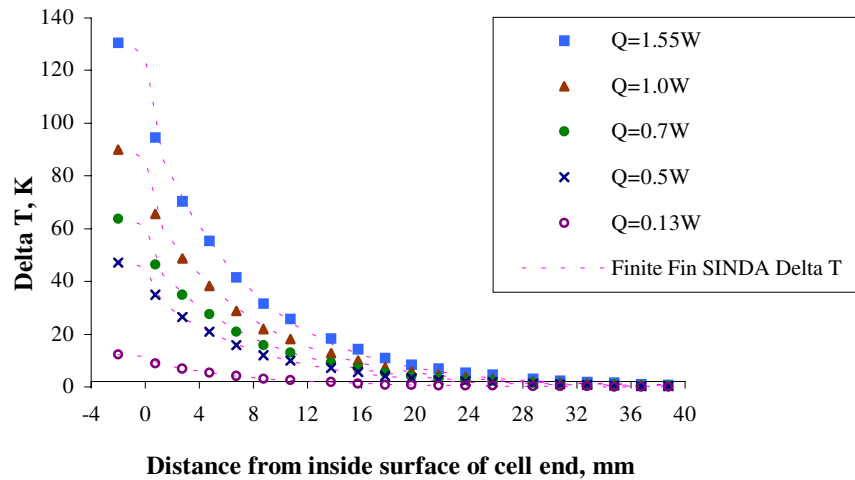


Figure 9. Experimental and Sinda Thermal Profiles of vertical CVB in air.

Although the average values of outside radiation h.t.c.'s seem to be low, some of the local values at the heater end were as high as $9.6 \text{ W/m}^2\text{-K}$, indicating the strong temperature dependence. This is of particular importance to us keeping in mind that space does not have convective currents and would probably exhibit similar high-end numbers.

The emissivity values were used to predict radiation losses and estimating the outside convective heat transfer coefficient for the cell. Figure 9 shows the experimental and Sinda temperature curves for CVB runs in air. The outside (natural) convective heat transfer coefficient was found to vary between $16\text{-}19 \text{ W/m}^2\text{-K}$. Heat transfer coefficients predicted by the model showed a good match to the theoretical values. The model values further indicated a slightly lower, but constant convection coefficient near the heater end due to the insulation/heater blocking off the convective air current path there. Experiments and modeling indicated that good heater insulation was a key factor for improving heat flow into the quartz cuvette. Other insulation like Vespel® resulted in decrease of power flowing into the cell end.

One important feature about the Sinda model is that it gives an actual value for the end-wall inside surface temperature (at $x=0$). Previously, power going into the cell was estimated by extrapolation of the experimental data to $x=0$. Table 3 summarizes some of the power-input estimation based on model and extrapolation. Losses were within the lower and upper range for intermediate power levels. It is evident that the power actually entering the cell is *underestimated* when an extrapolation technique is used. The Sinda model helps in calculating a more accurate power input (and loss) in to the cell. Q_{heater} is the power delivered to the heater by the voltage supply. The losses amounted to 40-45% in air and 23-37% in vacuum indicating that convection and radiation play a significant role in the operation.

Table 3. Comparison of Q_{SINDA} vs. $Q_{\text{extrapolation}}$

$Q_{\text{heater}}, \text{ W}$	Mode of operation	$Q_{\text{SINDA}}, \text{ W}$	$Q_{\text{extrapolation}}, \text{ W}$
0.13	Vacuum	0.10	0.07
1.06		0.69	0.48
1.55		0.98	0.47
0.13	Air	0.08	0.05
1.01		0.60	0.32
1.55		0.88	0.54

CONCLUSIONS

Experiments were conducted in vacuum and air on the vertical, dry/evacuated CVB heat pipe. The results in conjunction with the 2-dimensional Sinda model provide the following information:

- Effective thermal emissivity of the overall CVB heat pipe ranges between 0.57-0.67 corresponding to heater-power ranges of 1.55-0.13W respectively.
- The average thermal emissivity of the cell decreases with an increase in average temperature.
- View factors used for internal radiation effects was seen to vary between 0.2-0.8 depending on location of the element with respect to others.
- The radiation heat transfer coefficient is strongly dependent on temperature. The value in the 3-5 μ m range of operation is about 4.5W/m²-K.
- The outside convective heat transfer coefficient for the vertical heat pipe fin varies between 16-19W/m²-K.
- The presence of good heater insulation is critical in ensuring high heat inputs to the cell.
- Radiation heat transfer is fairly significant in the operation of the fin. The choice of material of the heat pipe dictates the level of importance. Above results indicate that even for low heater power the effects of radiation losses are not negligible.
- Convective heat transfer can be three times larger than radiation, for the same temperature difference. It reduces the efficiency of pumping power into the cell by increasing losses.
- The Sinda model provides a more accurate method of estimating the power entering the cuvette.

ACKNOWLEDGMENTS

This material is based on the work supported by the National Aeronautics and Space Administration and Federal Data Corporation. The author would like to express gratitude to Neil Rowe, Ray Margie and Paul West of FDC for their help. Any opinions, findings and conclusions expressed in this paper are those of the authors and do not necessarily reflect the view of NASA or FDC.

REFERENCES

- Bowman, W. J, Storey, J. K., Svensson, K. I., 1998, "Analytical comparison of constant area, adiabatic tip, standard fins and heat pipe fins", J. Thermophysics, Vol. 13, #2, pp. 269-272.
- Bowman, W. J, Moss, T. W., Maynes, D., Paulson, K. A., 1999, "Efficiency of a constant area, adiabatic tip heat pipe fin", J. Thermophysics, Vol. 14, #1, pp. 112-115.
- Incropera, F. P., DeWitt, D. P., 1996, "Introduction to heat transfer", Third Edition, Wiley Publications.
- Wang, Y., Zheng, L., Plawsky, J. L., Wayner, P. C. Jr., 2000, "Optical evaluation of the effect of curvature and apparent contact angle in droplet condensate removal", Paper submitted to Langmuir.
- Wayner, P. C. Jr., Plawsky, J. L., 1999, "Science Requirements Document for Constrained Vapor Bubble", NASA document # 60055-DOC-000.

AN ANALYSIS AND PROCEDURE FOR DETERMINING SPACE ENVIRONMENTAL SINK TEMPERATURES WITH SELECTED COMPUTATIONAL RESULTS

Albert J. Juhasz
National Aeronautics and Space Administration
Glenn Research Center
Cleveland, Ohio 44135

Summary

The purpose of this paper is to analyze the heat transfer problem posed by the determination of spacecraft temperatures and to incorporate the theoretically derived relationships into a computational code. Subject code is based on a theoretical analysis of thermal radiative equilibrium in space, particularly in the Solar System. Starting with the solar luminosity, the code takes into account a number of key variables, namely: the spacecraft-to-Sun distance expressed in AU (Astronomical Units), with 1 AU representing the average Sun-to-Earth distance of 149.6 million km; the angle (degrees of arc) at which solar radiation is incident on a spacecraft surface, the temperature of which is to be determined (i.e., a radiator or PV (photovoltaic) array); the absorptivity-to-emissivity ratio of the surface, α/ϵ , with respect to solar radiation; and the view factor of the surface to space.

Introduction

For the thermal design of spacecraft radiators it is necessary to determine a space background temperature or "equivalent space sink temperature" to which radiators reject their design heat load. This is especially true for radiators that operate at the relatively low temperature range of 300 to 500 K, a range for which early assumptions of 0 to 3 K for the sink temperature would introduce serious errors in the determination of required radiator area. This "equivalent, or space sink temperature" is not the temperature of the vacuum surrounding a spacecraft. It is rather an "equilibrium temperature" that a passive radiating surface would assume by exchanging thermal radiation energy with the space environment, without any "on board," or internally generated heat load, needing to be rejected to space. This "equilibrium temperature" is a function of the spacecraft-to-sun distance and the angle at which the surface intercepts solar radiation. It is also greatly influenced by the characteristics of the radiating surface itself. These include the view factor to space and the α/ϵ parameter, which expresses the ratio of a surface's

absorptivity of solar radiation to the emissivity at its final equilibrium temperature where it reradiates heat into space, usually in the infrared region of the spectrum.

Early reports (e.g., Goldman and Singer, 1957) assumed gray body characteristics for radiator surfaces, which implied α/ϵ values near unity. The work of Rittenhouse and Singletary (1968) showed that special metal oxide coatings, such as "Z-93," could be applied to surfaces in order to lower the amount of solar energy absorbed, while keeping infrared emissivity high. With the α/ϵ values near 0.1 achieved with these coatings, the space equivalent sink temperatures are effectively lowered, thus permitting more heat to be rejected by a radiator having a given surface area and effective radiating temperature.

The purpose of this paper is to derive the equilibrium temperatures that actual spacecraft radiating surfaces would experience due to the combined effects of solar and planetary radiation as well as "on board" heat to be rejected. The derivation is based on a new definition of the term "space sink temperature," which differs from earlier definitions. As an example, Gordon (1982) defined the "temperature of space as the equilibrium temperature that a small black sphere would experience."

In contrast to the above, the definition that the theoretical derivations in this paper are based upon is as follows: the "space sink temperature" is the equilibrium temperature that a radiating surface having a given α/ϵ would achieve in space, if the surface does not have any internal heat to be rejected, but is exposed to a given incident radiant energy flux from the Sun (or star) and planetary surfaces, part of which energy flux is reradiated to the space background." Of course the amount of thermal energy reradiates into space is controlled by characteristics of the radiating surface, such as the α/ϵ ratio and the view factor to space. Two additional observations can be made regarding our definition of space sink temperature:

1. If the incident radiant energy flux is reduced to zero, then the equilibrium sink temperature for a surface without internal heat generation would drop to 0 K. Note,

however, that this condition cannot be realistically achieved, even in interstellar space, where thermal equilibrium would be achieved at about 3 K.

2. For a radiating surface that is rejecting an internal heat load, the average equilibrium surface temperature will rise to a value consistent with the “warmer temperature value” in the Stefan - Boltzmann equation. Substituting the “sink temperature” as expressed by the new definition for the “colder temperature value,” in the same equation, the radiated heat will be equal to the internal heat load that needs to be rejected by the surface.

A mathematical analysis of radiation heat transfer in space is attempted next.

Analysis: Derivation of Equations

Radiative Heat Transfer, Q , between two bodies at temperatures T_1 and T_2 , where $T_2 < T_1$ (i.e., negligible reradiation), can be expressed according to the Stefan-Boltzmann Law as

$$Q = \sigma \epsilon F_v A_s (T_1^4 - T_2^4) \quad (1)$$

where

- Q is the radiated heat flow in Watts (Joules/sec)
- σ is the Stefan-Boltzmann Constant = $5.67 \times 10^{-8} \text{ W/m}^2 \text{K}^4$
- ϵ is the emissivity of the radiating surface ($\epsilon = 1$ for a “black” body; $\epsilon < 1$ for a “gray” body)
- F_v is the surface area view factor between the radiating bodies
- T_1, T_2 “hot” and “cold” temperatures in Kelvin (K)

Objects in the vacuum of space at arbitrary temperatures, T_R , lose heat by radiation to an environmental equilibrium, or space sink temperature, T_S , which is very near to absolute zero ($\sim 3 \text{ K}$) in interstellar space. However, as shown in the “Results” section of this paper, in the neighborhood of the inner planets of the Solar System, T_S , can be several hundred Kelvin. Hence to correctly size the areas for space satellite radiators which operate at temperatures between 300 to 400 K, the equivalent space sink temperatures have to be determined within an accuracy of a few tens of degrees.

For the space radiation case, Eq. (1) can be rewritten in terms of T_R and T_S . This is shown in Eq. (2).

$$Q = \sigma \epsilon F_v A_s (T_R^4 - T_S^4) \quad (2)$$

To calculate the equivalent space sink temperatures, T_S , in the neighborhood of planets of the Solar System, first consider the case of heat radiation from the Sun to Earth, as illustrated in Fig. 1. Starting with the solar energy generation rate or luminosity, L , the energy absorption rate per Earth unit surface area needs to be balanced by the emitted energy rate for thermal equilibrium, at temperature T_E , to be achieved. For this analysis F_v is set to unity.

Representing the Sun as a heat source at the center of a sphere whose radius is equal to mean distance between the Earth and Sun, d , the figure shows that about 1370 W fall on each square meter that is perpendicular to the radiating energy flux. The value, 1370 W/m^2 , is referred to as the Solar Constant at 1 AU (one Astronomical Unit, with $d = 1.496 \times 10^{11} \text{ m}$).

The value of the Solar Constant, S , can be determined by dividing the Luminosity, L , of the Sun by the area of the sphere with radius = 1 AU.

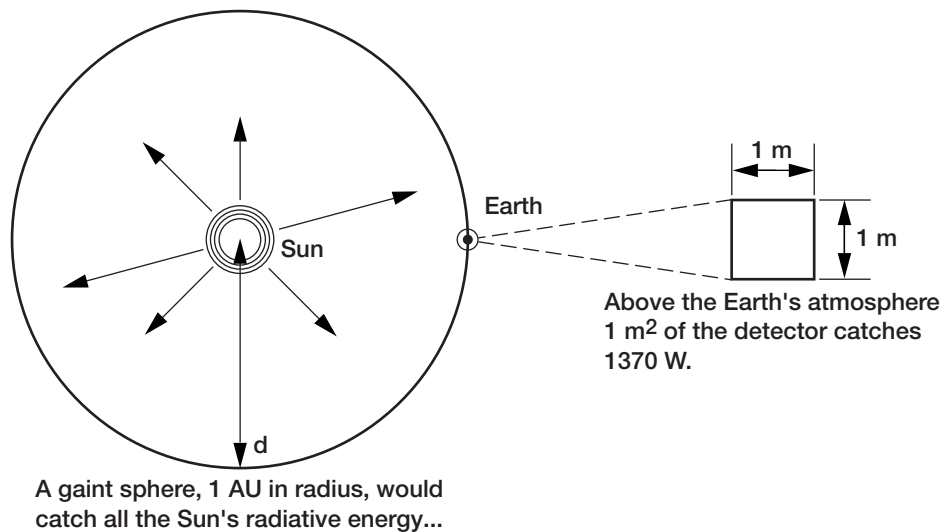


Figure 1.—Sun-Earth heat radiation case.

Expressing the above in equation form:

$$S = L / (4 \pi d^2) \quad (3)$$

Substituting variable values, with $L = 3.86 \times 10^{26} \text{ W}$ ($= 5.23 \times 10^{23} \text{ HP}$) and

$$S = 1372.5 \text{ W / m}^2 \text{ for } AU = 1 \quad (3b)$$

Which, when rounded to 3 significant figures, becomes

$$S = 1370 \text{ W / m}^2 \quad (3c)$$

Note that the result shown in (3c) represents the incident energy rate per unit Earth surface area, which is perpendicular to the solar energy flux. To determine the fraction of this energy flux, which is absorbed by the surface, some important relationships are reviewed in the next section.

Absorption, Reflection, and Transmission of Radiation

When electromagnetic radiation impinges on a body, it is partially absorbed (α), partially reflected (ρ), and partially transmitted (τ). The relation between the absorbed, reflected, and transmitted energy can be expressed as

$$\alpha + \rho + \tau = 1 \quad (4)$$

where

- α absorptivity, i.e., the fraction of the incident radiation absorbed by the body (Note: $\alpha = \epsilon = 1$ for black bodies; $\alpha = \epsilon < 1$ for gray bodies)
- ρ reflectivity, i.e., the fraction of the incident radiation reflected from the surface of the body
- τ transmissivity, i.e., the fraction of the incident radiation transmitted through the body

For opaque bodies like the planets, of course, transmissivity, $\tau = 0$.

Equation (4) then can be expressed as

$$\alpha + \rho = 1 \quad (5a)$$

Calculation of Planetary Temperatures in the Solar System

Since space radiators in planetary orbits are not only exposed to solar but also to planetary radiation, we first need to determine the equilibrium planetary temperatures

at which planets radiate to spacecraft, even if the spacecraft is in the planetary shadow and thus does not receive any solar radiation.

In addition to this planetary radiation, planets also reflect part of the incident solar radiation into space. Orbiting spacecraft may receive some of this reflected radiation, in addition to the direct radiation heating by the Sun.

The reflectivity of planets is also referred to as the albedo, denoted by A .

Thus, from Eq. (5a), the absorptivity can be expressed as

$$\alpha = 1 - A \quad (5b)$$

To proceed with calculation of equivalent space sink temperature, T_S , at a given planetary orbit distance from the Sun, the term energy flux or incident energy per second per unit area, f , is defined, where

$$f = \text{Energy rate (Watts) / Area(m}^2\text{)} \quad (6)$$

For thermal equilibrium at temperature T_E

$$f_{\text{emitted}} \times (\text{Radiating area}) = f_{\text{absorbed}} \times (\text{Absorbing area}) \quad (7)$$

where, from Fig. 1:

$$f_{\text{emitted}} = \sigma \epsilon T_E^4 \text{ and } f_{\text{absorbed}} = (1 - A)L / (4 \pi d^2) \quad (8)$$

Since the Earth rotates once every 24 hr it is a “rapidly rotating planet.” This means that, on average, its entire surface can be considered to be approximately at the same temperature. Hence the total surface energy (or heat) emitted will be

$$f_{\text{emitted}} \times 4 \pi R^2, \text{ where } R \text{ is the planetary radius – (eq. 6738 km for Earth).}$$

The total heat from the Sun, intercepted by the Earth, is the heat flux times the projected earth area on the imaginary sphere with radius = 1 AU. This area is πR^2 . Thus the total energy absorbed will be $f_{\text{absorbed}} \times \pi R^2$

Substituting the expressions from Eq. (7) results in

$$\sigma \epsilon T_E^4 \times 4 \pi R^2 = (1 - A) L \times \pi R^2 / (4 \pi d^2) \quad (9)$$

Solving (9) for T_E we obtain the expression

$$T_E = \sqrt[4]{(1 - A) \times L / 16 \pi \sigma \epsilon d^2} \quad (10)$$

Substituting the numerical values for L, d, and σ , and simplifying yields

$$T_E = 279 \sqrt[4]{(1-A)/(\epsilon d^2)} \text{ in Kelvin} \quad (11)$$

In Eq. (11) the term d is expressed in AU, where AU = 1 for Earth.

Substituting the approximate value for the Earth's albedo ($A \sim 0.3$) and $\epsilon \sim 0.8$ into Eq. (11) we obtain an approximate value for $T_E \sim 270$ K which will be used for calculating radiation from Earth to orbiting spacecraft.

The reader is reminded that Eq. (11) was derived for rapidly rotating planets, like Earth or Mars.

For "slowly rotating planets," like Mercury and the Moon, one must take into account that these bodies receive energy over their projected (disk) areas and emit energy, not over their full spherical surface areas, but only over the same projected areas. This is because the remaining surface area is considered to be "too cold" to radiate a significant amount of energy back into space. For these bodies the thermal equilibrium is thus established when

$$\sigma \epsilon T_E^4 \times \pi R^2 = (1-A) L \times \pi R^2 / (4 \pi d^2) \quad (12)$$

and

$$T_E = \sqrt[4]{(1-A) \times L / 4 \pi \sigma \epsilon d^2} \quad (13)$$

or

$$T_E = 394 \sqrt[4]{(1-A)/(\epsilon \times d^2)} \text{ in Kelvin}$$

where, as before, the Sun-Earth distance, d, is expressed in AU. Comparison of Eqs. (10) and (13) shows, that for slowly rotating planets the equilibrium temperature is higher by a factor equivalent the fourth root of the ratio of sphere surface-to-disk area (i.e., projected area), namely the fourth root of 4.

Applying Eq. (13) to Earth's moon, for which $d = 1$ AU, and $A = 0.07$, results in

$$\begin{aligned} T_E &= 394 \times \sqrt[4]{(1-0.07)/1^2} \\ &= 397 \text{ K} \end{aligned}$$

which is the maximum temperature at the lunar equator at noon. Note that on the dark side, i.e., during the 356 hr lunar night, the temperature is ~ 70 K.

Calculation of Spacecraft Temperatures in Planetary Orbits

Spacecraft in planetary orbits receive long wavelength infrared radiation from the planet they orbit, in addition to the electromagnetic radiation of the solar spectrum.

Near Spherical Satellites

For polyhedral spacecraft geometries that are approximately spherical, Eq. (10) will give a good approximation of the equilibrium temperature due to solar radiation. But the term $(1-A)/\epsilon$ which expresses the absorptivity-to-emissivity ratio for the planetary surface needs to be replaced by the absorptivity-to-emissivity ratio, α/ϵ , for the radiating surface material. Thus for near spherical shapes the equilibrium temperature for the rotating satellite, T_{ES} , becomes

$$T_{ES} = \sqrt[4]{(\alpha/\epsilon) \times (1/F_v) \times L / 16 \pi \sigma d^2} \quad (14)$$

Where the symbol F_v now represents the view factor to space. The value of F_v will normally be close to unity, but it can be lower, if the radiating surface is partially occulted by projecting parts of the spacecraft. Lowering of the view factor will cause T_{ES} to increase.

Flat Plate Radiator Surfaces

For flat plate radiators we need to include the solar illumination angle, θ_s , i.e., the angle at which the radiator plate intercepts the solar flux, in addition to the α/ϵ ratio.

The equilibrium temperature, T_E , due to reflected solar radiation can then be expressed as:

$$T_E = \sqrt[4]{((A \times L \times \sin \theta_s \times (\alpha/\epsilon) \times \tau / F_v (4 \pi \sigma d^2))} \quad (15)$$

where τ is the transmissivity of the atmosphere. If a satellite is outside a planetary atmosphere, as is normally the case, then τ is set to unity.

Albedo

Having previously defined the albedo, A, as the fraction of incident radiation reflected from a planetary surface, we have from Eq. (8) for Earth orbit:

$$f_{\text{reflected}} = (A L \tau / (4 \pi d^2)) \times (R_E / (R_E + H))^2 \quad (16a)$$

where (16a) is the reflected radiation energy flux per unit area at orbital altitude, H. Note that the atmospheric transmissivity, $\tau < 1$, will reduce the reflected radiation flux. Of this energy flux the fraction absorbed by a radiating surface will be

$$f_{\text{absorbed}} = f_{\text{reflected}} \times \sin \theta_p \times \alpha \quad (16b)$$

where

R_E is the radius of the Earth in meters (6.375×10^6 m)
 H is the orbital altitude in meters
 θ_p is the angle at which the radiator plate intercepts energy from a planet that the spacecraft is orbiting

Thus the equilibrium temperature of a satellite's radiating surface due to albedo alone is

$$T_E = \sqrt[4]{\left(A \times L \times \tau \times \sin \theta_p \times (\alpha / \epsilon) / F_V (4 \pi \sigma d^2) \right) \times (R_E / (R_E + H))^2} \quad (16c)$$

Earth Shine, or Direct Planetary Radiation

Similarly for Earth, or planetary, radiation at its previously determined equilibrium temperature to various orbital altitudes the radiation flux is

$$f_{\text{radiated}} = \sigma \epsilon \tau T_E^4 \quad (17a)$$

and the Earth (Planet) Shine equilibrium temperature is

$$T_E = \sqrt[4]{\left(f_{\text{radiated}} / F_V ((\alpha / \epsilon)_2 \times \tau \times \sin \theta_p \times (1 / \sigma)) \times (R_E / (R_E + H))^2 \right)} \quad (17b)$$

where $(\alpha/\epsilon)_2$ is the infrared planetary radiation absorptivity to emissivity ratio of the plate radiator surface. This value will in most cases be close to unity.

Internal Heat Generation

A spacecraft radiator surface normally needs to reject heat generated on board. This will cause its equilibrium radiating temperature to rise due to the internal heat flux,

or heat flow per unit cross sectional area, f_Q , which can be expressed as

$$f_Q = Q / F_V \epsilon \eta A_{RS} \quad (18)$$

In the absence of all other effects this equilibrium temperature would be represented by

$$T_E = \sqrt[4]{Q / F_V \epsilon \eta A_{RS}} \quad (19)$$

Where

Q is the on board heat generation in Watts
 F_V is the view factor to space
 ϵ is the radiator surface emissivity
 η is the surface fin effectiveness (efficiency)
 A_{RS} is the radiator surface area in m^2

Combined Effects

If one wants to know the combined effect of the heat transfer mechanisms, discussed above, (i.e., solar radiation, albedo, Earth radiation, and internal heat generation) on T_E , the individual radiation fluxes, f_i , are added and set equal to $\sigma \epsilon T_E^4$. The resulting expression can then be solved for T_E , as shown below.

Hence

$$T_E = \sqrt[4]{\sum f_i / F_V (\sigma \epsilon)} \quad (20)$$

The last equation expresses the combined effects of solar radiation, albedo, planetary surface temperature radiation in the long wavelength infrared region, and internal heat generation.

Results and Discussion

The equations expressing the thermal equilibrium relationships derived in the previous section were incorporated into a computer code, identified as "TSCALC." This code has been provided with several options to permit evaluating the effects of input variables, like: solar distance in AU, the angle at which thermal radiation energy is intercepted by a reradiating surface (ILUMANG), α/ϵ (AE) for both solar and infrared planetary radiation, and the view factor to space (FV). Note that FV can have a value up to 2 for flat plate radiators rejecting heat from both sides. If both sides do not have a full 2π steradian view of space, then the value will be less

than 2. For a sphere which receives thermal radiation over its projected area, but reradiates over the full surface area, FV can have a maximum value of 4.

An example showing the increase of equilibrium temperatures for a spacecraft surface approaching the Sun from the Heliopause, at 220 AU, is shown in Table 1.

Note that the near 2000 K temperature in the Corona, at the 0.02 AU position, represents the expected value at closest approach during the future "Perihelion Mission." A carbon-carbon heat shield having an α/ϵ (AE) of 0.6 and intercepting solar radiation at 25° (ILUMANG) may be used to shield the spacecraft.

Figure 2 depicts the heat flux and temperature information in graphic form. Note that the temperatures shown are for planetary orbit distances, but not for the planets themselves! However, planetary temperatures could be computed by the code if the proper input values (ILUMANG, FV, and AE) are used.

The effect of insolation angle at 1 AU, or angle at which a re-radiating surface without internal heat generation ($QW = 0$) intercepts the solar energy flux, is shown in Table 2. Note that for zero insolation angle the code returns

a value of 3 K, since the solar heat flux is eliminated and the equilibrium temperature will be that of interstellar space.

As an example of equilibrium temperatures determined primarily by planetary radiation in the infrared domain, consider the information shown in Table 3 for a space structure in geostationary orbit at 35,876 km altitude. By setting the insolation angle (ILUMANG) equal to 0.1° we have assumed that 99.9 percent of the solar heat flux can be eliminated, via clever shielding and insulation. Assuming an earth gravity gradient stabilized structure, we want to study how the space "sink" temperature will vary as direct radiation from earth is incident on a surface from 1 to 10° of arc. The results show that temperatures lower than 77 K (liquid nitrogen boiling point at atmospheric pressure) can be maintained if the angle of incident earth radiation can be kept to less than 5°.

Results of the type illustrated above have been used in the design of radiators for deep space probes (Juhasz et al. 1999). The computational code is also expected to be used for establishing environmental conditions for solar power generation structures in geostationary orbit.

TABLE 1: CONDITIONS FOR SPACECRAFT APPROACHING SUN TO AU=0.02

ILUMANG (DEG)	FV	EPS	AE	AU	Q/A(W/M2) (90 DEG.)	TS(K)	ORBIT
25.00	1.0	.88	.60	220.000	.03	18.9	HLPAUSE
25.00	1.0	.88	.60	39.438	.88	44.6	PLUTO
25.00	1.0	.88	.60	30.058	1.52	51.1	NEPTUNE
25.00	1.0	.88	.60	19.182	3.73	63.9	URANUS
25.00	1.0	.88	.60	9.539	15.08	90.6	SATURN
25.00	1.0	.88	.60	5.203	50.70	122.7	JUPITER
25.00	1.0	.88	.60	3.000	152.50	161.6	ASTRDS
25.00	1.0	.88	.60	1.524	591.18	226.8	MARS
25.00	1.0	.88	.60	1.000	1372.51	279.9	EARTH
25.00	1.0	.88	.60	.723	2623.26	329.1	VENUS
25.00	1.0	.88	.60	.387	9164.15	450.0	MERCURY
25.00	1.0	.88	.60	.020	3431265.02	1979.3	CORONA

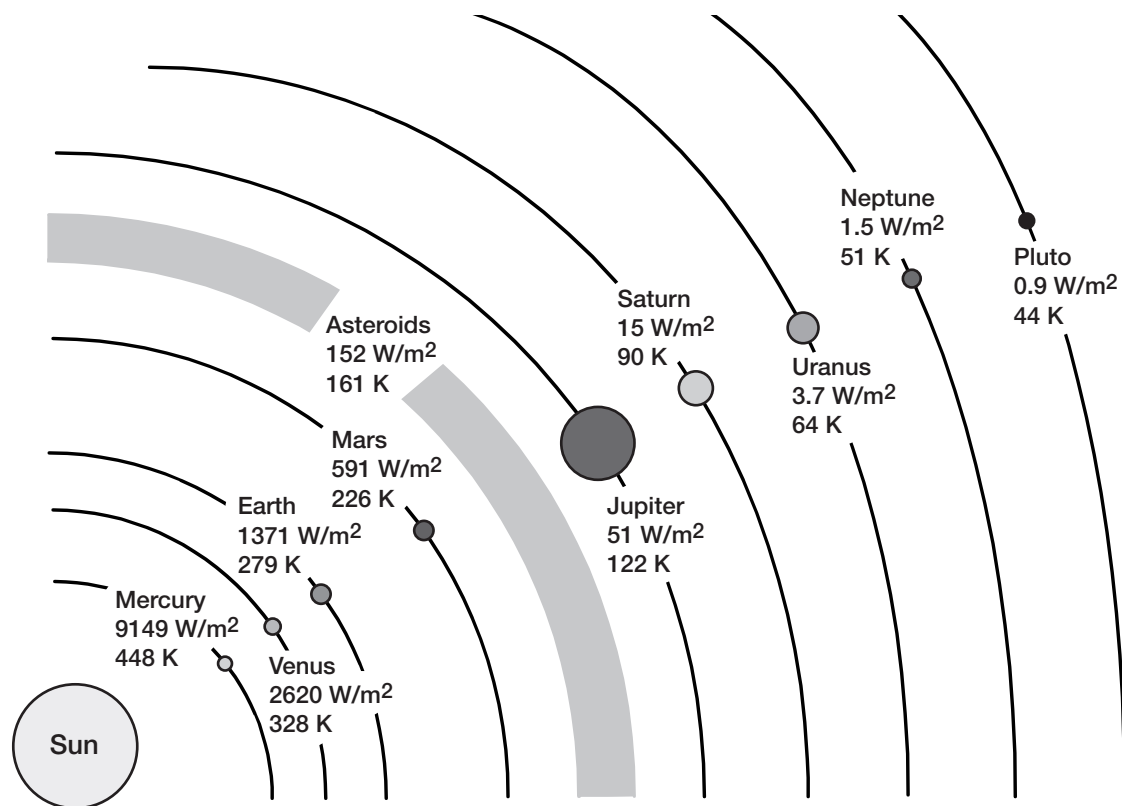


Figure 2.—Solar heat flux and spacecraft surface temperatures at various planetary orbit distances.

TABLE 2: SINK TEMPERATURE -TS- AS FUNCTION OF INSOLATION ANGLE AT 1 AU

ILUMANG (DEG)	FV	EPS	AE	AU	TS(K)	QW-WATTS
.00	1.5	.88	.18	1.000	3.0	.0
1.00	1.5	.88	.18	1.000	84.4	.0
2.00	1.5	.88	.18	1.000	100.3	.0
3.00	1.5	.88	.18	1.000	111.0	.0
4.00	1.5	.88	.18	1.000	119.3	.0
5.00	1.5	.88	.18	1.000	126.1	.0
10.00	1.5	.88	.18	1.000	149.9	.0
15.00	1.5	.88	.18	1.000	165.6	.0
20.00	1.5	.88	.18	1.000	177.5	.0
25.00	1.5	.88	.18	1.000	187.2	.0
30.00	1.5	.88	.18	1.000	195.2	.0
35.00	1.5	.88	.18	1.000	202.0	.0
40.00	1.5	.88	.18	1.000	207.9	.0
45.00	1.5	.88	.18	1.000	212.9	.0
50.00	1.5	.88	.18	1.000	217.2	.0
55.00	1.5	.88	.18	1.000	220.9	.0
60.00	1.5	.88	.18	1.000	224.0	.0
90.00	1.5	.88	.18	1.000	232.2	.0

TABLE 3: GEOSTATIONARY ORBIT EQUILIBRIUM TEMPERATURE AT NEAR ECLIPSE

ILUMANG (DEG)	ALTITUDE	FV	TR-K	TS-K	AE	AE2	AU	QW-WATTS
SUN EARTH	(K-KM)							
.1 1.0	35.88	1.0	300.0	59.5	.18	.80	1.000	.0
.1 2.0	35.88	1.0	300.0	64.6	.18	.80	1.000	.0
.1 3.0	35.88	1.0	300.0	68.7	.18	.80	1.000	.0
.1 4.0	35.88	1.0	300.0	72.2	.18	.80	1.000	.0
.1 5.0	35.88	1.0	300.0	75.2	.18	.80	1.000	.0
.1 6.0	35.88	1.0	300.0	77.9	.18	.80	1.000	.0
.1 7.0	35.88	1.0	300.0	80.4	.18	.80	1.000	.0
.1 8.0	35.88	1.0	300.0	82.6	.18	.80	1.000	.0
.1 9.0	35.88	1.0	300.0	84.7	.18	.80	1.000	.0
.1 10.0	35.88	1.0	300.0	86.6	.18	.80	1.000	.0

Concluding Remarks

A detailed derivation of the constitutive equations and relationships, which describe radiant energy exchange in space, has been completed and used as the basis for developing a computational code. The equations describe a spectrum of heat transfer mechanisms, including: solar or stellar radiation; reflected planetary radiation, also referred to as albedo; direct planetary radiation in the infrared portion of the electromagnetic spectrum; and any onboard generated heat that needs to be rejected to the space environment.

To rapidly evaluate any or a combination of the above heat transfer mechanisms a comprehensive multioptional computer code, TSCALC, was developed and tested against some independent determinations and measurements found in the literature. Results have also been used to determine equilibrium space sink temperatures for some specific applications.

References

Goldman, D.T. and Singer, S.F.: "Studies of a Minimum Orbital Unmanned Satellite of the Earth (MOUSE), Part III Radiation Equilibrium and Temperature," *Astronautica Acta*, Vol III, 1957.

Gordon, Gary D.: "Spacecraft Technology; Part II, Chapter 7—Thermal Control" *Comsat Laboratories*, March 1982, pp. 7-1 to 7-44.

Juhasz, Albert J., Tew, Roy C., and Thieme, Lanny G.: "Design and Analysis Code for Heat Pipe Radiators of Stirling Power Systems Applicable to Deep Space Probes" (Presented at the 11th International Heat Pipe Conference, Tokyo, Japan, Sept. 12-16, 1999.)

Rittenhouse, John B., and Singletary, John B. "Space Materials Handbook", Lockheed Tech. Report AFML-TR-60-205, 1968.

THERMAL DESIGN AND ANALYSIS OF THE STRATOSPHERIC AEROSOL AND GAS EXPERIMENT III (SAGE III) FOR THE ISS MISSION

Dana C. Gould

National Aeronautics and Space Administration
Langley Research Center
Hampton, Virginia 23681-2199

ABSTRACT

The Stratospheric Aerosol and Gas Experiment III (SAGE III) instrument is the fifth in a series of spaceborne remote sensing instruments developed by NASA Langley Research Center (LaRC) for monitoring global distribution of aerosols and gaseous constituents using the solar occultation approach. SAGE III will provide global profiles of atmospheric aerosol, ozone, water vapor, nitrogen dioxide, nitrogen trioxide, temperature, and chlorine dioxide in the mesosphere, stratosphere, and troposphere. The instrument is designed to be completely self-calibrating making it well-suited for long-term monitoring of atmospheric species which are important for global change study. To help achieve the desired long-term global coverage, three instruments have been built for different missions.

The thermal design of SAGE III is primarily passive using surface finishes and high thermal resistance spacers. Active thermal control consists of operational and survival heaters along with a thermoelectric cooler to maintain the CCD detector temperature within tolerances. While the overall thermal design is consistent among the three instruments, some modifications were necessary to meet the individual mission requirements.

The first SAGE III instrument is scheduled for launch on the Russian built METEOR-3M spacecraft in December 2000. This 2.5-ton spacecraft is 5 meters long and 1.5 meters in diameter and will fly a sun-synchronous, polar orbit at an altitude of 1020 km. The second instrument will fly on the International Space Station using an EXpedite the PROcessing of Experiments to Space Station (EXPRESS) Pallet Adapter. This flight has been particularly challenging for designers because of the constraints of the ISS as well as the differences in program schedules (the SAGE instrument has been fabricated and delivered while the EXPRESS project has yet to reach PDR.) For example, the attitude of the ISS can vary substantially making solar occultation difficult. To overcome this, a pointing system was added to the SAGE III instrument. However, the attitude variations also affect the instrument's thermal environment and therefore must be considered in the design of its thermal control system. This, along with other issues related to the thermal design of the SAGE III instrument for the ISS mission are presented in this paper.

INTRODUCTION

Program Background

The Stratospheric Aerosol and Gas Experiment III (SAGE III) project was authorized in 1991 under NASA's Earth Observing System (EOS) Program. SAGE III will provide data on the vertical distribution of aerosols and ozone in the Earth's atmosphere from the upper troposphere through the stratosphere. Profiles of certain trace gases that are important for the study of radiative and chemical processes in the atmosphere will also be obtained along with temperature distribution data in the stratosphere and mesosphere. SAGE III is the fifth in a series of spaceborne remote sensing instruments that have been obtaining climatic data for over 20 years. SAGE III will extend this data set into the future adding long-term data to enable a better understanding of climate and climate change.

To obtain the desired global coverage three instruments have been developed. The first instrument will fly on Russia's METEOR-3M spacecraft, scheduled for launch in December 2000. This spacecraft has a sun-synchronous orbit providing high latitude data (50 to 80 degrees North, and 30 to 50 degrees South). The second instrument will fly as an attached payload on the International Space Station (ISS). ISS's 51°-inclined orbit will allow this instrument to obtain data over the middle latitudes while also having some overlap at the higher latitudes with the METEOR instrument. A mission for the final instrument has not been selected, so it continues to serve as a backup until a launch is identified.

The three instruments were manufactured by Ball Aerospace in Boulder, Colorado. Approval for Phase C/D development was given in 1994 and the final instrument was delivered this year. The METEOR instrument has been shipped to the Russian Space Agency and integrated onto the METEOR-3M spacecraft. It is currently undergoing checkout testing. The last two instruments are currently in storage at NASA LaRC.

General Instrument Description

SAGE III uses the solar occultation technique for obtaining data. In this method, the instrument focuses on the sun during satellite sunrise and sunset events. As the sun rises, or sets depending on the event, its light is attenuated by the earth's atmosphere. By measuring the amount of attenuation at specific wavelengths, the constituents of the atmosphere can be determined. By continuing to operate for a short time after a sunrise or before a sunset, data for unattenuated sunlight can be obtained and used for calibration. This enables SAGE III to be self-calibrating. As SAGE III is the fifth in a series of instruments employing this technique, the method is well-established, has demonstrated good vertical resolution, high signal-to-noise ratio, and excellent accuracy with durability and long life. In addition, SAGE III will increase its global coverage by implementing lunar occultation. As the name suggests, this technique is the same as solar occultation except that sunlight reflected off the moon is used as opposed to direct solar light.

The SAGE III instrument consists of the Sensor Assembly (SA), the Instrument Control Electronics (ICE), and the Data Storage Unit (DSU). Figure 1 shows the major components of the SA. The top portion of the sensor is called the scan head and consists of the elevation scan mirror, solar attenuator, contamination door, motors, electronics, and scan head housing. Light enters the instrument through the aperture and is reflected off the scan mirror down through the azimuth tube to the telescope. The scan mirror motor rotates the mirror back and forth from the top of the solar (or lunar) disk to the bottom of the disk during data taking events. For solar events, a solar attenuator is inserted in the optical path to prevent saturation of the detector.

The mid-section of the SA is called the azimuth. Its major components include the telescope, azimuth tube, azimuth bearings, azimuth motor, azimuth housing structure, and the azimuth cover. The azimuth tube connects the scan head at its top to the spectrometer at its bottom. The telescope is located just above the spectrometer and consists of a primary and secondary mirror that focus the light on to the spectrometer's 30 x 300 μm entrance slit. The base of the azimuth structure is used for mounting the sensor assembly. The azimuth cover is a primary thermal control surface and functions as the SA radiator for the ISS mission.

The spectrometer is located at the bottom of the SA and consists of a fold mirror, diffraction grating and the detector assembly and associated electronics. The CCD detector is mounted on a thermoelectric cooler (TEC) to maintain a low, uniform, and stable operating temperature. Not shown in the figure are two electronics boards located just below the spectrometer and a thermal shroud that encloses both the spectrometer and electronics. The electronics boards provide power to and control the CCD/Detector package while the actively controlled thermal shroud provides a stable, uniform environment for the spectrometer thus minimizing thermal distortion of the optical path.

To acquire data, the scan head must be pointed at the sun (or moon). The scan head, azimuth tube, and spectrometer are assembled together and rotate in the azimuth housing to point the scan head at the sun (or moon) during an event. This points the sensor in the "horizontal direction", and once this has been done, the elevation mirror scans "vertically" to locate the sun and the instrument begins taking data. During the data acquisition period, the elevation mirror continues scanning, moving continuously between the top and bottom of the solar disk as the sun rises (or falls). The data is processed and then stored in the DSU until it can be downloaded.

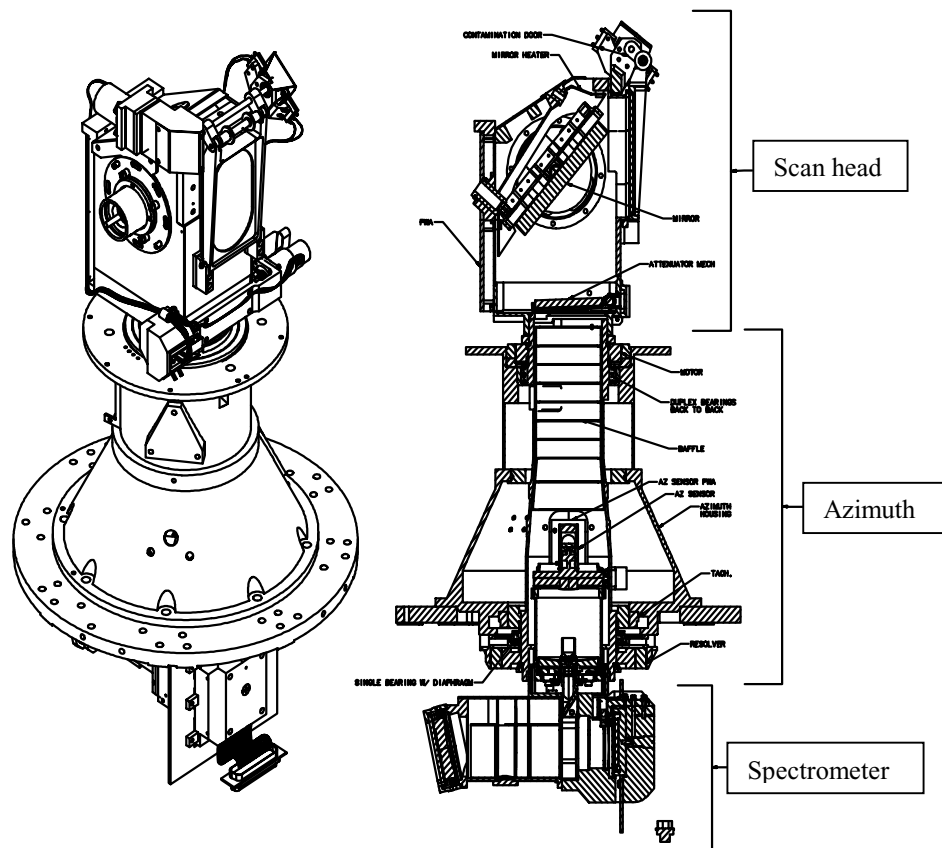


Figure 1. SAGE III Sensor Assembly (SA)

ISS Mission Issues

SAGE III will fly on the International Space Station (ISS) as one of the EXPRESS payloads. Flying on the ISS presents the SAGE III project with some unique challenges. The first of these challenges comes from the relatively tight pointing requirements of the instrument. SAGE III has been designed to fly on spacecraft that provide pointing to the Earth nadir within $\pm 1^\circ$. The ISS attitude can vary substantially more than that, so SAGE III required an external pointing system to compensate. In consideration for early utilization of ISS, the European Space Agency (ESA) agreed to provide a Hexapod pointing subsystem that would meet the SAGE III pointing requirements.

The pointing system consists of a Hexapod Mechanical Assembly (HMA) and Hexapod Electronics Unit (HEU). The HMA is essentially two rings attached by six actuators. The SAGE III SA mounts to the top ring of the HMA and the bottom ring of the HMA is attached to the EXPRESS Pallet Adapter (EXPA). By varying the length of the various actuators, the two rings move relative to each other to keep the SAGE instrument pointed in the nadir direction while the ISS (and therefore the EXPRESS pallet) moves due to attitude fluctuations. The entire SAGE III/Hexapod payload is shown on its EXPA in Figure 2. The payload consists of the following six major components: the SAGE III SA, ICE box, DSU, HMA, HEU, and the Interface Adapter Module (IAM). The IAM is being developed at NASA LaRC to provide a single electrical interface between the EXPRESS Pallet and both the SAGE III and Hexapod instruments.

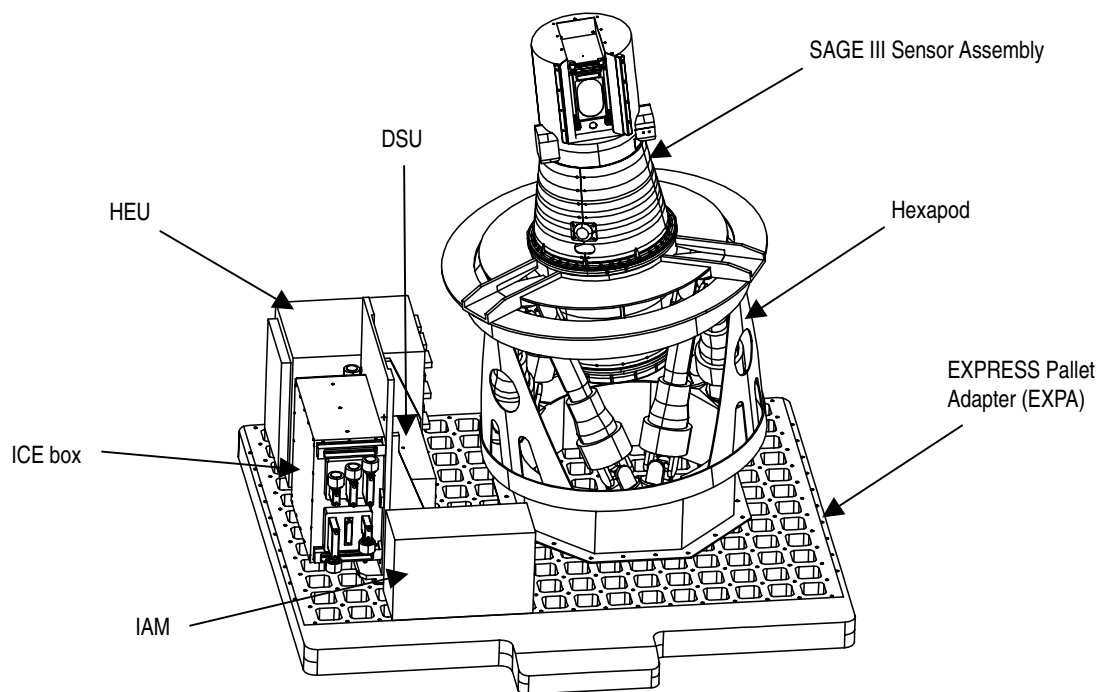


Figure 2: Sage III/Hexapod Payload

The Hexapod system has a long heritage of successful ground applications but has never been developed for flight. The design for the Hexapod flight system was therefore significantly behind (about four years) the SAGE III development. In addition, the design of EXPRESS is nearly two years behind the design of Hexapod. Thus the second major challenge for the SAGE III project is to successfully integrate these three systems which are in various phases of development. The difficulty lies in the instrument's need for definition of interface requirements and spacecraft services in order to complete their designs. However, the payload carrier is so early in its development that it is difficult to determine many of the interfaces to the level of detail needed by the payloads. In addition, the carrier has to ensure that its interface is robust enough to accommodate a variety of payloads.

One example of the schedule problem is the thermal design. The SAGE III instrument has been fabricated and is currently in storage NASA LaRC waiting for integration with Hexapod. Thus any changes to the thermal environment that was assumed in the SAGE III thermal system design could require hardware modifications to the instrument. The Hexapod project is currently in preparation for CDR; however, it is having difficulty meeting the preliminary requirements of the EXPRESS project. The reason for this is that since the EXPRESS project is so early in its design cycle (it is yet to reach PDR), the thermal analyses used to set the interface requirements have been based on extremely conservative assumptions. The cognizant engineers from both the EXPRESS and SAGE projects agree that the requirements are overly conservative, but until the design can be developed further, it would be imprudent to relax these assumptions.

Another issue related to the relative immaturity of the EXPRESS project is that SAGE III's neighboring payloads have yet to be defined on the EXPRESS pallet. Figure 3 shows a concept for a fully populated EXPRESS pallet, with SAGE III occupying the forward corner of the view. Each pallet has 6 payload bays arranged in a 2 x 3 grid. SAGE III has a confirmed payload location on its EXPRESS pallet; however the other 5 payloads on the pallet have not yet been selected. The adjacent payloads will directly impact the thermal environment (among others) of the SAGE III/Hexapod payload and must be accounted for in the thermal design of the instruments. Respective components for SAGE III and Hexapod are therefore designed to be thermally isolated from the neighboring

payloads. This will minimize the neighboring payload's influence on the SAGE III/Hexapod payload, but it will not eliminate it. As a result, for each thermal analysis case, the SAGE III/Hexapod thermal design is analyzed twice, first considering that all neighboring payloads fully utilize their envelope, and then considering that the neighboring payloads use none of their envelope (i.e. SAGE III is the only payload on the pallet).

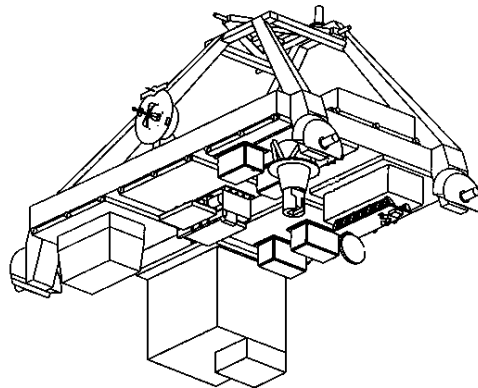


Figure 3: Conceptual view of an EXPRESS Pallet.

This complication ties into the third challenge for the ISS mission of SAGE III, which is to correctly identify and analyze all the critical thermal conditions throughout the mission. For example, although Hexapod will correct for variations in attitudes with regard to pointing the SAGE III instrument, the variations in ISS attitude are large enough (typically $\pm 15^\circ$) to impact the thermal environment of the instrument. Limiting the number of potential attitudes to just a minimum, mean, and maximum value for yaw, pitch and roll gives a total of 27 sub-cases for each beta angle case. Considering both maximum and minimum sized neighboring payloads mentioned above gives 54 sub-cases for each beta angle case. There are additional considerations that could affect the thermal environment of SAGE III as well; for example, the configuration of the ISS will be changing during the SAGE III mission. Some of these issues have been addressed by the analyses done to date, while others will be addressed in future analyses as data and resources become available.

THERMAL DESIGN AND ANALYSIS

Instrument Thermal Design

Since the three SAGE III instruments are to fly on different spacecraft, a primary design goal was to produce a robust design that would be thermally isolated, and thus independent, from the spacecraft. In addition to this goal, the following requirements were placed on the thermal control system:

- five year orbital life
- survive five hours without power
- maintain CCD detector array of 5°C during solar occultation and 23°C for lunar occultation
- maintain CCD temperature stable to $\pm 0.07^\circ\text{C}$ during data taking events
- maintain spectrometer temperature gradients within $\pm 0.006^\circ\text{C}$ during data taking events
- maintain all components within their survival and operating temperature limits
- heat the scan mirror above its surrounding temperature to minimize contamination

The thermal design of the first SAGE III instrument (for the METEOR) was modified because it relied on dissipating most of the SA heat to its mounting structure. Since the SAGE III ISS instrument was to be directly mounted to the HMA, this same approach would have thermally coupled the two components thus requiring an integrated design. To avoid this and allow for the independent design of each instrument's thermal systems a requirement to thermally isolate the SAGE III SA from the HMA (maximum conductance of $0.3 \text{ W}/^\circ\text{C}$) was imposed. Thus, SAGE III had to add a radiator to the SA to dissipate its heat. The azimuth housing cover was selected as the most appropriate

surface for the SA radiator. The base of the SAGE III azimuth hardware was modified to provide an efficient heat path from the spectrometer to the azimuth cover. In addition, the thermal isolators shown in Figure 4 were developed to meet the isolation requirement between the SAGE III SA and the HMA. The titanium isolators are 0.5 in. in length with a 0.5 in. OD and 0.04 in. wall thickness. The bolt and washers are stainless steel and combine with the isolator to give an overall joint conductance of 0.27 W/°C.

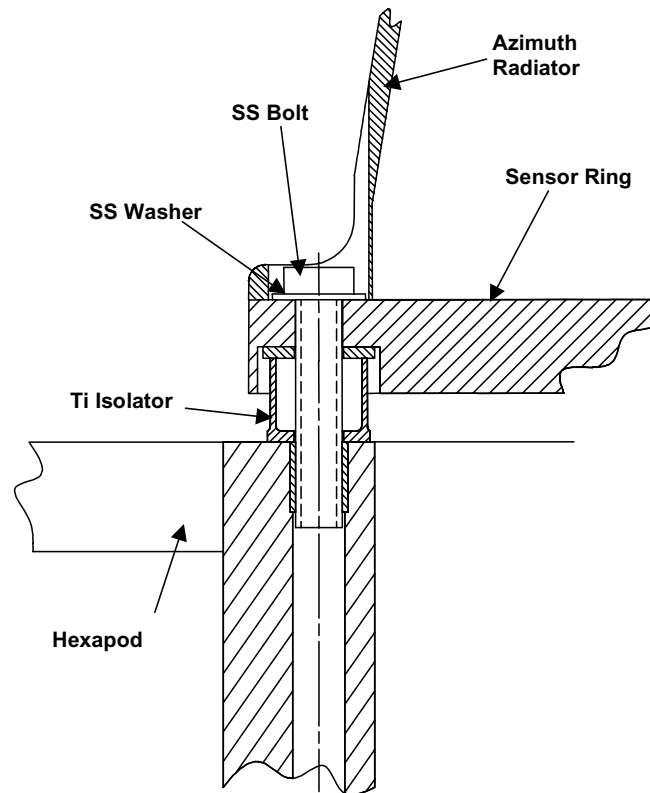
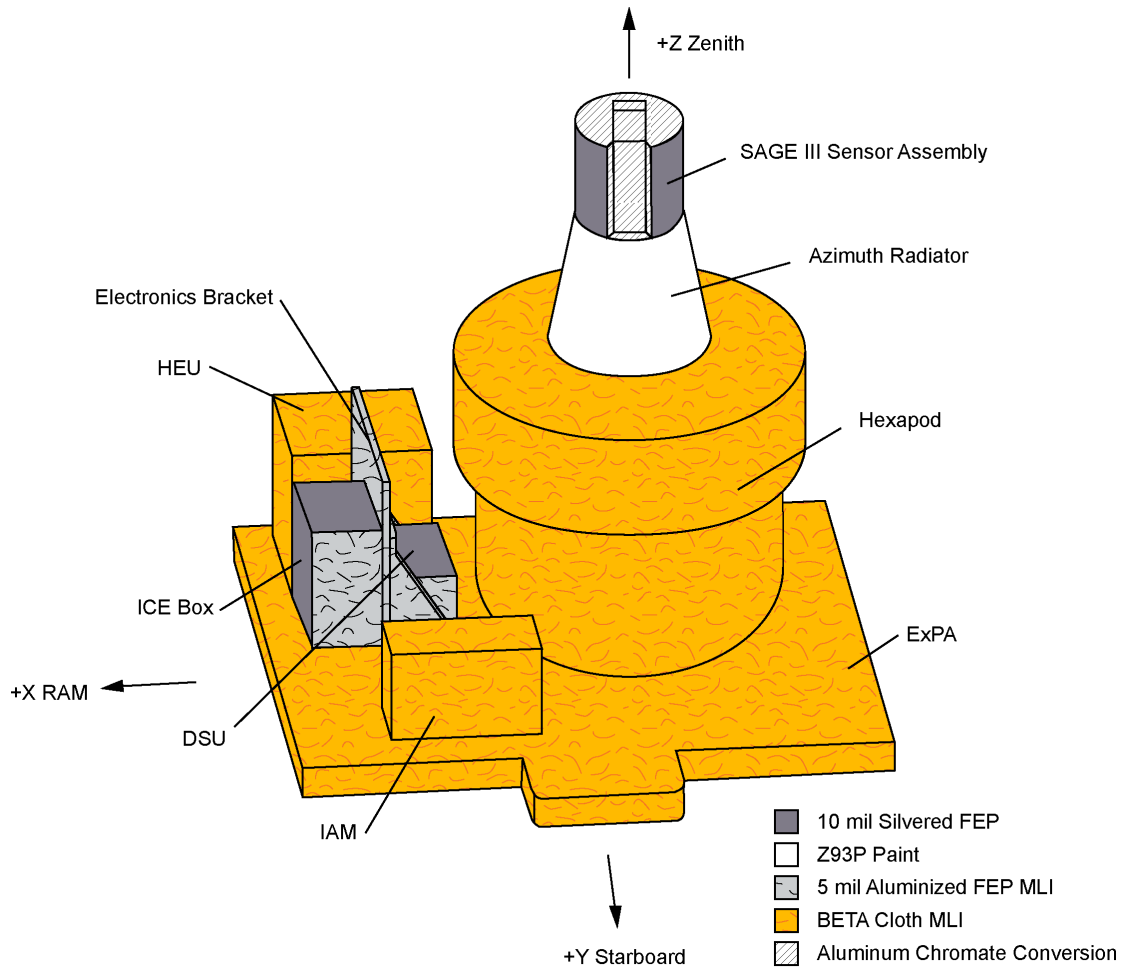


Figure 4: Thermal isolator configuration.

The optical properties of the external surfaces of the SAGE III instrument were also tailored for the ISS mission. The external surfaces of the SAGE III/Hexapod payload are shown in Figure 5 and their corresponding optical properties are listed in Table 1. Beginning Of Life (BOL) properties are based on measured values while End of Life (EOL) properties are estimated from research and heritage. In selecting the thermal control materials for the external surfaces of SAGE III, consideration was given to the atomic oxygen (AO) environment of ISS, which is considerably worse than the METEOR environment. Because of the AO concern, the radiator material on the ICE (ram and nadir faces) and DSU (nadir face) was switched from a 5-mil silvered FEP Teflon to 10-mil. The same concern led to a change in the outer surface of the external MLI blankets from Kapton to 5-mil aluminized FEP Teflon with Nomex netting. Beta cloth was also considered for the outer layer of the MLI blankets, but was not chosen because of concerns with darkening that were observed in the early 1990s. (This problem arose from an unreported change in the fabrication process, and has since been resolved. As indicated in the figure, Hexapod is planning to use it for the outer layer of their MLI blankets.) The MLI blankets consist of 10 layers of polyester netting and 10 layers of aluminized (both sides) Mylar film. The blankets are typically fastened in place with fiberglass studs and washers. Z93P white paint was chosen for the SA radiator over the 10-mil silvered FEP Teflon because of the difficulty in applying the Teflon film to a conical surface. To achieve 100% coverage would have required a number of cuts in the material and the resulting seams would be particularly susceptible to AO erosion. The scan head cover used the same 10-mil silvered FEP Teflon as the ICE and DSU radiators.

Table 1 . Optical Properties of External surfaces.

Description	BOL		EOL	
	ϵ	α	ϵ	α
10-mil, silvered FEP Teflon	0.870	0.067	0.870	0.100
5-mil, aluminized FEP Teflon with Nomex netting	0.803	0.127	0.803	0.150
Z93P paint	0.923	0.137	0.930	0.150
Aluminum Chromate Conversion Coating	0.067	0.269	0.067	0.350



A7275_003[30B]

Figure 5: External surface finishes for thermal control.

The active thermal control systems in the SAGE III design include heaters and a thermoelectric cooler (TEC). Operational Heaters are used to elevate the scan mirror temperature above that of its surroundings to minimize contamination accumulating on its surface. Operational heaters are used to control the spectrometer thermal environment as well. These heaters are mounted on the thermal shroud, which is an aluminum can surrounding the spectrometer. The heaters are thermostatically controlled to keep the shroud at $20 \pm 3^\circ\text{C}$ whenever the instrument is in standby or data acquisition modes. A final set of operational heaters is mounted to the azimuth structure and is also set to maintain a temperature of $20 \pm 3^\circ\text{C}$.

Since the heater elements have a high reliability factor, the azimuth and spectrometer thermal shroud heaters also serve as survival heaters. Additional survival heaters are located on the ICE and DSU boxes and have the same set points as listed above. The heaters have been sized for a low voltage condition (25V vs. the 28V nominal).

The final active thermal control element is the thermoelectric cooler (TEC) which is used to maintain a relatively cool, stable thermal environment for the CCD detector. The detector is mounted on the cool side of the TEC, while the hot side of the TEC is mounted to a large aluminum block that serves as a radiation shield as well as a thermal sink. This heat sink forms one end of the spectrometer and radiates its heat to the spectrometer thermal shroud. Since the spectrometer thermal shroud is also actively controlled, the detector is effectively controlled by two independent systems one inside of the other. In addition to providing the TEC a uniform heat sink, the thermal shroud also provides a uniform environment for the spectrometer, thus minimizing any potential gradients in the spectrometer and meeting the requirement to maintain the spectrometer temperature gradients within $\pm 0.006^{\circ}\text{C}$ during data taking events. (Note it is not possible to directly verify this requirement; verification is inferred from the calibration results during ground testing.)

ISS Analysis

The thermal analysis of SAGE III consists of a set of Geometric Math Models (GMMs) and Thermal Math Models (TMMs). The GMMs use the Thermal Radiation Analyzer System (TRASYS) to compute radiation conductors and orbital fluxes. The TMMs use the Thermal Analysis Kit III (TAK3) program to compute steady state and transient temperatures.

The ISS's orbit is inclined at 51.6° and its altitude will vary from 351 to 460 km with an orbital period of approximately 90 minutes. The SAGE III is scheduled for deployment on ISS mission UF-4 in 2003. The payload will be located in the ram-starboard location of the nadir-outboard EXPRESS pallet. The pallet, shown in Figure 6, will be located at the S3 truss location. As mentioned above, the thermal analysis of the SAGE III/Hexapod ISS mission is complex involving many variables. But because the SAGE III project was significantly ahead of the EXPRESS project, the thermal design of the instrument was carried out using an extremely simplified model of the ISS and the EXPRESS pallets. The TRASYS models included only the starboard solar arrays and radiator, and several MLI screens representing the neighboring payloads. Because of SAGE III's outboard starboard-nadir location on the EXPRESS pallet, the neighboring payloads effectively blocked the instrument's view of the entire ISS. The only hardware not blocked by the neighboring payloads are the starboard solar array and radiator, which are farther outboard than the EXPRESS pallet (see Figure 6). These models also assumed a fixed solar array position, which greatly simplified the model. Figure 7 shows the external TRASYS model and Figure 8 gives a close-up of the SAGE III/Hexapod payload.

ISS's 51.6° inclination angle produces a beta angle variation of $\pm 75^{\circ}$. The -75° case produces the hottest environment as the solar flux illuminates the pallet from the starboard side. Starboard facing surfaces are hit by the flux directly while port facing surfaces get a significant flux off the neighboring payloads. The coldest case occurs at a beta angle of $+75^{\circ}$ when the solar flux is coming from the port side of the pallet and the neighboring payloads effectively shade the SAGE III Hexapod payload. The surface property, orbital, and flux parameters used in the GMMs are given in Table 2.

The SAGE III TMMs are based on the thermally balanced TMM from the METEOR mission with modifications to account for the hardware changes unique to the ISS instrument. The model consists of approximately 270 nodes and over 5200 conductors. The vast majority of conductors are radiation conductors including both radiation transfer external and internal the instrument. Transient and steady state TMMs for the following cases were generated

- Hot conditions (beta angles of -60° and -75°)
- Cold operational
- Cold survival
- Transfer - five hour no power (transient only)

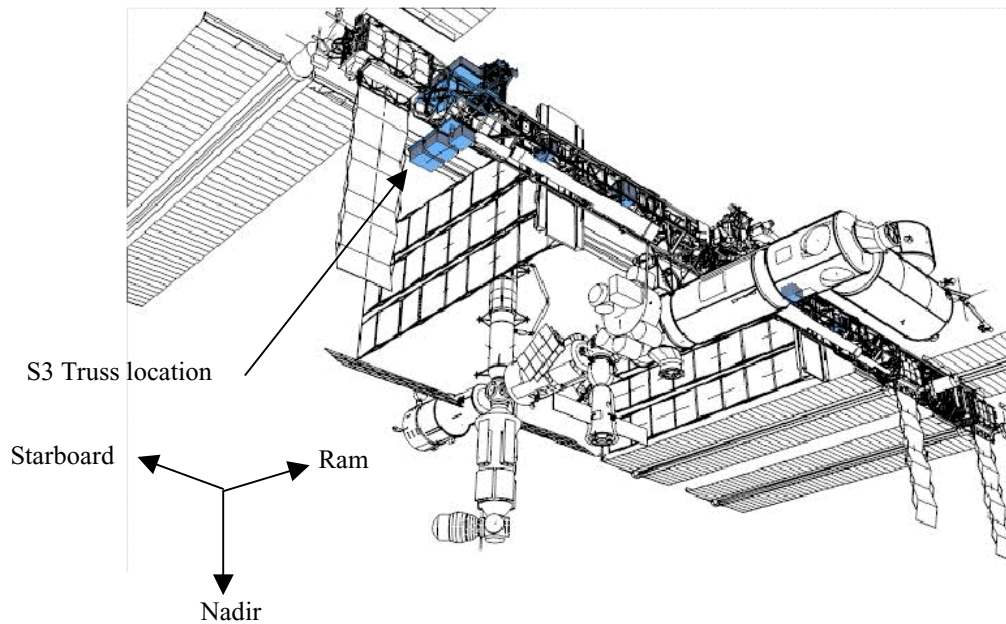


Figure 6 : SAGE III/Hexapod EXPRESS Pallet Adapter on ISS

Table 2: Orbital Flux Parameters

Description [units]	Cold	Hot
Surface Properties [-]	BOL	EOL
Solar Flux [W/m^2]	1320	1423
Earthshine [W/m^2]	206	241
Albedo [-]	0.20	0.32
Altitude [km]	460	352
β -angle [$^\circ$ from orbit plane to solar vector]	75	-75

Table 3 shows the orbital flux case, instrument status, power status, and boundary conditions for each case. Note the extremely cold EXPA boundary temperatures in the table. These temperatures are the worst case temperature predictions used in designing the EXPA. They are based on a bare aluminum plate exposed to full sun in the hot case and deep space in the cold case. However, at this early stage of the EXPRESS project, they are the only temperature predictions for the EXPA and have thus become the interface requirements that the payloads must meet. It is anticipated that the EXPA temperatures will moderate considerably once the effects of active payloads and thermal blankets are considered.

Initial runs of the hot case at a beta angle of -75° indicated problems maintaining the CCD detector within its operating range for solar events. Several options, mostly based on increasing the SA radiator area were investigated but proved ineffective. However, the CCD can operate at higher temperatures for lunar events without degrading the science data, and it turns out that solar events are not possible at beta angles below -60° (or greater than $+60^\circ$ for that matter). Hot case analysis at a beta angle of -60° verified that the instrument would operate within temperature limits at that beta angle. The instrument software was then modified to allow the detector to run at a higher temperature for the lunar events occurring below a beta angle of -60° .

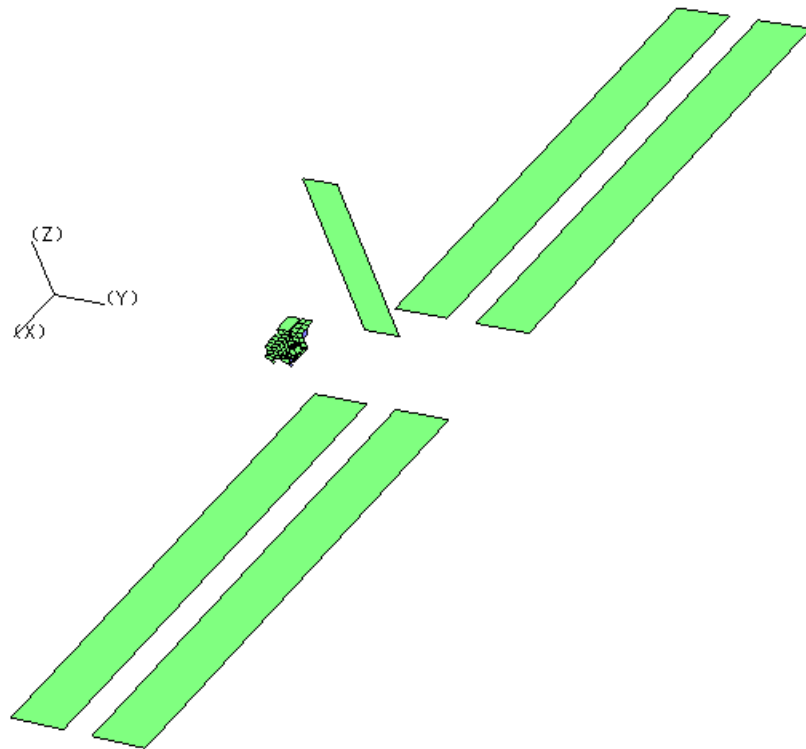


Figure 7 : TRASYS model used in SAGE III design analysis.

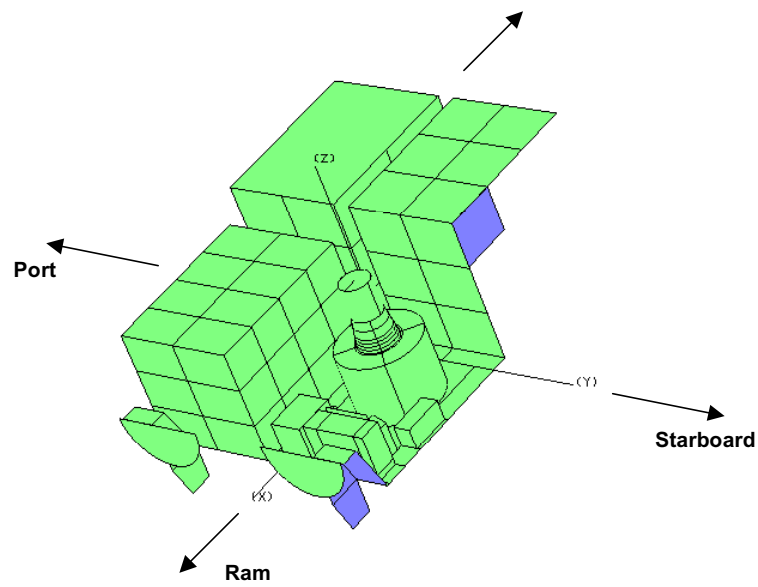


Figure 8: SAGE III ExPA Layout

Table 3 : Environment, power, and interface parameters for the thermal analysis cases.

Description [units]	Case			
	Cold	Hot	Survival	Transfer
TRASYS Case [-]	Cold	Hot	Cold	Cold
Operational Power Factor [-]	0.9	1.0	-	-
Scan [-]	Yes	Yes	No	No
Instrument Power [-]	Yes	Yes	No	No
Heater Power [W]	25	30	25	0
ExPA Boundary Temperature [°C]	-107	38	-107	-129
Hexapod Boundary Temperature [°C]	0	35	-10	-10
Interface Conductance to ExPA [W/K]	0.26	0.26	0.26	0.26
Interface Conductance to Hexapod [W/K]	0.27	0.27	0.27	0.27

Results for the two hot cases are shown in Table 4. The temperatures listed include a 5°C margin to account for uncertainty. Temperatures are all within their limits except for the CCD shield. The limit listed for the CCD shield applies only to the $\beta=-60^\circ$ so the prediction of 41°C results in a reduced margin (from 5°C to 4°C).

Table 4: On-Orbit Hot Case Temperature Predictions

Description	Hot		
	$\beta=-75^\circ$	$\beta=-60^\circ$	Limit
CCD shield	51	41	40
Spectrometer barrel, zenith	50	40	50
ICE Box	38	34	55
DSU	39	34	55
Spect. Thermal Shroud, -Y	44	33	50
CCD Controller PWA	53	43	55
Azimuth Housing, zenith	43	32	50
Scan Head Panel, nadir	37	27	50
Sensor Ring, +Y	41	30	50
Azimuth Outer Housing, -X	39	28	50

All temperatures in °C

All temperatures include 5°C margin

Results for the cold, survival, and transfer cases are shown in Table 5. The ICE box and DSU exceed their temperature limits in the cold operational and survival cases, and just reach their limits at the end of the transfer case. These results are based on the extreme cold boundary conditions discussed earlier, and additional analyses have shown that with a more reasonable value for the ExPA temperature (value provided by the EXPRESS project) the instrument will not exceed its temperature limits.

The SAGE III thermal analysis is continuing with a second generation of TRASYS models that include full models of the ISS and EXPRESS pallets. These models have significantly more surfaces and include fully articulating components (solar arrays, radiators). Although the resulting radiation conductors and orbital heat flux data sets are post-processed to extract only the most relevant data for the SAGE III/Hexapod payload, the resulting data files are quite large. These data sets have been incorporated into the SAGE III thermal models and are also being used for Hexapod thermal analyses. In addition to providing more refined environmental data, these models begin to explore some of the complicating factors of the ISS mission mentioned earlier. These models include additional mission phases (cargo-bay cases, ISS approach cases, cargo-bay docked to ISS, etc.), off-nominal attitudes, and minimum and maximum neighboring payload envelopes. The SAGE III project is working with the EXPRESS project and

Hexapod developer Alenia Aerospazio to identify additional critical thermal analyses cases and refine interface requirements; however, the relative immaturity of the EXPRESS design continues to be a problem. In particular, significant problems exist in designing the Hexapod to the extreme cold EXPA interface temperature defined by EXPRESS. These analyses also confirm the SAGE III results just presented that indicate the SAGE III hardware will have to be modified unless relief from the extreme thermal environments is obtained.

Table 5: On-orbit Cold Case Temperature Results

Description	Cold $\beta=+75^\circ$	Op. Limit	Steady State Survival	Translation	Non-op. Limit
CCD shield	17	-25	4	4	-30
Spectrometer barrel, zenith	17	-25	4	6	-30
ICE Box	-30	-25	-38	-30	-30
DSU	-31	-25	-39	-30	-30
Spect. Thermal Shroud, -Y	14	-25	4	-12	-30
CCD Controller PWA	23	-25	5	-10	-30
Azimuth Housing, zenith	15	-25	13	-2	-30
Scan Head Panel, nadir	-7	-25	-30	-17	-30
Sensor Ring, +Y	7	-25	-1	-13	-30
Azimuth Outer Housing, -X	3	-25	-4	-15	-30

All temperatures in $^\circ\text{C}$

All temperatures include 5°C margin

CONCLUSION

Thermal analyses of the SAGE III ISS instrument show acceptable temperatures except for the DSU, ICE, and CCD shield components. The thermal design of the SAGE III/Hexapod payload on ISS has proven to be a challenging task because of the complexity of the spacecraft and hardware as well as technical issues arising from the difference in design maturity of the three projects involved. The complexity of the thermal models along with the large number of variables affecting the thermal environments require careful consideration to produce a reasonable number of thermal cases that can be analyzed. The thermal analyses to date have been based on conservative interface conditions due to the lack of maturity in the EXPRESS design. Results from these analyses indicate that without relief from the severe interface boundary conditions, modification to the SAGE III hardware will be required. In addition, no thermal design for Hexapod has been developed that can meet the current interface requirements. However, it is believed that as the design of the EXPRESS matures, the severity of the thermal environments will diminish.

ACKNOWLEDGMENTS

The thermal models described here were substantially developed by Armen Melikian and Adrian Nagle of Ball Aerospace & Technologies Corporation under contract NAS1-18900.

REFERENCES

Ball Aerospace & Technologies Corporation, *Thermal Analysis and Mathematical Models for the ISS Mission of the Stratospheric Aerosol and Gas Experiment (SAGE III)*, Contract No. NAS1-18900, IN0053-220, DRL Item 69-Rev. C., October, 1999.

Ball Aerospace & Technologies Corporation, *Thermal Analysis and Mathematical Models for the METEOR-3M Mission of the Stratospheric Aerosol and Gas Experiment (SAGE III)*, Contract No. NAS1-18900, DRL Item 69-Rev. B., September, 1998.

Ball Aerospace & Technologies Corporation, *ISS Flight Instrument Operations Manual for the Stratospheric Aerosol and Gas Experiment (SAGE III)*, Contract No. NAS1-18900, IN0053-220, DRL Item 96, August, 1999.

NASA Langley Research Center, *SAGE III/Hexapod/ISS Interface Design Specification*, Revision 1.3, July, 1999.

SSP 52000-IDD-EPP, *EXpedite the Processing of Experiments to Space Station (EXPRESS) Pallet Payloads Interface Definition Document*, Working Draft 2, December, 1999.

SSP 52000-PAH-EPP, *International Space Station Payload Accommodations Handbook EXpedite the PProcessing of Experiments to Space Station (EXPRESS) Pallet Payloads*, Working Draft, October, 1999.

THERMAL ANALYSIS OF AN MEMS BROADBAND LIGHT SOURCE

Eric Golliher

National Aeronautics and Space Administration
Glenn Research Center
Cleveland, Ohio 44135

ABSTRACT

Thermal Synthesizer System (TSS) was used to perform a thermal assessment of a proposed broadband light source. The device uses MEMS (Microelectromechanical Systems) technology to form structural and thermal components of the package. Silicon and Silicon Nitride are the primary structural materials. The Tungsten filament will radiate as a blackbody at 2650 °C. The analysis shows that the detector located near the bottom of the device will be sufficiently cooled without any special effort, despite the close proximity to the filament. Also, the transparent Silicon Nitride window will remain below maximum temperature limits.

INTRODUCTION

A team consisting of engineers and scientists from JPL, Glenn Research Center (GRC) and Lighting Innovations Institute are developing a MEMS-based, low-power, incandescent broadband light source for aeronautics and spacecraft applications. Since the predicted temperature of the Tungsten element is very high, concern was raised as to whether the Tungsten element would overheat other components within the device. The Thermo-mechanical Systems Branch (5490) at GRC was asked to briefly review the preliminary design and make comments and suggestions with regard to thermal characteristics of the device. The following paper attempts to answer some of the concerns and document results for future efforts. A description of the device is provided, with comments as to the thermal design aspects of the components. A preliminary TSS model is described which includes detailed finite difference thermal model nodalization of the MEMS structure and all thermal characteristics. Temperature predictions for the four reference analysis cases are included. Design techniques at the MEMS level for thermal control are discussed. Further recommendations for additional thermal design considerations and analysis are provided.

BACKGROUND

This MEMS device is a broadband light source which can be used to interrogate optical sensors or as a calibration light source for spectrometers. The narrow bandwidth of commercially available lasers and light emitting diodes makes them unsuitable for the applications intended for this device. Also, the commercially available broadband light sources are heavy, bulky, expensive, short-lived, and dissipate relatively large amounts of heat.¹

The packaged device is very small, measuring approximately 1.2 mm thick by 8 mm length and 5.4 mm width. Several alternating layers of Silicon, Silicon Nitride, Silver Oxide, and Titanium/Platinum/Gold build the basic mechanical structure. A square cavity in the center of this “box” suspends a spiral Tungsten filament. The filament emits light and heat that bounces off the reflective walls of the cavity and exits through the Silicon Nitride window at the “top” of the device. The light travels some distance to a separate sensor. Below the filament, attached to the lower-most layer, is a detector that must be kept cool. This detector provides a reference signal for comparison to a signal from a sensor located far from the filament. Further function and application background can be found in Reference 1.

The small size of the device has several engineering advantages over state-of-the-art (SOA). The mechanical design integration on to the platform is simplified greatly due to the small size. Further, by reducing the size and optimizing the filament geometry, the thermal power dissipation (waste heat) is reduced, and the resultant thermal impact on the platform is minimized. The low-weight advantages are especially attractive in airborne and spacecraft applications.

THERMAL MODEL

TSS for Windows NT from Space Design version 9.1 Revision D was used to model the device because of past familiarity by the author. Many other thermal analysis packages would have been suitable. The accompanying necessary external programs were Hummingbird Exceed 3D Version 6.2 and Compaq FORTRAN. The platform was a Dell Optiplex GXi 200 MHz Windows NT machine purchased in July of 1997 with 64 MB of RAM. No “computer problems” were encountered during the model build-up or execution.

For the purposes of this paper, the author will refer to “conductivity” and “emissivity” as a property *independent* of geometry and intrinsic to the material with units $[W/m^2 K]$. The author will use “conductance” and “emittance” as a property *dependent* on the geometry with units of $[W/K]$. The author realizes that these terms are frequently interchangeable both in the literature and in common practice. The entire model used SI units.

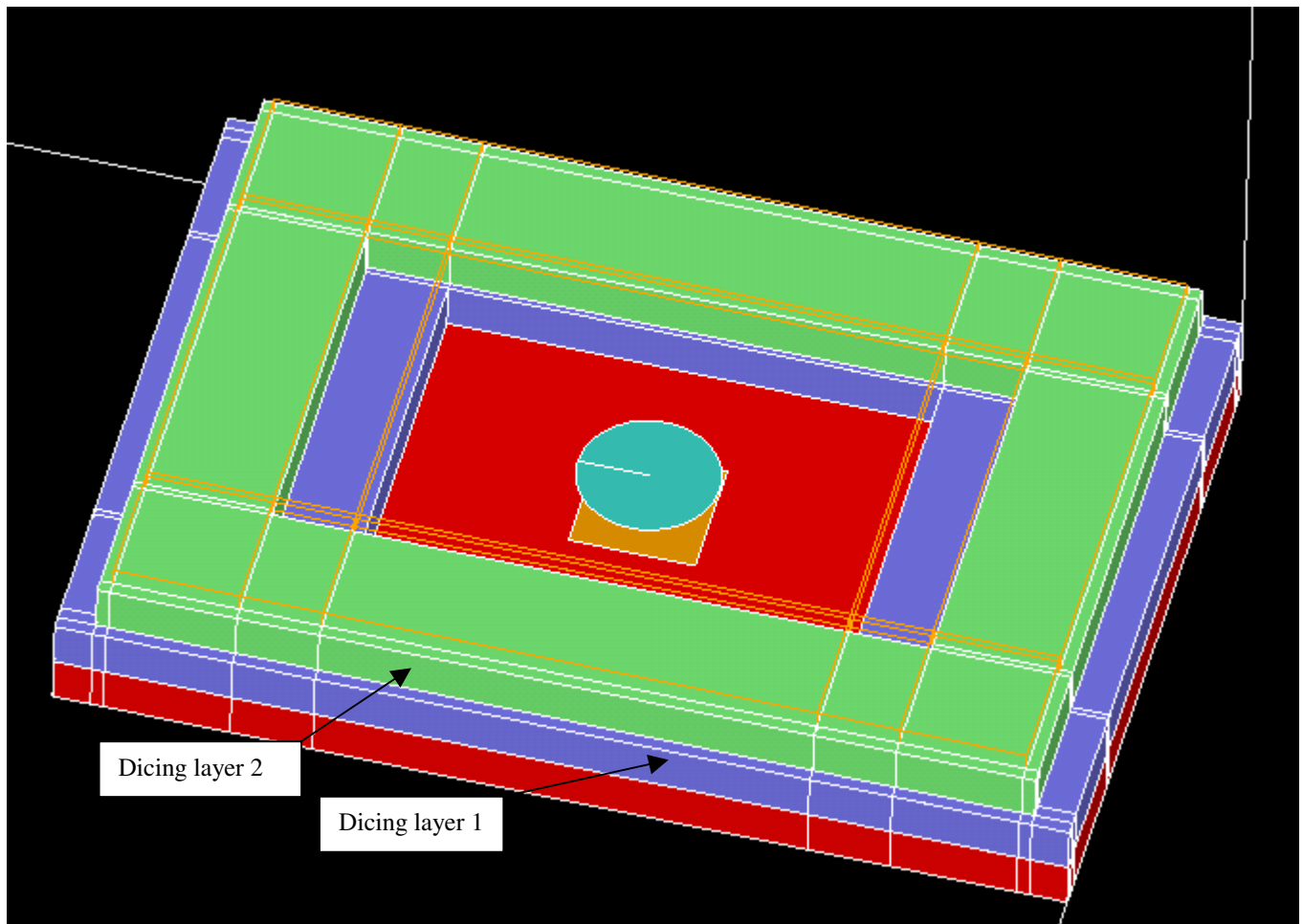
There were four different cases analyzed representing four different environmental conditions. Case 1 considered the device to be in vacuum with heat conduction to a heat sink on the bottom of the device. Case 2 considered vacuum, but no heat sink. Case 3 was in air with a fan directed on the device and a heat sink on the bottom layer. Case 4 considered a fan directed towards the device but no heat sink. All cases included thermal radiation. The total heat dissipated by the filament was 1.35 Watts¹.

Conduction Model - The total number of nodes was 229. TSS nodes corresponded exactly to SINDA nodes. SINDA is a typical well-known spacecraft thermal analysis tool, and is used as the thermal analyzer application in TSS. It is an acronym for Systems Improved Numerical Differencing Analyzer. In the 1960's, TRW Systems was awarded a contract to improve a generic thermal analyzer. TRW gave this improved software the company name. SINDA has since been improved by many companies and organizations since that time, but is still a popular thermal analysis tool for the aerospace industry. Solids were used for the structural layers and divided into enough nodes such that every node had a square interface to the adjacent node. ConCap, the conductor calculator application in TSS, was used to determine the linear conductors between nodes. There are basically three layers of silicon, each with thickness 0.4 mm. Each layer has a coating that is very thin. Because the SiN (Silicon Nitride) insulating layers were only 0.0015 mm thick, they were initially not included in the ConCap calculations. The SiN window was modeled as a square surface covering the entire package. Figure 1 shows this surface, so that the inner thermal model surfaces can be seen. The inner surfaces exposed to the filament light are coated with a very thin layer of AgO₂ for high reflectance. Since the thickness was 0.00002 mm, it was assumed to have no thermal resistance through the thickness and no conductance laterally. Similarly, the Ti/Pt/Au electrical conductor bonding pads were 0.0003 mm thick and not considered in the model. The filament was modeled as a circle surface. The detector was modeled as a square surface in perfect conductance to the bottom layer. The bottom layer was conductive to the heat sink with a value of 150 W/m²K for the contact conductance. This represents some thin layer of filler material such as thermal paste or bonding epoxy between the device and heat sink.

One calculation is worth special attention. The SiN layers are intended to provide thermal insulation, as well as electrical insulation between the silicon layers. However, the SiN layers are only 0.0015 mm thick, while the Si layers are 0.4 mm thick. By comparing the k/l values (conductivity/conductive path length), one can compare the relative conductance of the SiN versus the Si. The conductivity of Si is 148 W/mK, and of SiN, 16 W/mK. If you sandwich four SiN layers in between 2 Si layers, the effective overall sandwich Si/SiN/Si conductance is about 88% of the original Si to Si conductance. The addition of four SiN layers between the Si layers reduces the thermal conductance to only 0.88 of the original value, a relatively small difference. Case 1 was analyzed with the SINDA conductors between dicing layers 1 and 2 multiplied by 0.88. As described in the Results section, this produced less

than 1 °C of difference in the temperature predictions. Even though SiN is a poor thermal conductor, the layers are too thin to provide much thermal insulation between the Si layers. This is due to the conductivity of Si being very high, and that of SiN being very low.

Figure 1. TSS Thermal Model Geometry Application Showing Nodalization. (SiN window is rendered as “wire”



for clarity. This does not affect the temperature calculations.)

Radiation Model – Several points can be made with respect to radiation modeling. First, Silicon is partially transparent at room temperature IR wavelengths. However, the Silicon layers here were considered to be optically thick and considered to be a gray body with emittance of 0.8. Second, since TSS is a Monte Carlo ray-tracing code, there was no worry that the detector surface would block a portion of the bottom layer and produce incorrect radiation conductors for the bottom layer. For TRASYS or other radiation analysis codes that use the double integration or unit-sphere technique to determine form factors, then use the Gebhart method to establish conductors, this modeling would lead to erroneous results. The total RADK of the lower surface would be wrong and the FFSUM for this surface would not equal one. It would be a very big challenge to model MEMS-scale devices with TRASYS or other such codes accurately. Special cutouts and approximate surfaces would be needed for correct results. It may be that only ray-tracing codes such as TSS, RadCAD, TMG, NEVADA, and others, provide enough modeling flexibility to complete a MEMS-scale job in a reasonable amount of time and computer resources. Third, the SiN window is mostly transparent to thermal radiation on the order of a blackbody at 2650 °C. Data shows there is some absorption, however, and an absorptance value of 0.2 was used in the radiation model. Since the

temperature predictions show less than 2 °C degrees variation throughout the device, the absorptance does not greatly affect the temperature predictions.

Environment Model – The effective radiation sink temperature is 27 °C. The bottom of the package is in good contact with a conductive heat sink at 27 °C. For the case of forced convection (fan), the heat transfer coefficient was 45 W/m² K.

RESULTS

The device is very isothermal, due to the relatively high conductivity of silicon. The average temperature varies by only 2 °C throughout the device. As shown in Table 1, this device must have a heat sink attached to the bottom layer for the detector and SiN window to remain below the maximum allowable temperature of 125 °C. This bulk temperature is very sensitive to the boundary conditions, that is, the temperature of the attached heat sink. The maximum desired allowable temperature for the detector and SiN window was 125 °C, the typical maximum hot limit for semiconductor electronics. Although the SiN window does have 0.2 absorptance included in the model, the practically isothermal results show that the device is not sensitive to the absorptance value.

The results show the detector will receive a maximum of 34 W/cm² heat flux on its surface. With a good heat sink, it is possible to dissipate this flux passively (with conduction) and not exceed the maximum allowable temperature for semiconductor devices, 125 °C. This assumes that the heat sink is at the ambient temperature of 27 °C, which should be easy to achieve with a relatively large (> 2 kg) heat sink. Results show that the SiN window will be about 2 °C cooler than the detector in all cases. Case 1 was analyzed with the SINDA conductors between dicing layers 1 and 2 multiplied by 0.88. This produced less than one degree difference in the temperature predictions, and is not listed in Table 1. Case 2 shows that SINDA cannot calculate the temperature for the radiation case, because the predicted temperature is unrealistically high. The device might overheat and fail in this situation, and should not be operated under the conditions in Case 2. Case 3 shows that adding a fan will lower the temperature by about 20 °C. If Case 1 and 3 are compared, it is seen that a fan is not necessary if a good heat sink is available. Case 4 shows that a fan alone will not provide enough cooling and that a heat sink is necessary.

Case	Vacuum	Heat Sink	Convection	Radiation	Predicted Temperature of Detector
1	Yes	Yes	No	Yes	98 °C
2	Yes	No	No	Yes	Model did not converge
3	No	Yes	Yes	Yes	73°C
4	No	No	Yes	Yes	164 °C

Table 1. Temperature Results of SINDA Based on Modeling Assumptions

FURTHER WORK

This paper has described a preliminary thermal model and analysis results based on early design information. It is extremely fortunate that thermal engineering was considered so early in the design. As the mechanical and electrical design options narrow down to a few final candidates, a second –look thermal analysis should be performed. The nodalization may change to reflect new information. The thermal model could be better refined to include the conductive bonding pads transferring heat to the silicon mechanical structure. More nodes near the connection point would be necessary.

CONCLUSION

Preliminary thermal analysis has shown that there are no special cooling needs for the detector, and that the SiN window temperature will remain below the maximum allowable. The bottom of the device must be attached to a high-thermal-conductivity heat sink such as Copper, Aluminum, or some other high thermal conductance material. Between the heat sink and the device should be some thermal interface material (e.g. thermal paste or epoxy) to insure good thermal contact. Operating the device in air with no heat sink will produce unacceptably high temperatures. It was pointed out that even though SiN is a poor thermal conductor, the layers are too thin to provide much thermal insulation between the Si layers. As the project moves forward, thermal design must be considered carefully. More detailed thermal modeling is recommended once all of the options for mechanical and electrical designs become final.

ACKNOWLEDGMENTS

The author would like to acknowledge the efforts of Dr. Margaret Tuma in providing the author the key information and contacts to carry out the analysis. Also, the JPL and GRC contacts provided valuable insight and useful comments to improve the thermal modeling. Critical reviews of this paper by James Yuko, Wayne Wong and Dr. Margaret Tuma were exceptionally helpful. The author would also like to thank the Thermal-Mechanical Systems Branch for the analytical tools used.

REFERENCES

1. M. L. Tuma, L. Kim, R. Hansler, K. King, E. Jones, T. George, "MEMS Incandescent Light Source," SPIE Proceedings of the 45th Annual Meeting, Vol. 4134, San Diego, CA, August, 2000.
2. Y.S. Touloukian, D.P. DeWitt, "Thermal Radiative Properties," IFI/Plenum, 1970.
3. Incropera and DeWitt, "Fundamentals of Heat and Mass Transfer," John Wiley & Sons, 1985.

MODELING SPECULAR EXCHANGE BETWEEN CONCENTRIC CYLINDERS IN A RADIATIVE SHIELDED FURNACE

R. Gregory Schunk

Thermal and Fluid Systems Group
National Aeronautics and Space Administration
George C. Marshall Space Flight Center
Marshall Space Flight Center, AL 35812-0001

and

Francis C. Wessling

Department of Mechanical and Aerospace Engineering
University of Alabama in Huntsville
Huntsville, AL 35899-0100

ABSTRACT

The objective of this research is to develop and validate mathematical models to characterize the thermal performance of a radiative shielded furnace, the University of Alabama in Huntsville (UAH) Isothermal Diffusion Oven. The mathematical models are validated against experimental data obtained from testing the breadboard oven in a terrestrial laboratory environment. Development of math models to characterize the thermal behavior of the furnace is a challenging task due to the complexity of the interacting heat transfer modes. Important considerations in the analysis of the furnace include heat losses through power and instrumentation cables, buoyancy driven flows through and around exposed surfaces of the furnace, and specular radiation effects within the furnace. Due in part to the large aspect ratios of the cylindrical cavities formed by the radial shields within the furnace, a diffuse radiation exchange model was initially assumed with qualitative error bounds established through a simplified model of the furnace core and innermost shield. An improved correlation to the experimental data is obtained by directly modeling the specular radiative exchange between the radial shields of the furnace.

NOTATION

α	inner cylinder emitted ray exit angle (relative to surface normal)
α_i	average total absorptivity of surface i
β	intercept angle (relative to surface normal)
ϵ_i	average total emissivity of surface i
ϕ	elevation angle above the r- θ plane
γ	outer cylinder emitted ray exit angle (relative to surface normal)
ρ_i	average total reflectivity of surface i
σ	Stefan-Boltzmann Constant
A	area
B_i	radiosity of surface i
c_p	specific heat
Δr	shield spacing
E_{ij}	exchange factor between surfaces i and j
F_{ij}	form factor (or view factor) between surfaces i and j
G	linear coupling via conduction or convection
H	cylinder height
H_i	incident flux upon surface i
m	mass
Q,q	imposed heat load, imposed heat load per unit area
r_i, r_o	inner and outer radii, respectively

INTRODUCTION

The UAH Isothermal Diffusion Oven is designed to provide a thermal environment that is conducive to measuring the diffusion of high temperature liquid metals. In addition to achieving the temperatures required to melt a sample placed within the furnace, reducing or eliminating convective motions within the melt is an important design consideration [1]. Both of these influences are reflected in the design of the furnace. Reducing unwanted heat losses from the furnace is achieved through the use of low conductivity materials and reflective shielding. As evidenced by a highly conductive copper core used to house the sample within the furnace, convective motions can be greatly suppressed by providing an essentially uniform thermal environment.

A series of laboratory tests are conducted to measure the steady state and transient behavior of the furnace. To aid in the model correlation, the test conditions are chosen to isolate or enhance specific aspects of the thermal behavior of the furnace. Under vacuum, radiative exchange is the dominant heat transfer mechanism. At very low pressure, natural convection is suppressed and, along with radiation, gaseous conduction significantly influences the thermal performance of the furnace. Near atmospheric pressure, all three heat transfer modes, convection, conduction, and radiation, must be considered to adequately characterize the thermal behavior of the furnace. The test conditions are also chosen to parameterize the furnace core temperature versus heater power and to observe the influence of natural convection over a range of pressures. Actual testing of a sample within the furnace is excluded since the heat capacity of the sample is considered negligible relative to that of the core.

FURNACE DESIGN

A cross-sectional view of the oven is presented in Figure 1 with major components noted [2]. A cylindrical copper core and a quartz glass tube are used to house the test sample. The quartz glass tube and sample are absent in the breadboard furnace that is considered in this research. It is assumed that the thermal behavior of the furnace can be adequately characterized without the tube and sample since the heat capacities of these components are negligible compared to that of the copper core. The copper core is surrounded by a cylindrical boron nitride sleeve containing a graphite heater element. A thin layer of Fiberfrax™ insulation is used to enhance the heat transfer between the core and the concentric heater element. Two stainless steel end hubs, denoted long and short in the figure, are attached to opposite ends of the copper core. The top and bottom hubs contain four and six pins, respectively, that mate with matching penetrations in each end of the copper core. Fiberfrax™ gaskets are introduced between the hubs and the core to minimize heat losses and, thus, reduce axial temperature gradients through the core. The inner assembly (including core, sample, heater, and insulation) is suspended inside of the oven by stainless steel wires fastened between the two hubs and the top and bottom support rings. The stainless steel wires penetrate each of the interior end rings. Conduction from the core to the end rings is minimized by wrapping the stainless steel wire with Fiberfrax™ insulation within the penetrations. The overall design goal is to provide a stable and secure mount for the inner assembly while minimizing heat losses to the outside.

Three cylindrical radial shields (inner, middle, and outer) form a radiation barrier to reduce heat losses from the oven (although gaseous conduction is also present if the furnace is not placed in a vacuum). The inner surface of each radial shield has a vacuum deposited low emittance gold coating. The shields are constructed from Pyrex™ and the outer surfaces are uncoated. Visual inspection of the radial shields reveals that the inner surfaces are highly specular. The spacings between the three shields and the core are minimized to suppress convective exchange between the shields and to reduce specular losses from reflected energy escaping out the ends of the furnace. Each radial shield is supported by a matching pair of end rings on the opposite ends (top and bottom). At each end, Fiberfrax™ spacers are used to create a

gap between the radial shield and the end ring. Similarly, Fiberfrax™ washers are used to create a gap between the end rings and the end shields. The gaps reduce the direct contact area between the shields and the end rings and effectively limit the heat exchange to the energy that can be radiated and conducted (through the gaseous medium) across the gap. Like the radial shields, the three shields on each end of the oven form a radiation barrier to reduce heat leakage although the end shields on top of the furnace have a circular penetration to permit loading of the test sample (not used in these experiments). The lower end shields are made of stainless steel while the upper shields are aluminum and are polished as needed to remove accumulated oxidation (to create surfaces with as low an infrared emittance as possible). Three support rods hold the entire assembly together and are used to mount the oven onto a bronze baseplate containing a matching hole pattern. The oven and bronze baseplate are placed within a bell jar vacuum chamber for the experiments.

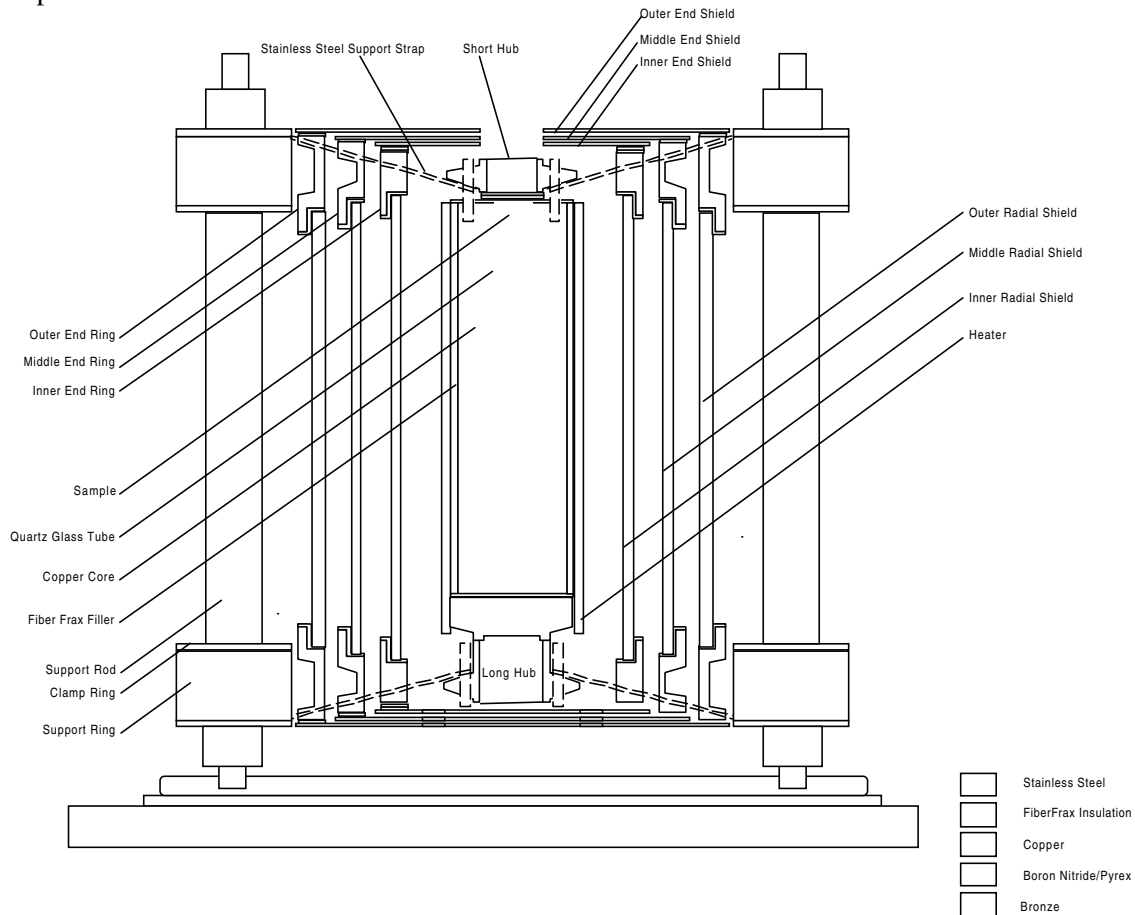


Figure 1 UAH Isothermal Diffusion Oven

Photographs of the disassembled furnace are contained in Figures 2 and 3. The first figure shows the bare copper core mounted atop the long hub on the bottom end ring assembly. The inner and middle radial shields are removed as well as the top end ring assembly containing the short hub, top support rings, and top end rings. The short hub and stainless steel support wires are visible within the top end ring assembly. The compact design of the oven is evidenced from a six inch scale included in the photograph.

The second figure shows the inner assembly (core and heater sleeve) mounted within the disassembled furnace. The long hub is obscured by the boron nitride heater sleeve which surrounds the core. Penetrations within the heater sleeve that are used to attach power cables are

visible in the photograph. Although not visible, the power cables are routed through penetrations underneath the furnace. The support rods, which hold the entire assembly together, are shown in the figure. The end shields, which attach directly to the end rings, are omitted from both photographs.

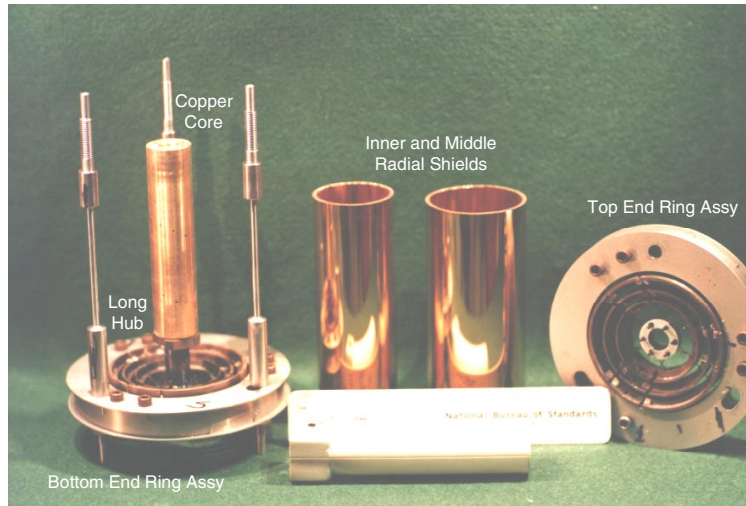


Figure 2 Disassembled View of the Furnace

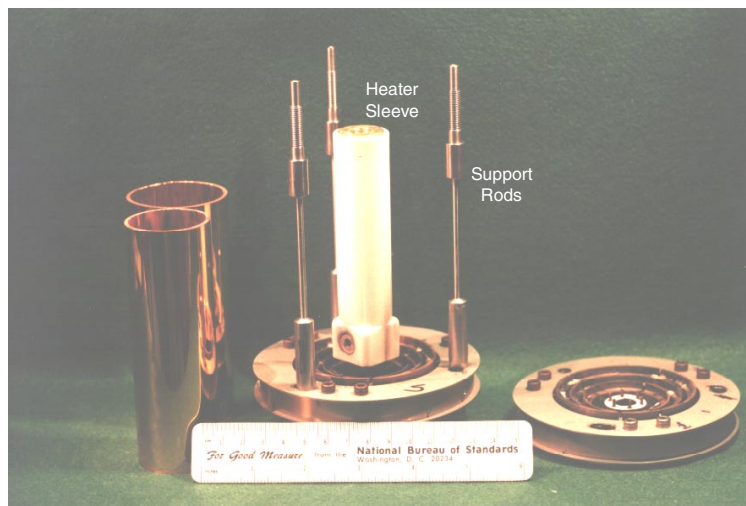


Figure 3 Furnace with Heater Sleeve

TESTING

Eight tests are conducted under vacuum and varying pressures of argon gas to measure the steady state and transient thermal performance of the furnace. Results from the tests are used to validate mathematical models of the furnace. To aid in the model correlation, the test conditions are chosen to isolate or enhance specific aspects of the thermal behavior of the furnace. Under vacuum, radiative exchange between the furnace core and radial shields is the dominant heat transfer mechanism. At very low pressure, natural convection is suppressed and, along with radiation, gaseous conduction between the core and radial shields significantly influences the thermal performance of the furnace. Near atmospheric pressure, all three heat transfer modes, convection, conduction, and radiation, must be considered to adequately characterize the thermal behavior of the furnace. The results from the eight tests are summarized

in Table 1. The first three tests are conducted under vacuum at power levels ranging between 5 and 20 watts. The final five tests are conducted under absolute pressures of argon gas ranging from 0.03 to 0.932 atmospheres at power levels between 11.6 and 12.0 watts.

Table 1 Steady State Test Results

Test	Date	Core (°C)	Radial #1 (°C)	Radial #3 (°C)	End (°C)	Chamber (°C)	Room (°C)	Voltage (volts)	Current (amps)	Power (watts)	Pressure (torr/atm)
1	12/13/95	390.6	268.7	43.2	113.0	25.3	24.7	12.2	0.92	11.2	3.90E-05 torr
2	12/15/95	262.9	170.9	34.6	72.1	27.2	27.1	8.6	0.60	5.2	8.60E-06 torr
3	12/30/95	506.5	368.1	56.2	153.2	22.8	22.7	19.0	1.06	20.1	3.60E-05 torr
4	1/20/96	201.5	121.3	45.9	53.7	23.5	23.0	11.6	1.00	11.6	0.667 atm
5	2/10/96	219.4	135.1	52.0	63.5	23.6	23.5	11.9	1.00	11.9	0.310 atm
6	2/12/96	228.0	143.4	60.1	72.1	28.4	28.3	12.0	1.00	12.0	0.146 atm
7	2/19/96	203.1	118.0	45.5	51.2	25.0	25.1	12.0	1.00	12.0	0.932 atm
8	2/21/96	230.5	145.4	61.8	73.6	28.0	28.0	12.0	1.00	12.0	0.030 atm

Experimental Configuration

The tests are conducted inside of a stainless steel bell jar vacuum chamber measuring approximately three feet in diameter by four feet in height. A schematic of the test configuration, with the furnace mounted inside of the bell jar on a circular brass adapter plate, is shown in Figure 4. The circular adapter plate is slightly larger than the outside diameter of the furnace support rings. An external power supply is used to drive the furnace through two power leads attached to the heater core. Four thermocouples are attached to the test article to measure the temperatures of the furnace core, inner and outer radial shields, and the bottom end shield. Additional thermocouples are placed externally to measure the temperature of the bell jar and the ambient temperature inside the laboratory.

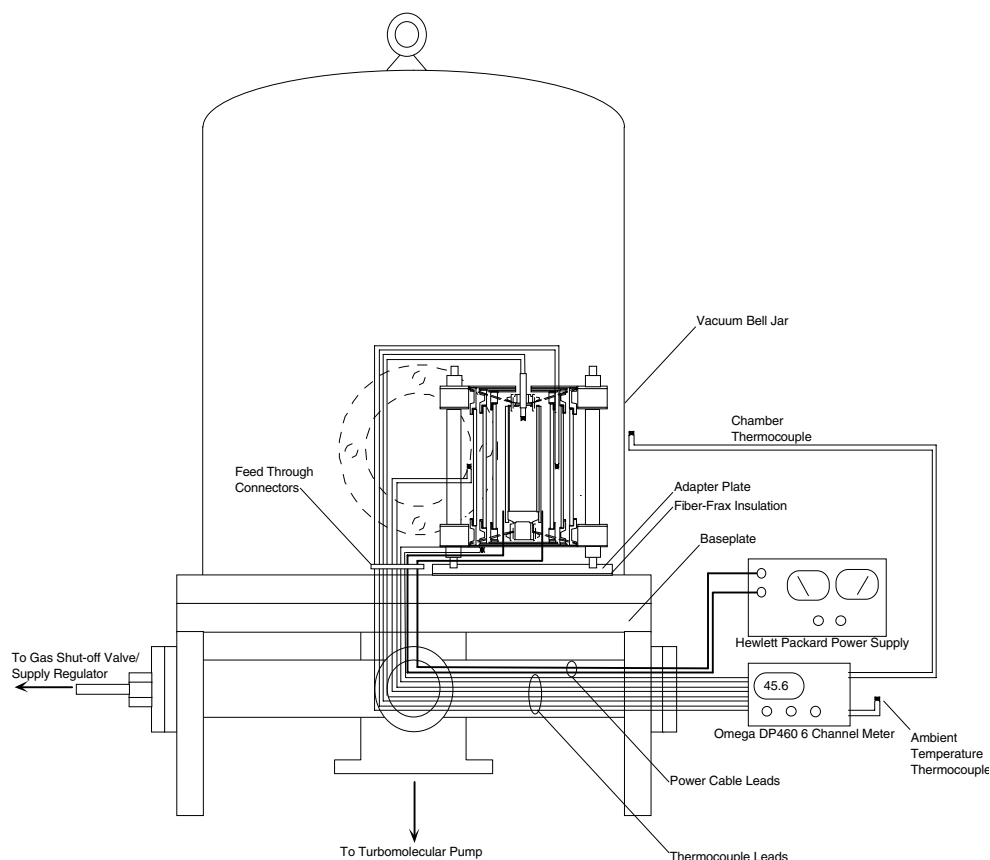


Figure 4 Test Setup

THERMAL MODEL

The Thermal Radiation AnalYSIS SYStem (TRASYS) [3] computer program is used to compute the radiation couplings between surfaces in the model. The Systems Improved Numerical Differencing AnalYZer (SINDA) [4] is used to solve the thermal network resulting from radiation conductors computed by TRASYS and user defined nodes, linear conductors, and imposed heat loads.

A cut-away view of the TRASYS furnace model is presented in Figure 5. Since TRASYS is only used to model planar surfaces and simple surfaces of revolution, many of the solid elements present in the furnace, such as the core and radial shields, are constructed by enclosing a volume with the available surface primitives. Thin solid elements, such as the end shields, are modeled directly using the planar surface primitives. By using surfaces to model opaque solid elements, only the exterior of each surface is declared active within TRASYS. Inactive surfaces, such as the interior of the radial shields and end rings, are visible in the cut-away view. Many of the surfaces are subdivided at common junctions with other surfaces (good practice to avoid view factor problems) or as necessary to support proper nodalization under SINDA.

The heater core and attached long and short hubs are shown in the figure. The core is modeled using a cylindrical surface subdivided into twelve rings axially with disk surfaces to close out each end. The disks are subdivided into three rings radially to match the footprint of the attached hubs and the thickness of the boron nitride heater element. The outer envelope of each hub is modeled using a combination of cylinders and cones.

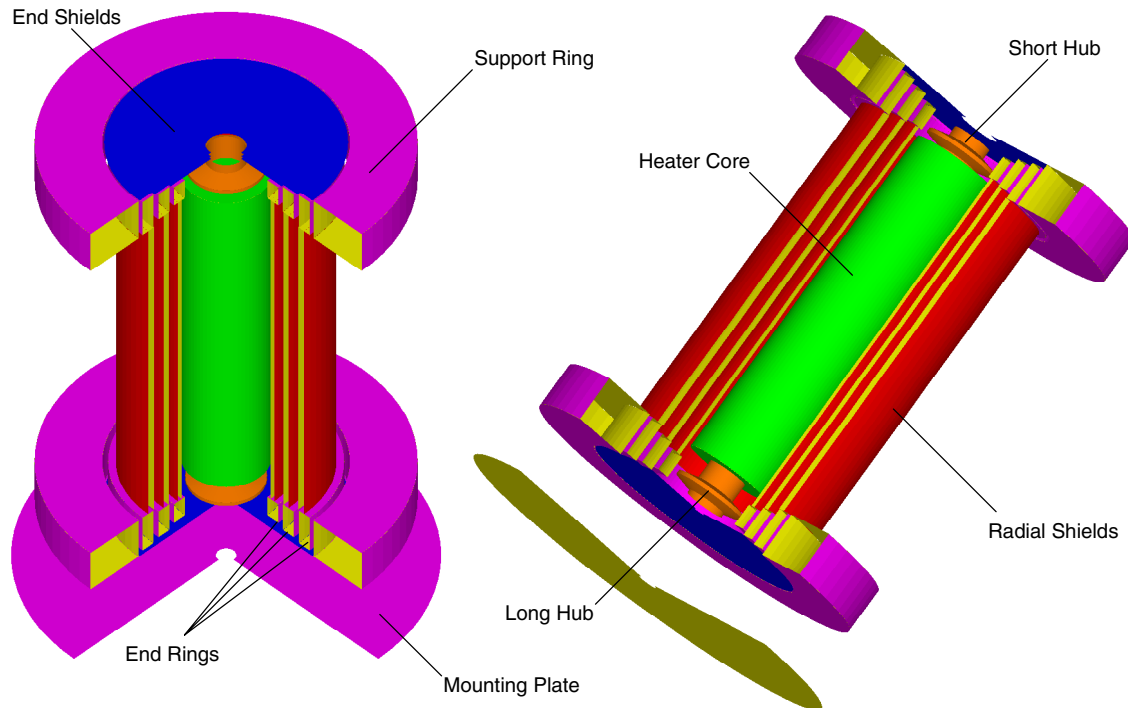


Figure 5 Cut-Away View of TRASYS Furnace Model

Like the core, the end rings are modeled with a combination of TRASYS disk and cylinder surface primitives. The primitives are used to form the rectangular cross section shown in the figure. The disk surfaces on top of the end rings are subdivided to match the footprint of the radial shields. Cylindrical surfaces define the radial faces of the end rings. The end shields are modeled using disk surfaces (that are active on both sides) and are subdivided to match the footprint of the end rings. The support rings and radial shields are modeled using cylinders for the exterior faces and disk surfaces for the top and bottom close-outs. The radial shields, end rings, and end shields are positioned to maintain proper clearance as determined by the Fiberfrax™ washers and spacers. As shown in the figure, the inside surfaces of the cylinders and disks forming the support rings and radial shields are not active in the TRASYS model.

Figure 6 contains a representation of the network for the thermal model. The network, containing nodes and conductors, is overlaid upon a cut-away view of the furnace in the r-z plane. Since axial symmetry is assumed, no conductors exist in the tangential direction. Diffusion and arithmetic nodes are represented as filled and open circles, respectively. Arithmetic nodes are used primarily to model exposed surfaces that participate radiatively and correspond one-to-one with the surfaces in the radiation model. Radiation couplings are not shown, but nodes with exposed surfaces that participate radiatively are indicated with two arrows. Linear conductors are represented with an electrical resistance symbol and imposed heat sources are represented with a large arrow placed directly upon the node.

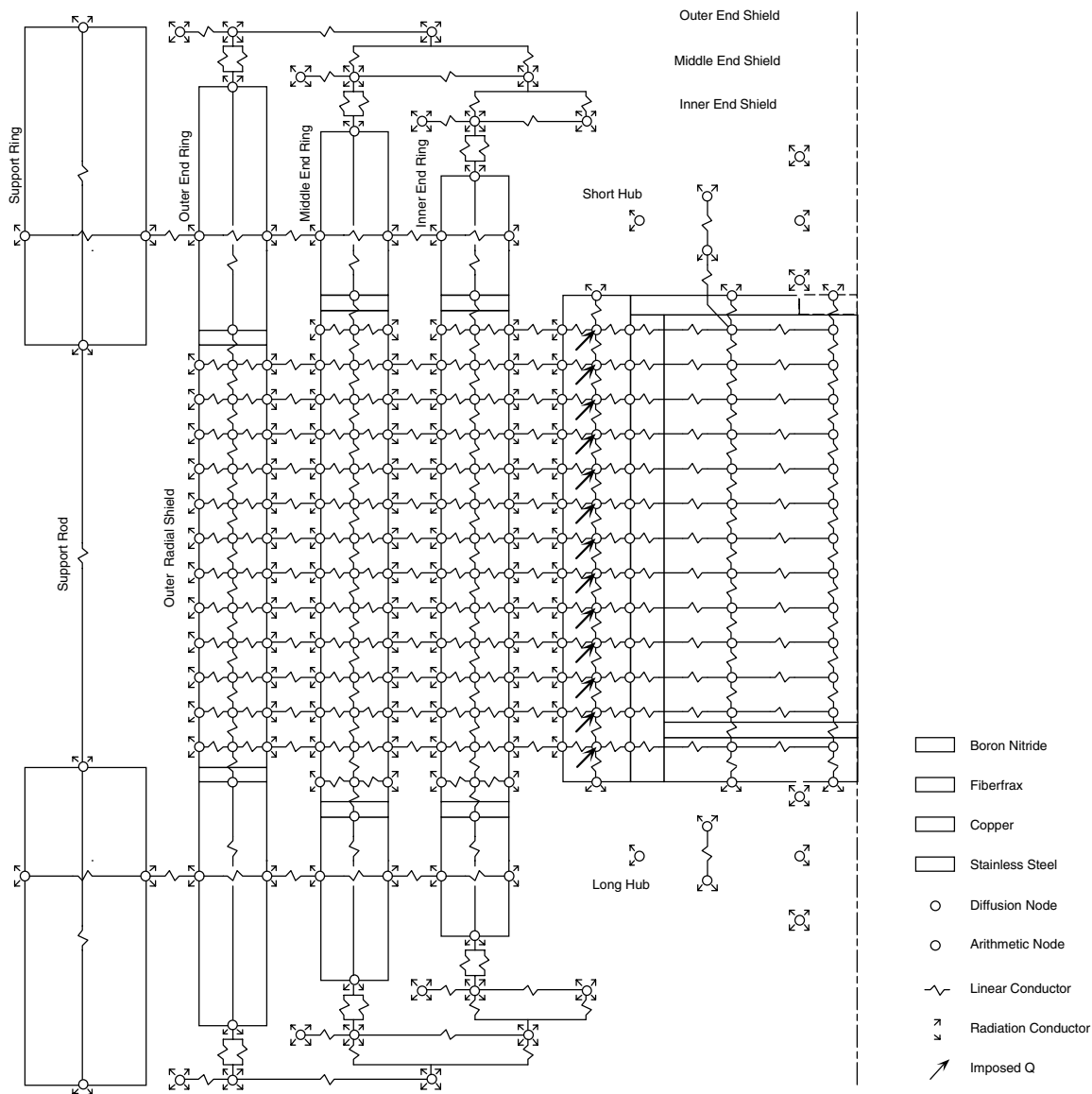


Figure 6 Thermal Network Model

The furnace core is discretized into a mesh of twelve diffusion nodes axially by two diffusion nodes in the radial direction. The core is surrounded by Fiberfrax™ insulation and a boron nitride heater sleeve. Linear conductors are included to account for the resistance through the insulation. The heater sleeve is discretized axially to match the nodalization of the furnace core and into three nodes radially to provide surface nodes that participate radiatively with the innermost radial shield. Imposed heat sources are placed upon the heater nodes and are varied to match test conditions. Linear conductors are also included to account for the heat flow from the ends of the core into the long (bottom) and short (top) hubs. The long and short hubs exchange heat radiatively with the surroundings. Although not shown in the figure, linear conductors are included to model the support wire connections between the end hubs and the outer support rings.

The inner, middle, and outer radial shields are axially discretized into nodes that are aligned to permit conductive couplings between the shields through the gas contained in the furnace. Gaseous conduction between the inner radial shield and the heater element is also included. To model the furnace under vacuum conditions, the gaseous conduction couplings are removed. Each shield is radially discretized into three nodes with an interior diffusion node to

account for the thermal capacitance of the shield and two arithmetic nodes for the exposed inner and outer surfaces. Each radial shield is also conductively coupled to end rings on the top and bottom of the furnace. Since Fiberfrax™ spacers are placed between the shields and the end rings, multiple conductors are included to model the resistance of the insulation as well as gaseous conduction through the gap formed by the spacers.

A single diffusion node is used to model each end ring with arithmetic nodes on all exposed surfaces. Conductors internal to the end ring include radial and axial couplings between the diffusion node and the arithmetic nodes on the exposed surfaces. The coupling between the radial shield and the end ring includes conductive paths through the Fiberfrax™ spacers and through the vapor gap formed between the end ring and radial shield. Gaseous conduction between the end rings (in the radial direction) is also included in the model.

SPECULAR RADIATIVE EXCHANGE BETWEEN CYLINDRICAL SURFACES

Heat transfer analyses of the furnace are performed assuming diffuse radiative exchange between the surfaces of the core, the inner radial shield, and the inner end shields. The inner surface of the innermost radial shield has a low emissivity, highly specular, vacuum deposited gold coating while the end shields and the highly emissive core are non-specular. Because of the large aspect ratio (i.e. $H/\Delta r$, where H is the height of the heater core and Δr is the shield spacing) of the vertical annulus formed by the furnace heater core, inner radial shield, and end shields, it is assumed (in the overall TRASYS model) that the specular interchange can be approximated with a diffuse model. It is expected that only if a significant fraction of the energy radiated by the core is directly reflected onto the end shields (from the inner radial shield) is the assumption compromised.

To validate the diffuse assumption, two simplified models of the vertical annulus (formed by the core, inner radial shield, and end shields), one diffuse and one specular, are developed for comparison. The models are based upon diffuse and specular radiosity analysis methods as described by Sparrow [5]. The conclusions presented are also applicable to the vertical annuli formed by the inner and middle radial shields and the middle and outer radial shields of the furnace. These annuli differ only in geometry since the outer surfaces of the radial shields are highly emissive and non-specular like the furnace heater core.

Simplified Model Geometry

The subsequent analyses are based upon the radiative exchange between two cylinders of height, H , and inner and outer radii, r_i and r_o , respectively as shown in Figure 7. An axisymmetric coordinate system is assumed. A single ray, at height of z , is emitted from the inner cylindrical surface as shown. The emitted ray exits at angle, α , relative to the surface normal of the inner cylinder and is intercepted by the outer cylinder at an angle, β , relative to the surface normal of the outer cylinder. Since the inner and outer surface normals have no component in the axial direction, the angles α and β are equivalent to the angle between the surface normal and the component of the ray in the r - θ plane. The elevation angle above the r - θ plane for the emitted ray is denoted ϕ . The elevation angle is an important parameter as the ray is specularly reflected between the surfaces of the cylinders; this angle (as well as the intercept angles α and β) is preserved on each successive specular bounce relative to the local surface normal. The end shields that close out the top and bottom ends of the vertical annulus are also shown.

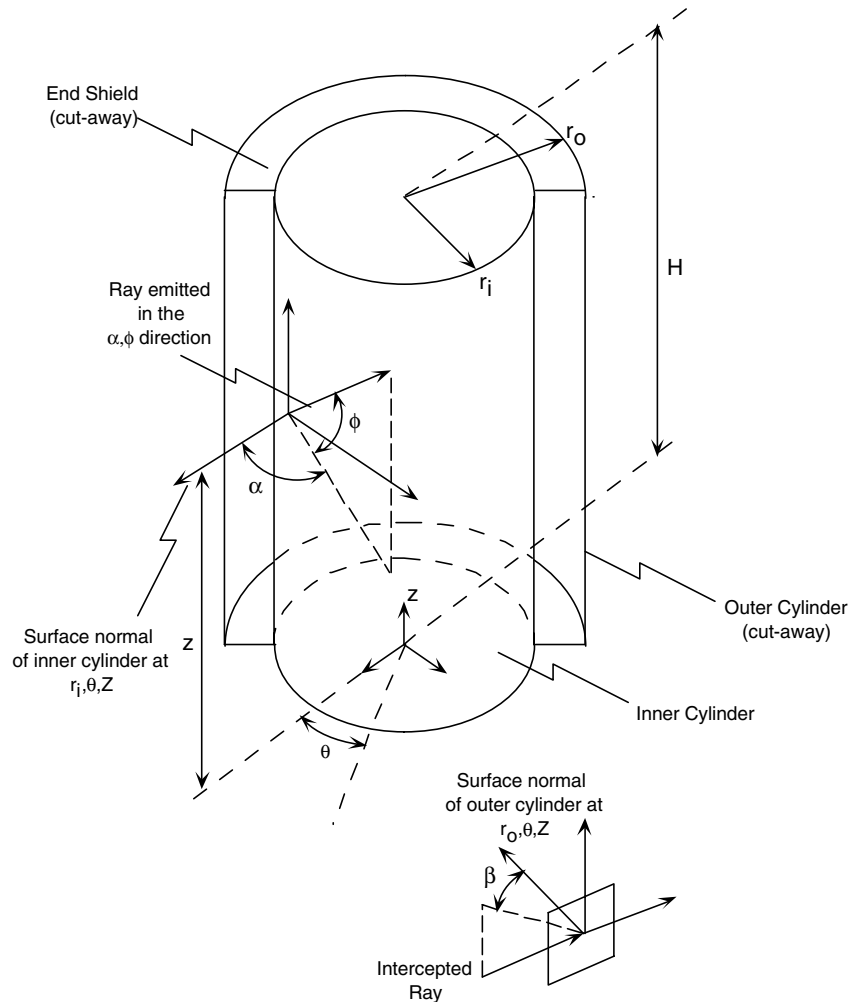


Figure 7 Axisymmetric Coordinate System

The relationship between the intercept angles α and β is shown in Figure 8. The relationship is mathematically expressed as $\beta = \sin^{-1}((r_i/r_o)\sin\alpha)$. An important characteristic for axisymmetric cylinders is that a ray emitted from the inner cylinder is always reflected back to the inner cylinder by a specular outer cylinder unless it escapes out of the annulus. The maximum intercept angle, β , for a ray emitted by the inner cylinder corresponds to $\alpha = \pi/2$ as shown in Figure 9. If a ray originating from the outer cylinder leaves at an angle γ that is greater than the maximum intercept angle, the ray will bounce along the surface of the outer cylinder indefinitely, essentially orbiting the inner cylinder until it escapes from the annulus. If the elevation angle, ϕ , is exactly zero, the ray will never escape.

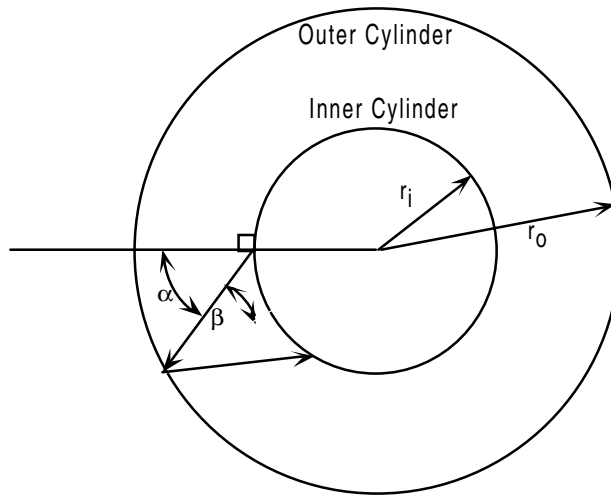


Figure 8 Relationship between Emitted and Reflected Ray

Diffuse Interchange Model

The theory behind the radiosity method [6] and its application to diffuse and specular models of a cylindrical vertical annulus are presented. An energy balance per unit area for a surface, denoted i , is provided in Figure 10. H_i is the incident flux upon the surface, $\rho_i H_i$ is the reflected incident flux, $\epsilon_i \sigma T_i^4$ is the heat flux emitted by the surface, and $q_i (=Q_i/A_i)$ is the net heat gained by the surface.

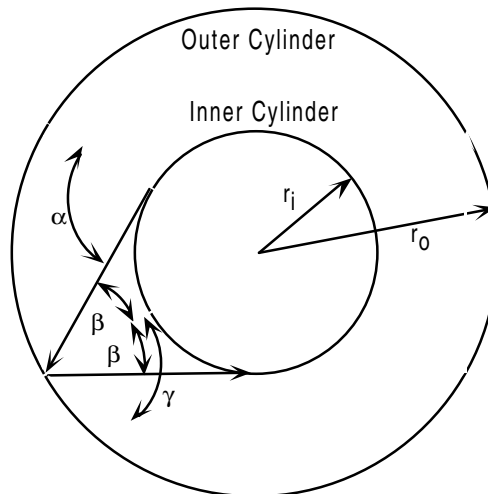


Figure 9 Emitted Ray Reflection to Inner Cylinder

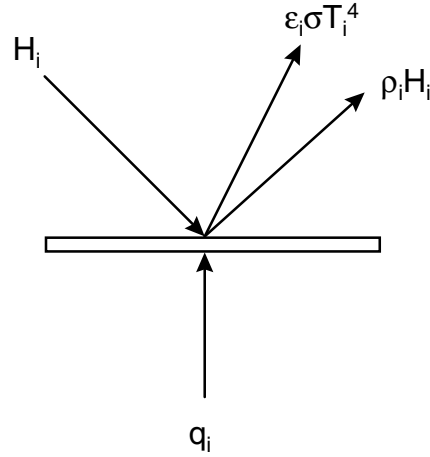


Figure 10 Energy Balance per Unit Area for a Diffusely Reflecting Surface

The radiosity of the surface, B_i , is defined as the total flux leaving the surface and is equal to the flux emitted by the surface plus the fraction of the incident flux that is reflected from the surface as shown in Equation 1.

$$B_i = \epsilon_i \sigma T_i^4 + \rho_i H_i \quad (1)$$

In Equation 2, an energy balance is constructed where the net flux, q_i , is equal to the incident flux absorbed by the surface, $\epsilon_i H_i$, minus the flux emitted by the surface, $\epsilon_i \sigma T_i^4$. The relation for the incident flux is based upon the assumption that the departure from thermal equilibrium is small enough that Kirchhoff's law [7] can be applied (i.e. $\epsilon_i = \alpha_i$). The net flux is equal to the rate of heat gained by the surface. Linear couplings (via conduction or convection, denoted by G_{ij}) to other surfaces, imposed heat loads (Q_i), and changes in the thermal mass (mc_p) of the surface are related to the net heat flux as shown in Equation 3.

$$q_i = \epsilon_i H_i - \epsilon_i \sigma T_i^4 \quad (2)$$

$$q_i = \frac{mc_p \frac{dT_i}{dt} - \sum G_{ij} (T_j - T_i) - Q_i}{A_i} \quad (3)$$

Substituting H_i from the definition of radiosity and simplifying yields an energy balance in terms of the radiosity (see Equation 4).

$$q_i = \frac{\epsilon_i}{(1 - \epsilon_i)} (B_i - \sigma T_i^4) \quad (4)$$

The definition of radiosity can be simplified to yield a set of equations in network form. Dividing both sides of the definition through by $(1 - \epsilon_i)$ and then subtracting $\frac{\epsilon_i B_i}{(1 - \epsilon_i)}$ from both sides yields Equation 5.

$$B_i = \frac{\epsilon_i}{(1 - \epsilon_i)} (\sigma T_i^4 - B_i) + H_i \quad (5)$$

Since the radiosity, B_i , represents the heat flux leaving a surface, the incident flux upon a surface, H_i , can be found by summing the contributions from all the surfaces within the enclosure as shown in Equation 6.

$$H_i = \frac{\sum_{j=1}^n F_{ji} A_j B_j}{A_i} = \sum_{j=1}^n F_{ij} B_j \quad (6)$$

Since the summation of form factors from a surface is equal to 1 (Equation 7), the relation can be simplified to express the radiosity in network form (numerical differences) as shown in Equations 8 and 9.

$$\sum_{j=1}^n F_{ij} = 1 \quad (7)$$

$$\sum_{j=1}^n F_{ij} B_i = \frac{\epsilon_i}{(1-\epsilon_i)} (\sigma T_i^4 - B_i) + \sum_{j=1}^n F_{ij} B_j \quad (8)$$

$$0 = \frac{\epsilon_i}{(1-\epsilon_i)} (\sigma T_i^4 - B_i) + \sum_{j=1}^n F_{ij} (B_j - B_i) \quad (9)$$

Equations 10 and 11 are generated by multiplying through by the surface area, A_i , to express the balances in terms of rate of heat transfer rather than flux.

$$Q_i = \frac{\epsilon_i A_i}{(1-\epsilon_i)} (B_i - \sigma T_i^4) \quad (10)$$

$$0 = \frac{\epsilon_i A_i}{(1-\epsilon_i)} (\sigma T_i^4 - B_i) + \sum_{j=1}^n A_i F_{ij} (B_j - B_i) \quad (11)$$

The application of Equations 10 and 11 to a three surface vertical annulus is provided in Figure 11. Because of the symmetry present in the simplified model, the end shields are combined and represented by one surface. This is only an approximation to the actual furnace geometry since the hubs attached to opposite ends of the furnace core are not identical. It should be noted that the single surface representing the two end shields views itself. The form factors between the surfaces within enclosure are available from the angle factor catalog in Sparrow [8].

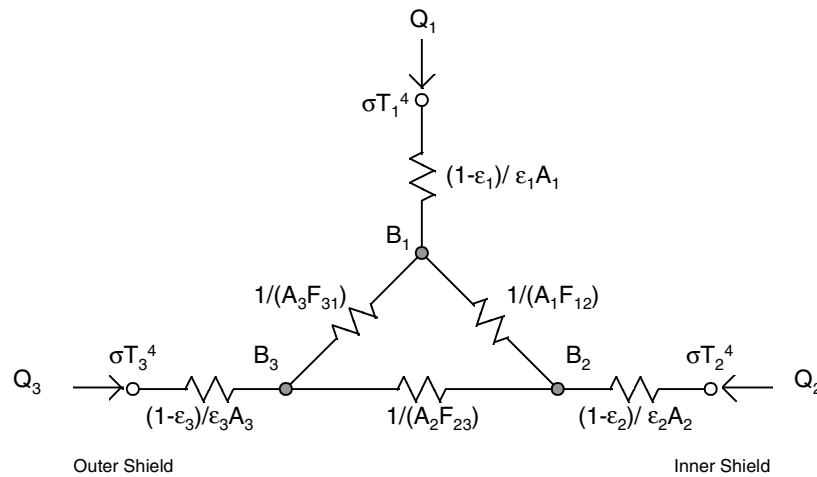


Figure 11 Radiosity Formulation for the Diffuse Model

Specular Interchange Model

A slightly different formulation is used to account for specularly reflecting surfaces within an enclosure. In the diffuse model, the energy exchange between two surfaces is directly proportional to the diffuse form factor between the surfaces. In an enclosure with one or more specular surfaces, an exchange factor is introduced to include reflected energy from specular surfaces. The exchange factor between two surfaces i and j is defined in Equation 12 where f_n is the fraction of energy originating at surface i that arrives at surface j after n intervening specular reflections. The reflectance of an intervening specular surface, k , is given by ρ_k (which is equal to $1 - \varepsilon_k$ for an opaque surface). With each successive reflection, a fraction of the incident energy is absorbed by the specular surface. The fraction of energy for $n=0$ is the energy originating at surface i that is directly incident upon surface j and corresponds to the diffuse form factor between surfaces i and j . The energy fractions for higher order reflections can be found by the diffuse form factor between the originating surface and a reflected image of the destination surface. Determining the exchange factors in this manner becomes complex for large numbers of specular surfaces or if the specular surfaces are curved.

$$E_{ij} = f_0 + f_1\rho_k + f_2\rho_k\rho_l + \dots \quad (12)$$

With the definition of the exchange factor, the radiative heat transfer between surfaces is defined as shown in Equation 13, where N_D is the number of diffusely reflecting surfaces and N is the total number of surfaces (the specular surfaces are numbered N_D+1 through N).

$$0 = \frac{\varepsilon_i A_i}{(1 - \varepsilon_i)} (\sigma T_i^4 - B_i) + \sum_{j=1}^{N_D} A_i E_{ij} (B_j - B_i) + \sum_{j=N_D+1}^N A_i E_{ij} \varepsilon_j (\sigma T_j^4 - B_i) \quad (13)$$

The net heat transfer rate from any of the diffusely reflecting surfaces is the same as in the diffuse formulation. Since the exchange factors already include reflections from specular surfaces, the net heat transfer from a specular surface, i , is defined as shown in Equation 14.

$$0 = \varepsilon_i A_i \left(\sigma T_i^4 - \sum_{j=1}^{N_D} E_{ij} B_j + \sum_{j=N_D+1}^N E_{ij} \varepsilon_j \sigma T_j^4 \right) \quad (14)$$

The application of Equations 13 and 14 to a three surface vertical annulus (with the outer cylinder specularly reflecting) is provided in Figure 12. In the following analysis for a specularly reflecting outer shield, it is assumed that the surface is completely specular (i.e. there is no diffuse component in the reflection). With this assumption, the two extreme cases are represented in the analysis and the problem is bounded. Because of symmetry, the top and bottom end shields are combined and represented by one surface that views itself.

Specular Exchange Factors

The diffuse network is easily solvable after determining the diffuse form factors from available angle factor correlations. The determination of the exchange factors contained within the specular model is more complex. For the exchange factor between surfaces 1 and 2, a ray originating from surface 2 may either be reflected back to surface 2 or reflected to surface 1. The ray may not sustain more than one intervening specular reflection before reaching surface 1 as shown in Equation 15. In Equation 16, the exchange factor E_{23} is identical to the form factor between the two surfaces since a ray emitted by surface 2 is either reflected back to surface 2 or reflected to surface 1. It is not possible for a ray originating at surface 2 to be reflected by surface 3 onto surface 3. As shown in Equation 17, it is possible for a ray emitted by surface 3 to be specularly reflected many times by surface 3 before reaching surface 1.

$$E_{21} = F_{21} + \rho_3 f_1 \quad (15)$$

$$E_{23} = F_{23} \quad (16)$$

$$E_{31} = F_{31} + \sum_{n=1}^{\infty} \rho_3^n f_n \quad (17)$$

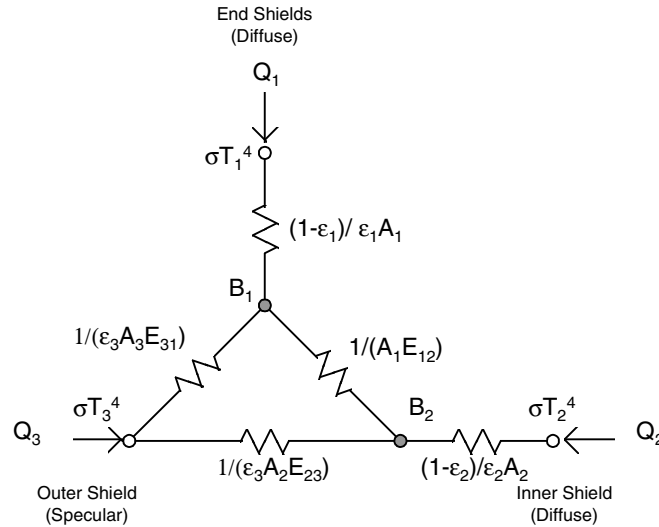


Figure 12 Radiosity Formulation for the Specular Model

The exchange factor between the surfaces 1 and 2 (the inner cylinder and end shields) is determined by subdividing the inner cylinder into axial segments and computing diffuse form factors from each segment to the outer cylinder. Radiation emitted by the inner cylinder may follow one of three paths as shown in Figure 13. In the first path (shown as dark gray in the figure), the radiation is directly incident upon the end shields. In the second path (medium gray), radiation incident upon the outer shield is reflected to one of the end shields on a single bounce. In the third path (light gray), the remaining radiation incident upon the outer shield is reflected back to the inner cylinder. This simplification is possible since no ray that is both emitted by the inner cylinder and incident upon the outer cylinder can be reflected back to the outer cylinder; the ray must return to the inner cylinder or be reflected to one of the end shields. The form factors from the inner cylinder to the outer cylinder and end shields are either computed directly from available correlations or derived from angle factor algebra (see Sparrow [9]).

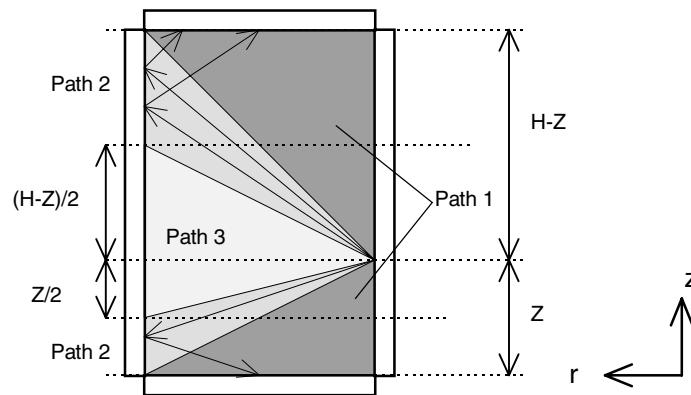


Figure 13 Destination of Radiation Emitted by the Inner Cylinder

The angle factor algebra necessary to determine the diffuse form factors corresponding to ray paths 1, 2, and 3 originating from a point on the inner cylinder is shown in Figure 14. Surface A is the originating surface and form factors to surfaces C, D, and E are desired (the form factor to surface F is known analytically). The process is illustrated for the upper region only and can be repeated to determine the form factors to corresponding surfaces in the lower region. Imaginary surfaces G and H are used to facilitate the calculation. Form factors F_{AC} , F_{AD} , and $F_{AE}+F_{AF}$ correspond to ray paths 1, 2, and 3 respectively. From analytical correlations it is possible to determine all possible form factors within a vertical annulus formed by concentric cylinders of equal height. The form factors known analytically are indicated with an apostrophe.

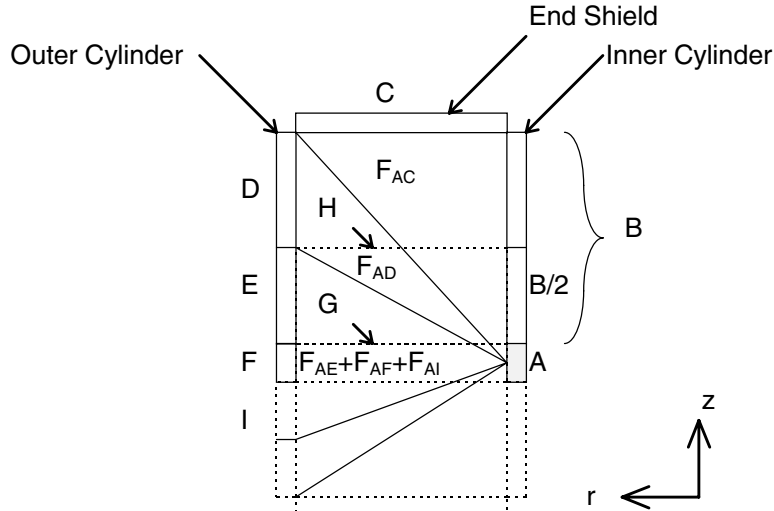


Figure 14 Angle Factor Algebra

The form factors between surface C and surfaces B and A+B are analytically known. The form factor from surface C to A is determined as shown in Equation 18. The form factor from surface A to C can be determined through reciprocity as shown in Equation 19. The form factor from surface A to C represents the fraction of energy emitted by surface A that is directly incident upon surface C (Path 1).

$$F_{C \rightarrow A} = F'_{C \rightarrow A+B} - F'_{C \rightarrow B} \quad (18)$$

$$F_{A \rightarrow C} = F_{C \rightarrow A} \frac{A_C}{A_A} = \left(F'_{C \rightarrow A+B} - F'_{C \rightarrow B} \right) \frac{A_C}{A_A} \quad (19)$$

The form factor from surface A to the imaginary surface H can be determined in a similar manner as shown in Equations 20 and 21.

$$F_{H \rightarrow A} = F'_{H \rightarrow A + \frac{B}{2}} - F'_{H \rightarrow \frac{B}{2}} \quad (20)$$

$$F_{A \rightarrow H} = F_{H \rightarrow A} \frac{A_H}{A_A} = \left(F'_{H \rightarrow A + \frac{B}{2}} - F'_{H \rightarrow \frac{B}{2}} \right) \frac{A_C}{A_H} \quad (21)$$

Using the imaginary surface G, the form factor between surface A and surface E can be determined from the relationship in Equation 22. This is one of three form factors required to compute the fraction of energy emitted by surface A that is directly incident upon the outer cylinder along path 3.

$$F'_{A \rightarrow G} = F_{A \rightarrow E} + F_{A \rightarrow H} \quad (22)$$

The combined view from surface A to surfaces D and E can be determined from the relationship in Equation 23 using imaginary surface G. The form factor from surface A to surface D is determined by subtracting the form factor to surface E determined previously from the

combined view (Equation 24). The form factor from A to D represents the fraction of energy emitted by surface A that is reflected onto surface C from the specular outer cylinder (path 2).

$$F'_{A \rightarrow G} = F_{A \rightarrow D+E} + F_{A \rightarrow C} \quad (23)$$

$$F_{A \rightarrow D} = F_{A \rightarrow D+E} - F_{A \rightarrow E} \quad (24)$$

To determine the total diffuse form factors corresponding to the energy fractions transmitted to the outer and end shields, the inner cylinder is axially subdivided into a number of segments as shown in Figure 15. The number of axial segments is incremented until the results returned by the computation vary by less than 1×10^{-4} with 2500 and 3000 segments typical of the number of divisions used. The diffuse form factors are determined at the vertical midpoint of each segment and are then numerically integrated over the height of the cylinder to find the total diffuse form factor from the inner surface. A trapezoidal approximation is used for the integration scheme.

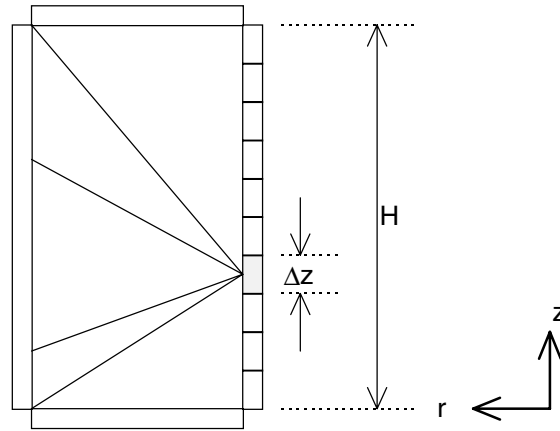


Figure 15 Determination of the Total Form Factors from the Inner Cylinder

Determining the exchange factor between surfaces 3 and 1 (the outer radial shield and the end shield) is complicated by the curvature of surface 3. Since surface 3 has a nonzero view of itself ($F_{33} \sim 0.25$), rays originating from surface 3 can be reflected many times before reaching the end shield (surface 1). This phenomenon is shown in Figure 16 for two different rays originating from surface 3.

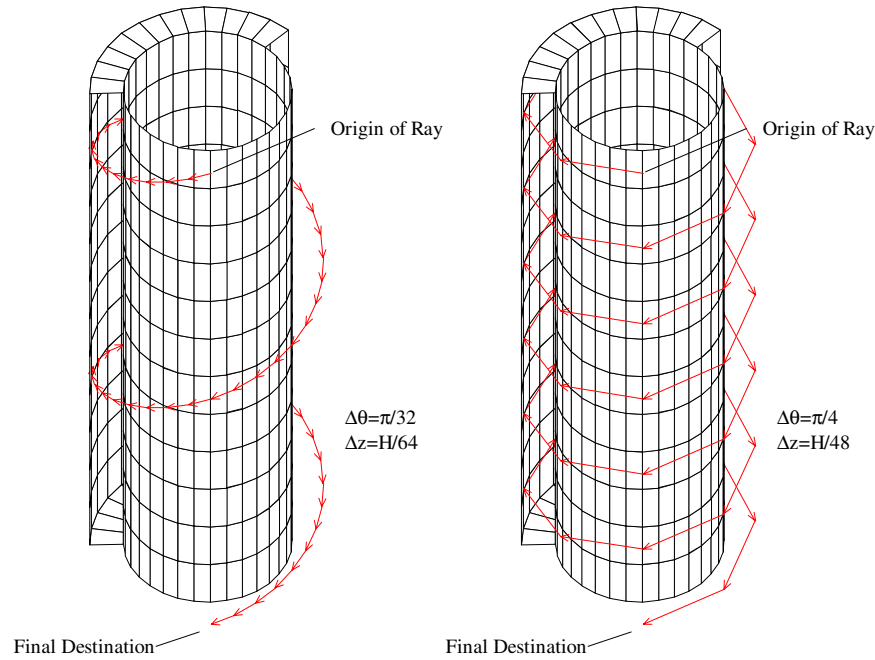


Figure 16 Anatomy of a Specular Reflection

Fortunately, no ray originating from surface 3 can be reflected by surface 3 onto surface 2. The indirect portion of the exchange factor between surfaces 3 and 1 is determined by numerically integrating the product of the diffuse form factor from surface 3 to itself multiplied by the reflectance raised to the integer number of bounces before reaching surface 1. Equation 25 represents the exchange factor between an infinitesimal area on surface 3 to surface 1. To obtain the total exchange factor between surface 3 and surface 1, the infinitesimal exchange factor is integrated over the entire area of surface 3 as shown in Equation 26. Definitions for the angles β_i and β_j and the segment r_{ij} (or r_{ji} for the reverse direction) connecting the two areas are illustrated in Figure 17.

$$(\rho_3^n f_n)_{dA_i \rightarrow A_j} = \int_{A_j} \frac{\rho_3^n \cos \beta_i \cos \beta_j dA_j}{\pi r^2} \quad (25)$$

$$\sum_{n=1}^{\infty} \rho_3^n f_n = \frac{1}{A_i} \int_{A_i} (\rho_3^n f_n)_{dA_i \rightarrow A_j} dA_i \quad (26)$$

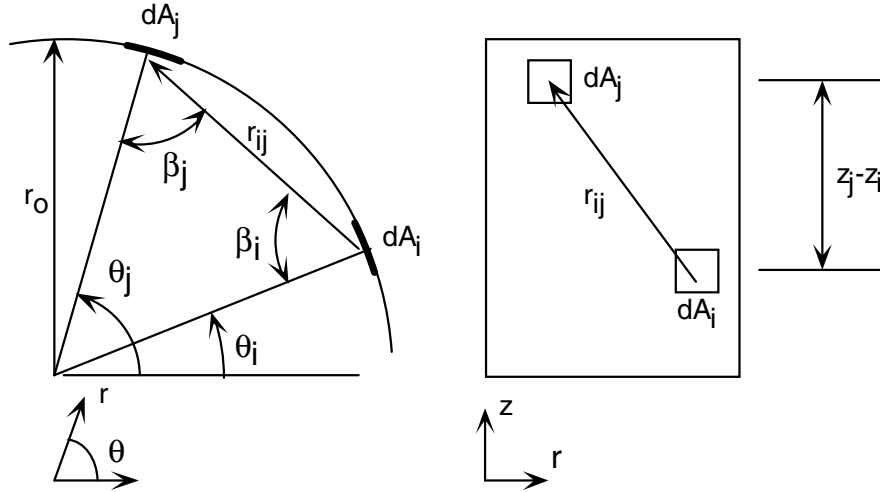


Figure 17 Form Factor Calculation Parameters

The exchange factor equations are simplified with the following definitions (in Equations 27, 28, and 29) for r_{ij} , $\cos \beta_i$, and $\cos \beta_j$, where \vec{n}_i and \vec{n}_j are the surface normals for the infinitesimal surfaces.

$$r_{ij} = \sqrt{2r_o^2(1 - \cos(\theta_j - \theta_i)) + (z_j - z_i)^2} \quad (27)$$

$$\cos \beta_i = \vec{n}_i \cdot \frac{\vec{r}_{ij}}{|\vec{r}_{ij}|} = \frac{r_o(1 - \cos(\theta_j - \theta_i))}{\sqrt{2r_o^2(1 - \cos(\theta_j - \theta_i)) + (z_j - z_i)^2}} \quad (28)$$

$$\cos \beta_j = \vec{n}_j \cdot \frac{\vec{r}_{ji}}{|\vec{r}_{ji}|} = \frac{r_o(1 - \cos(\theta_j - \theta_i))}{\sqrt{2r_o^2(1 - \cos(\theta_j - \theta_i)) + (z_j - z_i)^2}} \quad (29)$$

The final form of the integral over surface A_j is given in Equation 30. The exponent n , which is the integer number of reflections before a ray originating at A_i reaches the upper or lower end shield, is determined by dividing the distance from z_i to the upper or lower end shield by the difference in height between A_i and A_j . Which end shield is the final destination of the ray is determined by height of A_j relative A_i (e.g., if A_j is below A_i the ray will be reflected to the lower end shield).

$$(\rho_3^n f_n)_{dA_i \rightarrow A_j} = \int_{A_j} \rho_3^n \frac{r_o^2 (\cos(\theta_j - \theta_i) - 1)^2}{\pi (2r_o^2(1 - \cos(\theta_j - \theta_i)) + (z_j - z_i)^2)^2} dA_j \quad (30)$$

The infinitesimal surface area dA_j is equal to $r_o d\theta dz$. The limits for integration in the axial direction are from 0 to the height of the cylinder. The integration limits in the circumferential direction correspond to the unobstructed view that an infinitesimal area on the surface of the outer cylinder has of the outer cylinder. The half angle is illustrated in Figure 18 by a ray that just misses the inner cylinder. If the origin of the ray is set to $\theta=0$, the limits of integration are $\pm (\pi - 2\beta)$. The angle β of the grazing ray is equal to $\sin^{-1}(r_i/r_o)$.

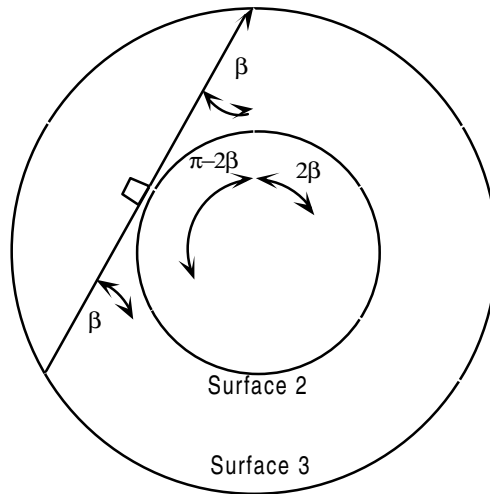


Figure 18 Integration Limits for Form Factor Integration

The final form of the integral to determine the exchange factor from dA_i to A_j is provided in Equation 31.

$$(\rho_3^n f_n)_{dA_i \rightarrow A_j} = \int_0^H \rho_3^n \int_{-(\pi-2\beta)}^{+(\pi-2\beta)} \frac{r_o^2 (\cos(\theta_j - \theta_i) - 1)^2}{\pi (2r_o^2 (1 - \cos(\theta_j - \theta_i)) + (z_j - z_i)^2)^2} r_o d\theta dz \quad (31)$$

Since the view of dA_i to A_j is dependent upon height only, the final form of the total integral can be expressed as shown in Equation 32.

$$\sum_{n=1}^{\infty} \rho_3^n f_n = \frac{1}{A_i} \int_{A_i} (\rho_3^n f_n)_{dA_i \rightarrow A_j} dA_i = \frac{1}{H} \int_0^H (\rho_3^n f_n)_{dA_i \rightarrow A_j} dz \quad (32)$$

Diffuse versus Specular Exchange – Analytical Model

The governing equations for the diffuse and specularly reflecting models are written in matrix form and solved. The diffuse and specular model results are shown parametrically in Table 2 for three furnace power levels. The heat rate is applied to the surface representing the inner cylinder. The outer cylinder and end shield are radiatively coupled to a boundary node representing the environment. The geometry and emissivities of the surfaces are chosen to be representative of the vertical annulus formed by the furnace heater core and inner radial shield. These results are based upon simplified models and are intended for comparison only.

Table 2 Results from the Diffuse and Specular Analyses

	Q ₂ =8.0 Watts			Q ₂ =4.0 Watts			Q ₂ =1.0 Watt		
	Diffuse °C	Specular °C	Delta °C	Diffuse °C	Specular °C	Delta °C	Diffuse °C	Specular °C	Delta °C
Core	626.4	639.5	-13.1	486.4	497.3	-10.9	276.1	283.3	-7.2
End Shield	527.4	525.0	2.3	404.4	402.5	1.9	222.9	221.7	1.2
Inner Radial Shield	537.4	539.4	-2.0	412.7	414.3	-1.6	228.2	229.2	-1.0

The specular surface of the outer cylinder (inner radial shield) does not appear to significantly influence the temperatures of either the end shield(s) or the inner radial shield

relative to a diffuse outer surface (the difference is less than 3°C). However, a specular outer cylinder results in a significantly warmer core. This result is not intuitively obvious since specular reflections from the inner radial shield would seem to reflect more heat to the ends of the furnace, which are less resistant to radiative heat leak to the environment (higher emissivity). However, the radial resistance to heat flow is much greater with a specular shield as demonstrated in Figure 19. With a diffuse outer surface, energy emitted by the core that is incident upon the inner radial shield is diffusely reflected back to the core with a form factor of only 0.7. Approximately 65% of the heat emitted by the core is reflected back to the core on the first exchange with the remainder diffusely reflected to the inner radial shield or to the end shield(s). With a specular shield, approximately 90% of the energy emitted by the core is returned to the core by specular reflections where it is readily absorbed by the highly emissive surface. This is both an unexpected and important result because it appears to be supported by the test data. Measured differences in temperature between the core and inner radial shield are greater than what are predicted by the diffuse assumptions in the overall furnace model.

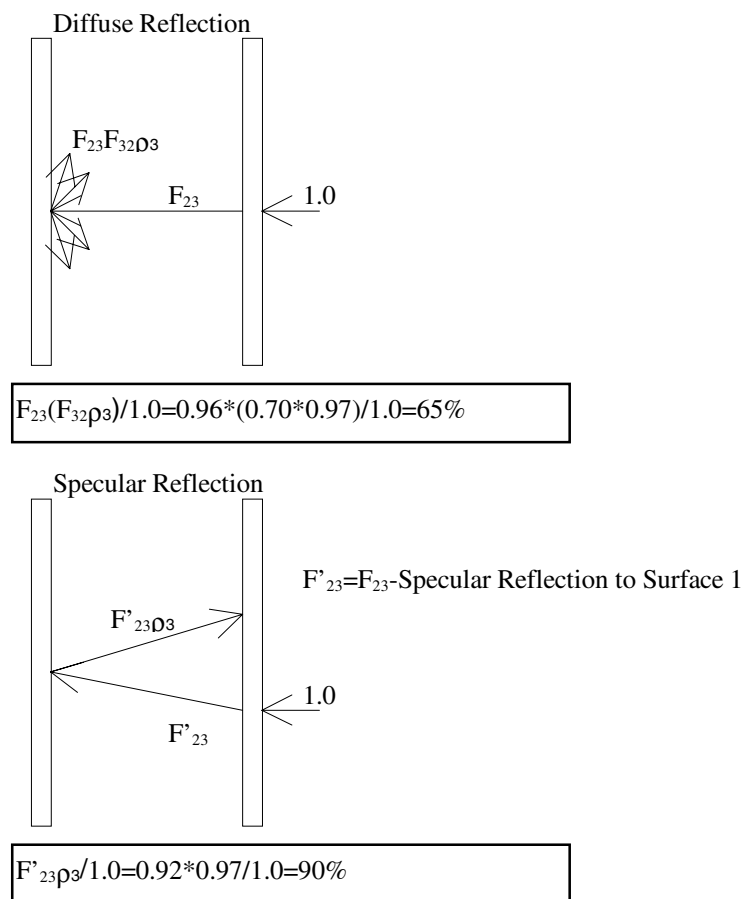


Figure 19 Diffuse and Specular Reflections

Diffuse versus Specular Exchange – Numerical Model

The numerical modeling of the radiative exchange between the diffuse and specular surfaces of the furnace is accomplished through the Thermal Desktop Radiation Analyzer (RadCAD) [10] developed by Cullimore and Ring Technologies. The diffuse TRASYS model is imported directly into the radiation analyzer with the inner surfaces of the inner, middle, and outer radial shields set to reflect 100% specularly. All remaining surfaces reflect diffusely. No directional dependence of the optical properties is assumed. The radiation conductors are

calculated via ray tracing with 1000 rays originating from each surface in the model. The Thermal Desktop outputs a radiation conductor file (much like TRASYS) and that is included during pre-processing of the SINDA model described above. The diffuse and specular model results are compared to the experimental results in Table 3 for three furnace power levels.

Table 3 Results from the Diffuse and Specular Analyses (Numerical)

Test	Core (°C)			Radial #1 (°C)			End (°C)			Power (Watts)
	Meas	Specular	Diffuse	Meas	Specular	Diffuse	Meas	Specular	Diffuse	
1	390.6	379.0	375.1	268.7	265.9	267.9	113.0	115.2	116.9	11.2
2	262.9	241.4	238.9	170.9	163.6	164.2	72.1	71.1	71.9	5.2
3	506.5	514.5	508.0	368.1	371.1	373.3	153.2	166.7	168.7	20.1

CONCLUSIONS

As shown in the table, the results with specularly reflecting radial shields offer a slight improvement over predictions based upon a diffuse exchange assumption. It should be noted that, compared with the diffuse model, the difference between the core and inner radial shield temperature is always larger for the specular model. This result is expected because, in the case of concentric cylinders, a specular reflection of a ray emitted from the inner cylinder is always returned to the inner cylinder (where a diffuse reflection is not).

REFERENCES

- [1] Jalbert, L. B., Banish, R. M., and Rosenberger, F., *Real Time Diffusivity Measurements in Liquids at Several Temperatures with One Sample*, Physical Review E, Volume 57, Number 2, 1998, p. 57.
- [2] Wessling, F. C., *Isothermal Diffusion Oven*, University of Alabama in Huntsville, 1994, drawings 94050 through 94457.
- [3] *Thermal Radiation Analyzer System (TRASYS), Version P25, User's Manual*, JSC-22964, Lockheed Engineering and Management Services Company, Houston, 1991.
- [4] *Systems Improved Numerical Differencing Analyzer and Fluid Integrator (SINDA/FLUINT), Version 2.4, User's Manual*, MCR-90-512, Martin Marietta Corporation, Denver, 1991.
- [5] Sparrow, E. M. and Cess, R. D., *Radiation Heat Transfer*, Brooks/Cole Publishing Company, Belmont, 1970, pp. 86-99.
- [6] Ibid., p 11.
- [7] Ibid., pp. 137-149.
- [8] Ibid., pp. 300-310.
- [9] Ibid., pp. 129-131.
- [10] Thermal Desktop Version 3.1, Cullimore and Ring Technologies, www.crtech.com.

PHOTOPHORESIS OF MICRONSIZED PARTICLES IN THE FREE-MOLECULAR REGIME

Shahram Tehranian

*Institute for Computational Sciences and Informatics, MS5C3,
George Mason University
Fairfax, VA 22030-4443*

Frank Giovane, Jurgen Blum

*Naval Research Laboratory
4555 Overlook Avenue SW
Washington, DC*

Yu-Lin Xu, Bo A. S. Gustafson

*Department of Astronomy
P.O. Box 112055
University of Florida
Gainesville, Florida 32611*

Abstract

The photophoretic force in the free-molecular regime has been calculated for a spherical particle using the Lorenz-Mie solution to the electromagnetic field within the particle. The temperature distribution on the surface of the suspended particle is calculated using a finite difference method. The effect of the complex refractive index $m=n+ik$ and the normalized size parameter defined as $\alpha=2\pi a/\lambda$ on the photophoretic force and particle velocity is also examined. We show that for a 1 solar constant illumination the photophoretic forces might be as high as 20 percent of the weight of the particles considered.

Nomenclature

a	sphere radius	T_g	gas temperature
B	non-dimensional electric field distribution function	T_p	temperature distribution function within the particle
c_p	specific heat of the particle	r	radial direction
k_p	thermal conductivity of the particle	R	specific gas constant
D	aerodynamic drag	V	photophoretic velocity
E	electric field distribution function	X, Y, Z	rectangular coordinates
E_0	incident electric field strength	α	normalized size parameter
F	photophoretic force	λ	wavelength of the light
H	magnetic field distribution function	r, θ, ϕ	spherical coordinates
I	light source intensity	ρ_p	particle density
k	imaginary part of the complex refractive index	μ	dynamic viscosity of the gas
Kn	Knudsen number		
l	average mean free path of the gas molecules		
m	complex refractive index		
n	real part of the complex refractive index		
P_g	gas pressure		
Q	heat generation function		

Introduction

Photophoresis owes its existence to a nonuniform temperature distribution of an illuminated particle in a gaseous medium. In a discussion of radiometric forces it is convenient to recognize three different flow regimes depending on the pressure of the gas and the size of the suspended particle. The similarity parameter that governs these different regimes is the Knudsen number, defined as $Kn = l/a$, where l is the average mean free path of the gas molecules and a is the radius of the sphere. The photophoretic force increases as the pressure is reduced in the continuum regime where the Knudsen number $Kn \ll 1$, reaching its maximum value in the transition regime for $Kn \sim 1$. As the pressure is further decreased, the photophoretic force will decrease proportionally with the gas pressure. This regime is called the free-molecular regime where the Knudsen number Kn is much greater than one. For the situation where the average mean free path of the gas molecules is much larger than the particle radius, that is for high Knudsen number flows, the photophoretic force can be calculated by considering the momentum transfer to and from the surface of the particle¹⁻³. For gas-suspended spherical particles photophoresis may result in a particle movement either away from or toward the light source. For positive photophoresis, the illuminated side is hotter and the movement is in the direction of the light beam; for negative photophoresis, the shaded side is hotter and the particle moves toward the light source.

Theory

The uneven temperature distribution on the surface of the particle depends on the source function representing the distribution radiant-energy absorption⁴. This source function is defined as

$$Q(r, \theta) = \frac{4\pi n k I}{\lambda} \frac{|E(r, \theta)|^2}{|E_0|^2} = \frac{4\pi n k I}{\lambda} B(r, \theta), \quad (1)$$

where n and k are the real and imaginary parts of the complex refractive index of the particle, λ the wavelength of the light, I the intensity of the light source and $E(r, \theta)$ the electric field within the particle. E_0 is the incident electric field strength and $B(r, \theta)$ the non-dimensional electric field distribution function. The starting point for a theory of photophoresis must be the determination of this source function in terms of the non-dimensional electric field represented by $B(r, \theta)$ in the equation above. The particle geometry and coordinates are depicted in figure 1. In this figure the spherical particle is illuminated by a monochromatic, parallel, linearly polarized wave propagating along the Z axis.

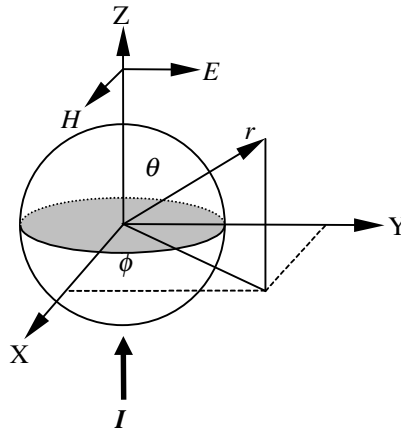


Figure 1. Geometry of illuminated particle for analysis.

For micron-sized particles where the radius of the particle is comparable to the wavelength of the light source the radiation absorption will be distributed within the entire volume of the illuminated particle^{5,6}. For a highly absorbing particle with a diameter much larger than the wavelength λ the absorption of the energy will most likely occur on the surface of the irradiated hemisphere with a resulting force directed away from the light source. This is referred to as positive photophoresis. For a less absorbing particle, however, the irradiated energy can be deposited anywhere within the particle depending on the normalized size parameter $\alpha=2\pi a/\lambda$ and the complex refractive index $m=n+ik$ of the particle. This may result in a negative photophoretic force where the particle moves toward the light source.

The internal electrical field was calculated through the use of Ricatti-Bessel functions, Legendre functions, and their derivatives. To obtain a sufficiently accurate internal field distribution for spherical particles in practical calculations, reliable numerical techniques are of crucial importance. Minor errors in the total rate of energy absorption will completely distort the temperature distribution within a particle and the associated photophoretic force. The normalized source function given by equation (1) depends strongly on the size parameter and the complex refractive index of the illuminated sphere. The pattern of the distribution of absorption centers in the a sphere changes dramatically with the change in size and refractive index. Figure 2 shows the non-dimensional electric field $B(r, \theta)$ for the X-Z plane ($\phi=0$) of the particle for different size parameters and a refractive index of $m=1.95-0.3i$. The electric field vector points in the Y-direction and the light is propagating in the Z-direction from negative (at the front side of the particle) to positive (at the back side of the particle). Since the present work aims at the photophoretic behavior of spherical particles we only give a brief description of the trends of the source function in terms of the non-dimensional electrical field. The calculation of the heat source function both for single spheres and for aggregates has been studies extensively by Xu et al⁷.

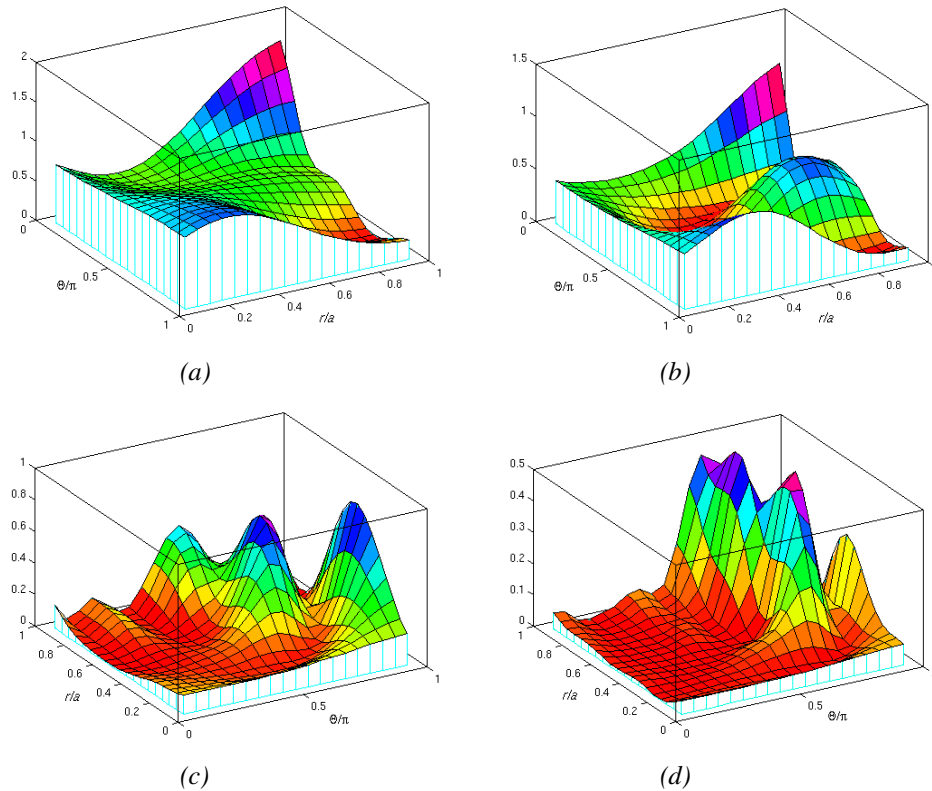


Figure 2. Non-dimensional electric field $B(r, \theta)$ for $m=1.95-0.3i$ with increasing size parameter α . (a) $\alpha=2.0$, (b) $\alpha=2.6$, (c) $\alpha=4.0$, (d) $\alpha=6.0$.

The non-dimensional electric field for a size parameter of 2.0 and a refractive index $m=1.95-0.3i$ is shown in figure 2a. For this combination of size parameter and refractive index the back absorption is clearly dominant. This would result in what is termed as negative photophoresis. Recall from figure 1. that $\theta = 0$ corresponds to the shaded side of the illuminated particle. In figure 2b the refractive index of the particle is kept constant while the size parameter α is increased to a value of 2.6. In this case both back and front absorption occur with the highest absorption center remaining on the shaded side of the sphere. As the size parameter is further increased as shown in figure 2c-d the absorption on the front side of the particle is strongly accentuated while the absorption within the particle and on the surface of the non-illuminated hemisphere becomes negligible. Hence the photophoretic force changes its direction from negative to positive.

Although, the internal field distribution and thus the direction and magnitude of the photophoretic force are highly dependant on the physical parameters of the particles, changing from particle to particle, some conclusions may be drawn. For highly absorptive particles, that is, spheres having a large value of the imaginary part of the refractive index, the incident radiation can hardly penetrate and absorption occurs all along the surface of the particle. For highly absorptive particles of a large size parameter only front absorption occurs, leading to positive photophoresis. However It should be noted that the effects of the size parameter, α , the real and imaginary part of the refractive index n and k on the source function are interrelated.

Analysis

Photophoretic force in the free-molecular regime

Consider a spherical particle of radius a suspended in gas with a pressure P_g and a temperature T_g and illuminated by a light beam of intensity I . It is assumed that the direct interaction of the light source with the surrounding medium is negligible. The temperature distribution T_p within the suspended particle is governed by the unsteady heat conduction equation given by

$$\rho_p c_p \frac{\partial T_p}{\partial t} = k_p \nabla^2 T_p + Q, \quad (2)$$

where ρ_p , c_p and k_p are the particle density, the specific heat and the thermal conductivity of the particle, respectively. Q is the heat source produced by electromagnetic wave absorption defined by equation (1). Neglecting the ϕ dependence of the temperature distribution of the particle and writing the heat conduction equation in spherical coordinates, equation (2) takes the form of

$$\rho_p c_p \frac{\partial T_p}{\partial t} = k_p \left[\frac{1}{r^2} \frac{\partial}{\partial r} \left(r^2 \frac{\partial T_p}{\partial r} \right) + \frac{1}{r^2 \sin \theta} \frac{\partial}{\partial \theta} \left(\sin \theta \frac{\partial T_p}{\partial \theta} \right) \right] + Q(r, \theta). \quad (3)$$

By using a Maxwellian distribution function for the incident and reflected gas molecules from the surface of the particle the local energy fluxes can be calculated. The boundary condition on the surface of the illuminated sphere is the sum of the incident energy flux H_i , the reflected energy flux H_r , the heat flux by conduction within the particle I_c , and the heat flux due to radiation to and from the surface of the particle I_r . Assuming that the surrounding medium is stationary, kinetic theory^{8,9} provides rather simple expressions for the energy fluxes of the incident and reflected gas molecules given by equations (4) and (5).

$$H_i = \frac{1}{2} P u. \quad (4)$$

$$H_r = \frac{1}{2} P \bar{u} \left(\frac{T_p}{T_g} \right)^{1/2}. \quad (5)$$

\bar{u} is the average molecular speed of the gas molecules given by

$$\bar{u} = \sqrt{\frac{8RT_g}{\pi}}, \quad (6)$$

with R being the specific gas constant.

The surface radiation energy flux I_r is given by the Stefan-Boltzman law and takes the form

$$I_r = \varepsilon \sigma (T_p^4 - T_g^4), \quad (7)$$

where the first part represents the radiation from the surface of the particle to the surrounding medium and the second part the radiation from the gas to the particle. ε is the emissivity of the particle and σ is the Stefan-Boltzmann constant.

The heat conducted from the particle surface is

$$I_c = -k_p \left(\frac{\partial T_p}{\partial r} \right)_{r=a}, \quad (8)$$

where k_p is the thermal heat conductivity of the particle.

Hence the boundary condition at the surface of the particle is given by

$$H_i - H_r - I_r + I_c = 0. \quad (10)$$

Once the heat generation function Q is determined the temperature distribution T_p within the particle can be calculated through equation (3) with the boundary condition given by equation (10).

In the free molecular regime, the incident momentum based on the freestream gas temperature is uniform over the entire surface of the particle and it makes zero contribution to the force. It is the uneven reflected momentum that results in the photophoretic force. Assuming that all the molecules are reflected diffusely from the surface of the particle, the pressure due to reflected molecules is given by

$$P_r = \frac{1}{2} P \left(\frac{T_p}{T_g} \right)^{1/2}. \quad (11)$$

Hence the photophoretic force will take the form

$$F = -\pi a^2 P \int_0^\pi \left(\frac{T_p}{T_g} \right)^{1/2} \cos \theta \sin \theta d\theta, \quad (12)$$

where the sign of the force is chosen such that F is considered positive in the direction of the propagating light. The photophoretic velocity V_p can be obtained by equating the photophoretic force given by equation (12) to the local aerodynamic drag on the body. The aerodynamic drag on the spherical particle is expressed as

$$D = \frac{6\pi \mu Va}{1 + Kn \left(c_1 + c_2 e^{-\frac{c_3}{Kn}} \right)}, \quad (13)$$

where $c_1=1.20$, $c_2=0.41$, and $c_3=0.88^4$.

Results

The temperature distribution for a spherical particle with a refractive index of $m=1.95-0.3i$ and two different size parameters is shown in figure 3. The non-dimensional electric field $B(r, \theta)$ for the same combination of size parameter and refractive index was previously shown in figure 2a and 2d. The normalized size parameter α is varied from 2 to 6 while the gas pressure is kept constant at 10 torr or 1330 Pa. The light intensity is put equal to the solar constant, 1353 W/m^2 . The specific heat c_p , the particle density ρ_p , the thermal conductivity k_p and the gas temperature T_g are 840 J/KgK , 1900 Kg/m^3 , 5.0 W/mK , and 273 K , respectively. For the particle considered, the angle $\theta = 0$ corresponds to the shaded or non-illuminated side of the particle, while $\theta = \pi$ represents the front side of the sphere.

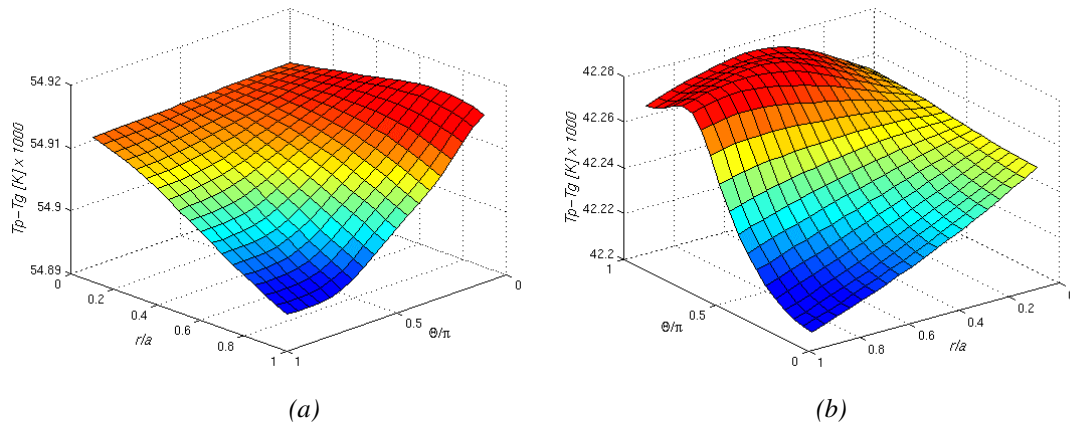


**Figure 3. Temperature distribution inside a spherical particle for $m=1.95-0.3i$.
(a) $\alpha=2.0$, (b) $\alpha=6.0$.**

For the first case with a size parameter of 2.0, the absorption center is located on the shaded side of the particle, resulting in higher temperatures on the non-illuminated hemisphere. Hence a negative photophoretic force is exerted. As the normalized size parameter is increased to a value of 6, the absorption peaks will move towards the front side of the suspended particle as shown in figure 2d. This behavior is clearly demonstrated in figure 3b showing higher temperatures on the front side of the particle. Hence a positive photophoretic force is obtained. Note that the difference between the temperature within the particle and the gas temperature, $T_p - T_g$ ranges only from 0.04 to 0.05 K. Hence a small temperature difference is sufficient enough to induce a photophoretic force on the spherical particle.

Figure 4 to 6 show the behavior of the photophoretic force for various refractive indices versus the normalized size parameter α . In figure 4 the photophoretic force F_p is shown for two different refractive indices versus the size parameter. In this case the imaginary part of the refractive index k is kept constant at a value of 0.001 while the real part n is increased from a value of 1.33 to 1.95. The photophoretic force is negative almost over the entire range of size parameters considered both for $m=1.33-0.001i$, and $1.95-0.001i$. For $m=1.33-0.001i$ the magnitude of the photophoretic force increases smoothly with α up to a size parameter of 5.0, where oscillations start to occur. For $m=1.95-0.001i$ the oscillations start to occur at a value of $\alpha=2.5$. Hence for higher values of the real part of the refractive index, the onset of oscillations occur at lower values of the size parameter. Furthermore for small values of the size parameter, the higher the real part of the refractive index, the larger is the magnitude of the photophoretic force.

Increasing the imaginary part of the refractive index to a value of 0.05 , the oscillatory behavior of the photophoretic force is even more dominated. This is shown in figure 5 for $m=1.33-0.05i$ and $1.95-0.05i$. In figure 6 the imaginary part of the refractive index is further increased to a value of 0.3 . Here the photophoretic force is initially negative for the smallest values of the size parameter and then becomes positive with increasing α . For $m=1.33-0.3i$, the oscillations are completely damped out while there still remains some oscillations for $m=1.95-0.3i$. For these highly absorptive particles with a large size, the incident radiation can hardly penetrate and the absorption occurs only on the front side of the particle, leading to positive photophoresis. Please note that the magnitude of the photophoretic force has increased with increasing k for these combinations of refractive index and size parameter.

Figure 7 shows the photophoretic force to weight ratio F_p/W_p versus the normalized size parameter for $m=1.33-0.3i$ and $1.95-0.3i$. It is interesting to note that for a refractive index of $1.95-0.3i$ and a normalized size parameter of 4.4 , the photophoretic force might be as high as about 20 percent of the weight of the particle considered. It is the authors' belief that even larger forces might be obtained with more suitable combinations of the refractive index and size parameter.

The photophoretic velocity V_p is obtained by equating the photophoretic force given by equation (12) to the local aerodynamic drag on the body given by equation (13). The sign convention on the photophoretic velocity V_p is chosen such that a particle movement in the direction of the light source is considered positive. Figure 8 to 10 show the photophoretic particle velocity for various refractive indices versus the size parameter. Since the particle velocity V_p is directly proportional to the photophoretic force through equation (13), it exhibits similar behavior as the photophoretic force. The highest photophoretic particle velocity obtained is about 8×10^{-6} m/s for a refractive index of $1.95-0.3i$ and a size parameter of 5.8 .

In figure 11 to 13 the present work is compared to the results of Kerker et al⁹. In these figures the photophoretic force is calculated based on the same parameters as given by ref. [9]. The normalized size parameter α is varied from 2 to 6 while the gas pressure is kept constant at 10 torr or 1330 Pa. The light intensity is put equal to the solar constant, 1353 W/m^2 . The light wave length λ , the specific heat c_p , the particle density ρ_p , the thermal conductivity k_p and the gas temperature T_g are $0.6 \text{ }\mu\text{m}$, 840 J/KgK , 1900 Kg/m^3 , 5.0 W/mK , and 273 K , respectively. Although the trends and the behavior of the photophoretic force calculated in the present work is quite similar to the results presented by ref. [9], the magnitude of the photophoretic force does not seem to match at all. It is interesting to note that the calculated photophoretic forces by ref. [9] are about 2×10^4 smaller than the results in the present work. Kerker et al⁹ state that their calculated photophoretic forces are within 2-4 percent of the gravitational forces in the size range $\alpha = 3-4$ for particles with the densities of carbon and water. For a particle density of 1900 Kg/m^3 , a light wave length of $0.6 \text{ }\mu\text{m}$, and a size parameter of 4, the particle weight is $4.4 \times 10^{-15} \text{ kg}$. Assuming that the photophoretic forces are 2-4 percent of the weight of the particle, F_p ranges from 8.7×10^{-17} to 1.7×10^{-16} and is not of the order of 10^{-21} to 10^{-22} as presented by ref. [8]. Hence it is believed that the authors made an error presenting their results. Disregarding from the differences in the magnitude of the photophoretic forces, there is good agreement between the present analysis and the work by ref [9]. However as the size parameter becomes larger, there appear obvious differences between our results and those of Kerker et al⁹. Such an example is shown in figure 13 where higher oscillations are achieved in our calculations. For a large size parameter, the calculation of the source function requires the evaluation of higher orders and degrees Ricatti-Bessel functions, which may cause larger numerical errors. This may be the reason that some approximations work reasonably well at low order function calculations and are not sufficiently accurate at higher orders⁷.

Conclusions

In this study we have calculated the photophoretic forces on spherical particles of various refractive indices and size parameters in the free molecular flow regime and for 1 solar constant illumination. It has been shown that for specific refractive indices and size parameters, the photophoretic force can amount to as much as 20 percent of the particle weights; this means that a substantial size/refractive index discrimination may occur in natural or artificial environments such as the upper atmosphere or in experiments under reduced gravity conditions.

Although absolute particle velocities due to photophoresis are quite small (few microns/sec), the net effect of an additional particle motion may not be negligible; for micron-sized particles the velocity due to Brownian motion is typically 1 mm/s and thus much larger than the photophoretic velocity; however, photophoresis is a directed motion whereas thermal motion is a diffusive motion, so that the drift distance due to photophoresis might be substantially larger than the thermal diffusion.

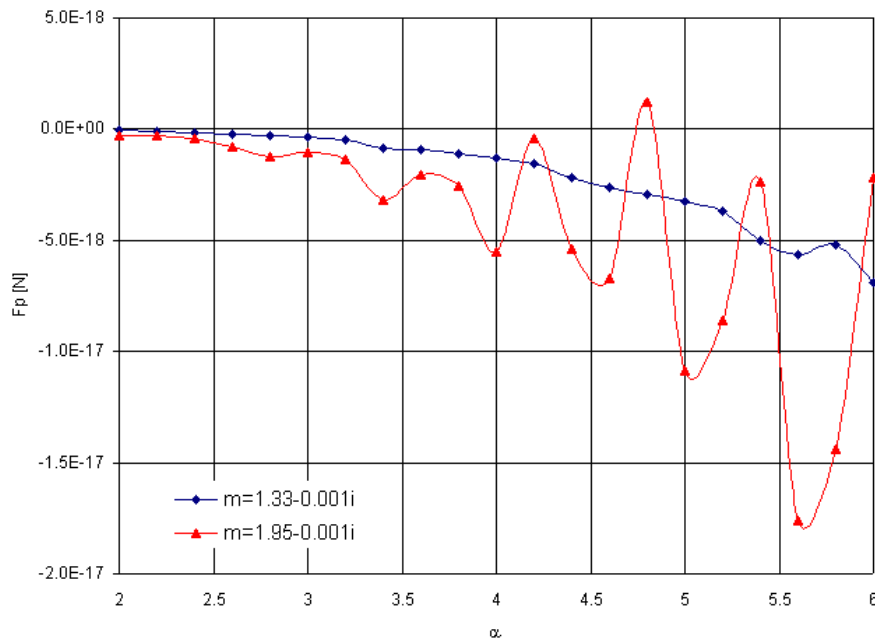


Figure 4. Photophoretic force F_p versus size parameter α for $m=1.33-0.001i$, $1.95-0.001i$.

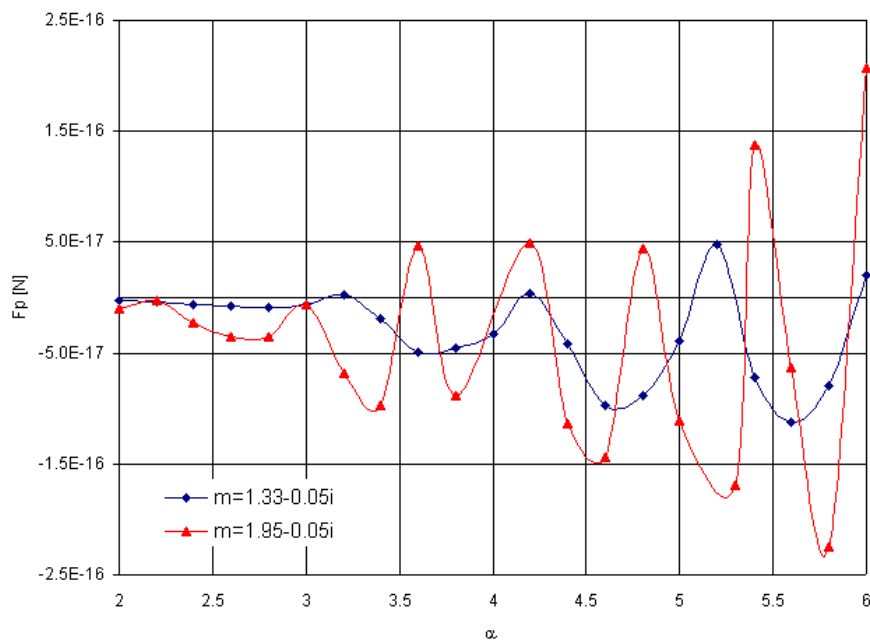


Figure 5. Photophoretic force F_p versus size parameter α for $m=1.33-0.05i$, $1.95-0.05i$.

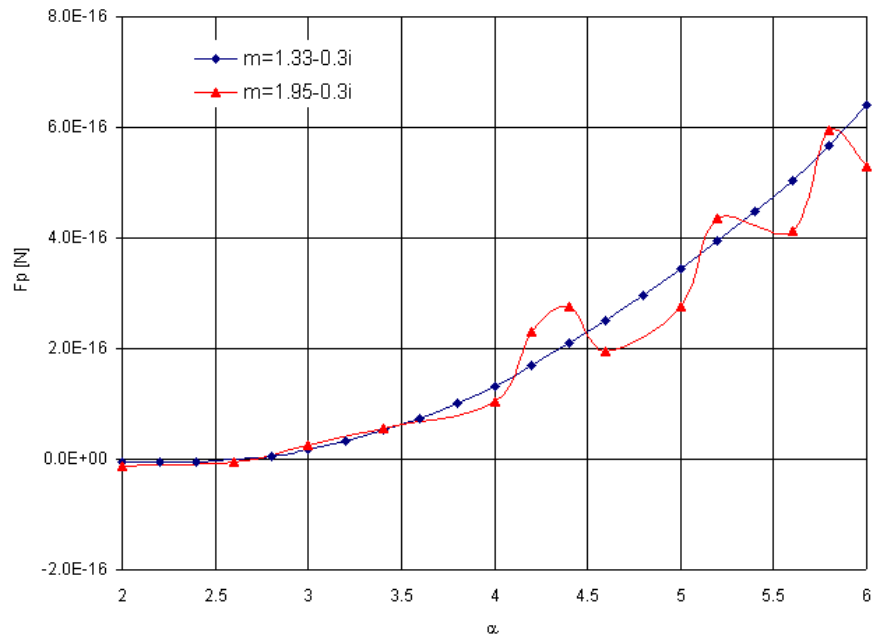


Figure 6. Photophoretic force F_p versus size parameter α for $m=1.33-0.3i$, $1.95-0.3i$.

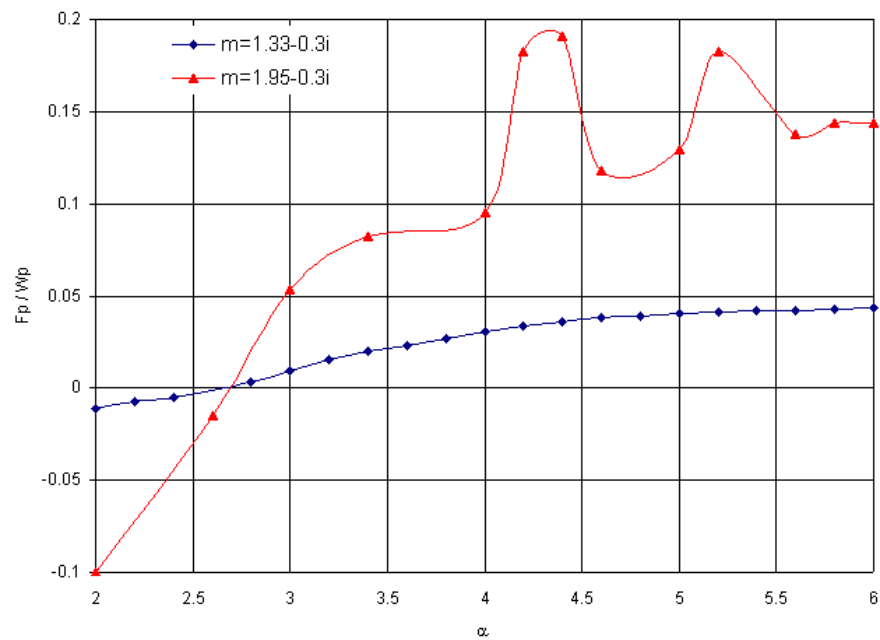


Figure 7. Photophoretic force to particle weight ratio F_p/W_p versus size parameter α for $m=1.33-0.3i$, $1.95-0.3i$.

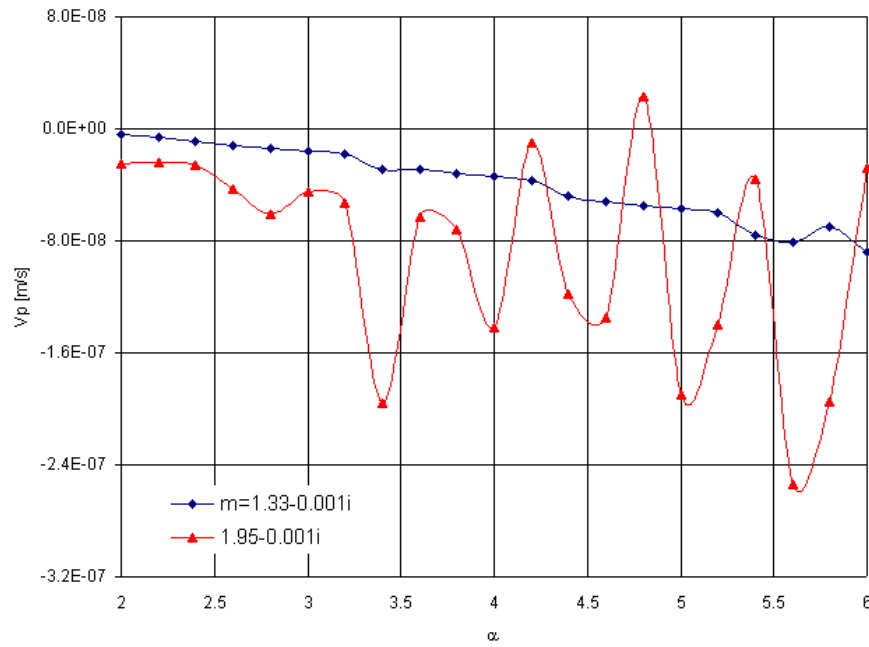


Figure 8. Photophoretic particle velocity V_p versus size parameter α for $m=1.33-0.001i$, $1.95-0.001i$.

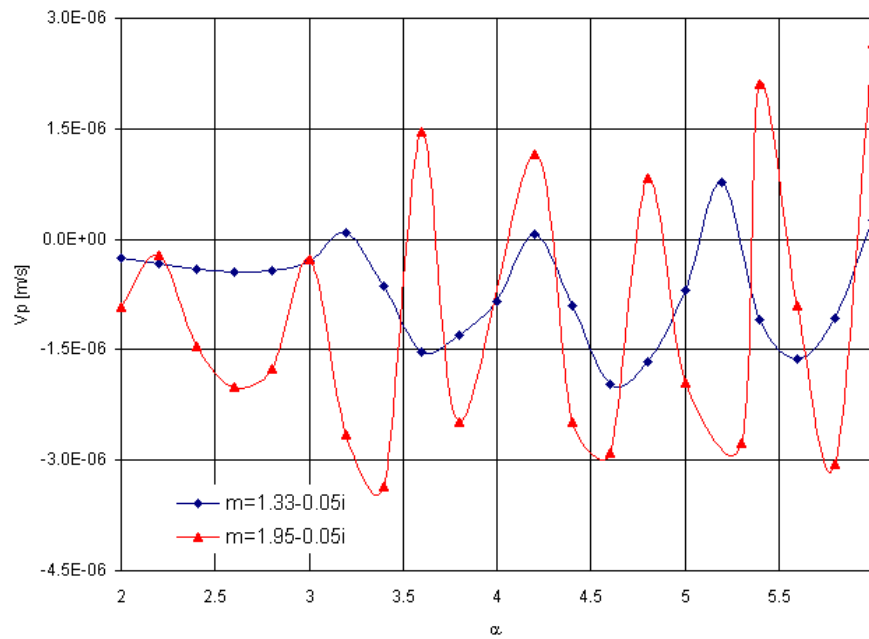


Figure 9. Photophoretic particle velocity V_p versus size parameter α for $m=1.33-0.05i$, $1.95-0.05i$.

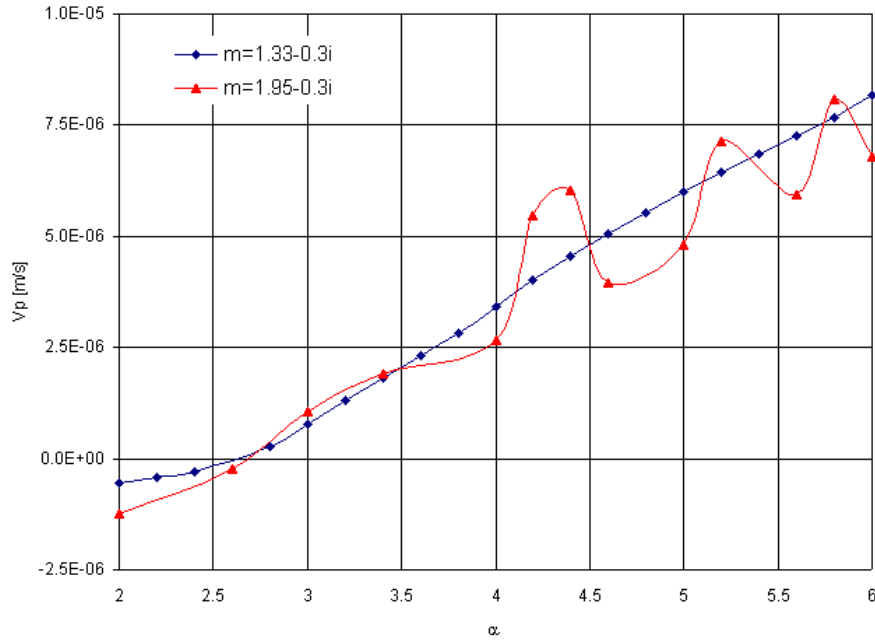


Figure 10. Photophoretic particle velocity V_p versus size parameter α for $m=1.33-0.3i$, $1.95-0.3i$.

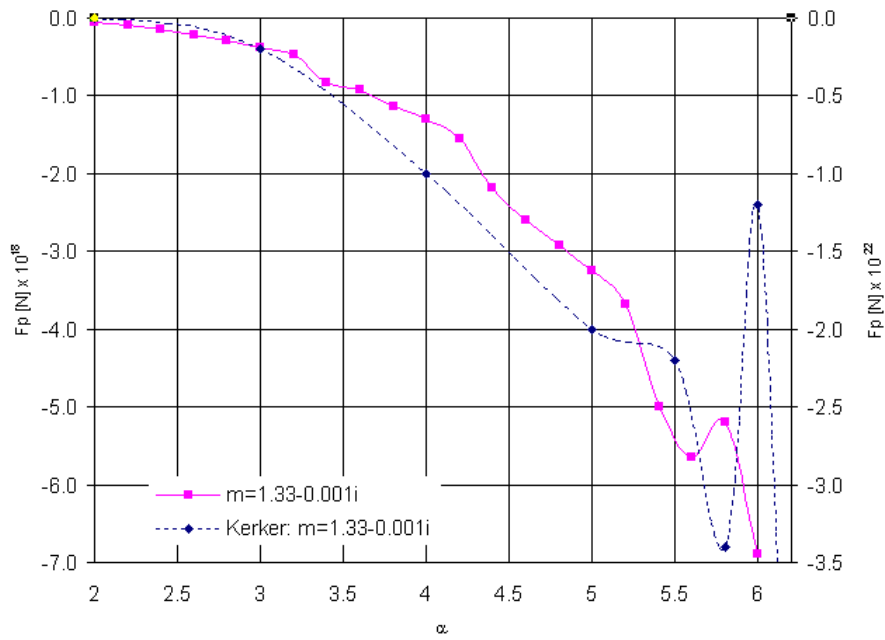


Figure 11. Photophoretic force F_p versus size parameter α for $m=1.33-0.001i$. Comparison of the present work with the results of ref [8].

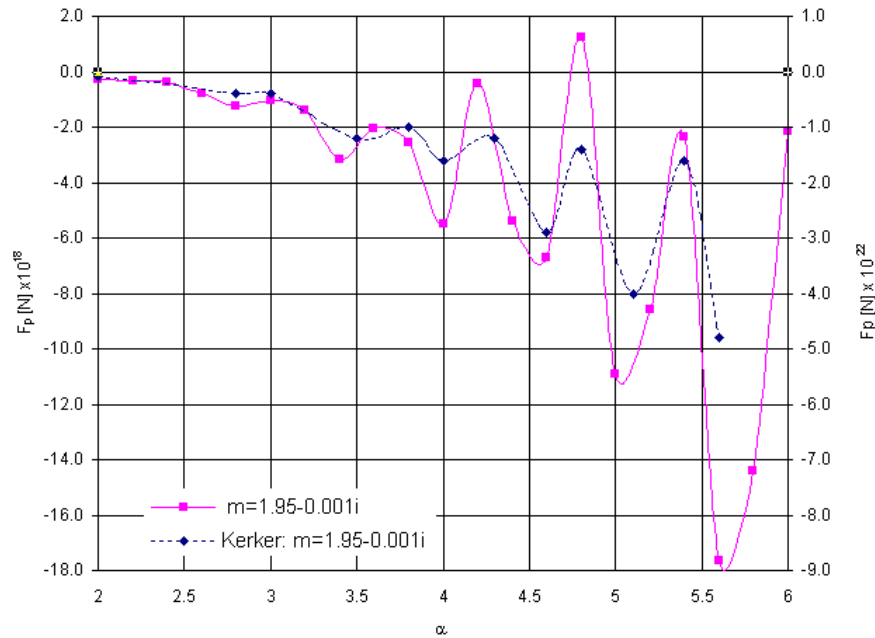


Figure 12. Photophoretic force F_p versus size parameter α for $m=1.95-0.001i$. Comparison of the present work with the results of ref [8].

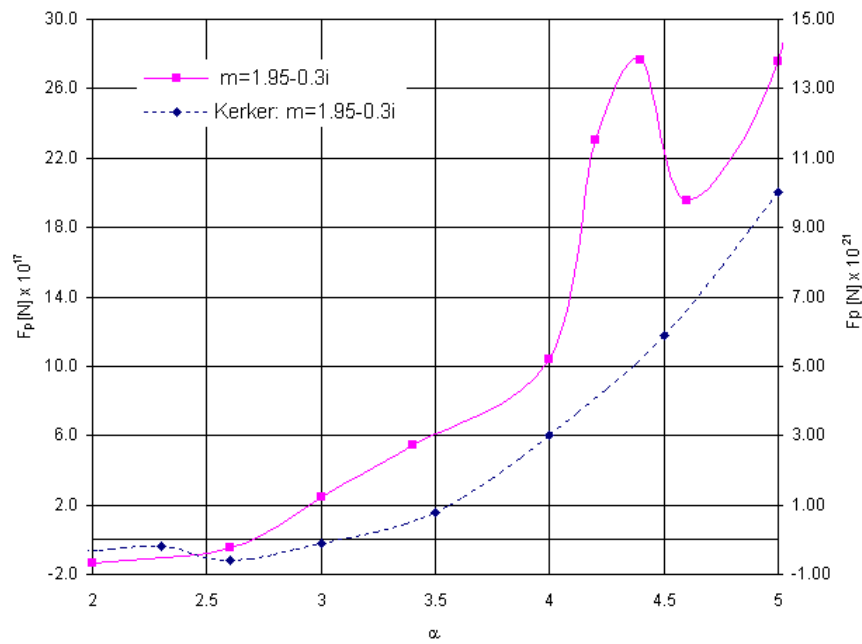


Figure 13. Photophoretic force F_p versus size parameter α for $m=1.95-0.3i$. Comparison of the present work with the results of ref [8].

References

1. N. T. Tong, "Photophoretic force in the free molecule and transition regime", *Journal of Colloid and Interface Science*, Vol. 43, No. 1, April 1973.
2. S. P. Lin, "On photophoresis", *Journal of Colloid and Interface Science*, Vol. 51, No. 1, April 1975.
3. A. Akhtaruzzaman, and S. P. Lin, "Photophoresis of absorbing particles", *Journal of Colloid and Interface Science*, Vol. 61, No. 1, August 1977.
4. D. W. Mackowski, "Photophoresis of aerosol particles in the free molecular and slip-flow regimes", *Int. J. Heat and Mass Transfer*, Vol. 32, No. 5, pp. 843-854, 1989.
5. W. M. Greene, R. E. Spjut, E. Bar-Ziv, A. F. Sarofim, J. P. Longwell, "Photophoresis of irradiated spheres: absorption centers", *J. Opt. Soc. Am. B/Vol. 2*, No. 6/June 1985.
6. P. W. Dusel, M. Kerker, D. D. Cooke, "Distribution of absorption centers within irradiated spheres", *J. Opt. Soc. Am. Vol. 69*, No. 1, January 1979.
7. Yu-Lin Xu, B. A. S. Gustafson, F. Giovane, J. Blum, S. Tehranian, "Calculation of the heat-source function in photophoresis of aggregated spheres", *Physical Review E*, August 1999.
8. G. A. Bird, "Molecular gas dynamics and the direct simulation of gas flows", *Oxford engineering science series*, 42.
9. M. Kerker, D. D. Cooke, "Photophoretic force on aerosol particles in the free molecular regime", *J. Opt. Soc. Am. Vol. 72*, No. 9, September 1982.

REMOTE THERMAL ANALYSIS THROUGH THE INTERNET

Eric T. Malroy

National Aeronautics and Space Administration
Glenn Research Center
Cleveland, Ohio 44135

ABSTRACT

The Heater of the Hypersonic Tunnel Facility (HTF) was modeled using SINDA/FLUINT thermal software. A description of the model is given. The project presented the opportunity of interfacing the thermal model with the Internet and was a demonstration that complex analysis is possible through the Internet. Some of the issues that need to be addressed related to interfacing software with the Internet are the following: justification for using the Internet, selection of the web server, choice of the CGI language, security of the system, communication among the parties, maintenance of state between web pages, and simultaneous users on the Internet system. The opportunities available for using the Internet for analysis are many and can present a significant jump in technology. This paper presents a vision how interfacing with the Internet could develop in the future. Using a separate Optical Internet (OI) for analysis, coupled with virtual reality analysis rooms (VRAR), could provide a synergistic environment to couple together engineering analysis within industry, academia, and government. The process of analysis could be broken down into sub-components so that specialization could occur resulting in superior quality, minimized cost and reduced time for engineering analysis and manufacturing. Some possible subcomponents of the system are solver routines, databases, Graphical User Interfaces, engineering design software, VRARs, computer processing, CAD systems, manufacturing, and a plethora of other options only limited by ones imagination. On a larger scope, the specialization of companies on the optical network would allow companies to rapidly construct and reconstruct their infrastructure based on changing economic conditions. This could transform business.

INTRODUCTION

The use of the Internet has grown at a staggering rate in the last five years. In January of 1995 the number of Internet domain hosts was just under ten million while in January of 2000 the number jumped to over 70 million [1]. The uses and opportunities related to the Internet are expanding and developing. Today the Internet offers the public online educational programs, Internet radio, instantaneous world-wide communication, accessible information, Internet shopping, entertainment, social activities, and a multitude of other opportunities. Since engineering and scientific communities are in the early stages of harvesting the full potential of the Internet, there are many areas of Internet usage that remain to be explored. Primarily, the use of the Internet is limited to information dissemination and educational purposes. The potential for performing analysis through the Internet has focused primarily on simplified models used for educational purposes. This paper presents the work of setting up an Internet system to perform remote thermal analysis of the Hypersonic Tunnel Facility (HTF). This new application of the Internet demonstrates that complex analysis is possible through the Internet. Additionally, the paper provides a visionary look into the future of possible applications of the Internet applied to engineering analysis.

The Hypersonic Tunnel Facility (HTF) had a major failure in 1997, so the facility had to be refurbished. The HTF engineers contacted EDAD (Engineering Design and Analysis Division at NASA Glenn Research Center) to perform a thermal analysis of the primary component, the induction heater. One of the requests was to have a thermal model that the facility engineers could operate to predict facility performance. The users did not want to purchase the software license nor learn the software. Also, the users wanted the ability to operate the software at the facility and at several external engineering offices. Given the requirements, it was decided to interface the thermal model with the Internet to input the relevant information. The primary task was to build the model and interface it with the Internet. The HTF heater project offered the opportunity to demonstrate the potential of using the Internet to perform thermal analysis.

HTF DESCRIPTION

The HTF is a nonvitrated free-jet facility used to test large-scale propulsion models up to Mach 7 [2]. A cutaway of the facility is located in Figure 1. The process of operating the HTF begins with the heat up of the 3-MW graphite heater, which lasts about 10 days. During this time, a low-pressure nitrogen purge gas cools the pedestal and flows through the holes of the block. After the heat up, the "blow down" begins where the high-pressure nitrogen gas flows through the heater. A GN₂ railcar provides the nitrogen at 1500 psi with a mass flow rate of approximately 130 lb/sec during the blow down. The hot Nitrogen flows through water-cooled graphite-lined piping, through an isolation valve, and into the mixer [3]. The injection flange is upstream from the mixer. At the injection flange, diluent nitrogen and oxygen are added to the hot nitrogen to model the specified test conditions. The fluid expands through the nozzle where it enters the test facility. Within the test facility the air stream can reach a velocity of Mach 7. After entering the test chamber, it goes through the diffuser and out the steam ejector to the free air. A typical run consists of ramp up where the test chamber reaches a steady flow rate and the ramp down where the flow is turned off in the test chamber. Normally, the length of the run is under a minute, but it can be longer.

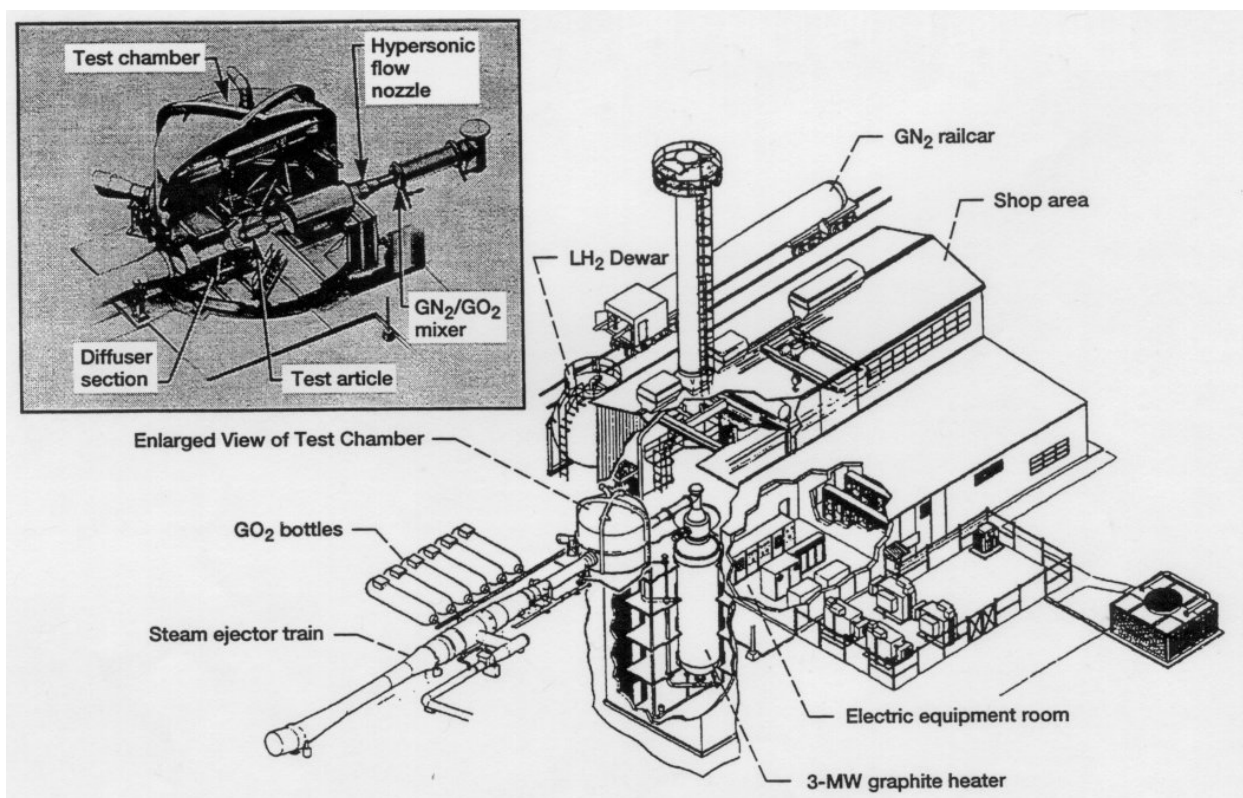


Figure 1. Cutaway view of Hypersonic Tunnel Facility

HTF HEATER MODEL DESCRIPTION

The HTF heater model has six main components: graphite blocks, bottom section, top section, annulus, nitrogen fluid (flow path), and logic simulating the induction heating. SINDA/FLUINT software models the HTF Heater. The thermal modeling software uses a finite difference solver in conjunction with nodes and conductors to analyze thermal systems. The heater is shown in Figure 2.

The first component is the graphite blocks. Fifteen blocks are stacked on each other and are about 30 ft in height. Each block has several thousand holes and is cylindrical in geometry. A hexagon graphite key aligns the blocks so the holes are aligned. The model is simplified by cutting the blocks into a 30-degree section. Included in this

component is the graphite insulation, which covers the block and the silicon tile. A MatLab program calculates the nodes and conductors and writes out the results in the SINDA/FLUINT convention.

The second component is the bottom section, which includes the support floor, silicon base, water-cooled steel jacket and stainless steel pedestal. The radiation shield is included in this component and acts as a shield to prevent the re-circulation piping from overheating. The next component is the top section, which includes the graphite transition cone, fibrous graphite insulation, and stainless steel water jacket. Both the bottom and top sections nodes and conductors are "hard coded" into the SINDA model. This means there is no way to change the conductor values for these sections of the model. Another component is the annulus, which models the silicon carbide spacers, GE Timber Stud-board and copper coils. Cooling water flows through the copper piping, but it is modeled by treating the inner copper piping temperature as a boundary condition.

The next component is the nitrogen fluid modeled with FLUINT. This component includes the flow of gas through the piping, annulus, graphite block and the transition cone. The "ties" that thermally connect the FLUINT model to the SINDA model are included as part of the component.

The last component is the FORTRAN logic that simulates the heating of the blocks. SINDA/FLUINT arrays were used to store the results of another induction heater model. The FORTRAN program uses interpolation routines to determine the heating based on radial distance, temperature and distance from the end block.

The thermal model simulates the run conditions of the heater – the main component of the Hypersonic Test Facility. The model simulates the heat up where induction heating coils are activated to slowly heat the graphite blocks. The heat up needs to be slow to ensure that hotspots don't develop. The main heating occurs in the outer four inches of the blocks. The FORTRAN logic simulates this heating. After the heating, the blow-down occurs where the nitrogen is allowed to flow rapidly through the test facility. The model can simulate the heat up of the facility, blow-down, or both the heat up and blow-down.

The first main inputs required to run the model are the induction coil amps settings and the corresponding times that the amps change. The second main input is the flow rate of the nitrogen gas, which is specified by an array that gives the times of change and the corresponding flow rates. Another main input is the time specifying the end of the heating and the end of the blow down. Included in this page is the increment time used for recalculating the heat rate. The third set of main inputs is the temperatures of the blocks. The other inputs are concerning boundary conditions and initial conditions. These are primarily the temperature settings of the walls and cooling water temperatures.

The purpose of the thermal model is to optimize the heater performance by minimizing the hotspots in the heater and maximizing the output Nitrogen temperature. Also, the model enables the HTF engineers to determine the best operation of the facility when customers request to operate the facility at specified test conditions.

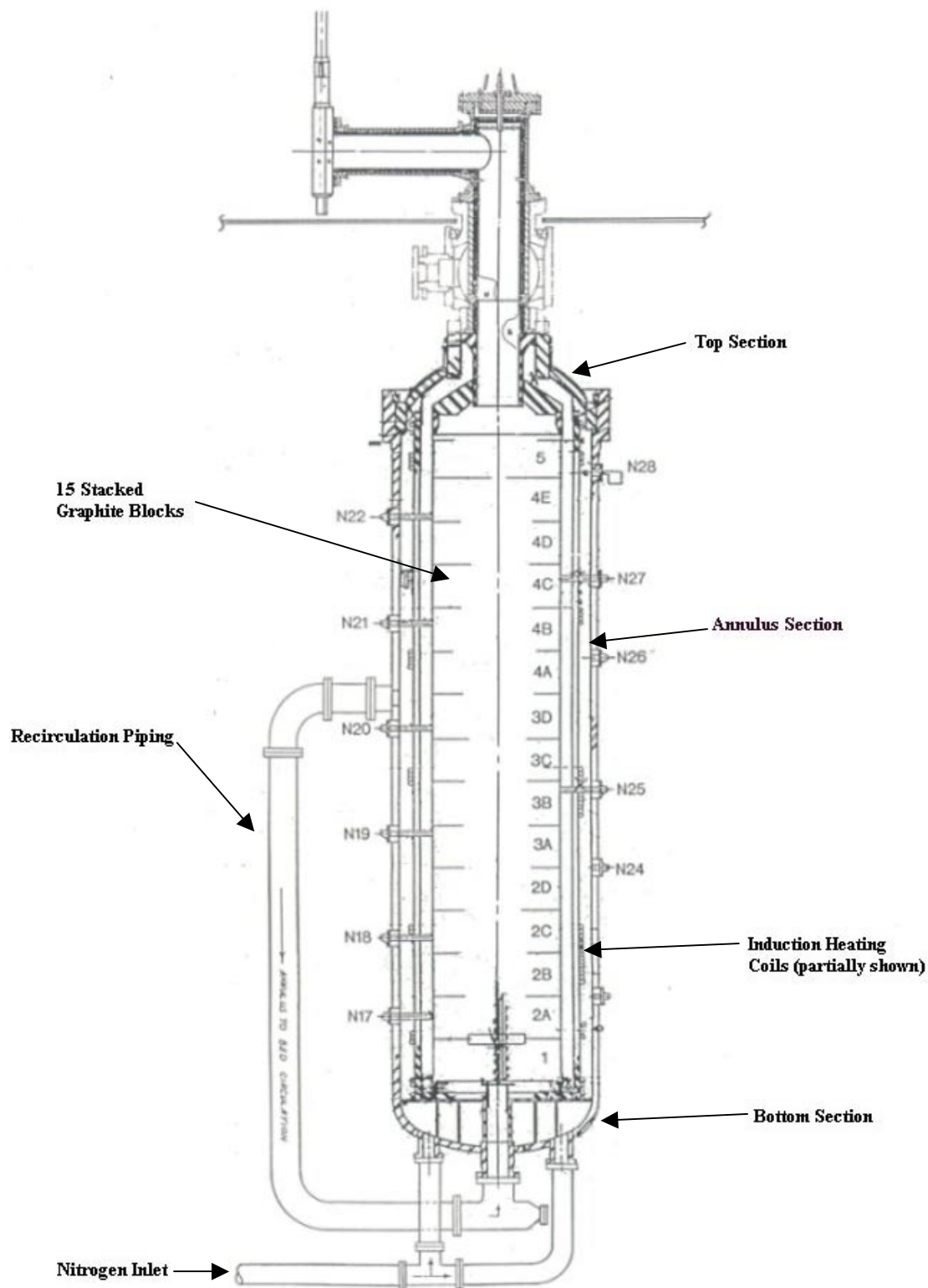


Figure 2. The Heater is the main component of the Hypersonic Tunnel Facility. Some of the main subcomponents and sections are labeled.

INITIAL CONSIDERATIONS WHEN INTERFACING SOFTWARE WITH THE INTERNET

There are a number of issues that need to be resolved prior to interfacing software with the Internet. First, there needs to be justification for interfacing software with the Internet. Typically, this should include a cost analysis comparing other alternative systems against the added benefit of using the Internet. The cost related with programming and developing the Internet system presented by the developers should be multiplied by a factor ranging from 3 to 10 depending on the experience of the developers. The second issue is the web server. Normally, the computer system has a built in web server that can be accessed with assistance from the system administrator. Consultation between the developer, system administrator, and security personnel should enable the best selection of web server. The developer and system administrator need to have a close working relationship when interfacing software over the Internet and using a Common Gateway Interface (CGI). This leads to the third issue, which is the choice of CGI language to use. FORTRAN, C, C++, Pascal, PERL and other computer languages can be used as the interface language. PERL was the computer language used for the CGI of the HTF Heater Model. Another issue was the security of the system. Initially, security was thought to have little impact on the project. As the project developed, security concerns became a significant concern, which required an increase in PERL programming and cost to the project. The fourth issue is the four-way relationship and interaction of the system administrator, CGI programmer, security personnel and organization developing the system. Ideally, the project should be clearly defined and presented by the project lead to insure that all parties are aware of the extent of the project and that feedback can be gathered from all parties. Initially, there was a lack of communication between these individuals for the HTF project resulting in slow progress. Over time, the difficulties were resolved but more time and cost was the result. The sixth issue was the need to maintain state between web pages. About twelve web pages of input information are required to complete an analysis of the HTF Heater Model. After each web page is complete, the system needs to be aware that the previous pages were inputted and know where to store the data. Passwords and user numbers are used to maintain state between web pages for the HTF Heater Model, but other methods can be used. The issue of maintaining state needs to be addressed at the beginning stages of the project. The final issue is the need to handle simultaneous users. For example, several users may be accessing the system at the same time, so the information needs protection from being overwritten. The passwords and user numbers also protect the system from simultaneous users on the HTF system, but again other methods could be used. As with maintaining state, the simultaneous user issues need to be addressed at the early stages of the project.

INTERFACING THE HTF HEATER MODEL WITH THE INTERNET

HTML was used as the graphical user interface (GUI) coupled with PERL programming. Requirements for the model evolved over time as the model was built. The requirements impacted the inputs and outputs of the model, which affect the GUI. Table 1 shows a general list of requirements of the model specified by the facility engineers.

Table 1. Requirements given for HTF heater model.

1. Have adaptable model that can model either heat up, blow-down or both for a given run of the facility.
2. Obtain the temperature distribution in the blocks.
3. Obtain temperature distribution of fluid from inlet of heater through exit of heater at varying time intervals.
4. Obtain temperatures at critical locations that may force facility to halt operation.
5. Have heater model able to simulate different cases of heating.
6. Have heater model able to simulate different cases of fluid flow.
7. Make adaptable model so that future changes can be made as required by facility engineers.

The process of using the GUI is illustrated in Figure 3 by the green boxes. The first process is to gather the inputs through the web pages. PERL programming is used to process the inputs and construct a MatLab input file (shown in purple). Figure 4 shows the dynamic web page used to select the web pages required to input the data. The second process is to use the web page to run the MatLab program that constructs the SINDA thermal model and SINDA include file based on the inputs and the template SINDA model. The third process is to execute the SINDA thermal program and write out the results in the MatLab format. The final process is to display the results. A MatLab program creates a HTML page with links to JPEG files that are also constructed by the MatLab program. The yellow boxes signify the final results. The generation of the results is a dynamic process enabling the user to specify which sections of the model to display. Table 2 shows the sections that the user has an option to display and if the option is currently operational. Some additional MatLab modules are needed to construct the non-operational sections, although the results are found in the MatLab result file. Figure 5 shows a graph that displays the temperature of the Nitrogen as a function of distance that the fluid travels within the holes of the blocks. The results can be generated automatically over the web. A colormap drawing can also be generated over the web that shows the temperature variation within the heater. This web page is dynamic, which enables the user to select a section of the heater to display.

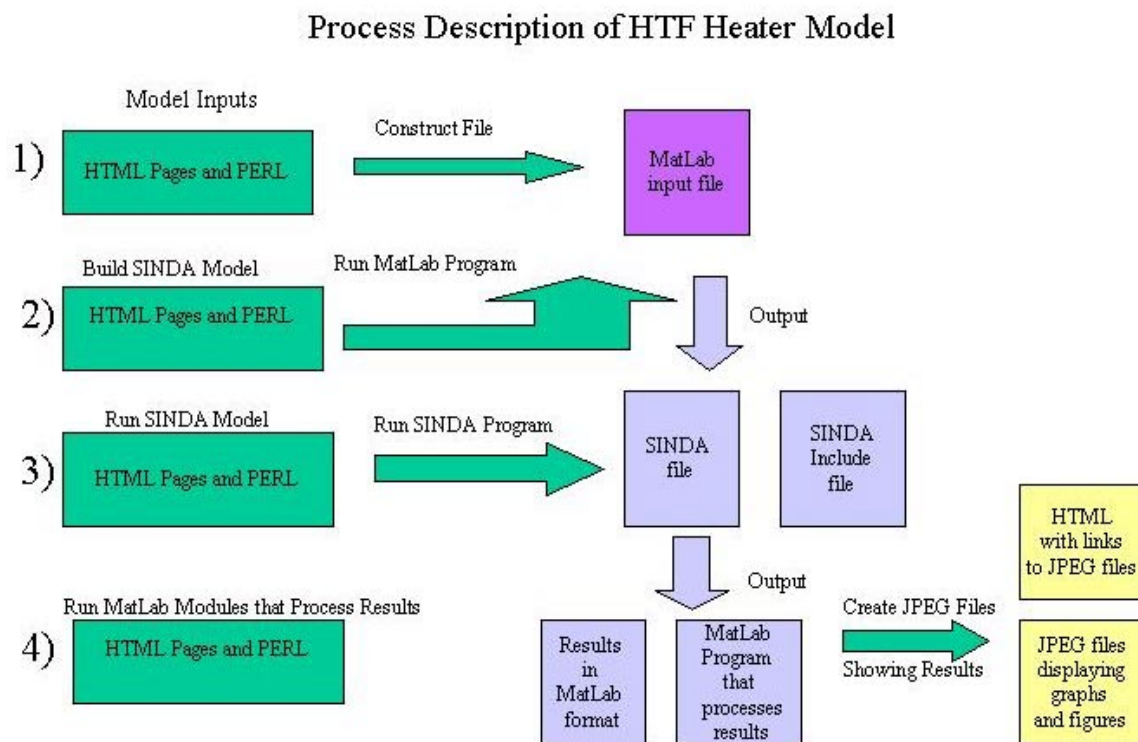


Figure 3. Diagram shows the processes activated by the web pages and the general process of solving the SINDA thermal model. The final results are highlighted in yellow, which are the JPEG graphic files and HTML web pages.

Select Inputs to modify

☒ Amps number of times that the amps change
☒ Flow number of pairs of inputs (doublet array: time,flowrate)
☒ Initial Conditions
☒ Time of Output
☒ Initial Temperature of Blocks [F]
☒ Water BC's in Coils and Tubes

User Number:

Password:

File Password:

Run Number:

Filename:

New File? Yes ☐ No ☒

Figure 4. Input page used to select web page to input data for HTF. This dynamic web page writes out links for the selected pages to input data. Also, it selects the MatLab input file if the file is old or it will construct a new file.

Table 2. Options for displaying the results.

Section	Is the option operational?
Bottom	yes
Top	yes
Radiation	no
Bottom section fluid results	no
Annular fluid results	no
Fluid recirculation results	no
Fluid in blocks	no
Vessel side walls	yes
SWALL sub-model nodes	no
Blocks 1-15 (each block can be selected individually)	yes

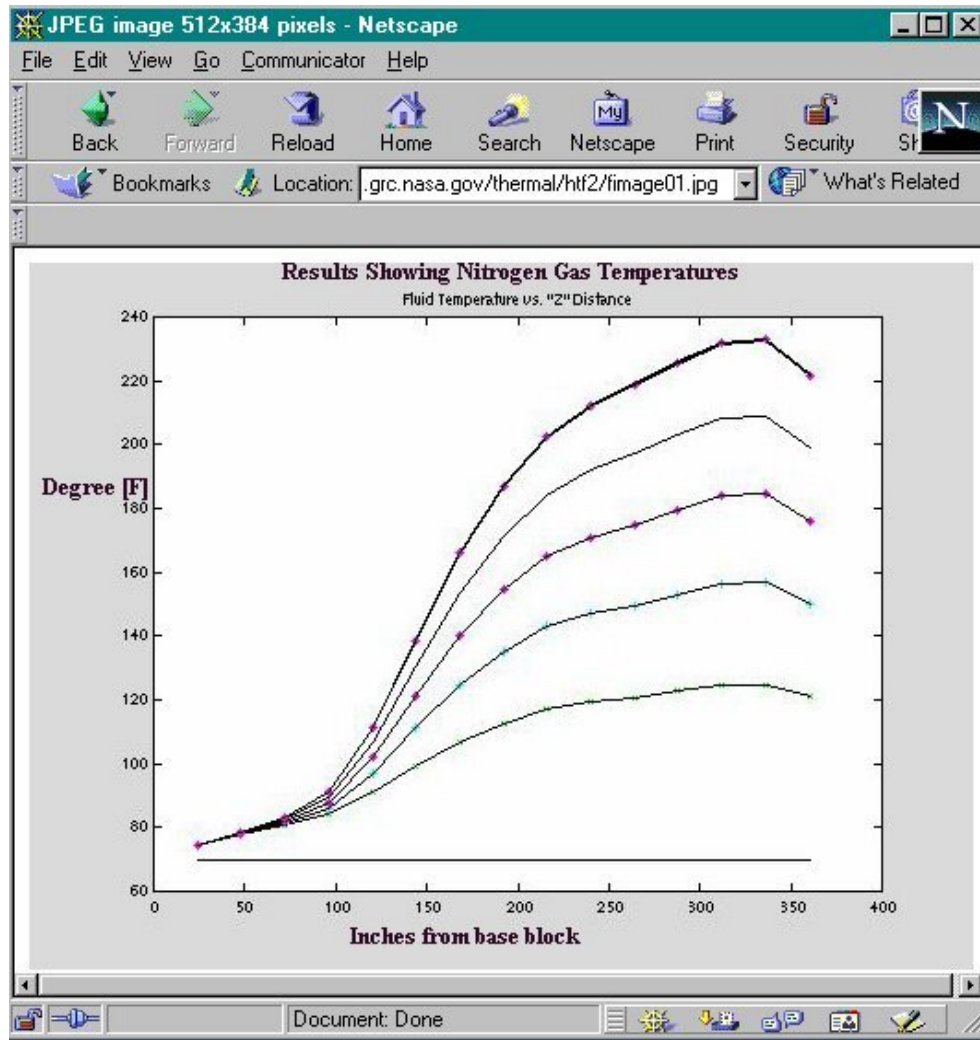


Figure 5. Results showing plot of Nitrogen gas temperature vs. the height in the blocks. Also, colormap drawings showing the HTF heater are constructed from the results of the SINDA model.

THE FUTURE OF ANALYSIS THROUGH THE INTERNET

The HTF Heater Model was a demonstration that complex analysis can be performed through the Internet. The engineering analysis community can expand the use of the Internet significantly, to include real engineering using complex models. Although the HTF heater model was primarily on one system, the future could see a distributed system over an optical Internet (OI) used exclusively for engineering analysis [4], which would be similar to Internet 2 [5]. Figure 6 shows a collage of ideas that could be included in the system. Such a system would allow for significant increases in data rates needed for high-speed analysis. A virtual reality station [6] would be built specifically for engineering analysis. The stations would be called virtual reality analysis rooms (VRAR) and would be found in government, industry and academia. The rooms would be voice operated, so that users could quickly build an engineering model. For example, the user could say, "Build a square box with dimensions of one cubic meter" and the system would construct a holographic image of a box with the dimensions [7]. Next the user could say, "Build a solid cone of radius one meter and height one meter." A holograph cone would appear with the specified dimensions. Next the user could either point to the holograph images or use a retina-tracking heads-up display [8] to construct the model by a combination of pointing and voice commands. The virtual analysis room would also be connected to a local database and other databases connected to the network. For example, if a user wanted to perform analysis on aero-shells, he could look into the local database connected to his VRAR on past

models and use one of the old models as the starting point. The option would also exist to pay data resource companies connected to the Internet to access information concerning aero-shell models if the user desired. For example, the VRAR user would say, "Search the Internet for aero-shell thermal models" and a list of pictures and names of aero-shells would be displayed. The VRAR user would then select a model and begin the analysis by modifying the model to fit their needs. Once the geometry was specified, materials would be selected for the geometry. Also, the boundary and initial conditions would be selected using the VRAR. The user of the VRAR could then use a local grid generation program or else use a grid generation company selected through the Internet. A finite element grid would then be generated for the model. The next process in the analysis would be to select the solve routine to do the analysis and the computer system to use. The VRAR would be smart enough to assist the user in this process. If the VRAR lacked the smarts (artificial intelligence [9,10]) then a company connected to the Internet specializing in artificial intelligence could be contacted for additional assistance. The VRAR or the company connected to the Internet would suggest the best solve routine for the given problem. Also, information concerning potential problem areas associated with the analysis could be given prior to actually performing the analysis based on the problem. A computer company would be selected over the Internet to perform the analysis. The companies would have parallel processors, which would operate at different speeds depending upon the system and the solve routine. The faster systems with the optimized solvers would cost more than the slower ones. The last part of the analysis would be the post-processing and the graphics. The VRAR user would have the option of using the local post-processing and graphics software or contracting over the Internet to display the results. The visual capabilities of the users VRAR system would be important concerning this choice. Once the analysis was complete the user could then contact manufacturing companies to request bids for manufacturing the components or part. This process could be automated if the parts were not too complex. The VRAR user would say, "Find manufacturer for aero-shell." Immediately, if the complexity of the aero-shell would not be extreme, the lowest bid manufacturers would be displayed so the user could select the specific company. The company selected would then download the CAD model and immediately begin manufacturing the aero-shell. If the bid for the aero-shell required human oversight, then a message would be given telling the VRAR user to wait for company personnel to examine the bid.

The aero-shell example is one of many possible types of analysis that could be done through the Optical Internet (OI) system. Fluids, structural, electronics, systems, combustion, thermal and any other type of analysis could be performed through the OI system and VRAR. The systems analysis could implement genetic algorithms to explore the design space to optimize the system. Failure analysis could be used to examine the life of the component or system. Companies specializing in cryptography could be used on the Internet to ensure confidentiality of the analysis. Initially, the VRAR would be consulted to construct the preliminary design. Companies specializing in artificial intelligent systems would be consulted to suggest the best tools for the analysis depending on what the user wanted from the analysis. Probability and statistics, neural networks, thermodynamic modules, property databases, Monte Carlo methods would be utilized as needed for the analysis. The smart computer system would use artificial intelligence to determine the best process and components for the analysis. Optimization could minimize the time required for the analysis, minimize cost of the analysis and maximize the probability for success. Not only would optimization occur in selecting the components for the analysis, but optimization could occur during the analysis. For example, if a selected solve routine started having problems then another solver module could be chosen during the analysis that would speed up the solve time. Also, optimization could minimize the manufacturing and material costs of the system or component under analysis. The production could begin almost immediately after the completion of the analysis and the selection of the manufacturers.

CONCLUSION

The HTF heater model demonstrates that complex models can be interfaced with the Internet enabling remote analysis. Rather than using the Internet only for simple educational purposes, the use can be expanded to include real engineering analysis using complex models. A revolutionary and visionary future is presented about engineering analysis being coupled with an optical Internet (OI). Although some of the ideas presented in this paper may seem equivalent to science fiction, the future of engineering analysis will see an explosion in technology when Virtual Reality Analysis Rooms (VRAR) are coupled with the OI. Specialization will occur enabling a synthesis of the best components of engineering analysis and manufacturing by optimizing the specific processes through artificial intelligent systems. Companies will become less geographically defined and more integrated as a whole – an integration that can be redefined instantaneously by specific engineering and manufacturing needs. On a larger

scope, this revolution could transform business by enabling companies to rapidly construct and reconstruct their infrastructure based on changing economic conditions utilizing smaller specialized companies, in some cases, geographically distributed around the globe. Engineering analysis, manufacturing, and business could be coupled together on OI systems enabling rapid development of products and services.

Analysis Specialization on the Optical Network

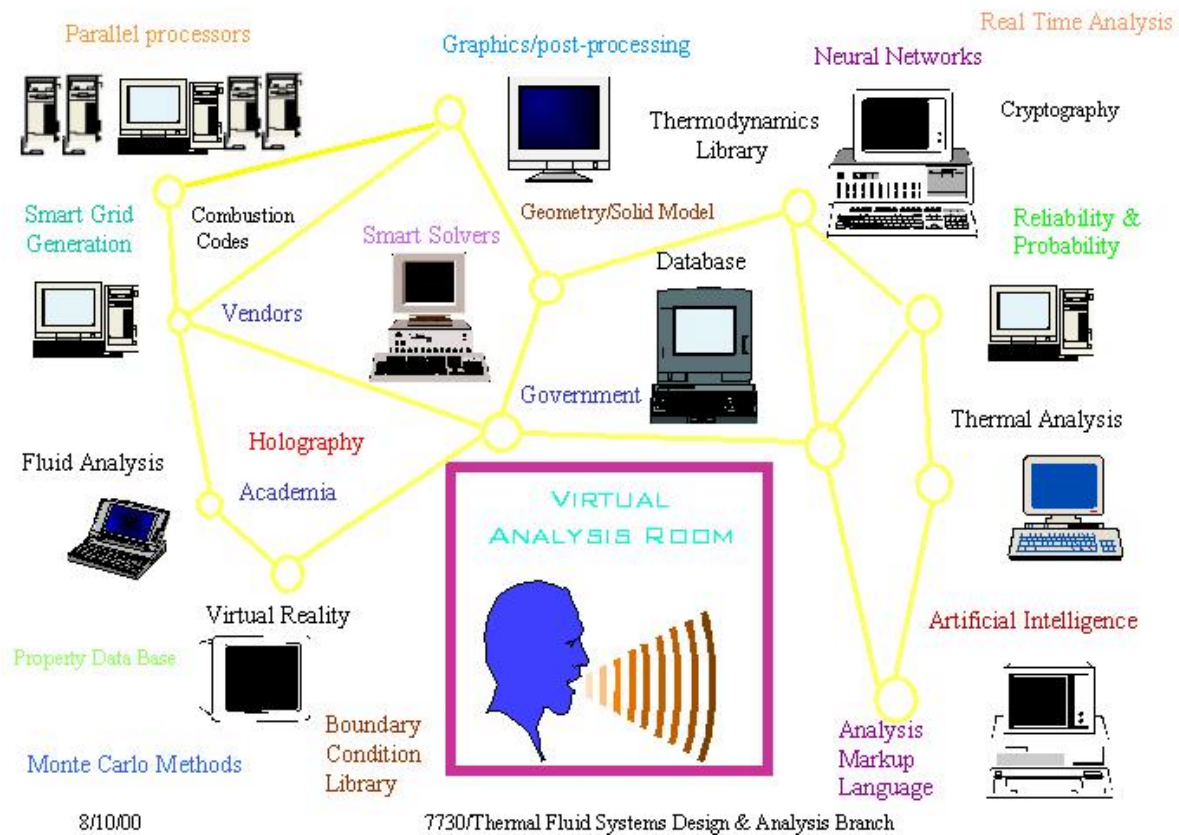


Figure 6. A collage of ideas is presented showing areas of engineering specialization that can be accessed using a VRAR over an optical Internet (OI) specifically used for engineering analysis.

ACKNOWLEDGMENTS

I would like to thank Barbara Sakowski for her patience with me concerning this paper. Also, I am grateful to Mike Stofcheck who provided encouragement as I worked on the project. NASA will miss his conscientious work and dedication, due to his regrettable death.

REFERENCES

1. <http://www.isc.org/ds/hosts.html> presents graph of Internet domain survey host count.
2. Thomas SR, Trefny CJ, Pack WD. Operating capability and current status of the reactive NASA Lewis Research Center Hypersonic Tunnel Facility. NASA TM-106808 1995.
3. Thomas SR, Woike MR, Pack WD. Mach-6 Integrated Systems Tests of the NASA Lewis Research Center Hypersonic Tunnel Facility. NASA TM 107083 1995.
4. http://www.actconferences.com/AllOptical/agenda_day1.htm conference on an “all optical” network.
5. <http://www.internet2.edu/> Internet2 informational web site.
6. http://www.grc.nasa.gov/WWW/MAELVRSTATION/news_info/vr_essay.html explains what is virtual reality and describes a virtual reality station.
7. <http://www.charlesriver.com/titles/holograms.html> link to new book called, “HOLOGRAMS and HOLOGRAPHY: Design, Techniques and Commercial Applications” by John Vacca. Presents all aspects of holography including uses over the Internet. Also, discusses the technology related to interactive virtual reality holodecks. Note, the book is out of print presently but the ISBN is 1-886801-96-7. Contact Eric.T.Malroy@grc.nasa.gov for copy of web pages related to the link above if it is not active.
8. <http://www.gallium.com/08/08fr.htm> example companies that sell and develop heads-up display units that use retina-tracking and scanning.
9. <http://www.isca-hq.org/special-IS.html> call for papers on intelligent systems by the International Journal of Computers and Their Applications. The link provides a list of the areas related to applied artificial intelligence. These areas related to artificial intelligence would be incorporated into the VRAR and the artificial intelligent companies connect to the OI. Contact Eric.T.Malroy@grc.nasa.gov for copy of old link or view most current conference call for papers related to intelligent systems at <http://www.isca-hq.org/> for similar list of areas related to artificial intelligence.
10. <http://www.dagstuhl.de/10Years/Abstracts/> Abstracts of the conference called “Informatics – 10 Years Back, 10 Years Ahead” on August 28-31, 2000. Embodied Artificial Intelligence, Pfeifer, Rolf 2000. Explains the new expanded view of artificial intelligence. This link has a large number of possible applications for the OI and VRAR system.

CORRELATION OF ANNULAR DIFFUSER PERFORMANCE WITH GEOMETRY, SWIRL, AND BLOCKAGE

Dr. David Japikse
Concepts ETI, Inc.
217 Billings Farm Road
White River Junction, Vermont 05001-9486

ABSTRACT

A correlation equation set for annular diffuser performance has been developed. The relationships are based on all of the experimental data available from the known open literature that covers basic diffuser geometry, inlet aerodynamic swirl, and inlet aerodynamic blockage. A sensible baseline correlation has been established which is suitable for preliminary design of some turbine systems. It has also been established, however, that the existing world's technical literature is deficient in a number of important variables and a resultant level of data variance has been established which ought to be reduced in future investigations. This paper establishes a baseline for current work and goals for future development.

NOMENCLATURE

α	Inlet average swirl angle	r_{1h}	Inlet hub radius
AR	Diffuser area ratio	r_{1t}	Inlet tip radius
b	Passage width	Tu	Turbulence intensity
B_1	Inlet aerodynamic blockage		
C_p	Static pressure recovery coefficient		Greek Symbols
C_{pi}	Ideal static pressure recovery	η	Diffuser effectiveness, C_p/C_{pi}
K	Total pressure loss coefficient	θ_i	Inner diffuser cone angle
$L/\Delta r$	Length to inlet passage height	θ_o	Outer diffuser cone angle
r	Radius		

INTRODUCTION

The purpose of this study is to investigate the level of knowledge, and in certain important areas the lack thereof, concerning the performance of annular diffusers. For decades investigators have conducted individual studies without a careful consideration of how all the studies may be interwoven. Patterns of consistent behavior among the database elements for annular diffusers is established in this investigation. However, it may be of even greater significance that the investigation reveals areas where critical design knowledge is missing. It will be observed that conducting individual investigations of annular diffuser performance has blinded most investigators from seeing the larger picture and the critical interactions between the different variables which have been discussed in the literature. This study begins by looking at historical data, then proceeds to investigate the parametric dependence, resulting in the development of a preliminary design set of equations and then finally by careful examination of further investigations which are needed before the annular diffuser design problem will be well understood.

HISTORICAL DATA

Much of the extant data covering annular diffusers comes from the period from the 1950s through the 1980s. In this period of time, a considerable amount of research was done in the experimental laboratory to uncover some of the unusual performance characteristics of annular diffusers. By the late 1980s, however, the experimental research had reduced substantially due to a lack of government funding in a number of countries where the work had previously been extensive. It is, therefore, useful to review the data which has been made available and to look for patterns within this data. It is also necessary to determine how this data may best be used in future design studies

Copyright © 2000 by Concepts ETI, Inc.

All rights reserved. No part of this publication may be reproduced, transmitted, transcribed, stored in a retrieval system, or translated into any language or computer language, in any form or by any means—electronic, mechanical, magnetic, optical, chemical, manual, or otherwise—without prior written permission from Concepts ETI, Inc., 217 Billings Farm Road, White River Junction, Vermont 05001, USA.

The U.S. Government is granted the right to use this document for use in the proceedings for the TFAWS meeting held August 21–25, 2000 in Cleveland, Ohio.

and where it needs to be further improved. Much of the original data was taken in order to support studies of axial compressor discharge diffusion as flow leaves a compressor and enters a combustion chamber. Other work was done for exhaust diffusers of hydroelectric turbines, small gas turbines, and turbochargers. While these topics are still important today and there are important unresolved questions, the level of activity has reduced. Now important research topics must be carefully selected for the more limited studies possible in future years.

Figure 1a shows a plot of many different annular diffuser data sets which cover a wide range of swirl angles, blockage, turbulence intensity, and geometric parameters. Figure 1b shows the classical diffuser performance map for an annular diffuser by Sovran and Klomp (1967)^[1]. This map was the first investigation to introduce the topic of aerodynamic blockage. The map actually is a generalized composite of many different investigations and the interested reader should review the Sovran and Klomp paper in detail, including a careful examination of the appendix to their paper in which their data sets are listed. The Sovran and Klomp map actually has accuracies of roughly ± 0.1 on C_p since the map itself is an aggregate of many different diffuser builds and does not correspond to one single or specific diffuser configuration. The difference in Figure 1a and Figure 1b is very important. Figure 1a is much less systematic than Figure 1b. Figure 1b is a systematic variation of certain geometric parameters, with many other parameters held constant. For example, Figure 1b corresponds to very low blockage (approximately 2%), low turbulence intensity, no swirl, and moderate variations of flow (wall) deflection angle. By contrast, Figure 1a has a wide variety of these parameters and forces the reviewer to think carefully about the role of these additional parameters. Ideally, one would like to see a very large collection of maps, such as in Figure 1b, to cover the list of variables just given, but these maps have never been prepared. To produce a map (such as Figure 1b) requires a large number of different geometries, a variety of inlet flow conditions and a large series of systematic tests. This has not been economically possible. Many dream of the day when this can be done by computational fluid dynamic methods (CFD), although this dream may still be quite remote (see later discussion). Consequently, it is important that we consider the variations in Figure 1a and attempt to determine how much of a systematic nature has been learned in the prior investigations.

Symbol	Source	θ_1	θ_2	r_2/r_1	r_{12}/r_{1t}	Blockage	Tu
○	Dovzhik	1°54'	8°	6.41	2.06	0.65	High
□	Lavrenko	8°	12°	6.51	2.18	0.65	High
●	Japikse	10°	15°	7.6	2.17	0.7	Med 0.03-
◆	Shaelen & Shabaka	0°	15°	18	6.7	0.38	Low
■	Hoadley & Hughes	0°	7.5°	19.05	4.57	0.40	Low
△	Coladipietro, et al.	20°	20°	12.65	3.0	0.63	0.10
▽	Coladipietro, et al.	20°	20°	12.65	3.0	0.63	0.06
▲	Coladipietro, et al.	20°	20°	1.4	1.25	0.63	0.10
▼	Coladipietro, et al.	20°	20°	1.6	1.25	0.63	0.06
◆	Srinath	-3.5°	3.5°	38	4.26	0.75	High

Notes: All Tests are at Low Mach No. (0.2 or less)

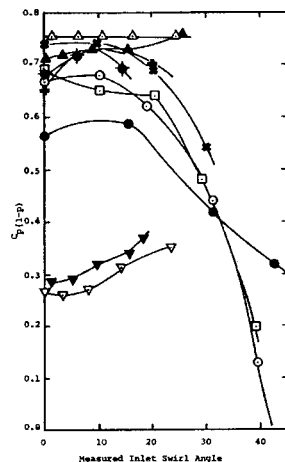


Figure 1a. Straight annular diffuser performance with swirl at various AR and blockage.

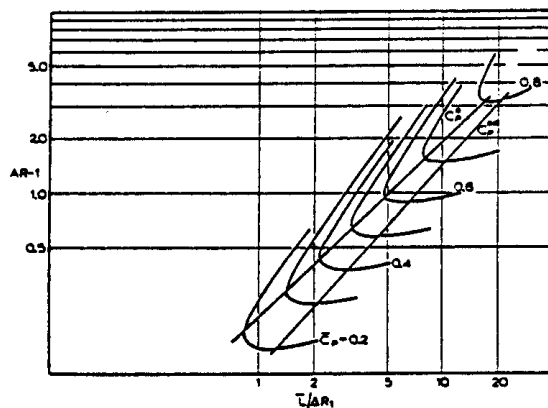


Figure 1b. Annular diffuser performance chart, $B_b \approx .02$ Sovran and Klomp (1967).

Figure 2 gives a clue as to how this might be done. In this early work of Hoadley and Hughes (1969)^[2], an ideal pressure recovery contour is plotted parallel to the actual pressure recovery. This suggests that much of the effect of geometry and swirl can be taken care of in the ideal pressure recovery and that a sensible way of developing a correlation for static pressure recovery performance will be to use diffuser effectiveness which is

$\eta = C_p/C_{pi}$ or in other words the ratio of the actual pressure recovery coefficient divided by the ideal pressure recovery coefficient. Figure 2 supports this basic notion and suggests that much of the swirl angle variation will be taken care of by this approach. However, Figure 2 also displays a second issue. On the far right-hand side of the figure, the data trend is no longer exactly parallel to the ideal pressure recovery and tends to fall away more quickly. A variety of past experiences suggests that there is some development of progressive stalling occurring which will not be reflected in the ideal pressure recovery, but must be dealt with in the actual pressure recovery (as discussed later). Clearly, a first step is to concentrate on diffuser effectiveness and not upon C_p . We must therefore, establish a proper definition of ideal pressure recovery coefficient.

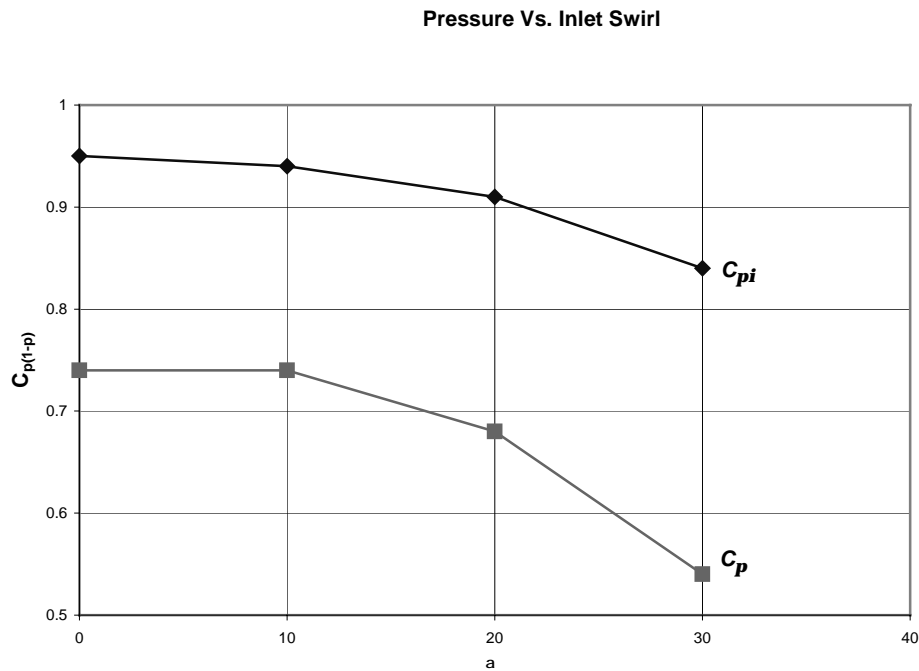


Figure 2. Pressure recovery versus inlet swirl, (adapted from Hoadley and Hughes, 1969).

The ideal pressure recovery coefficient is derived directly from basic principles. It is the pressure recovery that would be achieved if the flow was strictly one dimensional, inviscid, filled the entire passage and, therefore, by implication, has no blockage, no boundary layer buildup, and no deviation of flow either entering or leaving. When the definition of pressure recovery, the Bernoulli equation, and the conservation of mass and conservation of angular momentum principles are all employed, the following relationship is obtained for C_{pi} :

$$C_{pi} = 1 - \left(\frac{r_1}{r_2} \right)^2 \left\{ \frac{\tan^2 \alpha_1 + (b_1/b_2)^2}{\tan^2 \alpha_1 + 1} \right\} \quad (1)$$

Using this definition, we can now look at the entire data set. The first step is to partially remove the effect of geometry and swirl (as embodied in Figure 1) by using the definition of diffuser effectiveness, and then look for other dominate variables and trends.

A variety of parameters was considered in looking at basic trends for η . Area ratio, $L/\Delta r$, b_2/b_1 , r_{1h}/r_{1t} , r_2/r_1 , and such parameters were initially considered in a general parameter sensitivity investigation. It was found that all the remaining geometric effects (those not handled in the C_{pi} relationship above) were best handled simply by diffuser area ratio as shown in Figure 3. Figure 3 shows effectiveness versus area ratio and a clear exponential

decay form is suggested, but with data variance around an area ratio of 2.3. This first investigation was scoping in nature and pointed a direction in which to begin the modeling exercise. The step-by-step process is now being presented in the following section.

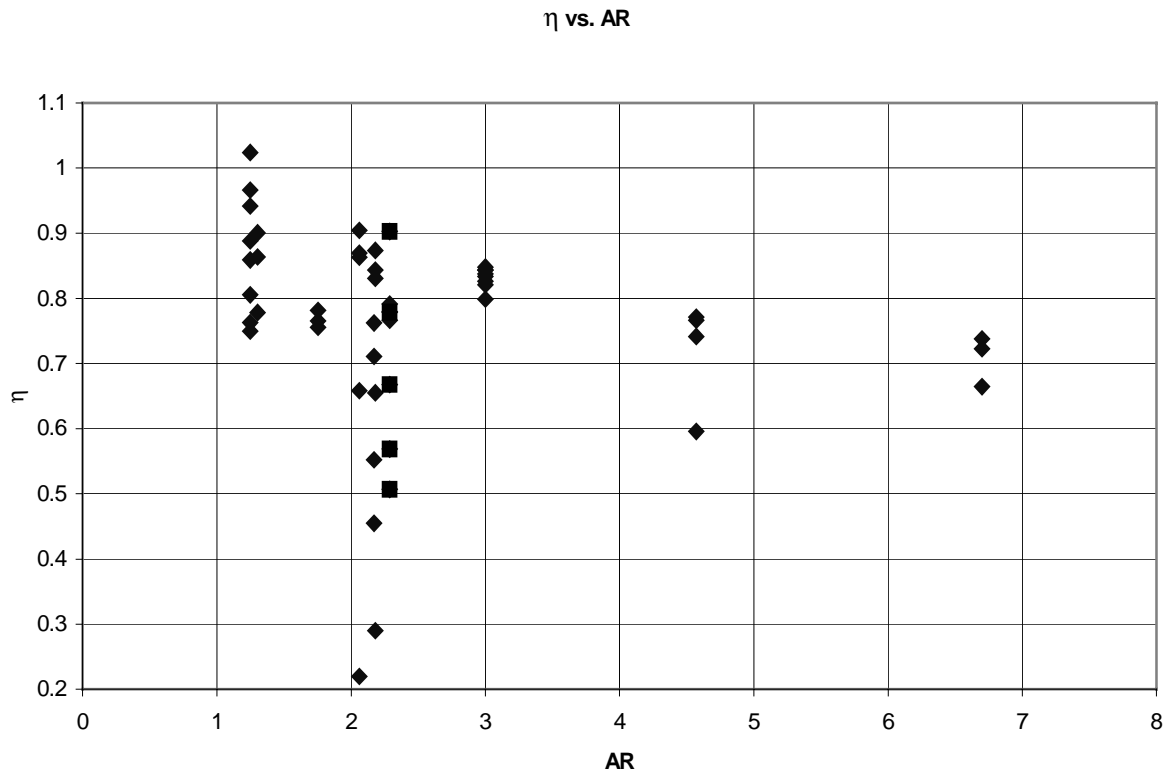


Figure 3. Display of all annular diffuser data which depends on geometry, inlet swirl angle, and inlet aerodynamic blockage. Plotted as diffuser effectiveness versus diffuser area ratio.

PARAMETRIC STUDIES (SIMILARITY VARIABLES)

Beginning with the concept of using the diffuser effectiveness, with some geometric variables and some degree of inlet swirl removed using Equation 1 as the denominator for the effectiveness, it has been found that area ratio is the dominant variable involved in Figure 3. It is recognized, of course, that aerodynamic blockage is another important variable and that Figure 3 includes different levels of aerodynamic blockage. Consequently, the data was screened to include only the data at low blockage (which essentially meant 3% to 5% based on the classes of data available). For reasons that will fall out later, the discriminating threshold was raised to 6% as shown in Figure 4 and it may be reported that the curve fit relationship established for the lower blockage works just as well for blockage levels all the way up to 6% as revealed in this figure. With the exception of a couple of low points at an area ratio of approximately 2.2, all the data tends to follow the exponential decay with reasonable variance. It is perfectly reasonable to use a relationship such as shown in Figure 4 in addition to the C_{pi} relationship presented in Equation 1. Area ratio is an important parameter, indirectly, in the C_{pi} relationship but it is not a complete relationship. The actual pressure recovery will depend on area ratio even beyond the C_{pi} dependency simply because diffusers at high area ratio will develop stalling characteristics and even at moderate area ratios there is no reason why C_p must completely follow C_{pi} on an area ratio basis. With the relationship of Figure 4 established, the investigation can move to additional parameters. This is done by removing from the effectiveness level of the original data the area ratio dependence by dividing out the new expression and this has been accomplished as shown in Figure 5.

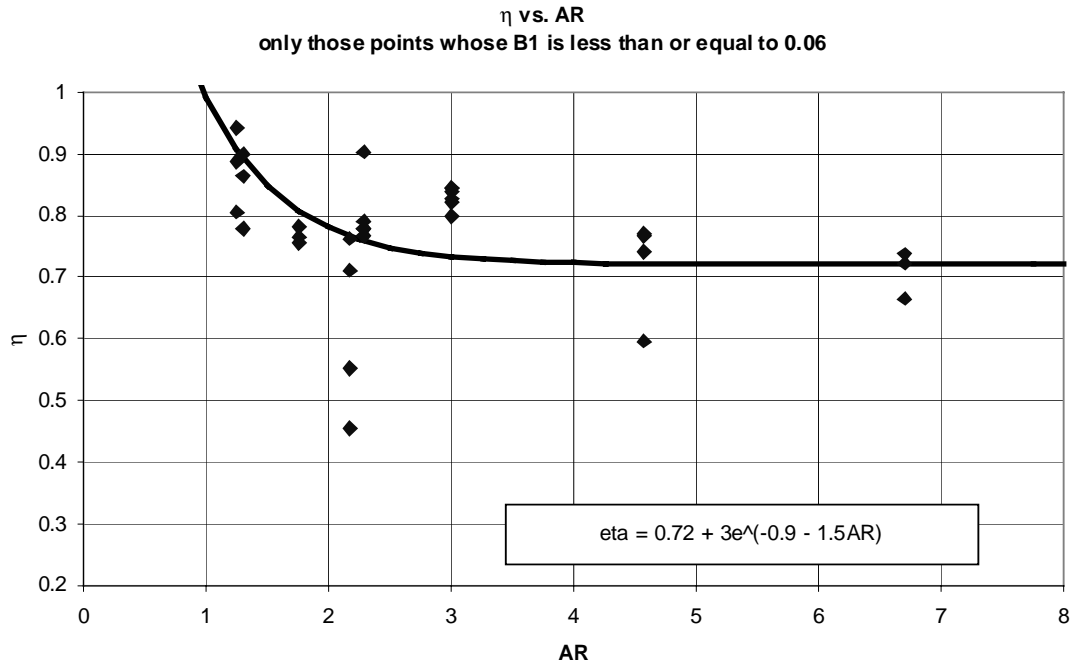


Figure 4. Diffuser effectiveness versus area ratio with low level inlet aerodynamic blockage and no inlet swirl.

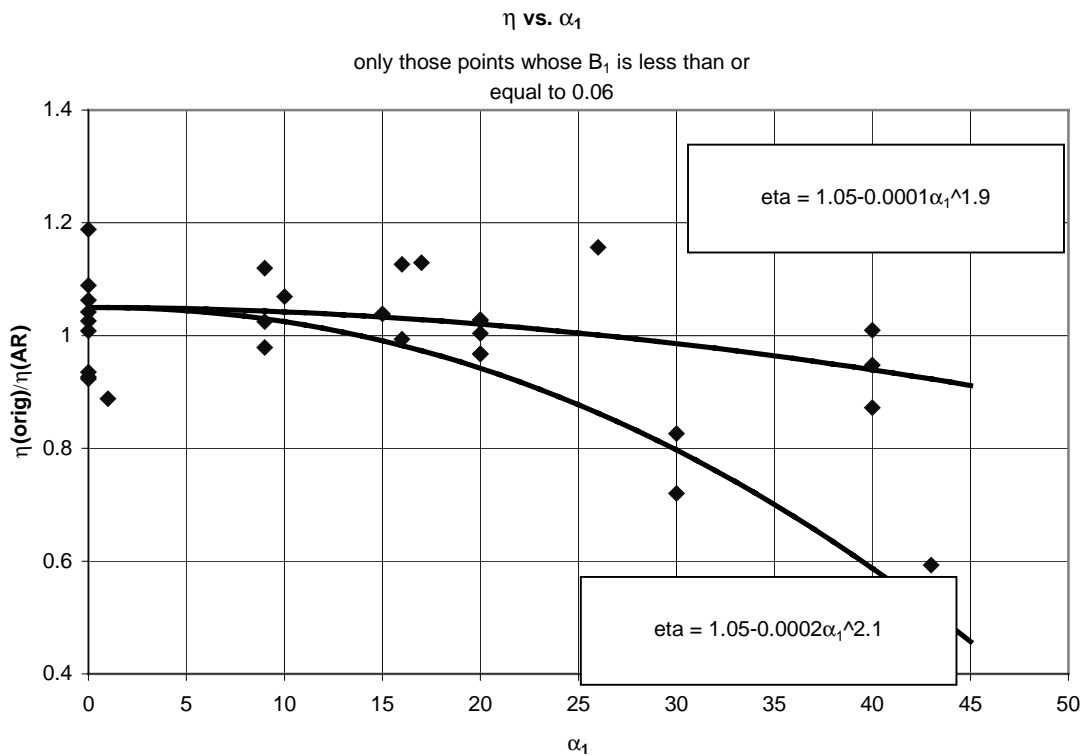


Figure 5. Diffuser effectiveness, with the principle effects of geometry removed, displayed as a function of inlet swirl angle. The two different trends may reflect the development of limited or more extensive diffuser stall.

Actually, two different trends are evident in Figure 5. The higher trend reflects the performance of diffusers with only mild stall developing at high swirl angles and the lower trend reflects data with substantial stall developing at high swirl angles. This will be discussed later.

A curve fitting study was made of each data trend. Below 18° of swirl, all the data was employed with blockage less than 6%; for the upper swirl angle trend, only the elevated data was used for supporting the higher curve fit and for the lower data trend, only the lower data points were used for establishing the lower curve fit. Clearly, this is quite subjective. This is a weakness, not of this paper, but of the data that is available for investigation and for guiding future designs. The present data might, at least tentatively, be thought of as revealing a strong stalling effect and other data sets revealing a milder stalling effect. It was for this part of the investigation that a critical blockage level of 6% was utilized simply to have enough data in order to develop at least first order but meaningful data trends (this is the reason why the barrier was raised from 5% to 6% in the area ratio study given above). Finally, it should be mentioned that the full effect of swirl is displayed in Figure 6 where all the data, and all blockage levels, is included. It can be seen that the relationships remain sensible, but there are blockage effects which are not included so far in this data processing. Consequently, the effects of both area ratio and swirl are removed from the original effectiveness data, by dividing out the correlations, using a new data set as shown in Figure 7. Again there is a low data set trend and a high data set trend and this apparent variation is much more complex to understand. Indeed, it can be widely debated.

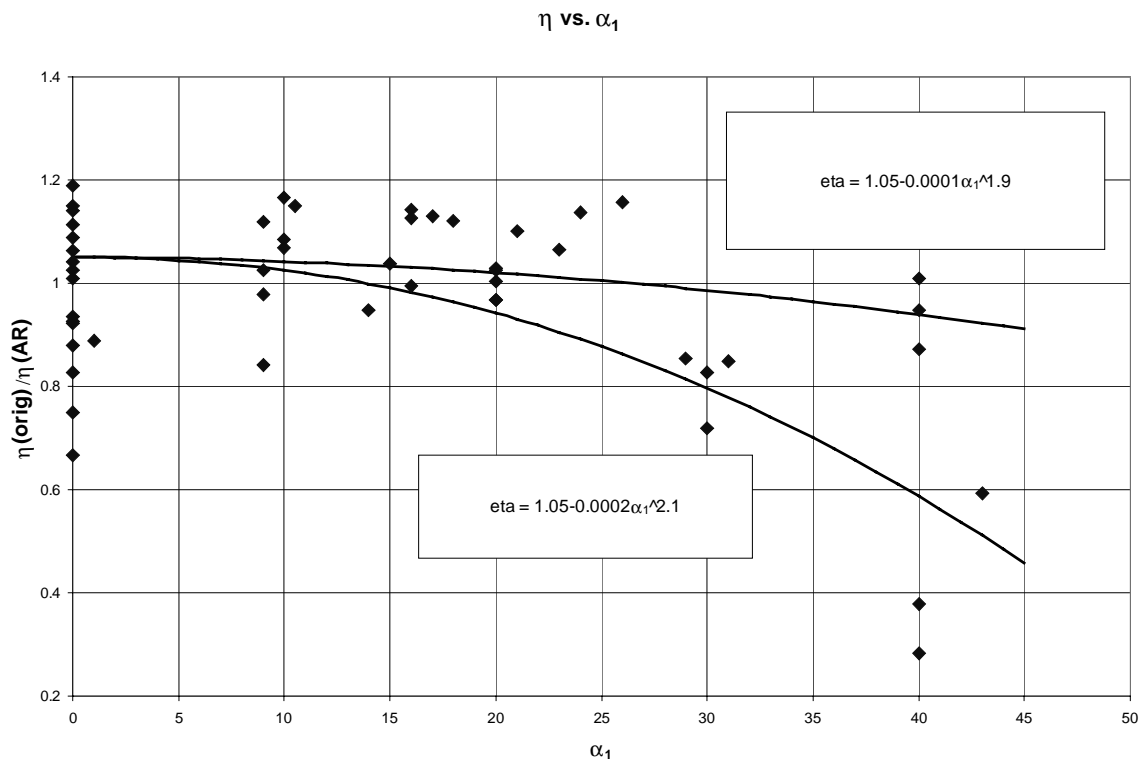


Figure 6. Diffuser effectiveness with principle geometric effects removed including data at all levels of inlet aerodynamic blockage.

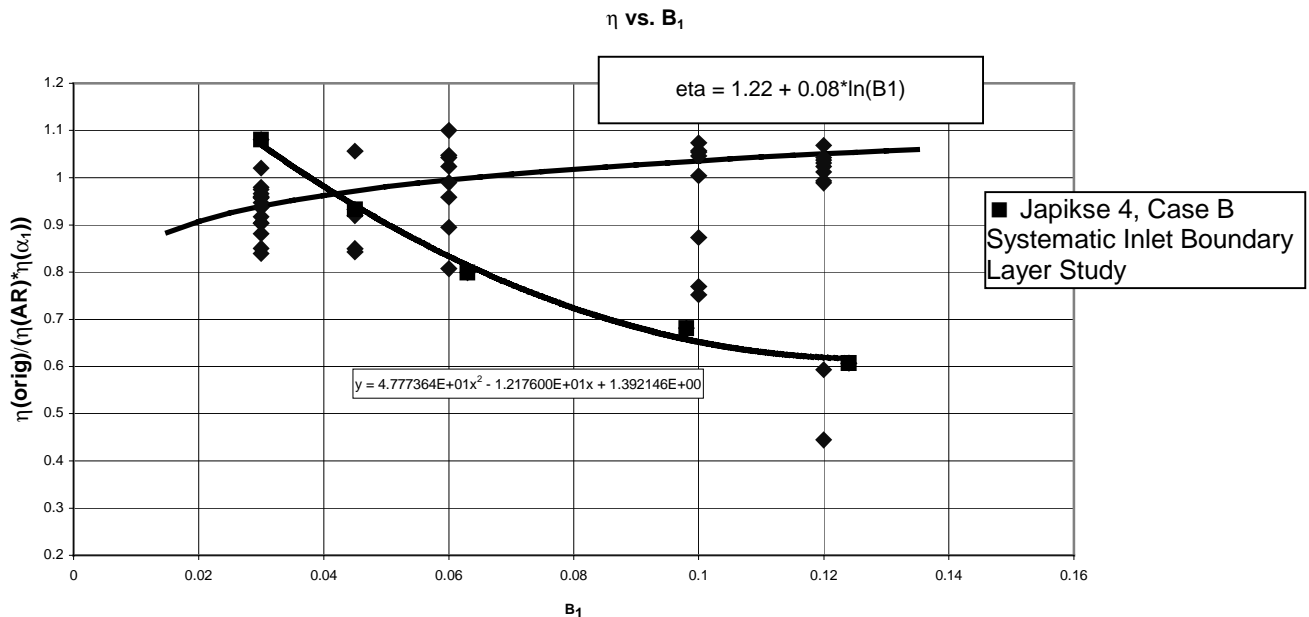


Figure 7. Diffuser effectiveness with the principle effects of geometry and inlet swirl removed according to preceding correlations; the resulting two trends display conflicting effects with respect to inlet aerodynamic blockage.

The low data set trend is a true fluid dynamic blockage effect (related directly to boundary displacement thickness). The square symbols are the *only* data from a study where blockage was systematically varied for more than two different conditions. It may be noted that Coladipietro^[3] conducted tests at two different blockage levels, but this is not a systematic test with respect to blockage and no one else considered any variation of inlet aerodynamic blockage at all. The data represented by square symbols was taken with a clean inlet velocity profile (uniform in the core) and with only changes in inlet boundary layer thickness. The decay relationship of the diffuser effectiveness with blockage is sensibly shown by the correlation through the square symbols. The curve fit was placed through this data as one of the answers for the blockage dependence trend. This relationship is shown also in Figure 8. Some of the data from Coladipietro and other diffuser studies by Japikse are also shown in this plot. The lower points from Coladipietro closely follow the square symbol blockage trend line while the upper two sets of point-pairs seem to parallel and closely approximate the trend displayed. Nonetheless, the Coladipietro data showed a drop from the 6% to the 10% blockage in every pair of points, which is a relationship similar to the square symbol data trend.

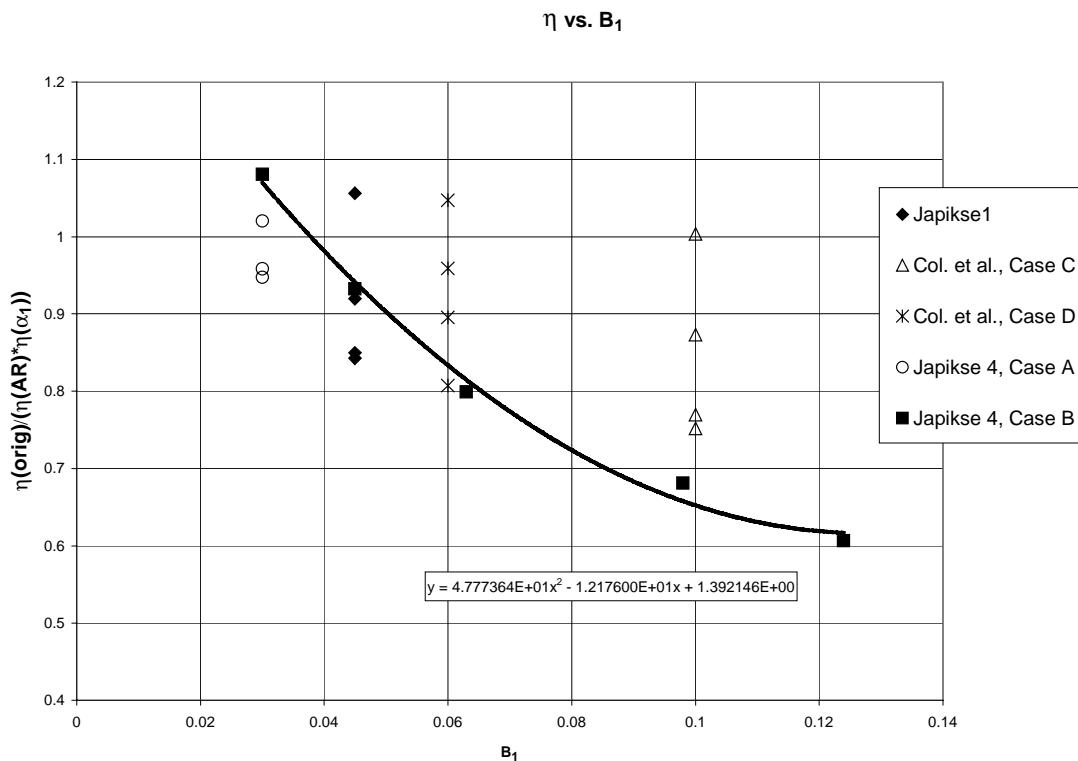


Figure 8. Diffuser effectiveness with principle geometric and swirl effects removed showing classical developing inlet boundary layer blockage development (square symbols are the only systematic test with controlled variation of inlet blockage). The variation displayed by other data sets may be the additional influence of inlet turbulence and vorticity.

Figure 9, which is the other subset of Figure 7, displays the results where the performance actually increases with the apparent inlet fluid dynamic blockage. In the minds of many people working with diffuser performance, recovery cannot increase with blockage and such a trend would appear to be fallacious. There is a problem, however, with the criticism. The school of work that shows effectiveness or pressure recovery decaying with blockage is a valid school of work that was centered basically in the United States with developing boundary layers (and principally through Stanford and related investigations). Many studies have been conducted showing this trend. However, another and equally vital school of thought was developed in England where a lot of work was done with fully developed flow or at least very long inlet passages. Figure 10 shows a set of this data. The argument was that combustors do not see thin inlet boundary layers and substantial velocity profiles are necessary in order to obtain meaningful data. In that case, results were shown where pressure recovery (or in turn, effectiveness) decayed initially with inlet fluid dynamic blockage at low levels of blockage but then actually rose again at high levels of blockage when very thick inlet boundary layers developed or as the flow became fully developed. The reasons for this appear to be increased levels of turbulence and vorticity which are generally recognized as a means to augment diffuser performance. Of course, the trend is not truly inlet aerodynamic blockage, but other effects which have not yet been sorted out and systematically or independently correlated. Consequently, the trend in Figure 9, even when plotted against blockage (since it is the only parameter available to tag this relationship), is not really one of blockage in all cases, but of other related profile effects. In this case, we see a mild increase in performance which has been demonstrated in a number of different studies. Consequently, two different sets of results are available, even though there is no strict guideline as to which one should be followed.

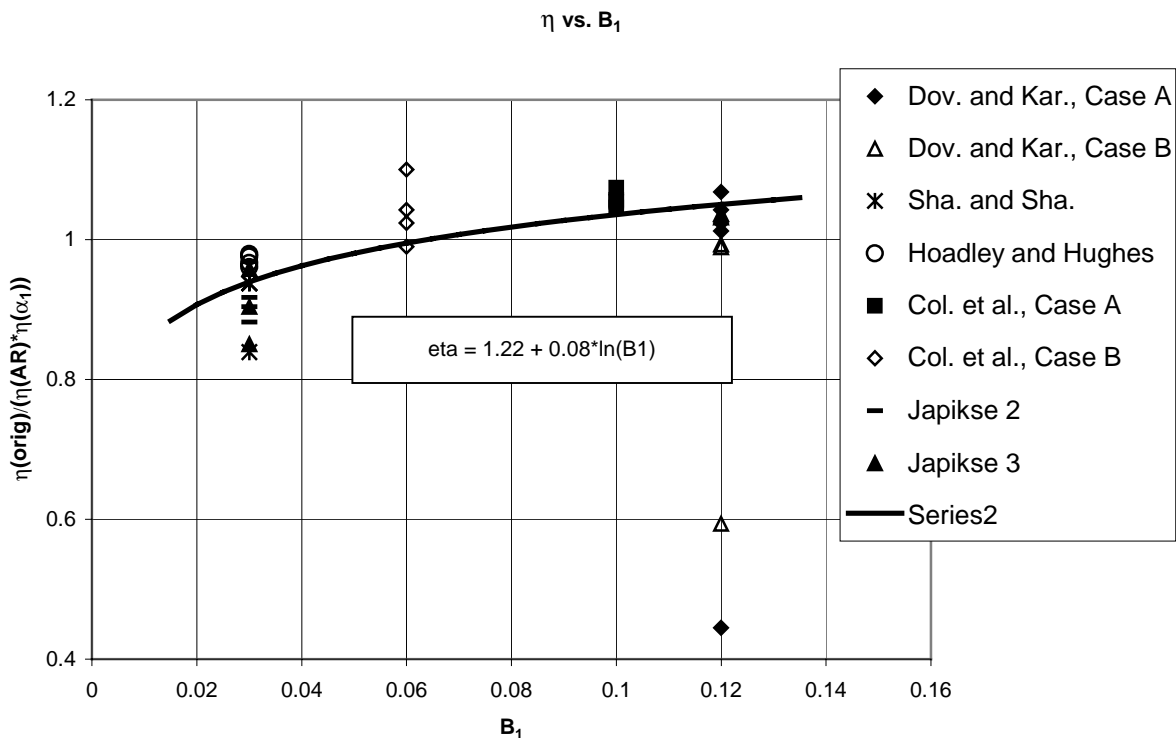


Figure 9. Diffuser effectiveness with the principle influence of geometry and inlet swirl removed, reflecting an optimistic effect of inlet blockage which is most likely due to turbulence and vorticity and not classical inlet boundary profile development.

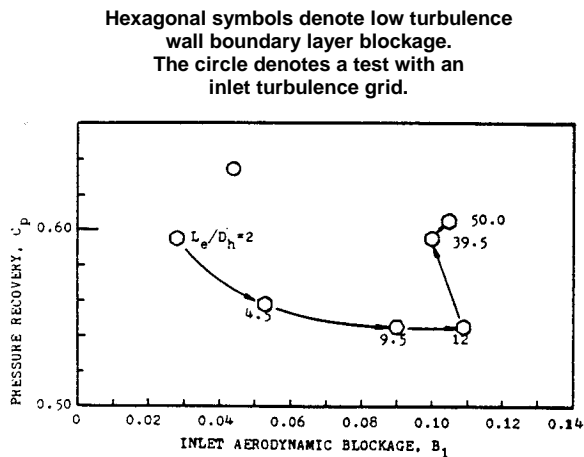


Figure 10. Pressure recovery for $AR = 2$, $L/\Delta r = 7.5$ straight centerbody annular diffuser. Japikse (1980)^[4] (adapted from *The Influence of Inlet Turbulence on Diffuser Performance*).

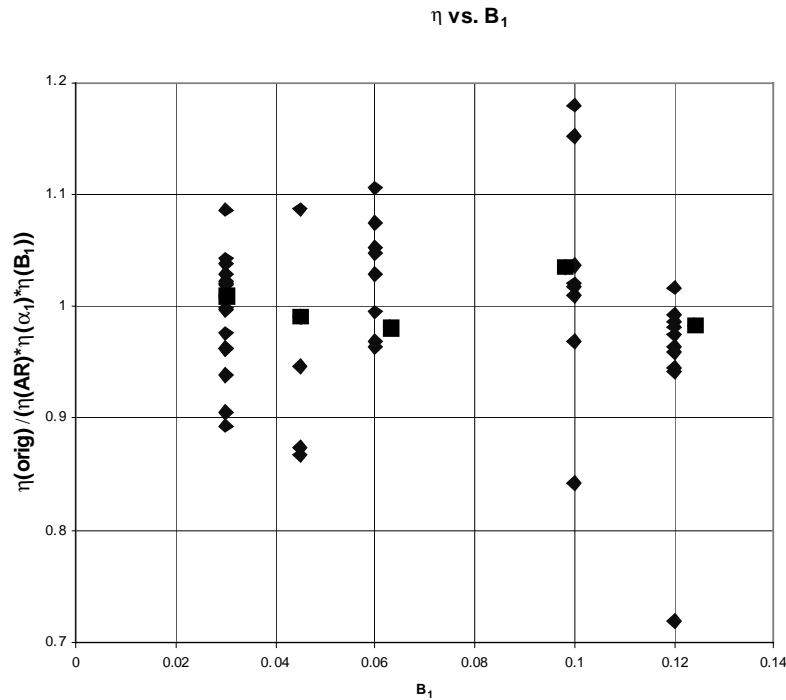


Figure 11. Diffuser effectiveness with the principle effects of geometry, inlet swirl, and inlet blockage removed; the resulting correlation assessment reflects the expected value of $1.0 \pm$ approximately 0.1 for most data and slightly larger for other points. The proposed correlations therefore, are approximately 10% accurate, but require a judicious estimate of the type of inlet profile and the type of stalling effects which develop in the diffuser.

DESIGN EQUATIONS

The preceding study of behavioral trends leads to the following set of suggested preliminary design equations:

$$C_p = C_{pi}(\alpha_1, r_2/r_1, b_2/b_1) \eta(AR) \eta(\alpha_1) \eta(B_1) \quad (2)$$

$$\eta(AR) = 0.72 + 3e^{(-0.9 - 1.5AR)} \quad (3)$$

$$\eta(\alpha_1) = 1.1 - 0.0001\alpha_1^{1.9} \quad \text{delayed stall} \quad (4)$$

$$\eta(\alpha_1) = 1.1 - 0.0002\alpha_1^{2.1} \quad \text{earlier stall} \quad (5)$$

$$\eta(B_1) = 47.77364B_1^2 - 12.17600B_1 + 1.392146 \quad \text{curve A, common blockage} \quad (6)$$

$$\eta(B_1) = 1.22 + 0.08 \ln(B_1) \quad \text{curve B classical profile blockage} \quad (7)$$

The Equation 2 is built around the definition of η using the ideal pressure recovery coefficient as given in Equation 1. Consequently, Equation 1 is the first term of the Equation 2 relationship. The following functions in Equation 2 give η trends, as a function of AR , α_1 and B_1 require the substitution of Equations 3 - 7. Unfortunately, as indicated before, a judgment must be made as to the character of developing stall and also as to the character of inlet blockage influence. The stall delay is a function of how well the diffuser can be designed and how it will

perform with various types of inlet distortion. The functional relationship clearly indicates possibilities for choosing other coefficients if even greater, or perhaps milder, effects are anticipated. The blockage decision is somewhat more difficult. The second option, classical profile blockage, is the easiest because it should be used whenever a uniform inlet flow has been established with thin wall boundary layers. However, the more optimistic estimation of performance, which the common blockage trend seems to suggest, is harder to justify from a design point of view. Clearly considerable data supports this trend, but there is no known set of design or performance related parameters which assure a designer of the suitability of using this more optimistic trend. In this case, a more conservative design approach would be recommended.

With the pressure recovery specified, a reasonable first order estimate of the diffuser total pressure loss can be based on the following equations:

$$\begin{aligned} K &= C_{pi} - C_p \\ &= C_{pi}(1-\eta) \end{aligned}$$

where the values for C_{pi} and η are given above. Incidentally, this equation is accurate only to a first order level of ± 0.05 or in some extreme cases to ± 0.1 (see Japikse, 1986^[5]).

When all the correlated relationships are used, according to the appropriate sets of data, a final plot is obtained as shown in Figure 11. In this case, most of the data falls around 1.0 ± 0.1 with a few outlying points. This shows a moderately good degree of success in correlating the data of many different workers using a wide variety of different annular diffusers, although it is somewhat frustrating that two different stall branches and two different blockage trends were, of necessity, utilized in the data correlating relationship. This is the data of Figure 1a which varies from 0.13 to 0.76!

It is recognized that the correlations presented above do reflect weaknesses in the available database and will provide some frustration to designers due to a lack of certainty of the swirl and blockage influences. Nonetheless, it is always beneficial to assess trends as found in nature in order to afford the best practical guidance available, and the preceding equations should help. In the following section, suggestions are made for future research.

FUTURE STUDIES: LABORATORY AND CFD

The search for consistent behavioral patterns has revealed weaknesses both in the data and in the opportunity to conduct meaningful additional investigations. For the first approximation, geometry has been reasonably modeled with the C_{pi} and the $\eta(AR)$ relationships. However, it is almost certain that additional tests with further geometric variations (and for annular diffusers a very wide range of geometric combinations is possible) would afford more precise correlations. Nonetheless, this is not a major area needing further investigation. The dual trend characteristics for both the swirl angle dependence and the inlet aerodynamic blockage dependence point to a clear need for further investigation.

Systematic tests are needed with a variety of diffusers to determine which parameters control the development with stall within the annular diffuser and, therefore, permit an extension to Equations 4 and 5. Indeed, Equations 4 and 5 should be reduced to a single relationship once further trends can be determined. The development of stall would depend not only on geometric variables, but on a variety of different inlet profile parameters.

Inlet velocity profiles constitute the area of greatest need for further investigation. The effects of inlet aerodynamic blockage as represented in Equation 6 must be extended with different information concerning turbulence at the inlet to the diffuser.

There is a common and prevalent notion at the time of writing this paper that most of these problems can be resolved by using computational fluid dynamics (CFD). CFD can certainly be used today to conduct 'what if' studies of different possible inlet profile parameters and different geometric variations. It should not, however, be considered a definitive tool at the present time. A recent investigation (see Japikse, 2000)^[6], establishes without a doubt that the modeling of annular diffuser performance by the best CFD tools today is imprecise at best. Consequently, for a number of years CFD must be used concurrently with good laboratory procedures so that only essential tests will be conducted in the laboratory. Several fundamental problems keep CFD from being used as the

definitive tool; these include serious problems in the basic turbulence model plus problems in discretization, artificial viscosity or damping, and effective grid generation.

CONCLUSIONS

This investigation of a diverse set of annular diffuser test results, including the effects of inlet swirl and inlet aerodynamic blockage, has led to a deeper understanding of performance issues concerning the annular diffuser. The specific conclusions are as follows:

1. A correlation has been developed which brings together the available data to approximately $\pm 10\%$ (occasionally worse); however, an interpretation must be made as to the type of inlet profiles and the consequential influence on inlet aerodynamic blockage, as well as to the rate of stall development.
2. Significant further experimental work is necessary to understand the impact of inlet velocity profile on the stall process and upon the overall performance as presently reflected through inlet aerodynamic blockage.
3. The available correlation is suitable for preliminary design studies subject to the stated uncertainty.
4. Computational fluid dynamics can be used to research essential geometric and inlet aerodynamic parameters that would best constitute an experimental test evaluation. Such hybrid investigations are necessary to develop a more complete scientific basis for the design application of annular diffusers.

REFERENCES

- 1] Sovran, G., Klomp, E.D., "Experimentally Determined Optimum Geometries for Rectilinear Diffusers with Rectangular, Conical or Annular Cross-Section," Fluid Dynamics of Internal Flow, Elsevier Publishing Company, 1967.
- 2] Hoadley, D., Hughes, D.W., "Swirling Flow in an Annular Diffuser," University of Cambridge, Department of Engineering, Report CUED/A-Turbo/TR5, 1969.
- 3] Coladipietro, R., Schneider, J.M., Sridhar, K. "Effects of Inlet Flow Conditions on the Performance of Equiangular Annular Diffusers," Trans. CSME 3 (2): pp. 75-82, 1974.
- 4] Japikse, D., "The Influence of Inlet Turbulence on Diffuser Performance," Concepts ETI, Inc., Design Data Sheet No. 1, 1980.
- 5] Japikse, D., "A New Diffuser Mapping Technique – Studies in Component Performance: Part 1," ASME Paper No. 84-GT-237, Amsterdam, June 1984; also, Journal of Fluids Engineering, Vol. 108, No. 2. pp. 148-156, 1986.
- 6] Japikse, D., "Performance of Annular Diffusers Subject to Inlet Flow Field Variations and Exit Distortion," presented at the ISROMAC conference in Honolulu, Hawaii, March 26-30, 2000.
- 7] Dovzhik, S.A., Kartavenko, V.M., "Measurement of the Effect of Flow Swirl on the Efficiency of Annular Ducts and exhaust Nozzles of Axial Turbomachines," Fluid Mechanics/Soviet Research 4(4): 156-172, 1975.
- 8] Japikse, D., and Pampreen, R., "Annular Diffuser Performance for an Automotive Gas Turbine," ASME Publication 78-GT-147. 1978.
- 9] Goebel, J. H., Japikse, D., "The Performance of an Annular Diffuser Subject to Various Inlet Blockage and Rotor Discharge Effects," Consortium Final Report, Creare TN-325, March 1981.
- 10] Shaalan, M.R.A., Shabaka, I.M.M., "An Experimental Investigation of the Swirling Flow Performance of an Annular Diffuser at Low Speed," ASME Paper No. 75-WA/FE-17, 1975.

THE EFFECT OF ORIENTATION ON FLOW BOILING IN SINGLE-SIDE HEATED CHANNELS

Quaid Peatiwala

71B Barakat A1-Haidry Memorial Market
Block "E", North Nazimabad
Karachi 74700, Pakistan
e-mail: qpeatiwala@hotmail.com

Ronald D. Boyd, Sr.

Honeywell Professor of Engineering and Director
of the Thermal Science Research Center (TSRC)
Department of Mechanical Engineering
Prairie View A&M University
Prairie View, Texas 77446
Fax: (936) 857-2325
e-mail: ronald_boyd@pvamu.edu

ABSTRACT

As part of a study on factors affecting the flow boiling in vertical tubes, the two-dimensional wall temperature profiles and the boiling heat transfer coefficient were measured for downward flowing Freon-11 in vertical channels for a single-side heating configuration. The results obtained were compared with identical test runs for Freon-11 flowing in horizontal channels with a top-side heating configuration. The single-side heated experiments show a significant effect of flow direction on local outside wall temperatures, the local (axial) heat transfer coefficient, and the averaged heat transfer coefficient.

INTRODUCTION AND LITERATURE SURVEY

Flow boiling is the most commonly used heat transfer technique in industry. Industries such as aerospace, nuclear, power generation, chemical processing, and electronics use flow boiling heat transfer processes to transport large quantities of power at fairly low wall temperatures.

Due to extensive use of flow boiling heat transfer in industries, basic features of the boiling phenomena have been extensively investigated for more than sixty (60) years, and large data base encompassing a variety of fluids with wide ranges of pressure and flow rates have been developed and correlated.

Most widely quoted flow boiling heat transfer coefficient (h) correlations have been developed from large data banks for vertical upflow with the majority of the data being in the vapor quality range from 0.0 to 0.5. These include correlations by Chen [1], Shah [2], Steiner et al. [3], and Winterton and his coworkers [4,5,6]. Very recently, Seo and Kim [7] used correlations developed by Kandlikar [8], Wright, Wright et al., Schrock and Grossman, Gungor and Winterton and Chen to make heat transfer coefficient comparisons with smooth tube R-22 data. Based on this comparison, they recommended correlations by Gungor and Winterton [5], Chen [1], and Wright et al. [9]. Some of these correlations have also been extended to flow boiling inside horizontal tubes. There are several causes for concern. First of all, above the stratified flow threshold criterion, it is assumed that there is no tube orientation effect on heat transfer. Below the threshold, there is a reduction in h because the tube circumference is only partially wetted with liquid and dry at the top. This reduction in h is predicted by adding an empirical correction term to the vertical tube correlation. However, some of these empirical corrections have been developed by statistical regression to improve the fit of the vertical tube correlation to the horizontal tube boiling data bank rather than by a direct comparison of experimental test data for vertical and horizontal flows at the same local test conditions. Consequently, effects other than stratification may be involved. Hence, these potentially important other effects (which could include other stratification influences; e.g. due to reduced gravity) will be manifested as weak influences in existing design correlations for horizontal tubes.

Several researchers have used the threshold criterion in their correlations for both vertical and horizontal flow. The most widely used stratified threshold criterion for applying vertical flow boiling correlations to horizontal flows is the liquid Froude number, defined as

$$Fr_L = G^2 / [g D \rho_L], \quad (1)$$

where G is the mass velocity, D is the inside channel diameter, g is the acceleration due to gravity, and ρ_L is the liquid density. For $Fr_L < 0.04$, Shah [2] recommended that both the convective boiling and nucleate boiling heat transfer coefficient be determined by separate correlations. Gungor and Winterton [5] on other hand defined the threshold for Fr_L to be 0.05. In addition, they modified both the convection enhancement factor (F) by multiplying by a factor E_2 and boiling suppression factor (S) by multiplying by a factor E_1 . Both E_2 and E_1 have a reducing effect and are given by

$$E_2 = Fr_L^{[0.1 - 2 Fr_L]} \quad (2)$$

$$E_1 = Fr_L^{0.5}.$$

Using a Shah type correlation, Kandlikar [8] developed a new correlation which retained the Shah threshold value of 0.04. More recently, Kattan et al [10] obtained experimental data on flow regimes and the threshold between stratified and unstratified flow. They found that the liquid Froude number criterion ($Fr_L = 0.04, 0.05$, etc.) used by many flow boiling correlations is incapable of delineating the transition between stratified and unstratified flow data of refrigerants, and called the use of vertical tube correlation to model heat transfer in horizontal tubes “questionable.”

Until recently very few researchers have investigated the effect of orientation based on fundamental flow analysis. Kattan et al. [10] studied orientation effects for R-134a flow boiling in horizontal flow, vertical upflow, and vertical downward flow using a 12 mm diameter tube over wide ranges of mass velocities, vapor qualities and heat flux. They found a significant effect of flow direction on local heat transfer coefficient. The experimental data showed that the horizontal tube heat transfer coefficients ranged from 47% to 38% below those for vertical upflow. The vertical downflow data were significantly below the data for h for both horizontal flow and vertical upward conditions. The lower coefficients for downflow compared to upflow and horizontal flow were not expected by Kattan et al. [10], and they tried to explain this by hypothesizing that buoyancy effects of vapor, which opposes downward flow may reduce its accelerating effects on the liquid and hence diminish the convective contribution to heat transfer. The lower heat transfer coefficients for horizontal flow as compared to vertical upward flow at low flow rates can be explained as a result of flow stratification in the horizontal tube. As they observed, these differences between horizontal and vertical upward flows diminish and even reversed in nature as the heat flux and quality increase.

One other fundamental difference between the boiling in upflow, downflow, and horizontal flow which can have significant effect of heat transfer was also hypothesized by Kattan et al. as the subcooling effect of the pressure gradient on the process. Kirk et al. [11] looked into the effect of low-velocity subcooled flow boiling at various orientations for R-113 flowing in rectangular channels. They found that at very low velocities where buoyancy is dominant, the effect of orientation is very pronounced. In the low-velocity domain, and as the channel is rotated from the horizontal position to the vertical upflow position, a significant enhancement of heat transfer takes place at low levels of heat flux with the enhancement diminishing as heat flux is increased. They also found that a limiting flow velocity exists beyond which the orientation and gravity can be completely neglected. Both the studies by Kattan et al. and Kirk et al., establishes the fact that the effect of flow velocity on heat transfer is very much dependent on flow orientation and has some surprising influences.

From the discussion above, it is clear that although efforts have just been started in understanding the orientation effects on heat transfer, more understanding is needed. In this work, we extend the previous studies to include single-side heated channels for downward and horizontal flow. Efforts will be made to study the effect of flow orientation using fundamental flow analysis by comparing quasi-boiling curves and heat transfer coefficients for identical flow conditions for a top-side heated horizontal flow and a single-side heated vertical downward flow.

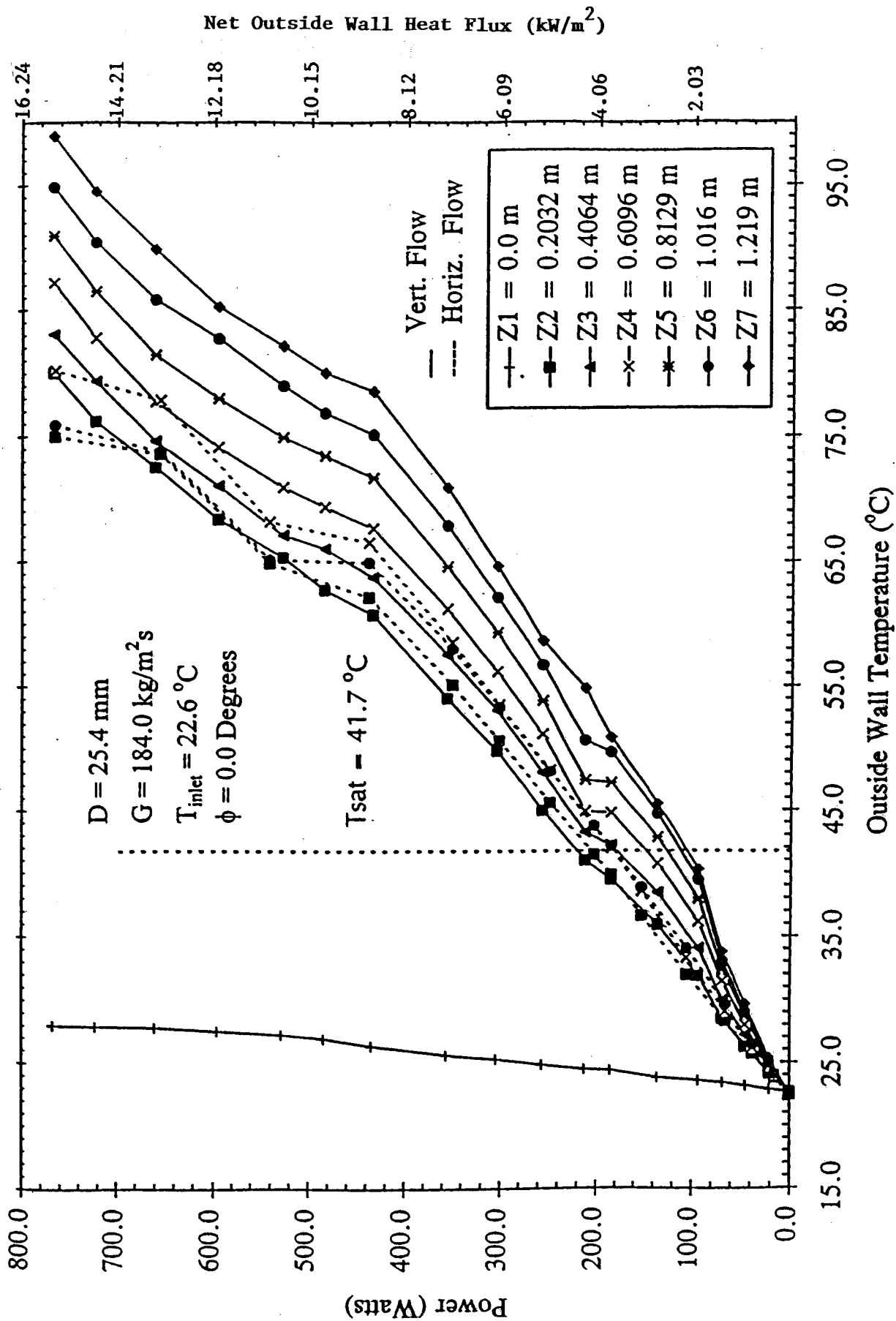


Figure 1a. Measured Outside Wall Temperature (Copper Channel) Axial Variation for $\phi = 0.0$ degrees as a Function of the Net Power Generation for a Single-Side Heated Smooth Channel, Vertical Downward and Horizontal Flow (Top-Side Heated) and $P_{\text{exit}} = 0.187 \text{ MPa absolute}$.

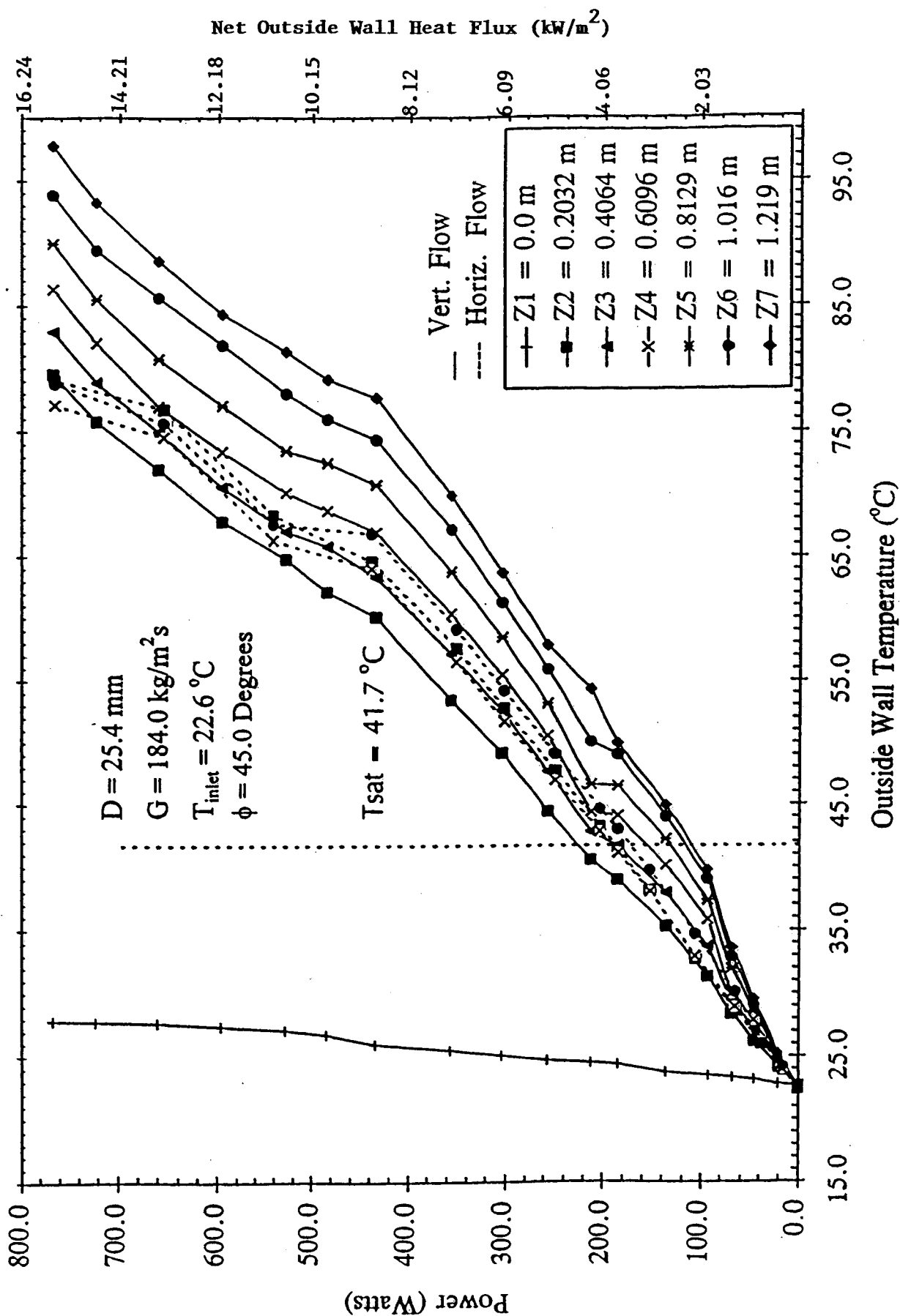


Figure 1b. Measured Outside Wall Temperature (Copper Channel) Axial Variation for $\phi = 45.0$ degrees as a Function of the Net Power Generation for a Single-Side Heated Smooth Channel, Vertical Downward and Horizontal Flow (Top-Side Heated) and $P_{\text{exit}} = 0.187 \text{ MPa}$ absolute.

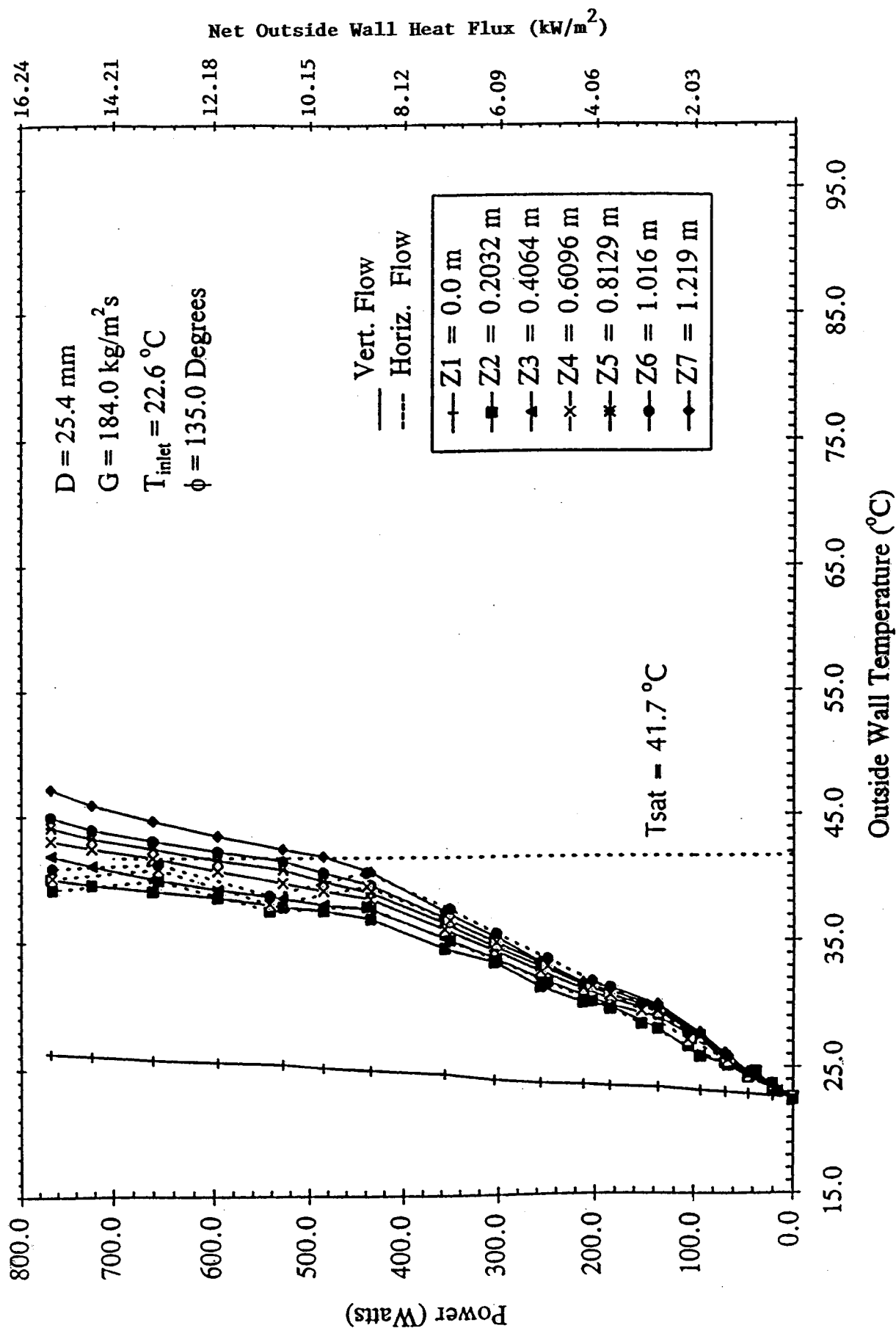


Figure 1c. Measured Outside Wall Temperature (Copper Channel) Axial Variation for $\phi = 135.0$ degrees as a Function of the Net Power Generation for a Single-Side Heated Smooth Channel, Vertical Downward and Horizontal Flow (Top-Side Heated) and $P_{\text{exit}} = 0.187 \text{ MPa}$ absolute.

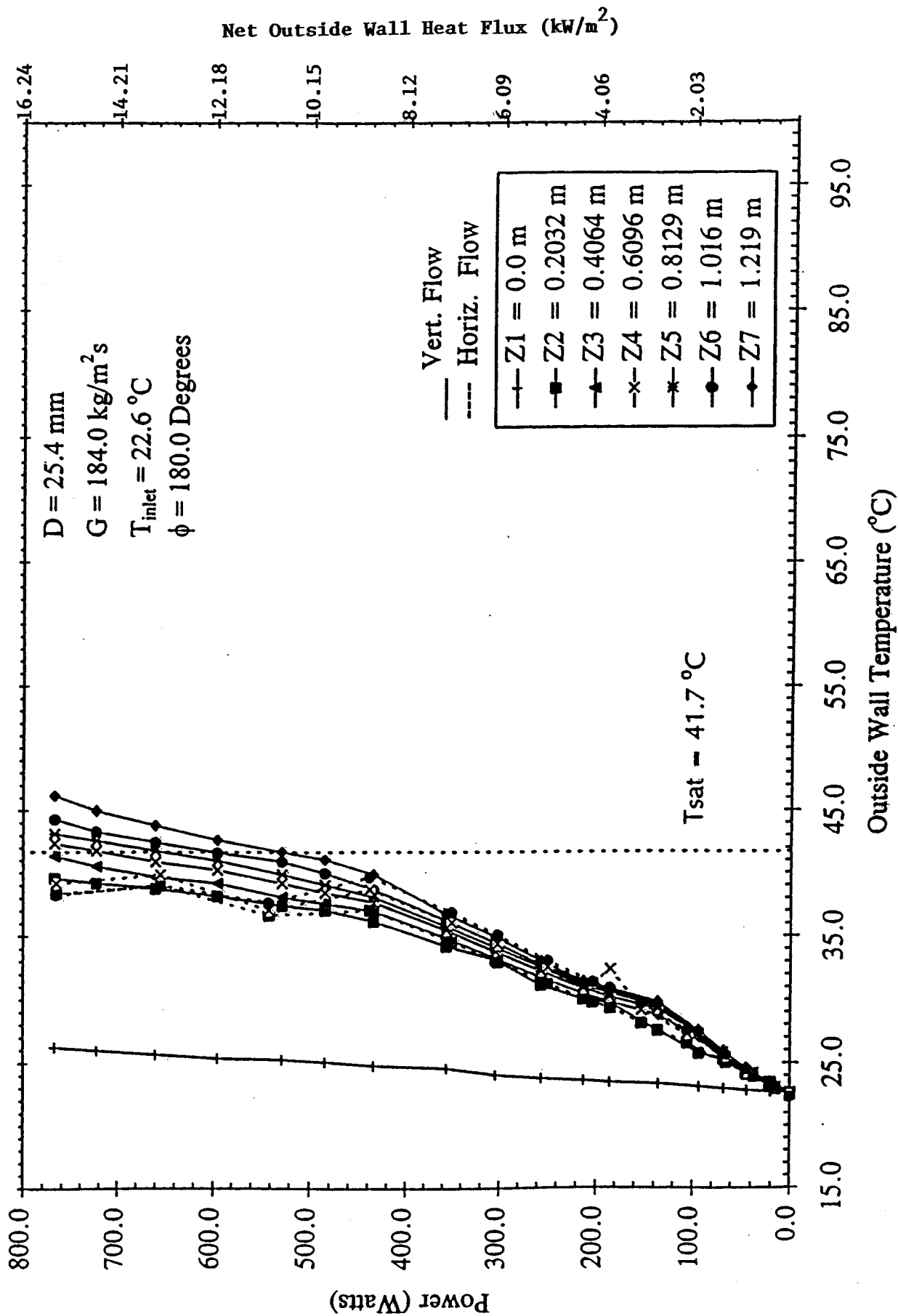


Figure 1d. Measured Outside Wall Temperature (Copper Channel) Axial Variation for $\phi = 180.0$ degrees as a Function of the Net Power Generation for a Single-Side Heated Smooth Channel, Vertical Downward and Horizontal Flow (Top-Side Heated) and $P_{\text{exit}} = 0.187 \text{ MPa}$ absolute.

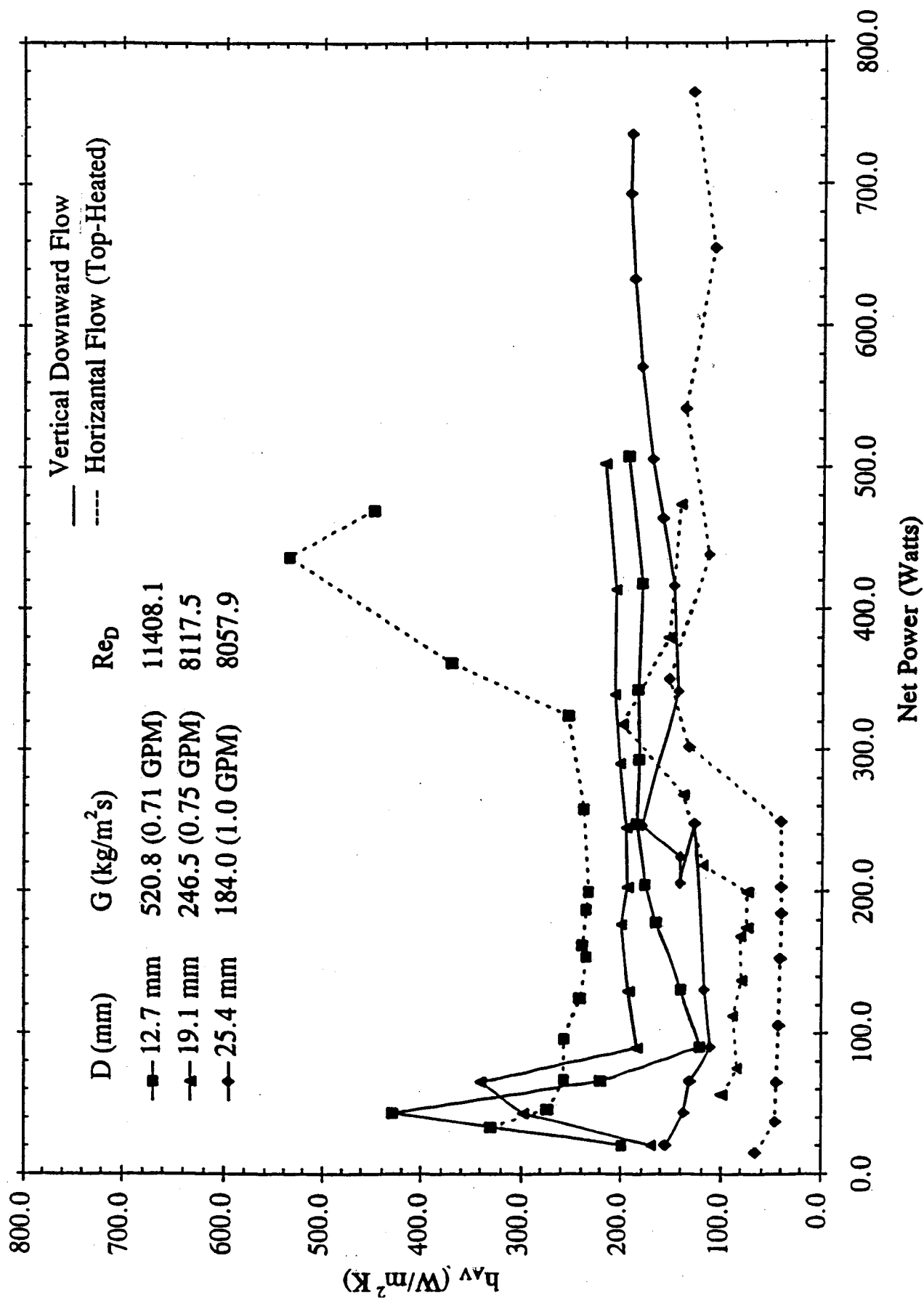


Figure 2. Comparison of Circumferentially and Axially Averaged Heat Transfer Coefficient as a Function of the Net Power Generation for a Single-Side Heated Smooth Channel for Vertical Downward and Horizontal Flows at Different Reynolds Numbers, with $T_{inlet} = 22.6^{\circ}C$, and $P_{ext} = 0.187 MPa$ absolute. The Outside Wall Heat Flux (in W/m^2) Corresponding to the Specific Channel Diameter Can be Obtained by Multiplying the Net Power by the Following Factor: 20.3 for $D = 25.4 mm$; 27.0 for $D = 19.1 mm$; and 40.6 for $D = 12.7 mm$.

Single-Side Heated Smooth Tube; I. D. = 25.4 mm; Inlet Temp. 22.6°C

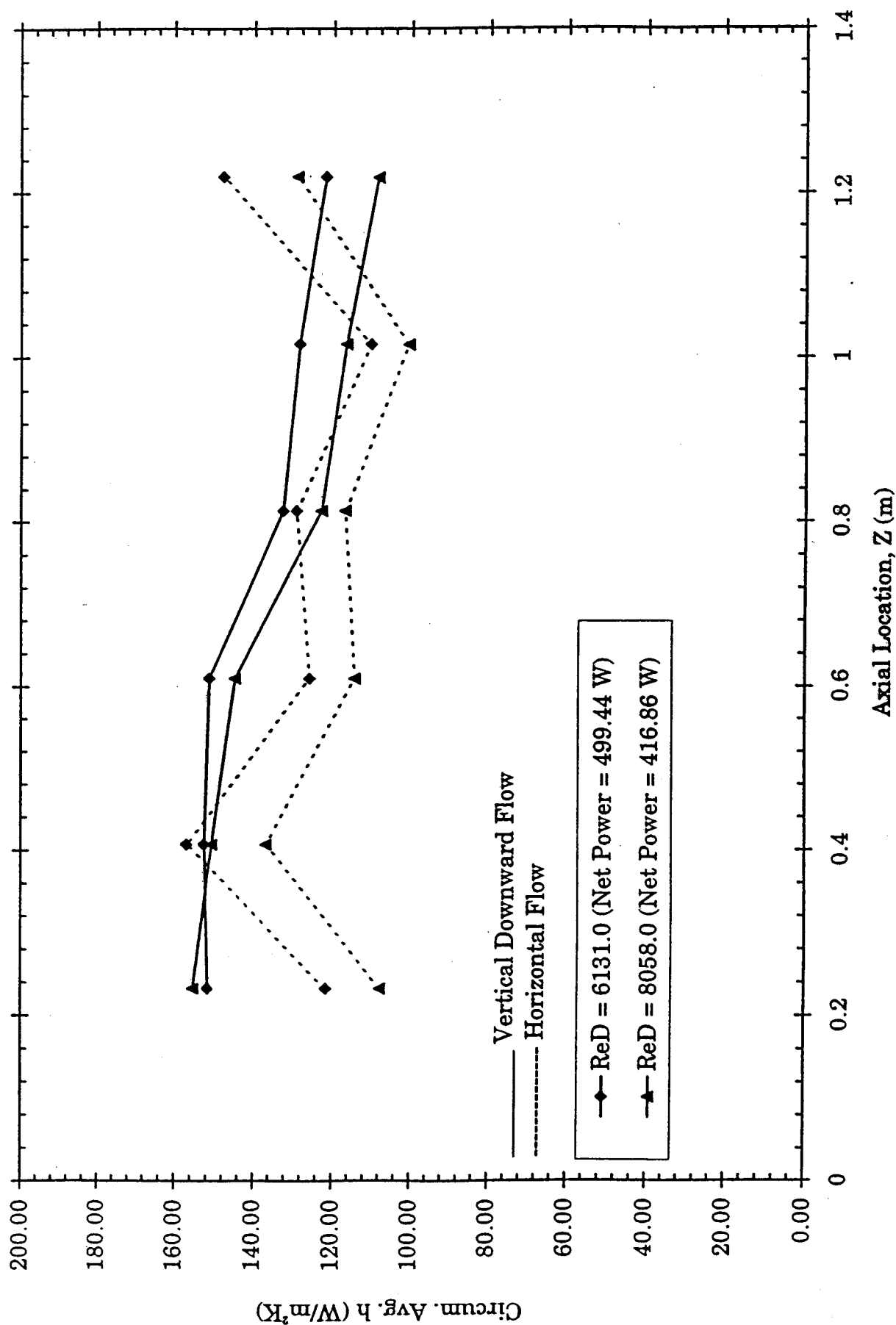


Figure 3. Axial Distribution of the Circumferentially-Average Heat Transfer Coefficient. Note: 499.44 W and 416.86 W correspond to Outside Channel Wall, Single-Side Heat Fluxes of 10.15 kW/m² and 8.47 kW/m², respectively.

power levels above 400.0 W for the horizontal flow, there appears to be a rewetting phenomenon which is initiated and then disappears as the power was increased.

In Figure 2, G is increasing and D is decreasing from case to case. However, the Reynolds number for the two largest values of D are almost identical. Although variations of h_{av} with power are different for the two cases, there are some similarities. When one take into account that the L/D s are quite different for the two cases, it indicates that a better correlation and comparison could be made by comparing the axial distributions of the circumferentially averaged heat transfer coefficient. For almost a fifty percent increase in the Reynolds number from 8,057.9 (and 8,117.5) to 11,408.1, h_{av} for the horizontal flow increased by a factor of two in some cases and actually exceeded h_{av} for the vertical downward flow for the case involving the highest Reynolds number (11,408.1) and the smallest inside diameter (12.7 mm). This demonstrates that increased top-surface wetting in the horizontal top-heated channel at higher Reynolds number results in increased heat transfer. The dashed curves (top-heated horizontal channel) in Figure 3 show axial fluctuations in the circumferentially-averaged heat transfer coefficient. At first glance, one may be tempted to conclude that this appears to indicate the axial locations where liquid crests are wetting the top-heated horizontal channel. Since the values shown either represent a relative maximum or minimum only at the measured axial locations, the indicated relative maxima cannot be used to deduce an axial period for the crests. However for the two lower Reynolds number cases (8,117.5 and 8,057.9) in Figure 2, the horizontal flow heat transfer is below that for the vertical downward flow. Figure 3 shows the axial distribution of the circumferentially-averaged heat transfer coefficient both at the lowest value of Reynolds number displayed in Figure 2 (8,057) and an even lower value of 6,131. This figure confirms the latter noted trend that at even lower levels of Reynolds number, the vertical downward flow has greater heat transfer coefficients at upstream locations. However, at downstream locations near the exit of the heated section, the top-heated horizontal flow has higher heat transfer coefficients. Finally, the above single-side heated channel flows had Froude numbers between 0.18 and 0.31, which are above the orientation liquid Froude number thresholds which have been used in the past by other investigators [2,5] for uniformly heated channels.

CONCLUSION

Results have been presented for identical test runs for horizontal top-side heated flow, and single-side heated vertical downward flow to study the effect of orientation on heat transfer. The results show that the horizontal flow heat transfer is lower than that for vertical downward flow at low Reynolds numbers, which is the opposite relationship observed for uniformly heated flow channels. However, as both the Reynolds number and heated axial coordinate increase, this trend is reversed in the flow boiling region.

ACKNOWLEDGMENT

This work was supported by NASA contract #NAG9-631 and DOE contract DEFG03-97ER54452.

REFERENCES

1. Chen, J. C., 1966, "A Correlation for Boiling Heat Transfer to Saturated Fluids in Convective Flows", *Industrial and Engineering Chemistry Process Design and Development*, Vol. 5, No. 3, pp. 322-329.
2. Shah, M. M., 1977, "A General Correlation for Heat Transfer During Subcooled Boiling in Pipes and Annuli," *ASHRAE Transactions*, Vol. 83, pp. 202-215.
3. Steiner, D. and Taborek, J., 1992, "Flow Boiling Heat Transfer in Vertical Tubes Correlated by an Asymptotic Model," *Heat Transfer Engineering*, Vol. 13, No. 2, pp. 43-66.
4. Liu, Z. and Winterton, R. H. S., 1991, "A General Correlation for Saturated and Subcooled Flow Boiling in Tubes and Annuli, Based on a Nucleate Pool Boiling Equation," *International J. Heat Mass Transfer*, Vol. 34, No 3, pp. 2759-2763.
5. Gungor, K. E. and Winterton, R. H. S., 1986, "A General Correlation for Flow Boiling in Tubes and Annuli," *International J. Heat Mass Transfer*, Vol. 29, No 3, pp. 351-358.
6. Gungor, K. E. and Winterton, R. H. S., 1986, "Simplified General Correlation for Saturated Flow Boiling and Comparison of Correlations with Data," *Chem. Eng. Res. Des.*, Vol. 65, pp. 148-156.
7. Seo, K., and Kim, Y., 2000, "Evaporation Heat Transfer and Pressure Drop of R-22 in 7.0 and 9.52 mm Smooth/Micro-Fin Tubes," *International J. Heat and Mass Transfer*, Vol. 43, #16, pp. 2869-2882.
8. Kandlikar, S. G., 1990, "A General Correlation of Saturated Two-Phase Flow Boiling Heat Transfer Inside

Mathematical Physics of the Propagation of a Laminar Aerodynamic Boundary Layer, Using the Kinetic Theory of Gases

Albert L. de Graffenried
Aeronautical & Electronics Research & Development engineer,
Aero-Electronic Leasing Corporation,
30 Washington Avenue,
Glen Head, L.I., New York
11545 + 1543 U.S.A.

Abstract

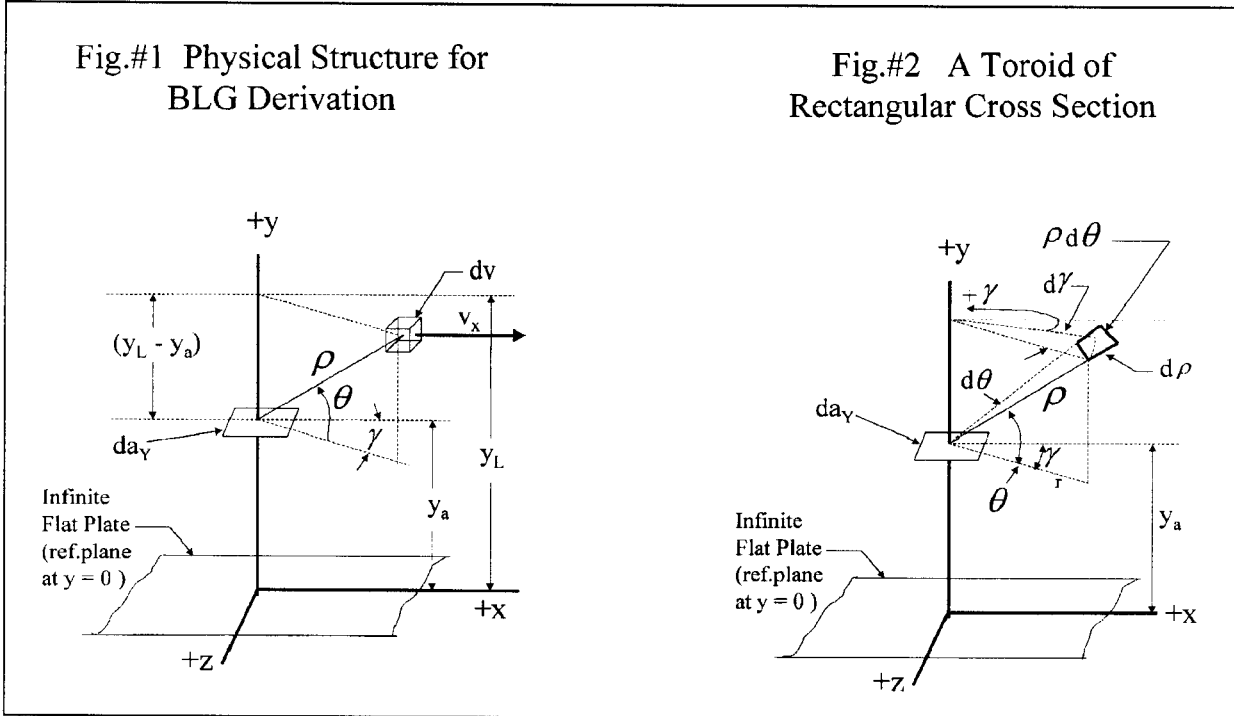
1. The paper presents a derivation showing the propagation mechanisms fundamental to the growth of the laminar aerodynamic boundary layer. The molecular mechanisms basic to such growth are those presented by James Clerk Maxwell in his classic derivation of μ , the viscosity of a gas, based on the Kinetic Theory of Gases. Maxwell's derivation is modified by moving the scene of the analysis from a free-stream location (where he assumes a linear velocity gradient) to a location immediately adjacent an infinite flat plate, using an unknown velocity profile.
2. Gas, initially quiescent above the flat plate, suddenly jumps to velocity U_0 at time $t=0+$. The resultant growth of a boundary-layer velocity profile, $v_x(y,t)$, is solved for in the following manner:
 - a. $\dot{\Phi}_{up}$, the stream momentum crossing an element of area, $da=dx dz$ per second per square centimeter, in an upward (+y) direction, is found by integrating through all volume below da , using an unknown velocity profile, $v_x(y,t)$;
 - b. similarly, $\dot{\Phi}_{down}$, the stream momentum crossing da in a downward (-y) direction is found by integrating through all volume above da ;
 - c. the net stream momentum, $\dot{\Phi}(y)$ equals $\dot{\Phi}_{up}$ minus $\dot{\Phi}_{down}$;
 - d. the acceleration, dv_x/dt of an element of mass dm , equal to ρ times $dx dy dz$ is set equal to minus the partial of $\dot{\Phi}$ with respect to y , the net momentum-flux gradient, based on Newton's Law;
 - e. in cylindrical coordinates, azimuth angle γ is promptly integrated out. Elevation angle θ is integrated-out numerically, using a short BASIC program on a PC;
 - f. Separation of Variables is assumed, specifically, $v_x(y,t)$ may be set equal to $f_1(y)f_2(t)$, thus producing two separate integro-differential equations which are each set equal to a common constant, $-\beta^2$;
 - g. LaPlace transforming these two equations into the s_y and s_t domains, applying the Method of Partial Fractions to the s_y equation, the FORM of the solution is found, viz., exponential and hyperbolic functions;
 - h. boundary conditions are satisfied in order to provide a closed solution.
3. The first experimental fall-out from this long-term boundary-layer-growth research project is: "BoundaryLayer-Growth Suppression" (BLG-S), a new boundary-layer control technique yielding more than 30% reduction in Profile Drag Coefficient of an infinite-aspect-ratio wing at low subsonic speeds, in the Hofstra University laminar-flow wind tunnel.
4. It is hoped that this new molecular analytical approach to boundary-layer growth will be able to mature and merge with current Computer Fluid Dynamics software, in order to provide a more realistic family of solutions, as well as a clearer picture of the molecular mechanisms present in the flow pattern.

The Physical Structure

1. This work is based squarely on the pioneering molecular derivation of μ , the coefficient of viscosity of a gas, generated by James Clerk Maxwell, a Scotchman who operated out of the University of Edinburgh in the mid-1800's.
2. The physical structure shown in figure #1 is Maxwell's figure. The Author has simply moved the axes from a free-stream location (where Maxwell assumed a linear velocity gradient) to a site adjacent an infinite flat plate. The viscosity of a gas, μ , is a CONTINUUM parameter and will not be mentioned again in this paper. Here one deals

directly with the *molecular* variables such as mean free path, molecular diameter, collisions/sec/molecule, and similar parameters.

3. This derivation assumes a gas quiescent above an infinite flat plate. The gas suddenly jumps to a streaming velocity U_0 at time $t=0+$. The final result of this derivation will be $v_x(y,t)$ which shows the one-dimensional propagation of a gaseous boundary layer with time. For those who are familiar with Maxwell's derivation, the first part



of this derivation will be a review, but this paper will generally cater to those who do not know Maxwell's molecular work on viscosity.

The Derivation

1. In a volume dv (see Fig.#1 & equation Q-1) are $n \cdot dv$ molecules, each making \underline{z} collisions/second. This produces $n \cdot \underline{z} \cdot dv \cdot dt$ new molecular paths/second in dv . Each molecule is assumed to be carrying a streaming-velocity component $v_x(y,t)$ characteristic of the horizontal lamina (Δy_L) in which it originated (which lamina is located

$$dN = n \cdot \underline{z} \cdot dv \cdot dt \quad (Q-1)$$

$$dM = n \cdot \underline{z} \cdot dv \cdot dt \cdot m \cdot v_x(y_L, t) \quad (Q-2)$$

$$= n \cdot m \cdot \underline{z} \cdot v_x(y_L, t) \cdot dv \cdot dt \quad (Q-3)$$

at y_L), as shown in figure #1 and equation Q-3.

2. The target area da , shown in fig.#1, is $dx \cdot dz$, and the *fractional solid angle* subtended by da , when viewed by an observer standing inside dv , is shown by Q-5, where $da \cdot \sin(\theta)$ is the area of da which is perpendicular to radius

$$da = dx \cdot dz \quad (\text{target area}) \quad (Q-4)$$

$$d\Omega = \left[\frac{da \cdot \sin(\theta)}{4 \cdot \pi \cdot \rho^2} \right] \quad (Q-5) \quad \text{Since: } \rho = \frac{(y_L - y_a)}{\sin(\theta)} \quad (Q-5a)$$

$$= \left[\frac{da \cdot \sin(\theta) \cdot \sin^2(\theta)}{4 \pi \cdot (y_L - y_a)^2} \right] \quad (Q-6)$$

$$= \left[\frac{da \cdot \sin^3(\theta)}{4 \pi \cdot (y_L - y_a)^2} \right] \quad (Q-7)$$

vector ρ , and $4 \cdot \pi \cdot (\rho)^2$ is the *total solid angle* surrounding an observer within dv . Note that θ is the angle to the *horizon*, not to zenith as is usually used.

3. Substituting Q-5a for ρ into Q-5 yields Q-6 and Q-7. Q-8 is the Free Path Distribution equation, and Q-9 is

$$\frac{n_\rho}{n_0} = e^{-\frac{\rho}{L}} \quad (Q-8)$$

$$\rho = \frac{(y_L - y_a)}{\sin(\theta)} \quad (Q-9)$$

$$\downarrow \dots \dots \dots \downarrow \dots \dots \dots (Q-10)$$

$$\therefore dM = \left\{ nm_z \cdot v_x(y_L, t) \cdot e^{-\frac{(y_L - y_a)}{L \cdot \sin(\theta)}} \cdot \frac{da \cdot \sin^3(\theta)}{4 \cdot \pi \cdot (y_L - y_a)^2} \cdot dv \cdot dt \right\}$$

substituted into Q-8 for ρ , to yield Q-10, the incremental amount of stream momentum carried by molecules originating in dv during time dt which reach da in *one free path*.

4. Q-11 defines Stream Momentum Flux. Q-13 shows constants collected out front, and an integration indicated in

$$\text{and: } \frac{dM}{da \cdot dt} = \frac{d^3}{d\Phi} \quad (\text{Momentum/sq.cm.} \cdot \text{second}) \quad (Q-11)$$

$\uparrow \dots \dots \dots$ the da located at $y = y_a$.

$$d^3\Phi = \left\{ nm_z \cdot v_x(y_L, t) \cdot e^{-\frac{(y_L - y_a)}{L \cdot \sin(\theta)}} \cdot \frac{\sin^3(\theta)}{4 \cdot \pi \cdot (y_L - y_a)^2} dv \right\} \quad (Q-12)$$

order to find $\Delta\Phi$. Q-14 defines the Net Stream Momentum Flux as as the total flux flowing through da from

$$\Delta\Phi = \left\{ \frac{nmz}{4 \cdot \pi} \left[v_x(y_L, t) \cdot e^{-\frac{(y_L - y_a)}{L \cdot \sin(\theta)}} \cdot \frac{\sin^3(\theta)}{(y_L - y_a)^2} \cdot dv \right] \right\} \quad (Q-13)$$

$$\text{net } \Phi = \frac{nmz}{4 \cdot \pi} \left[+ \int_0^{y_a} \dots \cdot dv - \int_{y_a}^{\infty} \dots \cdot dv \right] \quad (Q-14)$$

\uparrow
net stream-momentum flux crossing
 da requires (-) sign, because of
vector summation of $\Delta\Phi$ terms.

below da minus the total flux flowing through da from above da .

5. Since we are growing a one-dimensional boundary layer, the flow velocity will be *laminar* in the sense that, within any lamina dy , v_x will be independent of x and z . Thus the limits of integration will be in terms of y_a , and we must transform the integrands to a single differential, dy_L , where the subscript "L" stands for the lamina containing our dv .

6. Therefore, in Q-15 we convert to cylindrical coordinates (also see Fig.#2) using ρ , θ , and

$$dv = (d\rho) \cdot [\rho \cdot \cos(\theta) \cdot d\gamma] (\rho \cdot d\theta) \quad (\text{see fig.\#2}) \quad (Q-15)$$

$$= [\rho^2 \cdot \cos(\theta) \cdot d\rho \cdot d\theta \cdot d\gamma] \quad (Q-16)$$

$$= \frac{(y_L - y_a)^2}{\sin^2(\theta)} \cdot \cos(\theta) \cdot d\rho \cdot d\theta \cdot d\gamma \quad (Q-16A)$$

γ ...where θ is elevation angle above the horizon. If we integrate with respect to γ first, we generate a new increment of volume which is a doughnut-like-solid with a keystone cross section (see fig.#2).

7. Q-21 thru Q-24 express $d\rho$ in terms of y and θ . Substituting Q-24 into Q-20 for $d\rho$ produces a

$$d\rho = d\left[\frac{y_L - y_a}{\sin(\theta)} \right] = d\left\{ \underset{\substack{\uparrow \\ \text{"A"}}}{[y_L - y_a]} \cdot \underset{\substack{\uparrow \\ \text{"B"}}}{[\sin(\theta)]^{-1}} \right\} \quad (Q-21)$$

$$= (A \cdot dB + B \cdot dA) \quad \longleftarrow (Q-22)$$

$d\theta^2$, which term is considered negligible and is deleted.

$$\begin{aligned}
 & +\Phi(y_a, t)]_{\uparrow} = \quad \leftarrow \dots \downarrow \dots \downarrow \quad (Q-20) \\
 & \left[A_1 \cdot \int_{-\pi/2}^0 \int_0^{y_a} v_x(y_L, t) \cdot e^{-\frac{(y_L - y_a)}{L \cdot \sin(\theta)}} \cdot \sin(\theta) \cdot \cos(\theta) \cdot d\left[\frac{(y_L - y_a)}{\sin(\theta)}\right] \cdot d\theta \right]
 \end{aligned}$$

$$d\rho = d\left[\frac{y_L - y_a}{\sin(\theta)}\right] = d\left\{ \underset{\substack{\uparrow \\ \text{"A"}}}{y_L - y_a} \cdot \underset{\substack{\uparrow \\ \text{"B"}}}{[\sin(\theta)]^{-1}} \right\} \quad (Q-21)$$

$$= (A \cdot dB + B \cdot dA) \quad \leftarrow (Q-22)$$

$$= \left\{ [(y_L - y_a) \cdot (-1) \cdot (\sin\theta)^{-2} \cdot \cos\theta \cdot d\theta] + [(\sin(\theta))^{-1} \cdot dy_L] \right\} \quad \downarrow \dots \downarrow \dots \downarrow \quad (Q-23)$$

$$= \left[-(y_L - y_a) \cdot \frac{\cos(\theta)}{\sin^2(\theta)} \cdot d\theta + \frac{dy_L}{\sin(\theta)} \right] \quad \leftarrow \dots \quad (Q-24)$$

Resultant sign of exponent below must always be negative.

(Q-26)

$$+\Phi(y_a, t)]_{\uparrow} =$$

$$\left\{ A_1 \cdot \int_{-\pi/2}^0 \int_0^{y_a} v_x(y_L, t) \cdot e^{-\frac{(y_L - y_a)}{L \cdot \sin(\theta)}} \cdot \sin(\theta) \cdot \cos(\theta) \cdot \frac{dy_L}{\sin(\theta)} \cdot d\theta \right\}$$

↑...sin(θ) & (y_L-y_a) are each (-) in quadrant # IV.

8. Thus we have Q-26 which is in terms of y and θ . Q-27 and Q-27.10 show *both* integrals, viz., the UP-flux integral and the DOWN-flux integral. If we can integrate the θ functions, we will have arrived at our laminar or

$$\begin{array}{c}
 \text{(Q-27)} \\
 \downarrow \\
 \Phi(y_a, t) \Big|_{\uparrow} = \left[+A_1 \cdot \int_0^{y_a} v_x(y_L, t) \cdot \left\{ \int_{-\pi/2}^0 e^{-\frac{(y_L - y_a)}{L \cdot \sin(\theta)}} \cdot \cos(\theta) \cdot d\theta \right\} \cdot dy_L \right] \\
 \uparrow \dots \dots \dots \uparrow \\
 f(\theta) \text{ (up)} \\
 \\
 \downarrow \dots \dots \dots \downarrow \dots \dots \text{(Q-27.10)} \\
 \Phi(y_a, t) \Big|_{\downarrow} = \left[-A_1 \cdot \int_{y_a}^{\infty} v_x(y_L, t) \cdot \left\{ \int_0^{+\pi/2} e^{-\frac{(y_L - y_a)}{L \cdot \sin(\theta)}} \cdot \cos(\theta) \cdot d\theta \right\} \cdot dy_L \right] \\
 \uparrow \dots \dots \dots \uparrow \\
 f(\theta) \text{ (down)}
 \end{array}$$

dy_L -only condition.

9. Numerical integration, using BASIC, shows in Q-27.23, that the integral is of the form $(-a - b \cdot x)$ for f -of-

Therefore: raising both sides of Q-27.17 as a power of e gives:

$$\int_0^{+\pi/2} e^{-\frac{(y_L - y_a)}{L \cdot \sin(\theta)}} \cdot \cos(\theta) \cdot d\theta = \left[e^{-k_a - k_b \cdot \frac{(y_L - y_a)}{L}} \right] \quad \text{(Q-27.23)}$$

theta-down, and $(-a + b \cdot x)$ for f -of-theta-up. More recently, it has been shown analytically that k_a is zero, leaving only

k_b in place. Equation Q-27.40 is the laminar form desired.

$$\Phi(y_a, t)]_{\downarrow} = -A_1 \cdot e^{-k_a} \cdot \int_{y_a}^{\infty} v_x(y_L, t) \cdot e^{-k_b \cdot \frac{(y_L - y_a)}{L}} \cdot dy_L \quad (Q-27.40)$$

10. Separation of Variable is assumed in Q-27.45. Equations Q-27.47 & 27.48 together give the net stream

Assume Separation of Variables:

$$v_x(y_L, t) = f_1(y_L) \cdot f_2(t) \quad (Q-27.45)$$

Re-writing Q-27.40 gives:

$$\Phi(y_a, t)]_{\downarrow} = -A_1 \cdot e^{-k_a} \cdot f_2(t) \cdot \int_{y_a}^{\infty} f_1(y_L) \cdot e^{-k_b \cdot \frac{(y_L - y_a)}{L}} \cdot dy_L \quad (Q-27.47)$$

$$\Phi(y_a, t)]_{\uparrow} = +A_1 \cdot e^{-k_a} \cdot f_2(t) \cdot \int_0^{y_a} f_1(y_L) \cdot e^{+k_b \cdot \frac{(y_L - y_a)}{L}} \cdot dy_L \quad (Q-27.48)$$

$$\lambda = (y_L - y_a) \quad \therefore \quad y_L = (\lambda + y_a) \quad (Q-27.52)$$

$$\therefore \quad d\lambda = dy_L \quad (Q-27.53)$$

$$\text{when } y_L = y_a \quad \text{then } \lambda = 0 \quad (Q-27.54)$$

$$\text{when } y_L = \infty \quad \text{then } \lambda = \infty \quad (Q-27.55)$$

momentum flux across da . The form of Q-27.48 is the Real Convolution integral. The limits of integration of Q-27.47 may be changed (by using the substitution shown in Q-27.52 to .55) to make it conform to that of a real convolution.

11. Q-27.57 to Q-27.60 show the final form, with f_3 and f_4 defined.

$$\Phi(y_a, t)]_{\downarrow} = -A_1 \cdot e^{-k_a \cdot f_2(t)} \cdot \int_0^{\infty \text{ or } 5 \cdot L} f_1(\lambda + y_a) \cdot e^{-k_b \cdot \frac{\lambda}{L}} \cdot d\lambda \quad (\text{Q-27.57})$$

$$\text{where: } f_3 = e^{-k_b \cdot \frac{\lambda}{L}} \quad (\text{Q-27.58})$$

$$\Phi(y_a, t)]_{\uparrow} = +A_1 \cdot e^{-k_a \cdot f_2(t)} \cdot \int_0^{y_a} f_1(y_L) \cdot e^{+k_b \cdot \frac{(y_L - y_a)}{L}} \cdot dy_L \quad (\text{Q-27.59})$$

$$\text{where: } f_4 = e^{+k_b \cdot \frac{(y_L - y_a)}{L}} \quad (\text{Q-27.60})$$

12. By a straightforward continuum derivation, one may show Q-27t and Q-27u which lead to Q-28 and Q-28a. If

$$\begin{array}{c} n \cdot m \cdot da \cdot dy \cdot \frac{\partial v_x}{\partial t} = - \frac{\partial \Phi}{\partial y} \cdot dy \cdot da \\ \uparrow \dots \dots \uparrow \\ dm \end{array} \quad (\text{Q-27t})$$

$$\frac{\partial v_x}{\partial t} = - \frac{1}{n \cdot m} \frac{\partial \Phi}{\partial y} = - \frac{1}{n \cdot m} \cdot \frac{\partial}{\partial y} [\phi_{up} + \phi_{dn}] \quad (\text{Q27u})$$

we integrate Q-28a, the result is Q-28b.

13. Substituting the two convolution-form equations into Q-28b for $\partial \Phi / \partial y$ yields Q-29, Q-30, and Q-31.

$$\therefore dv_x = - \frac{1}{n \cdot m} \cdot \frac{\partial \Phi}{\partial y} \cdot dt \quad (\text{Q28})$$

$$dv_x = - \frac{1}{\rho_m} \cdot \frac{\partial \Phi}{\partial y} \cdot dt \quad (\text{Q28a})$$

↓.....↓.....↓..... (Q-28b)

$$\therefore \int_0^{v_x} dv_x(t) = v_x(y_a, t) = f_1(y_a) \cdot f_2(t) = - \frac{1}{\rho_m} \cdot \int_0^t \frac{\partial \Phi_y(y_a, t)}{\partial y} \cdot dt$$

14. In Q-32.10 we have a function of y on the right, a function of t on the left, and a negative constant, $-\beta^2$, in the

↓.....↓..... (Q-29)

$$\therefore v_x(y_a, t) = f_1(y_a) \cdot f_2(t)$$

$$= - \frac{A_1}{\rho_m} \int_0^t \frac{\partial}{\partial y} \left\{ + \int_0^{y_a} v_x(y_L, t) \cdot \int_{-\pi/2}^0 e^{-\frac{(y_L - y_a)}{L \cdot \sin(\theta)}} \cdot \cos(\theta) \cdot d\theta \cdot dy_L \right\}$$

↑.....f(θ)_{up}.....↑

$$- \int_{y_a}^{\infty} v_x(y_L, t) \cdot \int_0^{+\pi/2} e^{-\frac{(y_L - y_a)}{L \cdot \sin(\theta)}} \cdot \cos(\theta) \cdot d\theta \cdot dy_L \Big\} \cdot dt$$

↑.....f(θ)_{down}.....↑

$$\frac{A_1}{\rho_m} = \left[\frac{(n \cdot m \cdot \underline{z}) / 2}{n \cdot m} \right] = \frac{\underline{z}}{2} = A_3 \quad (Q-30)$$

middle. We may now LaPlace-transform both sides per Q-32.40, and proceed to solve the t-side first, per Q-34 thru equation Q-37....a decaying exponential.

$$\therefore v_x(y_a, t) = f_1(y_a) \cdot f_2(t) \quad \downarrow \dots \dots \dots \downarrow \dots (Q-31)$$

$$= -A_3 \cdot e^{-k_a} \cdot \int_0^t f_2(t) \cdot dt \cdot \frac{\partial}{\partial y} \left\{ + \int_0^{y_a} f_1(y_L) \cdot e^{+k_b \cdot \frac{(y_L - y_a)}{L}} \cdot dy_L \right. \\ \left. - \int_0^{\infty \text{ or } 5 \cdot L} f_1(\lambda + y_a) \cdot e^{-k_b \cdot \frac{\lambda}{L}} \cdot d\lambda \right\}$$

$$\therefore \frac{f_2(t)}{\int_0^t f_2(t) \cdot dt} = -\beta^2 = \quad \leftarrow \dots \dots \dots \downarrow \dots \dots \downarrow \dots (Q-32.10)$$

$$= -\frac{A_3 \cdot e^{-k_a}}{f_1(y_a)} \cdot \frac{\partial}{\partial y} \left[+ \int_0^{y_a} f_1(y_L) \cdot e^{+k_b \cdot \frac{(y_L - y_a)}{L}} \cdot dy_L \right. \\ \left. - \int_0^{\infty \text{ or } 5 \cdot L} f_1(\lambda + y_a) \cdot e^{-k_b \cdot \frac{\lambda}{L}} \cdot d\lambda \right]$$

$$z\text{-transforming to } s_t \text{ \& } s_y \text{ planes:} \quad \downarrow \dots \dots \downarrow \dots \dots \dots (Q-32.40)$$

$$\therefore \frac{F_2(s_t)}{\left[\frac{F_2(s_t)}{s_t} + \frac{f^{(-1)}(0+)}{s_t} \right]} = -\beta^2 \\ = -A_4 \cdot \left[\frac{[s_y \cdot F_1(s_y)]}{F_1(s_y)} \cdot \left[+ \frac{1}{(s_y - k_b/L)} - \frac{1}{(s_y + k_b/L)} \right] - f(0+) \right]$$

$$\therefore F_2(s_t) = -\beta^2 \cdot \left[\frac{F_2(s_t)}{s_t} + \frac{f^{(-1)}(0+)}{s_t} \right] \quad (Q-34)$$

$$s_t \cdot F_2(s_t) + \beta^2 \cdot F_2(s_t) = -\beta^2 \cdot f^{(-1)}(0+) \quad (Q-35)$$

$$\therefore F_2(s_t) = \frac{-\beta^2 \cdot f^{(-1)}(0+)}{(s_t + \beta^2)} \quad (Q-36)$$

$$\therefore f_2(t) = -\beta^2 \cdot f^{(-1)}(0+) \cdot e^{-\beta^2 \cdot t} \quad (Q-37)$$

15. QB-41 may be solved by the method of Partial Fractions to yield Q-42.35 . By re-arrangement, we find

$$\begin{array}{c} \downarrow \dots \dots \dots \downarrow \dots \dots \dots \downarrow \dots \dots \dots (QB-41) \\ -\beta^2 \cdot F_1(s_Y) = -A_4 \cdot \left[s_Y \cdot F_1(s_Y) \cdot \left[+\frac{1}{(s_Y - k_b/L)} - \frac{1}{(s_Y + k_b/L)} \right] - f(0+) \right] \end{array}$$

equation Q-42.60 . We may now combine the two solutions, $f_1(y_a)$ and $f_2(t)$, to show the *form or essence* of the

$$\begin{array}{c} \downarrow \dots \dots \dots \downarrow \dots \dots \dots (Q-42.35) \\ \frac{f_1(y_a)}{f(0+)} = A_5 \cdot u_1(y_a) + K_1 \cdot e^{(-k_3+k_4) \cdot y_a} + K_2 \cdot e^{(-k_3-k_4) \cdot y_a} \\ \uparrow \dots \text{unit impulse at } y_a = 0+ \end{array}$$

$$\begin{array}{c} \downarrow \dots \dots \dots \downarrow \dots \dots \dots (Q-42.60) \\ \frac{f_1(y_a)}{f(0+)} = \left\{ A_5 \cdot u_1(y_a) \right. \\ \left. - \frac{4 \cdot \kappa \cdot A_5}{(s_1 - s_2)} \cdot e^{-k_3 \cdot y_a} \cdot [k_3 \cdot \sinh \cdot (k_4 \cdot y_a) - k_4 \cdot \cosh \cdot (k_4 \cdot y_a)] \right\} \end{array}$$

solution, $v_x(y,t)$ in Q-42.65.

$$\begin{aligned} & \downarrow \dots \dots \dots \downarrow \dots \dots \dots (Q-42.65) \\ \therefore v_x(y,t) &= f_1(y_a) \cdot f_2(t) = \left[f(y_a=0+) \cdot \left\{ A_5 \cdot u_1(y_a) \right. \right. \\ & \quad \left. \left. - \frac{4 \cdot \kappa \cdot A_5}{(s_1 - s_2)} \cdot e^{-k_3 \cdot y_a} \cdot [k_3 \cdot \sinh(k_4 \cdot y_a) - k_4 \cdot \cosh(k_4 \cdot y_a)] \right\} \right. \\ & \quad \left. \cdot \left\{ -\beta^2 \cdot e^{-\beta^2 \cdot t} \right\} \cdot f^{(-1)}(t=0+) \right] \end{aligned}$$

16. However, boundary conditions must be satisfied, per Q-42.70 and tested in Q-42.80.

Boundary Conditions:

$$v_x(y=0+, t=0+) = U_0 \cdot u(t) \quad (Q-42.70)$$

$$\begin{aligned} & \downarrow \dots \dots \dots \downarrow \dots \dots \dots (Q-42.80) \\ \therefore v_x(y=0+, t=0+) &= U_0 \cdot u(t) \cdot \left[\left\{ A_5 \cdot u_1(y_a=0+) \right. \right. \\ & \quad \left. \left. + \frac{4 \cdot \kappa \cdot A_5}{(s_1 - s_2)} \cdot e^{-k_3 \cdot y_a=0+} \right. \right. \\ & \quad \left. \left. \cdot [k_3 \cdot \sinh(k_4 \cdot [y_a=0+]) - k_4 \cdot \cosh(k_4 \cdot [y_a=0+])] \right\} \right. \\ & \quad \left. \cdot \left\{ \beta^2 \cdot e^{-\beta^2 \cdot [t=0+]} \right\} \right] \\ & \quad \uparrow \dots = 0 \dots \uparrow \quad \uparrow \dots = 1 \dots \uparrow \\ & \quad \uparrow \dots = 1 \dots \uparrow \end{aligned}$$

17. Q-42.85 shows the final solution, but Q-42.95 displays a form which sheds additional light on the physical

↓.....↓..... (Q-42.85)

$$\therefore v_x(y,t) = U_o \cdot u(t) \cdot \left[A_5 \cdot u_1(y=0+) \right. \\ \left. + \left\{ 1 - \left[1 - e^{-\beta^2 \cdot t} \right] \cdot \left[e^{-k_3 \cdot y_a} \right] \cdot \left[\frac{4 \cdot k \cdot A_5 \cdot \beta^2}{(s_1 - s_2)} \right] \right. \right. \\ \left. \left. \cdot \left[k_3 \cdot \sinh(k_4 \cdot y) - k_4 \cdot \cosh(k_4 \cdot y) \right] \right\} \right]$$

↓.....↓..... (Q-42.95)

$$\therefore v_x(y=0+, t=0+) = U_o \cdot u(t) \cdot \left[A_5 \cdot u_1(y=0+) \right. \\ \left. + \left\{ 1 - \left[\frac{4 \cdot k \cdot A_5 \cdot \beta^2}{(s_1 - s_2)} \right] \cdot \left[e^{-k_3 \cdot y} \right] \cdot \right. \right. \\ \left. \left[\left[k_3 \cdot \sinh(k_4 \cdot y) - k_4 \cdot \cosh(k_4 \cdot y) \right] \right. \right. \\ \left. \left. - \left[k_3 \cdot \left\{ \frac{\overset{\downarrow \dots A \dots \downarrow}{e^{+k_4 \cdot y - \beta^2 \cdot t}} - \overset{\downarrow \dots B \dots \downarrow}{e^{-k_4 \cdot y - \beta^2 \cdot t}}} \right\} \right. \right. \right. \\ \left. \left. + k_4 \cdot \left\{ \frac{\overset{\downarrow \dots C \dots \downarrow}{e^{+k_4 \cdot y - \beta^2 \cdot t}} + \overset{\downarrow \dots D \dots \downarrow}{e^{-k_4 \cdot y - \beta^2 \cdot t}}} \right\} \right] \right] \right\} \right]$$

situation, since exponents A thru D show the relationship between y and t. Q-43.00 and 43.05 allow us to calculate the

RE: Vertically-propagating "Front" of Boundary Layer

$$\text{Let: } +k_4 \cdot y_f - \beta^2 \cdot t = 0 \quad (Q-43.00)$$

$$\text{Solve for } y_f: \quad y_f = \frac{\beta^2}{k_4} \cdot t = y\text{-location of "front".} \quad (Q-43.05) \\ (\text{at time } t)$$

y-location of the vertically-propagating "front" of the boundary layer at any time $t > 0+$.

Conclusions

1. It appears possible to find a closed solution of the velocity profile of a one-dimensional boundary layer, using:
 - a. James Clerk Maxwell's molecular derivation of Viscosity, μ ,
 - b. LaPlace transform techniques, and
 - c. A Partial Fractions expansion.
2. Work of this type should continue, in order to reach a closed solution to the two-dimensional boundary-layer case, i.e., growth over a semi-infinite (sharp leading edged) flat plate in order to understand what causes the occurrence of the Transition Region, where turbulence is initiated.

Acknowledgements

1. The Author acknowledges the generous assistance of the following:
 - a. Christopher de Graffenried, jr., (grandsdon) for hardware modifications and support,
 - b. Christopher de Graffenried, Sr., (son) for software modifications and support
 - c. Joan Laskey de Graffenried (beloved wife) for spiritual and financial support and encouragement.
2. In the early phases of this research (1940's):
 - a. Dr. Paul E. Hemke, (deceased), head, Aeronautical Engineering Dept., Rensselaer Polytechnic Institute, for enthusiastic support, and
 - b. Dr. Leonard B. Loeb, (deceased) Professor, Physics Dept., Univ. of California at Berkeley for consulting, and for writing a marvelous text book on the Kinetic Theory of Gases.

References

1. The Kinetic Theory of Gases, by Leonard B. Loeb, 2nd Edn., 3rd impression, McGraw-Hill Book Co., New York & London, 1934.
2. Transients In Linear Systems (studied by the LaPlace Transformation) by: Murray F. Gardner & John L. Barnes; Volume I, Lumped-Constant Systems John Wiley & Sons, Inc., New York, 2nd printing, 1945.

Hardware & Software

1. Computer = Gateway 2000, 4DX2-66V, 16 Mbytes fast RAM, 9.0 Gbytes hard disc.
2. μ -Soft WORD '97 (text & insertion of graphics from Corel software),
3. Corel Custom Photo (graphics handling of tiff and cps formats)
4. Techword (for mathematics and equations creation)
5. Flat-bed scanning of equations by Kinko, to bitmap format., plus assembly of individual files in WORD.

THE USE OF MATHCAD IN THERMAL/FLUIDS CALCULATIONS

B.K. Hodge and Robert P. Taylor

Mississippi State University
Mississippi State, MS 39762-9999

ABSTRACT

General computational software systems (such as Mathcad, Matlab, and Mathematica) with great flexibility are available for use on personal computers. This paper examines the application of one of these systems, Mathcad, to a number of preliminary thermal sciences calculations. Application examples include piping networks, steady-steady system simulation, and simple and generalized one-dimensional compressible flows. Mathcad is demonstrated to be a useful tool that offers great flexibility and generality as well as congruence with problem formulation.

INTRODUCTION

At some point in any engineering endeavor calculations must be made and “numbers” generated. The manner of doing calculations in the engineering workplace has continuously evolved, especially since World War II. Prior to that time engineering calculations were accomplished in a completely manual fashion using mechanical calculators, slide rules, log tables, and nomograms. Generating numbers was, until after World War II, a labor-intensive undertaking. Feynman’s (1) anecdotal account of neutron diffusion calculations at Los Alamos in the 1940’s is a good example of the drudgery and tediousness of extended pre-computer field calculations. He discusses how mechanical calculator results, recorded on cards, were sequenced and passed from operator to operator to accomplish manual finite-difference solutions. The digital computer fundamentally altered the use of “manual” calculations and replaced it with machine-based computations. Initial efforts were hard-wired (literally) with patch boards, but by the early 1950’s higher-level programming languages evolved. For engineering computations, FORTRAN became the dominant programming language. However, as these advances were taking place, the engineering workplace struggled to effectively utilize the promise of the “computer” and to define the relationship between computing and engineering.

In recent years, general computational software systems with great flexibility have become available for use on personal computers. Examples include Mathcad, Matlab, EES (Engineering Equation Solver), Polymath, Mathematica, Maple, Excel, and TK Solver. These “arithmetic engines” provide significant computational capability, often very congruent with problem formulation, without the need for extensive coding. Additionally, most of these systems possess ancillary plotting and word processing capabilities and some include units-tracking in computations. A very important feature of many of these arithmetic systems is that they include symbolic manipulation features that can dramatically shorten the time required for algebraic operations and can eliminate manipulation errors in solution developments.

The thesis of this paper is not that Mathcad (or any other arithmetic system) will replace accepted thermal/fluids software applications packages, but that such arithmetic systems can provide useful capabilities and rapid responses for many preliminary engineering calculations. The paper examines the Mathcad implementations for a number of procedures usually associated with preliminary thermal/fluids engineering calculations. Many of the Mathcad procedures possess significant generality that permit a wide range of problems to be solved with only minimal changes to the Mathcad “worksheets.”

MATHCAD FEATURES

Mathcad (www.mathsoft.com) is a general arithmetic software system that integrates text, equations, and graphics in a single worksheet. One reviewer (2) stated, “...Mathcad is the most broadly applicable of today’s technical computation programs...presents a word-processor-like notebook with live numerical and symbolic computations and live graphs, which taken together are more powerful and flexible than a spreadsheet.” In addition to live numerical computations, symbolic manipulations, and graphing facility, Mathcad possesses a number of other capabilities that are useful in engineering calculations. Not the least of these is congruency with problem formulation; that is, a Mathcad solution develops in a fashion congruent with the problem formulation and in a

fashion similar to a “by hand” solution. Mathcad can also include units as part of computations; indeed, both SI and US Customary can be specified and mixed, with units conversion taking place automatically. Mathcad offers formula evaluation, non-linear algebraic system solution, matrix evaluation, ordinary differential equations solvers, and some limited partial differential equation solvers. Taken together Mathcad’s capabilities are quite impressive and are relatively easy to assimilate, thus providing a new paradigm for many engineering calculations. Many preliminary thermal/fluids analysis and design procedures are iterative and were originally devised to permit hand solutions of non-linear algebraic equations or systems of non-linear algebraic equations. The SOLVE-block feature of Mathcad permits the routine solution of such equations or systems by a particularly robust solver.

The authors have been involved with Mathcad applications for several years and have implemented a number of Mathcad solutions for common thermal sciences problems. Some of these implementations are included in their book [Hodge and Taylor, (3)]. The authors’ extensive experiences using Mathcad in thermal sciences engineering education are discussed in References 4-6. The next section previews the salient features of a number of Mathcad approaches to solving thermal sciences problems.

EXAMPLES

Mathcad offers a wide range of capabilities that are useful in obtaining solutions to thermal sciences problems. The examples selected for inclusion were intended to demonstrate the many capabilities of Mathcad. Different examples and more details of the examples presented herein are in the references.

Example 1: Series Piping Systems

The same Mathcad approach can be used to solve all categories of series piping problems as well as for the operating point of a system with a specific pump. Consider, as in Figure 1, a series piping system with pipes of different diameters, a variety of major and minor losses, and a pump with an increase in head of W_s . If the flow is from a to b, the energy equation becomes

$$W_s \frac{g_c}{g} = \frac{P_b - P_a}{\gamma} + z_b - z_a + \sum_{i=1}^J \frac{8}{\pi^2} \frac{Q^2}{g D_i^4} \left[f_i \frac{L_i}{D_i} + C_i f_{T_i} + K_i \right] \quad (1)$$

Three different categories of problems are associated with series piping systems: (1) Category I in which the required increase in head, W_s , of the pump is the unknown, (2) Category II in which the flow rate Q is the desired results, and (3) Category III in which the pipe diameter is to be obtained. Category I problems are direct, but Categories II and III are iterative. However, the SOLVE-block structure of Mathcad permits all three category solutions to be obtained by simply indicating the required variable (unknown) in a FIND statement. Figure 2 presents a segment of a Mathcad worksheet illustrating the SOLVE block/FIND statement sequence for a Category II problem. For a Category I or Category III problem only the required solution variable (and an initial guess) must be changed. The Mathcad procedure for the solution of any series-piping problem is to apply and reduce the energy equation, define the known variables in Eq. (1), and specify the unknown. The explicit formulas for the friction factors are presented and are used as an alternative to the Moody diagram. Thus, in the Mathcad approach, the solution algorithm is of little concern and the problem formulation and results interpretation become the center of activities.

A slightly more complex series-piping example is the operating point of system with a given pump. Figure 3 is the Mathcad worksheet illustrating the addition of a specific pump in a system. The pump/system operating point determination requires the H-Q characteristics of the pump, which in this case is the first equation in the SOLVE block and results from a Mathcad curvefit. Since the SOLVE block contains two equations, the FIND statement requests two variables, W_s (the pump increase in head) and Q (the system flow rate). In essence the Mathcad SOLVE/FIND procedure solves simultaneously the two non-linear algebraic equations representing the pump and the system characteristics. Parallel piping systems, the next level of complexity after series systems, are examined next.

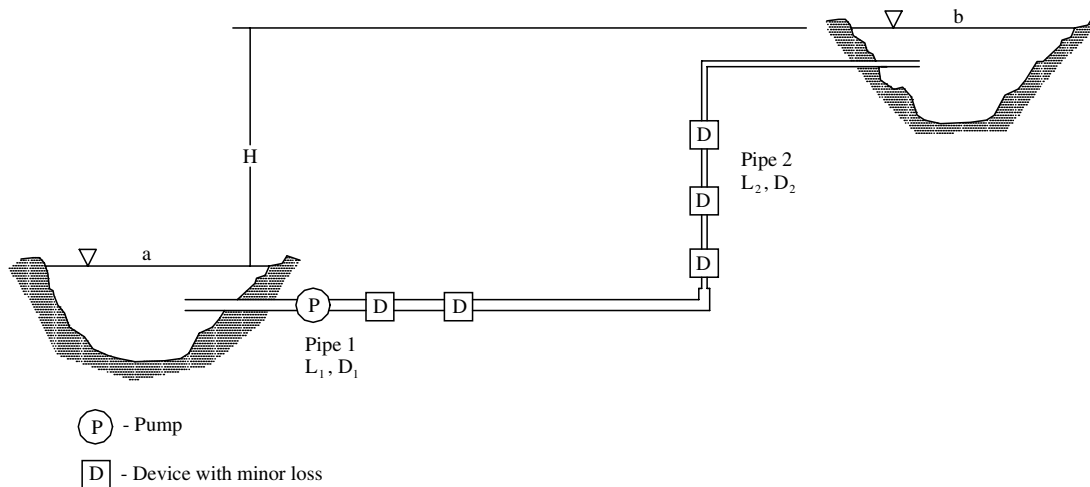


Figure 1. Series Piping System Schematic

Input the flow rate in cms:

$$Q := 1 \cdot \frac{\text{m}^3}{\text{sec}} \quad \text{Initial guess on flow rate.}$$

Increase in head of the pump:

$$W_s := 50 \cdot \text{newton} \cdot \frac{\text{m}}{\text{kg}}$$

Define the functions for Reynolds number, fully-rough friction factor, and friction factor:

$$\text{Re}(q, d) := \frac{4 \cdot q}{\pi \cdot d \cdot \nu}$$

$$f_T(d, \epsilon) := \frac{0.3086}{\log \left[\left(\frac{\epsilon}{3.7 \cdot d} \right)^{1.11} \right]^2}$$

$$f(q, d, \epsilon) := \begin{cases} \frac{0.3086}{\log \left[\frac{6.9}{\text{Re}(q, d)} + \left(\frac{\epsilon}{3.7 \cdot d} \right)^{1.11} \right]^2} & \text{if } \text{Re}(q, d) > 2300 \\ \frac{64}{\text{Re}(q, d)} & \text{otherwise} \end{cases}$$

The generalized energy equation is:

Given

$$W_s \cdot \frac{g_c}{g} = \frac{P_b - P_a}{\rho \cdot g} \cdot g_c + Z_b - Z_a + \sum_{i=1}^N \frac{8}{\pi^2} \cdot \frac{Q^2}{(D_i)^4 \cdot g} \cdot \left(f(Q, D_i, \epsilon_i) \cdot \frac{L_i}{D_i} + K_i + C_i \cdot f_T(D_i, \epsilon_i) \right)$$

$$q := \text{Find}(Q)$$

$$q = 0.452 \text{ m}^3 \cdot \text{sec}^{-1} \quad q = 2.713 \cdot 10^4 \frac{\text{liter}}{\text{min}}$$

Pump power (input to fluid):

$$\text{Power} := q \cdot \rho \cdot W_s$$

$$\text{Power} = 22.605 \text{ kW}$$

Figure 2. Series Piping Mathcad Worksheet

Additional output of useful quantities:

$$\begin{array}{llll}
 i := 1..N & V(q, D) := \frac{4 \cdot q}{\pi \cdot D^2} & D_i = \text{m} & V(q, D_i) = \text{m} \cdot \text{sec}^{-1} \\
 & & \begin{array}{|c|} \hline 0.3 \\ \hline 0.3 \\ \hline \end{array} & \begin{array}{|c|} \hline 6.396 \\ \hline 6.396 \\ \hline \end{array} \\
 & \text{Re}(q, D_i) = & f(q, D_i, \epsilon_i) = & f_T(D_i, \epsilon_i) = \\
 & \begin{array}{|c|} \hline 1.683 \cdot 10^6 \\ \hline 1.683 \cdot 10^6 \\ \hline \end{array} & \begin{array}{|c|} \hline 0.014 \\ \hline 0.014 \\ \hline \end{array} & \begin{array}{|c|} \hline 0.013 \\ \hline 0.013 \\ \hline \end{array}
 \end{array}$$

Figure 2. Series Piping Mathcad Worksheet (concluded)

Define the functions for Reynolds number, fully-rough friction factor, and friction factor:

$$\begin{aligned}
 \text{Re}(q, d) &:= \frac{4 \cdot \rho \cdot q}{\pi \cdot d \cdot \mu} & f_T(d, \epsilon) &:= \frac{0.3086}{\log \left[\left(\frac{\epsilon}{3.7 \cdot d} \right)^{1.11} \right]^2} \\
 f(q, d, \epsilon) &:= \begin{cases} \frac{0.3086}{\log \left[\frac{6.9}{\text{Re}(q, d)} + \left(\frac{\epsilon}{3.7 \cdot d} \right)^{1.11} \right]^2} & \text{if } \text{Re}(q, d) > 2300 \\ \frac{64}{\text{Re}(q, d)} & \text{otherwise} \end{cases}
 \end{aligned}$$

Specify initial guesses for the pump increase in head and the flow rate:

$$W_s := 100 \cdot \frac{\text{ft} \cdot \text{lbf}}{\text{lb}} \quad (\text{Initial guess of pump increase in head.}) \quad Q := 50 \cdot \frac{\text{gal}}{\text{min}} \quad (\text{Initial guess of flow rate.})$$

Given

$$\begin{aligned}
 W_s &= 414.894 \frac{\text{ft} \cdot \text{lbf}}{\text{lb}} + 0.07 \frac{\text{ft} \cdot \text{lbf} \cdot \text{min}}{\text{lb} \cdot \text{gal}} \cdot Q + -0.001545 \frac{\text{ft} \cdot \text{lbf} \cdot \text{min}^2}{\text{lb} \cdot \text{gal}^2} \cdot Q^2 + -0.0000161 \frac{\text{ft} \cdot \text{lbf} \cdot \text{min}^3}{\text{lb} \cdot \text{gal}^3} \cdot Q^3 \\
 W_s \cdot \frac{g_c}{g} &= \frac{P_b - P_a}{\rho \cdot g} \cdot g_c + Z_b - Z_a + \frac{8}{\pi^2} \cdot \frac{Q^2}{g \cdot (D)^4} \cdot \left(f(Q, D, \epsilon) \cdot \frac{L}{D} + K + C \cdot f_T(D, \epsilon) \right) \\
 \begin{bmatrix} W_s \\ Q \end{bmatrix} &:= \text{Find}(W_s, Q) \\
 W_s &= 390.505 \frac{\text{ft} \cdot \text{lbf}}{\text{lb}} \\
 Q &= 99.777 \frac{\text{gal}}{\text{min}}
 \end{aligned}$$

$$\text{Pump power (input to fluid):} \quad \text{Power} := Q \cdot \rho \cdot W_s \quad \text{Power} = 9.849 \text{ hp}$$

Figure 3. Pump/System Operating-Point Solution

Example 2: Parallel Piping Systems

No better example exists for the effects of Mathcad on solution techniques than that for parallel piping systems. Systems, such as that illustrated in Figure 4, have long been solved in iterative fashion by enforcing equality of change in head across each pipe and conservation of mass at the two nodes. The usual, pre-Mathcad procedure was to assume a flow rate in one pipe, compute the change in head in that pipe, compute the flow rate in the remaining pipes by requiring their changes in head to be equal to that of the first pipe, and iterating until convergence. In Mathcad, the procedure is more straightforward and closer to the formulation of the problem. Figure 5 presents a portion of the Mathcad worksheet illustrating the SOLVE-block arrangement. The formulation of the problem requires one equation summing the flow rates and one energy equation for each parallel piping segment. The Mathcad SOLVE block/FIND statement then solves the non-linear system for the total and individual flow rates given the increase in head of the pump (the pressures at a and b are equal). The solution algorithm is completely transparent to the user. One important salient feature of many Mathcad solutions is the general congruence of the problem formulation and the Mathcad implementation. In the case of parallel piping systems, this congruence is striking as the formulation process leads directly to the Mathcad input required for the solution.

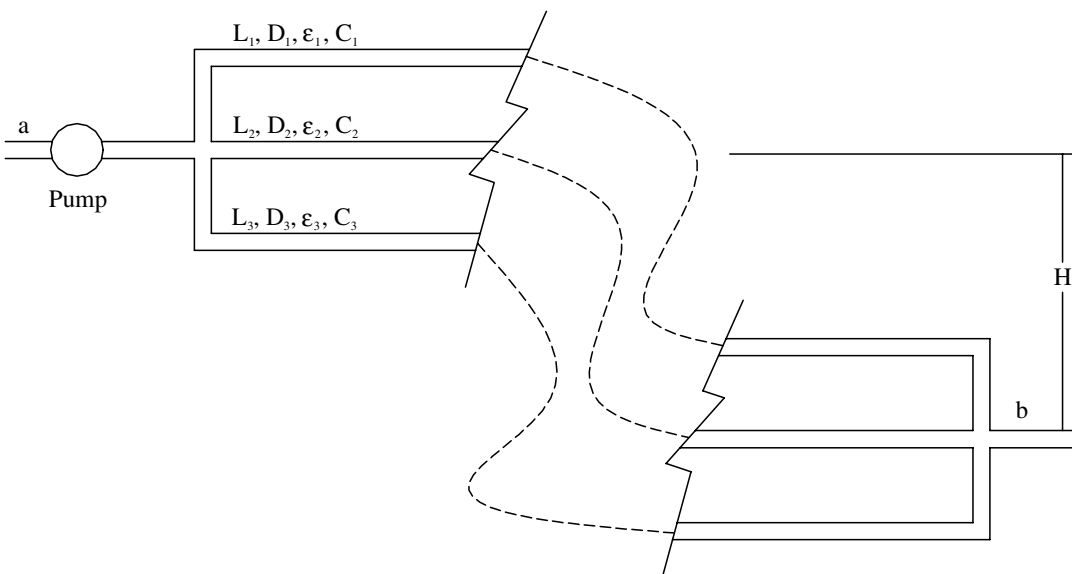


Figure 4. Parallel Piping System Schematic

Example 3: Piping Networks

Piping network analysis is built about the concept of loops, a series of pipes that form a closed path, and nodes, a point where two or more lines are joined. Conservation of mass must be maintained at each node, and the pressure change around each loop must be zero. Using these concepts a number of procedures can be devised to find the flow rate and change in pressure in each line. The most common of these procedures is the Hardy-Cross technique; see Hodge and Taylor (3) for details. The Hardy-Cross procedure was first devised for hand calculations, but its generality and utility make it the method of choice for computer-based approaches. Conservation of mass is enforced at each node and loop correction factors, ΔQ , are determined for each loop such that the change in pressure (or head) around a loop is zero. The Mathcad procedure for the iterative process is given in Figure 6, where $h(Q)$ represents the change in head in a pipe and $dH(Q)$ represents the change in head with respect to the flow rate Q . N is the connection matrix that describes the relationships between loops, nodes, and flow directions. The

Define the functions for Reynolds number and the friction factors:

$$\text{Re}(q, D) := \frac{4 \cdot \rho \cdot q}{\pi \cdot D \cdot \mu} \quad f_T(D, \varepsilon) := \frac{0.3086}{\log \left[\left(\frac{\varepsilon}{3.7 \cdot D} \right)^{1.11} \right]^2}$$

$$f(q, D, \varepsilon) := \begin{cases} \frac{0.3086}{\log \left[\frac{6.9}{\text{Re}(q, D)} + \left(\frac{\varepsilon}{3.7 \cdot D} \right)^{1.11} \right]^2} & \text{if } \text{Re}(q, D) > 2300 \\ \frac{64}{\text{Re}(q, D)} & \text{otherwise} \end{cases}$$

Setup Solve Block by defining specified inputs and guessed values:

$$Q_T := 5.3 \cdot \frac{\text{ft}^3}{\text{sec}} \quad Q_1 := \frac{Q_T}{N} \quad Q_2 := \frac{Q_T}{N} \quad W_s := 50 \cdot \text{ft} \cdot \frac{\text{lbf}}{\text{lb}}$$

Given

$$Q_T = Q_1 + Q_2$$

$$W_s \cdot \frac{g_c}{g} = Z_b - Z_a + \frac{8}{\pi^2} \cdot \frac{(Q_1)^2}{g \cdot (D_1)^4} \cdot \left(f(Q_1, D_1, \varepsilon_1) \cdot \frac{L_1}{D_1} + K_1 + C_1 \cdot f_T(D_1, \varepsilon_1) \right)$$

$$W_s \cdot \frac{g_c}{g} = Z_b - Z_a + \frac{8}{\pi^2} \cdot \frac{(Q_2)^2}{g \cdot (D_2)^4} \cdot \left(f(Q_2, D_2, \varepsilon_2) \cdot \frac{L_2}{D_2} + K_2 + C_2 \cdot f_T(D_2, \varepsilon_2) \right)$$

$$\begin{bmatrix} Q_T \\ Q_1 \\ Q_2 \end{bmatrix} := \text{Find}(Q_T, Q_1, Q_2)$$

$$Q_T = 9.396 \text{ ft}^3 \cdot \text{sec}^{-1} \quad Q_1 = 6.711 \text{ ft}^3 \cdot \text{sec}^{-1} \quad Q_2 = 2.684 \text{ ft}^3 \cdot \text{sec}^{-1}$$

Additional output of useful quantities:

$$i := 1..N \quad V(q, D) := \frac{4 \cdot q}{\pi \cdot (D)^2} \quad Q_1 := Q_1 \quad Q_2 := Q_2$$

$D_i =$	$V(Q_i, D_i)_{\text{ft} \cdot \text{sec}^{-1}}$	$\text{Re}(Q_i, D_i) =$	$f(Q_i, D_i, \varepsilon_i) =$	$f_T(D_i, \varepsilon_i) =$
1	8.545	$2.849 \cdot 10^5$	0.021	0.02
0.667	7.69	$1.709 \cdot 10^5$	0.017	0.013

Figure 5. Mathcad Parallel Piping Solution

Mathcad procedure in Figure 6 illustrates a Mathcad program element that in this case is an iterative process that uses the Hardy-Cross loop-correction equation to find the flow rate in each line. Convergence is attained when the root-sum-square of the loop corrections factors becomes less than an input tolerance, "tol." Major losses in piping networks can be described in terms of the Hazen-Williams relation, $h_f = KQ^n$, or in terms of the Darcy friction factor. The Hazen-Williams representation is common in water systems, but the friction factor representation is the most general. Figure 7 is the Mathcad worksheet for the friction factor Hardy-Cross solution of a seven-pipe, two-loop network with a heat exchanger and a pump in line one. The original problem was to determine the increase in head of the pump required to give a flow rate of 2 cfs through line one. By simply varying the increase in head of the pump, the value of 203.7 ft-lbf/lbm was determined.

HardyCross(h,dh,Q,N,tol)

This function executes the general Hardy-Cross solution algorithm. The return value is a vector of the flow rates.

N is a matrix which sets the loop sign convention--rows = # pipes and cols = # loops

Fill the matrix by columns:

If the pipe does not fall in the loop enter 0;

Enter 1 when the assumed flow direction is positive;

Enter -1 when the assumed flow direction is negative.

The counterclockwise sense for a loop is the positive sign convention.

tol is the convergence tolerance

```
HardyCross (h, dh, Q, N, tol) :=
  L ← cols(N)
  P ← rows(N)
  for l ∈ 1..L
    ΔQl ← 100
    while  $\sqrt{\sum_{i=1}^L (\Delta Q_i)^2} > \text{tol}$ 
      for i ∈ 1..L
        
$$\Delta Q_i \leftarrow 1 \cdot \frac{\sum_{j=1}^P N_{i,j} \cdot h(Q)_j}{\sum_{j=1}^P (N_{i,j})^2 \cdot dh(Q)_j}$$

      Q ← Q + N · ΔQ
  Q
```

Figure 6. Mathcad Hardy-Cross Function

Input the pipe geometry:

Diameter in inches: $d := (12 \ 8 \ 6 \ 6 \ 8 \ 8 \ 8)^T$ $D := \frac{d}{12}$

Length in feet: $L := (2000 \ 2000 \ 3000 \ 4000 \ 1000 \ 3000 \ 2000)^T$

Roughness in feet: $\varepsilon := (0.00015 \ 0.00015 \ 0.00015 \ 0.00015 \ 0.00015 \ 0.00015 \ 0.00015)^T$

Define physical properties: $\nu := 0.000016$

Define device head change vector:

$h_d(Q) := [50 \cdot Q_1 \mid Q_1 \mid -203.7 \ 0 \ 0 \ 0 \ 0 \ 0 \ 0]^T$ $dh_d(Q) := [100 \mid Q_1 \mid 0 \ 0 \ 0 \ 0 \ 0 \ 0]^T$

The usual functions for friction factor must be defined:

Figure 7. Mathcad Hardy-Cross Execution Example

$$\text{Re}(q, d) := \frac{4|q|}{\pi \cdot d \cdot \nu} \quad f_T(d, \varepsilon) := \frac{0.3086}{\log \left[\left(\frac{\varepsilon}{3.7 \cdot d} \right)^{1.11} \right]^2}$$

$$f(q, d, \varepsilon) := \begin{cases} \text{if } |q| > 0 \\ \frac{0.3086}{\log \left[\frac{6.9}{\text{Re}(q, d)} + \left(\frac{\varepsilon}{3.7 \cdot d} \right)^{1.11} \right]^2} & \text{if } \text{Re}(q, d) > 2300 \\ \frac{64}{\text{Re}(q, d)} & \text{otherwise} \\ 1 & \text{otherwise} \end{cases}$$

Define the minor loss coefficients K and the equivalent-lengths C:

$$K := (0 \ 0 \ 0 \ 0 \ 0 \ 0 \ 0)^T \quad C := (0 \ 0 \ 0 \ 0 \ 0 \ 0 \ 0)^T$$

Define the loss function for each line using the friction factor major loss expression:

$$h(Q) := \frac{8 \cdot Q \cdot |Q|}{\pi^2 \cdot g \cdot D^4} \cdot \left(f(Q, D, \varepsilon) \cdot \frac{L}{D} + K + C \cdot f_T(D, \varepsilon) \right) + h_d(Q)$$

Define the derivative of the loss function:

$$dh(Q) := \frac{16 \cdot |Q|}{\pi^2 \cdot g \cdot D^4} \cdot \left(f(Q, D, \varepsilon) \cdot \frac{L}{D} + K + C \cdot f_T(D, \varepsilon) \right) + dh_d(Q)$$

Starting guess for flow rates in cfs--must satisfy the conservation of mass at each node:

$$Q := (0.8 \ 0.2 \ 1.2 \ 1.2 \ 1 \ 1 \ 1)^T$$

The Matrix **N** relates the assumed positive flow rate in each pipe to the counter-clockwise loop rotation sign convention.

$$N := \begin{bmatrix} 1 & -1 & -1 & -1 & 0 & 0 & 0 \\ -1 & 0 & 0 & 0 & 1 & 1 & -1 \end{bmatrix}^T$$

☐ Reference: A:\HardyCross.mc

$$\text{ans} := \text{HardyCross}(h, dh, Q, N, 0.0001) \quad \text{ans}^T = (2.0009 \ -0.813 \ 0.187 \ 0.187 \ 0.8121 \ 0.8121 \ 1.1879)$$

Figure 7. Mathcad Hardy-Cross Execution Example (concluded)

Example 4: System Simulation

Steady-state system simulation problems can be solved using Mathcad by invoking the SOLVE-block feature. Consider the oil-cooling loop schematically illustrated in Figure 8. Q_T , the total flow rate entering the loop, is specified to be 250 gpm; a Goulds 2 x 3 -7 Model 3655 pump (at 3500 rpm) is in one leg of the system. Information is also given for head loss through the heat exchanger and a flow-rate dependent expression for U , the overall heat transfer coefficient, is provided. The system simulation is to determine the temperature out of the heat exchanger and the exit temperature, T_e , after mixing of the cooled oil and the oil bypassed by the heat exchanger. The solution requires the flow rates through each leg of the system, a heat exchanger analysis, and an energy balance. In all, 13 equations are used to define the operation of the system. The same closed-form expressions given in Examples 1-3 are provided for the friction factor calculations in this problem. Figure 9 presents part of the Mathcad worksheet for the solution to this system simulation problem. The vector “ans” contains the solution from the FIND command. This is a relatively involved problem that would require a significant amount of time to code

into a multi-variable Newton-Raphson routine, but the Mathcad solution is rapid and very congruent with problem formulation.

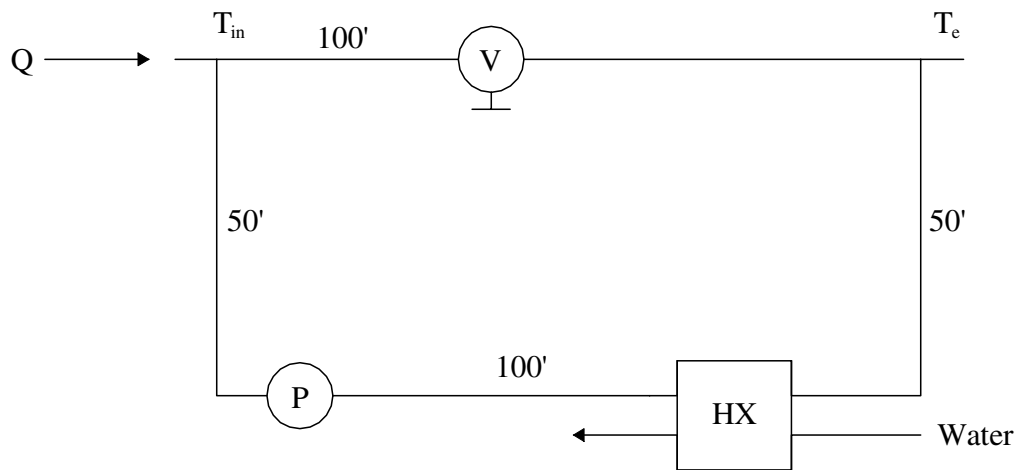


Figure 8. Schematic for System Simulation Example

The **solve** block equations are defined.

Given

$$Q_T = Q_1 + Q_2$$

$$Re_1 = \frac{Q_1}{A_c \cdot 7.481 \cdot 60} \cdot \frac{ID}{v}$$

$$Re_2 = \frac{Q_2}{A_c \cdot 7.481 \cdot 60} \cdot \frac{ID}{v}$$

$$HX = 0.0224 \cdot Q_2^{1.9}$$

$$HP = 218.0 - 0.072 \cdot Q_2 + 0.000704 \cdot Q_2^2$$

$$\frac{1}{2 \cdot g \cdot A_c^2} \cdot \left(\frac{Q_1}{7.481 \cdot 60} \right)^2 \cdot \left(2.85 + f_f(Re_1) \cdot \frac{L_1}{ID} \right) = \frac{1}{2 \cdot g \cdot A_c^2} \cdot \left(\frac{Q_2}{7.481 \cdot 60} \right)^2 \cdot f_f(Re_2) \cdot \frac{L_2}{ID} + HX - HP$$

$$C_{min} = \frac{Q_2}{7.481 \cdot 60} \cdot 0.48 \cdot 54.3$$

$$C = \frac{C_{min}}{C_{max}}$$

$$U = \frac{1}{\left(\frac{5.75}{Re_2^{0.8}} \right) + 0.004}$$

$$NTU = \frac{U \cdot A_{hx}}{C_{min} \cdot 3600}$$

$$\xi = \frac{1 - \exp(-NTU \cdot (1 - C))}{1 - C \cdot \exp(-NTU \cdot (1 - C))}$$

$$T_{out} = T_{in} - \xi \cdot (T_{in} - T_{water})$$

$$T_{exit} = \frac{Q_1}{Q_T} \cdot T_{in} + \frac{Q_2}{Q_T} \cdot T_{out}$$

Figure 9. Mathcad System Simulation Worksheet

ans := Find(Q₁, Q₂, HX, HP, Re₁, Re₂, C_{min}, C, U, NTU, ξ, T_{out}, T_{exit})

Q ₁ := ans ₀	Q ₁ = 130.206	Q ₂ := ans ₁	Q ₂ = 119.794
C := ans ₇	C = 0.232	U := ans ₈	U = 164.678
NTU := ans ₉	NTU = 2.63	ξ := ans ₁₀	ξ = 0.895
T _{out} := ans ₁₁	T _{out} = 83.66	T _{exit} := ans ₁₂	T _{exit} = 144.252

Figure 9. Mathcad System Simulation Worksheet (concluded)

Example 5: One-dimensional Generalized Flow

One-dimensional generalized flow refers to a one-dimensional flow in which area change $[A(x)]$, friction $[4f/D(x)]$, heat transfer $[T_o(x)]$, and mass addition $[\dot{m}(x)]$ can be simultaneously present (details are available in [4]). The differential equation for Mach number for generalized one-dimensional flow is as follows:

$$\frac{dM}{dx} = \frac{M\psi(M)}{1 - M^2} \left(\frac{-1}{A(x)} \frac{dA(x)}{dx} + \frac{\gamma M^2}{2} \frac{4f}{D(x)} + \frac{(1 + \gamma M^2)}{2} \frac{1}{T_o(x)} \frac{dT_o(x)}{dx} + (1 + \gamma M^2) \frac{1}{\dot{m}(x)} \frac{d\dot{m}(x)}{dx} \right) \quad (2)$$

where $\psi(M) = 1 + \frac{\gamma - 1}{2} M^2$.

The general procedure is to integrate the differential equation for Mach number as a function of x and then to use the “integral” relations (4) to find the remaining physical properties. The sequence is straightforward so long as M is not near unity: solve Eq. (2), the differential equation, for $M(x)$ and then use the integral relations to compute the various property ratios.

Since the sonic point is a singular point of the differential equation, generalized one-dimensional flow solutions with Mach numbers near unity require special procedures in the neighborhood of the sonic point. Beans (7) pointed out that if Eq. (2) is viewed as

$$\frac{dM}{dx} = \frac{M\psi(M)}{1 - M^2} G(x, \gamma, M) \quad (3)$$

where

$$G(x, \lambda, M) = \left(\frac{-1}{A(x)} \frac{dA(x)}{dx} + \frac{\gamma M^2}{2} \frac{4f}{D(x)} + \frac{(1 + \gamma M^2)}{2} \frac{1}{T_o(x)} \frac{dT_o(x)}{dx} + (1 + \gamma M^2) \frac{1}{\dot{m}(x)} \frac{d\dot{m}(x)}{dx} \right) \quad (4)$$

then at the sonic ($M = 1$) location a bounded dM/dx occurs only if $G(x, \gamma, 1) = 0$. The sonic location is determined as the root of $G(x, \gamma, 1) = 0$. If $G(x, \gamma, 1) = 0$ at the sonic location, Eq. (2) reduces to the indeterminate form $0/0$ and l’Hospital’s rule can be applied to give

$$\left(\frac{dM}{dx}\right)_{M=1}^2 = -\frac{\gamma+1}{8} \left[-2 \frac{d}{dx} \left(\frac{1}{A} \frac{dA}{dx} \right) + \gamma \frac{d}{dx} \left(\frac{4f}{D} \right) + (1+\gamma) \frac{d}{dx} \left(\frac{1}{T_o} \frac{dT_o}{dx} \right) + 2(1+\gamma) \frac{d}{dx} \left(\frac{1}{\dot{m}} \frac{d\dot{m}}{dx} \right) \right]_{M=1}$$

$$- \frac{\gamma+1}{8} \left(\frac{dM}{dx} \right)_{M=1} \left[2\gamma \left(\frac{4f}{D} \right) + 2\gamma \left(\frac{1}{T_o} \frac{dT_o}{dx} \right) + 4\gamma \left(\frac{1}{\dot{m}} \frac{d\dot{m}}{dx} \right) \right]_{M=1} \quad (5)$$

In the neighborhood of the sonic location, say $|1 - M| < 0.05$, Eq. 2 is replaced by the limiting value of dM/dx from Equation 5. Equation 5 has two roots—one positive and one negative. If the positive root is used, the solution traverses the $M = 1$ location and supersonic Mach numbers will result. If the negative root is used, subsonic flow will result. The sequence of calculations for a generalized one-dimensional flow with a sonic location is as follows:

1. Solve Eq. 4 in the form of $G(x, \gamma, 1) = 0$ for the sonic location, x_{sp} .
2. Use Eq. 5 to compute the limiting value of dM/dx at $M = 1$, located at x_{sp} .
3. Integrate Eq. 2, with the limiting value of dM/dx used in the neighborhood of $M = 1$, backwards from x_{sp} to $x = 0$. This establishes the Mach number at the inlet location, $x = 0$.
4. Using the inlet Mach number from step 3, integrate in the forward direction to find $M(x)$ for the entire domain and use the integral relations to find the various properties.

As an example, consider that a converging-diverging nozzle with the hyperbolic diameter distribution

$$D(x) = \sqrt{1 + 0.25(x - 3)^2} \quad (6)$$

is connected to a reservoir with stagnation conditions of 100 psia and 1000 R. Find the Mach number distribution if the nozzle is flowing supersonically. The nozzle shape is illustrated in Figure 10. The Mathcad worksheet for this example is given in Figure 11. The procedure follows that outlined in the previous paragraph for solutions with sonic locations present. The driving potentials are defined, and the Mathcad symbolic manipulation capability is used to find dA/dx . The sonic point is next located by extracting the root of Eq. 4 in the form of $G(x, \gamma, 1) = 0$. The sonic location is at $x_{sp} = 3.148$, although the minimum area is located at $x = 3$. After the sonic point is located, the limiting value of dM/dx at $M = 1$ is calculated using Eq. 5. Since Eq. 5 requires terms such as

$$\frac{d}{dx} \left[\frac{1}{A(x)} \frac{d}{dx} A(x) \right] \quad (10)$$

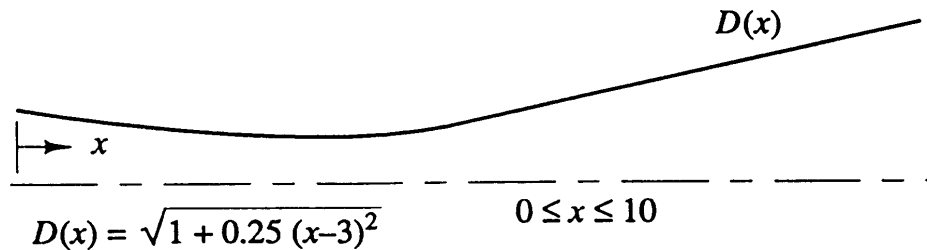


Figure 10. One-dimensional Generalized Flow Example Nozzle Geometry

Set the constant values: $f := 0.01$ $\gamma := 1.4$

Define the driving potentials:

$$\begin{aligned} T(x) &:= 1000 + 20 \cdot x & dTdx(x) &:= 20.0 \\ D(x) &:= \sqrt{1 + 0.25 \cdot (x - 3)^2} \\ A(x) &:= \frac{\pi}{4} \cdot [1 + 0.25 \cdot (x - 3)^2] & dAdx(x) &:= \frac{d}{dx} A(x) \\ m\dot{d}ot(x) &:= 1 + 0.01 \cdot x & dmdotdx(x) &:= 0.01 \end{aligned}$$

Determine the sonic point location:

The sonic point is defined by the vanishing of the function $G(x, \gamma, M)$ at $M = 1$.

The MathCad solve block, which requires an initial guess on the unknown, will be used to find the sonic point location, x_{sp} .

$x := 3$ Initial guess on the location of the sonic point.

Given

$$0 = \frac{-dAdx(x)}{A(x)} + \frac{\gamma}{2} \cdot \frac{4 \cdot f}{D(x)} + \frac{(1 + \gamma)}{2} \cdot \frac{dTdx(x)}{T(x)} + (1 + \gamma) \cdot \frac{dmdotdx(x)}{m\dot{d}ot(x)} \quad \text{Eq. 4 at } M = 1$$

$x_{sp} := \text{Find}(x)$ $x_{sp} = 3.148$ Sonic point location

The value of dM/dx at the sonic point is then evaluated using Eq. 5. The sonic point location is known from the previous calculation.

assume x Specifies x as a variable

$$Aterm(x) := \frac{d}{dx} \left(\frac{1}{A(x)} \cdot \frac{d}{dx} A(x) \right) \quad Aterm(x_{sp}) = 0.492$$

$$fterm(x) := \frac{d}{dx} \left(\frac{4 \cdot f}{D(x)} \right)$$

$$Tterm(x) := \frac{d}{dx} \left(\frac{1}{T(x)} \cdot \frac{d}{dx} T(x) \right) \quad Tterm(x_{sp}) = -3.54 \cdot 10^{-4}$$

$$mdotterm(x) := \frac{d}{dx} \left(\frac{1}{m\dot{d}ot(x)} \cdot \frac{d}{dx} m\dot{d}ot(x) \right) \quad mdotterm(x_{sp}) = -9.399 \cdot 10^{-5}$$

Compute dM/dx at the sonic point by using Eq. 5 in a Solve block. The sonic point location is x_{sp} .

$dMdx := 0.0$ Initial guess on dM/dx and $M = 1$ for Solve block.

Given

$$\begin{aligned} dMdx^2 &:= -\frac{\gamma + 1}{8} \cdot \left[-2 \cdot Aterm(x_{sp}) + \gamma \cdot fterm(x_{sp}) + (1 + \gamma) \cdot Tterm(x_{sp}) + 2 \cdot (1 + \gamma) \cdot mdotterm(x_{sp}) \right] \dots \\ &\quad + 2 \cdot \gamma \cdot \frac{\gamma + 1}{-8} \cdot dMdx \cdot \left(\frac{4 \cdot f}{D(x_{sp})} + \frac{1}{T(x_{sp})} \cdot dTdx(x_{sp}) + 2 \cdot \frac{1}{m\dot{d}ot(x_{sp})} \cdot dmdotdx(x_{sp}) \right) \end{aligned}$$

$dMdx := \text{Find}(dMdx)$ $dMdx = 0.512$ Limiting value of dM/dx near $M = 1$.

Figure 11. Mathcad Worksheet for Generalized Flow Example

Define Ψ and the differential equation:

$$\Psi(M) := 1 + \frac{\gamma - 1}{2} \cdot M^2$$

$$F(x, M) := \begin{cases} dM/dx & \text{if } |M - 1| \leq 0.05 \\ \frac{M \cdot \Psi(M)}{1 - M^2} \cdot \left[\frac{-dA/dx(x)}{A(x)} + \frac{\gamma \cdot M^2}{2} \cdot \frac{4 \cdot f}{D(x)} + \frac{(1 + \gamma \cdot M^2)}{2} \cdot \frac{dT/dx(x)}{T(x)} + (1 + \gamma \cdot M^2) \cdot \frac{dmdot/dx(x)}{mdot(x)} \right] & \text{otherwise} \end{cases}$$

Solve the differential equation from x_{sp} to 0 to find the inlet Mach number.

Set the initial condition: $M_0 := 1.0$

Solve the differential equation with the fixed-step Runge-Kutta:

$$Z := \text{rkfixed}(M, x_{sp}, 0, 15, F)$$

Extract x and M from the return matrix Z :

$$x := Z^{<0>} \quad Mach := Z^{<1>} \quad i := 0 \dots \text{last}(x) \quad Mach_{\text{last}(x)} = 0.164 \quad \text{Inlet Mach number}$$

Solve the differential equation from $x=0$ to $x = x_{max}$.

$M_0 := Mach_{\text{last}(x)}$ Set the inlet Mach number to start the forward integration.

$$Z := \text{rkfixed}(M, 0, 10, 40, F)$$

Extract x and M from the return matrix Z :

$$x := Z^{<0>} \quad Mach := Z^{<1>} \quad i := 0 \dots \text{last}(x) \quad Mach_{\text{last}(x)} = 2.681 \quad \text{Exit Mach number}$$

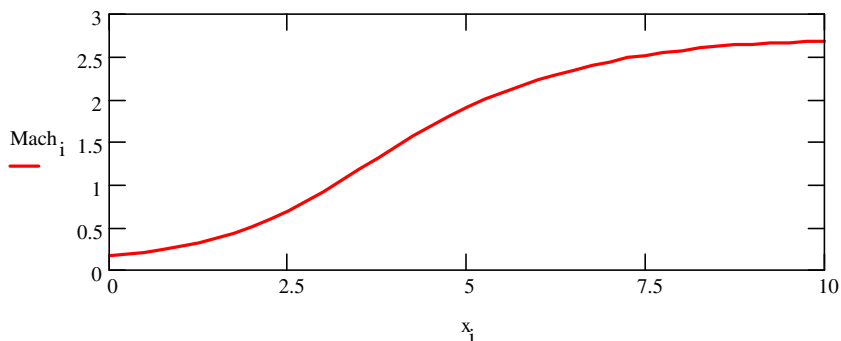


Figure 11. Mathcad Worksheet for Generalized Flow Example (concluded)

Mathcad's symbolic manipulation capability is used to avoid the tedious differentiations required, and Eq. 5 is solved to obtain $dM/dx = 0.512$ as the limiting value for this problem. **Rkfixed**, the Mathcad fixed-step Runge-Kutta integration element, is used to solve the differential equation from $x = x_{sp}$ to $x = 0$ to obtain the inlet Mach number. For integrations involving Mach numbers in the neighborhood of unity, the limiting value of dM/dx must be invoked, otherwise Eq. 2 is used. Mathcad permits the piecewise definition of the Eq. 2 and the limiting value of dM/dx as $F(x, M)$ and greatly simplifies the piecewise nature of the differential equation. The inlet Mach number that results is 0.164. Once the inlet Mach number is determined, **rklfixed** is used to integrate from $x = 0$ to $x = 10$ for $M(x)$. This is a complex problem, yet the MathCad approach is logical and straightforward.

Example 6: Simple Compressible Flow Calculations

Simple one-dimensional compressible flow forms the basis of understanding for compressible flow and is often used in preliminary calculations. Mathcad offers a problem-solution-congruent approach for the solution of simple one-dimensional compressible flow problems. The basis of Mathcad solutions for such flows is **Compmc.mcd** which contains all (simple area change, Fanno flow, Rayleigh flow, simple mass addition, normal shock wave, oblique shock wave, and Prandtl-Meyer process) the expressions for simple one-dimensional flow in the form of functions. The portion of **Compmc.mcd** containing the simple area change and normal shock wave functions is reproduced as Figure 12. The use of **Compmc.mcd** is illustrated by a simple compressible flow problem.

EXPRESSIONS FOR SIMPLE AREA CHANGE.

$$\begin{aligned} \text{Isar}(\gamma, M) &:= \frac{1}{M} \cdot \left[\left(\frac{2}{\gamma + 1} \right) \cdot \left[1 + 0.5 \cdot (\gamma - 1) \cdot M^2 \right] \right]^{\frac{\gamma + 1}{2 \cdot (\gamma - 1)}} \\ \text{Istr}(\gamma, M) &:= \left[1 + 0.5 \cdot (\gamma - 1) \cdot M^2 \right]^{-1} \\ \text{Ispr}(\gamma, M) &:= \left[1 + 0.5 \cdot (\gamma - 1) \cdot M^2 \right]^{\frac{-\gamma}{\gamma - 1}} \\ \text{Isdenr}(\gamma, M) &:= \left[1 + 0.5 \cdot (\gamma - 1) \cdot M^2 \right]^{\frac{-1}{\gamma - 1}} \\ \text{Ispstagr} &= 1 \end{aligned}$$

EXPRESSIONS FOR NORMAL SHOCK WAVE.

$$\begin{aligned} \text{Nspr}(\gamma, M1) &:= \frac{2 \cdot \gamma \cdot (M1)^2 - (\gamma - 1)}{\gamma + 1} \\ \text{Nsdenr}(\gamma, M1) &:= \frac{(\gamma + 1) \cdot (M1)^2}{(\gamma - 1) \cdot (M1)^2 + 2} \\ \text{Nstr}(\gamma, M1) &:= \left[1 + 0.5 \cdot (\gamma - 1) \cdot (M1)^2 \right] \cdot \frac{\left[-1 + (M1)^2 \cdot \frac{2 \cdot \gamma}{\gamma - 1} \right]}{(M1)^2 \cdot \left[0.5 \cdot (\gamma - 1) + \frac{2 \cdot \gamma}{\gamma - 1} \right]} \\ \text{NsM2}(\gamma, M1) &:= \sqrt{\frac{2 + (\gamma - 1) \cdot (M1)^2}{2 \cdot \gamma \cdot (M1)^2 - (\gamma - 1)}} \\ \text{Nspstagr}(\gamma, M1) &:= \left[\frac{0.5 \cdot (M1)^2 \cdot (\gamma + 1)}{1 + 0.5 \cdot (\gamma - 1) \cdot (M1)^2} \right]^{\frac{\gamma}{\gamma - 1}} \cdot \left(\frac{1}{\text{Nspr}(\gamma, M1)} \right)^{\frac{1}{\gamma - 1}} \end{aligned}$$

Figure 12. Simple Area Change and Normal Shock Wave Functions of Compmc.mcd

Consider, as schematically indicated in Figure 13, the determination of the nozzle exit Mach number and pressure for the converging-diverging nozzle ($A_4/A^* = 3.5$) with a normal shock wave located at $A_2/A^* = 2$. The Mathcad worksheet for the solution is given in Figure 14. The **Reference** statement invokes all the functions defined in **Compmc.mcd**. The problem solution proceeds as it would if worked “on paper,” except that all the function

evaluations and arithmetic are done by Mathcad. Where needed, the functions defined in **Compmc.mcd** can be used in SOLVE blocks as is the case for the determination of Mach number from area ratio in this example. This approach to compressible flow problems is very congruent with problem formulations.

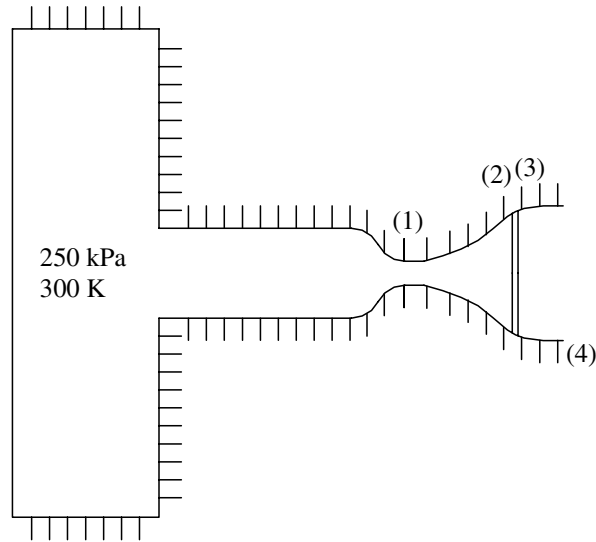


Figure 13. Converging-Diverging Nozzle Problem Schematic

Solution of Nozzle Flow Problem Illustrated in Figure 13.

☐ Reference: A:\compmc.mc

$$\begin{aligned} A1 &:= 3 \cdot \text{m}^2 & A2 &:= 6 \cdot \text{m}^2 & A3 &:= 6 \cdot \text{m}^2 & A4A1 &:= 3.5 \\ P0 &:= 250000 \cdot \text{Pa} & \gamma &:= 1.4 \end{aligned}$$

Conditions at state 2, the upstream side of the normal shock wave.

$$\begin{aligned} A2A1 &:= \frac{A2}{A1} & A2A1 &= 2 \\ M2 &:= 1.2 & \text{Guess for } M2 \text{ for SOLVE block.} \end{aligned}$$

Given

$$\begin{aligned} A2A1 &= \text{Isar}(\gamma, M2) \\ M2 &:= \text{Find}(M2) & M2 &= 2.197 \\ P2 &:= P0 \cdot \text{Ispr}(\gamma, M2) & P2 &= 2.348 \cdot 10^4 \cdot \text{Pa} \end{aligned}$$

Conditions downstream of the normal shock wave.

$$\begin{aligned} M3 &:= \text{NsM2}(\gamma, M2) & M3 &= 0.547 \\ P3P2 &:= \text{Nspr}(\gamma, M2) & P3P2 &= 5.466 & P3 &:= P3P2 \cdot P2 & P3 &= 1.284 \cdot 10^5 \cdot \text{Pa} \end{aligned}$$

Figure 14. Worksheet for Simple Compressible Flow Example

Conditions at the nozzle exit plane.

$$\begin{aligned}
 A3A1 &:= A2A1 & A4A3 &:= \frac{A4A1}{A3A1} & A4A3 &= 1.75 \\
 A3AS &:= \text{Isar}(\gamma, M3) & A3AS &= 1.259 \\
 A4AS &:= A4A3 \cdot A3AS & A4AS &= 2.203 \\
 M4 &:= \frac{M3}{1.2} & \text{Guess for M4 for SOLVE block.} \\
 \text{Giver} & & & & & \\
 A4AS &= \text{Isar}(\gamma, M4) \\
 M4 &:= \text{Find}(M4) & M4 &= 0.275 & \text{Mach number at nozzle exit plane.} \\
 P4 &:= \frac{\text{Ispr}(\gamma, M4) \cdot P3}{\text{Ispr}(\gamma, M3)} & P4 &= 1.493 \cdot 10^5 \cdot \text{Pa} \\
 P04 &:= \text{Nspstagr}(\gamma, M2) \cdot P0 & P04 &= 1.574 \cdot 10^5 \cdot \text{Pa}
 \end{aligned}$$

Figure 14. Worksheet for Simple Compressible Flow Example (concluded)

In some instances information similar to that provided in traditional tables and charts for simple compressible flow is desired. The SOLVE-block procedure is very useful for such information. Consider the case of oblique shock waves. As is the case for the previous problem, Mathcad expressions for the oblique shock (**mcos.mcd**) wave are invoked by a **Reference** statement and the SOLVE-block structure is used to obtain the solution. Figure 15 contains the equations describing the conditions and property variations across an oblique shock wave. Figure 16 is the Mathcad worksheet illustrating the complete solution for a weak shock wave given the upstream Mach number and the turning (deflection) angle. Casting this process as a Mathcad procedure provides a simpler, faster, and more accurate approach than reading the traditional oblique shock wave charts.

THESE EQUATIONS DESCRIBE THE BEHAVIOR OF OBLIQUE SHOCK WAVES.

$$\begin{aligned}
 \tan(\delta) &= \frac{2}{\tan(\theta)} \cdot \frac{M1^2 \cdot (\sin(\theta))^2 - 1}{M1^2 \cdot (\gamma + \cos(2 \cdot \theta)) + 2} & \text{Prat} &= \frac{2 \cdot \gamma \cdot (M1 \cdot \sin(\theta))^2 - (\gamma - 1)}{\gamma + 1} \\
 \text{Denrat} &= \frac{(\gamma + 1) \cdot (M1 \cdot \sin(\theta))^2}{(\gamma - 1) \cdot (M1 \cdot \sin(\theta))^2 + 2} \\
 \text{Trat} &= \left[1 + 0.5 \cdot (\gamma - 1) \cdot (M1 \cdot \sin(\theta))^2 \right] \cdot \frac{\left[-1 + (M1 \cdot \sin(\theta))^2 \cdot \frac{2 \cdot \gamma}{\gamma - 1} \right]}{(M1 \cdot \sin(\theta))^2 \cdot \left[0.5 \cdot (\gamma - 1) + \frac{2 \cdot \gamma}{\gamma - 1} \right]} \\
 (M2 \cdot \sin(\theta - \delta))^2 &= \frac{2 + (\gamma - 1) \cdot (M1 \cdot \sin(\theta))^2}{2 \cdot \gamma \cdot (M1 \cdot \sin(\theta))^2 - (\gamma - 1)} \\
 \text{Pstagr} &= \left[\frac{0.5 \cdot (M1 \cdot \sin(\theta))^2 \cdot (\gamma + 1)}{1 + 0.5 \cdot (\gamma - 1) \cdot (M1 \cdot \sin(\theta))^2} \right]^{\frac{\gamma}{\gamma - 1}} \cdot \left(\frac{1}{\text{Prat}} \right)^{\frac{1}{\gamma - 1}}
 \end{aligned}$$

Figure 15. Oblique Shock Wave Relations

$M1 := 3$ $\delta := 20 \cdot \text{deg}$ $\text{rattodeg} := \frac{180}{\pi}$
 $\theta := \delta$ set initial guess of shock wave angle to deflection angle for weak solution
 $\text{Prat} := 1$ $\text{Denrat} := 1$ $\text{Trat} := 1$ $\text{Pstagrat} := 1$
 $M2 := 0.7$

Given

☞ Reference:C:\cft\mcas.mc

$$\begin{bmatrix} \theta \\ M2 \\ \text{Prat} \\ \text{Denrat} \\ \text{Trat} \\ \text{Pstagrat} \end{bmatrix} := \text{Find}(\theta, M2, \text{Prat}, \text{Denrat}, \text{Trat}, \text{Pstagrat})$$

$$\begin{bmatrix} \theta \cdot \text{rattodeg} \\ \delta \cdot \text{rattodeg} \\ M1 \\ M2 \\ \text{Prat} \\ \text{Denrat} \\ \text{Trat} \\ \text{Pstagrat} \end{bmatrix} = \begin{bmatrix} 37.764 \\ 20 \\ 3 \\ 1.994 \\ 3.771 \\ 2.418 \\ 1.56 \\ 0.796 \end{bmatrix}$$

Figure 16. Oblique Shock Wave Mathcad Solution

CONCLUSION

Arithmetic systems, such as Mathcad, offer a new paradigm for engineering calculations. This new paradigm will not replace any existing techniques, but it does offer another option for preliminary calculations with the important advantage that engineering tasks not programming tasks become the focus. The examples in this paper illustrate the potency of arithmetic systems in preliminary thermal sciences calculations.

REFERENCES

1. Feynman, R. P. and Leighton, R., 1991, *Surely You're Joking, Mr. Feynman!*, QPBC, Camp Hill, PA.
2. Heller, M., 1999, "Mathcad's tools add up to excellence," *PC Week*, November 8, 1999.
3. Hodge, B. K., and Taylor, R. P., 1999, *Analysis and Design of Energy Systems*, 3rd ed, Prentice-Hall, Upper Saddle River, NJ.
4. Hodge, B. K., 1999, "Using MathCad for Generalized One-dimensional Compressible Flow in an Introductory Compressible Flow Course," Proceedings of the 1999 ASEE Annual Conference and Exposition, Session 2366, Charlotte, NC, June.

5. Hodge, B. K., and Taylor, R. P., 1998, "The Impact of MathCad in an Energy Systems Design Course," Proceedings of the 1998 ASEE Annual Conference, Session 2666, Seattle, WA, June.
6. Hodge, B. K., 1997, "The Use of Mathcad in Viscous Flow Courses," Proceedings of the 1997 ASEE Annual Conference, Session 2666, Milwaukee, WI, June.
7. Beans, E. W., 1970, "Computer Solutions to Generalized One-Dimensional Flow," *J. Spacecraft and Rockets*, No. 7, Vol. 12, pp. 1460-1464.

A MODIFIED NPARC CODE: THE BURNETT EQUATIONS SOLVER

K.L. Guo and G.S. Liaw
Department of Civil Engineering
Alabama A & M University
Normal, AL 35762

ABSTRACT

The conventional continuum Navier-Stokes equations gradually deteriorate when $Kn > 0.01$ because the transitional nonequilibrium effect begins to prevail. Therefore, the Navier-Stokes equations fail to predict the transitional flows accurately. In the past, many researchers have indicated that the Burnett equations can provide better solutions than the Navier-Stokes equations.

In this study, the NPARC code was modified to solve the Burnett solutions for near-continuum flows. Tests were conducted for flows over an ellipsoid and a blunt body at high speeds. The limitation and characteristics of the Burnett equations, Knudsen layer wall boundary conditions (slip velocity and temperature jump), numerical procedure and stability analysis are discussed. Comparisons of Burnett solutions and Navier-Stokes solutions and the DSMC results show that the Burnett equations can provide more accurate results than the Navier-Stokes equations in the near-continuum flow.

INTRODUCTION

A significant portion of the flight trajectory of the reusable launch vehicle is hypersonic speed at extremely high altitudes. Therefore, they are in the low Reynolds number and high Mach number ranges. The flow around these vehicles falls into the transitional regime, which can be characterized by the Knudsen number Kn . The Knudsen number can be defined as:

$$Kn = \frac{\lambda}{L} = 1.27 \gamma^{0.5} \frac{M}{Re}$$

where λ is the mean free path of the gas molecules, L is the characteristic length of the vehicle, M is the flight Mach number and Re is the Reynolds number. In general, the Knudsen number in the transitional regime is between 0.01 and 10. Since there is no appropriate ground test facility to provide windtunnel data, and flight experiment data is very expensive, the only alternative is numerical simulation.

As the Knudsen number increases, the Navier-Stokes equations gradually deteriorate because the transitional nonequilibrium effect prevails. It is natural to consider the Boltzmann equation as the governing equation for the transitional flow problems.

If only two-body collisions are considered, the Boltzmann equation is as follows:

$$\frac{\partial f}{\partial t} + \xi_i \frac{\partial f}{\partial x_i} = G(f, f) \quad (i=1,2,3) \quad (1)$$
$$G(f, \varphi) = \frac{1}{2} \int (f' \varphi'_1 + f'_1 \varphi' - f \varphi_1 - f_1 \varphi) g \cdot b \cdot db \cdot d\epsilon \cdot d\bar{\xi}$$

where $f(t, \bar{x}, \bar{\xi})$ is the distribution function, x_i and ξ_i are the physical coordinates and molecular velocities, g is the relative velocity, b and ϵ are impact parameters, and $d\bar{\xi} = d\xi_1 \cdot d\xi_2 \cdot d\xi_3$.

The non-dimensional Boltzmann equation can be written:

$$\frac{\partial f}{\partial t} + \xi_i \frac{\partial f}{\partial x_i} = \frac{1}{Kn} \cdot G(f, f) \quad (2)$$

The Boltzmann equation describes phenomena in gases at an arbitrary Knudsen number, and is a governing equation for the whole flow regime. It includes the continuum, transitional and free molecular flow regimes. However, the full Boltzmann equation is very difficult to solve because the collision term is very complex physically as well as numerically. Therefore, many investigations attempt to simplify the collision terms to solve the Boltzmann equation for the transitional flow. One such attempt is the Chapman-Enskog expansion method [1-8].

Based on the Chapman-Enskog expansion, the distribution function can be expanded into a regular series as follows:

$$f = f^{(0)} + Kn \cdot f^{(1)} + Kn^2 \cdot f^{(2)} + Kn^3 \cdot f^{(3)} + \dots$$

where the Knudsen number, a small perturbation parameter, must be less than 1.0. In general, the convergence of this expansion is asymptotic as Knudsen number $\rightarrow 0$.

As a consequence of the Chapman-Enskog expansion, the Euler equations are based on the zeroth order approximation. The Navier-Stokes equations are derived from the first order approximation. Based on a second order approximation of the expansion, the resulting equations of conservation of mass, momentum and energy are the Burnett equations. In recent years, other versions of the Burnett equations, the Augmented Burnett equations [9-14] and the BGK-Burnett equations [15-18], have also been proposed.

The Burnett equations in Cartesian coordinates can be written in a general tensor form as follows:

$$\begin{aligned} \frac{\partial \rho}{\partial t} + \rho_{,i} \cdot V_i + \rho \cdot V_{i,i} &= 0 \\ \rho \frac{\partial V_i}{\partial t} + \rho \cdot V_j \cdot V_{i,j} + \sigma_{ij,j} &= 0 \\ \rho \frac{\partial h}{\partial t} + \rho \cdot V_i \cdot h_{,i} - \frac{\partial p}{\partial t} - p_{,i} \cdot V_i - p \cdot V_{i,i} + \sigma_{ij} \cdot V_{j,i} + q_{i,i} &= 0 \end{aligned} \quad (3)$$

where

$$\begin{aligned} \sigma_{ij} &= \sigma_{ij}^{(0)} + \sigma_{ij}^{(1)} + \sigma_{ij}^{(2)} \\ q_i &= q_i^{(0)} + q_i^{(1)} + q_i^{(2)} \end{aligned} \quad (4)$$

Components of the second order terms or the Burnett terms ($\sigma_{ij}^{(2)}$ and $q_i^{(2)}$, $i, j = 1, 2, 3$) and forms of the Burnett equations were derived and given in Ref. [19-22].

Currently, the DSMC method can be considered as the most accurate and widely used technique for computation of low density flows [23-27]. However, in the near-continuum regime, where the densities are not low enough, the DSMC method requires a large number of particles for accurate simulation, making the technique prohibitively expensive. It is expensive in terms of computational time and memory requirements. In recent years, due to this limitation, many investigators have suggested an approach of CFD coupled with the DSMC. However, one of the most difficult problems is how to handle the interface of two regimes (transitional and continuum) and two point of views (micro- and macro-) for a general flow problem.

For the Burnett equations, discussions can be summarized in the following paragraphs:

Limitation of the Burnett Equations

The Burnett equations are only valid for Knudsen number less than 1.0, most likely much less than 1.0. For $Kn \rightarrow 0$, the flow approaches the continuum regime. When the Knudsen number is larger than 1.0, the Burnett equations become meaningless because the convergence of the Chapman-Enskog expansion is in trouble. Therefore, for $Kn > 1.0$, the term Kn^{-1} can be used as a small parameter to expand the distribution function and substitute into the Boltzmann equation. A solution is subsequently obtained by equating terms of the same order from the left and right hand sides. When $Kn \rightarrow 10$, it approaches the free molecule flow limit, where the distribution function is disturbed slightly from its collisionless value.

Kogan has pointed out that the convergence of the Chapman-Enskog method is in general asymptotic as $Kn \rightarrow 0$. Therefore, the Burnett equations improve the solution where the Navier-Stokes equations have a good accuracy. In general, however, it is not safe to say that we may progress in the direction of larger values of Kn by

means of the Burnett equations, i.e., toward more rarefied gases, in the cases when the Navier-Stokes equations are already unsuitable [2].

Muntz et al indicates that numerical experiments have been performed on a normal shock wave with DSMC to investigate the validity of continuum theories at very low Mach numbers. Results from the Navier-Stokes and the Burnett equations are compared to DSMC for both hard-sphere and Maxwell gases. It is found that the maximum slop shock thickness is described equally well (within the DSMC computational scatter) by either of the continuum formulations for Mach numbers smaller than about 1.2. For Mach numbers greater than 1.2, the Burnett predictions are more accurate than the Navier-Stokes results. Temperature-density profile separations are best described by the Burnett equations for Mach numbers greater than about 1.3. For all Mach number above one, the shock shapes are more accurately described by the Burnett equations [8].

Recently, some results of research work on the Burnett equations are really doubtful. For example, the Burnett solutions along stagnation streamline for Knudsen number 1.2 and the Navier-Stokes and the Burnett solutions for flow past a two-dimensional cylinder with Knudsen number 1.2 given in [10,12] are questionable. When the Knudsen number is greater than 1.0, convergence of the Chapman-Enskog expansion is in jeopardy. Then the Burnett equations or the “super” Burnett equations derived from this expansion becomes meaningless.

Can the Burnett equations be governing equations for the transitional regime at Knudsen number between 0.1 and 10? The answer is definitely negative. At this time, there is no evidence to show that any of the Burnett equations, the Augmented Burnett or the BGK-Burnett equations can be used as a governing equation for the transitional flow regime within this Knudsen number range.

Characteristics of the Burnett Equations

The Burnett equations are third-order nonlinear partial differential equations. In order to give closure to the equations and to uniquely determine the solution of the Burnett equations, an additional boundary condition is needed. Mathematically, it is very difficult to prove that the Burnett equations are well posed, which means that the solution exists, is unique and is stable, and can be solved directly.

It is noted by Cercignani that if we consider higher order approximations of the Chapman-Enskog method, we obtain differential equations of high order (the so-called Burnett and super-Burnett equations), about which nothing is known, not even the proper boundary conditions. These higher order equations have never achieved any noticeable success in describing departures from continuum fluid mechanics. Furthermore, a preliminary treatment of the connection problem for boundary layers seems to yield the same number of boundary conditions at any order of approximation, while the order of differentiation increases [4].

Lee also noted that the solution uniqueness and the proper boundary conditions of the Burnett equations remain as unresolved issues to date. This difficulty could disappear if we were to treat the Burnett terms as small perturbations from Navier-Stokes equations in a formal expansion procedure, as in the Burnett's original development [28].

Presently, a common numerical procedure is to explicitly calculate the Burnett terms and boundary conditions using the Navier-Stokes solution as an initial value. Then add them into source terms of the Navier-Stokes equation and finally solve them to obtain the Burnett solution. Therefore, the Burnett solution obtained by this procedure is a perturbation solution of the Navier-Stokes equations. Based on the Chapman-Enskog expansion, the Burnett terms (second order stresses and heat fluxes) are always smaller than the Navier-Stokes terms (first order stresses and heat fluxes). The Burnett equations can improve the accuracy of the Navier-Stokes solutions where the Navier-Stokes equations are still valid, but cannot be used when the Navier-Stokes equations already fail. As flow becomes rarefied, because Navier-Stokes convergence solutions are in doubt, the Burnett solutions fail [19].

Stability Problem

The Augmented Burnett equations did not present any stability problems when they were used to compute the hypersonic shock structure and hypersonic blunt body flows. However, attempts at computing the flow fields for

blunt body wakes and flat plate boundary layers with Augmented Burnett equations have not been entirely successful [15].

It is reported by Agarwal et al that both the Augmented Burnett and BGK-Burnett equations have the same forms of the stress tensor and heat flux terms in the second order approximation. However, the two sets of equations have different values for the coefficients. The third-order approximation represents the super Burnett equations. However, not all of the third order terms of the super Burnett equations are used in the Augmented Burnett and BGK-Burnett equations. Using linear stability analysis, it has been shown that these additional terms make the BGK-Burnett equations unconditionally stable for monatomic gases as well as polyatomic gases [18].

Chapman et. al. has pointed out that the linear stability analysis alone is not sufficient to explain the instability of the Burnett equations with increasing Knudsen numbers. This analysis does not take into account many non-linear terms, products of the first and higher order derivatives that are present in the Burnett equations. It may be due to the fact that the Burnett equations violate the second law of thermodynamics at higher Knudsen numbers [16].

It is reported by Comeaux et al that an expression describing the entropy production may be derived using the Gibbs equation in conjunction with the continuum conservation equations. Alternatively, the entropy production may be found by the concepts of kinetic theory directly by using Boltzmann's H-theorem. In either case, it is determined that the entropy source strength is not positive semi-definite as required by the second law. In addition, the two approaches produce completely equivalent expressions for the entropy balance equation. From thermodynamics analysis, for a monatomic gas it follows that

$$Kn_A \leq \frac{16}{5\sqrt{10\pi/3}} \cdot \frac{1}{M} = \frac{0.9889}{M}, \quad Kn_B \leq \frac{8}{5\sqrt{10\pi/3}} \cdot \frac{1}{M} = \frac{0.4944}{M} \quad (5)$$

This results indicates that when a gas is expanding, the first two entropy production terms are not positive semi-definite if the above restrictions on the local Knudsen and Mach number are not satisfied. From kinetic theory analysis, in an expanding flow the local Knudsen and Mach numbers are restricted by

$$Kn_{\hat{A}} \leq \frac{8}{5\sqrt{10\pi/3}} \cdot \frac{1}{M} = \frac{0.4944}{M}, \quad Kn_{\hat{B}} \leq \frac{8}{5\sqrt{10\pi/3}} \cdot \frac{1}{M} = \frac{0.2472}{M} \quad (6)$$

This finding may account for the many numerical problems experienced by researchers attempting to solve the Burnett equations over the past five decades [14].

According to this report, the Burnett equations violate the second law of thermodynamics if the restrictions, equations (5) and (6), on the local Knudsen and Mach number are not satisfied. Qualitatively, these restrictions are consistent with the convergence requirement of the Chapman-Enskog expansion. This means that the Burnett equations fail if the Knudsen number is too large. However, when these restrictions, equations (5) and (6) are applied to some subsonic flows, it seems that the Burnett equations are valid for the Knudsen number greater than 1.0 and does not violate the second law of thermodynamics. This contradicts the theory that the Knudsen number must be less than 1.0 for the Burnett equations. Therefore, more careful validations are needed.

Wall Boundary Conditions

In order to assure the accuracy of the Burnett equations solution, the conventional wall condition is replaced by the Knudsen layer wall condition. Since the flow becomes rarefied, a very thin layer exists near the wall, which makes the governing equations not applicable. The thickness of this kinetic boundary layer, or so-called Knudsen layer, is about a few mean free paths. The Knudsen layer may occur in a flow with velocity and/or temperature gradients. The gas may be restrained from relaxation toward thermal equilibrium by the boundary conditions. The Knudsen layer and the gas-wall interaction then create the slip velocity and temperature jump. Therefore, the Knudsen layer slip velocity and the temperature jump must be used as wall boundary conditions for the low density flow calculations.

For the boundary mesh points along the body surface, the flow variables on the surface were computed by the first-order Maxwell/Smoluchowski slip boundary conditions [10,11]. In the two-dimensional case, it can be written as:

$$\begin{aligned}
v_s &= 0 \\
u_s &= \frac{2-\sigma}{\sigma} \cdot l^* \cdot \left(\frac{\partial u}{\partial y}\right)_s + 0.75 \frac{\mu}{\rho_s T_s} \left(\frac{\partial T}{\partial x}\right)_s \\
T_s &= T_w + \frac{2-\sigma}{\sigma} \cdot \frac{2\gamma}{\gamma+1} \cdot \frac{l^*}{\text{Pr}} \left(\frac{\partial T}{\partial y}\right)_s
\end{aligned} \tag{7}$$

where

$$l^* = \sqrt{\frac{\pi}{2}} \frac{\mu}{\sqrt{P_s \rho_s}}$$

The subscript s represents the flow variables on the surface, and T_w is the temperature of the surface body. Also v is the velocity normal to the wall in the direction of y , u is the tangential velocity in the direction of x , σ is the reflection coefficient and α is the accommodation coefficient. In this study, complete accommodation was assumed, i.e., $\sigma = 1.0$ and $\alpha = 1.0$.

Beskok and Karniadakis [29] have recently derived the second order Maxwell/Smoluchowski boundary conditions as

$$\begin{aligned}
u_s &= \frac{2-\sigma}{\sigma} \left[l^* \left(\frac{\partial u}{\partial y}\right)_s + \frac{l^{*2}}{2} \left(\frac{\partial^2 u}{\partial y^2}\right)_s \right] + 0.75 \frac{\mu}{\rho T} \left(\frac{\partial T}{\partial x}\right)_s \\
T_s &= T_w + \frac{2-\sigma}{\sigma} \frac{2\gamma}{\gamma+1} \frac{1}{\text{Pr}} \left[l^* \left(\frac{\partial T}{\partial y}\right)_s + \frac{l^{*2}}{2} \left(\frac{\partial^2 T}{\partial y^2}\right)_s \right]
\end{aligned} \tag{8}$$

MODIFICATION OF THE NPARC CODE

The NPARC code is a general-purpose flow simulation computer program [30]. The basis of the algorithms used in the NPARC code is the complete Navier-Stokes equations in conservation law forms. The equations are solved using either the pentadiagonal form of the Beam and Warming approximate factorization algorithm or the Jameson multilevel scheme. The Beam and Warming algorithm is an implicit and robust scheme. The Jameson multilevel algorithm is second order accurate in time. The derived Burnett terms, second order stresses and heat fluxes, were implemented into the NPARC version 3.0 code [20]. The modified NPARC code extends the Navier-Stokes equation solver to the Burnett equations solver. To implement the Knudsen layer wall condition of equation (7) into the NPARC code, the non-dimensional form is need.

It is noted that the slip velocity and the temperature jump at the surface are inversely proportional to the Reynolds number. For the flow with Knudsen number 0.01, the magnitude of nondimensional slip velocity is less than 0.01. If the Knudsen number is less than 10^{-3} , most flow calculations adopt the Navier-Stokes equation with non-slip wall condition and the slip velocity is ignored. Similarly, the magnitude of temperature jump, $(T_s - T_w)$ is so small that the conventional isothermal wall can be used when the Knudsen number is less than 10^{-3} .

In order to implement the Knudsen layer wall condition, add one subroutine into the NPARC code, and modify two original subroutines of the code. The subroutine added is **KLWALL.F**, which is based on equation (7) and used to calculate the slip velocity and temperature jump at the wall. The two original subroutines that should be modified are **CTYPS.F** and **BC.F**, which are used to access the Knudsen layer condition. For the best result, this implementation of the wall condition requires that the grid lines are nearly normal to the body surface.

RESULTS AND DISCUSSION

In this study, the modified NPARC code was used to obtain the Burnett solutions. Validations of the Burnett equations solver were conducted on a CRAY SV1 platform. Tests were performed for flow past a six to one (6:1) ellipsoid and a blunt body at Mach number 2. In computations, the grids $35 \times 70 \times 21$, $(I \times J \times K)$ for an ellipsoid body were used. Singularities, which occurred at the places of $K=1$ and $K=21$, must be avoided in the grid generation. The O-grid overlap boundary conditions were used at the $J=1$ and $J=70$ locations. The residuals of the equations for the convergence solution were chosen to be less than 10^{-12} . Grid distribution, density and temperature contours on an ellipsoid body for flow Mach number 2 and Reynolds number 6000 are plotted in Figure 1. Calculated streamline profiles for azimuth angles 45, 90 and 135 degrees are shown in Figure 2. The streamline profile for 45 degrees and 135 degrees are almost the same, which shows that symmetry is very good. The comparison of the surface pressure coefficients for flow $M=2$ and $Re=300$ ($Kn=0.01$) demonstrates that the Burnett solutions are in good agreement with the DSMC results [19].

The stream line profile, density and temperature contours for flow past a blunt body with Mach number 2.0 and Reynolds number 10000 are plotted in Figure 3. It shows that two symmetrical recirculation zones exist in the near-wake area. Comparisons of the density and temperature contours obtained by the Burnett solution and the Navier-Stokes solution are displayed in Figure 4. Comparisons show that the contours given by Navier-Stokes equations and Burnett equations are almost the same in the shock area. However, in the near-wake area, the Burnett solutions are slightly different from the Navier-Stokes equations, because the local Knudsen number in the near-wake area is larger than that in the shock area. These differences will be increased when the upstream flow Mach number increases or the Reynolds number decreases, and hence the Knudsen number increases. In tests, it was found that magnitude of the ratio of the maximum value of the Burnett terms and the maximum value of the Navier-Stokes terms is about the same order of the Knudsen number. Therefore, for flow with a very small Knudsen number, such as $Kn < 0.001$, the effects of the Burnett terms on the Navier-Stokes solutions are negligible, and the slip velocity and temperature jump boundary conditions can also be ignored. For the transitional flow with a large Knudsen number, the Burnett equations will fail, and the DSMC method is the only alternative of the numerical approach.

CONCLUSIONS

Through development and validation tests of the Burnett equations solver, it was found that:

- (1). The Burnett equations are only valid for Knudsen numbers less than 1.0, most likely much less than 1.0. None of the Burnett equations, the Augmented Burnett equations, nor BGK-Burnett equations can be used as a governing equation for the transitional flow regime at Knudsen number between 0.1 and 10.
- (2). The Burnett equations, Augmented Burnett equations and BGK-Burnett equations are sets of nonlinear partial differential equations. Their stability problem cannot be determined by the linear stability theory.
- (3). Presently, the obtained Burnett solution is a perturbation solution of the Navier-Stokes equations. The Burnett equations can improve the accuracy of the Navier-Stokes solutions where the Navier-Stokes equations are still valid, but cannot be used when the Navier-Stokes equations have already failed. The DSMC method is the best approach to simulate transitional flows with a larger Knudsen number.

ACKNOWLEDGEMENTS

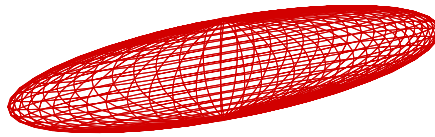
This work is supported by the U.S. Army Research Office (ARO) through a DoD EPSCoR grant and a NASA/MSFC research grant. The CPU time is provided by Alabama Research and Education Network (AREN).

REFERENCES

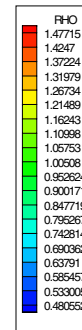
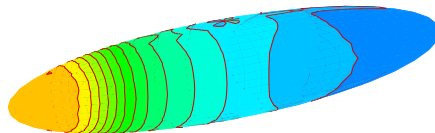
1. Vincenti, W. G. and Kruger, C. H., Jr, *Introduction to Physical Gasdynamics*, John Wiley and Sons, Inc., 1965.
2. Kogan, M. N., *Rarefied Gas Dynamics*, Plenum Press, New York, 1969.
3. Kogan, Mikhail. N., "Molecular Gas Dynamics", Annual Review of Fluid Mechanics, Vol. 5, 383-404, 1973.

4. Cercignani, Carlo, *Mathematical Method in Kinetic Theory*, Plenum Press, New York, 1969.
5. Chapman, S and Cowling, T. G., *The Mathematical Theory of Non-Uniform Gases*, Cambridge University Press, London, 1970
6. Wang Chang, C. S. and Uhlenbeck, G. E., "On the Transport Phenomena in Rarefied Gases", *Studied in Statistical Mechanics*, 5, 1948.
7. Muntz, E. P., "Rarefied Gas Dynamics", *Annual Review of Fluid Mechanics*, 21, 387-417, 1989.
8. Pham-van-diep, G. C., Erwin, D. A. and Muntz, E. P., "Testing Continuum Descriptions of Low-Mach-Number Shock Structures", *J. Fluid Mechanics*, 232, 403-413, 1991.
9. Fisco, K. A. and Chapman, D. R., "Hypersonic Shock Structure with Burnett Terms in the Viscous Stress and Heat Flux", AIAA paper 88-2733, 1988.
10. Zhong, X., McCormack, R. W. and Chapman, D. R., "Stabilization of the Burnett Equations and Application to High-Altitude Hypersonic Flows", AIAA paper 91-0770, 1991.
11. Zhong, X., McCormack, R. W. and Chapman, D. R., "Evaluation of Slip Boundary Conditions for the Burnett Equations with Application to Hypersonic Leading Edge Flow", *Proceedings of the 4th International Symposium on Computational Fluid Dynamics*, 1991
12. Zhong, X., McCormack, R. W. and Chapman, D. R., "Stabilization of the Burnett Equations and Application to Hypersonic Flows", *AIAA J*, Vol. 31, No. 6, 1993.
13. Lumpkin, F.E. and Chapman, D. "Accuracy of the Burnett Equations for Hypersonic Flows", AIAA Paper 91-0771.
14. Comeaux, K. A., Chapman, D. R. and McCormack, R. W., "An Analysis of the Burnett Equations Based on the Second Law of Thermodynamics", AIAA paper 95-0415, 1995.
15. Balakrishnan, Ramesh and Agarwal, Ramesh K., "A Kinetic Theory Based Scheme for the Numerical Solution of the BGK-Burnett Equations for Hypersonic Flows in the Continuum-Transition Regime", AIAA paper 96-0602, 1996.
16. Balakrishnan, R., Agarwal, Ramesh K. and Yun, Keon-Young, "Higher-Order Distribution Functions, BGK-Burnett Equations and Boltzmann's H-theorem", AIAA paper 97-2551, 1997.
17. Balakrishnan, Ramesh and Agarwal, Ramesh K., "Numerical Simulation of the BGK-Burnett Equations for Hypersonic Blunt Body Flows Using the Kinetic Wave-Particle Flux Splitting Algorithm", AIAA paper 98-0848, 1998.
18. Agarwal, Ramesh K., Yun, Keon-Young and Balakrishnan, Ramesh, "Beyond Navier Stokes: Burnett Equations for Flow Simulations in Continuum-Transition Regime", AIAA paper 99-3580, 1999.
19. Guo, K. L., Liaw, G. S. and Chou, L. C., "Numerical Predictions of the Transitional Flow Over an Elliptic Cylinder by the Burnett Equations and the DSMC Method", AIAA paper 99-3457, 1999.
20. Guo, K. L., Liaw, G. S. and Chou, L. C., "Implementation of the Burnett Terms into the NPARC Code for Predicting the Low Density Flows", AIAA paper 99-0746, 1999.
21. Liaw, G. S., Guo, K. L. and Chou, L. C., "Burnett Solutions Along the Stagnation Line of a Cooled Cylinder in Low-Density Hypersonic Flows", AIAA paper 93-2726, 1993.
22. Liaw, G. S., Guo, K. L., "Derivation of the Burnett Equations", Air Force Contract Final Report, Oct. 1993.
23. Bird, G. A., *Molecular Gas Dynamics and the Direct Simulations of Gas Flows*, Clarendon Press, Oxford, 1994.
24. Bird, G. A., *Molecular Gas Dynamics*, Clarendon Press, Oxford, 1976.
25. Guo, K. L., Liaw, G. S. and Chou, L. C., "The Prediction of the Blunt Body Near-Wake Flows by a Modified Direct Simulation Monte Carlo Method", AIAA paper 98-2672, 1998.
26. Guo, K. L., Liaw, G. S., Chou, L. C. and Mach, K. D., "Shock Structure Prediction By a Modified Direct Simulation Monte Carlo Method", AIAA paper 95-2049, 1995.
27. Guo, K. L., Liaw, G. S. and Chou, L. C., "Shock Structure Prediction for Gas Mixtures by a Modified Simulation Monte Carlo Method", AIAA paper 96-1818, 1996.
28. Lee, C. J., "Unique Determination of Solutions to the Burnett Equations", *AIAA J*, Vol. 32, No. 5, 1994.
29. Beskok, A. and Karniadakis, G., "Simulation of Heat and Momentum Transfer in Microgeometries", AIAA Paper 93-3269, 1993.
30. NPARC Alliance, *NPARC User's Guide*, Version 3.0, 1996.

GRIDS



DENSITY



TEMPERATURE

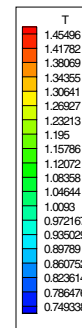
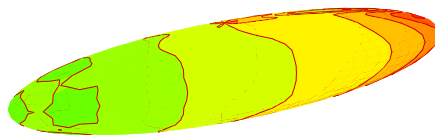
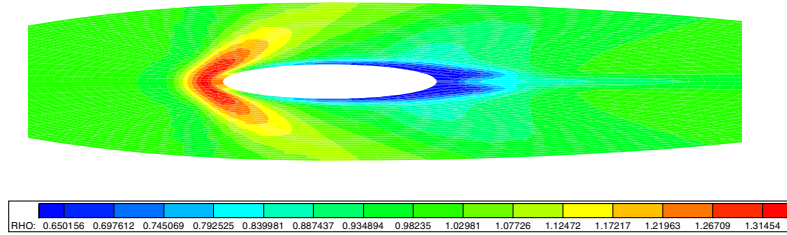
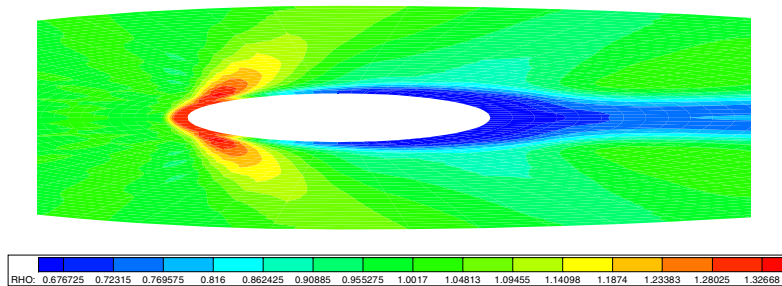


Figure 1. Grids, density and temperature contours on an ellipsoid surface for flow at $M=2$, $Re=6000$

Azimuth 45 deg



Azimuth 90 deg



Azimuth 135 deg

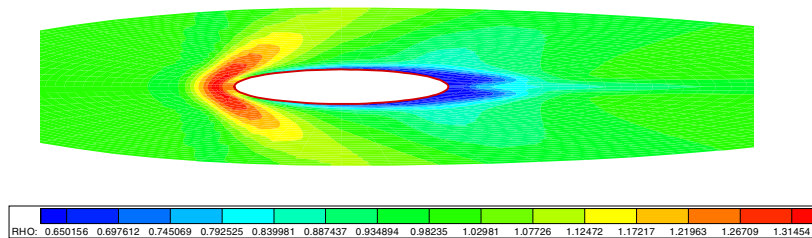
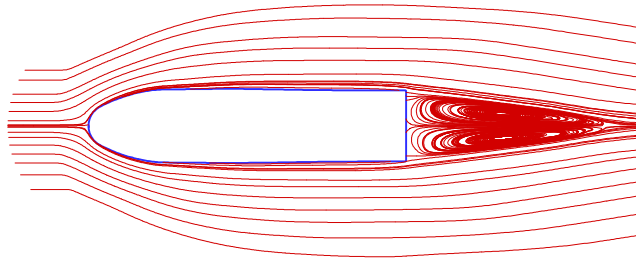
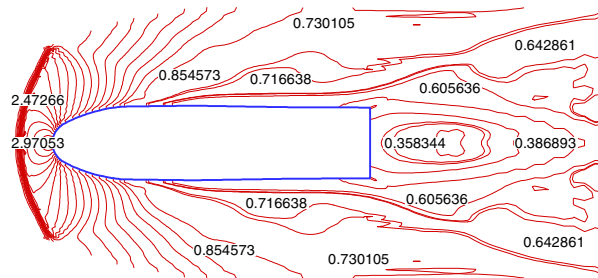


Figure 2. Density contours for Azimuth angles 45, 90 and 135 degrees of an ellipsoid for flow with $M=2$, $Re=6000$

STREAMLINE



DENSITY



TEMPERATURE

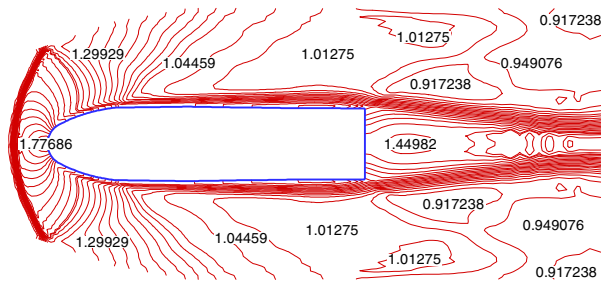
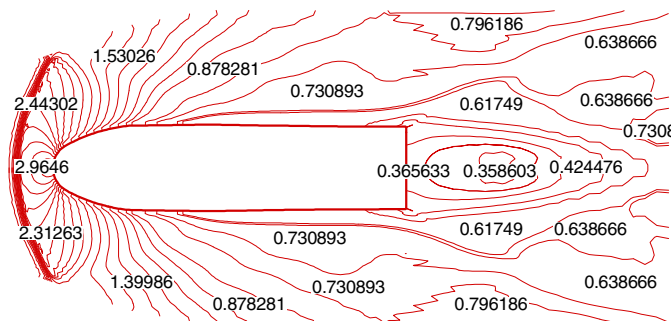


Figure 3. Streamline profiles, density and temperature contours of the flow past a blunt body at $M=2.0$, $Re=10000$

BURNETT



NAVIER-STOKES

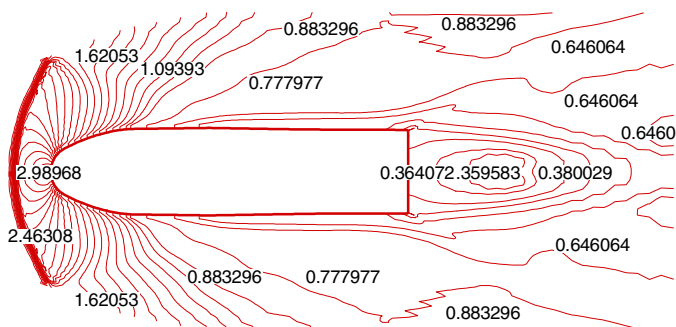
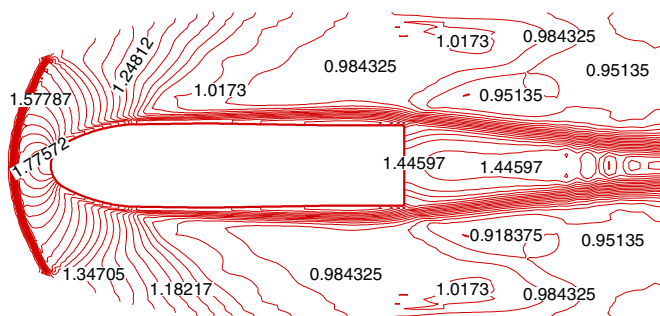


Figure 4. Comparison of density contours for flow $M=2.0$, $Re=10000$, by the Burnett and Navier-Stokes equations

BURNETT



NAVIER-STOKES

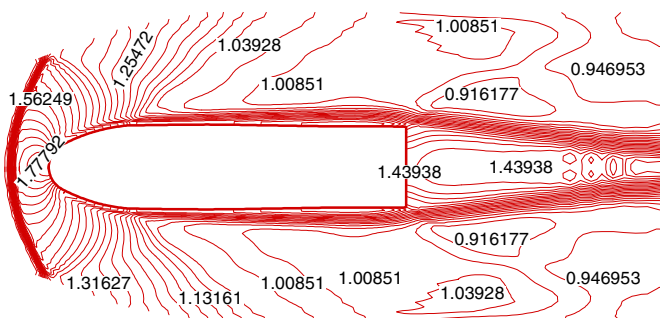


Figure 5. Comparison of temperature contours for flow $M=2.0$, $Re=10000$, by the Burnett and Navier-Stokes equations

MULTIDISCIPLINARY ANALYSIS OF A MICROSYSTEM DEVICE FOR THERMAL CONTROL

Matthew E. Moran

National Aeronautics and Space Administration
Glenn Research Center
Cleveland, Ohio 44135

ABSTRACT

A microelectromechanical (MEMS) device is under development that uses the Stirling cycle to provide cooling or heating directly to a thermally loaded surface. This MEMS cooler can be used strictly in the cooling mode, or switched between cooling and heating modes in milliseconds for precise temporal and spatial temperature control. Potential applications include cooling and thermal control of: microsystems, electronics, sensors, biomedical devices, and spacecraft components. A primary challenge for further development is the multidisciplinary analysis required to characterize and optimize its performance. This paper describes the first-order thermodynamic analysis performed on the MEMS cooler and the resulting ideal performance curves generated. The basis for additional coupled analyses such as fluid/gas dynamics, thermal, electrostatic, structural, dynamic, material, and processing is addressed. Scaling issues relevant to the device and the breakdown of continuum theory in the micro-domain is also examined.

INTRODUCTION

High capacity cooling options remain limited for many small-scale applications such as microelectronic components, miniature sensors, and MEMS devices. Passive techniques (e.g fins or conduction enhancing materials) are routinely used for some of these applications, but often fall short of the desired performance. Commonly used active cooling methods such as forced air and pumped liquid systems provide higher capacity, but are scale-limited. Other options have their own unique limitations: thermoelectrics (Peltier) coolers are relatively inefficient; heat pipes are designed for discrete temperature operation and are capacity-limited by the heat sink temperature; and various evaporation-compression/condensation cycles introduce greater complexity and generally involve distributed components.

There is a need for a high capacity micro-scalable cooling device with simple interfaces and the flexibility to be used in a variety of applications and temperature ranges. A MEMS cooler is being developed to meet this need by merging two core capabilities at the NASA Glenn Research Center: Stirling technology and microsystems. NASA Glenn has been developing Stirling machines for power generation and cooling for decades. More recently, NASA Glenn has proactively developed microsystems capabilities initially focused on sensors in harsh environments and now expanding to other devices.

Stirling Coolers

Figure 1 illustrates how an ideal Stirling cycle for refrigeration is produced using a traditional piston-bore geometry and a regenerative heat exchanger; along with the corresponding pressure-volume and temperature-entropy diagrams¹. The ideal cycle starts with compression of the working gas from state 1 to 2 in an isothermal process that increases the pressure and decreases the gas volume. The gas is then cooled in a constant volume process as it is forced through the regenerator into the expansion space (state 2 to 3). From state 3 to 4, the working gas is expanded in an isothermal process that decreases the pressure and increases the gas volume. The cycle returns to its original state (state 4 to 1) with the heating of the gas in a constant volume process as it is forced back to the compression space through the regenerator. During steady state operation, this cycle produces a cold region in the expansion space for cooling/refrigeration and a hot region in the compression space for heat dissipation. The regenerative heat exchanger functions as thermal capacitor transferring heat to and from the working gas as it is forced between the expansion and compression spaces by the pistons.

¹ Adapted from: Walker, Graham, Cryocoolers, Plenum Press, NY, 1983.

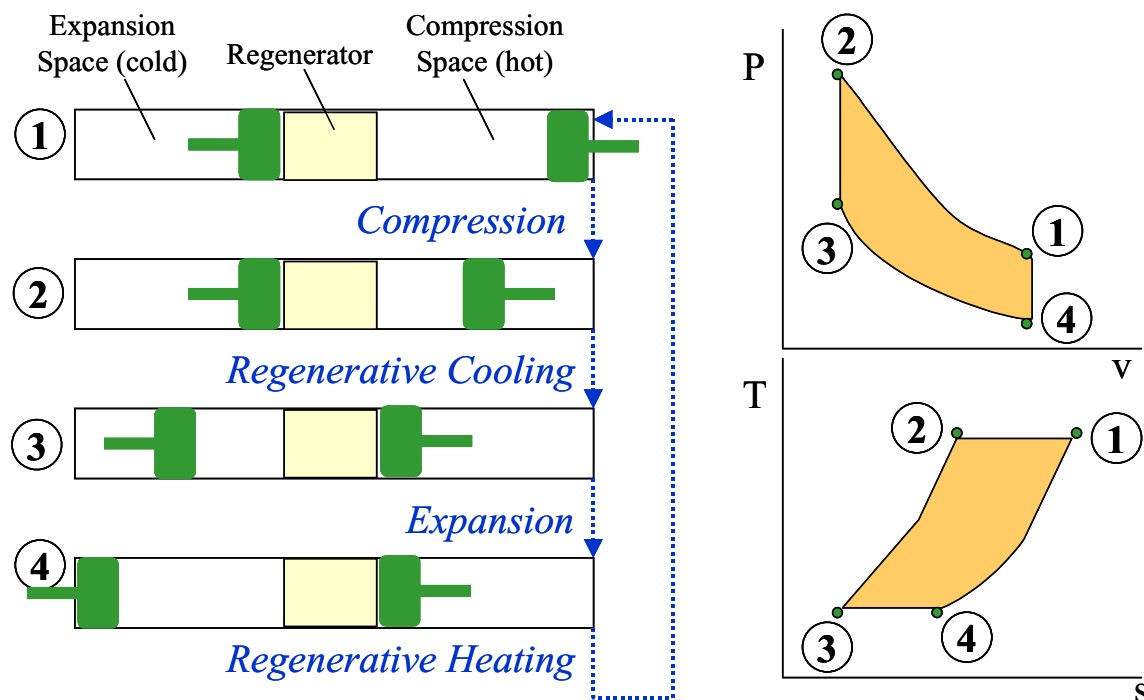


Figure 1. Ideal Stirling Cycle Refrigerator.

Stirling cycle coolers/refrigerators have been used for decades to produce cooling temperatures as low as the cryogenic range for a variety of applications. Historically, these machines have been made using pistons, mechanical linkages, and other standard engine components along with traditional materials and fabrication methods. More recently, the need for smaller-scale coolers has pushed the limits of these traditional components and assembly techniques. However, available coolers are still too large for many applications including certain electronic components, sensors, and MEMS devices.

Rapidly expanding capabilities in semiconductor processing in general, and microsystems packaging in particular, present a new opportunity to extend Stirling cycle cooling to the MEMS domain. The comparatively high capacity and efficiencies possible with a MEMS Stirling cooler provides a level of active cooling and thermal control that is currently impossible at the micro-scale with state-of-the-art techniques.

DEVICE DESCRIPTION

The MEMS cooler uses diaphragms instead of pistons to produce a Stirling cycle, and is fabricated with semiconductor processing techniques to produce a device with planar geometry. The result is a flat cold surface for extracting heat and an opposing flat hot surface for thermal dissipation. Figure 2 shows a partial crosssectional sketch of the MEMS cooler structure with three Stirling cycle “cells”. A typical device would be composed of numerous such cells arranged in parallel and/or in series.

The expansion and compression diaphragms are the only moving parts, and are deflected toward and away from the regenerator region in phase-shifted sinusoidal fashion to produce the Stirling cycle. Expansion of the working gas directly beneath the expansion diaphragm in each cycle creates a cold (top) end for extracting heat; while

compression at the other (bottom) end creates a hot region for dissipating heat. Heat is transferred to and from the working gas as it is forced through the regenerator region by the moving diaphragms. The slanted geometries of the diaphragm and regenerator surfaces are characteristic of the wet etching process used to create the structure, and advantageously increase the potential swept volume in the expansion and compression regions. A thin film temperature sensor deposited on the surface of the cap plate (not shown) provides control feedback. This sensor, along with the ability to switch hot and cold ends in milliseconds by altering the cycle with control software, permits the device to be used for precise thermal control as well as cooling.

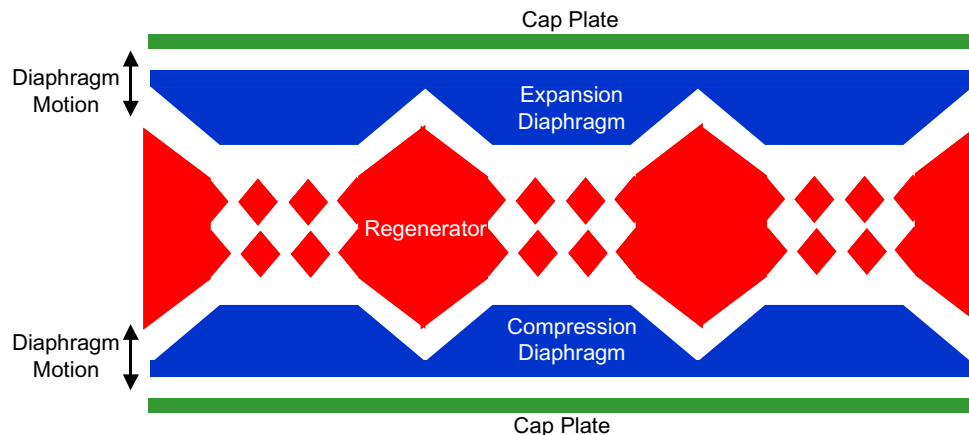


Figure 2. Partial Crosssection Sketch of MEMS Cooler.

Unique characteristics of the device include: scalability, modularity, simplified interfaces, robust design, and minimal vibration. The ability to fabricate the device at the microsystem level brings precise temperature control and cooling capabilities to a rapidly expanding variety of MEMS devices. Modular design allows for operation of identical devices in parallel to increase capacity, or staging of identical devices by stacking in series to obtain temperature ranges in the cryogenic region. Electrical power alone is required for operation; and structurally-deflected diaphragms are the sole moving parts of the device resulting in limited failure modes. Induced vibration is minimized by the low inertial forces produced by the diaphragms, and can be eliminated by the use of multiple devices operating out-of-phase with each other.

The MEMS cooler advances capabilities in four key areas: 1) extended environmental temperature range for sensors and other components in harsh environments, 2) precision spatial and temporal thermal control for temperature sensitive instruments, 3) lowered operating temperature for increased reliability of electronics, and 4) the enabling of microsystem devices that require active cooling and/or temperature control.

ANALYSIS

Characterizing the performance of the MEMS cooler requires a multidisciplinary analysis of the physics involved. Figure 3 shows the primary analyses, key subsequent results, and some of the basic input parameters needed. Most of these analyses are highly interrelated and must be properly coupled to accurately model the operation of the device. For example, the ideal performance results obtained from the thermodynamic analysis must be adjusted for the irreversibilities associated with frictional losses and non-ideal behavior of the working gas from the fluid analysis. Other inefficiencies must be incorporated from the thermal analysis of the regenerator and overall structure to ascertain a realistic estimate of the device's actual cooling capacity. Similarly, the operation of the actuators which drive the thermodynamic cycle are governed by the electrostatic forces produced and the structural response of the diaphragms. Interwoven within all the analyses is the selection and characterization of materials and fabrication processes which fundamentally affect the device performance.

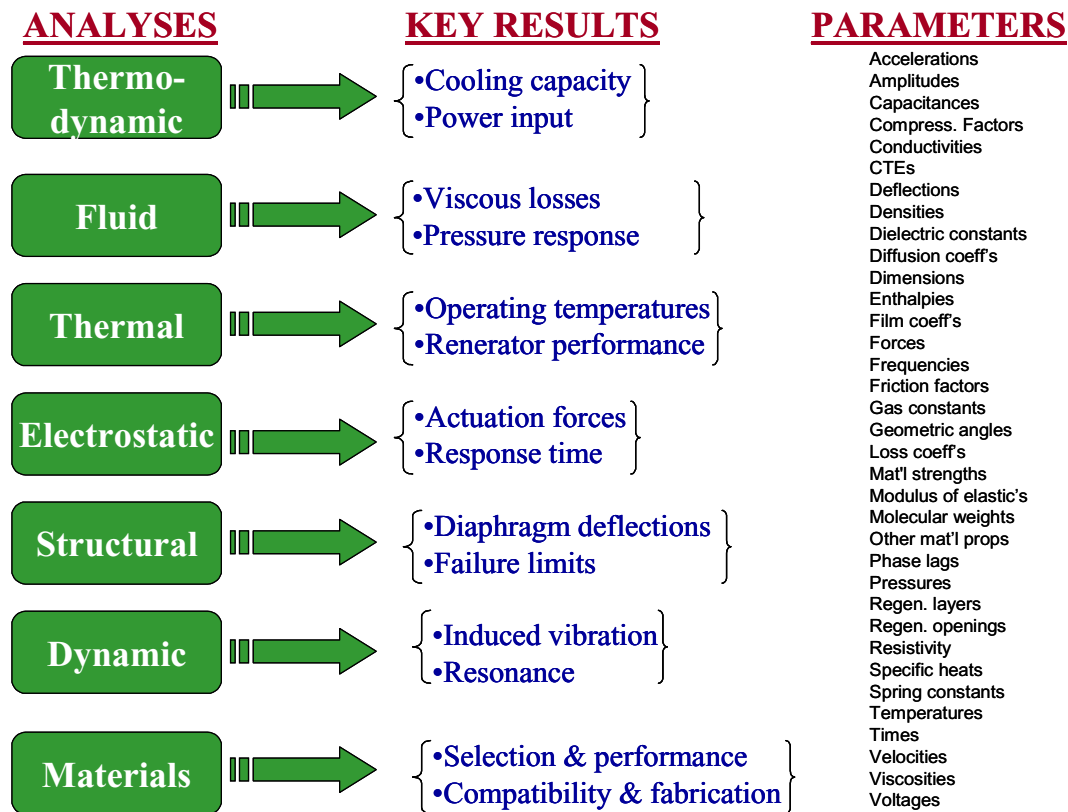


Figure 3. List of Coupled Analyses

Figure 4 illustrates the series of analytical steps envisioned for the development of the MEMS cooler device. This paper will discuss activities related to the first two steps shown which encompass first-order models aimed at characterizing the conceptual design and uncovering any fundamental issues. These analyses are based on first principles of the physics involved and provide intuition into the key design drivers and overall potential performance. The next step is to couple the various first-order analyses into an integrated system model. This system model is used to verify the operation of the device and allow for an initial optimization of the design.

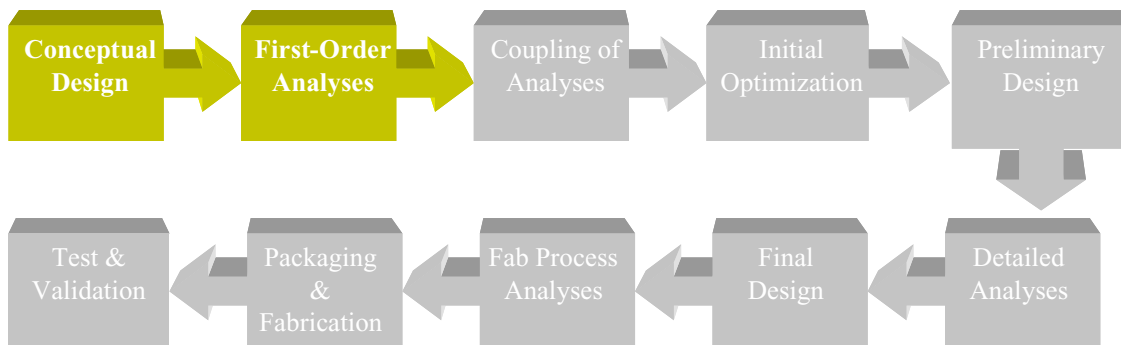


Figure 4. Overview of Analysis Steps

Based on the optimization results, the preliminary design of the MEMS cooler will be baselined and used to conduct a coupled set of detailed analyses. The detailed analyses will utilize sophisticated numerical codes (e.g. finite element, boundary element, finite difference, finite volume, etc.) to greatly refine the fidelity of the model. Design modifications based on the detailed analyses results will form the basis for the final device design.

There are a variety of fabrication and processing techniques available for MEMS devices. Since the experience base and standard practices for designing to these processes is limited, careful attention must be paid to assessing the effects of the fabrication process on the final device. Once a prototype has been assembled, testing will characterize the actual device performance and provide a means to validate the analyses.

Thermodynamics

Since the Stirling cycle is the heart of the MEMS cooler operation, it's appropriate to begin with a thermodynamic analysis of the device to find the ideal performance attainable. In addition, this analysis provides a basis for optimizing the device design parameters. A first-order analysis of an ideal Stirling cycle machine can be formulated subject to the following assumptions:

- The regenerative process is perfect
- The instantaneous pressure throughout the system is constant
- The working gas behaves as an ideal gas
- The working gas mass is constant; no leakage
- The working space volume variations occur sinusoidally
- No temperature gradients exist in the heat exchanger
- Temperatures in the “cylinder walls” and “pistons” are constant
- There is perfect mixing of the cylinder contents

Subject to the above assumptions, the dimensionless heat extracted by a Stirling cycle refrigerator/cooler per cycle can be found from [1]:

$$Q_{\max} = \frac{Q_E}{P_{\max} V_T} = \frac{\pi \delta \sin \theta \sqrt{1 - \delta}}{(1 + \kappa) \sqrt{1 + \delta} \left(1 + \sqrt{1 - \delta^2} \right)}$$

Where:

P_{\max} = maximum operating pressure

Q_E = heat extracted per cycle in the expansion space

V_T = combined swept volume = $V_c + V_E = (1 + \kappa)V_E$

V_c = swept volume in the compression (hot) space

V_E = swept volume in the expansion (cold) space

κ = swept volume ratio = V_c / V_E

$\delta = \frac{\sqrt{\tau^2 + \kappa^2 + 2\tau\kappa \cos \alpha}}{(\tau + \kappa + 2S)}$

τ = absolute temperature ratio = T_C / T_E

T_c = compression (hot) space absolute temperature

T_E = expansion (cold) space absolute temperature

α = lead phase angle between volume variations in the expansion & compression spaces {in fractions of π radians or degrees}

S = reduced dead volume = $2\tau X / (\tau + 1)$

X = dead volume ratio = V_D / V_E

V_D = total non - swept internal working gas volume

$\theta = \tan^{-1} \left[(\kappa \sin \alpha) / (\tau + \kappa \cos \alpha) \right]$

The dimensionless heat extracted (Q_{\max}) characterizes the ideal performance of a Stirling cooler in terms of its cycle frequency, maximum and minimum operating temperatures, fluid pressure, cycle phase angle, and machine dimensions/geometry. The utility of this formulation is the ability to optimize the cooler performance analytically by varying these parameters before selecting a final design for prototyping. Once the ideal heat extracted is determined other relevant thermodynamic performance measures can be found:

W = work input per cycle = $(\tau - 1)Q_E$

Q_C = heat dissipated in the compression space per cycle = τQ_E

COP_c = Carnot coefficient of performance = $1 / (1 - \tau) = T_E / (T_E - T_C)$

To make use of the first-order Stirling cycle equations, the various parameters must be defined in terms of the geometry of the MEMS cooler. Figure 5 illustrates an expansion diaphragm and a two-layer regenerator region along with key relevant dimensions. The openings in the regenerator layers are formed by wet etching each layer from the top and bottom resulting in the converging-diverging pattern shown. Anisotropic etching along the 1-1-1 crystal plane of the silicon results in a characteristic angle of 54.7° for all of the sidewalls. Note that the geometry is symmetric about a vertical axis drawn through the center of the device.

Referring to Fig. 5, the swept volume created by the expansion diaphragm as it deflects upward and downward a total of Y_E can be analytically defined by the combination of a cuboid of dimensions $D_p \times D_p \times Y_E$ (formed by the bottom face of the diaphragm) and four prismoids (formed by the sidewalls of the diaphragm). The prismoids have a short side width of D_p , long side width of D_b , length of $T_p / \cos 54.7^\circ$, and diagonal thickness of Y_E . The resulting equation for the total swept volume for the expansion diaphragm is,

$$V_E = Y_E D_p^2 + 2Y_E T_p (D_b + D_p) \tan(54.7^\circ)$$

Similarly, the swept volume in the compression space can be found from,

$$V_C = Y_C D_p^2 + 2Y_C T_p (D_b + D_p) \tan(54.7^\circ)$$

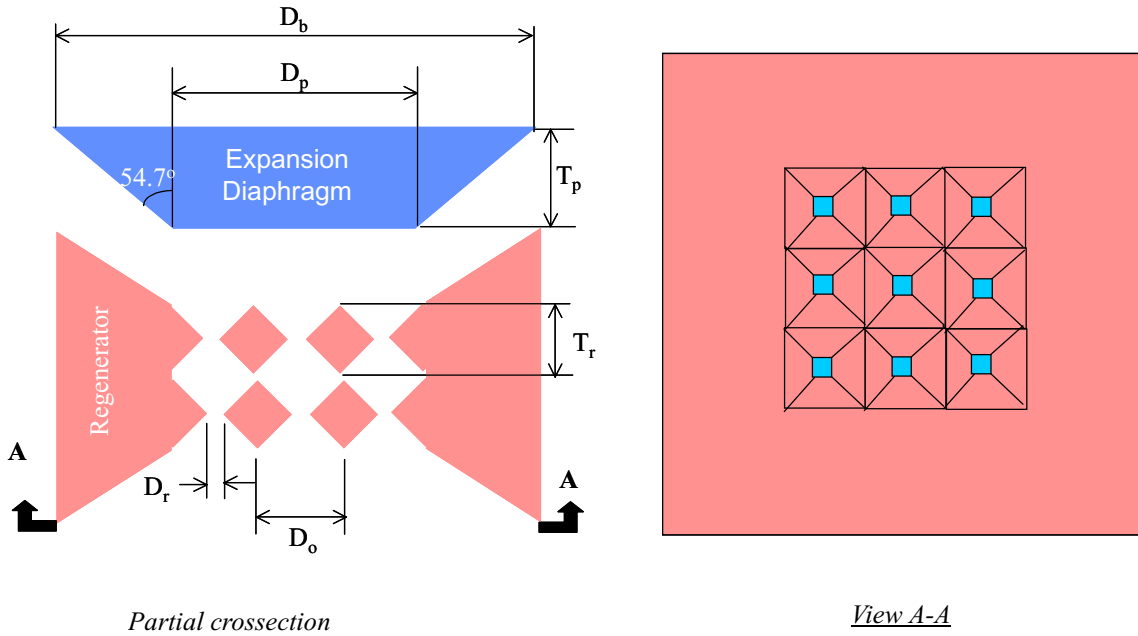


Figure 5. Geometry and Key Dimensions

The dead volume for the MEMS cooler is comprised of the internal volume of the regenerator region (V_r) plus the volume in both the expansion and compression spaces that are not swept out by the diaphragms (V_{ns}),

$$V_D = V_r + V_{ns}$$

For n_o number of regenerator openings and n_r number of regenerator layers, the internal volume of the regenerator can be found from,

$$V_r = T_r n_o n_r \left(\frac{D_o^2 + D_r^2}{2} \right)$$

The non-swept volume can be calculated by assuming the maximum travel of the diaphragms toward the regenerator is T_p , at which point the diaphragms are completely bottomed out against the regenerator. If the inward travel of the expansion and compression diaphragms are denoted by Y_{Ei} and Y_{Ci} , respectively, then the non-swept volume can be found from,

$$V_{ns} = (2T_p - Y_{Ci} - Y_{Ei})D_p^2 + 2T_p(2T_p - Y_{Ci} - Y_{Ei})(D_b + D_p)\tan(54.7^\circ)$$

With these parameters defined for the MEMS cooler, the ideal dimensionless heat extracted (Q_{\max}) can be calculated for any chosen device dimensions. In order to maximize the performance of a stirling cooler, Walker [1] generated design charts that provide the optimal swept volume ratio and phase angle for a given dead volume and temperature ratio. These design charts were used to optimize the MEMS cooler parameters as shown in Table 1 at discrete temperature ratios for a candidate configuration. Note that the swept volume for the MEMS cooler can be simply altered by adjusting the differential voltage used to actuate the diaphragms. The configuration dimensions and resulting ideal performance are given in Fig. 6.

<i>Table 1. Optimized Design Parameters and Resulting Ideal Performance</i>						
τ	κ	X	α	Q_E	W	Q_c
(K/K)			(π radians)	(mW/{KHz-mm ³ -bar})		
1.1	1.03	0.03	0.62	0.38	0.04	0.42
1.2	1.16	0.10	0.62	1.42	0.28	1.70
1.4	1.43	0.23	0.6	2.60	1.04	3.64
1.6	1.74	0.39	0.59	3.21	1.91	5.12
1.8	1.74	0.39	0.59	3.03	2.42	5.45
2.0	1.80	0.43	0.59	3.00	3.00	5.99
2.2	1.91	0.45	0.59	2.98	3.59	6.57
2.4	2.10	0.58	0.58	3.03	4.24	7.26
2.6	2.29	0.67	0.58	3.01	4.84	7.85
2.8	2.40	0.76	0.57	2.96	5.35	8.31
3.0	2.42	0.76	0.57	2.86	5.72	8.58
3.2	2.50	0.78	0.57	2.81	6.15	8.96

Individual Cell Parameters:

- Height = 0.310 mm
- Width = 0.145 mm
- Volume = 0.007 mm³
- Regenerator thickness = 10 microns/layer
- Regenerator layers = 4
- Regenerator orifice size = 2 microns
- Regenerator openings per layer = 4
- Diaphragm thickness = 45 microns

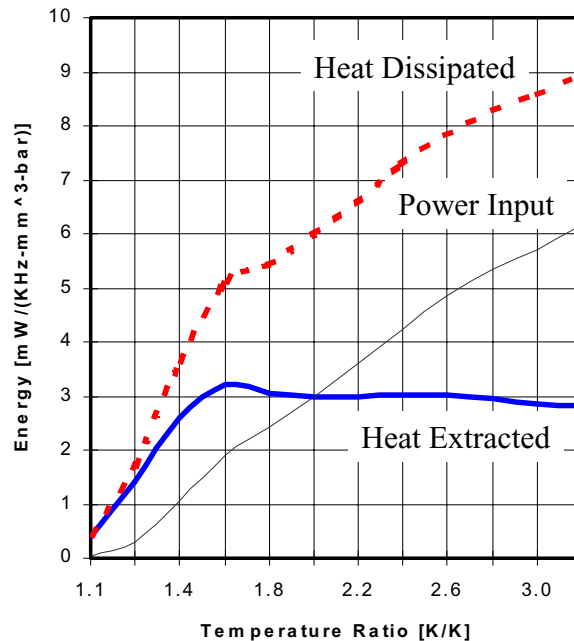


Figure 6. Ideal Thermodynamic Performance

Referring to Fig. 6, the temperature ratio is the ratio between the compression (hot) space absolute temperature and the expansion (cold) space absolute temperature. The energy axis is given in terms of the device operating frequency (in Hz), the device overall volume (in mm³), and the initial charge pressure (in bars). Presenting the results in this form allows quick estimation of the ideal heat extracted, power input, and heat dissipated for an application of interest.

For example, suppose a microprocessor chip needs to be cooled to a case temperature of 20C (293K). The volume available on the surface of the chip for mounting the MEMS cooler is approximately 6 cm³ (2.45 cm square by 1 cm thick). The hot (compression) end of the MEMS cooler at 80C (353K) will be dissipating heat to the ambient air. Therefore the resulting temperature ratio is 1.2. Using Fig. 6 (or Table 1) and assuming the MEMS cooler is

operating at 1KHz with an initial charge pressure of 20 bars (19.7 atm), the ideal performance of the cooler would be:

$$\text{Heat extracted} = [1.4 \text{ mW}/(\text{KHz}\cdot\text{mm}^3\cdot\text{bar})][1\text{KHz}][6000 \text{ mm}^3][20\text{bar}] = 168000\text{mw} = \underline{168\text{W}}$$

$$\text{Power input} = [0.3 \text{ mW}/(\text{KHz}\cdot\text{mm}^3\cdot\text{bar})][1\text{KHz}][6000 \text{ mm}^3][20\text{bar}] = 36000\text{mw} = \underline{36\text{W}}$$

$$\text{Heat dissipated} = [1.7 \text{ mW}/(\text{KHz}\cdot\text{mm}^3\cdot\text{bar})][1\text{KHz}][6000 \text{ mm}^3][20\text{bar}] = 204000\text{mw} = \underline{204\text{W}}$$

Note that in order to achieve this performance in a practical application, the system would have to be thermally balanced to dissipate the heat required. In practice, this might involve attachment of fins to the upper (hot) side of the MEMS cooler and/or use of cooling fans. However, the advantage is a relatively high overall cooling capacity of 168W with only 36W of input power while maintaining the processor chip case at a reduced temperature of 20C.

Coupled Analyses

As previously stated, the first-order Stirling cycle analysis presented above provides only an ideal estimate of the MEMS cooler performance. This ideal performance must be adjusted to account for real gas behavior and other effects that violate the assumptions of the first-order thermodynamic analysis. In addition, coupling of other analyses must be accomplished to predict the true performance of a chosen design. These other analyses include fluid/gas dynamics, electrostatics, thermal, structural, dynamics, and materials. Formulation of the coupled analyses is currently ongoing, and the basic considerations for each are described below.

Fluid/Gas Dynamics

A key assumption of traditional gas dynamics analysis is that the gas behaves as a continuum. This assumption is violated if the mean free path of the gas molecules begins to approach the characteristic dimension of the system. At that point, the gas behavior diverges from macroscopic (continuum) theory and enters the realm of microscopic (kinetic) theory. Two situations where this can occur are in rarified gases (e.g. upper atmosphere or partial vacuums) or very small scale systems (e.g. MEMS).

The Knudsen number provides a method of quantitatively testing the assumption of continuum behavior [2]:

$$Kn = \frac{\lambda}{d}$$

Where:

$$\lambda = \text{mean free molecular path length} = \frac{\mu}{\rho} \sqrt{\frac{\pi M}{2RT}} \quad (\text{for a gas at rest in local equilibrium})$$

d = smallest appropriate characteristic dimension

μ = dynamic viscosity ρ = density T = temperature M = molecular weight R = gas constant

Alternatively, the Knudsen number for flowing gases can be calculated from [2]:

$$Kn = \frac{Ma \sqrt{\pi \gamma / 2}}{Re}$$

Where:

$$Ma = \text{Mach number} = \frac{v}{\sqrt{\gamma R T / M}}$$

$$Re = \text{Reynolds number} = \frac{\rho v L}{\mu}$$

$$\gamma = \text{ratio of specific heats} = C_p / C_v$$

v = velocity T = temperature

If the Knudsen number is “negligibly small” then the continuum assumption is valid. If Kn is “everywhere large” then the flow is free molecular (non-continuum). Otherwise, for an “intermediate” value of Kn , the flow is transitional and limited theory or data exists. Wong and Bestok [3] provide more precise definitions of the flow regimes characterized by the Knudsen number:

$Kn < 0.01$ (continuum)

$0.01 < Kn < 0.1$ (slip flow)

$0.1 < Kn < 3$ (transition)

$Kn > 3$ (free molecular flow)

As the mean free path length approaches the characteristic system dimension, slip begins to occur at the flow boundary. Recall that for fully developed internal flow, continuum theory holds that no slip occurs at the solid-fluid boundary. This onset of boundary slip as free molecular flow begins to dominate results in a lower effective frictional factor at the boundary and a subsequent higher flowrate than would be anticipated by continuum theory. To account for this effect, Madou [4] provides a corrected Navier-Stokes equation for Poiseuille flow in the micro-domain:

$$f = \left(\frac{16}{Re} \right) \left(\frac{1}{1 + 8 \lambda / d} \right)$$

Analysis of the gas dynamics and associated viscous losses must begin with an assessment of which flow regime is present in every region of the MEMS cooler. Based on that assessment, the appropriate relations can be used to estimate the frictional losses and subsequent pressure drops in the device. Note that viscous effects scale favorably in the micro-domain due to the boundary slip phenomenon described.

Electrostatic Forces

The MEMS cooler design is compatible with a variety of microactuation techniques for deflecting the diaphragms. Selection of an optimum technique will be driven by the requirements for force, displacement, response time, power input, thermal effects, and other factors. Initially, pure electrostatic actuation will be investigated for the device.

An electrostatic force is produced by applying a voltage across two conducting surfaces with a gap between them. For two parallel opposing plates as shown in Fig. 7, the maximum electrostatic potential is given by [5]:

$$E_{em} = \frac{\epsilon_r \epsilon_0 h_w V_b^2}{2d}$$

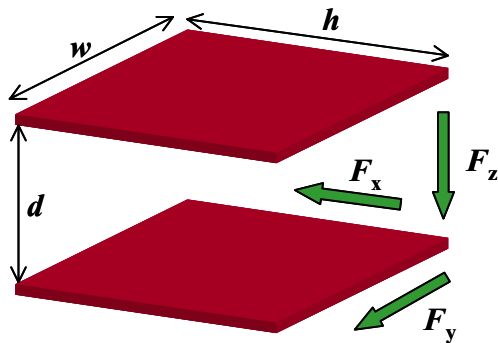
Where:

ϵ_r = relative permittivity of the dielectric (= 1 for vacuum and ~ 1 for air)

ϵ_0 = dielectric constant

V_b = breakdown voltage

It is evident from the above equation that the breakdown voltage drives the maximum electrostatic potential, and hence the maximum electrostatic force that can be produced. For gaps containing gases that can be treated as a continuum, the breakdown voltages decreases gradually as the product of the gas pressure and gap dimension decreases. However, when the conditions in the gap approach the non-continuum region (i.e. the mean free path length approaches the gap dimension), the breakdown voltage increases rapidly as the product of pressure and gap decreases. This relationship is determined experimentally, and the resulting graphs are known as Paschen curves with the general shape as shown in Fig. 8.



Breakdown Voltage

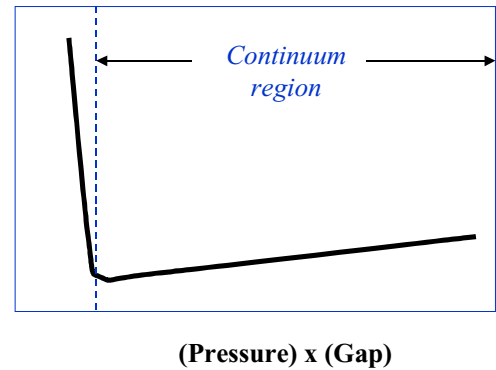


Figure 7. Electrostatic Forces Between Parallel Plates

Figure 8. Paschen Curve Shape

For air at one atmosphere, the transition between continuum and non-continuum behavior occurs at about 5 microns [4]. For example, the increase in breakdown voltage going from a gap of 10 microns to 2 microns is about an order of magnitude. However, another order of magnitude increase in breakdown voltage occurs with a mere decrease in gap from 2 microns to 1.5 microns [6, 7]. As a result, relatively high electrostatic forces can be generated in MEMS devices containing small gaps.

The attractive force between two parallel plates perpendicular to the plate surfaces (see Fig. 7) can be found from²:

$$F_z = -\frac{\partial E_e}{\partial z} = \frac{\epsilon_r \epsilon_0 h w V^2}{2d^2}$$

Where V is the applied voltage, and must be less than the breakdown voltage. The inverse relation of the electrostatic force to the square of the parallel plate gap distance demonstrates the potential to achieve exponentially large forces as the gap is reduced. Forces are also generated parallel to the plate surfaces if they are horizontally offset from each other. Comb drives are commonly used in micromachines to take advantage of this effect. The lateral forces generated by offset parallel plates can be found from:

$$F_x = -\frac{\partial E_e}{\partial x} = -\frac{\epsilon_r \epsilon_0 w V^2}{2d}$$

² Neglecting the effects of fringing fields which would result in a slightly higher predicted force.

$$F_y = -\frac{\partial E_e}{\partial y} = -\frac{\epsilon_r \epsilon_0 h V^2}{2d}$$

An added advantage of using pure electrostatic actuation is the ability to sense the displacement of the diaphragms by measuring the capacitance. The capacitance of two parallel plates is given by,

$$C = \frac{\epsilon_r \epsilon_0 h w}{d}$$

Referring back to Fig. 2, it can be seen that the physical geometry of the diaphragms and cap plates is equivalent to aligned parallel plates, and therefore generates a perpendicular attractive force when a differential voltage is applied. This scenario produces the outward deflection of each diaphragm. The inward deflection, however, is caused by an applied voltage between each diaphragm and the adjacent regenerator side walls. The resulting electrostatic forces have both perpendicular and parallel components.

Thermal Considerations

Perhaps the greatest deviation from the first-order thermodynamic analysis is due to thermal effects. The heat transfer between the gas and the regenerator is highly transient with both the gas temperatures and regenerator temperatures changing during each cycle in both space and time. In addition, changing temperature gradients exist in the regenerator, the expansion space, and the compression space. The cumulative effect of these deviations from the first-order analysis results in parasitic losses in the ideal performance of the device.

From a design standpoint, a key thermal challenge is to effectively transfer heat from the expansion and compression spaces to their respective adjoining cap plates. At the same time, heat transfer between the expansion and compression spaces must be minimized by thermally isolating the regenerator layers and maintaining a temperature gradient within the regenerator.

If the device dimensions result in gas flows in the non-continuum regime (i.e. free molecular flow), then the temperature difference between the flowing gas and the solid boundary increases due to the discontinuity introduced by boundary slip flow. Also, as the mean free path length approaches the characteristic dimension of the gap, the thermal conductivity of the gas decreases. To account for the latter effect, conduction across small gaps of dimension d can be approximated by [4]:

$$Q = \frac{k\Delta T}{d + 2g}$$

Where:

k = gas thermal conductivity

$2.4\lambda < g < 2.9\lambda$ (for air, oxygen, nitrogen, carbon dioxide, helium, & methane)

$g = 11.7\lambda$ (for hydrogen)

Similar to the gas dynamics analysis, heat transfer in the MEMS cooler must be evaluated for each region to ascertain whether continuum theory is valid. Once that determination is made, the appropriate heat transfer relations can be used to calculate the thermal performance of the device.

Other Coupled Analyses

Other key analyses – such as structural, dynamic, and materials - must be performed on the MEMS cooler device and properly coupled to characterize overall operation. For example, Fig. 9 shows a free body diagram of the forces acting on the device diaphragm as it is deflected inward by electrostatic actuation (assuming the diaphragm does not

make contact with the regenerator region). The electrostatic force is counteracted by a combination of three forces: reduced gas pressure above the diaphragm, increased gas pressure below the diaphragm, and the structural reactive force resulting from the deflection induced stress in the diaphragm. The structural reactive force will depend on the mounting configuration and material properties of the diaphragm. Together, these forces dictate the maximum deflection and acceleration of the diaphragm from its at rest position to fully actuated.

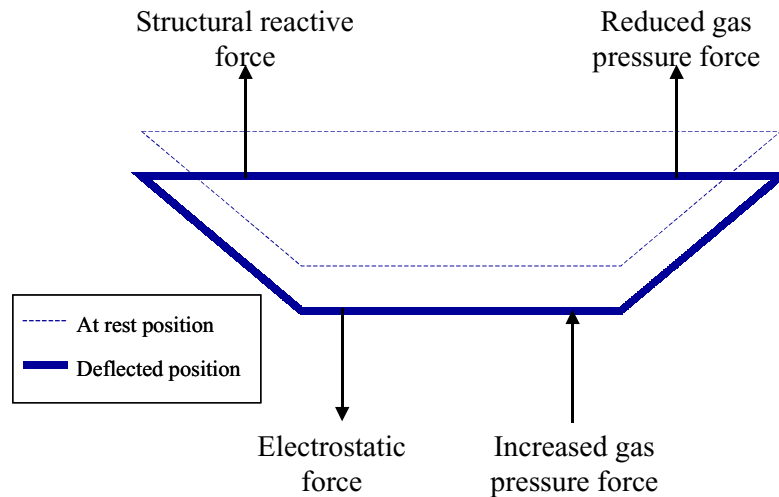


Figure 9. Forces Acting on Deflected Diaphragm

The forces denoted in Fig. 9 must be calculated in stepwise fashion using an incremental deflection value until all of the forces are balanced. This equilibrium condition will occur at the maximum deflection of the diaphragm, and is therefore a key design parameter that will dictate the appropriate actuation voltage.

Dynamic response of the device diaphragms is also critical. Induced vibrations caused by the oscillatory motion of the diaphragms will be of primary interest for some applications. In addition, the resonant frequencies of the diaphragms must be properly estimated since operation of MEMS devices near resonance can result in as much as an order of magnitude change in moving part displacements depending on the structures involved. As a result, resonance can be operationally avoided to prevent undesirable responses, or advantageously used to maximize displacements. In either case, the resonant frequencies must be known.

Finally, the effect of material properties and fabrication processes on the device must be understood to insure acceptable performance. Silicon, for example, is an excellent structural material at micro-scales with a higher yield strength and equivalent Young's modulus relative to steel; but having only about one-third the density of steel. However, silicon is known to be permeable to hydrogen (and probably helium) which is often used in Stirling cycle coolers due to its tendency to behave more like an ideal gas in terms of viscous losses. If hydrogen is used for the device, a diffusion-mitigating coating (e.g. nitride) will probably be necessary to keep the working gas at operating pressure throughout the device's life. In terms of fabrication processes, a variety of issues such as dimensional tolerances, layer-to-layer indexing, residual stresses, and many others must be addressed early in the conceptual design stage.

SUMMARY

Overall analysis of the MEMS cooler device requires the coupling of multiple separate analyses including: thermodynamic, fluid/gas dynamic, thermal, electrostatic, structural, dynamic, and materials. Early in the conceptual design stage, first-order analyses formulated from the basic physics involved allow rapid convergence on a workable

concept design and permit initial optimization of key parameters. This approach also uncovers key issues relative to the device operation early in the development process.

A first-order Stirling cycle analysis has been performed on the MEMS cooler by modifying established equations for the unique geometry of the device. The resulting equations have been optimized for a candidate design to provide ideal performance curves as a function of the expansion (cold) and compression (hot) space temperatures. An application example of cooling a microprocessor chip indicates that the MEMS cooler could ideally provide nearly 170W of overall cooling with an input power of less than 40W. Deviations from ideal performance require the coupling of other analyses to account for real gas behavior and other irreversibilities in the actual cycle.

One of the key assumptions that must be tested for the thermal, fluid, and electrostatic analyses is whether continuum theory is valid. In the micro-domain, the mean free molecular path length can approach the characteristic dimension of a MEMS device and invalidate continuum theory. The Knudsen number is used to test this condition for both fluid flow dynamics and fluid-solid heat transfer. Appropriate relationships have been identified for flow friction factors and gas conduction in the non-continuum regime. Regardless of the flow/thermal regime, the heat transfer between the working gas and the regenerator - as well as the between the diaphragms and caps plates - are key design issues.

For electrostatic analysis, the product of gap dimension and pressure defines the continuum domain. Paschen curves provide a means of estimating the breakdown voltage in both the continuum domain and the non-continuum regimes. Since the electrostatic force between two parallel plates in the perpendicular direction is inversely proportional to the square of the gap dimension between them, relatively high forces can be generated for micro-scale gaps. Relationships for this force and the parallel electrostatic forces produced by offset parallel plates have been identified for use in estimating the deflection of the MEMS cooler diaphragms. Also, since capacitance measurements can be used to indicate the gap magnitude, feedback on the diaphragm deflections can be acquired during operation.

Both fluid flow and electrostatic actuation scale favorably to the micro-domain. For fluid flow, as the mean free molecular path approaches the characteristic dimension, slip occurs at the solid-fluid boundary. As a result, the effective friction factor is reduced allowing higher potential flowrates for the same pressure differential. In terms of electrostatics, the breakdown voltage increases dramatically with decreasing gap dimension in the non-continuum domain allowing for the use of much higher driving voltage potentials.

Other analyses must also be performed and appropriately coupled to characterize the MEMS cooler performance. Structural analysis is needed to both verify that the device will not fail and to determine the structural reactive force produced by the electrostatic actuation of the diaphragms. Dynamic analysis is required to estimate induced vibrations caused by the device and to identify the resonant frequencies. Material properties and fabrication processes must also be carefully analyzed to insure proper device performance.

REFERENCES

1. Walker, G., Stirling Cycle Machines, 1976.
2. Rohsenow, et.al., Handbook of Heat Transfer Fundamentals, 2nd Ed., McGraw-Hill, 1985.
3. Wong, Chaney (1999) and Bestok, Ali (1995).
4. Madou, M., Fundamentals of Microfabrication, CRC Press, 1997.
5. Trimmer, T., "Micromechanical Systems", Proceedings of Integrated Micro-Motion Systems: Micromachining, Control, and Applications, pp1-15, October, 1990.
6. Bart, et.al., "Design Considerations for Micromachined Electric Actuators", *Sensors and Actuators*, Vol. 14, pp 269-292, 1988.
7. Busch-Vishniac, I.J., "The Case for Magnetically Driven Microactuators", *Sensors and Actuators*, Vol. A33, pp207-220, 1992.

THERMAL ANALYSIS METHODS FOR AN EARTH ENTRY VEHICLE

Ruth M. Amundsen, John A. Dec, Michael C. Lindell

National Aeronautics and Space Administration

Langley Research Center

Hampton, Virginia 23681-2199

ABSTRACT

Thermal analysis of a vehicle designed to return samples from another planet, such as the Earth Entry vehicle for the Mars Sample Return mission, presents several unique challenges. The Earth Entry Vehicle (EEV) must contain Martian material samples after they have been collected and protect them from the high heating rates of entry into the Earth's atmosphere. This requirement necessitates inclusion of detailed thermal analysis early in the design of the vehicle. This paper will describe the challenges and solutions for a preliminary thermal analysis of an Earth Entry Vehicle. The aeroheating on the vehicle during entry would be the main driver for the thermal behavior, and is a complex function of time, spatial position on the vehicle, vehicle temperature, and trajectory parameters. Thus, the thermal analysis must be closely tied to the aeroheating analysis in order to make accurate predictions. Also, the thermal analysis must account for the material response of the ablative thermal protection system (TPS). For the exo-atmospheric portion of the mission, the thermal analysis must include the orbital radiation fluxes on the surfaces. The thermal behavior must also be used to predict the structural response of the vehicle (the thermal stress and strains) and whether they remain within the capability of the materials. Thus, the thermal analysis requires ties to the three-dimensional geometry, the aeroheating analysis, the material response analysis, the orbital analysis, and the structural analysis. The goal of this paper is to describe to what degree that has been achieved.

INTRODUCTION

The purpose of the Mars Sample Return Mission is to return a sample of Martian material to Earth so that it may be studied here. In order for the return of the samples to the Earth's surface to be successful, the Earth Entry Vehicle (EEV) must be robust and extremely reliable. Some of the reasoning behind design of the vehicle is discussed in an earlier publication on a similar design.¹ This paper will describe the thermal modeling and design of one possible design of an EEV (CP5.7) of the many designs under evaluation. The design of a Mars Sample Return Earth Entry Vehicle has many unique finite element modeling challenges associated with it, both of a structural and thermal nature. The purpose of the Earth Entry Vehicle is to protect Mars samples from the mechanical and thermal environment encountered during Earth entry and landing, while assuring sample containment. The science requirement on thermal design is that the returned samples will not experience a temperature over 50°C throughout all mission phases. The system requirement is that no component should go outside its survival temperature range during cruise, or outside its operational temperature range during operation.

The EEV expected lifetime of about three years can be separated into several distinct thermal phases. For the most part of three years (phase 1), it would be attached to the spacecraft during the planetary travel and sample collection intervals. Several days before arrival into the Earth's atmosphere, the EEV would be spin-ejected from the spacecraft and begin the exo-atmospheric cruise portion (phase 2) of the journey. The entry into Earth's atmosphere would be the third phase, with aerodynamic heating boundary conditions very different than the first two phases. The fourth phase would be equilibration of the EEV to ambient temperature conditions on the Earth's surface after landing. Only the last three phases are discussed in this paper.

This paper will describe the challenges inherent in this analysis, and the solutions employed. One challenge is keeping up with rapid design changes and rapid trajectory changes. In order to be useful, the analysis must be able to respond with quick answers to "what-if" scenarios regarding geometry or trajectory changes. Another challenge is defining the exterior properties of the vehicle so that appropriate temperatures are maintained both while attached to the spacecraft, and after separation. The cruise after separation is in a hyperbolic orbit, which complicates the simulation. The heat pulse at entry challenges both the mesh density and the thermal solver. The material responses (such as pyrolysis) during the heat pulse must be taken into consideration. Finally, three-dimensional orthotropic properties on these randomly oriented components are a challenge to incorporate.

The thermal analysis results are valuable for several reasons. First, the thermal environment experienced by the returned samples can be predicted, and if not acceptable for science reasons, design modifications can be made. The thermal history of each material in the vehicle design can also be compared to its survival range, to ensure that all designed materials are adequate. The thermal predictions for operational mechanical and electronic components can be used to ensure they remain within their acceptable thermal range. Another use for the thermal predictions is to predict thermal stresses and deflections in the vehicle. The exo-atmospheric phases involve cold temperatures and slow changes, as well as a moderate gradient across the vehicle. The entry phase involves very rapid changes in temperature and gradients across the vehicle. Each thermal case can be used for structural analysis of the vehicle, to determine if unacceptable stresses or deflections are encountered.

DESIGN DESCRIPTION

This particular preliminary design of an EEV is shown in Figure 1. This is a concept called CP5.7, which incorporates a carbon-phenolic ablator. An earlier design concept utilizing a different ablator is described in an earlier publication². This is an on-going design process, and both the design and associated analysis are expected to change. The forebody thermal protection system (TPS) is carbon-phenolic, and the afterbody TPS is SLA-561V. Both materials have substantial heritage in aerospace missions. The substructure is carbon-carbon. The wing foam is a low density but stiff carbon foam. The samples are held within an orbiting sample canister (OS), and the OS is enclosed within a containment vessel (CV). The CV/OS is within an impact sphere filled with energy absorbing material. The entire forebody is covered with a 3-layer multi-layer insulation blanket (MLI) that extends back to the spin-eject ring on the aft side. The spin-eject ring is where the EEV is mounted to the spacecraft via a mechanism that accomplishes separation and spin-up.

During the 4-day exo-atmospheric cruise after separation, the spin stabilized EEV is in a hyperbolic orbit ending at atmospheric entry. The solar angle during this cruise is at roughly 45° off the nose, such that the solar flux falls only on the forebody.

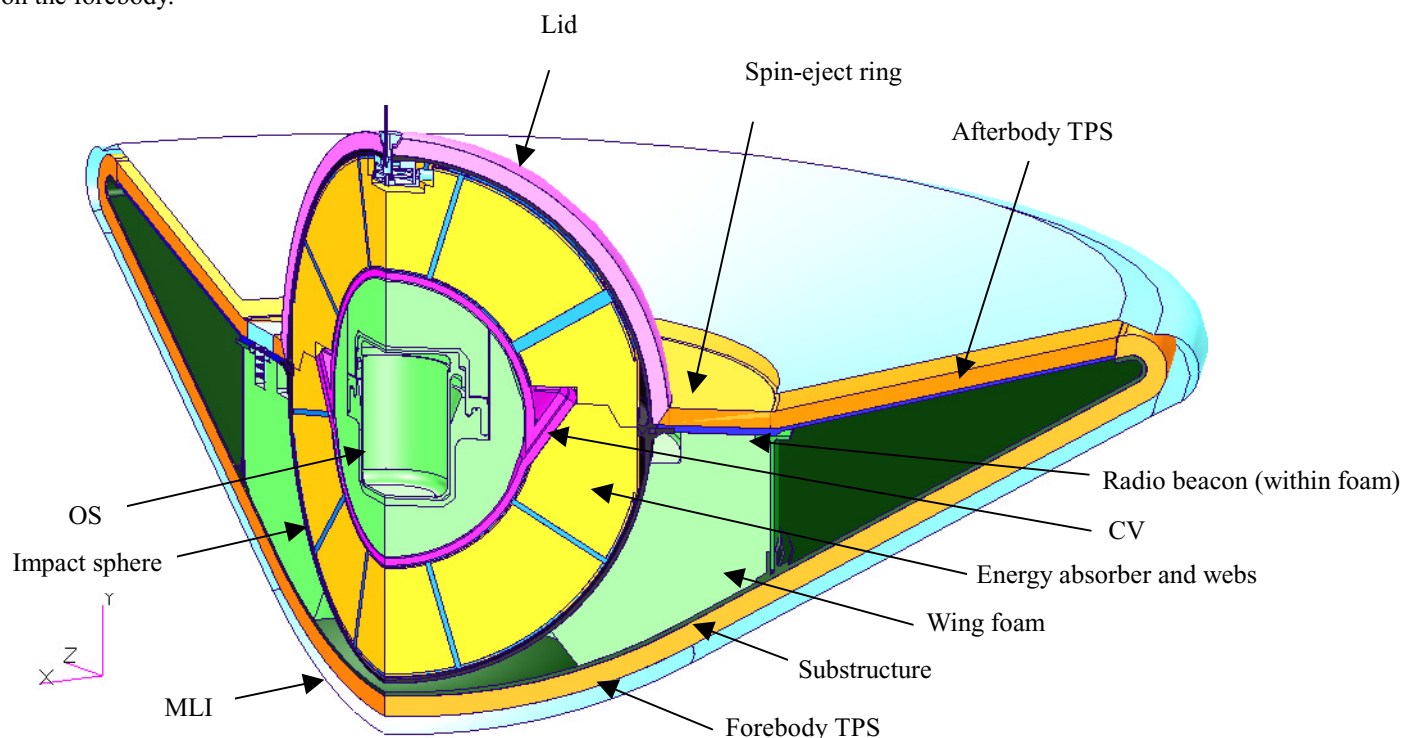


Figure 1. EEV model geometry (120°).

THERMAL MODELING

Geometry

One challenge in modeling an Earth Entry Vehicle (EEV) during preliminary design is tracking frequent design changes. It is important to have an analysis method that allows quick evaluation of potential design modifications. The method employed in this analysis is to import design geometry directly from the computer-aided design (CAD) software Pro/Engineer³ into the modeling software MSC/PATRAN^{4*}. This geometry can be directly meshed to create the analysis model. In some cases, a design modification can be evaluated by simply altering a material or boundary condition in the model. For a more substantial design change, a new geometry or part must be imported. Even when a new geometry is imported, re-analysis can be relatively fast since all the boundary conditions and materials applied to the geometry can be re-used. In this manner, design changes and updates can be rapidly incorporated, rather than necessitating long periods of manual dimension input to the modeling software.

The geometry comes into PATRAN with all parts separated into groups, which facilitates meshing, application of properties and boundary conditions, and model changes. The thermal solver is currently PATRAN Thermal 9.0. The thermal models capture only a portion of the vehicle since it is largely axially symmetric; 120° of the vehicle was modeled to capture non-symmetric items such as body mount bolts, radio beacon, push pads, etc. A previous study evaluated use of a 2D axi-symmetric model. 2D axi-symmetric and 3D partial models were developed, and solved for the same boundary conditions. The 2D axi-symmetric model did not give a faster solution time, and is actually more time-consuming to create from the CAD geometry. Three-dimensional models also allow capturing the behavior of the non-symmetric components. Thus, the 3D models were used for the remainder of the work.

Analysis Methodology

The overall analysis process is shown in Figure 2. Geometry, trajectory, heating and material response information are all incorporated in the PATRAN model. Thermal solution is done with PATRAN Thermal, and temperatures are passed to NASTRAN for structural analysis. Each of these steps will be described in later sections.

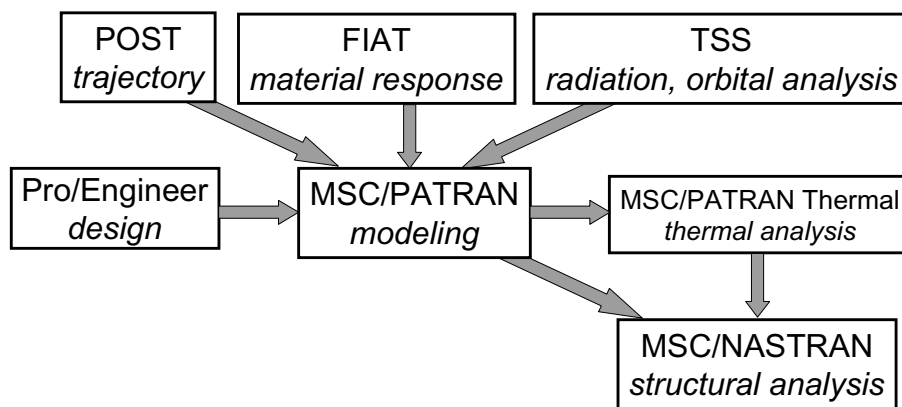


Figure 2. Integrated analysis process.

The modeling is separated into four distinct phases: cruise with the spacecraft, post-separation exo-atmospheric cruise, atmospheric entry to landing, and post-landing. The different phases of analysis have very different timelines and boundary conditions, as well as different requirements for integrating with other analysis. The exo-atmospheric cruise portion may last for several days, and it must include the effects of orbital radiation fluxes. The heat pulse at entry is less than a minute, the entire descent is less than seven minutes, and this model must include aerodynamic heating and material response. Each of these phases must be integrated with structural analysis in order to determine the structural behavior in each phase.

* The use of trademarks or names of manufacturers in this report is for accurate reporting and does not constitute an official endorsement, either expressed or implied, of such products or manufacturers by the National Aeronautics and Space Administration.

The exo-atmospheric cruise phase and the entry phase have similar boundary conditions in that both have heat fluxes, convection and radiation applied to the entire exterior of the vehicle. However, in the entry phase the heat pulse is severe enough that a very fine mesh must be used. This model is a transient that only lasts for 360 seconds, so the solution time can be kept reasonable even with a very fine mesh. If that dense a mesh were used on the exo-atmospheric case, where the transient is four days and there are many parametric cases to be run, solution time would be excessive. Thus, the same geometry and materials are shared between these two models, but the meshing is different. Temperatures are transferred between the model phases by mapping the results back to the geometry, independent of the differing meshes.

The post-landing model is very similar to the exo-atmospheric case in that it is a long-term transient (24 hours) where a coarse mesh is acceptable. Thus, the same geometry and mesh as the exo-atmospheric case are used, although most boundary conditions are different. The post-landing state of the vehicle presents a challenge since there are many possible alternatives. The vehicle may be in any one of many possible orientations, yielding a host of potential air convection and ground contact possibilities. The range of possible ground material compliance is wide, which can vary the amount of the vehicle in contact with the ground. Also, the time interval before the vehicle is located is variable, and the ambient temperature and wind conditions are difficult to predict. Thus, several general cases must be run to bound the problem.

Model Development

After import from Pro/Engineer, the model consists of trimmed solids. These are a type of solid that can be automatically meshed using tetrahedral (tet) elements in PATRAN, but cannot be automatically meshed with brick (6-sided) elements. Tetrahedral meshes were sufficient for the exo-atmospheric and landed models, since the heating levels were benign enough at the surface to allow a converged solution using tet elements. For these models the imported solids were meshed directly, leading to roughly 50,000 nodes. The exo-atmospheric model is shown in Figure 3 and Figure 4.

The entry model cannot use tet elements on the exterior surfaces. The heating levels drive the tet elements unstable and convergence cannot be achieved without extremely small elements. Also, meshing with tet elements does not allow the charring of the surface to be modeled in successive regular layers with a controlled depth. In order to mesh this model with appropriate bricks, quad surface meshes were developed on the open faces and swept through the model to create bricks that were associated to the original geometry. On some of the interior components, thermal change was slow enough to allow direct tet meshes of the solids. The complete model is shown in Figure 5. The total number of nodes in the model is much larger than in the exo-atmospheric model due to the finer mesh -- 350,000 nodes resulted when the interior was meshed with bricks; the brick-tet hybrid mesh yielded 181,000 nodes. The entry model did not include MLI since this is assumed to burn away very early in the descent.

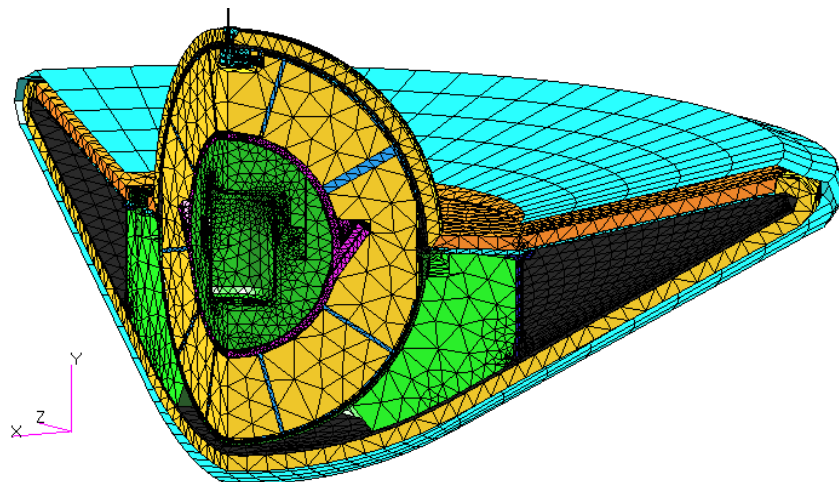


Figure 3. Mesh of exo-atmospheric model.

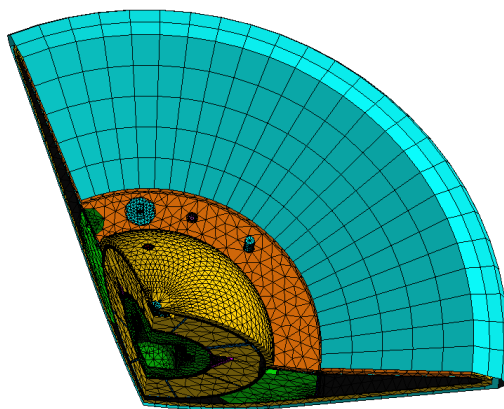


Figure 4. Exo-atmospheric model mesh, showing lid and aftbody penetrations.

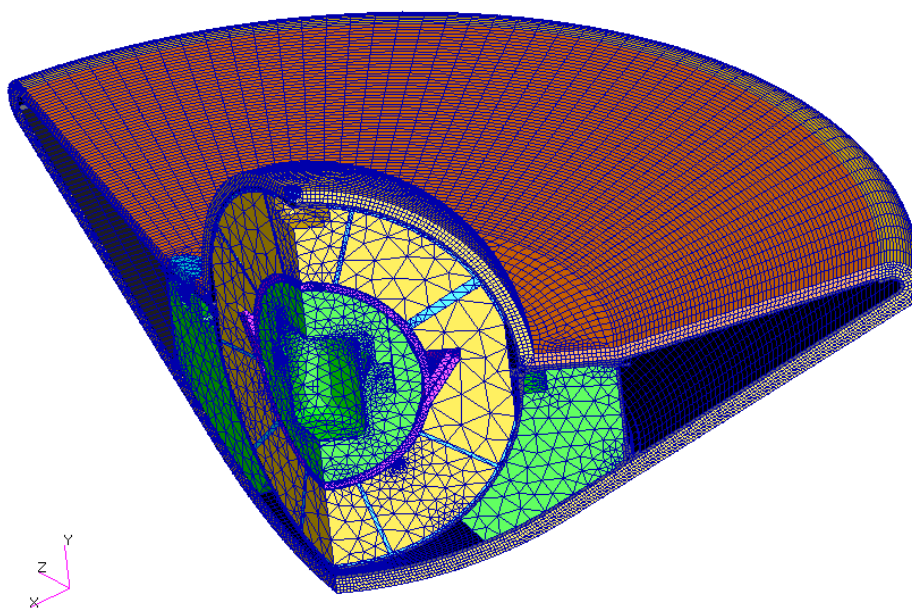


Figure 5. Mesh of entry model.

In both models, boundary conditions and material properties were applied to the geometric entities, rather than to the mesh. Applying boundary conditions to the geometry, rather than the mesh, facilitates both the evaluation of different mesh densities as well as re-meshing when necessary.

Heat Flux Boundary Conditions

A common change that must be anticipated when performing detailed thermal analysis early in the design of the vehicle is modifications to the trajectory and heating rates. When the trajectory changes, both the exo-atmospheric cruise and entry heating loads are affected. Rapid evaluation of the changes is beneficial in allowing final trajectory design. Heat flux boundary conditions are applied via an external text file, so that changes to the trajectory and heating rates can be easily made via substitutions in that file.

Integration with Orbital Analysis

The modeling of orbital fluxes could not be done using PATRAN, so the Thermal Synthesizer System (TSS)⁵ software was used. The orbital heat loads during the exo-atmospheric phase must be calculated for a hyperbolic orbit. Many of the available orbital/radiation analysis tools do not handle hyperbolic orbits. TSS was used because of its capability to handle a hyperbolic orbit analysis via input of discrete trajectory points. TSS does not currently have geometry import capability from Pro/Engineer or PATRAN. Thus, this model was developed independently.

This was not a large effort since only the main exterior shapes of the vehicle need to be captured. In order to allow rapid response to design changes, the model was built using variables. By changing one or many of only five variables, the entire outer shape of the vehicle could be modified. This method allowed quick calculation of orbital heating on the exterior of the vehicle, from both solar and planetary sources, for a variety of vehicle shapes, exterior properties and trajectory definitions.

Figure 6 shows an example TSS model with heat fluxes on the vehicle surface, as well as a representation of the final orbit points. Visual verification of the trajectory, orientation and exterior heat fluxes is of significant benefit in the analysis. The vehicle is spinning at 2 rpm, so calculated fluxes were averaged around the vehicle to account for the spin. The averaged fluxes were applied to the PATRAN model as a surface boundary condition. The heat loads from this analysis are automatically captured in a single file, thus simplifying the incorporation of this data into the overall thermal analysis and the evaluation of several trajectories for a single vehicle design.

Since the TSS model is developed independently, this is not a complete analysis integration. However, for this simple exterior, development and modification of the separate model is relatively trivial. Although a tighter integration would be preferable for a more complex model, in this case it is not essential. Future revisions of this process are planned whereby the orbital model will be developed from a STEP* format output of the geometry. Also, the output heat load file format will be modified such that no manual editing is required.

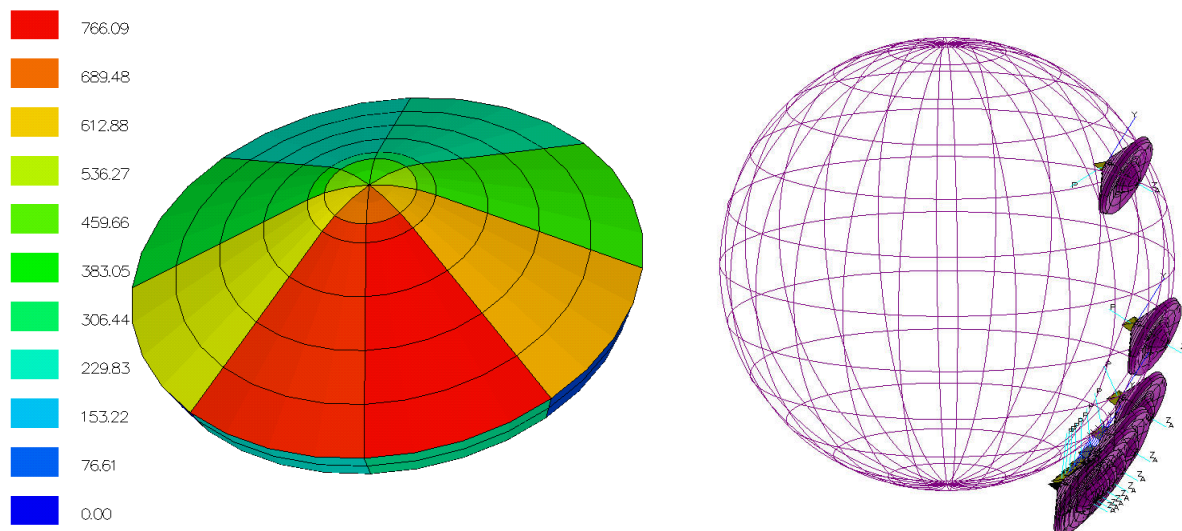


Figure 6. TSS solar flux prediction (W/m²) and trajectory orientation.

Integration with Aeroheating and Material Response

The heat pulse of an earth entry must be modeled precisely in order to fully understand its effect on the subsequent thermal behavior. The aerodynamic heating is a function not only of time, since velocity and atmosphere are both altering radically with time, but also of the position on the vehicle surface. Unique methods were developed to incorporate an accurate representation of this heating into the model.

CFD predictions of heating on the vehicle surface were performed for several discrete time points. In order to have a transient heating profile that includes trajectory effects, the Program to Optimize Simulated Trajectories (POST) code was run. The aerodynamic heating values from this code were corrected using CFD results. This code predicts cold-wall heating values, and does not account for the blocking effect due to ablation and pyrolysis of the TPS material. These material response effects are captured in the Fully Implicit Ablation and Thermal Analysis Program (FIAT)⁶ used by NASA Ames for preliminary TPS sizing. FIAT accounts for all of the physical and chemical

* Standard for the Exchange of Product Model Data (STEP)

processes occurring in the TPS material. The output used from FIAT for this thermal analysis was the hot wall ablative heat flux. This heat flux includes the effects of the actual temperature of the vehicle surface as well as ablation and pyrolysis blocking of heat (blowing factor). This heat flux was used as the input to the PATRAN model. The FIAT analysis is currently only 1D, so several discrete points were used with appropriate spatial factors between them in accordance with the shape of the heating observed in CFD analysis.

These heat flux predictions on the forebody showed gradients both in time and spatial position. To capture this on the forebody, the stagnation point heating (convective plus radiative) as a function of time (Figure 7) was multiplied by the spatial factor on the forebody as function of radial distance (Figure 8). This spatial factor was thus assumed to be constant with time, when it actually changes with time. This will be improved in later modeling, but since the factor is only important over a short time period (about 30 seconds), the approximation is good enough for preliminary design evaluation.

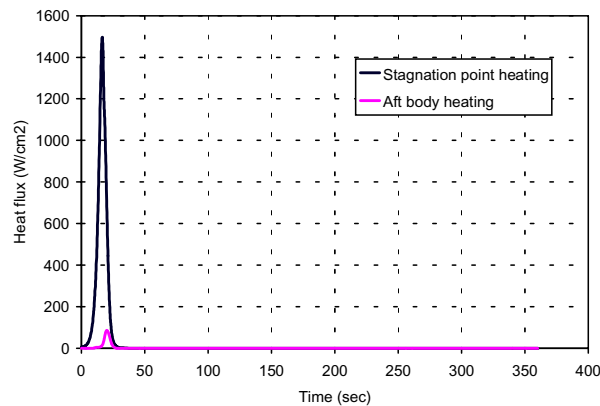


Figure 7. Heat flux versus time on EEV (CP5.7).

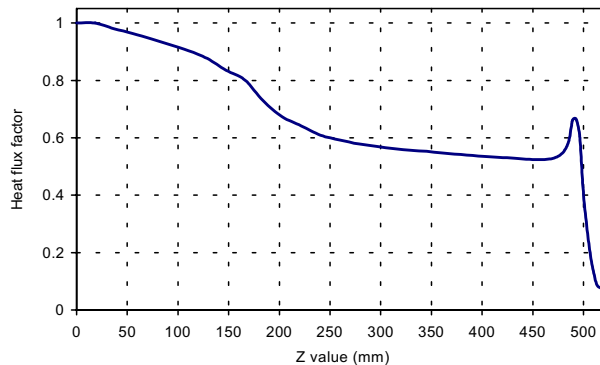


Figure 8. Spatial factor on forebody (CP5.7).

On the afterbody, due to the uncertainty in the spatial variation of afterbody CFD predictions, three points were used for heat flux predictions. The three points were at the aft body stagnation point on the lid, the interior corner where the lid TPS meets the aft TPS, and a point on the shoulder at the max vehicle diameter. Then time-varying spatial factors were developed to interpolate heating between the points. Figure 7 shows the aft body stagnation point flux. Two boundary conditions were created, one between the stagnation point and the interior corner, the other between the shoulder and interior corner. The spatial factors for these boundary conditions were found by dividing the flux at the interior corner by the flux at the stagnation point and flux at the shoulder for each respective set, then interpolating between 1.0 and these ratios. When the flux ratios were plotted over time, they were found to vary. Fortunately, the variations could be separated into three different time intervals in which they were generally constant, and therefore three different spatial fields could be created for each area, and three heat flux boundary conditions could be applied to the lid TPS and aft TPS. To ensure that each boundary condition was active only

during the appropriate time interval, the heat flux boundary conditions were created with unit step-function multipliers to turn them on and off. As an example, the flux applied to the lid TPS was thus the product of the flux at the stagnation point, the spatial factor between the stagnation point and interior corner, and a step function that changed between 1 or 0 based on time.

The heating data when applied in this manner does not account for the charring effects of the ablative TPS materials. In order to correct this, the thermal predictions for TPS sizing at the stagnation point (done by YK Chen at NASA Ames) were used as a baseline for comparison. Several layers of the TPS elements in the model were constructed to include charring as a function of time by changing their properties. By correlating the response of the PATRAN model with the FIAT results, the actual char layer behavior could be corrected such that the PATRAN model shows accurate 3D behavior of the material.

Other Boundary Conditions

Contacts between the components are modeled via pseudo-convection boundary conditions. All components are connected via a 0.25-mm adhesive bond, which gives a contact conductance of $750 \text{ W/m}^2\text{K}$. Several parametrics were run with other contact conductances and the variation had little effect. The only unbonded attachment is the OS within the CV; since this is a loose contact connection it is rated at a lower conductance of $100 \text{ W/m}^2\text{K}$.

Current assumptions for the exo-atmospheric model include an EEV temperature at release of -80°C . This value is not critical to later operations, since regardless of the release temperature, the EEV will come to the same equilibrium during the four-day cruise before Earth entry. During exo-atmospheric cruise there is an MLI blanket in place that extends over the entire forebody and afterbody up to the spin-eject ring. There is no blanket over the spherical aft lid or the flat disk where the spin-eject ring mounts. The effective emissivity (ϵ^*) of the blanket, driven by JPL heater power limits, is 0.03. The exterior of the MLI, and the non-insulated portions of the vehicle, radiate to deep space and absorb solar fluxes as determined by their optical properties. The solar orientation during the four-day cruise varies from 45.2 degrees off the nose at separation to 47.5 degrees off the nose at entry.

The entry phase model includes the heat flux loads as discussed above. It also includes radiation between parts and radiation to the atmosphere. The atmospheric temperature as a function of time was derived from the altitude using a GRAM-95 model. Convection cooling to the atmosphere after the heat pulse will be added as a refinement later in the modeling. Radiation to the atmosphere is the driver in decreasing EEV surface temperatures. It is assumed that the MLI breaks away rapidly (as designed), so the surface emissivity used (0.8) is for the TPS itself.

The post-landing model includes the initial temperature from the entry phase, as well as radiation and convection to a 25°C ambient. The 25°C ambient is considered conservative since the projected landing in October in Utah would yield a colder ambient than that. All assumptions are designed to be conservative in the sense of predicting the warmest possible OS temperature.

Material Properties

Material properties for the TPS materials were taken from the TPSX software⁷, with some modifications by NASA Ames personnel. Carbon-carbon and other composite properties were from Langley reports.^{8,9} Other material properties were from vendor literature, from the PATRAN Thermal materials database, and from independent calculations. All material properties with substantial temperature variation were input as tables versus temperature.

Initially the materials were modeled as isotropic, which is not a valid assumption for some of the fiber-based materials such as the carbon-carbon structure. For these orthotropic materials, through-thickness and in-plane conductivity properties were added. In general, the in-plane conductivity is appreciably higher than the through-thickness property due to the in-plane orientation of the fibers. Thus, this model refinement makes a substantial difference in the heat flow and overall thermal behavior.

The difficulty in adding the orthotropic properties is that the materials are not oriented in any constant axis of the model. On the forebody carbon-carbon spherical cap, for example, the direction of the through-thickness property is changing continuously in two directions of rotation. In PATRAN, the orientation of an orthotropic material is

defined by three Eulerian rotation angles about the x, y and z axes. Since the Eulerian rotation of the material is different at each point on most of these components, a spatial field was used to define these rotations. By making the spatial field a specific function of two spatial variables, the field could be defined as exactly the Eulerian rotation necessary to bring the material axes into the correct orientation at each position. Each field was written as an equation of the following form:

$$\phi = \sin^{-1}\left(\frac{Z}{R}\right) * \cos\left(\tan^{-1}\left(\frac{X}{Z}\right)\right) \quad (1)$$

where ϕ is the material rotation around the x-axis, R is the component radius at that point, and X and Z are the location in the x and z axes. This equation was modified for the conical parts, as well as for parts such as the lid where the curvature was inverted (concave rather than convex). Each of the curved orthotropic components had x-rotation and z-rotation defined in this manner (no rotation around y since it was the axis of symmetry). Changes due to refining the material properties in this way are shown in the results sections.

Transfer to Structural Analysis

Transfer of temperatures to the structural model was very straightforward in the exo-atmospheric case. A routine within PATRAN's thermal solver (patq) can interpolate temperatures from one model to another, provided the models have the same geometry, even if the meshes are entirely different. The structural model was constructed from the same Pro/Engineer geometry used for the thermal model and was meshed with solid elements. The structural model mesh includes only structurally significant material, with the remaining components as distributed masses. Temperatures from the thermal-to-structural interpolation were used to assess stress and deformation under the thermal gradients. For the entry case, two methods were used. One was the same as previously described. In the second method, the structural model used meters as the length unit, and used mainly shell elements since this is how final models will probably be done. In this case, the structural model was scaled to the same units to allow thermal interpolation, and fields were applied to shells rather than solids. The process for interpolating the temperatures onto the meter-scale shell model were as follows: scale structural model back to millimeters for temperature interpolation, rotate scaled FEM to align with thermal FEM, interpolate temperatures from thermal to structural model, and run thermal strain analysis using scaled, rotated shell FEM.

RESULTS

Exo-Atmospheric Phase Results

After separation from the spacecraft, the EEV comes to equilibrium within several hours, and there are no major changes until the vehicle has a substantial view of Earth (in the last hour). Thus, the thermal behavior is constant over a majority of the time. This being the case, this model was usually run as steady state in order to quickly evaluate the effect of different boundary conditions and materials. Once a set of materials and coatings were selected, this model was run as a transient to evaluate the real-time behavior.

The thermal response during exo-atmospheric cruise is almost completely driven by the orientation of the EEV with respect to the sun, and by the coatings and coverings on the exterior of the EEV. Currently, it is assumed that MLI will be needed on the exterior of the EEV in order to minimize the heater power needed while attached to the spacecraft. The drivers on selecting exterior properties were as follows. The OS must be kept at a reasonably low temperature, well below the limit of 50°C. The adhesive bondlines should all be kept above -80°C to maintain structural integrity. The beacon assembly, which is located within the wing foam, should be kept above -40°C. In order to facilitate flight testing, it is desired that most structural components be kept as near room temperature as possible. Several parametric cases were run on an earlier concept to determine an optimum set of exterior properties², which were used for this analysis. The MLI was assumed to have exterior properties of $\alpha/\epsilon = 0.6/0.3$. The aft lid was assumed to have a high virgin emissivity of 0.88, and the spin eject ring was slightly lower at 0.58.

The results are shown in Figure 9. The gradient across the vehicle is mainly driven by the solar flux on the forebody and by the absence of heating or MLI on the aft body. However, all components are within acceptable thermal ranges. It is expected that a lower emissivity coating will be selected for the aft body, thus bringing up the aft body temperatures and decreasing the overall gradient. The incorporation of 3D orthotropic properties in the analysis

decreased the predicted gradient across the vehicle by roughly 35°C to its current value of 81°C. The structural effects due to this thermal gradient are shown on the structural model in Figure 10. These strains are well within the materials' capability.

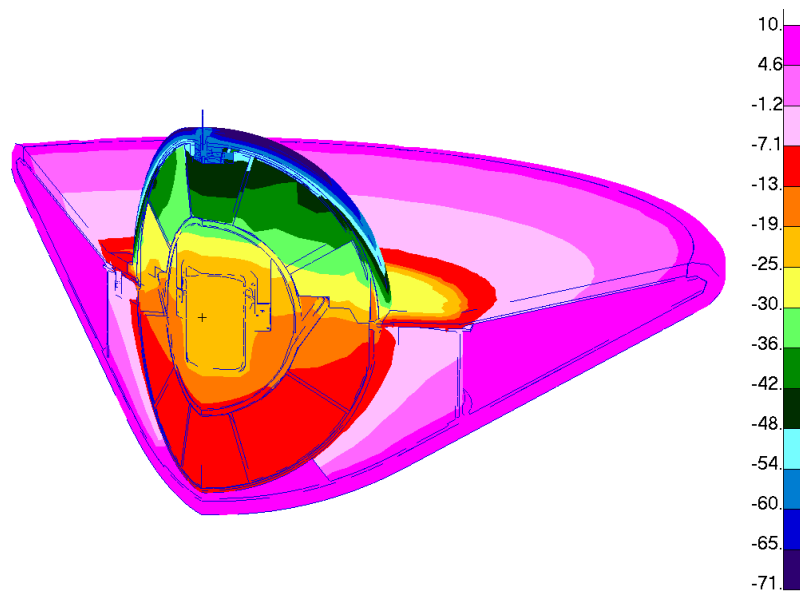


Figure 9. Exo-atmospheric temperature distribution (°C).

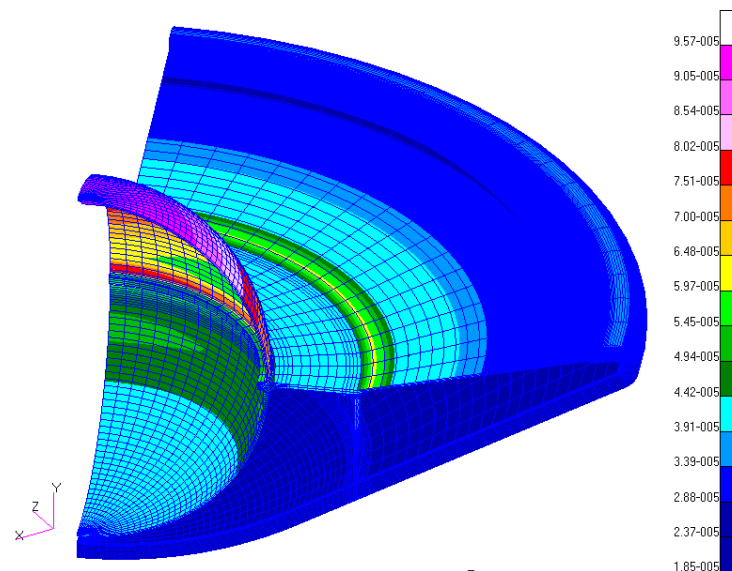


Figure 10. Structural model principal strain predictions based on temperature field.

Entry Phase Correlation to FIAT Model

The forebody and aftbody heating during entry dominate the thermal response of the EEV in this phase of the mission. Initial temperature predictions did not account for the energy loss due to charring and property change. The predicted temperature distribution at 45 seconds for this initial run without correlation is shown in Figure 11. Figure 12 shows the temperature history at the stagnation point through entry up to landing for both the PATRAN Thermal and FIAT models. At peak heating (17 seconds), a temperature difference of 149°C between the PATRAN and FIAT model occurred. At landing (360 seconds), there was a maximum temperature difference of 174°C. The temperature distribution at landing is shown in Figure 13. Obviously, neglecting the material charring has a substantial effect.

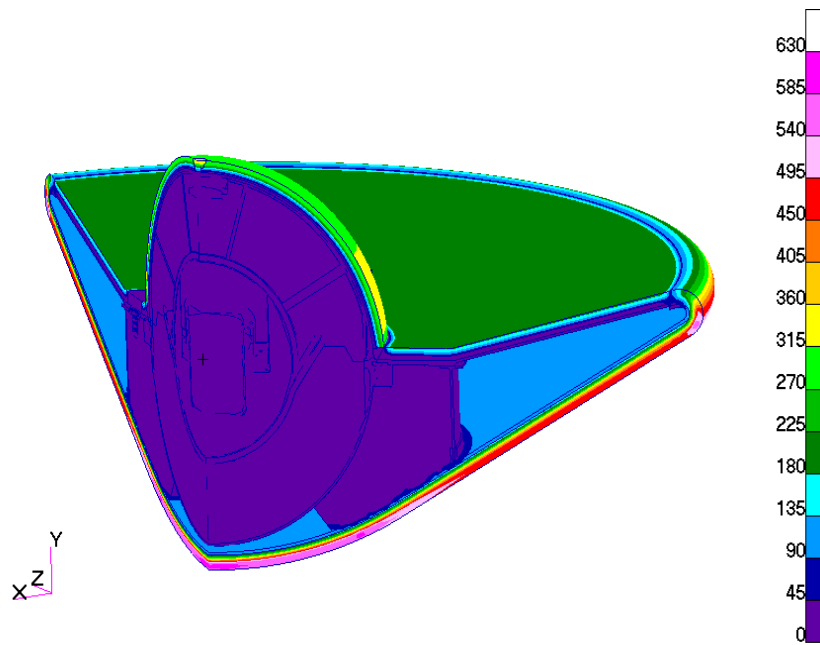


Figure 11. Entry temperature distribution at 45 sec (°C) -- uncorrelated.

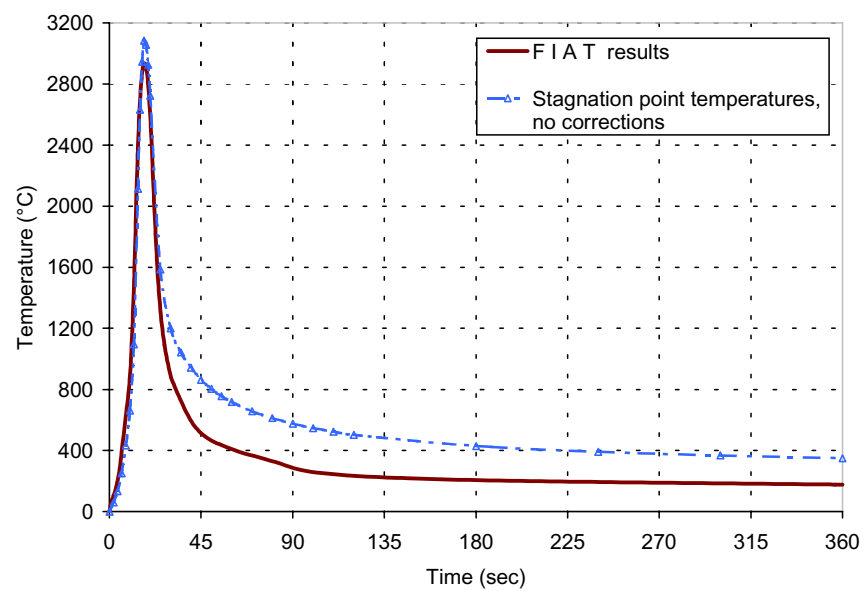


Figure 12. Stagnation point temperatures during entry for uncorrelated model.

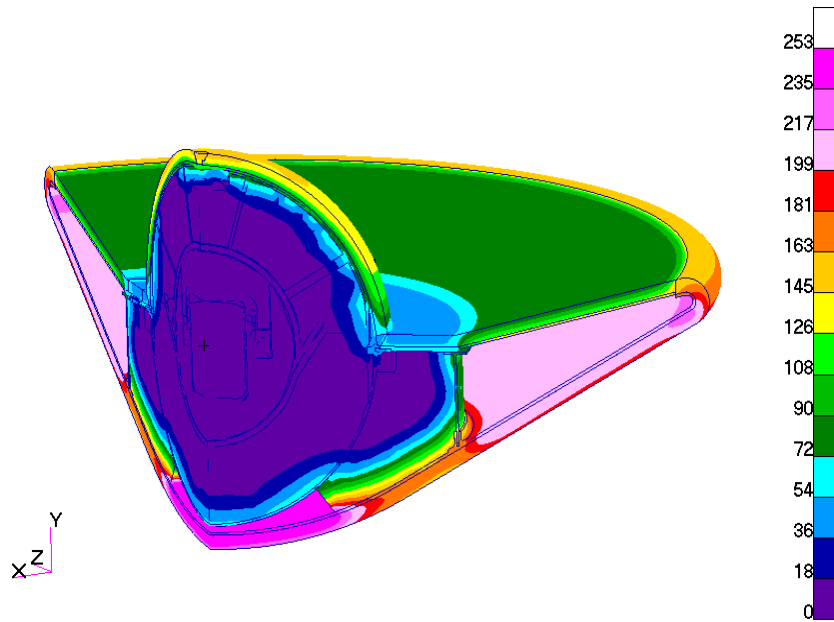


Figure 13. Entry temperature distribution at 360 sec (°C) -- uncorrelated.

These initial results showed unsatisfactory correlation largely due to the inability of PATRAN to directly model the ablative nature of the TPS material. In order to simulate the physical and chemical processes and achieve satisfactory correlation, an engineering adjustment to the PATRAN model was needed. Applying the hot wall heat flux from FIAT to the PATRAN model was an improvement from previous analyses in that it more closely approximated the actual heating on the vehicle, and thus a complex set of heat reduction functions were not needed. A time-varying reduction factor on the heat pulse was needed, however, to account for the energy lost due to mass loss. A peak reduction factor of 22.5% at 17 sec was all that was required to correlate the temperatures from 16 to 25 seconds. The form of the heat flux reduction, originally developed for a previous design configuration², was a simple sine function with time as the independent variable. This was used to smoothly transition from the baseline heating profile to the maximum reduction at peak heating in the following form:

$$Q_f = (A \sin^4 \omega t + B \sin^2 \omega t + C \sin \omega t + D) * Q_o \quad (2)$$

where t is time, Q_f is the corrected heat flux, Q_o is the FIAT hot-wall heat flux, and ω is the frequency of the sine function. The coefficients A, B, C, and D were determined by bounding the reduction factor between a given time interval, specifying the time the maximum occurs, and specifying the maximum value of the reduction factor. After 25 seconds, the effect of charring in changing the bulk material properties becomes significant enough to diverge the results. The FIAT code models charring directly such that the vehicle loses mass and hence loses some of its ability to store energy. Therefore, to simulate the loss of mass and energy in the PATRAN model, the first two layers of elements on the forward TPS were assigned material properties of charred carbon phenolic after 16 seconds (to average the time at which charring became significant). These two layers of elements were also given time-varying, decreasing density in order to simulate the loss of mass. With the combination of the heat reduction factor and the time varying char properties, the PATRAN results showed good correlation with the FIAT model. Figure 14 shows the correlation for the stagnation point, where the temperature difference is only 11.6°C at peak heating and 16.0°C at landing. A similar correlation was obtained for interior nodes in line with the stagnation point.

Slight adjustments to the aftbody heating were necessary to produce a satisfactory correlation at peak heating. A reduction factor of 20% when applied at 20 seconds to the aft body heating reduced the temperature difference from 96.3°C to 15.8°C. A charring approximation was not necessary as the PATRAN and FIAT models were in good agreement at landing where the temperature difference was 12.3°C. Figure 15 shows the temperatures at the stagnation point on the aft body. The reason for such close correlation without any major corrections was that the aftbody TPS material, SLA-561V, was not exposed to heating rates high enough to cause significant charring.

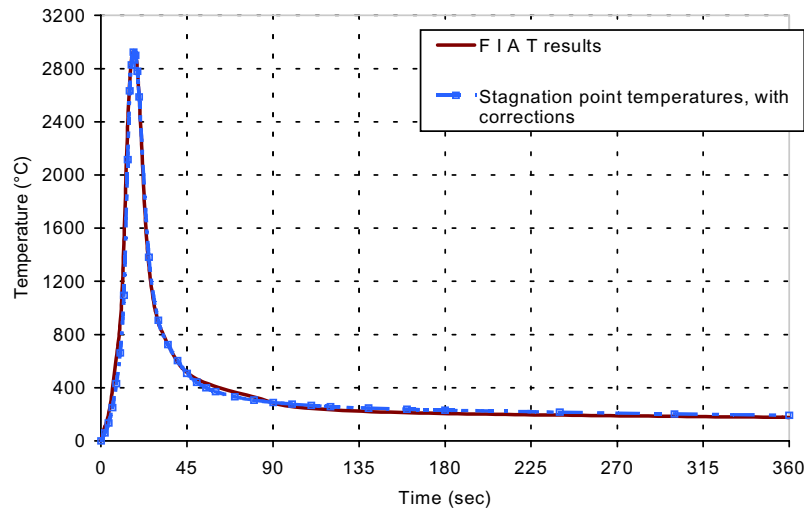


Figure 14. Correlated stagnation temperatures.

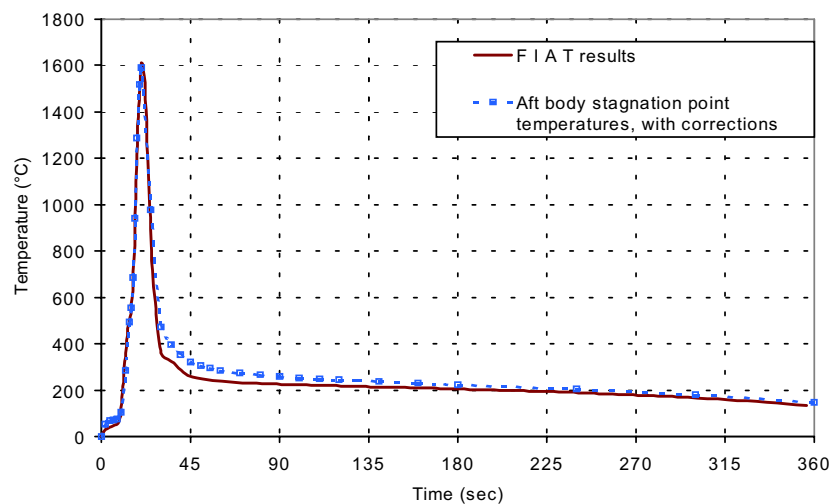


Figure 15. Correlated aft body stagnation temperatures.

Entry Phase Results

The prediction for Earth entry used these engineering adjustments, adds the refinement of 3D orthotropic properties, and included the initial temperatures from the exo-atmospheric phase of the mission. The results are shown in Figure 16 and Figure 17. The addition of the orthotropic properties increased the conduction through the energy absorbing core web material, which is directed towards the center of the energy-absorbing core. The effect of the orthotropic properties can also be seen in the forward TPS and structure, where the higher in-plane conductivity of the structure helped to evenly distribute the energy across itself and the TPS. Including the orthotropic properties decreased the temperature at the stagnation point, increased the temperature near the body foam and decreased the temperature in the shoulder region. The 3D orthotropic model was also analyzed starting at 0°C to allow direct comparison with the correlation runs that used a global initial temperature of 0°C. This verified that the orthotropic nature of the material, and not the initial temperature, caused the changes in thermal distribution. Figure 18 shows the temperature distribution at landing for this case, and shows the same trends are present as in the case with the initial temperatures from the exo-atmospheric phase.

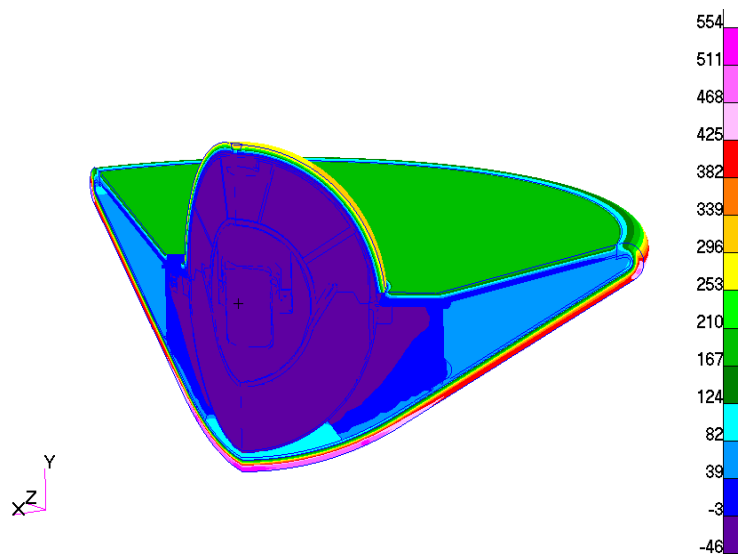


Figure 16. Entry phase temperature prediction at 45 s (°C).

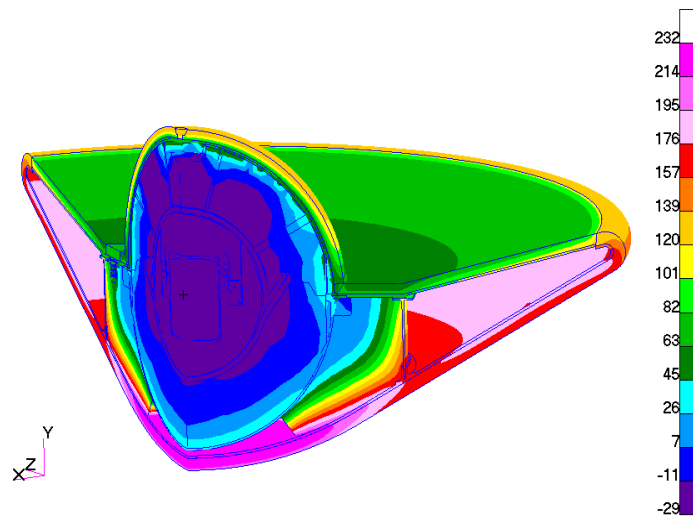


Figure 17. Entry phase temperature prediction at 360 s (°C).

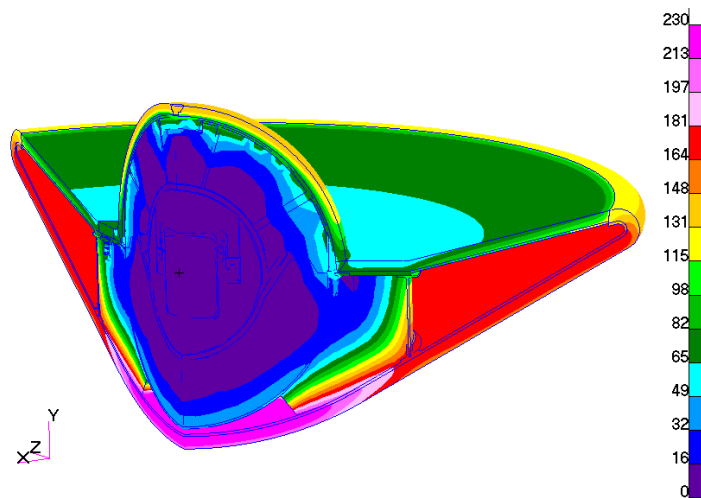


Figure 18. Entry phase temperature prediction at 360s (with 0°C initial temperature).

The structural predictions for the entry phase are shown in Figure 19 for the direct transfer to a solid model, and in Figure 20 for the interpolation to a shell model that used meters as the unit. These results are for the maximum pressure point in the trajectory, when the stresses on the material would be maximized. The interpolations give very similar results, except that in the shell model, thermal gradients across solids are not captured so some stresses are neglected. Strains are shown rather than stresses since these can be directly compared between solid and shell models. The strains are well within the capability of the carbon-carbon structural material. The pressure loads due to entry deceleration have not yet been combined with the thermal effects, but this is a relatively simple operation.

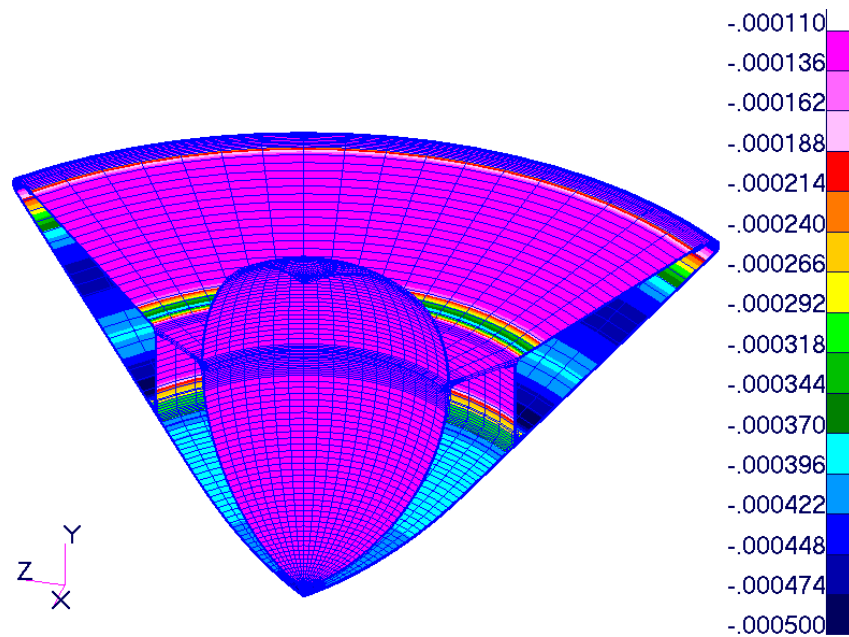


Figure 19. Strains for maximum pressure point at entry using solid model.

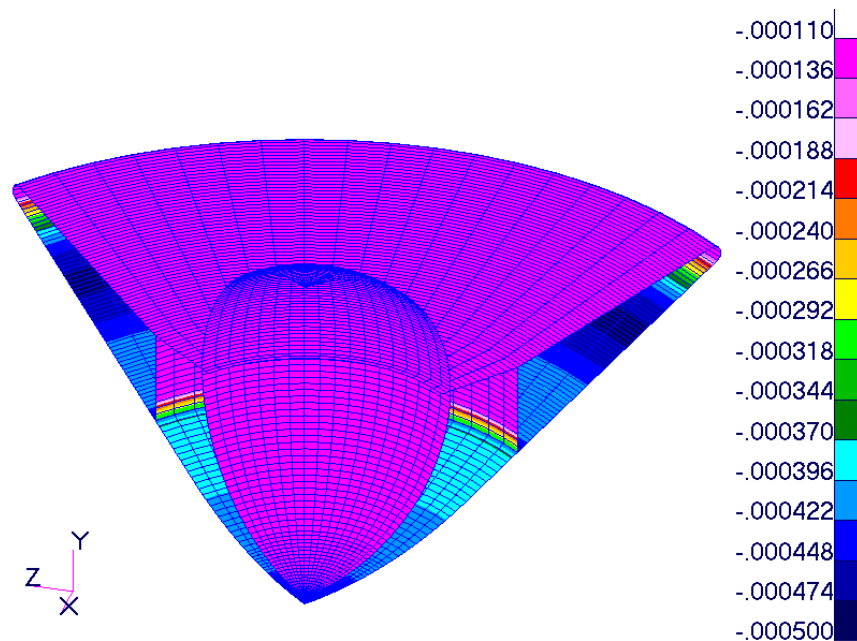


Figure 20. Strains for maximum pressure point at entry using shell model.

Landed Phase Results

After landing, the vehicle begins to come to thermal equilibrium. Figure 21 shows results of an example analysis of the progression. By four hours after landing, the vehicle is close to thermal equilibrium and few changes are occurring. At no time does the OS exceed the ambient temperature of 25°C. No combination of assumptions such as convection to ambient and which parts of the vehicle come in contact with the ground raise the OS temperature above 25°C.

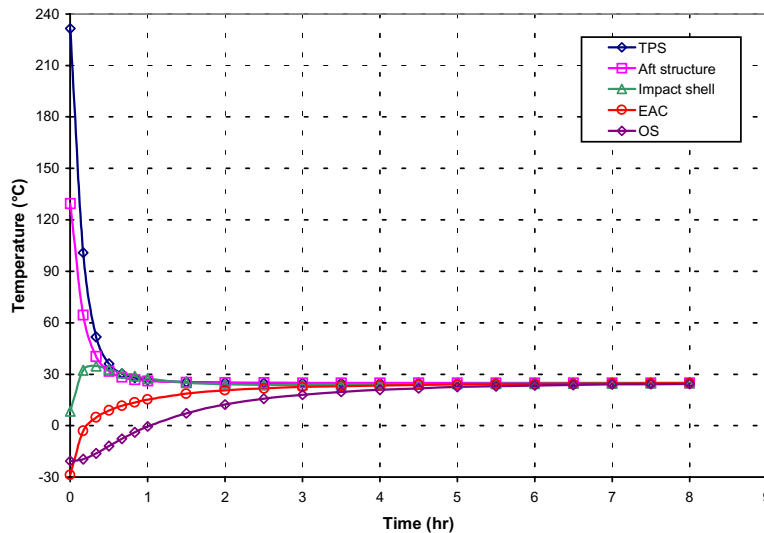


Figure 21. Transient after landing (°C).

CONCLUSIONS

A procedure was developed to perform detailed thermal analysis early in the design phase of the EEV for the Mars Sample Return mission. Results from this procedure indicate the passive design EEV was successful in maintaining all parts within their designed thermal limits. The thermal analysis was successfully coupled with the CAD design tool, aeroheating and material response analysis, orbital radiation analysis and structural analysis. While some improvements in the integration are planned, the current implementation linking the processes was of immense benefit in producing an accurate prediction of the EEV behavior. Orthotropic material properties were successfully added to all models using complex spatial fields, and produced meaningful changes in the predicted gradients.

ACKNOWLEDGEMENTS

The work of YK Chen at NASA Ames in analyzing the material response during entry, which allowed correlation of this analysis, is acknowledged with deep gratitude. The work of Stephen Hughes and Robert Dillman at NASA Langley in preparing CAD models is greatly appreciated.

ACRONYMS

CAD	Computer-aided design
CV	Containment vessel
EEV	Earth Entry Vehicle
FIAT	Fully Implicit Ablation and Thermal Analysis Program
MLI	Multi-layer insulation

OS	Orbiting samples
POST	Program to Optimize Simulated Trajectories
STEP	Standard for the Exchange of Product Model Data
TSS	Thermal Synthesizer System
TPS	Thermal protection system

REFERENCES

- ¹ R. A. Mitcheltree, S. Kellas, J. T. Dorsey, P. N. Desai and C. J. Martin, Jr., "A Passive Earth-Entry Capsule for Mars Sample Return," 7th AIAA/ASME Joint Thermodynamics and Heat Transfer Conference, Albuquerque, New Mexico, AIAA 98-2851, June 15-18, 1998.
- ² R. M. Amundsen, J. A. Dec, R. A. Mitcheltree, M. C. Lindell and R. A. Dillman, "Preliminary Thermal Analysis of a Mars Earth Entry Vehicle," 34th AIAA Thermophysics Conference, Denver, Colorado, June 19-22, 2000.
- ³ Pro/ENGINEER Fundamentals Manual, Parametric Technology Corporation, Release 20.0 (June 1998).
- ⁴ MSC/PATRAN User Manual, MacNeal-Schwendler Corporation, Version 9.0 (May 1999).
- ⁵ User Manual, Thermal Synthesizer System, Release 6.01, Lockheed Martin Space Mission Systems, NAS9-19100, October 1997.
- ⁶ Y. K. Chen and F. S. Milos, "Ablation and Thermal Response Program for Spacecraft Heatshield Analysis," *Journal of Spacecraft and Rockets*, Vol. 36, No. 3, 1999, pp. 475-482.
- ⁷ TPSX, Thermal Protection Systems Expert and Material Properties Database, February 1998, NASA Ames Research Center (<http://asm.arc.nasa.gov/tpsx/>).
- ⁸ C. W. Ohlhorst, W. L. Vaughn, P. O. Ransone, H. Tsou, "Thermal Conductivity Database of Various Structural Carbon-Carbon Composite Materials," NASA TM-4787, NASA Langley Research Center, November 1997.
- ⁹ E. M. Silverman, "Composite Spacecraft Structures Design Guide," NASA Contractor Report 4708, Contract NAS1-19319, March 1996.

INCLUSION OF THERMAL PROTECTION SYSTEMS IN SPACECRAFT THERMAL-STRESS ANALYSIS USING CONCURRENT ENGINEERING TECHNIQUES

Steven L. Rickman
ES3/Thermal Branch
Structures and Mechanics Division
Engineering Directorate
National Aeronautics and Space Administration
Lyndon B. Johnson Space Center
Houston, Texas 77058-3696

ABSTRACT

Creating compatible thermal and structural mathematical models is complicated by the different meshing requirements of the thermal and structural disciplines. Often times, the structural model is of significantly higher fidelity requiring the thermal model to grow to an intractable size if full compatibility is to be assured. Given that the structural finite element mesh can be transformed into a thermal model, the network description remains incomplete until the appropriate thermal protection system (TPS) features are added. For entry heating studies, a high fidelity TPS mesh is required to accurately predict structural temperatures. Additionally, local pressure, temperature and heating variations further complicate the analysis. A technique for the efficient extraction of thermal protection system thickness data from CAD geometry is presented. The technique allows for application of complicated TPS cross-sections consisting of different materials and permits local pressure and heating rate variations. The resulting process has been successfully demonstrated on the X-38 crew return vehicle configuration and serves as a prototype for concurrent engineering techniques using a combination of custom and commercial software tools¹.

INTRODUCTION

Thermal-stress analysis of atmospheric entry spacecraft has been plagued due to the differences in methodologies used by the structural and thermal disciplines. Traditionally, the thermal analyst uses a finite difference discretization while the structural analyst employs finite element techniques. Not only do the methodologies differ; the mesh density of the structural model is often quite higher than that of the thermal model. To adequately model the atmospheric entry phase and predict structural temperatures, the addition of TPS is required. Providing thermal analysis results that are entirely compatible with the structural model is further complicated by the fact that the structural mesh is only a small part of the overall thermal model. Due to the high heating rates and large temperature gradients experienced in the TPS, proper modeling methodology requires a high mesh density in these materials.

Additional obstacles arise when the following factors are considered:

- a. discretization of the TPS must be compatible with the structural mesh;
- b. the TPS thickness and composition varies as a function of location on the vehicle;
- c. the TPS cross-section is comprised of multiple materials;
- d. the materials' thermal conductivity varies as a function of temperature and pressure;
- e. pressure versus time distributions vary as a function of location on the vehicle;
- f. heating rates vary as a function of time and location on the vehicle.

¹ Thermal Desktop[®], RadCad[®] and SINDA/FLUINT[®] are registered trademarks of Cullimore and Ring Technologies. Patran[®] and NASTRAN[®] are trademarks of the MacNeal-Schwendler Corporation. I-DEAS[®] is a registered trademark of the Structural Dynamics Research Corporation. ProEngineer[®] is a registered trademark of Parametric Technology Corporation.

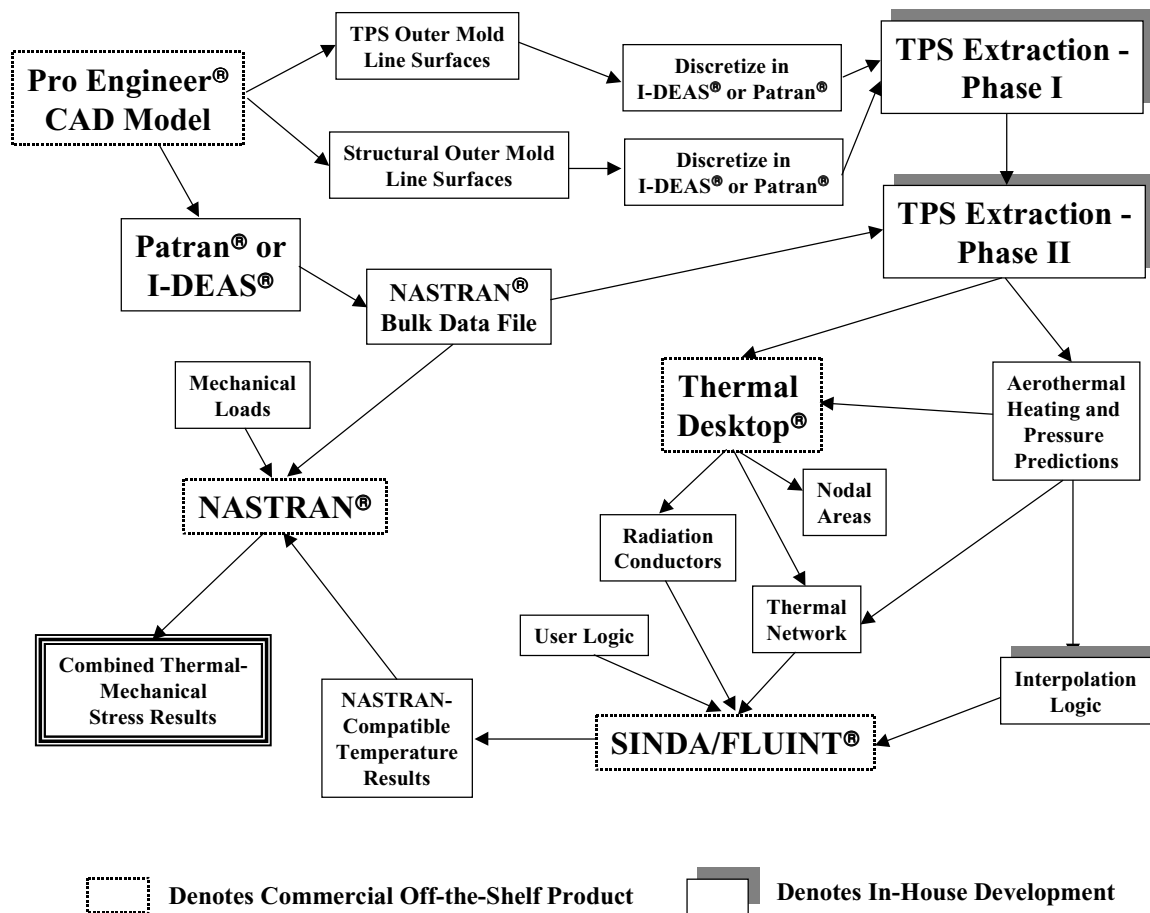


Figure 1 – Process Overview

The proposed process, depicted schematically in Figure 1, overcomes these obstacles through a combination of user-developed software and commercial product enhancements. The details of the technique are presented herein.

TECHNIQUE DESCRIPTION

An important facet of a new process is that it does not constrain any other phase of the design or analysis cycle. The proposed technique relies on the availability of three CAD/CAE products: 1) a surface description of the vehicle outer mold line (referred to as the TPS outer mold line, TOML); 2) a surface description of the vehicle structural outer mold line (SOML); and 3) a FEM representation of the spacecraft structure.

Extraction of TPS Thickness from CAD Data - (Phase I)

The first step in the process is to create a high-density mesh on the TOML and SOML surfaces in order to facilitate extraction of the TPS thickness data. This is readily accomplished using any of a number of commercially available meshing tools such as Patran® or I-DEAS®. The dense nature of the mesh is necessary to ensure the desired accuracy in thickness extraction.

Once the TOML and SOML meshes are generated – only the grid points are needed – a simple distance program using the Pythagorean Theorem is used to determine the closest TOML point to a given SOML grid location (X_{SOML} , Y_{SOML} , Z_{SOML}). The process is illustrated in Figure 2 where d is the distance between grids, t is the true local TPS thickness and r is the distance to the closest point on the TOML

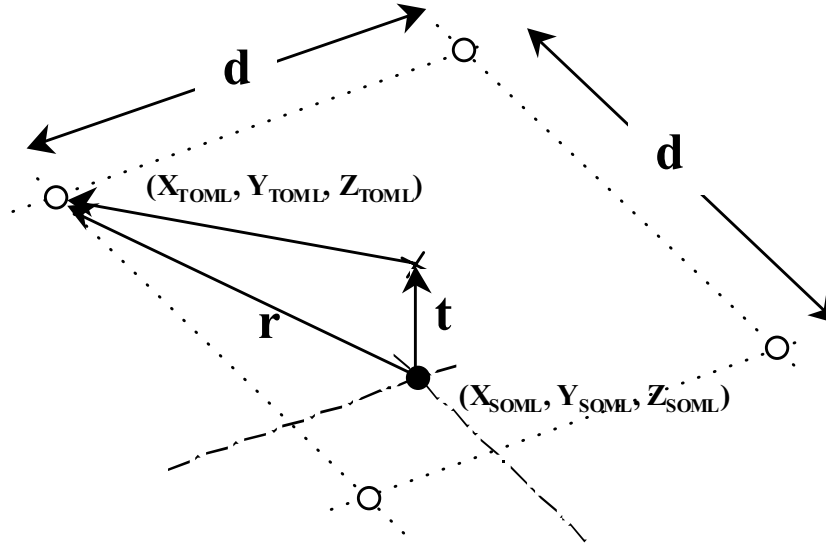


Figure 2 – Finding the Closest Grid Point on the TOML Mesh

$(X_{TOML}, Y_{TOML}, Z_{TOML})$. As the mesh density increases, r becomes an increasingly better approximation of t .

The distance formula is simply:

$$r = \sqrt{t^2 + \frac{d^2}{2}} = \sqrt{(X_{TOML} - X_{SOML})^2 + (Y_{TOML} - Y_{SOML})^2 + (Z_{TOML} - Z_{SOML})^2}$$

The accuracy of the extracted thickness is determined by comparing the calculated distance, r , with the true TPS thickness, t . But since r is the approximation of t , we can look at the accuracy parametrically. That is, we can formulate a relation between error, d and t . If the minimum TPS thickness is known, the grid spacing may be determined such that the TPS at every location on the vehicle can be extracted with the desired accuracy. This is given by:

$$Error(\%) = \frac{100(r-t)}{t} = \frac{100\left(-t + \sqrt{t^2 + \frac{d^2}{2}}\right)}{t}$$

where, here, t is the minimum vehicle TPS thickness.

A plot of the extraction accuracy as a function of d and t is presented in Figure 4.

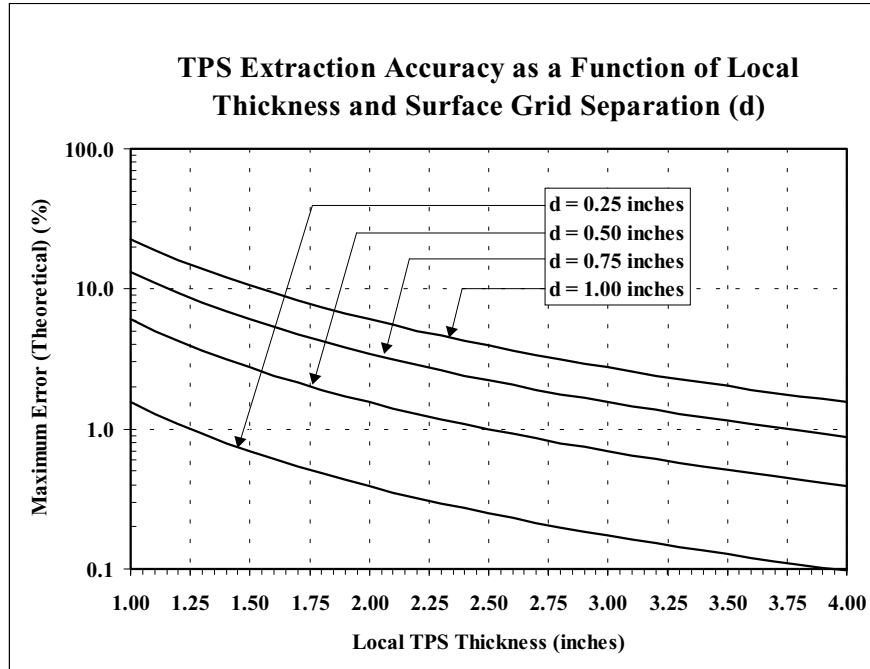
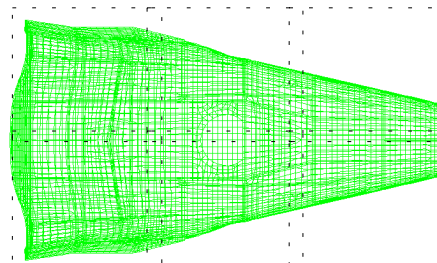


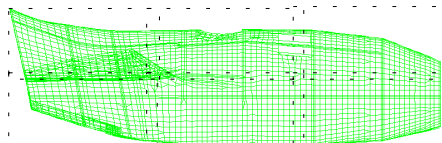
Figure 4 – TPS Thickness Accuracy

For example, if $< 2\%$ error in TPS thickness modeling is acceptable and the minimum vehicle TPS thickness is 1 inch, then, a grid spacing of 0.25 inches is acceptable. The error for any thickness greater than 1 inch will be lower.

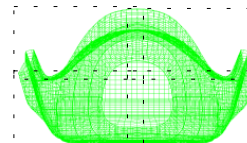
For large vehicles, finding the minimum distance between large sets of points can be a time consuming process. This can be accelerated dramatically by using a bounding volume technique to significantly reduce the number of grid combinations to be tested. Consider, for example, the bounding volumes established for the geometry presented below in Figure 3.



Top View



Side View



Front View

Figure 3 – X-38 Model Showing Overlapping Bounding Volumes

For each SOML grid, determine its parent bounding volume. Next, perform distance calculations to all TOML grids that occupy the same bounding volume. Since there is a slight overlap in the bounding volumes, the technique certain to catch a potentially closer grid which might normally have been eliminated from a non-overlapping scheme.

Associating TPS Thickness with the Finite Element Model - (Phase II)

The finite element model (FEM) is an abstraction of the true geometric description. Often, the spacecraft skin is modeled as shell elements. In the situation where the skin may actually consist of composite panels, the FEM shell model may use a mid-plane approach for representing the structure. This, in essence, offsets the shell representation from the true SOML. If TPS thickness was extracted using the FEM mid-plane and the TOML only, the resulting TPS thickness would be in error by an amount equivalent to the half-thickness of the composite panels in *addition* to the error previously discussed. Since structural skin temperatures are sensitive to TPS thickness, this would introduce a significant error into the thermal analysis results.

In a manner identical to the extraction process described earlier, the thickness database is associated with the closest grid location on the structural finite element model. This process is identical to the previous process except that the mesh density of the FEM is significantly less than that of the SOML. This phase of the process is considerably faster but still benefits from the use of the bounding volume technique previously described. Overall, the two step extraction and association process is summarized below in Figure 5.

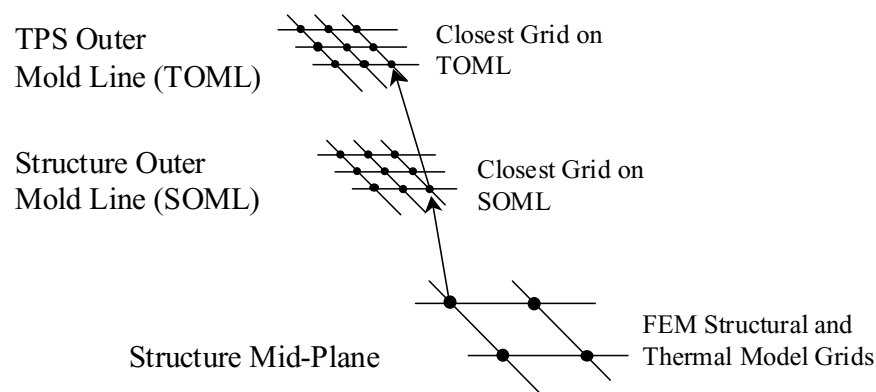


Figure 5 – Extraction and Association of TPS Thickness

Associating the Entry Heating Fluxes and Pressure with the Model

As a byproduct of the extraction and association processes, data regarding surface grid numbers and coordinates are formatted and entry heating flux and pressure histories are associated with each grid location. The resulting data are formatted in SINDA/FLUINT[®] array format. An additional file containing spatial location data for pressure data (generated from a computational fluid dynamics model) is also returned and is used, subsequently, to allow local pressure variations in the model.

Constructing the Model

In order to proceed with model construction, it was necessary to find a modeling tool that supports the following features:

- a) variable thickness extrusion supporting multiple materials;
- b) allows temperature and pressure dependent properties;
- c) allows local pressure variations with time.

Of the tools surveyed, the Thermal Desktop[®] suite best met the requirements.

The structural finite element model geometry was loaded into the software and collected into groups convenient for model development and manipulation. Of particular importance was the ability to create groups containing only the external skin -- elements destined to act as a substrate for the TPS. These are depicted in Figure 6.

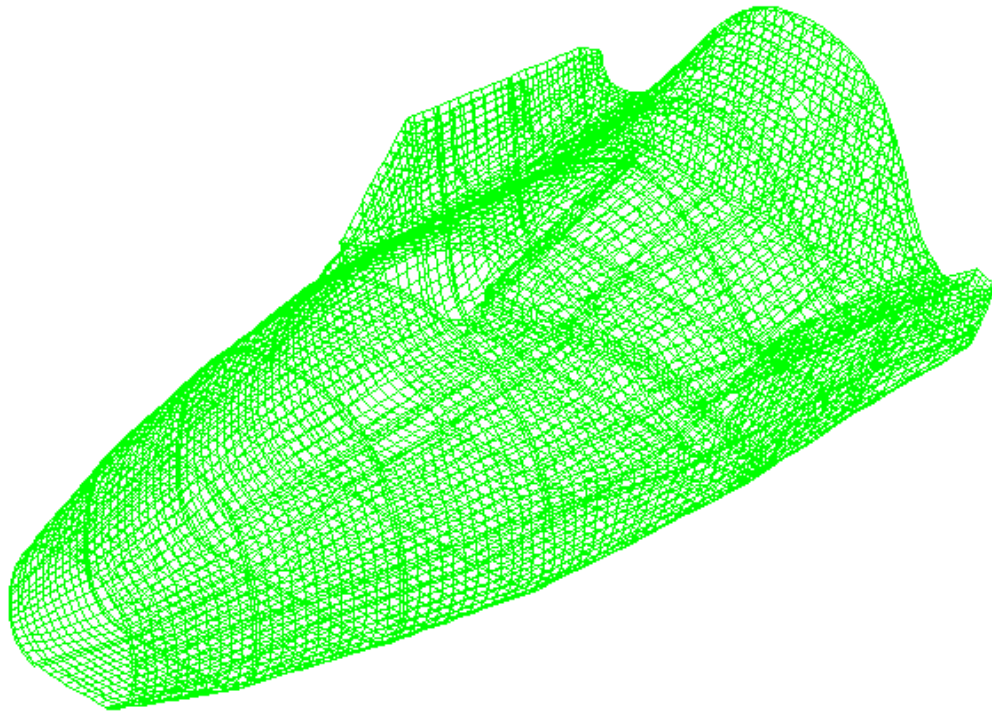


Figure 6 – Skin Elements Used for TPS Extrusion

Once grouped, the extrusion operations could begin. The capability of Thermal Desktop[®] was extended to allow extrusion of variable thickness TPS data onto the geometry. The required inputs were the variable thickness data that was extracted from the CAD model as well as a list of thickness for each component – external coating, densified tile layer, and strain isolator pad. The thickness of the tile material is not specifically input to the list. Rather, it is derived from the difference between the CAD-extracted thickness and the known fixed-thicknesses input with the list.

In practice, there is an advantage to adding the external coating in a separate extrusion operation because there was a need to maintain a correspondence between the coating SINDA node numbers and the underlying skin node numbers. The separate extrusion operations allowed for easy grouping of the resulting elements and facilitated renumbering to accommodate the required scheme. Subsequent to this analysis, however, improvements to the technique were recognized and splitting of the extrusion into separate operations will no longer be required.

The tool employs a number of features to simplify creation of the associated thermal radiation model. For example, the ability to add a zero-thickness surface to the extrusion process resulted in the creation of the TOML external radiation surface geometry. This replaced a more cumbersome operation using surface coating which necessitated a great deal of user interaction to remove surfaces created on the free sides of

solid elements. Normal extrusion operations were used in areas with constant thickness TPS. A sample extrusion on the X-38 chute door is depicted in Figure 7.

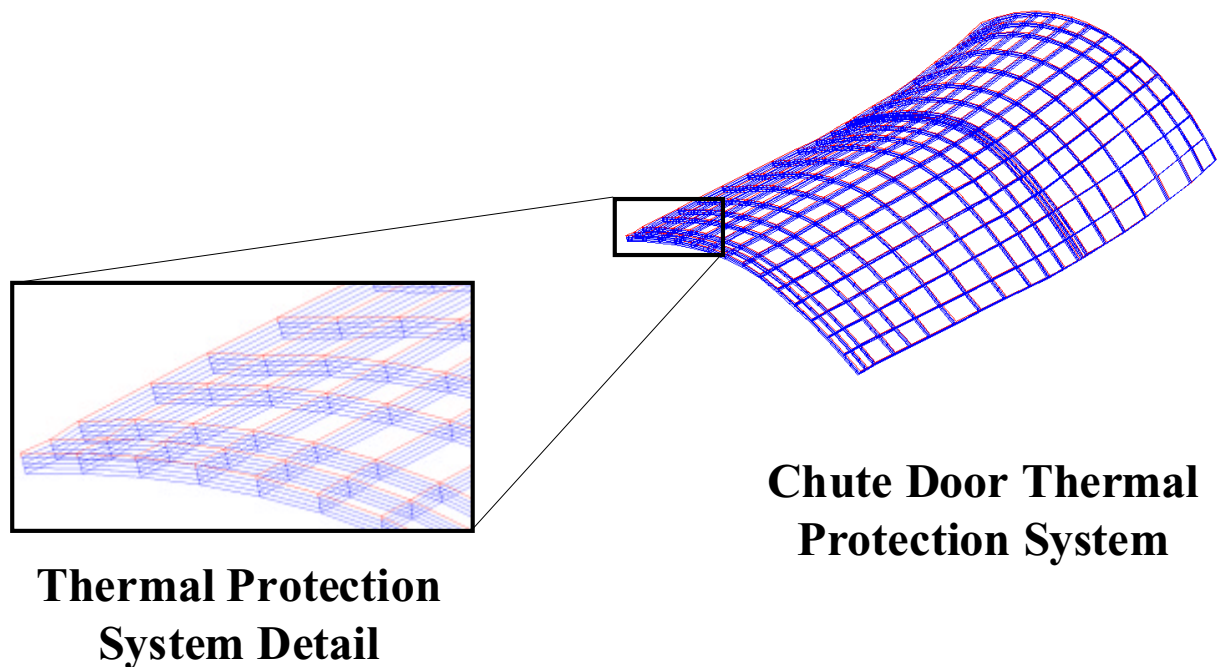


Figure 7 – Thermal Protection System (TPS) Extrusion Detail

Convection film coefficients versus time were added to the model and a conservative profile was used. Separate assignments were made to internal structure and external structure to allow easy variation of either component during the analysis phase.

Association of local pressure data with temperature and pressure varying TPS material thermal conductivity was easily accomplished. Thermal Desktop[®] allows for association of a pressure or pressure versus time array with a specific spatial location. Selected nodes will find the closest pressure location and automatically associate the node with the given profile. The resulting PIV calls are automatically generated as the model input deck is output. This capability gives the engineer the ability to easily model not just $p = p(t)$ but $p = p(x, y, z, t)$ as well.

With the model construction completed, radiation and network analysis began. The model was output in SINDA/FLUINT[®] format and augmented with entry heating flux and pressure versus time arrays. Radiation conductances were inserted and logic to generate NASTRAN[®]-compatible TEMP cards was added. Hence, results from the transient analysis were used directly as input to the FEM structural model. The total thermal model consisted of 129,861 nodes and 944,026 conductors.

Analysis and Results

Radiation conductances (Radks) and transient thermal analysis were processed on a PC (300 MHz Pentium^{®2} II with 320 Mbytes RAM and 8 Gbytes of hard disk space). Due to the limitations of the available computational resources, it was necessary to break the radiation model into three parts – one external and two internal. The Radks were calculated using a monte-carlo scheme with 2000 rays/node in RadCad[®]. This was sufficient for accurate characterization for the external view to space as well as the main radiative heat flow paths internal to the vehicle. The transient analysis, covering the period from

² Pentium[®] is a registered trademark of the Intel Corporation.

entry interface through landing (approximately 2350 seconds) plus an additional 600 seconds was accomplished in approximately four hours of which almost one hour was devoted to pre-processing and another fifteen minutes to one half hour devoted to model compilation. Structural temperature data were output for use in thermal-mechanical stress analysis at 100-second intervals (after entry interface plus 1500 seconds) and at specified event times such as drogue chute deploy and landing.

Sample structural temperature distributions are presented in Figures 8 and 9.

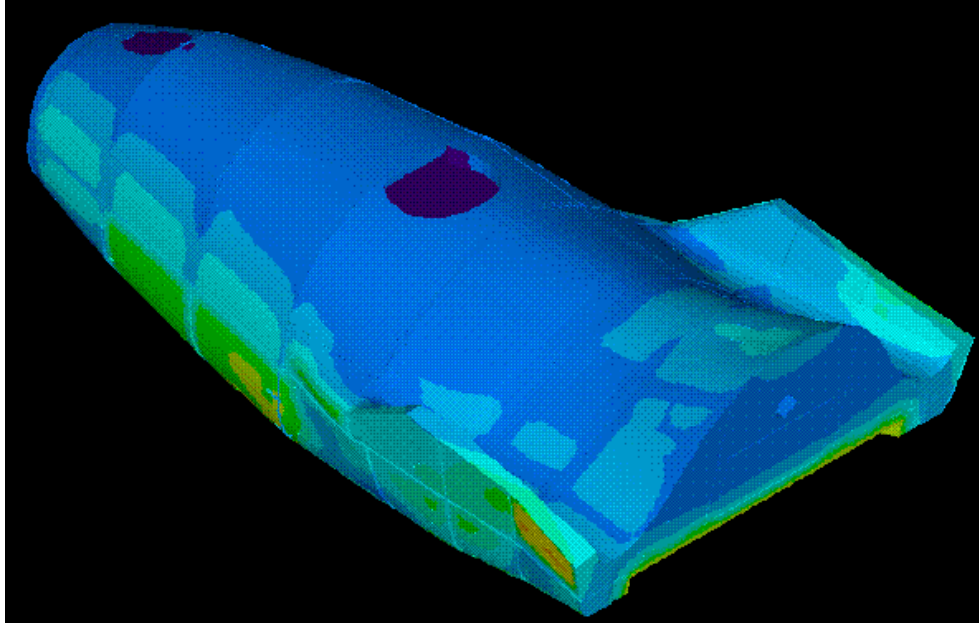


Figure 8 – X-38 Structural Temperatures at Touchdown (View from Port-Aft Quadrant)

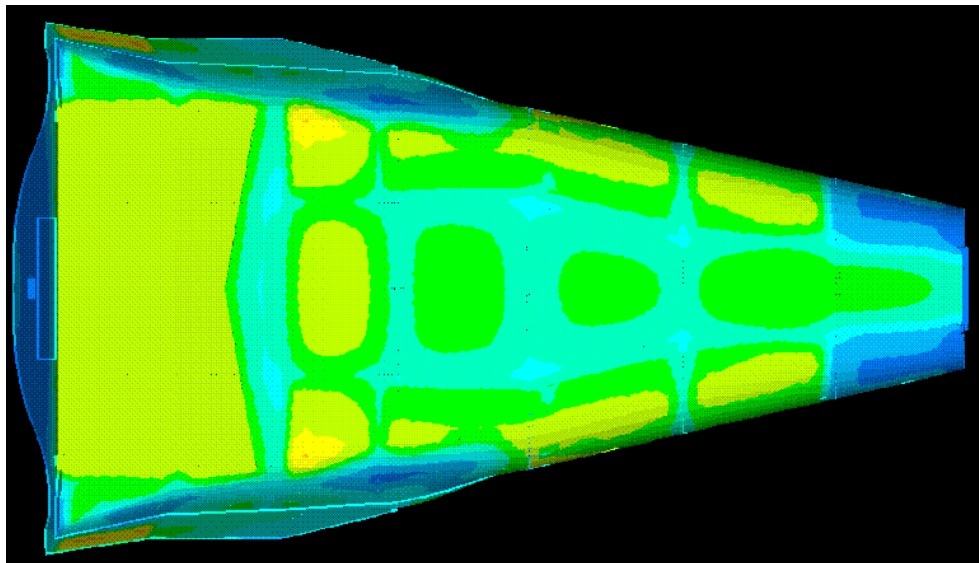


Figure 9 – X-38 Structural Temperatures at Touchdown (View from Bottom)

A sample thermal-mechanical stress distribution is presented in Figure 10.

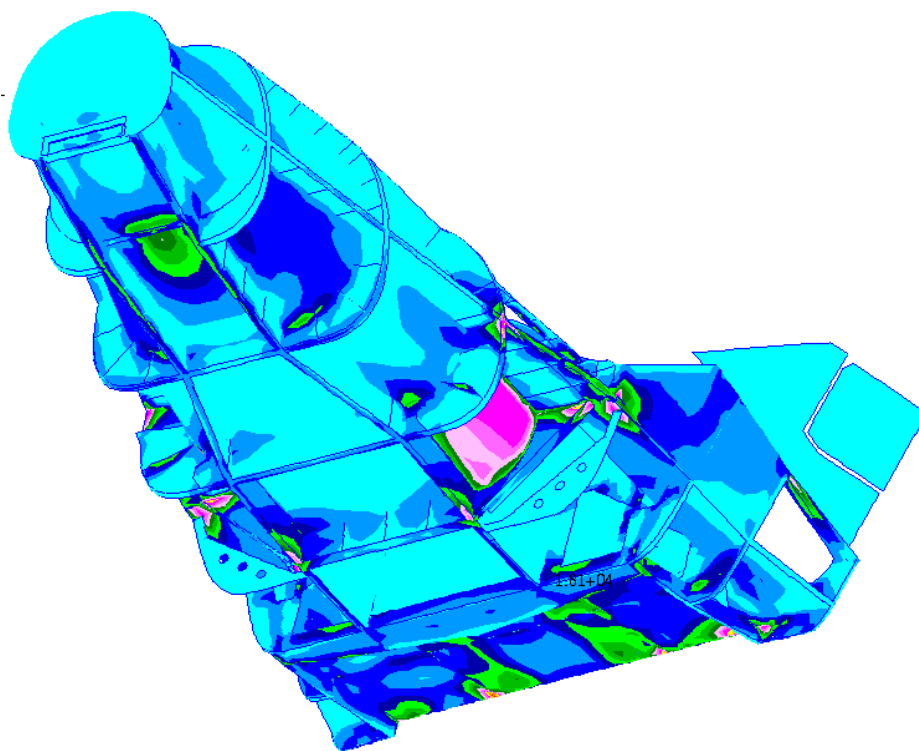


Figure 10 – X-38 Sample Combined Thermal-Mechanical Stress

CONCLUSION

The technique described here has successfully demonstrated a means of developing thermal models with fidelity sufficient to support combined thermal-mechanical stress analysis. The extraction of model information from CAD geometry and augmentation of an existing structural finite element model serves as a prototype for future concurrent engineering efforts. Potential enhancements to this technique to be investigated in the future include automatic sizing of TPS for new entry vehicles.

ACKNOWLEDGEMENTS

The success of this study is due to the assistance and creative input of many people. The author is grateful to the X-38 project for providing the impetus to develop this technique. Britney Sandell (Lockheed-Martin) and Chris Lupo (JSC) provided CAD geometry and consultation. Ronny Baccus and James Smith, both of JSC, provided consultation on MSC NASTRAN[®]. Galen Overstreet (JSC) performed the combined thermal-mechanical stress analysis and provided the output presented herein. Ron Lewis and Andy Hong, also of JSC, provided boundary temperature predictions for the body flap cavity and the nose region. Special acknowledgement is given to Steve Fitzgerald (JSC) for providing the entry heating fluxes and the local pressure profiles as well as developing the code to facilitate the exchange of data. Finally, this project would not have been possible without the product enhancements, creative talents and user support provided by Mark Welch, Tim Panczak, Dave Johnson, Steve Ring, and Cindy Beer of Cullimore and Ring Technologies.

THE U.S. STEP-TAS PILOT

Georg Siebes

Jet Propulsion Laboratory
California Institute of Technology

Hans Peter de Koning

European Space Research & Technology Centre/European Space Agency

Eric Lebegue

SIMULOG

ABSTRACT

In January 2000, the STEP for Aerospace Workshop at JPL brought together representatives from the standards developer, tool vendor and user community. It served as the catalyst for further STEP implementation activities in NASA. The most mature of these activities is the US STEP-TAS pilot. Five US thermal tool vendors are participating. In alphabetical order they are Cullimore and Ring Inc. (Thermal Desktop), Harvard Thermal Inc. (TAS), Network Analysis Inc. (SINDA/ATM), SpaceDesign (TSS), and TAC Inc. (NEVADA).

The scope of this pilot is limited to the development of a prototype bi-directional STEP-TAS interface of defined and limited capability. The word prototype is used in the sense of a feasibility demonstration. This specifically means that the final product is not required to support all capabilities that are typically found in a radiation analysis tool. The prototype is limited to the bi-directional exchange of pre-defined surface geometry and thermal properties.

The current status of this pilot and future plans are reported in this paper.

INTRODUCTION

Before delving into the subject matter it is helpful to gain some perspective. This can be accomplished by viewing the same topic from different angles. Two useful views are the history of STEP and the context STEP provides today for the current pilot activity. But for starters, let us do away with the acronym and spell it out. STEP stands for **Standard for the Exchange of Product model data**. That is quite a construct and it is probably as indicative as anything about the nature of STEP.

Short History of STEP

Without reaching too far into the past, STEP can be viewed as the evolutionary result of many efforts. The following summary has been derived from information in [Ref. 1].

U.S. Efforts

Starting in the 1970s, the American National Standards Institute (ANSI) developed the notion that data should be described independent of particular uses or computer technologies. During the same time frame, the U.S. Airforce developed formal methods of information modeling as part of its Integrated Computer Aided Manufacturing (ICAM) program. Later, ICAM made a significant contribution to IGES through its Product Data Definition Interface (PDDI), which was to develop a replacement for blueprints. The Computer-Aided Manufacturing – International (CAM-I) organization developed mathematical presentations of geometry and topology, which contributed significantly to the formal description of Boundary Representation (B-REP) data. At the beginning of the 1980s, the National Bureau of Standards (NBS) formed the IGES organization (IGES = Interim Graphics Exchange Specification) with the goal of developing a common translator for CAD applications.

International Efforts

Problems in the exchange of product data were also recognized early on in Europe. In 1977, the European Association of Aerospace Industries (AECMA) developed a format that allowed the exchange of simple surface geometry. The German Verband der Deutschen Automobil Industrie (VDA) was created in 1982 to address the exchange of free form surfaces and curves needed by the automotive industry. In 1983 the French Standard

d'Echange et de Transfer (SET) project was started by Aerospatiale because of the need for a common database capability. And in 1984 the European Commission funded a project called CAD Interfaces (CAD*I), which worked mainly in the exchange of product model data and finite element analysis. In 1987, CAD*I achieved the first ever B-REP solid model exchange between different CAD systems.

The Beginning of STEP

In the mid 80's, many of these efforts had produced results and the focus shifted towards a common solution. From within the IGES organization, the first Product Data Exchange Specification was released in 1984. It was a "proof of concept" to validate methodology and turned eventually into a specification for the international effort led by ISO TC184/SC4 responsible for the development of ISO 10303, informally known as STEP. Since then the enormous number of product data entities has been gathered into many specific Application Protocols, which define the context and scope for various industrial needs.

STEP Today

Today STEP has evolved into over 30 Application Protocols. Some see increasing industrial use, whereas others are still in the developmental stages. A subset of these AP's is particularly suited for the Aerospace industry and is described in [Ref. 2]. This subset includes AP's for System Engineering, Engineering Analysis, 3D Design, and Technical Data Packages. U.S. companies such as Boeing and Lockheed Martin, are taking the lead to create an interoperating suite of Engineering Analysis (EA) APs.

Here, the STEP AP development pattern has similarities with a traditional design pattern, which starts with a CAD model, followed by engineering analysis. Whereas the 3D Design AP (AP 203) has already found widespread acceptance and is incorporated in most commercial CAD packages, STEP development in the engineering analysis area is most advanced in the finite element structural analysis domain through AP209 – Composite and Metallic Structural Analysis and related design who's first commercial incarnation is available through MSC PATRAN. Currently, ISO TC184/SC4 is engaged in the development of an Engineering Analysis Core Model (EACM) with the goal of harmonization and interoperability of new EA APs, which address aero-thermo/elasticity, dynamics and materials.

In parallel with these developments, the European Space Agency (ESA) in 1996 initiated the development of two STEP-based companion standards called STEP-NRF and STEP-TAS. NRF, the **N**etwork-model **R**esults **F**ormat, is a generic, discipline-independent protocol, which provides representation of engineering objects by network models consisting of nodes and nodal relationships. TAS, the **T**hermal Analysis for **S**pace protocol, specifies the resources necessary for the electronic exchange of data in the domain of thermal control engineering for space applications.

STEP-TAS

STEP-TAS is a protocol for the definitions of space missions and models used in thermal analysis. The space missions part comprises definitions of orbit, space thermal environment, material property environment and kinematic articulation. The model definition comprises surface geometry (including boolean constructive surface geometry), thermal-radiative properties and meshing, kinematic structure, materials and physical properties. STEP-TAS is a pure extension of STEP-NRF. It adds - or specializes - the specific constructs that are needed for space thermal analysis applications.

The following are within the scope of STEP-TAS:

- The representation of an engineering object by a network model of discrete nodes and relationships between those nodes.
- A hierarchical tree structure of network models and submodels.
- The definition and representation of properties of engineering objects. Both quantitative properties (with numerical value) and descriptive properties (with descriptive content) are supported.
- The representation of values of properties as scalars, vectors and tensors.
- The definition and representation of analysis, test and operation runs, which produce bulk results.

- The definition and representation of product structure, in the form of assembly trees, and the relationships between items in the product structure and in the network model representation.

Examples of three typical STEP-TAS objects are given below in Figure 1 –3 below.

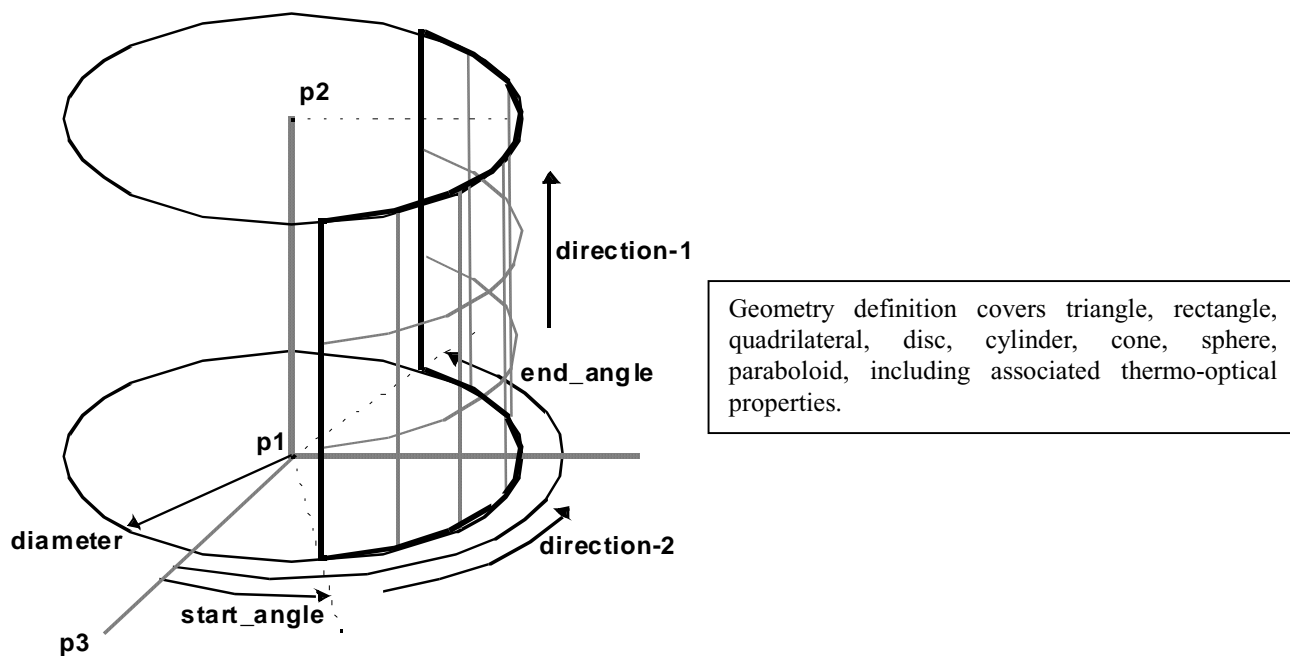


Figure 1 Example of STEP-TAS geometry definition

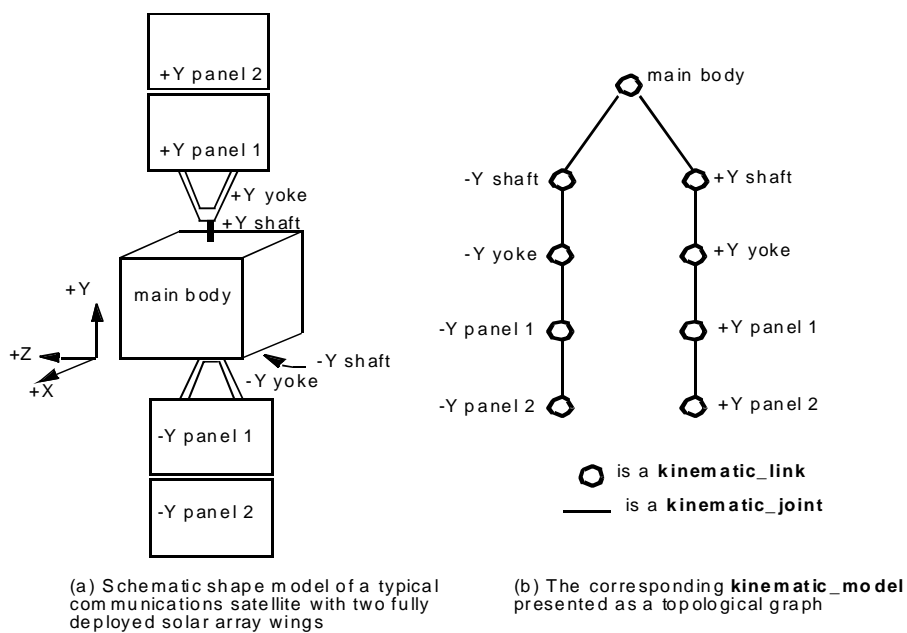


Figure 2 Product structure and kinematic structure in STEP-TAS

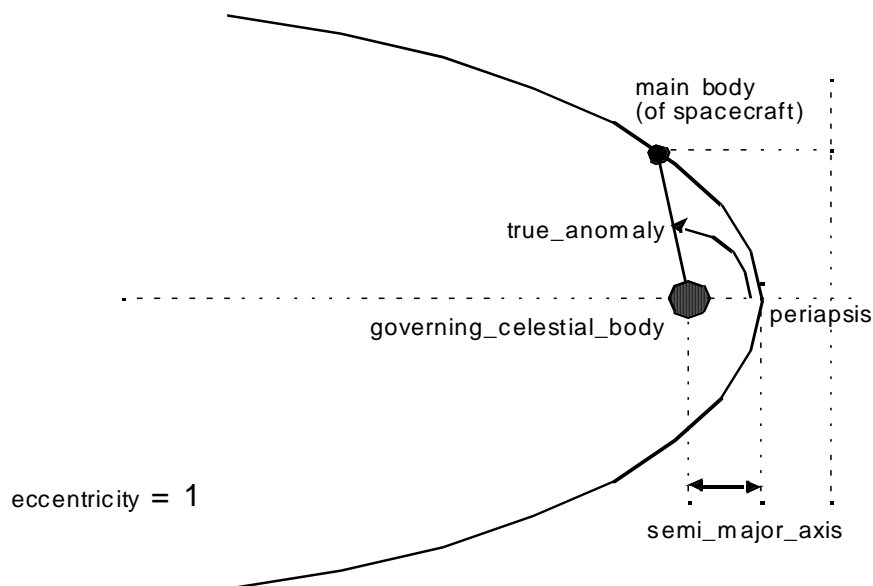


Figure 3 STEP-TAS Orbit Definition

STEP-TAS has passed rigorous testing by ESA and is now industrially implemented in two European analysis tools, ESARAD (ESA/ESTEC) and THERMICA (Matra Marconi Space). A third implementation is planned for CORATHERM (Alcatel Space).

THE U.S. STEP-TAS PILOT

STEP-TAS was first introduced to the U.S. thermal engineering community during TFAWS in 1998. In the two years that have since passed, substantial progress has been made to introduce STEP-TAS in the U.S., culminating in the current pilot activity.

Pilot Scope

The scope of this effort is limited to the development of a prototype bi-directional STEP-TAS interface of defined and limited capability. The word prototype is used in the sense of a feasibility demonstration. This specifically means that the final product is not required to support all activities that are typically found in a radiation model. The prototype is limited to the bi-directional exchange of the surface geometry and thermal properties.

Pilot Objectives

The pilot can be compared to planting a seed. It is intended to raise awareness and to demonstrate the feasibility of STEP-TAS. The hope is that it grows and matures into a full implementation of STEP-TAS into our thermal analysis tools and engineering processes.

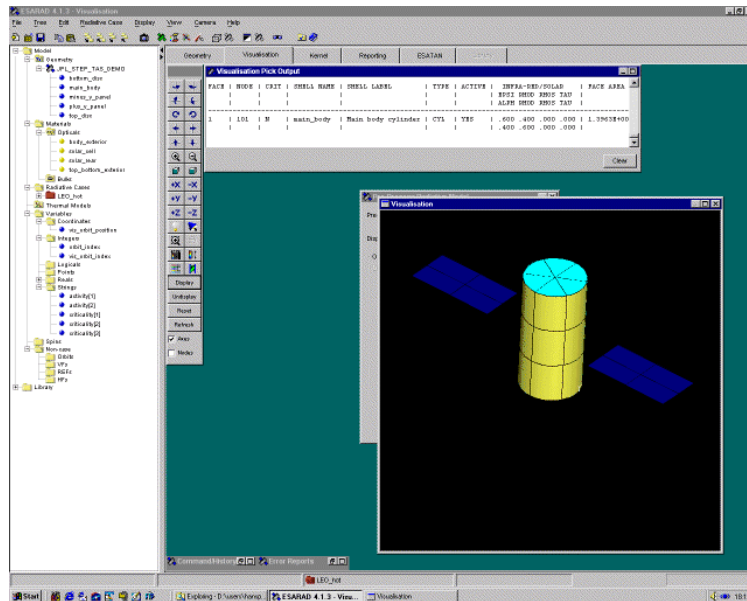
The pilot addresses the following objectives:

1. Develop a STEP-TAS prototype interface based on SIMULOG/ESA provided APIs.
 - This prototype can either be embedded into the respective radiation analysis tool or a stand-alone product.
 - The prototype shall be bi-directional (tool to STEP-TAS, STEP-TAS to tool).
2. Demonstrate a visual comparison of the native and STEP-TAS based geometry. For the STEP-TAS geometry visualization, apply the visualization tools developed by ESA.

3. The Prototype interface shall be capable of successful bi-directional exchange of the defined geometry. "Successful" is defined as a bi-directional exchange from an analysis tool into STEP and back from STEP into the tool without loss of information. The metric used shall be a defined set of radiation exchange factors calculated before and after the exchange.
4. Once all prototypes have been developed, STEP-TAS models from all developers will be collected and made available to all developers. An attempt shall be made to read and visualize all STEP-TAS files received.

Pilot Geometry

The pilot geometry is purposely kept simple and consists of a cylinder, disks, and quadrilaterals. Figure 4 below shows a rendering of this geometry.



```
ISO-10303-21;
HEADER;
...
#109=TYPE_QUALIFIER('diffuse');
#110=TYPE_QUALIFIER('infra_red');
#111=ATR_PROPERTY_NAME('transmittanc
e');
#112=ATR_PROPERTY_QUANTITATIVE(#1
11,,SYMMETRICAL.);
#113=ATR_PROPERTY_USAGE(#71,#112,#1
14);
#114=ATR_PROPERTY_MEANING((#109,#1
10));
#115=SI_UNIT(*$,.METRE.);
#116=SI_UNIT(*$,.DEGREE_CELSIUS.);
#117=GLOBAL_UNIT_ASSIGNED_CONTE
XT("",( #115,#116));
#118=GLOBAL_UNCERTAINTY_ASSIGNE
D_CONTEXT("",( #119,#120));
#119=UNCERTAINTY_MEASURE_WITH_U
NIT(LENGTH_MEASURE(1.E-
008),#115,
```

Figure 4 Pilot Geometry in ESARAD and Excerpt of STEP-TAS File

Pilot Status

Five US thermal tool vendors are participating. In alphabetical order they are Cullimore and Ring Inc. (Thermal Desktop), Harvard Thermal Inc. (TAS), Network Analysis Inc. (SINDA/ATM), SpaceDesign (TSS), and TAC Inc. (NEVADA). The pilot implementation was ongoing at the writing of this paper. The status given below is as of late July 2000.

Status of Cullimore and Ring Inc. (Thermal Desktop)

The STEP-TAS pilot for Thermal Desktop has been completed. In addition to the tasks defined in the pilot, C&R added the capability to import/export triangles, quads, cones, spheres, and paraboloids. The ability to import/export entities that have uneven nodalization has also been implemented in Thermal Desktop. Thermal Desktop already had a TRASYS import/export function, so when you combine this with the STEP-TAS importer, a user will be able to take a TRASYS model and convert it to STEP-TAS or vice versa. The Beta release of Thermal Desktop that contains the STEP-TAS translators will be version 3.3 and will be available in mid August of 2000.

We found the pilot very useful as an introductory process, but would like to see the protocol and the API expanded to handle items such as submodels, uneven nodalization, registers, finite elements, and Thermophysical entities such as thickness, insulators, and contact conductance.

Status of Harvard Thermal Inc. (TAS)

The Baghera viewer is installed and working and we got the STEP-TAS examples to compile and run using the MS VC++ compiler. We had to modify the Include Files so they are compatible with the C++ environment. When we created a class from Example 1 and added it to TAS, TAS crashed.

When we created a simple project and added the class to it, it worked fine. Our conclusion is that there is something in TAS that is incompatible with the STEP-TAS libraries. The problem we have is that there is no way for us to find what it is.

We plan to install our VC++ compiler on a laptop for TFAWS. Maybe we can find the problem. We would like to complete the pilot. What we could do is to write a simpler translator that reads a TAS model file and writes out a STEP-TAS file. We could do the reverse as well. Maybe we will try this before TFAWS.

Status of Network Analysis Inc. (SINDA/ATM)

Network Analysis has added the ability to export a STEP-TAS file from our FEMAP based model builder (SINDA/ATM). This interface was created so any radiation code that can read a STEP-TAS file could interface to SINDA/ATM for solving the thermal radiation/orbital portion of a thermal model. We only support triangles, quads and rectangles since a FEA meshing program like FEMAP divides shapes such as cylinders into flat finite elements. Before adding the STEP-TAS export, we wrote 4 different file types, TRASYS, NEVADA, THERMICA and TSS. If all of these codes had supported STEP, we would have only had to create one type of file export.

Because our product is a graphical model builder, and not a radiation program, importing a STEP-TAS file is not as important to the user of SINDA/ATM. This is because a thermal radiation STEP-TAS model does not contain the complete information that is needed to build a thermal model. The missing information is thickness, thermal conductivity, density and specific. The surfaces (plate geometry) can be imported, and for a small model it is a relatively easy task to assign material properties and thickness to these surfaces. For a large model with many surfaces, this task could be very time consuming. We are currently working the import feature and it should be finished by early August.

The basic flow to interfacing a radiation code to the SINDA/ATM graphical modeler is to export the STEP-TAS radiation file, run the radiation code to produce the radiation conductors and absorbed flux data and finally bring these radiation results back into the thermal model. The STEP-TAS file does not contain the results, so we need to read this data from each radiation code that we support (currently 4 different file formats). Having this data available from all of the radiation codes in a STEP-NRF file would reduce maintaining 4 different interfaces to just one. Also, since file formats sometimes change from one version to the next for a radiation code, we have a total of 8 (4 import and 4 export) formats to keep current. Interfacing to STEP-TAS and STEP-NRF would eliminate us from having the latest version of each radiation code.

In summery, we think exporting STEP-TAS will simplify our SINDA/ATM product, if all of the radiation codes we support add this interface. In order to build a thermal model, the radiation results need to be imported, and this data could come from a STEP/NRF file if the radiation codes produced this file. We currently have to maintain 4 export and 4 import (radiation results) formats, but with STEP-TAS and STEP-NRF this could be reduced to two imports (one for geometry and one for results) and one export and interface to all radiation codes that support this format. Because the STEP-TAS data from a radiation code contains no surface thickness or material properties, it may not be very useful to import a STEP-TAS model into our SINDA/ATM model builder. While one could manually add this missing information for a small model, it may be time consuming for large models.

Status of SpaceDesign (TSS)

With a later start than the other participants, TSS has so far progressed to install the viewing and API software. An initial set of surface primitives has been successfully exported to the STEP-TAS format. It is expected that the pilot is completed for at the time of the TFAWS workshop. A full bi-directional implementation is planned.

TAC has completed the NEVADA to STEP portion of the code for the basic shapes required by the example file. Other basic shapes have been coded into the translator, but will not be included into production code until the requirements for the STEP-TAS Pilot are met. The STEP to NEVADA code is currently under development. The NEVADA file writing routines are completed with most of the development efforts concentrating on reading and translating the STEP file.

EUROPEAN CONTRIBUTION

The U.S. STEP-TAS pilot is an implementation of information technology developed by several European organizations under the lead of ESA. The obvious contribution is, of course, the development of the STEP-TAS format. But two other developments are essential for an efficient STEP-TAS implementation into U.S. thermal analysis tools. One is the development of high level Application Programming Interfaces (APIs) by SIMULOG. These APIs permit the development of translators without the need to completely understand STEP-TAS on the lowest level of detail. The critical function of these APIs is demonstrated in Figure 5 below.

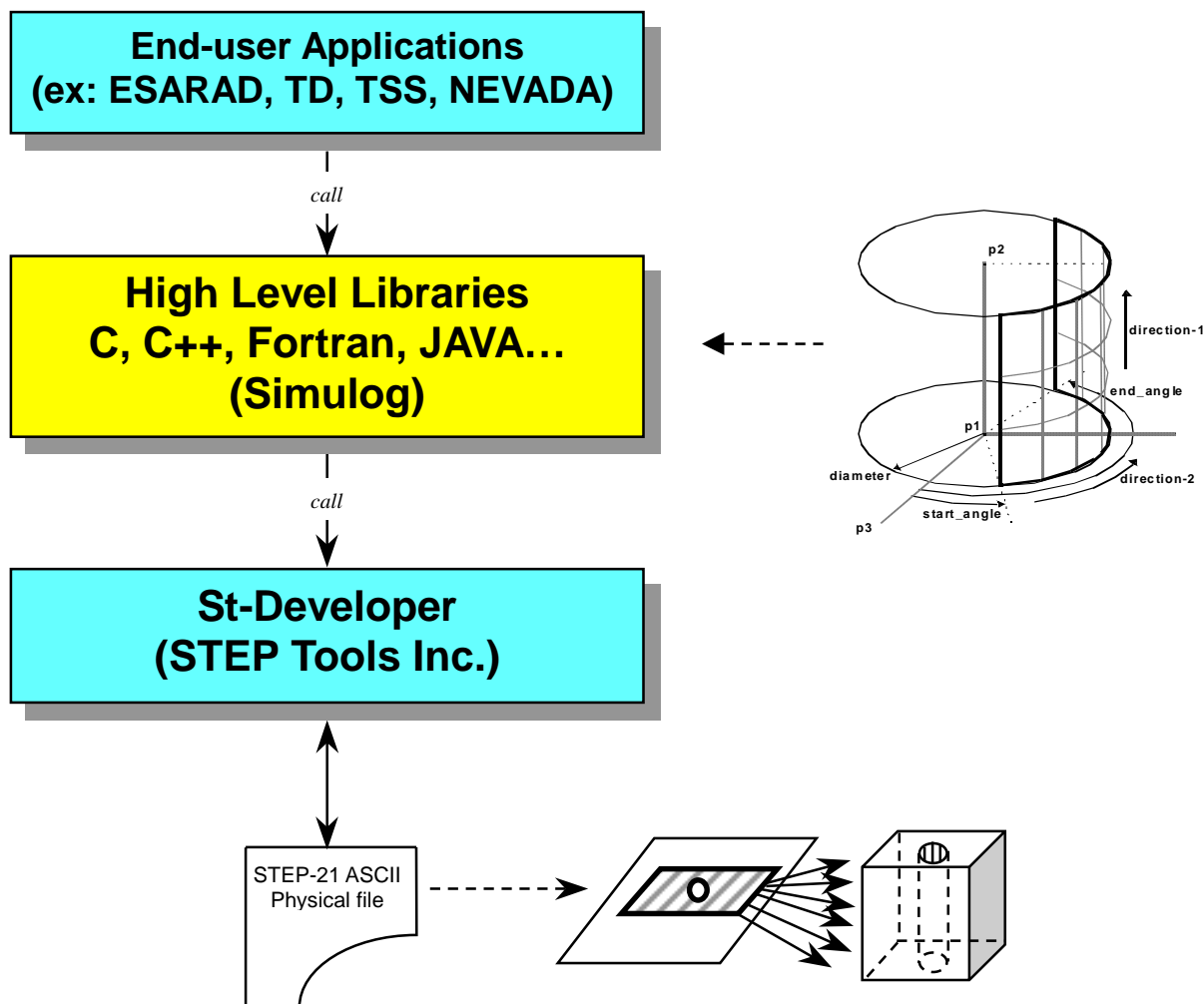


Figure 5 STEP-TAS APIs

The other contribution is Baghera View, a visualization tool developed by SIMULOG under contract to CNES. As can be readily appreciated by anybody who has modeled geometry, visualization is essential for the validation process. An example of Baghera View is shown below in Figure 6.

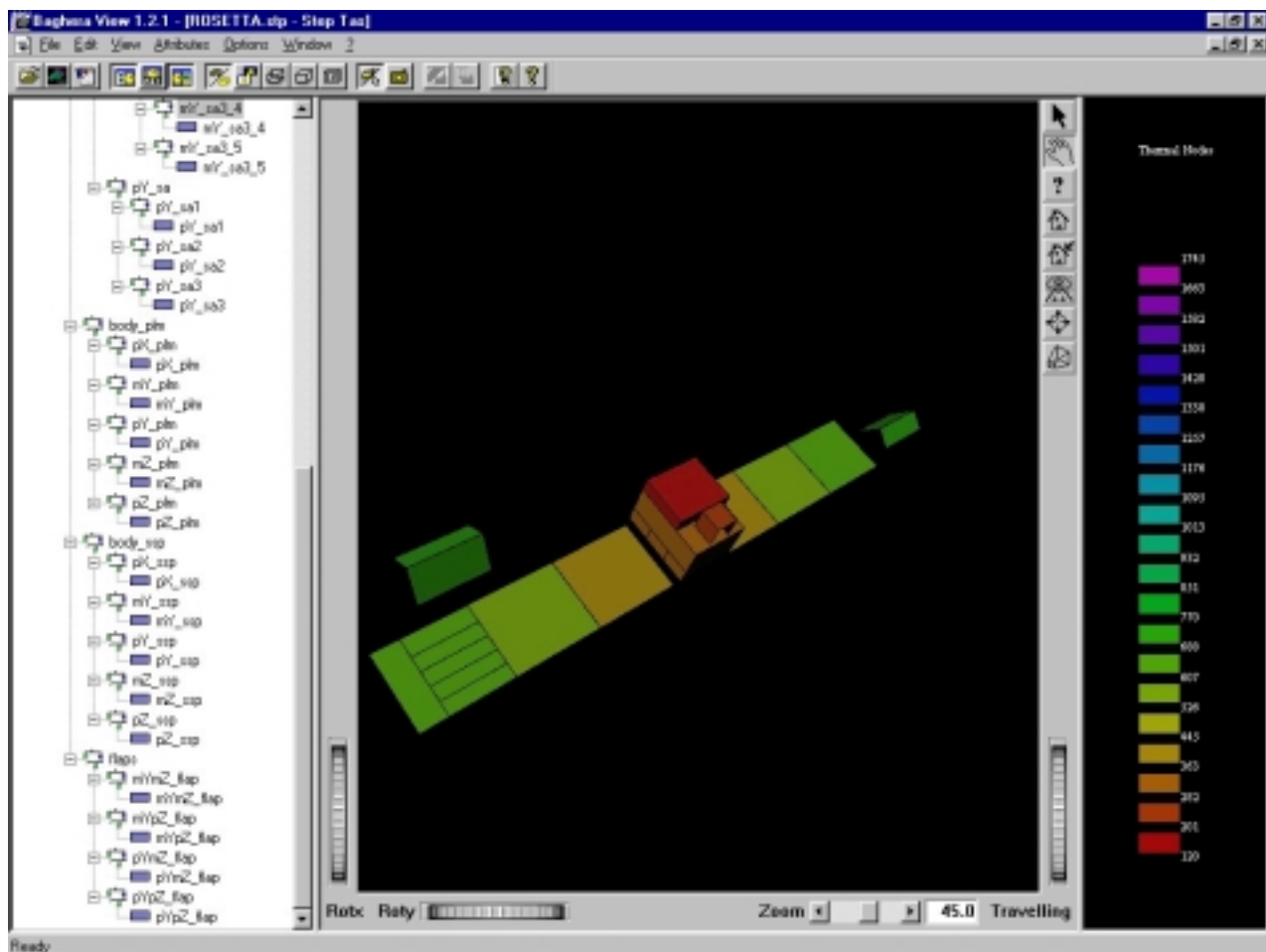


Figure 6 Sample Screen of Baghera View

CONCLUSION

The U.S STEP-TAS pilot holds great promise. Success is already evident at this intermediate stage and it is expected that all pilot objectives will be met. But this pilot is also remarkably successful in demonstrating cooperation between many diverse organizations. When it is concluded in a few weeks, the results represent the efforts of five U.S. thermal software vendors, SIMULOG, CNES, ESA and NASA.

The pilot is a significant step towards full interchangeability of thermal radiative models and independence of analysis tools. Once a full implementation of STEP-TAS has been achieved, the results will be liberation from error prone data format translation and a renewed focus on engineering and its underlying processes. The increases in productivity, especially in areas of tight integration of multiple partnering organizations, such as ISS or a new Mars project, are expected to be significant.

And finally, this pilot is hoped to be the first of many more to come, when, starting with STEP-NRF, other engineering analysis application protocols are going to be implemented ...

ACKNOWLEDGEMENTS

The work described in this paper was funded through the Develop New Products (DNP) domain of the Jet Propulsion Laboratory, California Institute of Technology, under contract with the National Aeronautics and Space Administration. STEP-NRF and STEP-TAS protocols as well as the ESARAD / STEP-TAS converter were developed under contract from ESA with support from CNES. Baghera View was developed under CNES contract

The pilot objectives require a substantial step towards a complete STEP-TAS implementation in the respective thermal analysis tools and could not have been met without additional contributions of resources from the participating tool vendors.

REFERENCES

- [Ref. 1] Sharon J. Kemmerer (Editor), The Grand Experience, NIST Special Publication 939
- [Ref. 2] Eric Lebegue, Georg Siebes, Charles Stroom, Thermal Analysis Data Exchange between ESA and NASA with STEP, ICES 99ES-39

RELIABILITY ENGINEERING AND ROBUST DESIGN: NEW METHODS FOR THERMAL/FLUID ENGINEERING

Brent A. Cullimore
C&R Technologies, Inc.
Littleton, Colorado 80127-5710

Glenn T. Tsuyuki
Jet Propulsion Laboratory
Pasadena, California 91109-8099

ABSTRACT

Recent years have witnessed more improvement to the SINDA/FLUINT thermohydraulic analyzer than at any other time in its long history. These improvements have included not only expansions in analytic power, but also the additions of high-level modules that offer revolutions in thermal/fluid engineering itself.

One such high-level module, "Reliability Engineering," is described in this paper. Reliability Engineering means considering tolerances in design parameters, uncertainties in environments, uncertainties in application (e.g. usage scenarios), and variations in manufacturing as the stochastic phenomena that they are. Using this approach, the probability that a design will achieve its required performance (i.e., the reliability) is calculated, providing an assessment of risk or confidence in the design, and quantifying the amount of over- or under-design present.

The design to be evaluated for reliability will likely have been produced using traditional methods. Possibly, the design was generated using the Solver optimizer, another high-level module available in SINDA/FLUINT. Using design optimization, the user quantifies the goals that make one design better than another (mass, efficiency, etc.), and specifies the thresholds or requirements which render a given design viable or useless (exceeding a performance limit, etc.). SINDA/FLUINT then automatically searches for an optimal design.

Robust Design means factoring reliability into the development of the design itself: designing for a target reliability and thereby avoiding either costly over-design or dangerous under-design in the first place. Such an approach eliminates a deterministic stack-up of tolerances, worst-case scenarios, safety factors, and margins that have been the traditional approaches for treating uncertainties.

In any real system or product, heat transfer and fluid flow play a limited role: there are many other aspects to a successful design than the realm of thermal/fluids that is encompassed by SINDA/FLUINT. Therefore, this paper concludes with brief descriptions of methods for performing interdisciplinary design tasks.

INTRODUCTION: THE NEED FOR A NEW METHOD

Overdesign is common and expensive. In large scale projects, each discipline (thermal, structural, power, etc.) communicates worst-case requirements to other disciplines rather than attempting to couple the design analyses. This leads to designs that are heavier and more costly than they need to be, *and in some cases does not even result in a safer or more reliable design.*

For example, it is common for power specialists to require that nickel-hydrogen batteries never exceed 15°C. This creates a serious thermal control challenge, requiring additional structural mass, technology risk, and, ironically, heater power. In fact, nickel-hydrogen batteries do not fail at 15°C, they simply become less reliable and more likely to fail the longer they operate at elevated temperatures. Occasional exposure temperatures up to as high as 30°C are tolerable but undesirable, yet total avoidance of any temperature greater than 15°C during any mission phase becomes the task of the thermal control specialist. The thermal control specialist might even resort to fancier and therefore more risky thermal control options to achieve this requirement, resulting in a *less* reliable overall design than if temperature excursions had been better tolerated in the battery design requirements! Examples of such overdesign abound.

Even within one discipline, overdesign exists due to stack-up of margins and worst-case scenarios until the design case is unrealistic and will likely never occur. A worst-case (*unlikely*) spacecraft attitude is combined with end-of-life

expected degradations of optical coatings, *estimations* of worst-case electronic dissipations, and *predictions* of worst-case conductive interface performance, etc. Additional margin is then added to cover *uncertainties* in thermal modeling, environment, and component sizing (11°C prediction margin plus either 10°C margin from qualification on passive designs or 25% control authority on active designs, per MIL-STD 1540c). Only when meeting an extreme stack-up of margins and uncertainties becomes impossible does a renegotiation of adequate margin begin, and such renegotiations are seldom based on any mathematical rigor or true knowledge of the underlying risk.

In the aerospace industry, which is heavily influenced by understandably cautious military standards, such over-design compensates for unknowns and unforeseen problems. Success in such a design environment is a necessity, and cost is a secondary consideration.

In commercial satellites, on the other hand, cost is a primary consideration. An overall satellite reliability of 99% may be desired, but if significant savings result from a reduced reliability of 98%, the latter option will be seriously considered. For example, it is common to apply a 5°C uncertainty to thermal analysis predictions in a commercial environment versus an 11°C uncertainty dictated by MIL STD 1540c. “Safer” is also much more costly.

NASA’s “faster, better, cheaper” campaign in many ways represents a shift from a military perspective to a commercial one: additional risk may be *intelligently* traded against reduced mission cost.

Statistical variations and uncertainties are intrinsic to thermal/fluid designs. They occur in the form of:

1. Dimensional tolerances and property or performance uncertainties. Examples: interference fits, epoxy bond line thicknesses, as-built insulation performance, degradation of optical coatings, conductance across interfaces, convection coefficients, two-phase pressure drops.
2. Boundary conditions. Examples: weather, orbital environments, solar constants.
3. Requirements and design margin. Examples: battery dissipation levels, equipment failure (temperature control) limits, heat pipe excess capacity, heater margin.

Uncertainties abound in thermal design, and performance specifications (design requirements) are usually negotiable, meaning that they can be violated occasionally or under certain circumstances. As an alternative to stacking up worst-case margins, uncertainties, the engineer could combine these factors statistically to yield information about the degree of confidence (“reliability”) in a particular point design. In other words, the engineer could generate not just a single performance predictions but also a distribution of performance predictions with associated probabilities of occurrence, as shown graphically in Figure 1.

Consider an example. During the design of the space station single-phase ammonia coolant loop, the question arose of compliance with requirements given the uncertainty in the manufacture of flow control orifices. In other words, the baseline design included specific orifice sizes as needed to achieve a balance of flow rates between parallel legs such that no single payload would have less than the required flow rate (and hence be at risk of overheating). Even slight changes in the orifice dimension could result in uneven flow distributions, such that a worst-case stack-up of orifice sizes would definitely cause a lower or upper temperature control limit to be exceeded. Recognizing that such a problem should not be treated using a worst-case but rather a probability distribution, the confidence in the final design was determined quantitatively using statistical combinations of various orifice sizes. Unfortunately, since an older version of SINDA/FLUINT was employed which had no such statistical design features, considerable work was expended to perform the analysis.

Another space station example is the “design-to-freeze” radiator. Thawing ammonia ice can rupture fluid lines, and hence high strength materials and other design measures were used to overcome the problem. The number of expected fatigue cycles had to be treated statistically combining estimates of loads and environments over the life of the station. Also, the worst case design point for the thaw stress resulted from a stack-up of various uncertainties in radiator performance, environmental heating rates, etc. Because a worst-case stack-up resulted in an unrealistically harsh design case with no potential design solution, development and negotiation of a reasonable design case had to

be performed to provide adequate confidence in the resulting design. The resulting design case was also used as the basis for the validation test program.

Although only two examples are provided above, opportunities for treating limits not as fixed “goal posts” but as probabilistic distributions abound in most engineering problems. Engineers are simply not accustomed to dealing with design problems in this manner in part because of training and in part because of lack of tools.

INTRODUCTION: SINDA/FLUINT

SINDA/FLUINT (Ref 1) is the NASA-standard heat transfer and fluid flow analyzer for thermal control systems. Because of its general formulation, it is also used in other aerospace specialties such as environmental control (ECLSS) and liquid propulsion, and in terrestrial industries such as electronics packaging, automotive, refrigeration, and power generation.

SINDA/FLUINT is used to design and simulate thermal/fluid systems that can be represented in networks corresponding to finite difference, finite element, and/or lumped parameter equations. In addition to conduction, convection, and radiation heat transfer, the program can model steady or unsteady single- and two-phase flow networks, including nonreacting mixtures and nonequilibrium phenomena.

SINDA

SINDA uses a thermal network approach, breaking a problem down into points at which energy is conserved (*nodes*), and into the paths (*conductors*) through which these points exchange energy via radiation and conduction. While often applied as a lumped-parameter modeling tool, the program can also be used to solve the finite difference

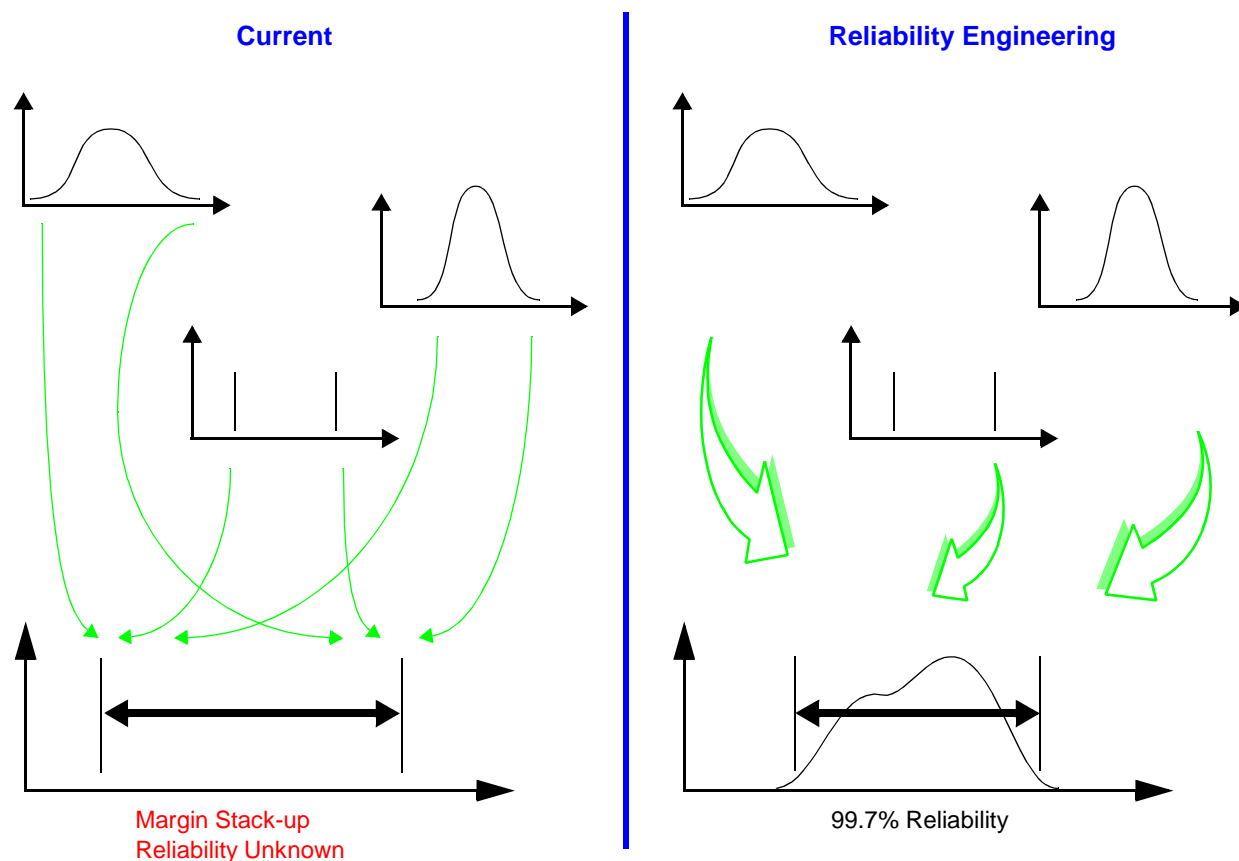


Figure 1: Avoiding Overdesign by Combining Uncertainties and Meeting Requirements Statistically

(FDM) or finite element (FEM) equations for conduction in appropriately meshed shells or solids. One can employ finite difference, finite element, and arbitrary (lumped parameter) nodes all within the same model.

An important improvement over ancestral versions of SINDA is the inclusion of submodels, which enable analysts to subdivide a large network of nodes and conductors into collections of subnetworks consisting of nodes, conductors, or both. Submodels represent a convenient means of combining separately developed models, each with its own control variables, customization logic, solution method, and perhaps conflicting node and conductor numbering schemes. More often, they are simply used to improve the organization and legibility of the model, or to perform high-level simulation manipulations such as dynamically swapping sets of boundary conditions, evaluating alternate designs or components, or simulating variable configurations.

Solutions may be performed in single- or double-precision without any model or logic changes. Also, either iterative or simultaneous (optimally reordered sparse matrix) solutions may be used in steady-state or transient analyses. SINDA/FLUINT provides a powerful means for creating highly customized solution schemes by permitting the user to vary the underlying methods on a submodel-by-submodel basis.

FLUINT

To answer the need to model two-phase fluid systems and to replace the cumbersome and limited “one-way conductor” methods employed by ancestral versions of SINDA for fluid flow simulation, FLUINT development was initiated by NASA in the 1980’s as a major expansion of SINDA. All major development has been completed, providing unmatched thermohydraulic analysis capability. Thermal and fluid models may be used alone or together to solve conjugate heat transfer problems as typically found in thermal control, propulsion, and energy systems.

FLUINT introduced a new type of submodel composed of network elements, *lumps* and *paths*, which are analogous to traditional thermal nodes and conductors, but which are much more suited to fluid system modeling. Unlike thermal networks, fluid networks are able to simultaneously conserve mass and momentum as well as energy.

Built-in Spreadsheet

A built-in spreadsheet enables the user to define custom (and perhaps interrelated) variables (Figure 2) call *registers*. The user can also define complex self-resolving interrelationships between inputs, and also between inputs and outputs. This spreadsheet allows rapid and consistent model changes, minimizes the need for user logic, and makes parametric and sensitivity studies trivially easy to perform.

The ability to create a SINDA/FLUINT model whose network parameters and logic are completely controlled by a few centralized registers enables high-level modules to be added. One of these high-level modules is the focus of this paper, but to fully explain it, another high-level module must first be introduced.

The Solver

The Solver was the first top-level design module in SINDA/FLUINT. It was released in 1997 as part of Version 4.0. The Solver is a fully featured nonlinear programming system that can be used for a variety of purposes:

1. Goal Seeking: the ability to solve for an input value given a desired response (output value). When used in this mode, the Solver eliminates the need to write iteration logic. For example, the user might wish to know what coolant pump flow rate results in an electronics temperature of 20°C. Or, the user may wish to find the conductivity of a plate or fin required to achieve a heat rejection efficiency of 95%.
2. Optimization (design synthesis): the ability to use SINDA/FLUINT to help size or select design parameters. The user defines which parameters are to be sized or selected along with an objective (“What makes one design better than another?”) and possibly some constraints (“What limits render a particular design viable or useless?”).

Registers				
Exit Save/Show Rows Post Processing Help				
	Int	Name	Expression	Comment
	<input type="checkbox"/>	disp	0.00017777	compressor volumetric displacement per revolution
	<input type="checkbox"/>	DmanC	$0.6 \cdot T_{coreC} / 0.6$	manifold hydraulic diameter, condenser
	<input type="checkbox"/>	DmanE	$0.5 \cdot T_{coreE}$	manifold hydraulic diameter, evaporator
	<input type="checkbox"/>	dtactual	refr.dtimuf	for diagnostics
	<input type="checkbox"/>	dtchar	10.0	expected time constant for time-dependent
	<input type="checkbox"/>	DtubeC	$1.72 \cdot 0.9$	refr side hydraulic dia, condenser, mm, 1.72 +/- 1.0
	<input type="checkbox"/>	DtubeE	$1.8 \cdot 2.0$	refr side hydraulic dia, evaporator, mm, 1.8 +/- 1.0
	<input type="checkbox"/>	emcomp	$\eta_{vol} \cdot (\text{disp} \cdot \text{rpm} / 60) \cdot \text{refr.dl} / 1000$	mass flowrate in compressor
	<input type="checkbox"/>	emlags	0.7	delay in adopting emcomp steady state
	<input type="checkbox"/>	emlagt	0.95	emlag for transients
	<input type="checkbox"/>	etalsen	$1.0 - \max(0, \min(1, (\text{cb}0 / (\text{pr}at \cdot \text{rpm}f) + \text{cb}1 / \text{pr}a$	isentropic efficiency
	<input type="checkbox"/>	etaVol	$1.0 - \max(0, \min(1, (\text{ca}0 / \text{rpm}f + \text{ca}1 + \text{ca}2 \cdot \text{pr}a$	volumetric efficiency
	<input type="checkbox"/>			

Figure 2: Part of the Built-in Spreadsheet: User-defined Registers

3. Test Correlation (calibration): the ability to adjust the model (not the design) until best-estimate values for uncertain parameters are generated. The user defines which parameters are uncertain, and provides test data to match against. Many correlation methods are available along with various data handling and comparison utilities: automated test data correlation is currently the primary use of the Solver module.

In all of the above cases, the user defines an *evaluation procedure*, or an arbitrarily complex series of SINDA/FLUINT solutions that tell the Solver how a particular design (for optimization) or model (for correlation) stacks up against the goals and requirements. Frequently, this procedure is no more complicated than a single steady state solution, but it can use any solutions or utilities available in SINDA/FLUINT to perform the task. In essence, using the Solver is like tasking a traditional SINDA/FLUINT model to run itself repeatedly until it achieves some user-defined objective (Figure 3).

Further description on the Solver is available in Reference 2. Knowledge of this module is a prerequisite for the subsequent discussion on Robust Design. However, a few key points need to be made before leaving this topic.

Without the high-level modules, SINDA/FLUINT is used in a traditional point-design fashion: given a specific and deterministic design and a fixed environment and usage scenario, steady-state and/or transient simulations are run to determine how the design performed. This method is *not* a natural way of performing common engineering tasks. Rather, it is readily available because it is what is “easily” achieved using numerical solutions. Because this type of software is all that has been available, a generation of engineers has been trained in these point-design evaluation methods, forgetting perhaps what the original intent of using them was: to produce good designs, and not just to evaluate point designs.

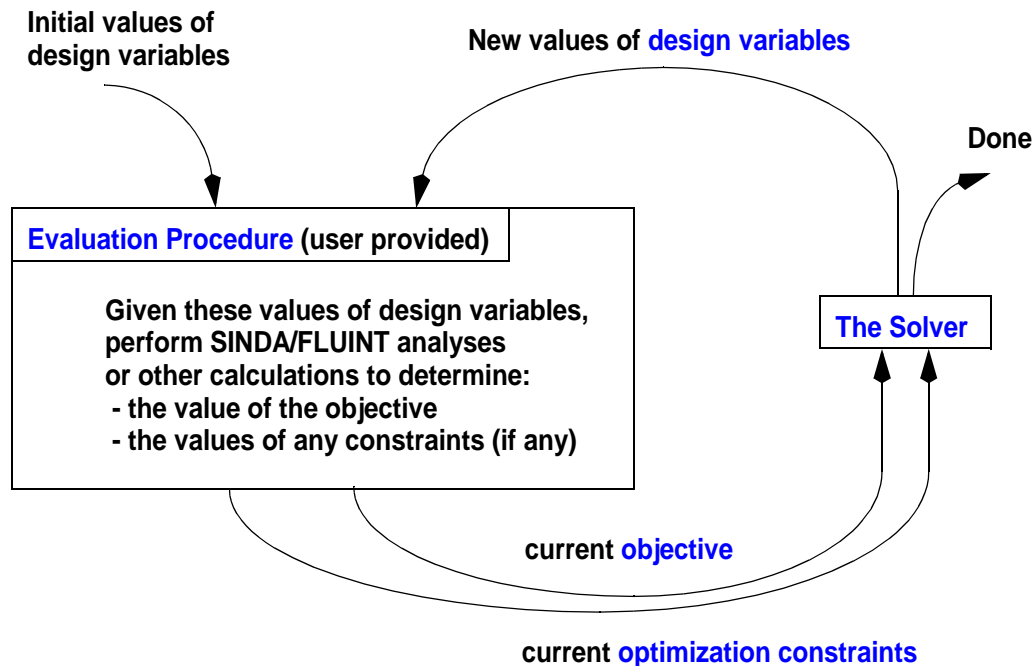


Figure 3: “The Solver:” Optimization and Test Data Correlation Module

The Solver module offers a revolution in SINDA/FLUINT usage because it represents an automation of the design process itself, and not an automation of a subprocess: point-design evaluation. Reliability Engineering offers a similar revolution because it permits many point-designs to be evaluated at a higher level. Combining the Solver and Reliability Engineering yields Robust Design: factoring reliability into the automated process of design synthesis itself, and thereby producing a design quantitatively balances risk and cost.

Accessibility

Concurrent developments have made advanced design features in SINDA/FLUINT more accessible. C&R’s *SinapsPlus*® is a complete nongeometric (circuit sketchpad) pre- and postprocessor for SINDA/FLUINT. C&R’s *Thermal Desktop*® (with the optional *RadCAD*® radiation analyzer) is a geometric (CAD/FEM/FDM) interface that brings traditional thermal modeling practices into a concurrent engineering environment. A freely distributed plotting program is also available: *EZ-XY*™.

RANDOM VARIABLES AND THEIR DISTRIBUTIONS

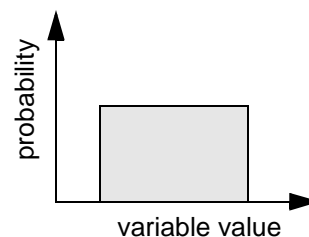
To use the Reliability Engineering module in SINDA/FLUINT, the user starts by identifying which parameters (dimensions, properties, boundary conditions, etc.) are uncertain. These *random variables* will be allowed to vary over a prescribed range, and any one value of such a random variable has a given probability of occurrence, at least in comparison to other values. This variation is called a *probability distribution*.

Once a parametric model is built using registers, a subset of these variables are identified as random. The user must then describe the distribution function of each random variable using one of three methods described next.

Uniform Distributions

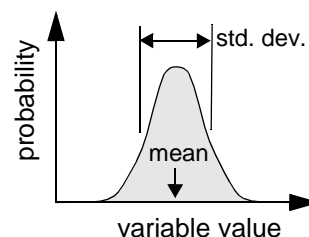
The simplest type of distribution is a uniform one: the random variable may assume any value with equal probability between a lower limit and an upper limit, as shown at the right.

This is an important class of distributions because it represents an easy transition from the current margin-based approach of worst-case high and low values. The margin-based approach to handling uncertainty is excessively conservative, corresponding to two delta (spike) distribution functions at the upper and lower limits, whereas the uniform distribution acknowledges that values in between are at least as likely to occur as the extremes. Unlike the margin-based approach to uncertainty, the Reliability Engineering approach makes no presumptions about which *combinations* of upper and lower limits yield problematic performance. Nonetheless, the uniform distribution is very simplistic: in most distributions values near the extremes are much less likely to occur than values near the middle.

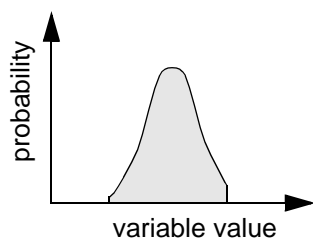


Normal Distributions

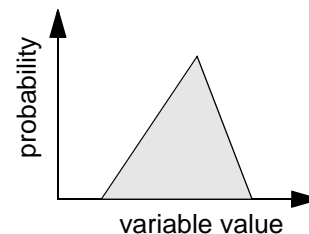
The most common type of nontrivial distribution is the normal or Gaussian distribution. It is a symmetric distribution that can be completely described by a mean value and a standard deviation. Many times, an engineer will know the nominal value of a parameter along with an upper and/or lower limit. Frequently these upper and lower limits correspond to a known number of standard deviations (usually about three) off the mean.



Arbitrary Distributions



Sometimes, a normal (Gaussian) distribution is appropriate, but a theoretical range between negative and positive infinity is nonphysical or would cause numerical problems: a truncated normal distribution is required (shown at left). Another possibility is a triangular (witch's hat) distribution, useful when all that is known is a most likely value plus a lower and upper bound (shown at



right).

In fact, there are many types of distributions available (e.g., log normal, Weibull, Chi-square, etc.), each suited for a different purpose. It is also possible that a distribution function is produced from test or manufacturing data or from a previous analysis.

To support any such distribution, SINDA/FLUINT accepts a user-supplied table (array) of value versus probability. Any number of points can be used to define the distribution function. SINDA/FLUINT itself can be used to generate the function for use in a future run using Fortran-style calculations.

RELIABILITY CONSTRAINTS (FAILURE LIMITS)

“Reliability” is the probability that a design will not exceed limits defining failure. For example, a design might be considered a failure if a critical component exceeded an upper or lower bound on a temperature, if a heater switched on and off excessively, if a pressure exceeded 25% of the burst pressure, etc. There may be many such failure limits.

A list of responses of interest to the designer (e.g., the temperature of the critical component) can be created as well as upper and/or lower limits on those responses (the failure limits). Collectively, these are referred to as *reliability constraints*. One such reliability constraint might appear as follows:

$$T_{min} \leq \text{battery.T100} \leq T_{max}$$

meaning that a failure will be assumed to exist if the temperature of node 100 in submodel “battery” goes below T_{min} or above T_{max} .

While the program must know what responses are desired and what the limits are on those responses in order to calculate reliability, such foresight is helpful but strictly not required. A user might forget to define any responses, or may indicate a response of interest without applying any limits to it.

In other words, the user might decide after having made a run to impose a new limit, or to investigate a new response. Such hindsight is afforded by expansions to postprocessing tools such as EZ-XY.

RELIABILITY ESTIMATION METHODS

SINDA/FLUINT offers three very different statistical analysis routines. These routines all perturb random variables according to their specified distributions, execute the evaluation procedure provided by the user (perhaps just a single steady state solution), and monitor reliability constraints (if any) to produce statistics regarding those responses, including the probability of a successful design. Figure 4 indicates this top-level data flow for the Reliability Engineering module.

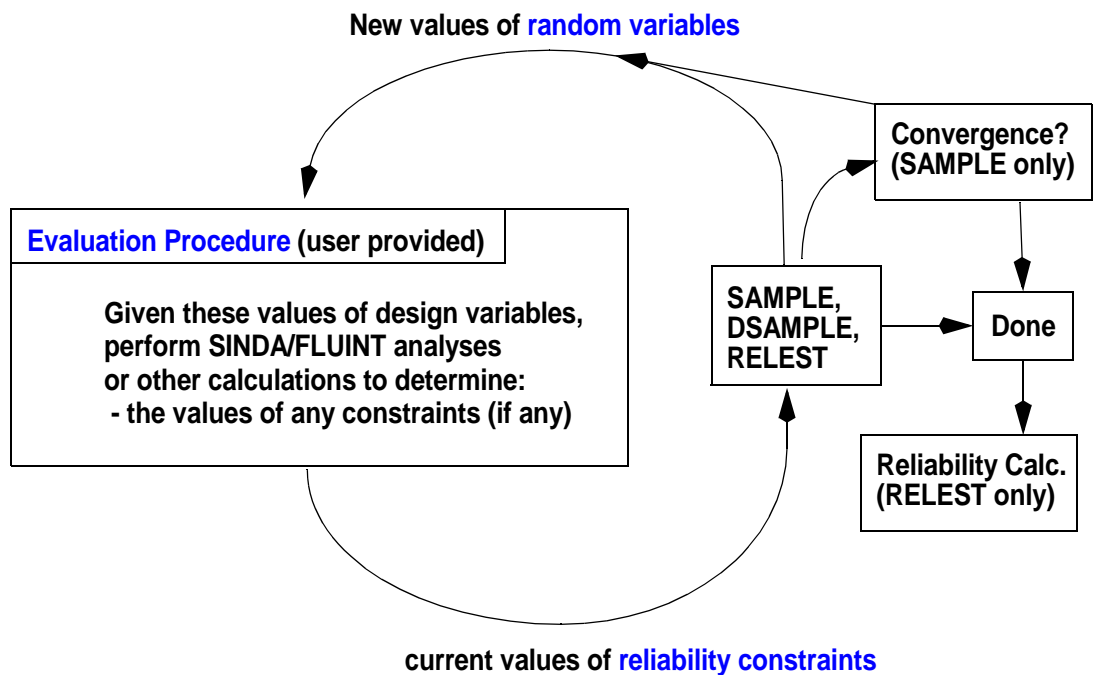


Figure 4: Flow Chart for Reliability Prediction Methods

However, the methods used by each of the three routines are intentionally very different, providing the user with a wide range of options. These statistical analysis routines are described next. Table 1 is a summary of the options available.

Monte Carlo Sampling

The simplest approach is that taken by the SAMPLE routine: a Monte Carlo method in which values of random variables are selected randomly according to their probability distribution functions. As an example, for a uniform distribution any value within the valid range is selected using a uniform random number generator. For normal distributions, random values are selected, but values near the center (the mean) will be generated more frequently than those at the extremes.

Table 1: Comparison of Reliability Estimation Routines

Routine	SAMPLE	DSAMPLE	RELEST
Method	Monte Carlo sampling	Descriptive sampling	Gradient method
Speed	Slow	Intermediate	Fast
Convergence Detected?	Yes	No	No
Fixed Execution Cost?	No	Yes	Yes
Overall Reliability?	Yes	Yes	No
Cumulative?	Yes	Somewhat	No
Applicability?	Unlimited	Unlimited	Limited. Assumes: - Gaussian variables - Linear responses - Continuous responses - Fixed failure limits

The Monte Carlo approach requires many samples (on the order of 1000: 100 to 10,000) and is therefore expensive. However, it yields the most information. Furthermore, the accuracy of the estimation can be controlled at least relatively if not absolutely: the SAMPLE routine detects convergence as defined by negligible change in the selected responses and their associated limits (i.e., the reliability constraints) between any two consecutive samples.

Monte Carlo Sampling provides two methods of predicting reliability. The first is a simple tally of the number of times a failure limit was not exceeded divided by the total number of samples. A similar method is used to predict overall reliability: * the percent of all sampled cases that did not exceed any limits. (In the limit of a single constraint with only an upper or only a lower limit, the overall reliability is the same as the reliability for that constraint.)

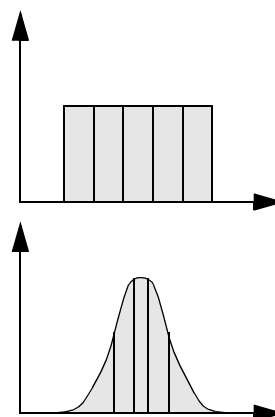
A second method is to accumulate statistics (mean and standard deviation) about every indicated response, and then to assume a normal (Gaussian) distribution for that response. The probability of exceeding any limit can then be calculated using the assumed profile.

Descriptive Sampling

A faster alternative to Monte Carlo sampling is descriptive sampling, which is used in the DSAMPLE routine. This approach has a known cost: the user specifies the number of samples to be made (based on what they can afford). This number becomes the resolution with which the distributions in the random variables are subdivided.

For example, if 100 samples are to be used, each input profile will be divided into 100 regions of equal probability. For uniform distributions, one hundred equal regions will be used. For normal distributions, the region near the mean will be more finely subdivided than the extremes such that each region is equally probably and therefore contains the same area (integral of probability over the random variable values: the *cumulative distribution function*). This subdivision is illustrated at the right using five subdivisions.

Once the distributions of the random variables have been subdivided, only one value from each subdivision (the center of the corresponding region in the cumulative distribution function) is sampled, since each of these values is as probable as any of the others. There is still randomness involved for more than one random variable: each cell, while sampled only once, is selected at random. For example, the 5th cell of variable #1 might be combined with the 88th cell of variable #2 in one run, but the 5th cell of variable #1 might be combined with the 42nd cell of variable #2 in a second run.



* This method only works if all the reliability constraints are independent (in series).

For the same number of samples, descriptive sampling yields more accurate results than Monte Carlo sampling. Typically, descriptive sampling takes only 10 to 20% as many samples as does the Monte Carlo method does to achieve the same accuracy. However, Monte Carlo sampling retains certain advantages, the most important of which is a measure of confidence that enough samples have been taken for the given problem. In other words, there is no convergence test possible in descriptive sampling. Furthermore, Monte Carlo sampling is more readily cumulative (repeated runs can be combined for more accuracy than can repeated runs of descriptive sampling), and it can yield a more accurate prediction of the overall reliability than can descriptive sampling.

Gradient Method

A method for estimating reliability is available that is even faster than DSAMPLE, but has even more limitations: RELEST. This technique is not a sampling technique at all. Rather, it estimates reliability by measuring gradients in the responses with respect to the random variables, and by assuming (but not requiring) that all distributions (both input and response) are normal (Gaussian). It further assumes that the mean of the responses can be predicted using the mean values of the random variables, and that response variations from that point are linear with respect to changes in inputs.

RELEST requires only $N+1$ evaluations, where N is the number of random variables. This is often an order of magnitude smaller than what DSAMPLE requires, which is itself often an order of magnitude smaller than what SAM-
PLE requires: *RELEST is comparatively cheap.*

The first evaluation uses the mean values of random variables, and assumes that the resulting responses are the means of those functions. The next (and final) N evaluations perturb each random variable (in input order) such that the gradients of each response with respect to each input variable can be estimated using finite differences. RELEST then assumes a first order Taylor series of variance (the square of standard deviation) can be applied to estimate the variance (and therefore standard deviation) of each response given the variance of each random variable, whether those variables are normal or not. Now the code has enough information to predict reliabilities: it has an estimate for the mean and standard deviation of each response, and can therefore predict the likelihood that a response will assume any given value.

RELEST cannot predict overall reliability much less the tallied estimate of reliability that a sampling routine can, and should be used with caution in cases with nonlinear responses and non-normal random variables. It also cannot handle variable failure limits. Furthermore, unlike sampling techniques, the accuracy of RELEST is not cumulative: repeated calls do not affect the accuracy of the results. However, because it is so inexpensive, RELEST is often plays an important role in Robust Resign (described later).

DATABASE AND POSTPROCESSING

An important part of the Reliability Engineering module is the database that can be created to store the samples or gradient perturbations made in the previously described routines.

One purpose of creating such a database is to be able to accumulate results in subsequent runs. For example, it may be desired to add 1000 more Monte Carlo samples to the samples taken in a previous run, in order to add to the accuracy of the predictions.

A second purpose of creating the databases is to be able to visualize the resulting response distributions by plotting histograms, such as the two EZ-XY histograms displayed in Figure 5. The user can also produce scatter plots to see how any two parameters are related to each other.

However, the most important use of the database is to be able to apply hindsight while postprocessing: to be able to define new responses of interest, or new limits to previously defined responses. Generating the samples can be an expensive proposition when using sampling methods, and so storing a database is very important in case failure thresholds change or are redefined, or simply if the user forgot to define a reliability constraint in the first place.

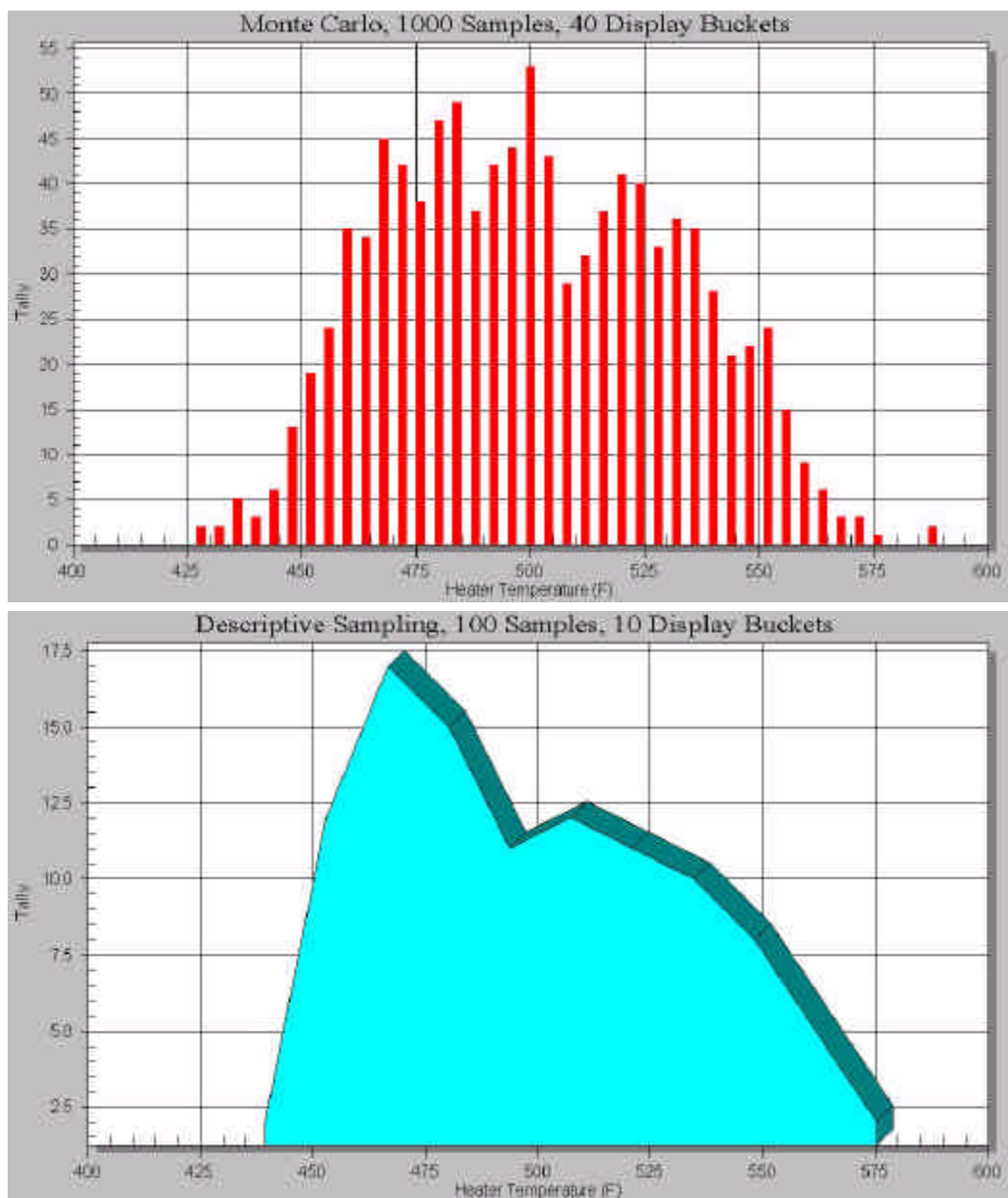


Figure 5: Sample Postprocessing: EX-ZY Histograms

A BRIEF EXAMPLE

Consider a metal bar that is heated on one end and which radiates to deep space on the other end, and is otherwise insulated. The length and thickness of the bar are known, as are the material properties. However, the width of the bar, the power applied, and the emissivity of the exposed (radiating) surface are less certain. The emissivity can assume any value from 0.08 to 0.12. The width of the bar is nominally 1 inch, and is expected to have a Gaussian distribution with a standard deviation of 0.01 inch. Similarly, the input power is nominally 10W but has a Gaussian distribution with a standard deviation of 0.5W.

What are the chances that the temperature of the heated side of the bar will not exceed 500°F under steady conditions?

A one-dimensional SINDA model of the bar is built using registers to define key dimensions and properties. Three of these registers are defined as random variables: WIDE, POWER, and EMIS corresponding to the above three uncertain terms. The definition of these registers, their identification as random variables, and the specification of their distributions is as follows:

```
HEADER REGISTER DATA
```

```
    . . .
    EMIS              = 0.1
    WIDE              = 1.0
    POWER             = 10.0
```

```
HEADER RANDOM DATA
```

```
    EMIS, UNIFORM,    0.08, 0.12
    WIDE, NORMAL,     SD = 0.01
    POWER, NORMAL,    SD = 0.5
```

The heated side of the bar corresponds to node #1 in submodel “sub1,” and therefore the reliability constraint is simply defined as:

```
HEADER RELCONSTRAINT DATA
```

```
    SUB1.T1 <= 500.0
```

The evaluation procedure is simply a steady state solution:

```
HEADER RELPROCEDURE
```

```
    CALL STEADY
```

Now one of more of the reliability routines (SAMPLE, DSAMPLE, RELEST) can be called from the main solution block of SINDA/FLUINT (called “OPERATIONS”), along with calls for output and/or database write operations. The following calls for descriptive sampling (100 samples by default) plus tabulated output of the predicted reliability:

```
    CALL DSAMPLE
    CALL RCSTTAB
```

Details of the SINDA model are omitted for brevity, but the above sample illustrates how easily Reliability Engineering can be applied to an existing model that uses registers. Older models not originally built using registers and expressions can be easily retrofitted, adding multiplying factors that are initially equal to unity.

In the above case, due to the presence of a non-normal random variable and the highly non-linear behavior of this radiation dominated problem, the RELEST routine can only be used as a first approximation. Such a fast but approximate calculation is ideal if reliability is estimated as a part of the evaluation procedure for a design optimization, as described next.

ROBUST DESIGN

Assume that a thermal control system is being designed for a component whose temperature cannot exceed 40°C. Traditionally, the user would iteratively develop such a design, and then stack up worst case conditions to assure that the temperature would never exceed some lower threshold (perhaps 30°C) allowing for safety factors or margin, which hopefully have some basis in experience if not test data.

If the degree of uncertainty in the inputs can be quantified, then the probability of exceeding 30°C or 40°C could be determined using the Reliability Engineering module described above.

Perhaps the Solver optimization module could be used to find a deterministic (nonrandom) design that will just meet the 30°C threshold. Any variation in parameters will then result in a reliability of roughly 50% relative to 30°C, with a higher probability of not exceeding 40°C. If the chances of exceeding 40°C are too great, the design must be regenerated using a greater safety margin: applying perhaps a 25°C limit during the redesign process (whether manual or automated). In other words, even with automated design synthesis using the Solver optimization module, *the margin is itself unknown and must be estimated iteratively.*

Robust Design means being able to factor the ultimate reliability into the design process: using reliability as a basis for synthesizing the design in the first place, and avoiding high-level design iterations.

The Reliability Engineering module described in this paper enables a user to estimate the reliability of a point design based on uncertainties in the dimensions, properties, boundary conditions, etc. The Solver optimization module enables a user to size or select dimensions, properties, etc. such that mass is minimized, or such that performance is maximized, etc. This section lists ways in which these two modules can be combined to yield even more powerful design tools.

Listed below are a few possible combinations of these modules:

1. a design can be selected using the Solver, and then (in the same or later run) the reliability of that design can be estimated
2. the reliability of a design can be used as an objective (“maximize reliability” or “minimize the chances of failure”)
3. the reliability of a design can be used as an optimization constraint (“find the minimum mass design that achieves a reliability of at least 99%”)
4. the range or variance of a random variable can be used as a design variable (“what variation can be tolerated: how tight must tolerances be?”)

In the first case, the Solver and Reliability Engineering modules are not combined so much as executed in series. Often, the random variable is expressed as the uncertainty in a parameter rather than the parameter itself. For example, a pipe diameter might be defined as a mean value plus a random value (whose mean is zero):

$$D_H = D_{\text{mean}} + D_{\text{random}}$$

The mean diameter (D_{mean}) might be selected using the optimizer (with D_{random} equal to zero), and then the reliability of the design might be evaluated about that mean using D_{random} as a random variable.

However, the real power of Robust Design is reflected by the second, third, and fourth cases listed above: reliability-based optimization to replace a margin or safety factor approach.

Example: Traditional Approach

Assume a computer chip fails when the semiconductor junction temperature exceeds 125°C: its *qualification* temperature. During acceptance testing of any particular unit, the junction temperature is stressed to 115°C, and it is therefore intended that this temperature (115°C) should never be exceeded during the life of the electronics: a 10°C margin exists as a minimum.

During the product design the junction temperature is not allowed to exceed 104°C, adding another 11°C of margin (using U.S. military standard MIL-STD-1540c for passive thermal designs as an example) to cover uncertainties in inputs (performance, environments) as well as uncertainties or inaccuracies in the model itself.

Worst case stack-ups are produced of hot and cold cases (environments, dissipations, etc.), beginning-of life (undegraded) properties versus end-of-life (degraded) properties, etc. and the designs are adjusted until the predictions show 21°C margin from the upper and lower bounds of qualification temperatures, and 11°C margin from the acceptance temperatures.*

The margins are shown graphically at the top of Figure 6 for the upper end of the temperature limits.

Expanding the Traditional Approach

Optimization and Reliability Engineering can be used to enhance the current design process.

Most designs are produced iteratively and manually. The Solver optimization module can be tasked to synthesize a design automatically or at least semi-automatically. In the above example, this would be performed by applying the limits as *optimization constraint* (similar to but independent from reliability constraints):

$$T_{junc} \leq 125.0 - 10.0 - 11.0$$

Whether the design has been produced manually or the Solver has been used, the reliability of the design can still be estimated using the Reliability Engineering module. In this case, a *reliability constraint* of

$$T_{junc} \leq 125.0 - 10.0$$

is applied as a failure limit. In other words, the reliability is defined as the chances of not exceeding the acceptance temperatures. In essence, *the validity of the 11°C margin (which was used to generate the design) is being tested*, as shown in Figure 6. The 11°C margin will either be too cautious, resulting in costly over-design, or will be inadequate, resulting in risky under-design.

The amount of over- or under-design can only be quantitatively measured using reliability estimation methods. Either way, a truly optimal design will achieve exactly the required reliability for the thermal subsystem and thus be neither over- nor under-designed. Any excesses in either direction are justification for revisiting the design itself.

Replacing the Traditional Approach

Revisiting a design is costly: it would have been far better to have achieved the target reliability in the first place using Robust Design methods.

To use Robust Design methods, the reliability constraint is still applied

$$T_{junc} \leq 125.0 - 10.0$$

but the optimization constraint is replaced by:

$$0.997 \leq RelAct$$

where “0.997” is the required thermal subsystem reliability, and “*RelAct*” is the actual reliability predicted for the current design using the Reliability Engineering module. In other words, *reliability estimation becomes part of the design evaluation process*.

As was noted above, meeting a reliability requirement is but one possible option. Other options include maximizing reliability (making *RelAct* the objective) while meeting some other mass or power budget. Also, presuming the engineer had some control on tolerancing (machining, subassembly acceptance criteria, etc.), Robust Design can also be used to calculate what range of uncertainties is acceptable.

* This description oversimplifies for clarity. Generally, an even greater uncertainty margin (17°C) is recommended during preliminary design, and 11°C is applied to a model that has been calibrated (perhaps using the Solver module) to test data to within about 3°C.

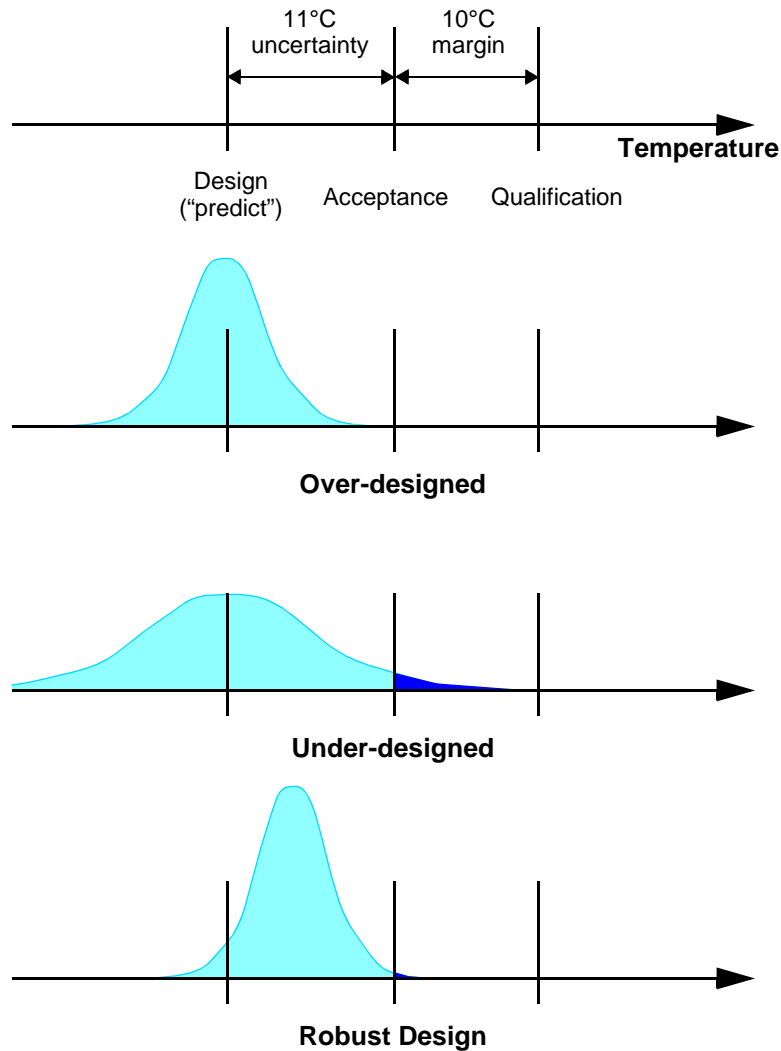


Figure 6: Traditional vs. Robust Design

MULTIDISCIPLINARY DESIGN GENERATION AND EVALUATION

Extending the previous example, note that even the 125°C limit levied upon the thermal designer is itself uncertain: it contains margins and/or a hidden reliability predictions. A truly optimal multidisciplinary design would factor in the reliability of the chip directly, rather than indirectly as an inflexible limit imposed upon the thermal designer. Even the final 10°C margin would be subject to replacement by statistical methods.

Commercial tools exist such as Engineous' iSIGHT® (www.engineous.com) that can perform optimization, reliability estimation, and robust design generation at a higher level than what can be accomplished within a thermal/fluid analyzer such as SINDA/FLUINT. Codes such as iSIGHT enable the inclusion of almost any point-design simulation tool within any arbitrarily complex design evaluation process. SINDA/FLUINT is being expanded to provide direct links to iSIGHT to encourage such high-level integration.

RELEVANT THERMAL DESKTOP EXPANSIONS

C&R's Thermal Desktop® has been expanded to be parametric, allowing geometry, orbits, optical and material properties, etc. to be defined using expressions and symbols (analogous to SINDA/FLUINT registers).

More importantly, a direct link is being established between SINDA/FLUINT and Thermal Desktop: *Thermal Desktop calculations can be invoked dynamically from within SINDA/FLUINT during processor executions.* This provides the ability to include variations in radiation and geometric conductance/capacitance results while using the optimization, correlation, and reliability engineering modules. For this reason, interfaces to these modules are currently being added to Thermal Desktop. *The traditional separation of thermal math models (TMM) and geometric math models (GMM) is being eliminated.*

CONCLUSIONS

The ability to determine the amount of over- or under-design present in a thermal/fluid system has been added to SINDA/FLUINT, permitting uncertainties to be treated statistically in addition to traditional deterministic methods. More importantly, the potential to eliminate over-design due to stack-ups of margins, safety factors, and tolerances has been added, taking into account uncertainties early in the design process by designing for reliability.

Good software automates existing processes, reducing the effort required to create new products. Great software revolutionizes the processes, empowering the creation of better products. The addition of the Reliability Engineering module to SINDA/FLUINT, especially combined with previously existing modules such as optimization, attempts to assure SINDA/FLUINT's place in the latter category.

ACKNOWLEDGMENTS

SINDA/FLUINT would not exist were it not for the continuing support of the Crew and Thermal Systems Division of the NASA Johnson Space Center. Dr. Eugene Ungar was the technical advisor for the Reliability Engineering module, among other improvements.

REFERENCES

User's manuals, tutorials, and training notes for all software discussed are freely available in PDF format at www.crtech.com

1. Cullimore, B. et al; "Thermohydraulic Solutions for Thermal Control, Propulsion, Fire Suppression, and Environmental Control Systems;" SAE 1999-01-2159.
2. Cullimore, B; "Optimization, Data Correlation, and Parametric Analysis Features in SINDA/FLUINT Version 4.0;" SAE-981574.

DESIGN STUDY OF A LOW-COST LOX TURBOPUMP

Dr. David Japikse
Dr. Nicholas Baines
Michael J. Platt
Concepts ETI, Inc.
217 Billings Farm Road
White River Junction, Vermont 05001-9486

ABSTRACT

A preliminary design study, focusing on potential component selections and Design for Manufacturing and Assembly (DFMA®¹) analysis, is presented in this study. The investigation was focused on a nominal cost liquid oxygen turbopump suitable for a private launch class vehicle. Utilizing a “turbocharger-like” design philosophy, preliminary feasibility studies of the basic pump design class, the rotordynamic design class, and the turbine design class were conducted with associated DFMA evaluations. Reasonable cost levels and sensible levels of product assurance have been established.

NOMENCLATURE

β_{1bt}	Inlet blade angle at the shroud	p_{00}	Inlet stagnation pressure
β_{2b}	Impeller exit blade angle	p_{exit}	Exit static pressure
η_{calc}	Calculated stage efficiency	pr_{tt}	Total-to-total pressure ratio
η_{goal}	Desired stage efficiency	pr_{ts}	Total-to-static pressure ratio
b_2	Impeller exit width	r_{1t}	Inducer eye radius
b_5	Diffuser exit width	r_2	Impeller exit radius
m	Flow rate	r_5	Diffuser exit radius
N	Rotational speed	T_{00}	Inlet stagnation temperature
$NPSH$	net positive suction head		

PROJECT OBJECTIVES

The fundamental objective of this preliminary scoping project was to establish a reasonable estimate of the most likely cost of producing, in series production, both a LOX and a LH2 rocket turbopump for a 40K upper-stage engine. The LH2 study will be presented elsewhere (see Japikse, et al., 2000^[1]). The operating parameters for this stage were established by an external study as displayed in Table 1. It is understood that these numbers will change as further iterations on the design cycle are conducted. However, the range of conditions envisioned do not present concerns; the feasibility questions will not be materially affected by such considerations.

¹ DFMA® is a registered trademark of Boothroyd Dewhurst, Inc.

Copyright © 2000 by Concepts ETI, Inc.

All rights reserved. No part of this publication may be reproduced, transmitted, transcribed, stored in a retrieval system, or translated into any language or computer language, in any form or by any means—electronic, mechanical, magnetic, optical, chemical, manual, or otherwise—without prior written permission from Concepts ETI, Inc., 217 Billings Farm Road, White River Junction, Vermont 05001, USA.

The U.S. Government is granted the right to use this document for use in the proceedings for the TFAWS meeting held August 21–25, 2000 in Cleveland, Ohio.

Table 1. Oxidizer Turbopump Turbomachinery Variables		
Inlet Flow Rate	lb/sec	78.16
Inlet Pressure	psia	50
Inlet Temperature	R	183
Inlet Vapor Pressure	psia	42
Inlet NPSH	ft	17.1
Discharge Flow Rate	lb/sec	78.16
Discharge Total Pressure	psia	585
Pump Head Rise	ft-lb/lb	1133
Pump Head Coefficient		0.5
Pump State Ns		≈1500
Pump Torque	ft-lb	93.5
Pump Horsepower	Hp	212
Desired Pump Isentropic Efficiency		75%
Turbine Inlet Flow Rate	lb/s	0.914
Turbine inlet flange tot temperature	R	.1132
Turbine Inlet flange tot pressure	psia	75
Turbine disch flow rate	lb/s	0.914
Turbine disch static pressure	psia	30
Isentropic velocity ratio		0.131
Turbine pressure ratio (T-S)		2.5
Turbine torque	ft-lb	93.5
Turbine horsepower	hp	212
Desired turbine isentropic efficiency (T-S)		42%
Turbine speed (estimated)	rpm	11905

In order to reach the appropriate determination of probable production costs, CETI has conducted a preliminary, but comprehensive design of a LOX turbopump. The actual numbers should not be construed as suitable for any construction at the present time; they represent a pump that would work, with nominal life, but definitely do not represent a fully iterated design of final quality. Due to the existence of the Agile Engineering Design System², it was possible to look at all elements in a quick, initial design in order to establish sufficient details for costing purposes. These details are reasonably assured of meeting a ten-minute life with one restart capability. While further work must be conducted in order to effect the final design, it may be safely taken that the preliminary design configuration gives fair confidence for establishing reasonable component costs.

FEASIBILITY APPROACH

The objectives presented above should lead to the eventual design, prototyping, and production of a liquid oxygen turbopump. Early cycle studies suggested that a single-stage pump might be feasible and that a two-stage turbine may be required. In order to conduct the necessary feasibility studies, a preliminary (but intentionally incomplete) design of the full liquid oxygen pump was prepared. This is shown in Figure 1. This design focused only on the broad aspects of the principal features of the design. A preliminary pump design, a preliminary turbine design, a preliminary rotordynamic system including bearings and seals, and preliminary structural and cost assessments were conducted. In order to perform these evaluations, the highly flexible, concurrent, Agile Engineering Design System of Concepts ETI, Inc. (CETI) was employed. This Agile Engineering Design System is illustrated in Figure 2.

² Agile Engineering Design System® is a registered trademark of Concepts ETI, Inc.

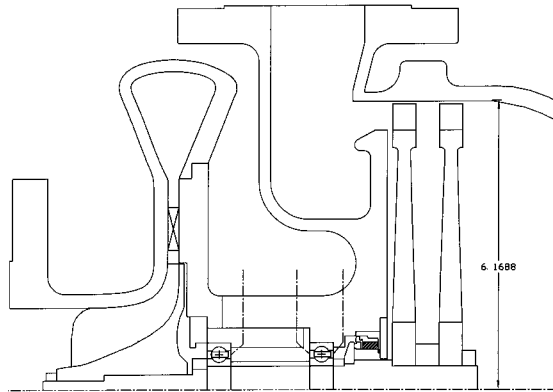


Figure 1. Conceptual LOX pump layout (subject to detail revisions).

The Agile Engineering Design System includes all engineering tools necessary for the complete design and subsequent development of advanced rocket turbopumps. A copy of this system is in use at NASA MSFC (Marshall Space Flight Center), which has aided in its development through various SBIR projects. Section 1 refers to meanline analyses, which are conducted after the cycle calculations (upper left-hand corner, "A") are conducted. The cycle calculations were conducted externally and iterated with CETI engineers. Initial one-dimensional calculations, as indicated in Section 1, were conducted for all components of the LOX pump and then preliminary blading designs were conducted, as illustrated in Section 2. CFD calculations (Sections 3-5) were not conducted or pursued for this evaluation. Structural calculations of pump impellers and turbine rotors were conducted on a scoping basis. This covers Sections 6-7 of Figure 2. Subsequently, rotordynamic calculations, as shown in Section 8 were conducted and appropriate bearings and seals were selected for this preliminary evaluation. In addition, the design for manufacturing (DFM) and design for assembly (DFA) evaluations of Block B, upper right-hand corner of Figure 2, were of great value.

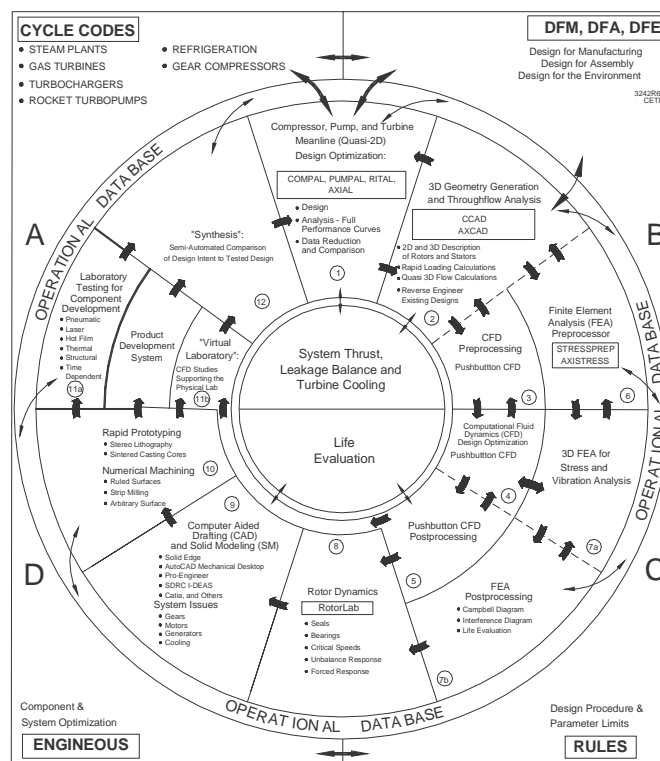


Figure 2. The integrated turbomachinery agile engineering design and technology system. The arrows indicate the flow of information (Japikse 1999[2]).

The resulting preliminary design is shown on a provisional basis in Figure 1, as mentioned. This conceptual figure shows roughly the type of layout (to scale) that could be developed into a successful turbopump. However, further modifications are expected. Considering Figure 1, several notes can be offered. The two-stage turbine, as shown on the right-hand side, does not, as yet, illustrate the location of nozzle guide vanes. These would be added in a later stage of design and development. Additionally, the direction of flow through the turbine has not yet been set. This would be chosen as details of thrust balancing are evaluated later. Appropriate seals on the backface of the pump impeller and additional seals around the turbine rotors would be considered as the overall thrust balancing is achieved. This detailed leakage path calculation and force balancing would be done later with a separate analysis, suggested at the center of Figure 2. This is a tedious exercise, but not particularly difficult in practice; there is no risk in this area when the work is carefully executed, and, hence the details were saved for later. The precise location of the mechanical face seal may very well be modified at a later time, but the initial configuration offers a very sensible ‘strawman’ for review and analysis. A continuous, low level of leakage from the pump impeller backface through the bearings and back into the pump inlet (not shown) is anticipated in order to maintain appropriate bearing temperatures and acceptable life.

The housing layout is strictly preliminary. Modifications to the pump diffuser configuration on the left are certainly to be expected and the size of the housing components will be adapted with some design synergy developed between the pump and turbine housing components. It is possible that a single casting may be employed for the inner housing (although the part line above the pump side bearing suggests a two-piece construction). The overall configuration resembles a high-performance turbocharger. Manufacturing techniques have been widely developed for nearly one century for the economic production of turbochargers and much good insight enters from this industry. The only significant difference is the existence of a two-stage turbine rather than a single-stage turbine which is common for the turbocharger application. All other elements may be found in turbocharger systems.

CETI has worked very closely with MSFC and with Boothroyd Dewhurst, Inc. (BDI) to develop a preliminary costing system for rocket turbopumps. Substantial progress has been made and correlated data have been thoroughly exploited in this investigation. Details of the preliminary design studies are now given in the subsequent sections.

PUMP DESIGN

The design of the LOX pump was a straightforward process. CETI presently has under development several high-performance rocket turbopump configurations that have evolved from a careful business relationship with one of the leading suppliers to NASA MSFC and to the Phillips Laboratory, USAF (also a major SBIR source for CETI system development). These designs incorporate a single-piece inducer and pump which can achieve a suction specific speed on the order of 30,000. Full design head can easily be made in a single stage. CETI has designed such stages and taken water-rig test data to confirm these design levels. There are no significant hydrodynamic or structural problems associated with the pumps which have not been addressed in past design and laboratory experimental evaluations. Several alternative diffuser options are available; for the purpose of the preliminary study, a cascade or airfoil type diffuser was utilized. However, in the final design study, channel diffusers, conical diffusers, vaneless diffusers, and other types of compact diffusers will be considered.

The pump design process begins with finding the optimum meanline design specifications using PUMPAL®³ (Section 1, Figure 2). An extensive database is available to guide the sensible application of PUMPAL and this was utilized to establish the expected impeller exit radius, impeller exit tip depth, and appropriate blade angles. Likewise, the diffuser and volute parameters were laid out using PUMPAL. Following the meanline analysis, the CCAD™⁴ program (Section 2, Figure 2) was used to lay out a preliminary impeller geometry. While this geometry is far from optimized and complete, it closely resembles previous impellers. This follows naturally, since design information from previous designs was imported into this particular evaluation for purposes of expediency. It is expected that the final design will differ in meaningful, but comparatively small, ways. All design calculations were made using real fluid properties as the PUMPAL calculations used a compressible evaluation of the liquid oxygen.

Table 2 summarizes the important design parameters for the LOX pump. The basic size parameters, critical flow angles, design head, and efficiency conditions are displayed. A reasonable estimate, at the point of this scoping

³ PUMPAL® is a registered trademark of Concepts ETI, Inc.

⁴ CCAD™ is a trademark of Concepts ETI, Inc.

study, is that the efficiency of the pump is approximately 74%, +2, -3. A broad band of uncertainty is projected at this point, pending final design optimization. It is anticipated that efficiencies in the higher range cited may very well result from the final optimization study. The design is considered to be advanced, but not high risk.

Table 2. LOX pump design specifications and results (preliminary).

Specification	
P_{00}	50 psia
T_{00}	183°
m	78.2 lbm/s
N	11,905 rpm
NPSH	17.1 ft
P_{exit}	585 psia
η_{goal}	75%
Preliminary Design Results	
r_{1t}	1.745 in.
β_{1bt}	8.40°
r_2	2.680 in.
b_2	0.283 in.
β_{2b}	32°
r_5	4.50 in.
b_5	0.241 in.
η_{calc}	0.75

TURBINE AERODYNAMIC DESIGN

Preliminary design studies were undertaken for turbines to drive the LOX pump. These studies were limited to a basic scoping and proof of concept, and further effort would be required for design optimization and detail design. The operating speed and power output were defined by the pump requirements. The inlet conditions to the LOX pump turbine were defined by the analysis of the complete turbopump cycle although in practice, because the two turbines operate in series, the inlet temperature and pressure for the LOX turbine depends on the power and expansion ratio of the fuel turbine. However, the design concept for the LOX turbine is not particularly sensitive to changes in these parameters. The working fluid is products of oxygen and hydrogen combustion in the gas generator, and comprises gaseous hydrogen and steam. The operating conditions are summarized in Table 3.

Table 3. LOX turbine operating conditions.

Mass flow rate (lb/s) (44% H ₂ , 56% H ₂ O)	0.914
Inlet total pressure (psia)	75
Inlet total temperature (R)	1420
Shaft speed (rpm)	11905
Power (hp)	217*

* Pump power + 2% bearing loss assumed.

The turbine design approach was to select a range of values of stage loading and flow coefficients. These are fundamental non-dimensional parameters which describe the power output per unit flow rate, and the flow rate itself, respectively, for the turbine. The maximum blade speed was dependent on the rotor and disk material limits, and to determine that the aerodynamic and mechanical designs were carried out in parallel with iteration between

them. Multistage concepts were also investigated because of the high powers required in both applications. With these parameters the basic velocity triangles at inlet and exit of each blade row could be calculated, and from that preliminary estimates of the key blade geometric parameters, such as mean radius, blade height, and blade angle, were made. Candidate designs were then set up and analyzed in CETI's axial turbine meanline analysis program AXIAL^{TM5} (Section 1, Figure 2), which permits the performance of a single or multistage axial turbine to be calculated. Once a satisfactory design was achieved, the results were transferred into AXCAD^{TM6} (Section 2, Figure 2), where the actual blade shapes were set out. No optimization of the blade profiles was attempted, but experience was used as a guide to provide suitable forms. The output of AXCAD was used for structural evaluation (Sections 6 and 7, Figure 2).

Several design concepts were considered for the LOX pump turbine. The requirements of output power, blade speed, and shaft speed for this application were such that it was possible to design a single-stage turbine, albeit a very highly loaded one. The final design, summarized in Table 4, is a supersonic impulse turbine with a high level of exit swirl. A limited amount of partial admission (0.82 of the total number of blade passages are open and flowing, the remainder are closed) was required to keep the blade height and the passage aspect ratios within reasonable limits. The stator exit Mach number is 1.306. The design of nozzles to achieve such a high Mach number is a complex task that would almost certainly require some experimental development. Furthermore, such nozzles do not operate well at conditions other than the design point.

Table 4. Summary of LOX turbine design concepts.

	Description	pr_{tt}	pr_{ts}	Efficiency tt	Efficiency ts	Stator exit Mach no.	Rotor exit relative Mach no.	Exit swirl angle	Partial admission	Mean radius (in.)	Inlet blade height (in.)
LOX Pump Turbine	Single-stage supersonic impulse turbine	3.50	3.968	0.238	0.220	1.306	0.551	-57.5	0.82	5.804	0.392
	Two-stage subsonic impulse turbine	1.67	1.693	0.534	0.521	S1: 0.840 S2: 0.706	R1: 0.244 R2: 0.212	-10.4	0.79	5.790	0.434

The principal limitation of this design, however, is the low efficiency and the corresponding large expansion ratio that is required. The overall turbopump cycle analysis shows a gas generator delivery pressure of 394 psia. The fuel pump turbine inlet pressure was assumed to be 384 psia, allowing 10 psia for piping losses. For a fuel pump turbine expansion ratio of 5.5, which should be achievable with some exhaust diffusion, the LOX turbine inlet pressure is 70 psia. With a LOX turbine total-to-static pressure ratio of 3.97 shown in Table 4, the LOX turbine exhaust pressure is only 18 psia, or possibly as high as 20 psia with some exhaust diffusion. The acceptable limit for this pressure is uncertain at present, but an early turbopump cycle analysis showed a LOX turbine exhaust pressure of 30 psia, which is considerably larger than achievable with the single-stage turbine. Even if this expansion ratio proves to be acceptable, there are still considerable design difficulties associated with the single-stage concept, because of the high supersonic flow and the high blade loading, and, therefore, an alternative was sought.

The two-stage turbine, also shown in Table 4, represents a somewhat more conservative design, but also one which can be considered to have a much higher probability of success. The expansion ratio is much lower, at 1.67 total-to-total and 1.69 total-to-static, and this corresponds to an exhaust pressure of approximately 43 psia. The Mach numbers are well below sonic in all of the blade rows, and the exit swirl angle, at -10° , is quite small. In this case, the rotors of the two stages are identical in section, and so too are the stators of the two stages. All of the blades are two-dimensional. Although the two-stage concept will be heavier than the single-stage, these design measures will at least keep down the design and manufacturing costs, and overall it can be considered to be a much more feasible design solution. The best compromise between the conflicting requirements of aerodynamic performance, structural integrity, size, and manufacturing cost appears to be a two-stage turbine. The oxidizer pump

⁵ AXIALTM is a trademark of Concepts ETI, Inc.

⁶ AXCADTM is a trademark of Concepts ETI, Inc.

turbine is not particularly highly loaded, but is still a moderately challenging design. The design efficiency is estimated at $\eta_T = 0.53 \pm 0.05$. Although low, it will be quite acceptable in the intended cycle.

The turbine design is intended only to demonstrate that the concept is feasible and to provide first-order estimates of performance. The designs are not optimized and it is clear that further development would be required so that the performance estimates can be refined, and before detail design is undertaken. It is important that the design and development process should include experimental testing of prototype turbines. Because of the inevitable uncertainties in the design of such highly loaded machines, experimental testing is necessary to ensure that the design goals are met.

STRUCTURAL AND ROTODYNAMIC EVALUATION

With its impact on bearings, seals, and rotor bore stress, the initial step in the structural evaluation of the LOX pump was sizing the shaft. The main consideration was carrying the torque from the turbine, including the stress concentrations at the shaft shoulders. Using a torque of 94 ft-lb, and a design stress of 150 ksi, the minimum shaft diameter will be roughly 0.39 in. for fillets in torsion. The rotor engagement *could* be a simple clamped stackup, an area where CETI has considerable experience. In addition to a clamp load, either splines or a polygon drive could be used, but the high stress concentrations would rule out a simple keyway. Although these limits do not present any immediate problems, the steady-state and transient thermal effects on the shaft strength will need to be evaluated in detail.

The final bearing selection for this pump will be an easy task, as this falls well within the capability of preloaded angular contact ball bearings. The turbopump layouts show that the bearing bore diameter will likely fall in the 20 - 25 mm range, putting the DN values in the 250,000 – 300,000 range. Such low DN values will allow some latitude in setting the preload and choosing the component materials. The bearing races will most likely be either 52100 or 440C alloy races, with steel or silicon nitride balls.

It is assumed that the bearings would be required to run without lubrication, and would be cooled with a metered flow of the pumpage. To assure zero leakage, this will require a mechanical seal, possibly backed up with a gas-buffered labyrinth, between the bearing and the turbine. The mechanical seal will most likely be a face seal, although a gas-buffered segmented seal could also work in this application. The face seal package would utilize a carbon seal and a stainless steel mating ring. The secondary seal would be either a metal bellows or a polymer, such as Vespel. The surface speeds for the seal will be on the order of 100 fps, which is well below the 450 fps working limit of typical face seals. Another limit of such seals is pV, where the upper limit is generally in the 500k-1M psi-fpm range. In this case, the pV limit translates into a pressure differential upwards of 100 psi across the seal face. Since the thrust loads have not yet been balanced, there is still work to do before the seal configuration is finalized.

The pump rotor stress analysis, see Platt and Marscher, 1993^[3], was conducted with a combination of 2D and 3D FEA models using blade shape information from CCAD linked through OLE to the STRESSPREP^{TM7} model generation and post-processing code. Given the low tip speed, the stress and deflection on the pump is well below the material yield. Within reasonable limits, this will allow the selection of the most economical materials and manufacturing processes. The blade and disk natural frequencies are very high compared to running speed-related excitations and are not likely to present problems.

The turbine stress analysis was done in a similar fashion – making 3D FEA models with AXCAD blade shape information linked to AXISTRESS^{TM8} for model generation and post-processing. Only the first turbine stage was analyzed since the two stages are very similar in terms of blade shape, tip speed, etc. As with the pump stress analysis, the results for the turbine reflect the relatively low tip speed. The results, with only minimal disk shape iterations, show roughly 30 ksi at the disk bore and 20 ksi at the blade root. While the blade and disk natural frequencies are expected to change somewhat as the final geometry is defined, the preliminary check shows no areas for concern.

⁷ STRESSPREPTM is a trademark of Concepts ETI, Inc.

⁸ AXISTRESSTM is a trademark of Concepts ETI, Inc.

The rotor dynamics was investigated using the RotorLab™⁹ software package, and critical speed maps and forced response predictions were made for a variety of turbopump layouts. The results show that the LOX turbopump will run sub-critical with a good margin of safety relative to the first critical speed. This margin will give some latitude in the final design, since small changes in the layout can be accommodated and the shaft size could always be increased if needed because of the already conservative DN and pV values for the bearings and seals. The final analytical results will vary depending on the bearing preload and stiffness, added mass and damping effects from the liquid, and contributions from the labyrinth seals.

DFMA ANALYSIS AND PROJECT COSTS

The last principal step of the feasibility assessment for the LOX and LH2 rocket turbopumps was the preparation of a proper analysis (albeit on a preliminary basis) in order to ascertain the expected unit cost in both low numbers and high volume (50 per year) production. In order to do this, a typical turbopump was laid out and every part identified. Figure 3 shows the identification of every piece in the LOX turbopump. Additionally, the heat shield and the associated bolting ring was assumed, which is not shown in this figure. Otherwise, a very reasonable (preliminary) assessment of all components is presented. The components identified in Figure 3 are listed in Table 5. A prior example of a turbopump and a turbocharger DFMA study is given by Gauthier, et al., (2000^[4]).

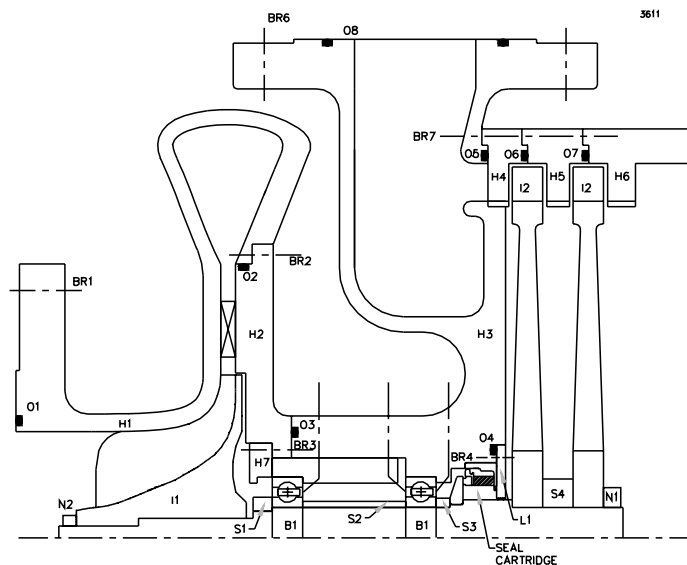


**Figure 3. LOX Turbopump component identification.
Also used for the LH2 study.**

⁹ RotorLab™ is a trademark of Concepts ETI, Inc.

Table 5. LOX pump component listing.

HOUSINGS
H1 – pump front
H2 – pump rear
H3 – bearing
H4 – stator 1
H5 – stator 2
H6 – stator 3
H7 – retain ring (use cover cost 4” size)
SHAFT
1 – main rotor
BEARINGS
B1 - Ball bearings (2)
SPACERS
S1
S2
S3
S4
SPRINGS
1 set (12 pieces)
SEAL CARTRIDGE
1 primary seal set
LABYRINTH SEALS
L1 - piece, turbine side
IMPELLERS
1 – pump impeller (machined)
2 – turbine impeller (2 pieces) cast
O-RINGS
O1 – inlet and outlet flanges (4)
O2 – volute flanges
O3 – bearing housing
O4 – seal housing (1)
O5 – seal housing (2)
O6 – turbine housing (1)
O7 – turbine housing (2)
O8 – turbine housing (3)
NUT
N1 - turbine/shaft
BOLTS W/TAB LOCKS
BR1 - inlet flange (12 pieces)
BR2 - volute flange (12 pieces)
BR3 - inner locking ring (12 pieces)
BR4 - seal assembly (8 pieces)
BR5 - heat shield (12 pieces)
BR6 - turbine inlet (12 pieces)
BR7 - turbine housing (24 pieces)
BR8 - pump exit flange (12 pieces)
BR9 - turbine exit flange (12 pieces)
HEAT SHIELD
1 – sheet metal – flat

PRE-ASSEMBLY MACHINING OPERATIONS

1. Pump stationary cover (H1)
2. Diffuser ring 6” diameter
3. Housing H2 (2x’s 8” diff plate)
4. Bearing house H3 (3x’s 8” diff plate)
5. Nozzle faces
H4
H5
H6 + exit flange
6. Impeller bores and facing and tip dia. Trimming (2 x’s) 25% increase due to hardness in above
Cleaning 2 x 40 hours (initial) + support
Assembly 2 x 40 hours + support
Inspection 40 hours + support
Special capital equipment amortized Balance, machine centers, inspection equipment
Miscellaneous (place holder – forgot what?)
Balancing (4x’s) use 5” size
Tooling, special fixtures
MATERIALS
Pump imp. 100 in ³
Shaft 25 in ³
Labyrinth 25 in ³
H3 ring 25 in ³
Spacers 4x’s 2 in ³

As presented previously, (Japikse, et al., 2000^[5]; Gauthier, et al., 2000^[4]), CETI has already established manufacturing costs of each individual component in rocket turbopumps under contract for NASA MSFC. Further refinement of these charts is ongoing at the present time, but they are sufficiently accurate to provide a very sensible preliminary assessment. Additionally, based on data being acquired for the DFMA analysis for MSFC, reasonable estimates of assembly time, clean room operation, and cleaning have been made. The charts of component costs include the cost for making a first item, the cost for making a second item, the cost for making a fifth item, then the 20th item and then the 100th item. This database has been checked, partially, with other manufacturers so as to begin the process of detailed validation. The specific listing of individual costs is proprietary information and not included here.

Based on the analysis conducted, the probability is high that the LOX pump can be built for approximately \$100,000, probably for slightly less.

It is important to justify the costs above from a practical perspective. Compared with current rocket turbopump manufacturing costs, these costs may seem overly competitive (i.e., too low). There are important factors to consider. First, all the costing is based on reliable estimates representing parts of the type to be used in these actual projects. Virtually all these parts, in some form or another, have all ready been manufactured at CETI. The CETI database goes back over 18 years of prototype component manufacturing and has been thoroughly reviewed and incorporated in the DFMA database. All parts which are required for these turbopumps can either be manufactured at CETI or procured from outside shops. The pricing assumes that the lowest cost source of quality parts will be used. In other words, the CETI internal shop (small but extremely comprehensive) will bid against outside vendors and vice versa. All outside vendors understand that any part requested from CETI can, in fact, be also manufactured within CETI. Consequently, CETI holds an advantage against a late delivery of parts, so-called “acts of God or acts of war,” which would upset a flow of components. At the same time, this approach utilizes good cost savings from outside vendors.

Early in this report, a reference was made to turbocharger design and development. Turbochargers of approximately the same size and comparatively similar complexity, are manufactured for large off-road automotive applications, small marine applications, aviation applications, and very small locomotive applications. Mass-produced common truck turbochargers generally cost on the order of \$350 to \$1,000. Small marine turbochargers will cost anywhere from a minimum of \$2,000 or \$3,000 up to \$10,000. Turbochargers of this size and complexity, but used for the light (piston engine driven) aircraft industry, are priced up to \$25,000 per copy (but 40% of this price is purely insurance costs). The biggest differences between the rocket turbopump application and the turbocharger application are the two-stage turbine which is required for these turbopumps, the much higher production level of the turbocharger, and the great difficulty brought about by rapid thermal transients during start-up of the rocket turbopump. It may be noted, however, that the production levels for aircraft turbochargers are roughly on the same order of magnitude as the production levels for these rocket turbopumps. Additionally, production levels for some of the marine turbochargers are approximately the same. The dimensional accuracy of the turbochargers is approximately the same as that required with these rocket turbopumps in many key areas, particularly in the shaft and bearing system and the balancing requirements. The higher prices quoted herein for the rocket turbopump reflect the differences mentioned plus the need to assure traceable manufacturing and assembly methods and the requirements for extreme cleanliness.

SUMMARY

An appropriate feasibility study has been conducted of a preliminary design layout for a liquid oxygen rocket turbopump. No insurmountable technical problems have been identified. To achieve a practical design configuration, the turbopump is designed so that it roughly resembles a modern turbocharger. By following turbocharger design and manufacturing practices, as closely as feasible, reasonable costs can be achieved. Pump efficiencies in the range of 74%, +2, -3, are considered realistic; turbine efficiencies are on the order of 53% for the LOX turbopump. These efficiencies are ± 5 points at the present time. The purpose of a subsequent design optimization study would be to simplify the design further, to reduce the cost further (if possible), and to increase efficiency wherever possible. The LOX turbopump operates well below its first shaft critical speed.

It is recognized that the cycle specifications will change. The parameters of this study can be readily adapted to new configurations. However, it is not anticipated that any fundamental hurdles will be raised by subsequent modifications in the operating cycle.

Subsequent analysis will concentrate on further steady-state operating conditions and the full design optimization required for eventual product release. However, comprehensive transient analysis must also be conducted to look at questions of heat soak and thermal response of the entire system. No assessment of these transient problems has been conducted and it is expected that some tailoring of the internal leakage/cooling system will be required. This is a common step in the design of a rocket turbopump. Due to the simplicity of the present design, it is unlikely that any insurmountable problems would be found on the transient basis, given sufficient time and resources to carefully conduct appropriate analyses and adapt the design accordingly.

It is presently concluded that the LOX turbopump can be manufactured for a cost of approximately \$100,000 per copy in lots of 50 per year for a private launch business. Nominal assumptions have been made for clean-room requirements, and for documentation according to standard requirements of any quality, engineered product process. No allowance has been made for government/military level reviews, documentation, or traceability. If additional burden is introduced in this area, some nominal increases in estimated costs are to be expected.

REFERENCES

- 1] Japikse, D., Baines, N. C., Platt, M., "Design Study for a Low-Cost LH2 Turbopump," to be presented at the Joint Army-Navy-NASA-Air Force (JANNAF) Propulsion Meeting, November 13 – 17, 2000.
- 2] Japikse, D., "Restructuring of Engineering Design and the Role of DFMA," Proceedings at the Committee for the Advancement of Competitive Manufacturing, University of Rhode Island, March 24, 1999.
- 3] Platt, M., and Marscher, W.D., "Rapid FEA of Impeller Stress and Vibration in the Agile Engineering Process," ASME Rotating Machinery Conference and Exposition, Somerset, NJ, November 10-12, 1993.
- 4] Gauthier, B., Dewhurst, P., Japikse, D. "Application of Design for Manufacture and Assembly Methodologies to Complex Aerospace Products," to be presented at the 36th AIAA/ASME/SAE/ASEE Joint Propulsion Conference and Exhibit, July 16-19, 2000.
- 5] Japikse, D., "Precision Turbomachinery Products in the Agile Engineering Era," Keynote address presented at The Pacific Center of Thermal-Fluids Engineering, Maui, Hawaii, March 26-30, 2000.

UNSTEADY PHENOMENA DURING OPERATION OF THE SSME FUEL FLOWMETER

Bogdan Marcu

Boeing

Rocketdyne Propulsion and Power

6633 Canoga Ave

Canoga Park, California 91309-7922

ABSTRACT

This report describes a part of the analysis carried in support of the SSME Fuel Flowmeter redesign, addressing a particular phenomenon known as “shifting” of the flowmeter constant value. It consists of a sudden change in the flowmeter indication, which occurs simultaneously with the onset of an oscillatory variation of the rotor speed. The change in the flowmeter indications does not correspond to a real change in the volumetric flow through the device. Several causes have been investigated in detail, in the past, without conclusive evidence towards a cause of this phenomenon. The present analysis addresses the flow physics through the flowmeter by assembling results from 3-D CFD calculations, airfoil C_D/C_L performance curves and mass moment of inertia characteristics of the rotor into a synergistic calculation which simulates the unsteady regime of the flowmeter operation. The results show that the 4-bladed rotor interacts with the periodic flow pattern created behind the flow straightener upstream in a manner that generates a steady, periodic fluctuation in the rotor’s speed. The amplitude of this fluctuation is significantly smaller than the 0.5% of mean speed threshold which constitutes a flight operational limit. When manufacturing variations occur, however, the fluctuations are amplified and can generate a significant apparent change in the flowmeter indication. Two types of possible fabrication variations—which can occur even for parts fabricated within the accepted tolerances for the blade airfoil—are presented, together with their effect on the flowmeter operation.

NOMENCLATURE

U	blade tangential velocity
Ca	fluid axial velocity
W	fluid relative velocity
ρ	fluid density
α	blade stagger angle
β	angle of relative fluid velocity
i	flow incidence angle on the blade
θ	blade angular position
C_D, C_L	drag and lift coefficients
ρ	fluid density
b	blade chord length
K_f	flow meter calibration constant for engine operation
K_{fw}	flow meter calibration constant determined from water flow test

1. INTRODUCTION

The Space Shuttle Main Engine uses a turbine type flow meter [6] to control the amount of fuel delivered to the engine and the mixture ratio between the fuel and oxidizer. The flow meter is located in a duct between the low pressure fuel pump discharge and the high pressure fuel pump inlet. The meter translates the volume flow of the liquid hydrogen based on its rotor speed and a calibration constant, denominated as K_f , which relates the fuel volume flow rate to the rotor's rotational speed though a proportionality relationship $K_f = 4 \text{ RPM/GPM}$, where **RPM** is the rotor speed in rotations per minute and **GPM** the fuel volumetric flow rate in gallons per minute.

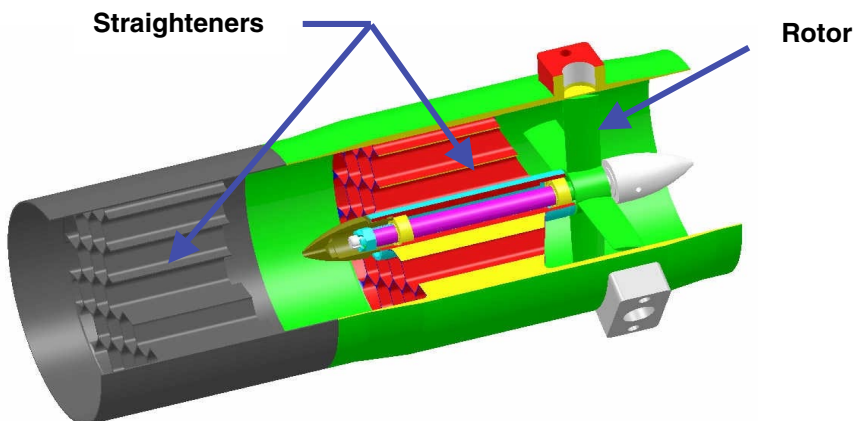


Figure 1. SSME Fuel Flowmeter Configuration

The flowmeter—shown in figure 1—consists of a set of honeycomb flow straighteners, followed by a 4-blade turbine rotor whose speed of rotation is picked up by a magnetic sensor.

Over the years of the Space Shuttle Main Engine (SSME) operation, a certain behavior was observed in the flowmeter operation [1, 2]. At certain regimes, an apparent shift seems to occur in the K_f value, without a real change in the fuel volume flow rate. The K_f shift phenomenon also appears to be associated with a fluctuation in the rotor's speed. A typical example of such behavior is shown in figure 2. The detailed plot of the onset of the anomalous behavior shows that, while the real volume flow (denoted as facility flow) decreases slightly, the flowmeter indicates a slight increase. Sometimes it is apparent that the onset of such behavior is associated with significant fluctuations in the flowmeter speed, as shown in figure 3. Such fluctuations may be of high frequency, but since the rotation is only sampled 4 times per one complete revolution, aliasing occurs in the measurements. Hence, the term of “aliasing” has been associated with the rotor speed fluctuations, occurring simultaneously with the K_f shifting.

Several authors have investigated the phenomenon. The effects of engine vibrations on the duct flow have been assessed [2]. Also, a different analysis [3] has demonstrated a rotor sensitivity to the flow turbulence intensity. No conclusive evidence was found that either condition is the cause of the shifting. Recently, an unsteady 2-D CFD analysis by A. Hadid [5], and a pseudo-unsteady 3-D CFD analysis by E. Ascoli et al. [4] have found that when the blade passes the strong wakes in the flow pattern generated behind the hex flow straightener, there are momentary stall-like flow regimes on the blade, which slow down the rotor. Both authors suggests that the occurrence of successive stalls may produce effects similar the K_f shifting phenomenon, associated with a high frequency oscillation in the rotor.

The present analysis addresses the problem in its entire physics, i.e. the coupling of the flow field distortions with the blade aerodynamics and the rotor's dynamics, in an effort towards explaining the underlying nature of the K_f shifting phenomenon.

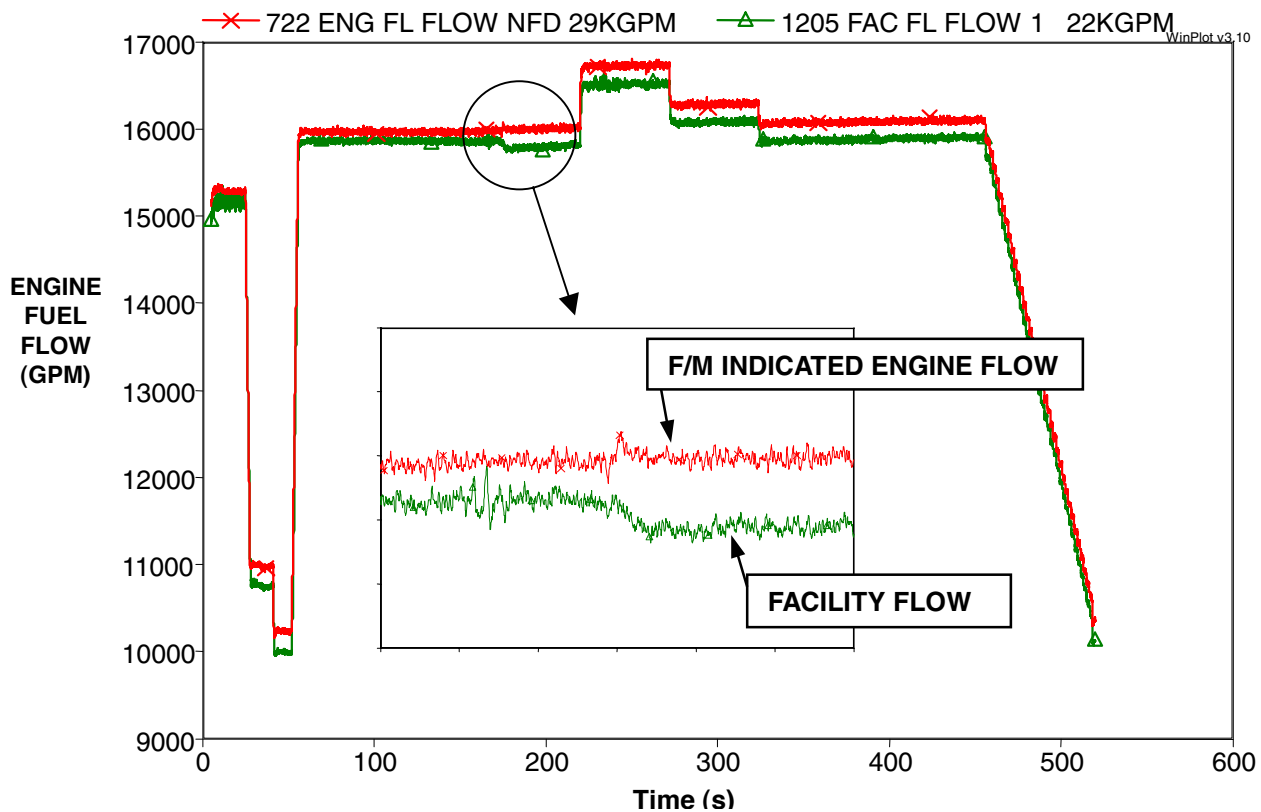


Figure 2. An example of an apparent shift of the flowmeter's indication. While the volume flow actually decreases slightly—as shown by the ground test facility flow measurement—the flowmeter indication increases slightly. Since the meter indication is derived from its speed measurement, it turns out that the meter's rotor rotates faster than it should (i.e. faster than it did when it was calibrated). In most other instances, it appears to be rotating slower. Such a situation is equivalent to a change in the proportionality constant K_f which relates the rotor speed to the volume flow, hence the expression “ K_f shifting”..

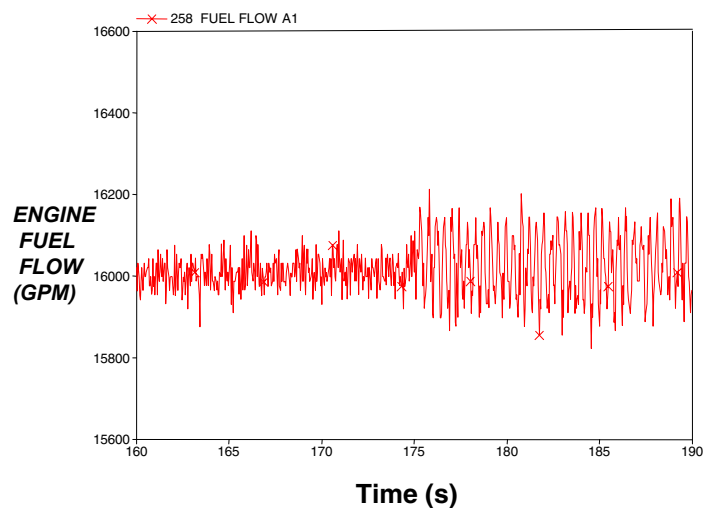


Figure 3. In most of the cases of K_f shifting, the onset of the K_f apparent value shift is associated with oscillations in the flowmeter's reading.

2. THE FLOWMETER MODEL

In order to organize a fluid dynamics model for the flowmeter, one must understand a significant difference between a typical turbine destined to produce power, and the turbine flowmeter rotor at hand. A typical turbine rotor operates by organizing the working fluid flow within the channel formed between two adjacent blades in a way that maximizes blade loading and allows a high degree of turning of the fluid, thus producing a significant torque. The flowmeter rotor on the other hand (shown in figure 4), uses only 4 blades that operate practically independent of each other—in the sense that one cannot speak of a channel flow in between these blades—as isolated rotating airfoils. If the rotor were to operate in a smooth, uniform incoming flow, its blades should operate at very small incidence angles at every radius. The situation is depicted in figure 5. The incoming flow has a uniform axial velocity C_a while the rotor blade has the tangential velocity U as shown. Adding the two vector velocities results in the relative velocity with respect to the blade, W . The blade stagger angle α is not quite aligned with the relative velocity angle β , as the relative velocity impinges on the blade's leading edge at a small incidence angle i . Since the blade profile is symmetric, the small incidence angle is necessary to produce some lift, besides drag. Only the tangential components of the forces acting on the rotor blade are of interest here. The blade will adjust its tangential velocity in a way that will produce a very small incidence angle i for which the tangential component of the drag force and rotor miscellaneous friction resistances R_f will be compensated by the tangential component of lift. Due to the free-vortex blade twist $\alpha = \alpha(R)$ (figure 5b), this situation occurs at every radius R of the blade.

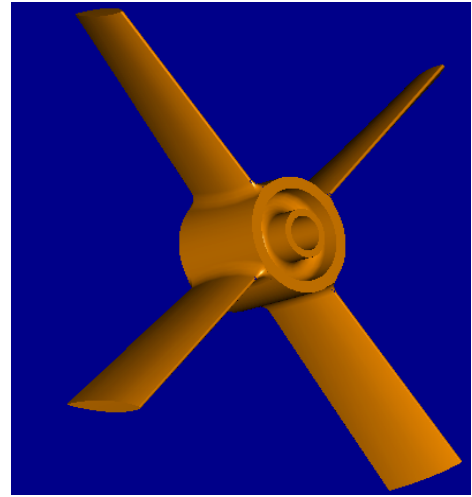


Figure 4. The flow meter rotor.

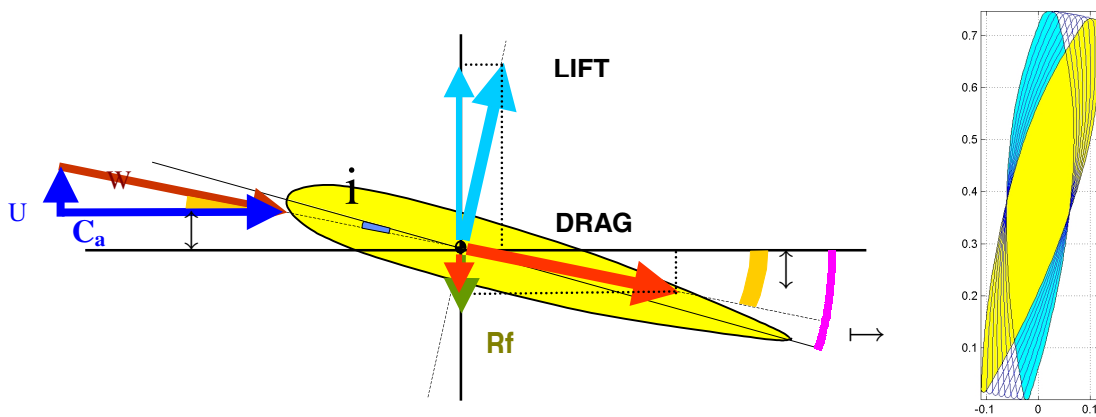


Figure 5. a) The blade load and force decomposition on the rotor blade b) The blade radial twist

However, the incoming flow is not uniform. The hexagonal channels of the straightener generate a flow pattern as shown in figure 6. The pattern is periodic in the tangential direction, characterized by a 12N and 18 N periodicity in the axial fluid velocity, therefore, in the model shown in figure 5 the axial fluid velocity becomes a forcing function $C_a = C_a(t)$, since the rotor will “feel” an unsteady incoming fluid axial velocity as it passes through the wakes existent in the flow pattern behind the flow straightener. If the rotor has a mass moment of inertia I , at every moment it's motion is governed by the dynamic equation of motion

$$I \frac{d^2 \theta(t)}{dt^2} = T[\theta(t), \alpha(R), C(R, \alpha, \theta(t))] \quad (1.)$$

where $\theta = \theta(t)$ is the rotor's angular position, t is the time, and T is the torque produced by the resultant force on the blade according to the model in figure 5, i.e. $T = T[\theta(t), \alpha(R), Ca(R, \alpha, \theta(t))]$. The torque expression in (1.) is a complicated relationship due to the simultaneous nonlinear two-way coupling between the rotor position and the aerodynamic forces on the blade. In order to solve for the dynamic equation of motion, one must rely on numerical procedures. A numerical model has been assembled as follows.

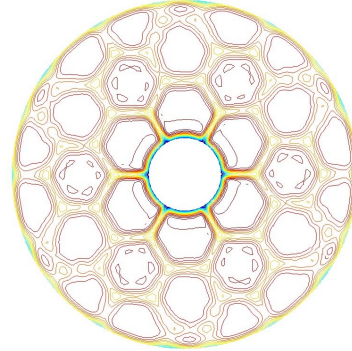


Figure 6. Axial fluid velocity field intensity pattern (from CFD calculations) behind the flow straightener

The flow field behind the flow straightener $Ca(R, \alpha, \theta)$ has been generated by a 3-D CFD calculation in reference [4]. One can assume that the coupling between the flow field and the rotor motion is strong in the direction flowfield→rotor motion and very weak in the reverse direction rotor motion→flowfield, or otherwise stated, the presence of the rotor does not influence the flow pattern since the rotor has only 4 blades (very small blockage) and carries no load, while the flow is extremely energetic during the SSME operation. Relying on a numerically known incoming flowfield, the instantaneous value of the blade torque T can be computed by an integration along the radius of the local torque produced at each radial location (in fact a narrow bin) by the aerodynamic forces described in figure 5 (see also figure 7).

$$T(t) = \int_{r_{hub}}^{r_{tip}} dT \quad (2.)$$

$$dT = dF_T R \quad (3.)$$

$$dF_T = \frac{1}{2} \rho \cdot b \cdot W^2(R) \times \quad (4.)$$

$$[C_L(R) \cdot \cos(\beta(R)) - \zeta \cdot C_D(R) \cdot \sin(\beta(R))] \cdot dR$$

where ζ is an empirical parameter allowing for the calibration of the numerical model with experimental data. Equation (1) is integrated numerically using a 4th order Runge-Kutta scheme, considering each of the 4 blades simultaneously, clocked at 90 degrees from each other. The C_D and C_L performance is modeled from NACA 4 digit series airfoils. The airfoil of each blade is divided in 32 radial bins for which the Drag and Lift forces are calculated at each time step based on C_D/C_L modeling, incidence i and incoming relative flow velocity W . The numbers are then integrated according to expressions (2) through (5).

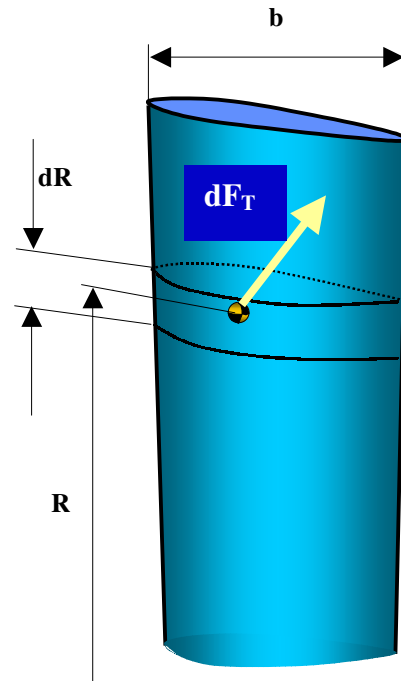


Figure 7. Force/Torque integration on a rotor blade.

3. ANALYSIS

3.1 Quasi-steady regime

The numerical procedure presented in the previous section has been applied for the computation of the rotor response time to a sudden change in the flow rate. The results are presented in Figure 8 for two flowmeter configurations using the original SSME flowmeter rotor with $I=0.0035$ lbm ft², and a redesigned rotor with $I=0.0039$ lbm ft² [7]. The simulation results confirm the measured response time, which is of the order of 6 milliseconds for both rotors.

One important detail can be observed in figure 8a. After the rotor responds to a change in the volumetric flow rate, it operates at a quasi-steady regime characterized by a stable and periodic fluctuation in speed, with very small amplitude. The amplitude of the fluctuations shown is 0.28% and 0.21% of the mean speed value for the original and the new design respectively. Figure 8b show the fluctuating component of the rotor speed for the original rotor, calculated at 115% engine Rated Power Level (RPL). The spectral analysis of the fluctuation is shown in figure 8c. The dominant frequency (791 Hz) corresponds to the 12N symmetry of the hexagonal flow straightener pattern.

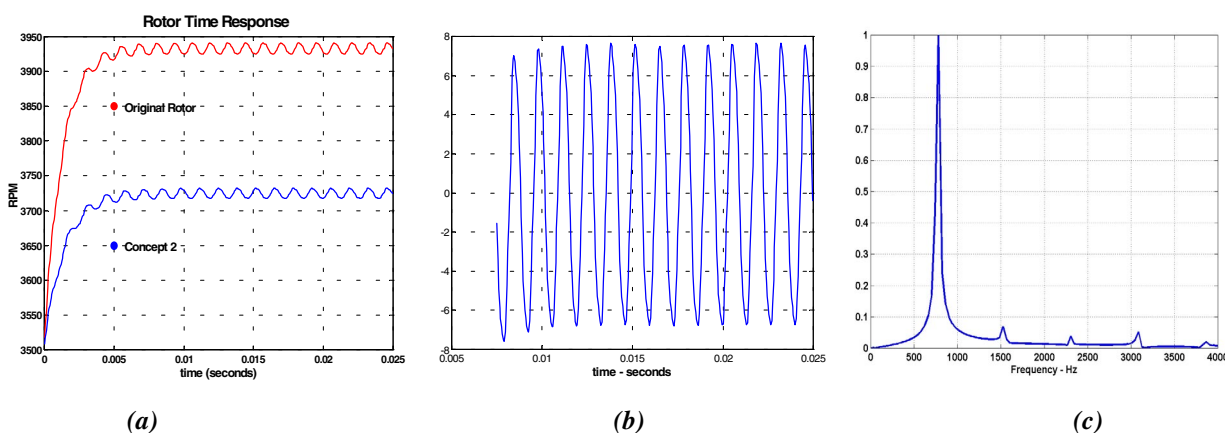


Figure 8. a) Rotor time response to a change in flow volumetric rate. b) Rotor speed fluctuation component during quasi-steady operation. c) spectral analysis of the fluctuating component: the peak corresponds to 12N frequency.

3.2 Possible manufacturing errors and their effects

The shifting and speed oscillation occurrences during the flowmeter operations have been, in several cases, well correlated with “off-print” rotor parts. Specifically, the blade airfoil had been manufactured outside the tolerance field. This correlation has led to a careful assessment of the possible type of variations which can occur, and their effect on then rotor operation [7]. In the following, a classification of the airfoil errors is presented from the point of view of their aerodynamic effect.

One type of a manufacturing variation is one during which the blade airfoil at a certain radius is twisted, or rotated, within the accepted tolerance field. The situation is shown in figure 9. All points on the fabricated blade are within tolerance, yet, by a biased distribution of differences from

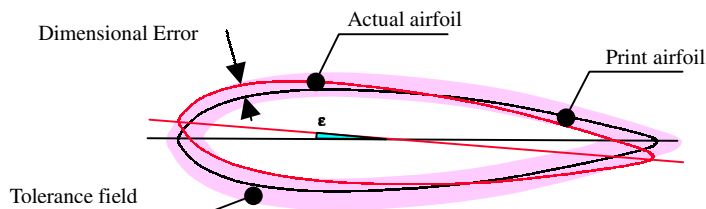


Figure 9. Manufacturing variation of Type I, altering the blade stagger angle by a fraction ϵ .

print, the profile has an extra twist, which adds to the design blade stagger angle α as an alteration ϵ . A tolerance band of ± 0.003 inches will allow for a maximum of $\pm 0.556^\circ$ deviation from the intended blade stagger angle. For a case of ± 0.010 inches tolerance band, the deviation from the intended blade stagger angle can be as large as $\pm 2.0^\circ$.

Another type of manufacturing variation is one that disturbs the symmetry of the blade. The deviations from the blade profile print, while within the accepted tolerance band, group as shown in figure 10, distorting the geometry of the profile from a symmetric profile to an asymmetric one with a cambered mean line. Such a distortion changes the airfoil lift and drag characteristics. In order to perform a simulation which to include the effects of such errors, the maximum possible camber of the blade profile mean line was estimated, and an altered, non-symmetric C_D/C_L performance curve

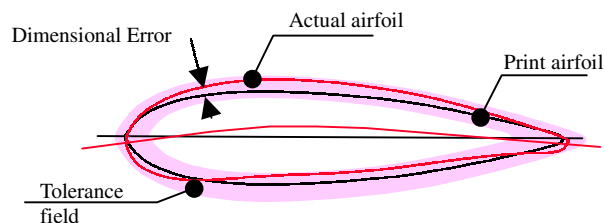


Figure 10. Manufacturing error of Type II, altering the blade mean line camber.

Repeated simulations have been performed to assess the individual effects of each type of variation. The blade stagger angle distortions appear to induce changes in the fluctuation component one order of magnitude larger than the non-symmetry effects. Results from a simulation for which 2 blades out of 4 had stagger angle deviations and the other two had profile mean line camber, are shown in Figure 11. Shown is only the fluctuating component of the rotor's speed for each distortion magnitude and its spectrum. The observable effect of the blade profile deviations

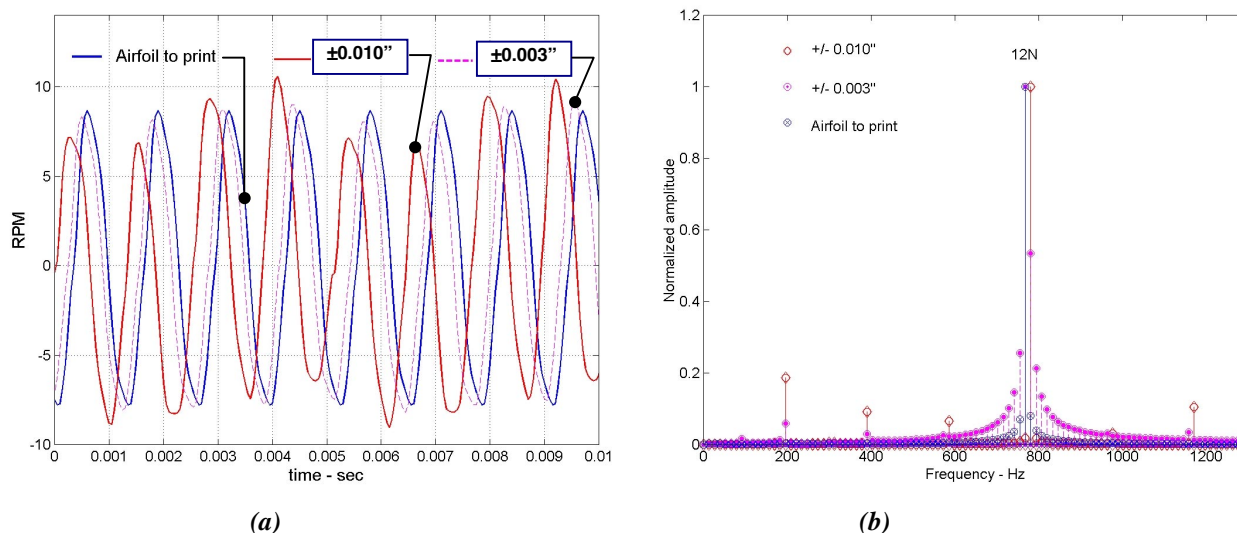


Figure 11. Combined effects due to blade geometry distortions. Both type I and type II geometry distortions are included: two non-consecutive blades have blade stagger angle distortions of \pm max value allowed by the specified tolerance band, while the other two blades have a camber of the mean line also max and min allowed by the tolerance field. a) rotor speed fluctuating component. b) spectrum of the fluctuation. While the 12N base frequency remains unchanged, lower and upper harmonics are created.

is a certain amplification of the fluctuations' amplitude—proportional to the magnitude of the deviation—as well as the creation of upper and lower harmonics in the fluctuation. Furthermore, a phase shift is introduced in the fluctuating speed component. This is an important effect, which will be addressed in detail in the next section. While for the ± 0.003 tolerance band the fluctuation change is minimal, the distortions allowed by the ± 0.010 tolerance band have a noticeable effect.

3.3 An explanation of the shifting phenomenon

Many authors, mentioned in the introduction section of this study, have addressed the topic. The analysis by L. K. Sharma [3] showed analytically that the flowmeter indication is very sensitive to the incoming flow turbulence and distortions of the flow velocity field. The results of Sharma's analysis show a sensitivity to flow turbulence intensity leading to a change of 1% in the flowmeter indication for a flow turbulence intensity increase from 5% to 7%.

Here, we will show that the flowmeter's sensitivity to flow turbulence intensity couples with three other operating characteristics described in the subsections 3.1 and 3.2, and generate a change in the device's indication. Specifically the three characteristics are i) the permanent presence of a fluctuating rotor speed component, ii) the amplification of the amplitude of the fluctuation by distortions in the blade geometry, and iii) the introduction of a phase shift in the wavy fluctuation component by distortions in the blade geometry.

A simulation of the flowmeter operation at 109% Rated Power Lever has been performed for a "to print" flowmeter rotor (i.e. no geometry distortion). The results are shown in figure 12. The darker curve represents the fluctuating speed component, at constant amplitude, for zero turbulence intensity. The light color curve represents the fluctuating speed component in the presence of 5% flow turbulence intensity, added into the calculation via a Monte-Carlo procedure. The flowmeter speed is measured at each blade passage by the detector, thus there are as many readings per rotation as many blades the rotor has, which is a number of four. This is somewhat equivalent to sampling of the real speed at a rate of 4 times per revolution. For the situation with zero turbulence intensity, this

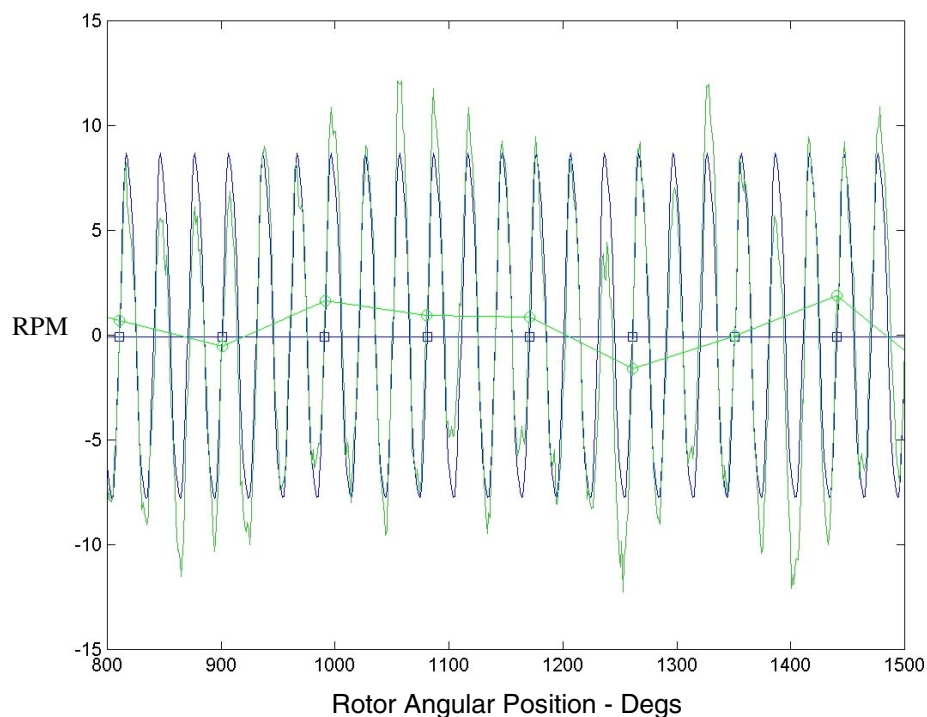


Figure 12. Speed fluctuation component for a "to print" rotor. The darker curve corresponds to zero turbulence intensity, while the light colored curve corresponds to 5% flow turbulence intensity. For each curve, the actual reading, as sampled is shown, □ - zero turbulence intensity, ●- 5% turbulence intensity

is shown by the square data points, which align at the same value. The perfect constant reading is due to the fact that the fluctuating component has a 12N periodicity, and the reading is every 4N, therefore the same value is read at every 3rd wave period. When 5 % turbulence intensity is introduced, the fluctuating speed component is perturbed in amplitude, but remains 12N periodic with no phase shift. Slight differences in the speed sampled readings reflect the amplitude perturbations, but the mean of the speed reading is essentially unchanged.

A second simulation of the flowmeter operation at 109% Rated Power Level has been performed for a distorted rotor geometry corresponding to a $+2^\circ$ and -2° distortions in the blade stagger angle for two non-consecutive blades. The results are presented in Figure 13. The darker curve represents the fluctuating speed component, for zero turbulence intensity while the light color curve represents the fluctuating speed component in the presence of 5% flow turbulence intensity. The square symbols represent the speed sampling for the zero turbulence intensity. Due to the amplification and phase shift effects introduced by the distorted geometry, the sampled speed does not align at constant value, but rather fluctuates itself and introduces a small (-2.12 RPM) bias into the reading. In the presence of 5% turbulence intensity, the rotor speed fluctuations are amplified even more. The amplification is associated with a larger phase shift, which, in turn, changes the value of the sampled speed data points. This is due to the fact that the wave phase shift changed the quasi-periodical location where the wave is sampled. The mean of the sampled speed has shifted to a negative bias of -8.103 RPM, which is equivalent to an apparent shift of -0.21% in the calibration constant K_f .

The simulation presented in figure 13 explains the underlying nature of the K_f shifting phenomenon. A flowmeter with a rotor affected by distorted geometry due to manufacturing variation may shift the value of its calibration

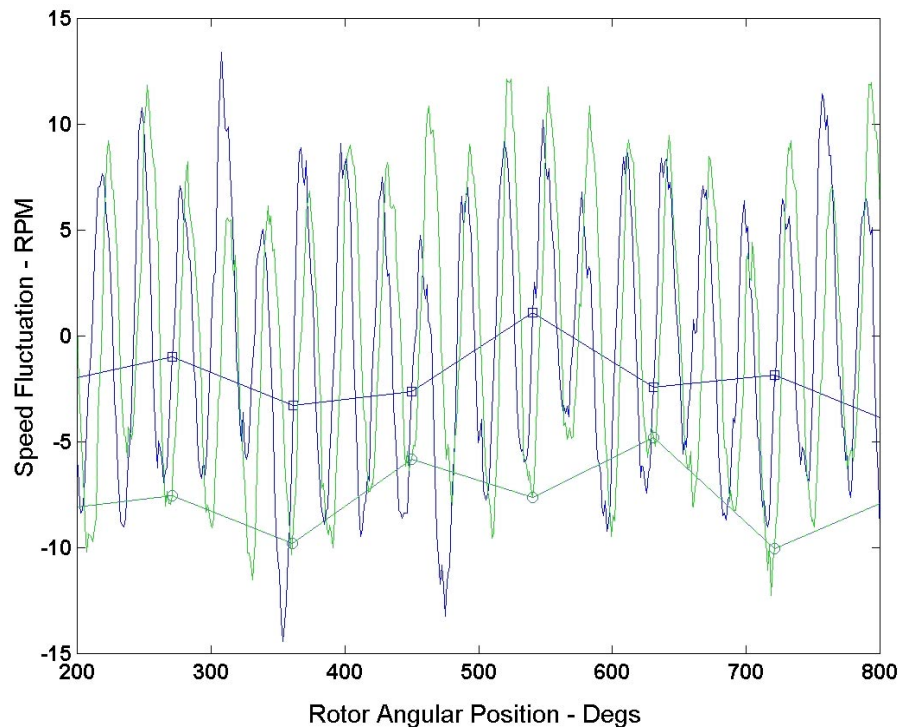


Figure 13. Speed fluctuation component for a rotor with geometry distortions due to manufacturing errors. The darker curve corresponds to zero turbulence intensity, while the light colored curve corresponds to 5% flow turbulence intensity. For each curve, the actual reading, as sampled is shown, \square - zero turbulence intensity, \bullet - 5% turbulence intensity

constant due to a change in the flow turbulence intensity, or due to any change in the nature of the unsteadiness characterizing the flow field behind the honeycomb flow straightener. The maximum potential value for the shifting is roughly equivalent to the span of the rotor speed fluctuation values (max to min). The new flowmeter design [7] incorporates tight tolerances and well-studied manufacturing process to eliminate or minimize the blade geometry distortions. Furthermore, the distance from the straightener vanes to the rotors has been increased, thus allowing for a decay of the wakes in the flow field. This is equivalent to a reduction in amplitude of the rotor speed fluctuation, and thus a significant reduction in the potential value for a shift in the K_f value.

CONCLUSIONS

The present study addressed the phenomenon known as calibration constant “shifting” observed during the operation of the Space Shuttle Main Engine fuel flowmeter. The calculations are based on a synergistic model, which assembles 3-D CFD results, blade aerodynamic C_D/C_L modeling and physical dynamics of the rotor. It has been found that due to the 12N symmetry of the flow field behind the hexagonal straightener, the flowmeter rotor always operates with a rotor speed fluctuating component, which—for a “to print” rotor geometry—is stable, periodic, and of small amplitude. Distortions in the blade geometry, which alter the blade stagger angle and introduce camber to the blade airfoil mean line, are found to amplify the fluctuations in rotor speed, and introduce a phase shift. A detailed explanation as to how these effects couple with effects due to flow turbulence and generate an apparent shift in the flowmeter indications has been provided. One should note that, while the model used in the calculations reflect the physics of the phenomenon in the best possible manner, it does not capture details related to the full three-dimensionality of the flow, the effects of the rotor’s presence on the flow and some details of speed sampling that were simplified for this study.

ACKNOWLEDGEMENTS

The author wishes to acknowledge the contributions of William Bowling-Jr for the innovative solid modeling of the rotor geometry, and error analysis for discrepant rotors. Mr. Bowling’s feed back and graphic data interpretation has been extremely helpful.

Special thanks to Dr. Edward D. Lynch for providing the CFD flow field data behind the hexagonal straightener, and for the interesting discussions regarding the flow regimes and instabilities past the rotor blades.

This work was made possible through the wonderful support of the SSME management team, Gary E. Gilmartin, Henry Loureiro, and John Ubowski. Their determination towards the research and understanding of the problem addressed are fully appreciated.

REFERENCES

1. Fenwick, J.R., “Discussion of the SSME Fuel Flowmeter Anomaly”, Rocketdyne Internal Report, October 13, 1993.
2. Fox, T.H., “Possible Mechanism for Flowmeter Oscillations Seen on STS-8”, Marshall Space Flight Center Letter, April 9, 1984
3. L. K. Sharma, “Fuel Flowmeter Problem: Drop in Calibration Constant with Power Level”, Rocketdyne Internal Report, May 13, 1988.
4. Ascoli, E. et. al. “Application of CFD to Explain Stall Behavior of the SSME Flowmeter”, AIAA paper 99-2458, presented at the 35th AIAA/ASME/SAE/ASEE Joint Propulsion Conference and Exhibit.
5. Hadid, A. “Transient CFD Analysis of the SSME Fuel Flowmeter Anomaly” Rocketdyne Internal Report, May 5, 1998.
6. J.T. France, “The Measurement of Fuel Flow”, AGARD Flight Test Instrumentation Series, Volume 3, NATO publication, 1972.
7. Marcu, B., “Rotor Design for the SSME Fuel Flowmeter”, TWAFS 1999, NASA Marshall, Huntsville, Alabama.
8. Schlichting, H. “Boundary Layer Theory”, McGraw Hill, 1979
9. Abbot, I.H. and von Doenhoff, A. E., “Theory of Wing Sections”, Dover, 1949.

INTERFACING SINDA/FLUINT WITH ROCETS

Barbara A. Sakowski

National Aeronautics and Space Administration
Glenn Research Center
Cleveland, Ohio 44135

ABSTRACT

A complete thermal and fluid systems analysis for a Rocket-Based Combined Cycle (RBCC) type vehicle would optimally link the cycle analysis of the vehicle with the thermal and fluid systems analysis of the vehicle. Furthermore it would be advantageous if the cycle analysis could be dynamically linked to the thermal and fluids systems analysis. This would avoid the repetitive and tedious process of manually inputting the results of the cycle analysis as boundary conditions in the thermal and fluids systems analysis, and subsequently inputting those results as boundary conditions in the cycle analysis until a converged solution is achieved. The goal of this paper is to illustrate such an interface between the ROCKET Engine Transient Simulator (ROCETS), a cycle analysis code, and a thermal and fluid systems analysis code, SINDA/FLUINT.

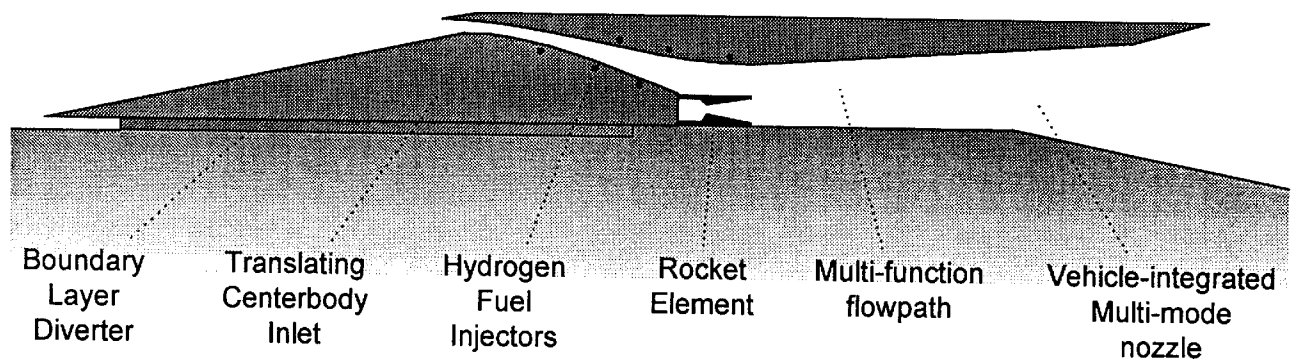
INTRODUCTION

The reasoning behind choosing ROCETS for the cycle analysis code and SINDA/FLUINT for the thermal and fluids system analysis code is simultaneously multi-faceted and quite simple. ROCETS is unique in that it enables the user to input “modules” representing various components of the vehicle’s system. In the case of an RBCC-type vehicle, the user can input tailor made subroutines representing the inlet, rocket, combustor, mixer, and or nozzle. ROCETS runs these subroutines in a user defined order and performs any system balances that are required. SINDA/FLUINT is an extremely versatile thermal and fluid systems analysis code that has many features to model the active and passive cooling systems of an RBCC-type vehicle. Such features include the ability to model multiphase flow and heat transfer, and turbines and pumps. One of the main advantages in using SINDA/FLUINT is that it can easily incorporate user-defined subroutines. In this case the user-defined subroutine would be ROCETS. Finally, the simple reason for using the respective codes ROCETS and SINDA/FLUINT is that they are available and more or less ready to use.

This paper will describe the challenges in interfacing ROCETS and SINDA/FLUINT, and the process through which they communicate. In discussing these points, it is assumed the reader has a rudimentary working knowledge of ROCETS and SINDA/FLUINT.

ROCETS PROCESS DESCRIPTION

There are five modules implemented in the ROCETS code that describe the cycle analysis for an RBCC-type vehicle. They represent the inlet, rocket, combustor, mixer, and nozzle. A depiction of such a vehicle with these components is shown in Figure 1. The hierarchy in which the respective modules are called is illustrated in Figure 2. The various modes of the vehicle’s operation are outlined in Table 1.



Four operating modes from lift-off to orbit:

- 1) Ejector-Ramjet**
- 2) Subsonic combustion ramjet**
- 3) Supersonic combustion ramjet**
- 4) High area-ratio rocket**

Figure 1. RBCC-Type Vehicle

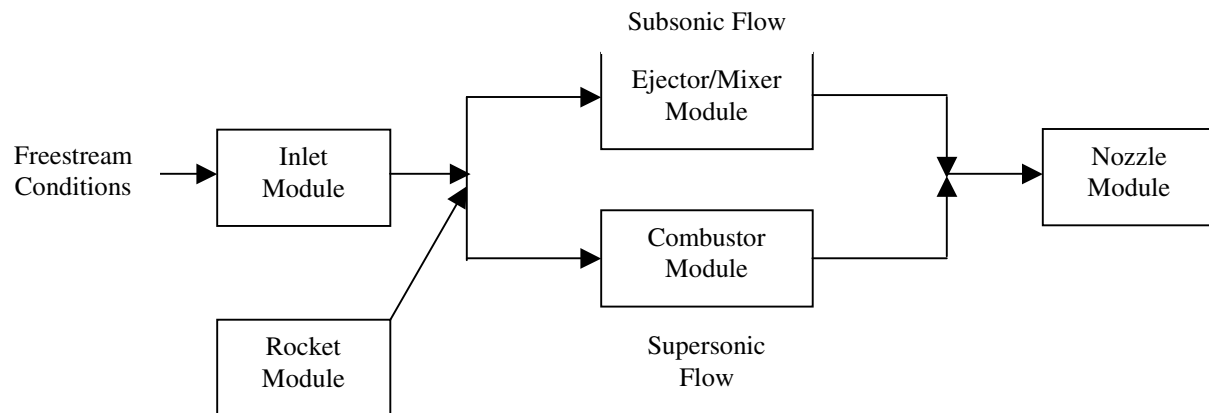


Figure 2. ROCETS Cycle Layout

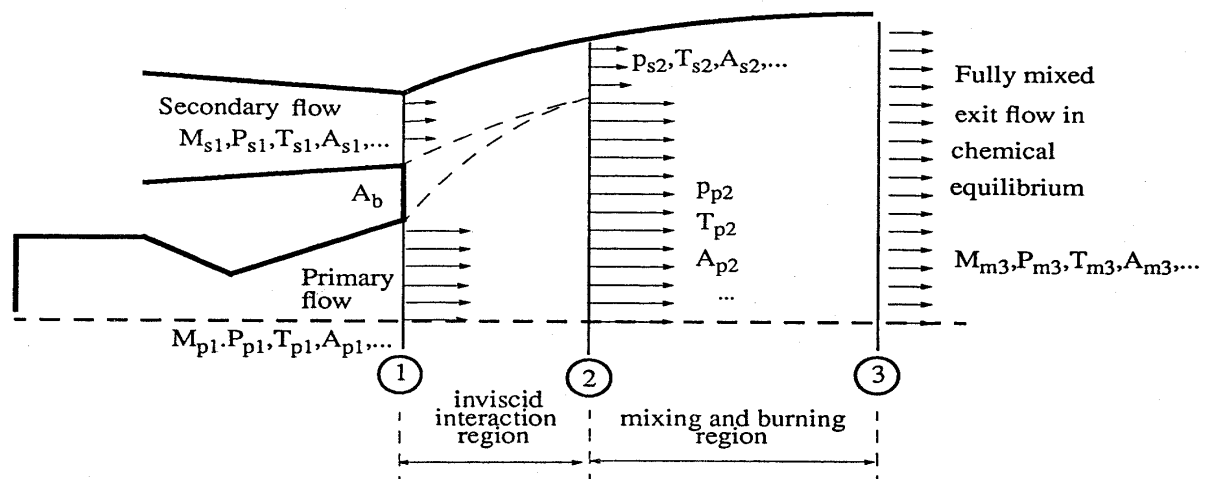
	Mach Number	Inlet	Ejector/Mixer	Combustor	Rocket	Nozzle
Mode 1	0.0 – 2.5	ON	ON	OFF	ON	ON
Mode 2-3	2.5 – 12.0	ON	OFF	ON	OFF	ON
Mode 4	12.0 – 25.0	OFF	OFF	OFF	ON	ON

Table 1. Vehicle Modes of Operation

The inlet module uses the LARge Perturbation INlet (LAPIN) code. LAPIN is a one dimensional transient inlet code that can model both supersonic and subsonic freestream and outlet conditions. Its many versatile modeling abilities include moving shocks, bleeds and bypasses, and rotating and translating centerbodies. LAPIN is modified for use in ROCETS to accommodate the modeling of RBCC-type vehicles specifically in the hypersonic regime. Normally the user inputs a constant value of γ (ratio of specific heats) into LAPIN and obtains a solution based on that constant value of γ . However when LAPIN is used in ROCETS, a constant value of γ is still employed, but it is an average value for the inlet calculated from the flow properties. Flow properties are determined by the Chemical Equilibrium Code (CSDTTP). On the first pass through the inlet a “guessed” value of γ is used to obtain a solution. From this solution an average value of γ is recalculated based on the flow properties. This value of γ is then used as the new “guessed” value of γ for the inlet whereupon a new solution is obtained. This iterative process is continued until γ no longer changes. The second modification made to LAPIN for use in ROCETS for RBCC-type vehicles is to accommodate non-axisymmetric area distributions through inlets. LAPIN normally can model two-dimensional and axisymmetric flows. Area modification factors are incorporated into the axisymmetric area terms. These factors are based on the “real” area distribution through the inlet.

The rocket module uses the Chemical Equilibrium Code (CSDTTP) to model the rocket component of the vehicle. The rocket module can model the rocket component as “one-dimensional” by discretizing the domain as a function of area ratio. This allows for greater refinement in calculating heat transfer coefficients through the rocket.

The combustor and ejector/mixer modules also use the Chemical Equilibrium Code (CSDTTP). Unfortunately they cannot simulate any “one-dimensionality”, so to speak, only a single thermodynamic state. This leads to a poor resolution of heat transfer distribution in that region of the vehicle. According to Table 1. The combustor does not operate when the rocket is “on”. The ejector/mixer does operate when the rocket is “on”. A schematic of the mixer is shown in Figure 3. The secondary flow from the inlet (station 1) mixes with the primary flow from the rocket (station 1).



$M = \text{Mach Number}, P = \text{Pressure}, T = \text{Temperature}, A = \text{Area}$

Subscripts: p = primary flow, s = secondary flow, m = mixed flow

Figure 3. Schematic of Ejector/Mixer

Finally, the nozzle module uses the Chemical Equilibrium Code (CSDTTP) to model this vehicle component. This model can also be made “one-dimensional” by discretizing the domain as a function of area ratio.

ROCETS fullest capabilities are utilized for subsonic freestream conditions (mode 1). In this mode ROCETS performs a mass flow balance between the inlet and the ejector/mixer. At the start of the run, an initial guess on either the exit mach number or exit pressure of the inlet is input by the user. The inlet module (LAPIN) calculates a mass flow rate based on one of these exit boundary conditions. This calculated mass flow rate value as well as the exit boundary condition of pressure or Mach number is sent to the ejector/mixer module as a “guess”. The ejector/mixer module then calculates a new mass flow rate so that the exit of the mixer is choked. ROCETS continues to perturb the inlet exit boundary condition of pressure or Mach number until the calculated values of mass flow from the inlet and ejector/mixer modules match.

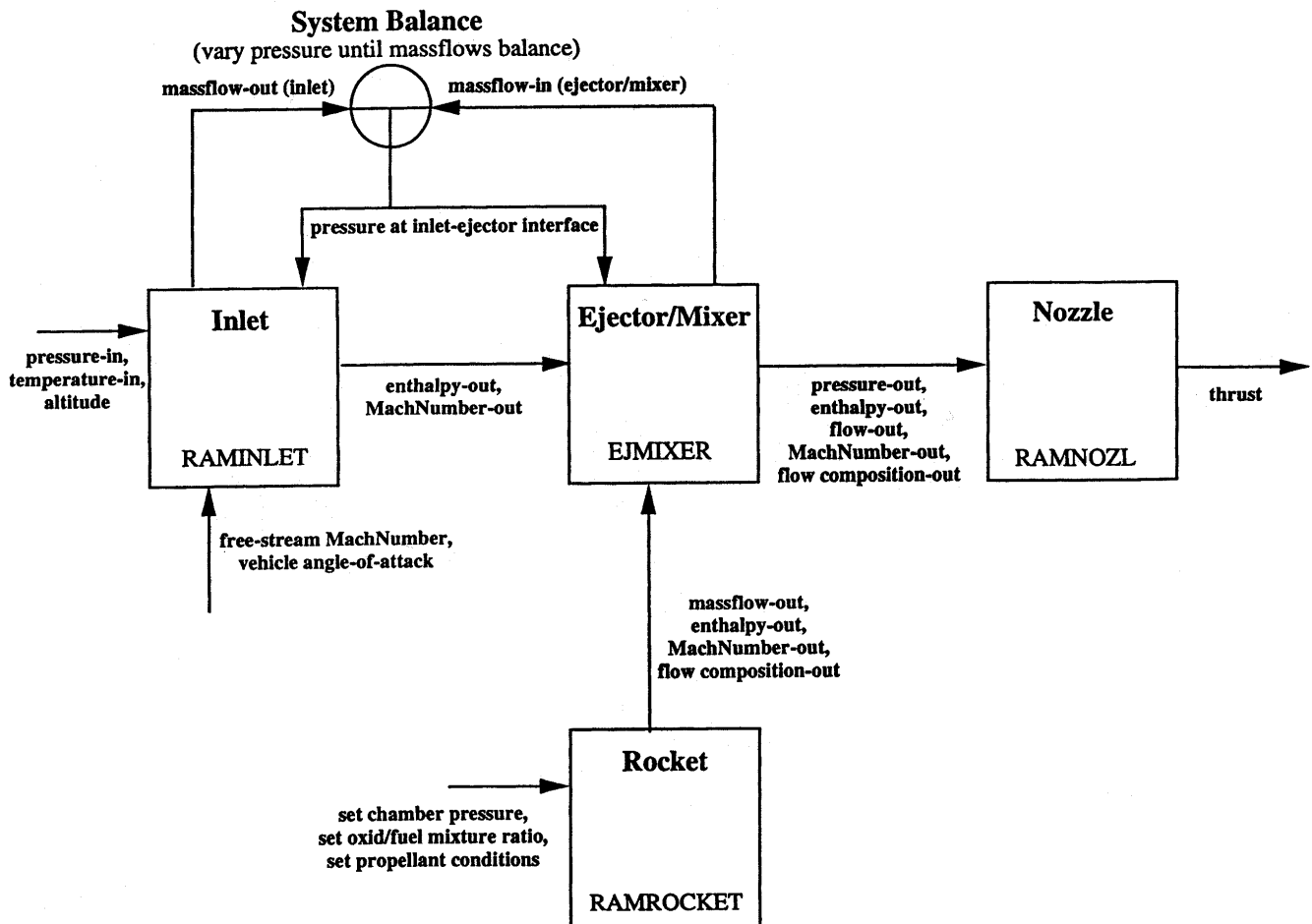


Figure 4. ROCETS System Configuration for Subsonic Freestream Conditions

For supersonic flow no such balancing is required, i.e., the combustor “accepts” the downstream conditions of the inlet and the combustion is supersonic.

SINDA/FLUINT

SINDA/FLUINT is used to model the active cooling system of the vehicle which also serves as the fuel feed system of the vehicle. The detailed components of the feed system such as the pumps and turbines have not been incorporated into the model yet. They will be incorporated in future models. The cooling fluid is hydrogen and properties are generated for SINDA/FLUINT using GASPLUS. Currently the mass flow rate of the cooling system set is set by the user. Future models will determine an optimal flow rate through the system to yield an appropriate power balance in the cycle analysis. Thus the SINDA/FLUINT model of the cooling system to date is a one dimensional model represented by a bundle of tubes with the hydrogen flowing through it. These tubes pass over each of the components (i.e., inlet, rocket, combustor, ejector/mixer, nozzle) of the vehicle. Heat conduction through the vehicle “walls” is also modeled

HEAT TRANSFER

Heat rates are calculated in each of the component modules of ROCETS using wall temperatures from SINDA/FLUINT. The heat transfer coefficient, H_c , is calculated in the inlet, mixer/combustor, and nozzle modules using the Colburn Equation:

$$H_c = Nud * K \quad (1)$$

where the Nusselt number is defined by:

$$Nud = 0.023 * Re^{.8} * Pr^{.34} \quad (2)$$

The heat transfer coefficient, H_c , is calculated in the rocket module using the Bartz Equation:

$$H_c = 0.026 * (W/A)^{.8} * (Ts/Tam)^{.8} * K^{.6} / D^{.2} * (Cp/Mu)^{.4} * (D/Rc)^{.1} \quad (3)$$

where the Stanton number is defined by:

$$St = Stthrt * (D/Rc)^{.1} * Ar^{.9} * (Ts/Tam)^{.8} \quad (4)$$

or

$$H_c = St * W/A * Cp \quad (5)$$

given that

W = Mass Flow Rate

T_s = Static Temperature

T_{wall} = Wall Temperature

T_{am} = Arithmetic Mean Film Temperature: $(T_s + T_{wall})/2.0$

$(T_s/T_{am})^{.8}$ = Property Correction

K = Conductivity

C_p = Specific Heat

Mu	= Viscosity
Re	= Reynolds Number
Pr	= Prandtl Number
Stthrt	= Stanton Number at the Throat: ($0.026 \cdot Re^{-.2} \cdot Pr^{-.6}$)
D	= Hydraulic Diameter
Rc	= Radius of Curvature
A	= Cross Sectional Area
Ar	= Cross Sectional Area / Throat Cross Sectional Area
$(D/Rc)^{.1} \cdot Ar^{-.9}$ = Corrects from Throat to Local Geometry	

Calculated heat rates are imposed on the SINDA/FLUINT “wall” nodes. SINDA/FLUINT then calculates new wall temperatures which are passed back to the respective ROCETS subroutines. This process continues until SINDA/FLUINT meets convergence criteria for changes in energy and temperature.

RESULTS

The hierarchical structure of the interface between ROCETS and SINDA/FLUINT places ROCETS as a subroutine to SINDA/FLUINT. This is the easiest methodology because of the input file structure of SINDA/FLUINT. The main calling subroutine of ROCETS is called from the OPERATIONS BLOCK of SINDA/FLUINT. A steady-state flow field is first established in ROCETS. Heat rates are calculated based on guessed “wall” temperatures. Then SINDA/FLUINT performs a steady-state analysis on the cooling/feed system with the given heat rates. At the beginning of every iteration in the SINDA/FLUINT analysis, the heat rates on the “wall” are updated by calls to the heat transfer subroutines. The heat rates are continually updated until SINDA/FLUINT converges. Currently the model runs with no update to the initial steady-state flow calculation of the vehicle so as to obtain results in a faster run time. However each component module does have the ability to add heat to or subtract heat from the flow.

The main obstacle in interfacing such a large code, ROCETS, with all the accompanied subroutines representing the vehicle’s components, is the overlap of subroutine and common block names. It is helpful when the FORTRAN compiler flags an overlap in subroutine or common block names, otherwise, things will go very awry. Fortunately only a handful of subroutine and common block names need to be altered. Most of these changes are in the utility subroutines used to model the vehicle’s components in the cycle analysis. The only ROCETS specific subroutine that needs to be changed for use in SINDA/FLUINT is the subroutine (COMPRS).

Another annoyance in interfacing multiple codes is the duplication of unit numbers. No unit numbers are changed in the ROCETS subroutines interfaced with SINDA/FLUINT. However modifications were made to the unit numbers in the utility subroutines used to model the vehicle’s components in the cycle analysis.

To expedite the compilation of the SINDA/FLUINT input file, the entire ROCETS source code is placed in the SINDA/FLUINT library. Basically a new library is created containing the ROCETS source code and the SINDA/FLUINT library is appended to this new library. Only two subroutines from the ROCETS code are placed in the SINDA/FLUINT input file’s SUBROUTINE DATA BLOCK. These subroutines, which are created from the ROCETS preprocessor, are the initial guess file of values for the ROCETS run (GUESS), and the subroutine (ROCETS). The subroutine (ROCETS) sets up the unique cycle run determined by the ROCETS configuration file. Subroutine (GUESS) is left out of the SINDA/FLUINT library so that the user may change initial conditions as desired without having to recompile the SINDA/FLUINT library. The subroutine (ROCETS) changes with every

new configuration file so it is also advantageous to omit this file from the library. These two files are placed in the same working directory as the SINDA/FLUINT input file.

Another note about the ROCETS routines interfaced with SINDA/FLUINT. The ROCETS program has a set of preprocessing subroutines that process a configuration file which the user constructs. These subroutines are not interfaced with the SINDA/FLUINT library. The user must first, outside of the SINDA/FLUINT environment, run these subroutines to create the (ROCETS) and (GUESS) subroutines respectively. A modification to the subroutine (COPEN) is made so that the SIZES.INC file can be copied into the SINDA/FLUINT working directory and the ROCETS RUNIN directory. The SIZES.INC is not created by the ROCETS preprocessing source code but is set by the user as the maximum fixed size.

A final note on the passing of arguments between ROCETS modules. The original intent of ROCETS was to pass all variables through the argument lists of the subroutines. However with the interfacing of large modules to model the vehicle's components this turned out to be quite impossible. Common blocks are used to communicate between these large codes used to represent the inlet, rocket, combustor, ejector/mixer, and nozzle. They are also used in the various property calculation subroutines. Otherwise the argument lists for these modules would have ungodly sizes. Most of these variables would be undesirable and unnecessary system variables and cause the user a lot of stress to book-keep.

CONCLUSIONS

A dynamic interface was successfully created between ROCETS and SINDA/FLUINT to link the thermal and fluid systems analysis to the cycle analysis for a Rocket-Based Combined Cycle (RBCC) type vehicle. Future models will incorporate the use of Thermal Desktop to model the entire vehicle. This way the user can easily visualize the thermal loads on the entire vehicle from the cycle and thermal and fluid systems analysis. Furthermore, future models will also incorporate the pumping and turbomachinery in the fuel feed system, and will also determine an optimal flow rate through the fuel feed system to yield an appropriate power balance in the cycle analysis.

NUMERICAL MODELING OF DRYING RESIDUAL RP-1 IN ROCKET ENGINES

Alok Majumdar, Robert Polsgrove and Bruce Tiller

Thermodynamics and Heat Transfer Group
National Aeronautics and Space Administration
Marshall Space Flight Center
Huntsville, Alabama 35812-0001

Abstract

This paper describes a numerical model of evaporative heat and mass transfer of liquid RP-1 in a stream of inert gas such as nitrogen or helium. A heat and mass transfer model was created using the Generalized Fluid System Simulation Program (GFSSP). GFSSP solves for time dependent mass, momentum, energy and specie conservation equation in a flow network. The heat and mass transfer model was developed using one of GFSSP's three modules, the User Subroutine. This paper provides results to parametric studies performed using the GFSSP model, which show that nitrogen is a better dryer than helium, and drying rate increases with reduced supply pressure and increases with increasing supply temperature and flowrate.

Introduction

When a liquid rocket engine shuts down under a fuel rich environment, a significant amount of unburned fuel can be trapped in the engine. It is necessary to clean this residual fuel prior to subsequent engine firing to avoid any explosion due to detonation. The conventional method of drying a Kerosene (RP-1) fueled engine is to flow an inert gas such as nitrogen or helium through the engine. It is difficult, however, to estimate the time necessary to dry the engine unless the engine is adequately equipped with instruments to trace RP-1 during the drying process. Such instrumentation in flight hardware is often impractical and costly. On the other hand, numerical modeling of the drying process can provide a good insight for a satisfactory operation of the process. A numerical model can provide answer to questions such as a) how long it takes for the engine to dry, b) which fluid is a better dryer for RP-1, and c) how drying time can be reduced.

The purpose of this paper is to describe a numerical model that simulates the drying of RP-1 trapped in a cavity by flowing nitrogen or helium. The numerical model assumes a one-dimensional flow of the drying fluid in contact with a liquid pool of RP-1 (Figure 1). A simultaneous heat and mass transfer takes place across the contact surface. The task was to find the rate of mass transfer of RP-1 into a nitrogen stream for a given pressure, temperature and flowrate, with simultaneous heat transfer between the RP-1 and nitrogen. It was also assumed that mass transfer between the liquid and gas occurs through a thin film separating two streams. The temperature of this film at the interface of the two streams was assumed to be equal to the liquid temperature.

Governing Equations

The equations governing the mass transfer of liquid to a gaseous stream can be expressed as¹:

Mass Transfer Rate, W_A (lb-mol/sec)

$$W_A = k_{xm} A \frac{x_{A0} - x_{A\infty}}{1 - x_{A0}} \quad (1)$$

Where x_{A0} is the mole fraction of vapor of the saturated film near the liquid surface and $x_{A\infty}$ is the mole fraction of vapor in the gaseous stream. A is the surface area of the liquid-vapor interface, and k_{xm} is the mass transfer coefficient, given by:

Mass Transfer Coefficient, k_{xm} (lb-mol/ft²-sec)

$$\frac{k_{xm}L}{\rho_{mol}D_{AB}} = 2.0 + 0.60 \left(\frac{\rho_f v_{\infty} L}{\mu_f} \right)^{0.5} \left(\frac{\mu_f}{\rho_f D_{AB}} \right)^{0.33} \quad (2)$$

L is a characteristic length scale, and ρ_f and μ_f are density and viscosity of vapor at film temperature, respectively. The molar density of the stream is denoted ρ_{mol} , and the freestream velocity of gas near the liquid surface is denoted v_{∞} . The diffusivity between liquid and gas, D_{AB} , is given by:

Mass Diffusivity, D_{AB} (ft²/sec)

$$\frac{pD_{AB}}{\left(p_{cA} p_{cB} \right)^{1/3} \left(T_{cA} T_{cB} \right)^{5/12} \left[\frac{1}{M_A} + \frac{1}{M_B} \right]^{0.5}} = a \left(\frac{T}{\sqrt{T_{cA} T_{cB}}} \right)^b \quad (3)$$

The subscripts a and b refer to liquid and gas, respectively. The subscript c refers to the critical point, and p and T are pressure and temperature respectively.

The mass transfer process represented by Equations 1 through 3 is temperature dependent. Therefore, heat transfer between liquid RP-1 and an inert stream must be considered to accurately predict the mass transfer process. The equations governing the heat transfer between a liquid and a gaseous stream can be expressed as:

Heat Transfer Rate, \dot{Q} (Btu/sec)

$$\dot{Q} = hA(T_{gas} - T_{liquid}) \quad (4)$$

h is the heat transfer coefficient. T_{gas} and T_{liquid} are temperatures of drying gas and liquid respectively.

Heat Transfer Coefficient, h (Btu/ft² °F sec)

$$\frac{hL}{k_{mix}} = 0.023 \left(\frac{\rho_{mix} v_{\infty} L}{\mu_{mix}} \right)^{0.8} \left(\frac{\mu_{mix}}{\rho_{mix} \alpha_{mix}} \right)^{0.4} \quad (5)$$

k_{mix} , ρ_{mix} , μ_{mix} and α_{mix} are thermal conductivity, density, viscosity and thermal diffusivity of gas and vapor mixture.

Equations 1 through 5 are solved in conjunction with conservation equations for mass, momentum, energy, and specie concentration. The conservation equations are described in the GFSSP User's Manual². Figure 2 shows a schematic representation of the numerical model of the drying process. The inputs to the model are supply pressure, temperature, and geometry. The required outputs are drying rate, flowrate, and chamber pressure, temperature, and concentrations. GFSSP solves mass, momentum, energy and specie conservation equations in conjunction with the above heat and mass transfer equations to generate the required outputs. The GFSSP User Subroutines module provides the heat and mass transfer model.

GFSSP Model

A simple transient GFSSP (Generalized Fluid System Simulation Program²) model was constructed to estimate the evaporative mass transfer rate of RP-1 using nitrogen and helium as the drying fluid. The model is shown in Figure 3. The Figure shows that nitrogen is flowing through a duct and is in contact with RP-1 stored in a cavity. Nodes 1 and 3 are boundary nodes where pressure and temperature are specified. Nodes 2 and 5 are internal nodes where all scalar properties such as pressure, temperature and concentrations are calculated. Node 5 is an internal node that contains RP-1 of known initial mass, volume and temperature.

The GFSSP process flow diagram is shown in Figure 4. The code consists of three major modules: 1) Preprocessor, 2) Solver and Property Program, and 3) User Subroutines. The Preprocessor module aids the user in creating the input data file. GFSSP has two preprocessors, namely, command line and visual. The second module, the Solver and Property Program, generates and solves all pertinent equations with the help of fluid property routines. Finally, the User Subroutines module is a set of blank subroutines called by the solver module that allows the user to add or modify the governing equations according to their need. The developed User Subroutine is then compiled and linked with the solver module to create a customized executable file. The heat and mass transfer model described in equations 1 through 5 was implemented in the User Subroutine module of GFSSP. The User Subroutine capability of GFSSP is an effective way of incorporating a new physical model into the code.

Results

Several cases were run to study the effect of various parameters on drying time. The results of the parametric study are shown in Table 1. The parametric study was designed to determine the effect that supply temperature, pressure, flowrate, and fluid has on drying time. Cavity volume and surface area of heat and mass transfer were kept constant (shown in Figure 3) in all cases. The transient nature of the problem is due to heat transfer. Initially, there is a temperature difference between RP-1 and supply gas. As the temperature difference decreases, the problem becomes steady state. The mass transfer rate becomes constant and drying time is estimated from residual mass in the cavity. Figure 5 shows temperature variation of nitrogen and RP-1 for Case 1 during transient operation. It can be noted from the figure that transient operation exists only for 90 seconds, whereas it takes about 2 hours to completely dry the cavity. The mass transfer, seen in Figure 6, is a slow process. The steady state mass transfer rate is less than 10^{-5} lbm/sec.

The effect of supply temperature on drying time is shown in Figure 7. As expected, drying time reduces with an increase in supply temperature. By increasing temperature from 75 to 125 °F, drying time can be reduced by half. Using helium instead of nitrogen as the drying fluid, drying takes approximately six times longer. The drying time is related to the mass transfer coefficient, listed in Table 1. It may be noted that the mass transfer coefficient for helium is an order of magnitude lower than nitrogen.

The effect of supply pressure on drying time is shown in Figure 8. Drying time is found to increase with an increase in pressure. Helium, once again, is a less efficient dryer than nitrogen. Molar concentration of RP-1 in the fluid film is less at higher pressure than at lower pressure. The reduced driving potential of

mass transfer is the cause of increase in drying time. Even a higher mass transfer coefficient (Table 1) does not compensate for reduction in the concentration gradient.

The effect of flowrate on drying rate is shown in Figure 9. As expected, drying time reduces with an increased flowrate. After a certain flowrate is reached, though, it appears that drying time asymptotically converges to a constant value and becomes independent of flowrate.

Conclusions

A simultaneous heat and mass transfer model of drying liquid propellant with inert gas was developed using GFSSP's User Subroutines module. Results indicate that a) nitrogen is a better dryer of RP-1 than helium, and b) drying rate significantly decreases with supply pressure and increases with supply temperature and flowrates.

References

1. "Transport Phenomenon" Bird, R. B., Stewart, W. E. and Lightfoot, E. N., John Wiley & Sons, 1960.
2. "Generalized Fluid System Simulation Program (GFSSP) Version 3.0" Alok Majumdar, Sverdrup Technology Report No. MG-99-290, Marshall Space Flight Center Contract NAS 8-40836, November 1999.

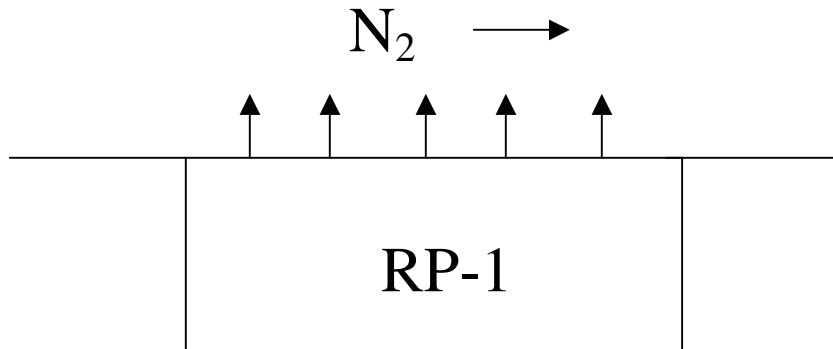


Figure 1: Drying of liquid RP-1 by gaseous Nitrogen

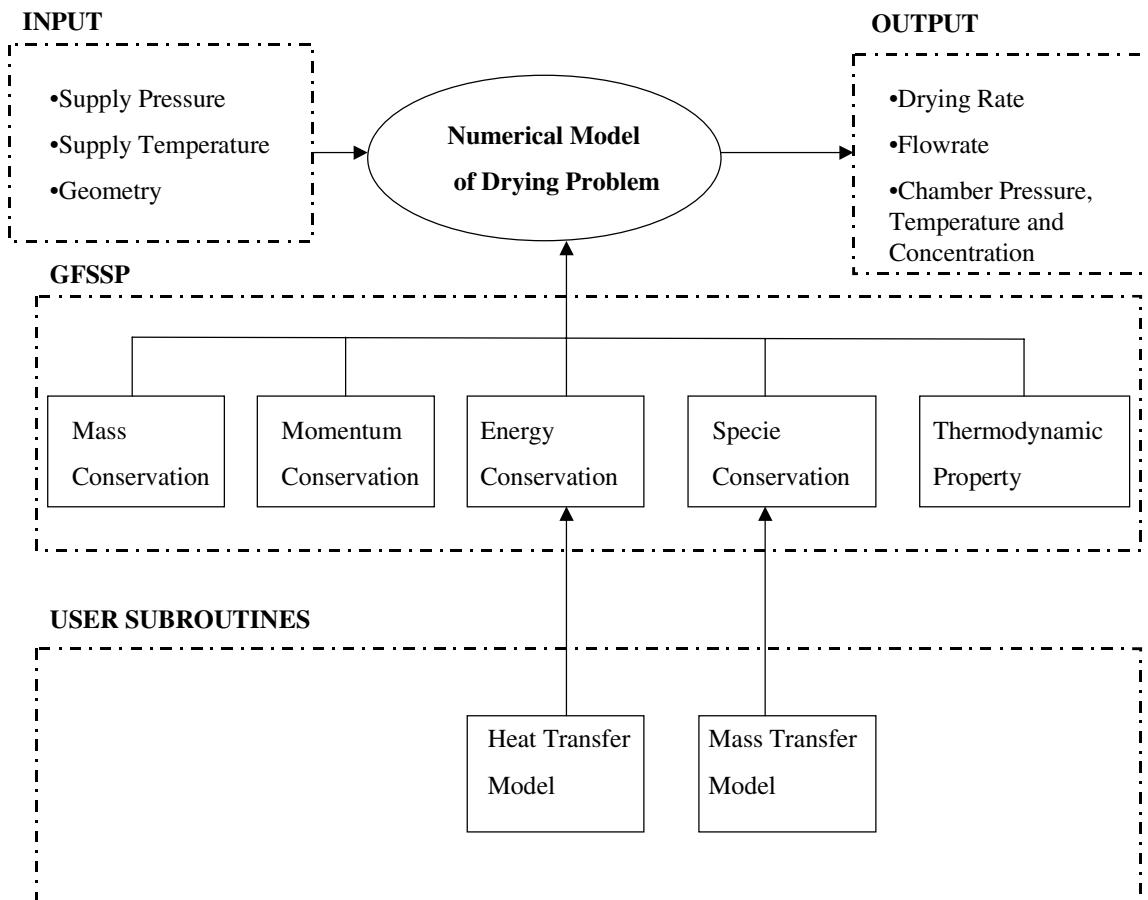
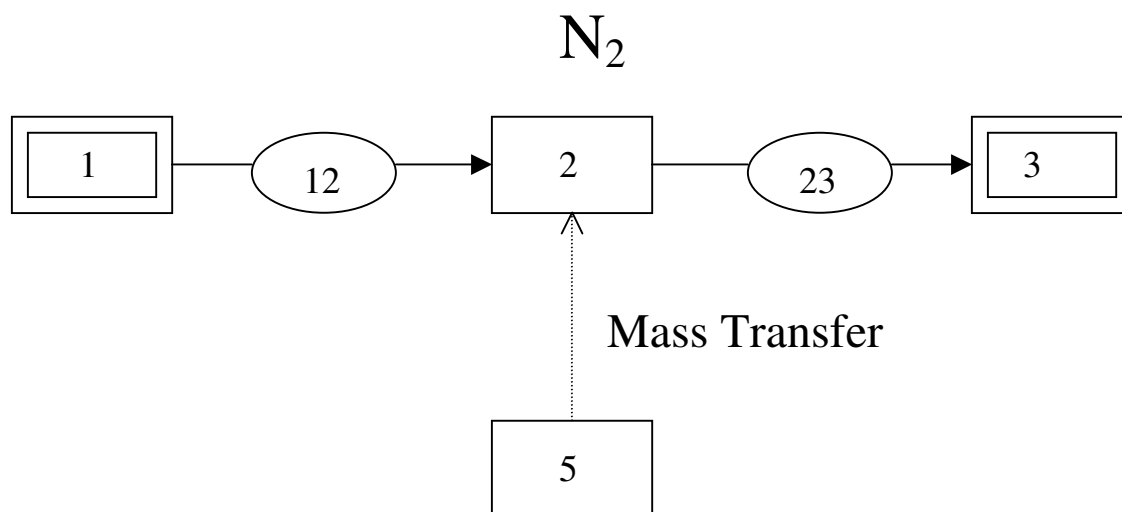


Figure 2: Schematic of the Numerical Model showing interaction of input/output with Governing Equations



RP-1

M = 0.0745 lbm; V = 2.5 in³; A = 5 in²; T = 60 ° F

Figure 3: GFSSP Model of mass transfer

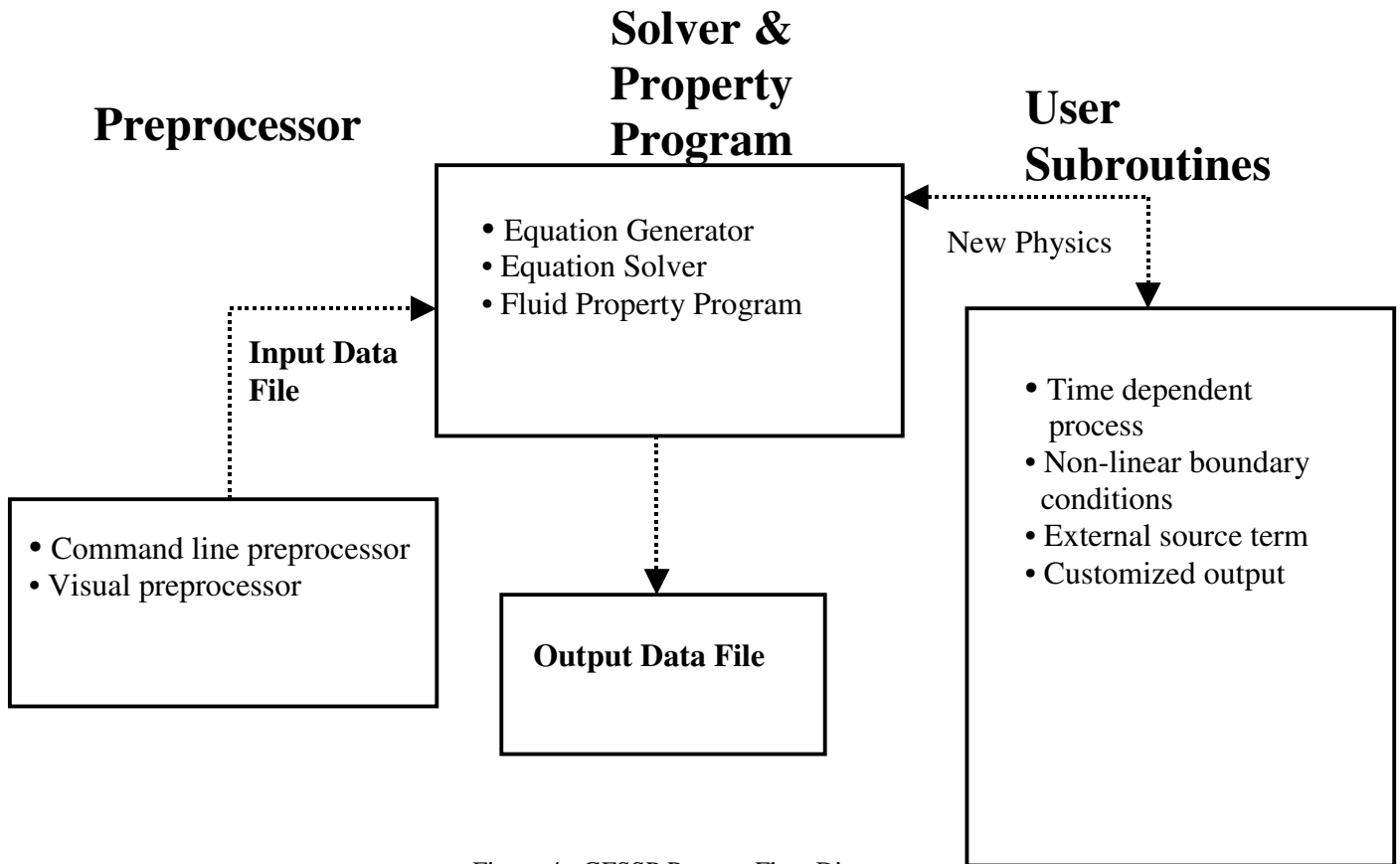


Figure 4: GFSSP Process Flow Diagram

Case No.	Drying Fluid	Supply Pressure (psia)	Exit Pressure (psia)	Supply Temperature (°F)	Initial RP-1 Temp (°F)	Flowrate (lbm/sec)	Heat Tr. Coeff Btu/ft ² sec °F	Mass Tr. Coeff x 10 ⁴ Lbmol/ft ² sec	Drying Time (Hr)
1	Nitrogen	2.5	20	100	60	0.117	0.0328	1.185	2.101
2	Nitrogen	2.5	20	100	75	0.117	0.0328	1.185	2.081
3	Nitrogen	2.5	20	100	90	0.117	0.0328	1.185	2.06
4	Nitrogen	2.5	20	75	90	0.120	0.0331	1.179	2.759
5	Nitrogen	2.5	20	125	90	0.114	0.0323	1.191	1.432
6	Nitrogen	2.5	22	100	90	0.089	0.0273	1.084	2.251
7	Nitrogen	2.5	24	100	90	0.0489	0.0174	0.084	2.898
8	Nitrogen	5.5	50	100	90	0.183	0.0492	1.581	3.420
9	Nitrogen	10.5	100	100	90	0.263	0.0668	1.941	5.341
10	Helium	2.5	20	100	90	0.039	0.0721	0.183	13.32
11	Helium	2.5	20	75	90	0.040	0.0734	0.182	17.93
12	Helium	2.5	20	125	90	0.038	0.0709	0.184	9.269
13	Helium	5.5	50	100	90	0.062	0.1084	0.244	22.13
14	Helium	10.5	100	100	90	0.088	0.1476	0.300	34.31
15	Helium	2.5	22	100	90	0.0297	0.0598	0.167	14.59
16	Helium	2.5	24	100	90	0.0162	0.0379	0.129	18.79

Table 1: Results of Parametric Study

Supply Pressure = 25 psia
Supply Temperature = 100 F

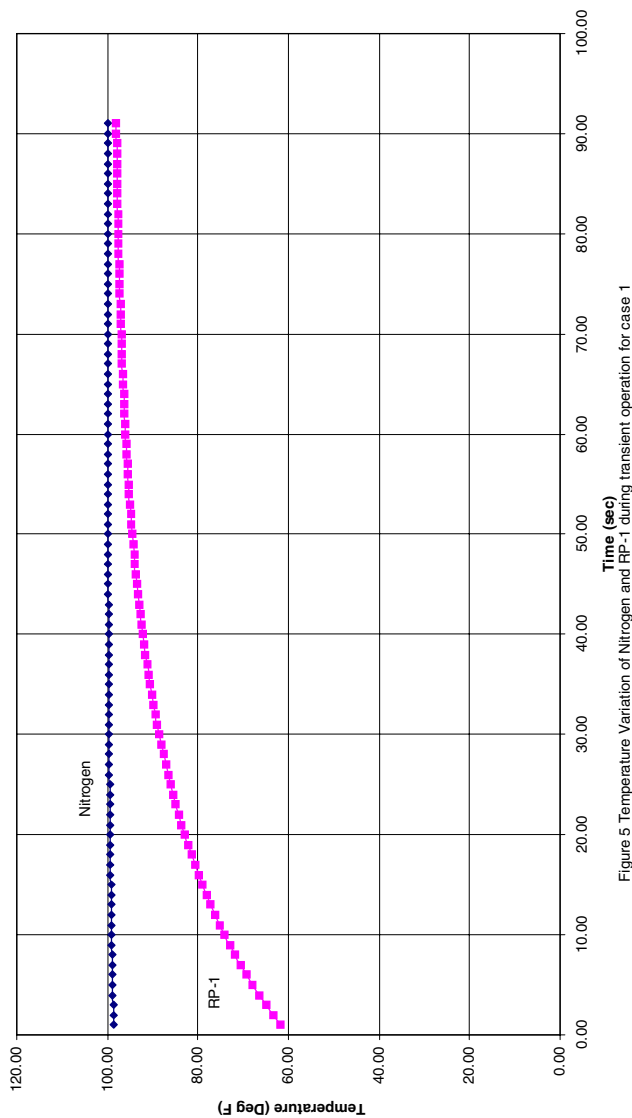


Figure 5 Temperature Variation of Nitrogen and RP-1 during transient operation for case 1

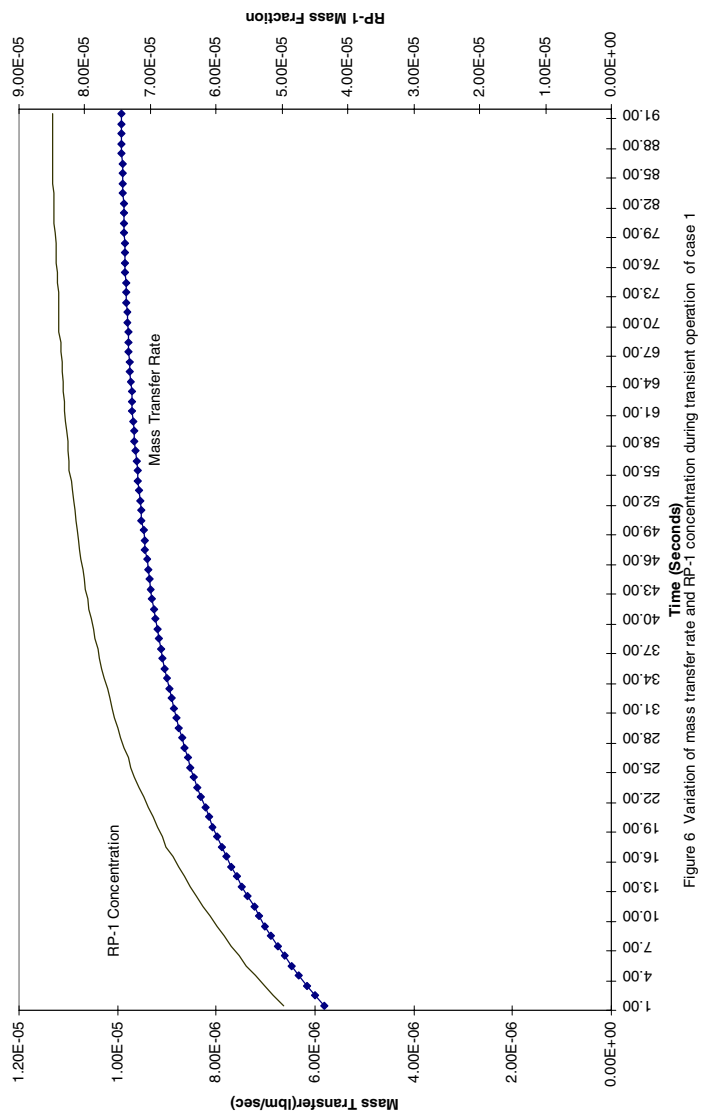


Figure 6 Variation of mass transfer rate and RP-1 concentration during transient operation of case 1

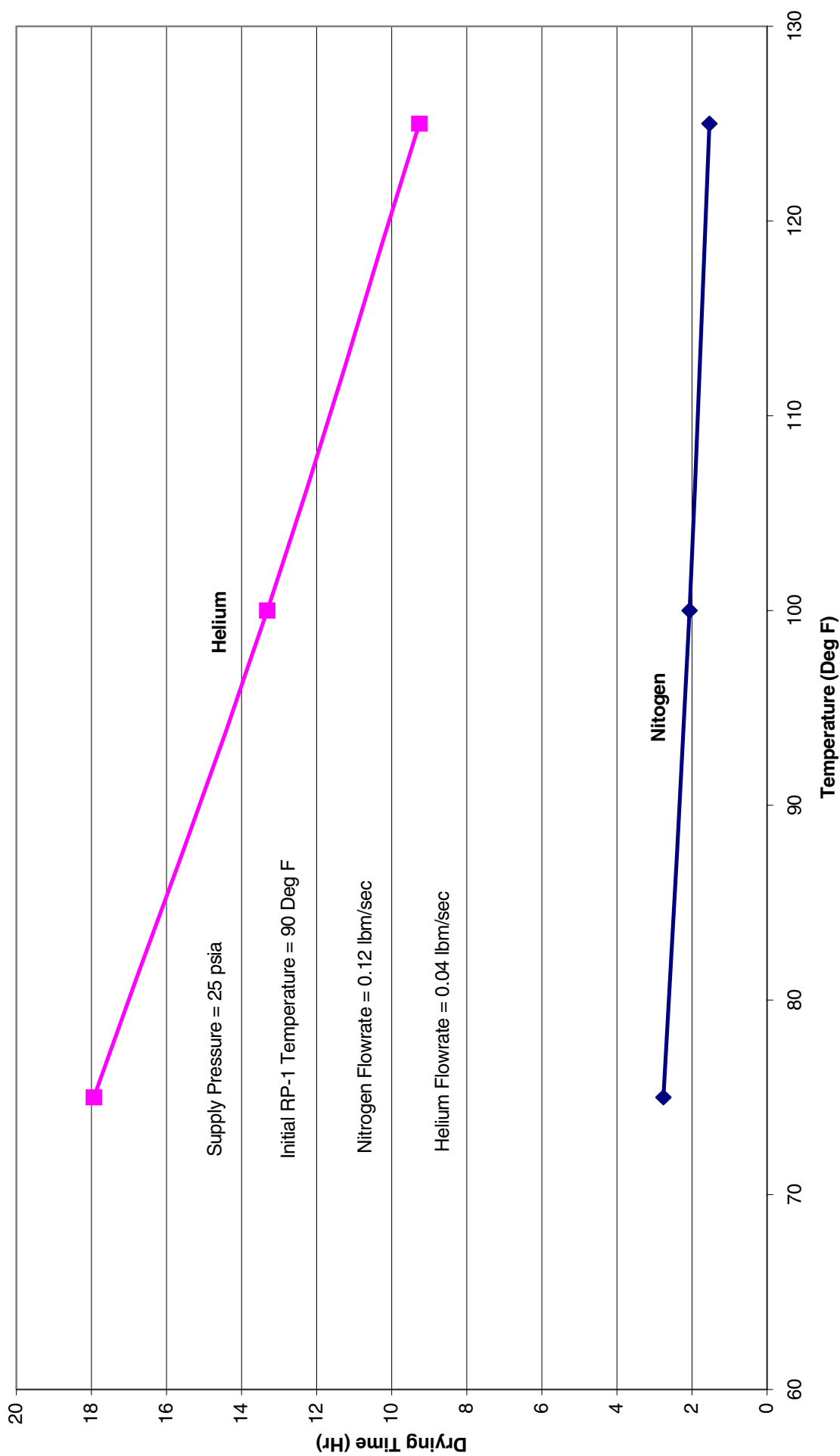


Figure 7. Effect of Supply Temperature on Drying Rate

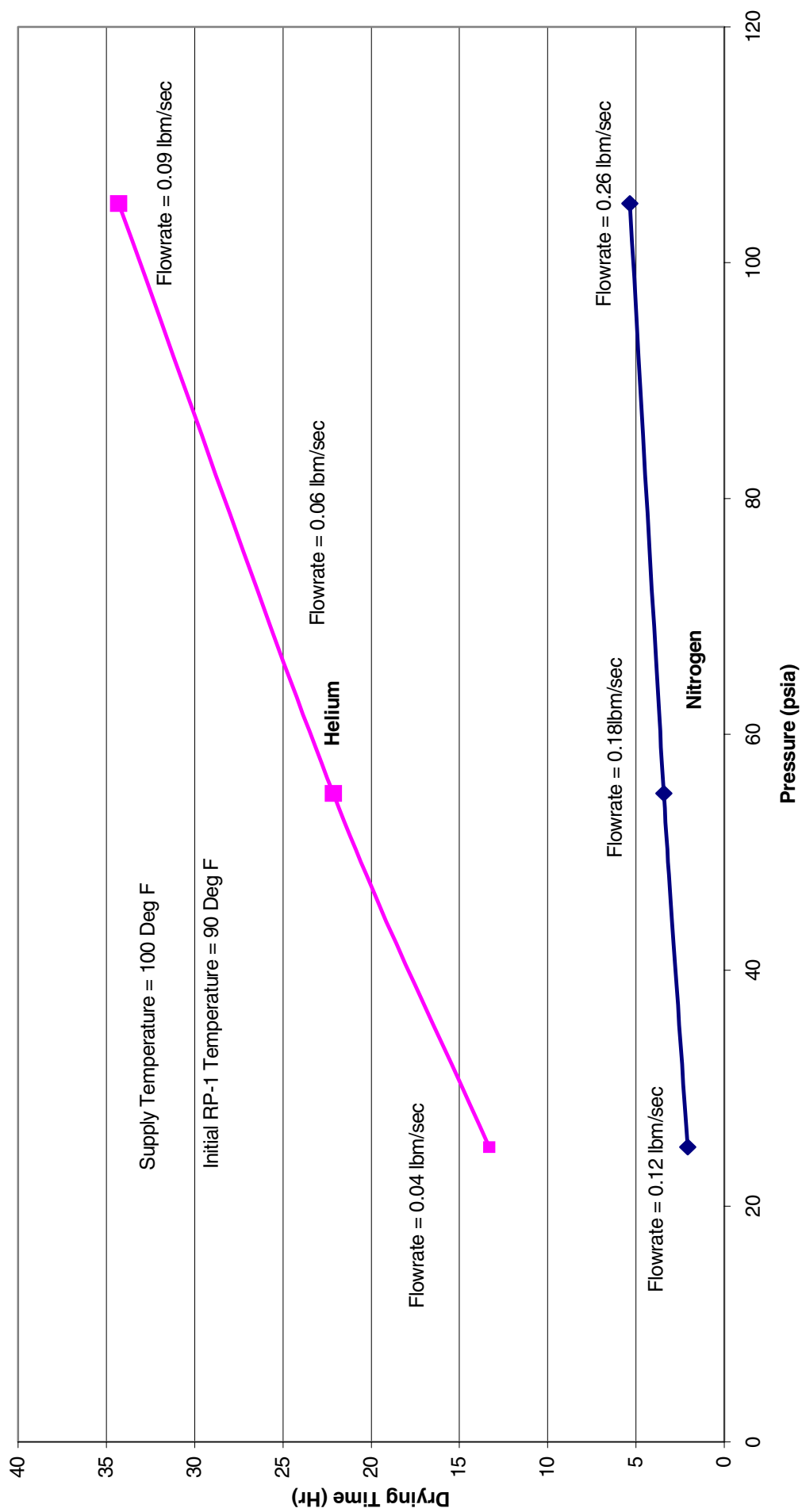


Figure 8. Effect of Supply Pressure on Drying Rate

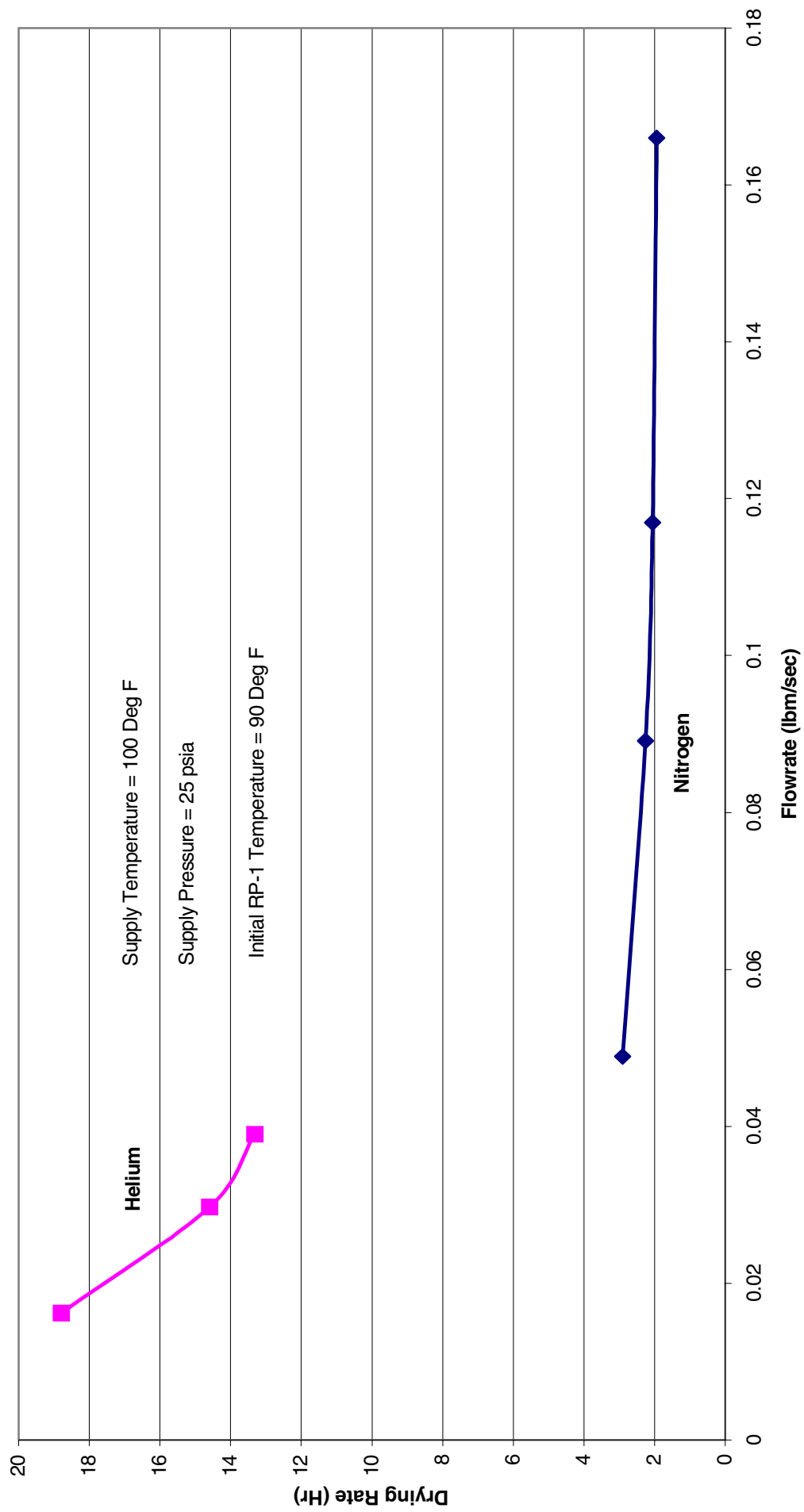


Figure 9. Effect of Flowrate on Drying Rate

REPORT DOCUMENTATION PAGE			Form Approved OMB No. 0704-0188	
Public reporting burden for this collection of information is estimated to average 1 hour per response, including the time for reviewing instructions, searching existing data sources, gathering and maintaining the data needed, and completing and reviewing the collection of information. Send comments regarding this burden estimate or any other aspect of this collection of information, including suggestions for reducing this burden, to Washington Headquarters Services, Directorate for Information Operations and Reports, 1215 Jefferson Davis Highway, Suite 1204, Arlington, VA 22202-4302, and to the Office of Management and Budget, Paperwork Reduction Project (0704-0188), Washington, DC 20503.				
1. AGENCY USE ONLY (Leave blank)		2. REPORT DATE July 2002		3. REPORT TYPE AND DATES COVERED Conference Publication
4. TITLE AND SUBTITLE Proceedings of the 11th Thermal and Fluids Analysis Workshop			5. FUNDING NUMBERS WU-940-30-09-21	
6. AUTHOR(S) Barbara Sakowski, compiler				
7. PERFORMING ORGANIZATION NAME(S) AND ADDRESS(ES) National Aeronautics and Space Administration John H. Glenn Research Center at Lewis Field Cleveland, Ohio 44135-3191			8. PERFORMING ORGANIZATION REPORT NUMBER E-13254	
9. SPONSORING/MONITORING AGENCY NAME(S) AND ADDRESS(ES) National Aeronautics and Space Administration Washington, DC 20546-0001			10. SPONSORING/MONITORING AGENCY REPORT NUMBER NASA CP-2002-211486	
11. SUPPLEMENTARY NOTES Responsible person, Barbara Sakowski, organization code 7730, 216-433-8725.				
12a. DISTRIBUTION/AVAILABILITY STATEMENT Unclassified - Unlimited Subject Categories: 07, 18, 34 and 20 Available electronically at http://gltrs.grc.nasa.gov/GLTRS This publication is available from the NASA Center for AeroSpace Information, 301-621-0390.			12b. DISTRIBUTION CODE	
13. ABSTRACT (Maximum 200 words) The Eleventh Thermal & Fluids Analysis WorkShop (TFAWS 2000) was held the week of August 21-25 at The Forum in downtown Cleveland. This year's annual event focused on building stronger links between research community and the engineering design/application world and celebrated the theme "Bridging the Gap Between Research and Design". Dr. Simon Ostrach delivered the keynote address "Research for Design (R4D)" and encouraged a more deliberate approach to performing research with near-term engineering design applications in mind. Over 100 persons attended TFAWS 2000, including participants from five different countries. This year's conference devoted a full-day seminar to the discussion of analysis and design tools associated with aeropropulsion research at the Glenn Research Center. As in previous years, the workshop also included hands-on instruction in state-of-the-art analysis tools, paper sessions on selected topics, short courses and application software demonstrations. TFAWS 2000 was co-hosted by the Thermal/Fluids Systems Design and Analysis Branch of NASA GRC and by the Ohio Aerospace Institute and was co-chaired by Barbara A. Sakowski and James R. Yuko. The annual NASA Delegates meeting is a standard component of TFAWS where the civil servants of the various centers represented discuss current and future events which affect the Community of Applied Thermal and Fluid Analysts (CATFANS). At this year's delegates meeting the following goals (among others) were set by the collective body of delegates participation of all Centers in the NASA material properties database (TPSX) update; developing and collaboratively supporting multi-center proposals; expanding the scope of TFAWS to include other federal laboratories; initiation of a white papers on thermal tools and standards; formation of an Agency-wide TFAWS steering committee.				
14. SUBJECT TERMS Computational fluid dynamics; CFD; Heat transfer; Thermal analysis; Concurrent engineering; TFAWS; STEP; Computational heat transfer; SINDA			15. NUMBER OF PAGES 289	
			16. PRICE CODE	
17. SECURITY CLASSIFICATION OF REPORT Unclassified	18. SECURITY CLASSIFICATION OF THIS PAGE Unclassified	19. SECURITY CLASSIFICATION OF ABSTRACT Unclassified	20. LIMITATION OF ABSTRACT	